Construction chemicals

Arnd Bernd Eberhardt

On the mechanisms of shrinkage reducing admixtures in self consolidating mortars and concretes

SHAKER
VERLAG

On the mechanisms of shrinkage reducing admixtures in self consolidating mortars and concretes

Dissertation zur Erlangung des akademischen Grades

Doktor Ingenieur

an der Fakultät Bauingenieurwesen
der
Bauhaus Universität Weimar

vorgelegt von
Arnd Bernd Eberhardt
aus
Saalfeld/Saale

Weimar 2010

Gutachter:

Prof. Dr.-Ing. habil. Jochen Stark (Weimar/D)
Prof. Dr. rer. nat. Dr.-Ing. habil. Max Setzer (Krailling/D)
Prof. Dr.-Ing. Horst-Michael Ludwig (Weimar/D)
Prof. Dr. ès. sc. Robert J. Flatt (Zürich/CH)

Tag der öffentlichen Disputation 02.02.2011

Berichte aus der Materialwissenschaft

Arnd Bernd Eberhardt

On the mechanisms of shrinkage reducing admixtures in self consolidating mortars and concretes

Shaker Verlag
Aachen 2011

Bibliographic information published by the Deutsche Nationalbibliothek
The Deutsche Nationalbibliothek lists this publication in the Deutsche Nationalbibliografie; detailed bibliographic data are available in the Internet at http://dnb.d-nb.de.

Zugl.: Weimar, BU, Diss., 2011

Printed in Germany.

ISBN 978-3-8440-0027-6
ISSN 1618-5722

Shaker Verlag GmbH • P.O. BOX 101818 • D-52018 Aachen
Phone: 0049/2407/9596-0 • Telefax: 0049/2407/9596-9
Internet: www.shaker.de • e-mail: info@shaker.de

Zusammenfassung zur Promotionsschrift

„Zur Wirkungsweise schwindreduzierender Zusatzmittel in selbstverdichtenden Mörteln und Betonen“

Problemstellung und Zielsetzung

1. Der Einsatz selbstverdichtender Mörtel und Betone im Bauwesen erbringt klare Vorteile. Dies sind im Wesentlichen eine erhöhte Betonierleistung, verbesserte Betonierqualität für bewehrten Beton im Allgemeinen und für filigrane, eng bewehrte Bauteile im Besonderen. Die mit den traditionellen Methoden des Betonbaus verbundenen Lärmemissionen werden erheblich reduziert. Der Wegfall der für herkömmlichen Beton notwendigen Verdichtungsarbeit reduziert den manuellen Aufwand und die damit verbundenen Gesundheitsrisiken.
   Das im selbstverdichtenden Beton benötigte hohe Bindemittelleimvolumen ist der Betondauerhaftigkeit abträglich. Es bewirkt, dass selbstverdichtende Betone ein erhöhtes Schwindmaß sowie eine höhere Rissneigung aufweisen. Ersteres kann für Betonbauteile zu erheblichen Verformungen oder Zwangsspannungen führen, während Letzteres die Dauerhaftigkeit des Baustoffes Beton aufgrund einer Begünstigung rissinduzierter Schädigungsmechanismen stark beeinträchtigt.
2. Herkömmliche Methoden zur Schwindreduktion und Rissvermeidung verfolgen hauptsächlich das Ziel, die im Beton einzusetzenden Bindemittelmengen zu reduzieren. Für selbstverdichtende Betone ist dieses Konzept nur sehr begrenzt anwendbar, da die Selbstverdichtung dieser Betone relativ hohe Bindemittelleimvolumen erfordert. Eine Möglichkeit das Ausmaß des Schwindens und damit die Rissanfälligkeit selbstverdichtender Betone zu senken, besteht in der Anwendung schwindreduzierender Betonzusatzmittel. Eingeführt in den achtziger Jahren des 20ten Jahrhunderts in Japan, erweisen sich diese Zusatzmittel als effiziente Methode zur Verbesserung der Qualität bindemittelreicher Hochleistungsbetone im Allgemeinen und selbstverdichtender Betone im Besonderen.
3. Während die Wirksamkeit schwindreduzierender Betonzusatzmittel in zahlreichen anwendungsorientierten Studien nachgewiesen werden konnte, ist das Wirkprinzip nur unzureichend erforscht. Eines der Hauptziele dieser Arbeit ist deshalb die gründliche Erforschung des Wirkmechanismus schwindreduzierender Betonzusatzmittel.
4. Weiterhin besteht Unklarheit, wie diese Zusätze in den Chemismus der Zementhydratation eingreifen und ob dies der allgemeinen Dauerhaftigkeit des Baustoffes Beton abträglich ist. Ein wichtiges Ziel dieser Arbeit ist deshalb die gründliche Erforschung der Zementhydratation in Gegenwart einer repräsentativen Auswahl verschiedener Typen schwindreduzierender Betonzusatzmittel.
5. Die Nachhaltigkeit der Anwendung schwindreduzierender Zusatzmittel ist bedeutend für die Betondauerhaftigkeit. Ob schwindreduzierende Zusatzmittel auslaugbar sind und ob eine Auslaugung die Schwindreduktion langfristig beeinträchtigt, sind weitere Fragen, denen im Rahmen dieser Arbeit nachgegangen wird.

Stand der Wissenschaft

6. Schwinden und Quellen von zementären Baustoffen wird im Allgemeinen mittels makroskopisch-thermodynamischer Ansätze beschrieben. Der stark vereinfachte Ansatz kapillaren Unterdrucks bzw. hydrostatischen Drucks als treibende Kraft für hygrische Verformungen wird weitgehend abgelehnt. Vielmehr wird im Bereich moderater Luftfeuchten der Spaltdruck und im Bereich niedriger Luftfeuchten die Oberflächenenergie zur Beschreibung der hygrischen Volumenstabilität herangezogen.

7. Schwindreduzierende Betonzusatzmittel bestehen überwiegend aus synergistischen Abmischungen nicht-ionischer Tenside mit Glykolen. Die amphiphilen Eigenschaften der nicht-ionischen Tenside führen zu einer Senkung der Oberflächenspannung des Zementporenwassers. In Abhängigkeit ihrer Konzentration in wässrigen Elektrolyten bilden nicht-ionische Tenside Mizellen und/oder Flüssigkristalle. Beobachtet wurden Mischungslücken und Aussalzungen dieser organischen, oberflächenaktiven Substanzen. Durch die Zugabe von Glykolen wird die Mischbarkeit nicht-ionischer Tenside mit wässrigen Elektrolyten stark erhöht und führt zu einer Absenkung der Bildung von Flüssigkristallen und organischen Aussalzungen sowie zu einer verminderten Adsorption des Tensides an Feststoffoberflächen. Der ausschließlich in der Patentliteratur erwähnte Synergieeffekt bei der Abmischung nicht-ionischer Tenside mit Glykolen zu Schwindreduzierern bezieht sich auf eine erhöhte Schwindreduktionskapazität des Zusatzmittels und beruht auf der Abmilderung aller Effekte, die zu einer Abscheidung des Tensides aus der wässrigen Lösung führen.
8. Eine Implementierung der spezifischen chemisch-physikalischen Eigenschaften schwindreduzierender Zusatzmittel in bestehende Modelle zur Beschreibung des Trocknungsschwindens ist der Fachliteratur nicht zu entnehmen. Mit Ausnahme des Kapillardruckmodells zur Vorhersage des Trocknungsschwindens lassen sich Charakteristika schwindreduzierender Betonzusatzmittel, im Speziellen ihrer Oberflächenaktivität, nicht bzw. nur unzureichend in bestehende Modelle zum Trocknungsschwinden implementieren.

Methodik

9. Die Oberflächenaktivität einer repräsentativen Auswahl an Schwindreduzierern wurde in makroskopischen Versuchen an synthetischen als auch an extrahierten Zementporenwässern quantifiziert. Dies umfasste auch die Quantifizierung von Mischungslücken und organischen Aussalzungen.
10. Ein in dieser Arbeit entwickelter theoretischer Ansatz zur Auswertung herkömmlicher Messungen der Oberflächenspannung erlaubt eine Abschätzung der Oberflächenspannung der Porenlösung im trocknenden, zementären Porensystem.
11. Der Einfluss schwindreduzierender Zusatzmittel auf den Hydratationsmechanismus, d.h. Hydratphasenbestand und Hydratationskinetik, wurde mittels Thermogravimetrie, Röntgenphasenanalyse bzw. isothermer Wärmeleitungskalorimetrie erfasst. Zusätzlich wurde Elektronenmikroskopie zur Beschreibung der Mikrostrukturen und energiedispersive Röntgenspektroskopie zur qualitativen Bestimmung von niedrig konzentrierten Hydratphasen eingesetzt. Die Veränderungen der Komposition des Zementporenwassers in Gegenwart schwindreduzierender Zusatzmittel wurden analysiert. Die spezifische Adsorption schwindreduzierender Zusatzmittel an Zementhydraten wurde an hydratisierendem Zement als auch an synthetischen Hydratphasen untersucht.
12. Der Mechanismus der Auslaugung schwindreduzierender Zusatzmittel wurde in Standtests untersucht, während praxisnahe Konditionen mittels zyklischer Auslaugung und Trocknung in Langzeittests simuliert wurden.
13. Die Beschreibung der hygrischen Eigenschaften von Zementstein und Mörteln erfolgte anhand von Schwind- und Desorptionsisothermen. Basierend auf thermodynamischen Ansätzen wurden unter Verwendung dieser Schwind- und Desorptionsisothermen Energiebilanzen erstellt, die eine Unterscheidung zwischen Verformungsenergie und Energie zur Erzeugung von Oberfläche im Trocknungsprozess zementärer Baustoffe zulassen und somit eine Abgrenzung der Einflussnahme von Schwindreduzierern auf diese spezifische Energieverteilung ermöglichen.

Im Wesentlichen erzielte Ergebnisse

14. Schwindreduzierende Betonzusatzmittel nehmen aufgrund ihrer amphiphilen Eigenschaften Einfluss auf den Hydratationsmechanismus von Portlandzementen. In Gegenwart dieser Zusatzmittel ist die Löslichkeit für anorganische Salze verringert. Die Konzentration von Calcium-, Kalium- und Sulfationen sinkt mit zunehmender Konzentration des Zusatzmittels. Während der Induktionsperiode der Portlandzementhydratation führt dies zur temporären Ausfällung von Calcium-Kalium-Sulfathydrat. Eine Veränderung des Hydratphasenbestandes in Gegenwart von schwindreduzierenden Zusatzmitteln kann nicht signifikant unterschieden werden. Somit sind nachteilige Auswirkungen auf die Dauerhaftigkeit derartig modifizierter Betone aufgrund eines veränderten Hydratphasenbestandes nicht zu erwarten.
15. Die stark verzögernde Wirkung von Schwindreduzierern in Kombination mit polycarboxylatbasierten Fließmitteln beruht nicht auf der Adsorption des Schwindreduzierers am hydratisierenden Klinker. Vielmehr kann davon ausgegangen werden, dass die verminderte Löslichkeit für Salze in der Porenlösung den Reaktionsumsatz absenkt und/oder eine spezifische Adsorption des nicht-ionischen Tensides an Portlanditkeimen deren Wachstum hemmt und damit die Auflösung von silikatischen Klinkerphasen.
16. Schwindreduzierende Zusatzmittel weisen eine spezifische Adsorption an Portlandit auf, einem Nebenprodukt der Hydratationsreaktionen eines Hauptbestandteils von Portlandzement. Ein verstärktes Kristallwachstum von Portlandit in lateraler Dimension führt zu einer Zunahme der spezifischen Oberfläche des hydratisierten Zementsteines. Für nass nachbehandelte Zementsteine bedeutet dies eine Zunahme der Gelporosität auf Kosten der Kapillarporosität. Eine Einflussnahme auf die Gesamtporosität lässt sich nicht feststellen.
17. Die Zunahme der spezifischen Oberfläche von Zementstein in Gegenwart von Schwindreduzierern bewirkt eine verstärkte physikalische Adsorption von Zementporenwasser am Feststoff. Für Betone mit niedrigem w/z-Wert oder unzureichender Nachbehandlung kann dieser Prozess zu einer Reduktion des für die Hydratation verfügbaren Wassers führen und in einem vermindertem Hydratationsgrad resultieren. Dies könnte eine Ursache für die in der Literatur beschriebenen Einbußen bezüglich mechanischer Eigenschaften beim Einsatz von Schwindreduzieren sein.
18. Schwindreduzierer sind im hohen Maße auslaugbar. Jedoch zeigen zyklische Langzeittests, dass ein signifikanter Austrag des Zusatzmittels in vorwiegend trockener Exposition nicht zu erwarten ist. Die Nachhaltigkeit des Einsatzes dieser Zusatzmittel ist gegeben, wenn die Anwendung im Beton das Ziel der Reduktion des Trocknungsschwindens verfolgt.
19. Die schwindreduzierende Wirkung der nicht-ionischen Tenside beruht vorwiegend auf der Reduktion der Oberflächenspannung der Grenzfläche „flüssig/gasförmig“ des trocknenden Zementsteines. Inwieweit diese Oberflächenspannung durch das nicht-ionischeTensid herabgesetzt wird, ist von der Gesamtkonzentration im Allgemeinen und im Speziellen von der Konzentration des Tensides in der Oberfläche abhängig. Da im Zuge des Trocknens diese Grenzfläche wächst, kann bei gegebener Gesamtkonzentration des Zusatzmittels im Beton dessen Konzentration in der Grenzfläche sinken, woraufhin die Oberflächenspannung ansteigt und die Schwindreduktion sinkt.
20. Im Ergebnis dieser Arbeit ist es möglich, die Entwicklung sowohl der Oberfläche als auch ihrer Oberflächenspannung im Trocknungsprozess zu quantifizieren und diese Ergebnisse in einen einfachen konzeptionellen, thermodynamischen Ansatz zur Minimierung der freien Energie des trocknenden, zementären Porensystems zu überführen. Die Verwendung dieses konzeptionellen Ansatzes erlaubt es, den Wirkmechanismus schwindreduzierender Betonzusatzmittel zu beschreiben.

Acknowledgements

I would like to thank the following people for their contributions to this work:

- Professor Jochen Stark, my thesis supervisor, for accepting me as an external PhD-student at the F.A. Finger Institute in Weimar, for the confidence he placed in my work throughout the thesis as well as for the support during synthesis and compilation. I also want to express my gratitude to Professor Stark for his very stimulating lectures that I so much enjoyed during my undergraduate studies and his reputation that opened me many doors after graduating from Weimar.
- Dr. J.P. Kaufmann, my thesis co-supervisor at the Swiss federal laboratories (EMPA), for all his support during the experimental part of this thesis, for his trust in my judgements that allowed me to freely exploit the measuring equipments that the Swiss federal laboratories provide. I also want to thank Dr. Kaufmann for encouraging me to carry out my internship at Purdue University, West Lafayette, US, which was not only scientifically stimulating but also an experience of life.
- Professor Max J. Setzer for sharing his excellent understanding of the hygral properties of cementitious material and for the challenging discussions on that subject during synthesis and compilation of this work.
- Professor Robert J. Flatt, for providing extreme availability for discussions I benefitted from a lot. I also want to express my gratitude to Robert Flatt for doing invaluable fundamental scientific work in an industrial setting and for his trust in me to contribute to this. Working in his group I experienced considerable progress in how to do scientific work. Without a doubt, this contributed a lot the quality of this thesis.
- The team of “concrete & construction chemicals laboratories” at the Swiss federal laboratories for their warm welcome when I arrived in Switzerland and for their support during the time I spent in this place, in particular: Dr. Barbara Lothenbach and Dr. Frank Winnefeld, for their scientific advice and Walter Trindler for his outstanding contributions in organizing required equipment and lab support, which enabled me to combine real work on the one hand and experimental work for my thesis on the other. Special thanks go to Marcel Käppeli and Luigi Brunetti for attending to long term leaching experiments during my absence, Jakob Burckhardt and Boris Ingold for their help on demand, again Marcel Käppeli for translating shrinkage strain values from Thuringian to Swiss german into real numbers, a delicate task for him and a special service for me that facilitated the shrinkage measurement of several hundreds of specimens. I would like to thank Cornelia Seiler for all her support in successfully separating superplasticizers from shrinkage reducing admixtures. I also want to emphasise the pleasure I had in working, discussing and “living” with my PhD-colleagues Goeril, Anatol, Astrid, Belay & Schmidti as well as the “visitors” Martin & Nina.
- Dr. Christiane Roessler and Dr. Lorenz Holzer for the support in electron microscopy.
- Harald Gundelwein from enertec engineering AG for providing office space on weekends after leaving the Swiss federal laboratories.
- Gaurav Sant, my PhD-colleague from abroad, for taking care of me during my visit at Purdue University, for all the fruitful discussions on and far beyond the subject.
- My family in Germany, for their great support throughout decades.
- To my friends whose support I appreciated throughout the years.
- Most important, I want to express my deepest gratitude to “the grey tiger and the blond cat”.

Finally, I want to express my gratitude to the members of my thesis jury for reviewing this work:
Professor J. Stark; Professor M.J. Setzer; Professor H.-M. Ludwig and Professor R. J. Flatt.

Table of content

1 Introduction 1

2 Thesis objectives 5

2.1 Surface activity and phase transitions of SRA 5

2.2 Evolution of surface tension in the course of hydration and drying 5

2.3 Influence of SRA on microstructure 6

2.4 Cement hydration in the presence of SRA and SP 6

2.5 Leaching of SRA 7

2.6 Physical impact of SRA on drying and shrinkage 8

3 State of the art – "Drying shrinkage of cementitious materials" 9

3.1 Standard thermodynamics of isothermal drying and shrinkage 9

3.1.1 The liquid/vapour equilibrium 10

3.1.2 Creation of liquid/vapour interface in the course of drying 11

3.1.3 Stress created in the course of drying 12

3.1.4 The concept of average pore pressure 14

3.1.5 Deformation upon drying induced pressure 17

3.2 Impact of cement specificity on drying & shrinkage 20

3.2.1 Ionic strength of cement pore solution 20

3.2.2 Surface tension of cement pore solution 21

3.2.3 The microstructure of cement paste 22

3.3 Irreversible shrinkage of cement paste 25

3.4 Impact of SRA on drying shrinkage 26

3.5 Summary 26

4 State of the art "Shrinkage Reducing Admixture (SRA)" 27

4.1 General introduction 27

4.2 Properties of non-ionic surfactants 28

4.2.1 General introduction 28

4.2.2 Surface activity 28

4.2.3 Association and self-aggregation of non-ionic surfactants in aqueous solution 31

4.2.4 Association and self-aggregation of non-ionic surfactants in electrolyte solution 33

4.2.5 Adsorption of non-ionic surfactants on the solid/liquid interface 35

4.2.6 Influence of non-ionic surfactant on surface forces 36

4.2.7 Summary 37

4.3 Mixtures of non-ionic surfactants and glycols in aqueous solution 38

4.3.1 Interfacial phenomena 38

4.3.2 Implications on cementitious environmental conditions 39

4.4 SRAs in concrete – Phenomenological overview ... 40
4.4.1 Characterisation of SRA used in scientific studies ... 40
4.4.2 Surface activity of SRA ... 41
4.4.3 Efficiency of SRA in shrinkage reduction ... 41
4.4.4 Influence of SRA on cement hydration and microstructure ... 43
4.4.5 Influence of SRA on mechanical properties ... 44
4.4.6 Influence of SRA on durability ... 45
4.5 Summary ... 45

5 Theoretical considerations ... 47
5.1 Thoughts about a suitable model for drying and shrinkage ... 47
5.2 Impacts of SRAs on mechanisms of drying & shrinkage ... 49
5.2.1 Impact of SRA on drying ... 49
5.2.2 Impact of surface tension on drying shrinkage of deformable systems ... 52
5.3 Conclusions ... 54
5.4 Summary ... 55

6 Materials and methods ... 57
6.1 Model systems ... 57
6.2 Materials ... 57
6.3 Methods ... 58
6.3.1 Preparation and curing of cement paste, mortar and concrete ... 58
6.3.2 Analytical methods ... 59
6.3.3 Microstructural investigations ... 62
6.3.4 Drying shrinkage and water vapour desorption isotherms ... 63
6.3.5 Leaching of SRA ... 65
6.3.6 Thermodynamic modelling of cement hydration using GEMS-PSI ... 70

7 Surface activity of SRA/SP and Phase transitions of SRA in aqueous and aqueous electrolyte solution ... 73
7.1 General introduction ... 73
7.2 Specific materials and methods ... 73
7.3 Results and discussion ... 74
7.3.1 Surface activity of SRA, SP-PCE and SRA/SP-PCE ... 74
7.3.2 Phase transitions of SRA ... 80
7.3.3 Impact of volume-interface ratio on efficient surface activity ... 88
7.4 Concluding remarks ... 93
7.4.1 Surface activity in aqueous solution ... 93
7.4.2 Surface activity in aqueous electrolyte solution ... 94
7.4.3 Phase behaviour of SRA ... 94

7.4.4 Impact of the interfacial area on surface activity 94
7.4.5 Possible impact on the hydration of Portland cement 94
7.4.6 Implications for modeling of shrinkage 95

8 Influence of SRA on the hydration of normal Portland cement 97
8.1 General introduction 97
8.2 Specific materials and working approach 97
8.3 Results and discussion 97
8.3.1 Influence of SRA on the hydration kinetics of Portland cement 97
8.3.2 Influence of SRA/SP-PCE on hydrated phase composition 106
8.3.3 Properties of pore solution during hydration progress 111
8.3.4 Influence of SRA on the hydration of C_3S and adsorption measurements on pure hydrates 120
8.3.5 Concluding remarks 129

9 Impact of SRA on microstructure 131
9.1 General introduction 131
9.2 Specific materials and working approach 131
9.3 Impact of SRA on microstructure of cement paste during wet curing 132
9.3.1 Chemical shrinkage of cement paste and mortars 132
9.3.2 Porosity of cement paste and mortar 135
9.3.3 Summary 139

10 Sustainability of SRA application for self compacting mortars and concretes – How long will concrete benefit from SRA addition? 141
10.1 General introduction 141
10.2 Specific materials and methods 141
10.2.1 Materials 141
10.2.2 Methods 141
10.3 Permanent leaching 142
10.3.1 Results – tank test 142
10.3.2 Differentiated analysis of leached SRA & SP-PCE 143
10.3.3 Discrimination between the mobile and the immobile fraction of SRA 145
10.3.4 Successive equilibrium hypothesis 147
10.3.5 Determination of effective diffusion coefficients 148
10.3.6 Diffusion in sample and in eluate 152
10.3.7 Summary 157
10.4 Cyclic leaching and drying 157
10.4.1 Results 157
10.4.2 Discussion 158
10.5 Impact of leaching on shrinkage reduction 158

10.5.1 Results - permanent leaching ... 158
10.5.2 Discussions on permanent leaching ... 160
10.5.3 Results on cyclic leaching and drying ... 162
10.5.4 Discrimination between ageing and leaching phenomena ... 164
10.6 Concluding remarks ... 166

11 Physical impact of SRA on drying and shrinkage ... 169
11.1 General introduction ... 169
11.2 Synthesis of theoretical and experimental results that matter dyring and shrinkage ... 169
11.3 Results ... 171
11.3.1 Drying ... 171
11.3.2 Free drying shrinkage ... 173
11.3.3 Irreversible shrinkage ... 174
11.3.4 Mechanical properties of paste and mortars ... 175
11.4 Energy balances for drying and shrinkage ... 176
11.4.1 Separation of the energy of deformation ... 176
11.4.2 Specific energy of deformation ... 177
11.4.3 Concluding remarks ... 181
11.5 Evolution of interfacial area and surface tension in the course of drying ... 182
11.5.1 Surface activity of SRA1 in hydrated mortars and paste ... 183
11.5.2 Interfacial area exposed in the course of drying ... 183
11.6 The role of average capillary pressure for drying shrinkage ... 186
11.7 The role of SRA in drying and shrinkage of cementitious material ... 188
11.7.1 Basic concept for drying and shrinkage of cementitious material ... 188
11.7.2 The shrinkage reducing mechanism of SRAs ... 191
11.7.3 Perspectives on the SRA mechanism ... 194

12 Overall conclusions ... 197
12.1 Cement hydration in presence of SRA ... 197
12.2 Sustainability of the SRA application ... 198
12.3 Drying and shrinkage of cementitious material in presence of SRA ... 199

13 References ... 201

14 List of tables ... 215

15 List of figures ... 217

16 Abbreviations ... 223

17 Appendix ... 225

1 Introduction

Self Consolidating Concrete – a dream has come true!(?)

Self Consolidating Concrete (SCC) is mainly characterised by its special rheological properties. Without any vibration this concrete can be placed and compacted under its own weight, without segregation or bleeding. The use of such concrete can increase the productivity on construction sites and enable the use of a higher degree of well distributed reinforcement for thin walled structural members. This new technology also reduces health risks since in contrast to the traditional handling of concrete, the emission of noise and vibration are substantially decreased.
The specific mix design for self consolidating concretes was introduced around the 1980s in Japan. In comparison to normal vibrated concrete an increased paste volume enables a good distribution of aggregates within the paste matrix, minimising the influence of aggregates friction on the concrete flow property. The introduction of inert and/or pozzolanic additives as part of the paste provides the required excess paste volume without using disproportionally high amounts of plain cement. Due to further developments of concrete admixtures such as superplasticizers, the cement paste can gain self levelling properties without causing segregation of aggregates.
Whereas SCC differs from normal vibrated concrete in its fresh attributes, it should reach similar properties in the hardened state. Due to the increased paste volume it usually shows higher shrinkage. Furthermore, owing to strength requirements, SCC is often produced at low water to cement ratios and hence may additionally suffer from autogenous shrinkage. This means that cracking caused by drying or autogenous shrinkage is a real risk for SCC and can compromise its durability as cracks may serve as ingression paths for gases and salts or might permit leaching. For the time being SCC still exhibits increased shrinkage and cracking probability and hence may be discarded in many practical applications. This can be overcome by a better understanding of those mechanisms and the ways to mitigate them. It is a target of this thesis to contribute to this.

How to cope with increased shrinkage of SCC?

In general, engineers are facing severe problems related to shrinkage and cracking. Even for normal and high performance concrete, containing moderate amounts of binder, a lot of effort was put on counteracting shrinkage and avoiding cracking. For the time being these efforts resulted in the knowledge of how to distribute cracks rather to avoid them.
The most efficient way to decrease shrinkage turned out to be to decrease the cement content of concrete down to a minimum but still sufficient amount. For SCC this obviously seems to be contradictory with the requirement of a high paste volume. Indeed, the potential for shrinkage reduction is limited to some small range modifications in the mix design following two major concepts. The first one is the reduction of the required paste volume by optimising the aggregate grading curve. The second one involves high volume substitution of cement, preferentially using inert mineral additives.
The optimization of grading curves is limited by several severe practical issues. Problems start with the availability of sufficiently fractionated aggregates. Usually attempts fail because of the enormous effort in composing application-optimized grading curves or mix designs. Due to durability reasons, the substitution rate for cement is limited depending on the application purpose and on environmental exposure of the hardened concrete.
In the early 1980s Shrinkage Reducing Admixtures (SRA) were introduced to counteract drying shrinkage of concrete. The first publications explicitly dealing with SRA go back to Goto and Sato (Japan). They were published in 1983, which is also the time when the SCC concept was introduced.

SRA modified concretes showed a substantial reduction of free drying shrinkage contributing to crack prevention or at least a significant decrease of crack width in situations of restrained drying shrinkage.

Will shrinkage reducing admixtures contribute to a broader application of SCC?

Within the last three decades performance tests on several types of concrete proved the efficiency of shrinkage reducing admixtures. So, at least in terms of shrinkage and cracking, concretes in general and SCC in particular can benefit from SRA application. But "One man's meat is another man's poison" and with respect to long term performance of SRA modified concretes there are still several issues to be clarified.

One of these concerns the impact of SRAs on cement hydration. It is therefore an issue to know if changes in the hydrated phase composition, induced by SRA, result in undesired properties or decreased durability.

Another issue is that the long term shrinkage reduction has to be evaluated. For example, one can wonder if SRA leaching may diminish or even eliminate long term shrinkage reduction and if the release of admixtures could be a severe environmental issue.

It should also be noted that the basic mechanism or physical impact of SRA as well as its implementation in recent models for shrinkage of concrete is still being discussed.

The present thesis tries to shed light on the role of SRA in self consolidating concrete focusing on the three questions outlined above: basic mechanisms of cement hydration, physical impact on shrinkage and the sustainability of SRA-application.

Which contributions result from this study?

Based on an extensive patent search, commercial SRAs could be identified to be synergistic mixtures of non-ionic surfactants and glycols. This turns out to be most important information for more than one reason and is the subject of chapter 4:

An abundant literature focuses on properties of these non-ionic surfactants. Moreover, from this rich pool of information, the behaviour of SRAs and their interactions in cementitious systems were better understood through this thesis. For example, it could be anticipated how SRAs behave in strong electrolytes and how surface activity, i.e. surface tension, and interparticle forces might be affected. The synergy effect regarding enhanced performance induced by the presence of additional glycol in SRAs could be derived from the literature on the co-surfactant nature of glycols. Generally it now can be said that glycols ensure that the non-ionic surfactant is properly distributed onto the paste interfaces to efficiently reduce surface tension.

In literature, the impact of organic matter on cement hydration was extensively studied for other admixtures like superplasticizer. From there, main impact factors related to the nature of these molecules could be identified. In addition, here again, the literature on non-ionic surfactants provides sufficient information to anticipate possible interactions of SRA with cement hydration based on the nature of non-ionic surfactants.

All in all, the extensive study on the nature of non-ionic surfactants, presented in chapter 4, provides fundamental understanding of the behaviour of SRAs in cement paste. Taking a step further to relate this to the impact on drying and shrinkage required to review recent models for drying and shrinkage of cement paste as presented in chapter 3. There, it is shown that macroscopic thermodynamics of the open pore systems can be successfully applied to predict drying induced deformation, but that surface activity of SRA still has to be implemented to explain the shrinkage reduction it causes. Because of severe issues concerning the importance of capillary pressure on shrinkage, a new macroscopic thermodynamic model was derived in a way that meets requirements to properly incorporate surface activity of SRA. This is the subject of chapter 5.

Based on theoretical considerations, in chapter 5 the broader impact of SRA on drying cementitious matter could be outlined. In a next step, cement paste was treated as a deformable, open drying pore system. Thereby, the drying phenomena of SRA modified mortars and concrete observed by other authors could be retrieved. This phenomenological consistency of the model constitutes an important contribution towards the understanding of SRA mechanisms.

Another main contribution of this work came from introducing an artificial pore system, denominated the normcube. Using this model system, it could be shown how the evolution of interfacial area and its properties interact in presence of SRAs and how this impacts drying characteristics.

In chapter 7, the surface activity of commercial SRAs in aqueous solution and synthetic pore solution was investigated. This shows how the electrolyte concentration of synthetic pore solution impacts the phase behaviour of SRA and conversely, how the presence of SRA impacts the aqueous electrolyte solution. Whilst electrolytes enhance self-aggregation of SRAs into micelles and liquid crystals, the presence of SRAs leads to precipitation of minerals as syngenite and mirabilite. Moreover, electrolyte solutions containing SRAs comprise limited miscibility or rather show miscibility gaps, where the liquid separates into isotropic micellar solutions and surfactant rich reverse micellar solutions.

The investigation of surface activity and phase behaviour of SRA unravelled another important contribution. From macroscopic surface tension measurements, a relationship between excess surface concentration of SRA, bulk concentration of SRA and exposed interfacial area could be derived. Based on this, it is now possible to predict the actual surface tension of the pore fluid in the course of drying once the evolution of internal interfacial area is known. This is used later in this thesis to describe the specific drying and shrinkage behaviour of SRA modified pastes and mortars.

Calorimetric studies on normal Portland cement and composite binders revealed that SRA alone show only minor impact on hydration kinetics. In presence of superplasticizer however the cement hydration can be significantly decelerated. The delaying impact of SRA could be related to a selective deceleration of silicate phase hydration. Moreover, it could be shown that portlandite precipitation in presence of SRA is changed, turning the compact habitus into more or less layered structures. Thereby, the specific surface increases, causing the amount of physically bound water to increase, which in turn reduces the maximum degree of hydration achievable for sealed systems.

Extensive phase analysis shows that the hydrated phase composition of SRA modified binders remains almost unaffected. The appearance of a temporary mineral phase could be detected by environmental scanning electron microscopy. As could be shown for synthetic pore solutions, syngenite precipitates during early hydration stages and is later consumed in the course of aluminate hydration, i.e. when sulphates are depleted. Moreover, for some SRAs, the salting out phenomena supposed to be enhanced in strong electrolytes could also be shown to take place. The resulting organic precipitates could be identified by SEM-EDX in cement paste and by X-ray diffraction on solid residues of synthetic pore solution.

The presence of SRAs could also be identified to impact microstructure of well cured cement paste. Based on nitrogen adsorption measurements and mercury intrusion porosimetry the amount of small pores is seen to increase with SRA dosage, whilst the overall porosity remains unchanged.

The question regarding sustainability of SRA application is the subject of chapter 10. By means of leaching studies it could be shown that SRA can be leached significantly. The mechanism could be identified as a diffusion process and a range of effective diffusion coefficients could be estimated. Thereby, the leaching of SRA can now be estimated for real structural members. However, while the admixture can be leached to high extents in tank tests, the leaching rates in practical applications can be assumed to be low because of much reduced contact with water. This could be proven by quantifying admixture loss during long term drying and rewetting cycles. Despite a loss of admixture shrinkage reduction is hardly impacted. Moreover, the cyclic tests revealed that the total deformations in presence of SRA remain low due to a lower extent of irreversibly shrinkage deformations.

Another important contribution towards the better understanding of the working mechanism of SRA for drying and shrinkage came from the same leaching tests. A significant fraction of SRA is found to be immobile and does not diffuse in leaching. This fraction of SRA is probably strongly associated to cement phases as the calcium-silicate-hydrates or portlandite. Based on these findings, it is now also possible to quantify the amount of admixture active at the interfaces. This means that, the evolution of

surface tension in the course of drying can be approximated, which is a fundamental requirement for modeling shrinkage in presence of SRA.

The last experimental chapter of this study focuses on the working mechanism and impact of SRA on drying and shrinkage. Based on the thermodynamics of the open deformable pore system introduced in chapter 5, energy balances are set up using desorption and shrinkage isotherms of actual samples. Information on distribution of SRA in the hydrated paste is used to estimate the actual surface tensions of the pore solution. In other words, this is the first time that the surface activity of the SRA in the course of the drying is fully accounted for. From the energy balances the evolution and properties of the internal interface are then obtained.
This made it possible to explain why SRAs impact drying and shrinkage and in what specific range of relative humidity they are active.

Summarising the findings of this thesis it can be said that the understanding of the impact of SRAs on hydration, drying and shrinkage was brought forward. Many of the new insights came from the careful investigation of the theory of non-ionic surfactants, something that the cement community had generally overlooked up to now.

2 Thesis objectives

In this chapter the main objectives of this thesis are outlined as well as the intermediate steps that had to be taken in order to fulfil these objectives. As previously explained, the overriding objective is to understand the effect of SRAs on cement hydration, drying and shrinkage.
For this we first of all must recognize that SRAs belong to the family of non-ionic surfactants of which the basic behaviour must be taken into account. In particular this means that the evaluation of surface tension with dosage must be characterized (chapter 2.1).
When used in cement, SRAs largely remain in aqueous phase of which the composition evolves with time due to hydration. Understanding how this impacts surface tension is another objective (chapter 2.2).

SRAs are reported to increase the specific surface of hydrated cement paste and may additionally impact the hygral properties of these porous systems. Examining the impact of these admixtures on the microstructure of cement paste is in particular important towards a clear discrimination between their main and side effects on drying and shrinkage (chapter 2.3).

We must recognize that the presence of SRAs impacts hydration kinetics of cement paste. Moreover, this is in particular true when SRAs are combined with superplasticizers, which is often the case of SCC. How SRAs impact cement hydration and whether this causes undesired properties, as for instance for durability, is another important objective (chapter 2.4).
Since SRAs belong to the family of surface active agents (surfactants), their presence at interfaces might subject them to enhanced leaching. An important objective of this thesis is, whether SRAs are leachable and if so, whether this impacts long term shrinkage reduction or is on itself an environmental issue.

2.1 Surface activity and phase transitions of SRA

Surface activity is an essential property of surfactant containing systems and can be evaluated by means of surface tension measurements. The method returns a relationship between bulk concentrations of the surface active component of the species. More in detail, a relationship between excess surface concentration and surface tension can be obtained. Commercially available SRAs as well as non-ionic surfactants are to be characterised by such measurements.

It is known that the electrolytes impact surface activity and can cause phase transition. To determine if this is an issue in cement systems, surface tension measurements are therefore to be conducted in SRA solutions with and without electrolytes as well as in synthetic cement pore solution with SRAs.

This part of the study also includes miscibility tests on mixtures of SRA with water and synthetic pore solution to receive information on:

a) Miscibility in general

b) Phase transitions

c) Electrolyte induced salting out effects of the surfactant

d) Surfactant induced mineral precipitations in synthetic pore solution

2.2 Evolution of surface tension in the course of hydration and drying

The evolution of surface tension of the interfaces in the course of drying is of high interest for implementing SRAs into shrinkage modeling. So far, authors account for the initial surface activity in aqueous solution. Therefore, a method is lacking to properly describe the change of the surface tension of the pore fluid as a function of either water consumption by cement hydration or water loss due to evaporation.
Usually the initial SRA dosages are well below the critical micellation concentrations. However, in the course of drying water evaporates, which increases the bulk concentration of SRA.

The challenge is therefore to know how the surface tension of the remaining pore solution changes due to that. This is obtained from an improved evaluation of the surface tension measurements mentioned above.
For this we must recognize that the relationship between excess surface concentration and bulk concentration of SRA depends on the ratio of solution volume to the interfacial area. Therefore, the surface tension can be back calculated from the bulk concentration of SRA, the solution volume and the interfacial area at which the surfactant is supposed to be active.

Whereas this surface tension can be obtained from macroscopic measurements, the ability to predict it at discrete time steps requires knowing the actual distribution of SRA between

a) pore solution

b) the solid surfaces (adsorbed)

c) self-aggregation of SRA (inactive)

where a) can be obtained from appropriate macroscopic studies on b) and c).

2.3 Influence of SRA on microstructure

Concerning the impact of SRAs on microstructure, an increase in specific surface area was observed by some authors. Though not proven, this increase was suggested to come from enhanced formation of low density C-S-H.

This increased interfacial area can be expected to impact drying and shrinkage. On the one hand, the excess Gibbs free energy utilized at these interfaces would increase; hence shrinkage deformation would also increase. On the other hand, an increased amount of low density C-S-H can be assumed to increase the extent of irreversible deformation in the course of drying.

The evolution of specific surface area will be determined by nitrogen adsorption. However, a lot of issues concerning nitrogen sorption measurements on hydrated paste can be found in literature. An important argument is that an ingression limit for nitrogen can be found for pores smaller than 2-3 nm. Therefore, a significant fraction of calcium-silicate hydrate porosity cannot be tracked by such a sorbate. However in presence of SRA, the alternative of water vapour sorption is most probably perturbed by these surfactants, so that nitrogen sorption is retained as characterization method.

On the topic of microstructure deformation, it is particularly important to distinguish between irreversible deformations that do not cause stress and reversible ones that do. Distinction between both is obtained by including length change measurements after resaturation at the end of shrinkage isotherms.

As far as the hydrate phase assemblage is concerned, some authors reported the appearance of additional mineral phases due to SRA.
Using Environmental Scanning Electron Microscopy (ESEM), which significantly reduces sample pretreatment artefacts, we find that:

a) minor phases can be detected and qualitatively described

b) changes in morphology can be proven quantitatively

2.4 Cement hydration in the presence of SRA and SP

In literature it is reported that SRA has only minor impact on hydration kinetics. However, a disproportional delay of hydration in presence of both SRA and SP can occur. This is particularly relevant for self consolidating mortar and concrete as a combination of these admixtures is most likely.

The kinetics of cement hydration in presence of SRAs and in combination with SP are therefore examined using isothermal heat conduction calorimetry. From this type of measurement time schedules can be developed so that, despite significant impacts on hydration kinetics, pastes can be studied at comparable hydration stages.
In analogy to studies on the impact of superplasticizers on Portland cement hydration, the adsorption

of SRA onto clinker and hydration phases is of high interest. Admixture adsorption measurements on synthetic phases as well as on hydrated paste at different stages of hydration are performed. This reveals most important information on the distribution of the admixture in bulk. Furthermore, from specific adsorption it can be derived what causes the hydration to be altered.

As far as drying shrinkage is concerned, the distribution of SRA between liquid and solid phases is of high interest. From adsorption measurements and, more important, the nature of adsorption, one can deduce how much of the admixture can be supposed “active” on the liquid/vapour interface of the pore system.

Concerning durability of SRA containing systems, it is of particular interest whether a hydrate phase assemblage can be found that leads to undesired properties or decreases the long term performance of concrete. This can be examined using X-ray powder diffraction. Selected phases are properly quantified using thermogravimetric analysis. Furthermore, the pore solution is a mirror image of hydration. Its change in presence of admixture is therefore relevant to the questions at hand. On the one hand, information towards the electrolyte composition can be obtained; on the other hand it reveals, how much of the admixture is part of the pore solution. The latter is especially important concerning the surface tension of pore solution and its importance for shrinkage mechanisms.

We have to recognize that for SCC a combination of SRA and SP is most likely, requiring a proper discrimination of these species for analysing pore solutions. Due to different molecular masses a clear discrimination is possible by gas chromatography. In this method the non-volatile SP can be supposed to be separated from SRA, comprising a relative low molecular weight.

In regard to the physical impact of SRA on drying and shrinkage, the examination of this requires a preferably complete description of the hydration process in presence of the admixtures.

2.5 Leaching of SRA

SRA-type surfactants are intended to preferably adsorb at the liquid/vapour interface to reduce surface tension. To do so they have to be part of the pore fluid. For mortar and concrete this implies the potential risk of leaching upon cyclic drying and rewetting.

Once the SRA is leached out, concrete may no longer benefit from shrinkage reduction and one long term its crack probability could increase. Up to now the application of SRA in concrete is relatively expensive and answering the question of “How long will concrete benefit from SRA?” is of high interest. Moreover, release of SRA might cause environmental issues.

To examine these issues, one needs a proper leaching methodology that must

a) enable a clear view on the dominating mechanism of leaching

b) comprise test conditions exploitable towards practical application/prediction.

We have to recognize that leaching tests on cement paste might not reflect field conditions, because the release of SRA from mortar and concrete can be significantly higher due to an enhanced porosity of the paste/aggregate interface. Leaching tests therefore have to be performed on mortars or concrete.

Cyclic drying and leaching can be seen as the exposition that mortars and concretes are subjected to in practice. However, the evaluation of leaching mechanisms will be perturbed by resaturation prior to leaching. We recognize that the governing mechanism has to be examined using tank tests and permanent leaching, whereas the extent of leaching for practical application can be evaluated on cyclic drying and leaching.

As far as leaching and ageing impact microstructure and overall properties of the material, a representative reference has to be introduced as a measure for shrinkage and shrinkage reducing effect of SRA. These reference series preferably comprise properties that enable a clear distinction between ageing and leaching phenomena.

For both test conditions, permanent and cyclic leaching, the admixture release is to be quantified. Again, the combined use of SRA and SP requires a proper distinction between both admixtures. This can be done as outlined in the previous subchapter.

2.6 Physical impact of SRA on drying and shrinkage

Recent models for drying induced shrinkage of cement paste are based on the thermodynamics of the open pore system exchanging water with its environment. Deformation predictions are mainly based on energy balances accounting for the cumulative character of Helmholtz free energy. This states that changes of Gibbs free energy can be separated as follows:

a) energy utilized for creation of interfacial area

b) energy utilized in deformation of the solid skeleton

Based on drying and shrinkage isotherms of cement paste such energy balances can be drawn. The impact of SRA is evaluated by means of changes due to surface activity of SRA.

Again, the determination of actual amounts of admixtures active at interfaces is of high interest.

3 State of the art – “Drying shrinkage of cementitious materials”

Hydrated cement paste is very porous and comprises a wide pore size distribution from macro capillary [µm] down to gel porosity [nm]. Due to this it is subjected to the so-called hygral deformations during adsorption and desorption of water vapour. The mechanical action of molecular forces on porous material during the formation of adsorption-solvation layers causes swelling. Conversely, desorption of these layers causes shrinkage.

The first attempts in relating drying and shrinkage of porous matter to standard thermodynamics go back to Bangham’s work on charcoal published between1930-37 [1-4]. Later on Powers 1968 [5] published the “Thermodynamics of volume change and creep”, suggesting a combined action of surface free energy, disjoining pressure and capillary pressure within the porous cementitious material, all derived from standard thermodynamics. Setzer proposed a thermodynamic approach for calculation of pore space distributions using water vapour sorption isotherms in 1973 [6], providing the basis for modeling the drying of a porous matter. Later, Setzer 1974 [7] and Hansen 1987 [8] successfully related changes of surface free energy to the deformation of drying/swelling of cement paste, primary for the low humidity range (<50% RH).

Beltzung and Wittmann 2005 [9] as well as Setzer et al. 2006 [10] summarized that deformations of cement paste below an ambient relative humidity of 50% clearly follow Bangham’s law, i.e. changes of free surface energy, whilst above 50% RH deformations are to be dominantly due to disjoining pressure.

Throughout the literature on shrinkage of cementitious material one often finds authors referring to the capillary force model, in which said capillary forces exert tensile stress to the pore walls, causing the solid skeleton to deform. However, there are severe doubts on the capillary force model because it comprises major shortcomings as outlined in the following. A first issue occurs for the humidity range where menisci are supposed to break down (<50% RH) and capillary pressure or rather the hydrostatic average fluid pressure is no more supposed to impact drying shrinkage. It is widely agreed that capillary pressure is limited to relative humidity at which menisci are still present but, even then, there are severe doubts on its importance for drying deformation. More important, concerning the tensile character of capillary pressure, swelling of cementitious materials cannot be explained.

Coussy et al. [11-13] propose a more global treatment for drying induced shrinkage based on thermoporoelasticity (saturated and partially saturated). This allows them to derive the deformation of the drying/swelling porous matter without referring to different ranges of humidity. Coussy´s approach [11, 13] allows to clarify the issue related to the action of pore fluid pressure versus surface energy contributions. However, some aspects of this work are still being under discussion.

In what follows, the basic equations for describing drying and shrinkage of cementitious porous matter are derived from standard thermodynamics. The main goal for this is to find out how SRAs might act on drying and shrinkage in order to implement them appropriately into current models.

3.1 Standard thermodynamics of isothermal drying and shrinkage

The drying cementitious material can be viewed as an open thermodynamic system exchanging water and gas with the surrounding environment. Due to its constitution at any drying state and referring to full saturation, the multi-phase cementitious system comprises a Gibbs free energy given by:

$$G = \sum n_i \cdot \mu_i \tag{1}$$

where

G: Gibbs free energy [J]

n: quantity of component i [mol]

µ: chemical potential of component i [J/mol]

i: components; *w*-water; *a*-air; *v*-water vapour; s-solid matter

The chemical potential is a function of the intensive variables T-temperature and p-pressure, so that for the isothermal drying process it is a function of pressure only

$$\mu = \mu(p) \tag{2}$$

and

$$d\mu = v_{m;i} dp_i \tag{3}$$

where

v_{m_i}: molar volume of component i

The chemical potentials of the gaseous μ_g and liquid phases μ_l can be expressed as a function of apparent pressure and volume. However, for the solid skeleton (*s*) a more convenient expression for μ_s was introduced by Landau and Lifschitz [14]:

$$\mu_s = \Psi_s - \sigma\varepsilon \tag{4}$$

and

$$d\mu_s = \sigma d\varepsilon \tag{5}$$

where

Ψ_s: Helmholtz free energy of the solid skeleton

σ: stress tensor

ε: infinitesimal reversible strain

According to the Gibbs-Duhem equality for a reversible evolution between two successive isothermal drying states of the open cementitious system one derives:

$$dG = d\Psi = \sigma d\varepsilon + \mu_w dn_w + \mu_a dn_a + \mu_v dn_v \tag{6}$$

In (6) the total difference in free energy between two isothermal drying states is expressed as a function of change in chemical potential of the components and the change in the components quantity within the open system. Note that the mass of the solid skeleton is usually assumed to be invariant. Moreover, equation (6) exclusively accounts for incremental changes of the open porous system between two close isothermal drying states.

3.1.1 The liquid/vapour equilibrium

According to Clausius-Clapeyron the chemical potential of all constituents in the system has to be equal. This requires changes of chemical potentials to be similar also. The equilibrium between liquid and vapour reads:

$$d\mu_v \equiv d\mu_w \tag{7}$$

Assuming ideal gas (g) behaviour for air (a) and water vapour (w) so that the molar volume of the gas phase is given by

$$v_{m;g} = RT / p_g \tag{8}$$

and incompressibility for water ($v_{m,w}$ = const.) Kelvin’s law is obtained by integration of equation (7):

$$\int_{p_{v,0}}^{p_{v,0}+\Delta p} v_{m,w}\,dp_w = \int_{p_{v,0}}^{p_{v,1}} \frac{RT}{p_v}\,dp_v \tag{9}$$

or

$$\Delta p = \frac{RT \cdot ln(\frac{p_{v,1}}{p_{v,0}})}{v_{m,w}} \tag{10}$$

where

Δp:	pressure due to curvature of the interface; capillary pressure
$p_{v,0}$:	vapour pressure over a plane surface
$p_{v,1}$:	vapour pressure in equilibrium
p_w:	liquid pressure

Equation (9) describes the energy balance for a fluid in equilibrium with its vapour. The left term describes the work done at constant molar volume and varying liquid pressure due to curvature of the interface, and the right term the appropriate work done at the interface.

For drying cementitious matter one usually finds the atmospheric pressure imposed to the boundaries of the open system. Further on the change in vapour chemical potential is referred to as the ratio of actual vapour pressure and saturation pressure, i.e. the relative humidity (RH). For total liquid saturation of the cementitious system, the water pressure is assumed to be equal to the atmospheric pressure. Accordingly Kelvin’s law then reads:

$$\Delta p = \frac{RT}{v_{m,w}} \cdot ln(RH) \tag{11}$$

where the relative humidity imposed at the boundaries of the cementitious porous system determines the pressure of the liquid phase, i.e. the pore solution.

3.1.2 Creation of liquid/vapour interface in the course of drying

The pore fluid comprises a certain surface tension at the liquid vapour interface that is determined by its electrolyte constitution and, in the context of this study, by the presence of non-ionic surface active admixtures.

In the course of water evaporation from the saturated porous material, the pores empty. According to Scherer 1990 [15], the removal of pore fluid from the porous body causes a replacement of a low energetic liquid/solid interface by a high energetic solid/vapour interface. To prevent this increase of energy, or rather to maintain a low interfacial energy, the remaining pore fluid tends to cover the solid interface.

Following the approach of Brunauer et al. [16, 17] one can assume a rigid drying porous material where $d\varepsilon$=0 and the total difference in free energy of the system is stored by creating interfacial area at the liquid/vapour interface

$$dG = dw = \gamma da \tag{12}$$

where

dw: energy required to create interfacial area

γ: surface tension at the liquid/vapour interface

da: change of interfacial area due to water loss

The total difference in free energy can by obtained from the total mass loss, i.e. evaporated water according to equation (6), and one reads:

$$-\frac{dv_{water}}{v_{m,w}} \cdot RT\, ln(RH) = \gamma da \tag{13}$$

where

dv_{water}: water loss due to drying

3.1.3 Stress created in the course of drying

Generally one can distinguish between two types of forces potentially causing shrinkage of cement paste.

a) capillary forces, acting similar to a hydrostatic pressure

b) disjoining pressure, acting normal to the solid interfacial planes

3.1.3.1 Capillary pressure

The liquid/vapour interface created in the course of drying is highly curved. This is due to the nanoscopic features of the hydrated cement paste microstructure. Capillary pressure can be however derived from standard thermodynamics, as follows:

Let us assume an ideal rigid open pore system where the change in Gibbs free energy is exclusively utilised in creating interfacial area as in eq. (12). Furthermore we consider that this energy change comes from a volume work given by *Δpdv*, so that:

$$\Delta p dv_{water} = \gamma da\,;\, \Delta p = \gamma \frac{da}{dv_{water}} \tag{14}$$

For a saturated pore with a given geometry the removal of water causes the interface to be increased. Moreover, if now the liquid tends to cover the solid interface the liquid/vapour interface comprises a curvature. In equilibrium with a curved surface the pore fluid pressure is depressed (cap. pressure) to maintain force balance. For a spherical liquid/vapour interfaces Laplace equation (17) is obtained from (11), (12), (13) and (14) reading:

$$a = 4\pi r^2\ ;\ da = 8\pi r dr \tag{15}$$

and

$$v = 4/3 \cdot \pi r^3\,;\ dv = 4\pi r^2 dr \tag{16}$$

so that

$$\Delta p = \gamma \frac{8\pi r}{4\pi r^2} = \frac{2\gamma}{r} \tag{17}$$

and returns a special case of Lord Kelvin’s law usually applied to pore systems comprising cylindrical pores and the radius r is the so-called Kelvin radius r_k, which is also the radius of the largest water filled cylindrical pore.

Concerning the impact of SRAs, it can be stated that the capillary condensation equilibrium is changed if the surface tension of the pore fluid decreases. Assuming that the capillary pressure exclusively depends on the imposed relative humidity in accordance with equation (11), this pressure should not be changed by SRAs and therefore has to be assumed a constant.
The following scenario can therefore be thought of to explain why SRAs reduce shrinkage:
Aqueous solutions of SRAs have decreased the surface tensions which changes the capillary condensation equilibrium. More specifically, for a given humidity, the so called Kelvin radius r_K decreases with surface tension according equation (17). Consequently, the water loss of pore systems with SRA should increase with increasing SRA content.

3.1.3.2 Disjoining pressure

In the literature on drying and shrinkage of hydrated cement paste one can find serious doubts on the importance of capillary pressure and disjoining pressure is often presented to be the dominating mechanism [9, 10, 18-21]. According to Scherer [15], disjoining pressure result from short range forces at solid/liquid interfaces. Due to its structuring in vicinity of a solid interface, water would not be easily displaced in the course of drying, and would in particular resist solid surfaces from being brought together. Disjoining pressure is therefore defined to act normal to the solid/liquid interface. Unlike capillary pressure, the concept of disjoining pressure describes both, drying and swelling of porous matter. In regard to cement paste Powers 1968 [5] introduced the principle of hindered adsorption and gave a basic thermodynamic expression for disjoining pressure $p_{\text{disj.}}$ derived from Clausius-Clapeyron:

$$\Delta p_{disj.} = \frac{RT}{v_{m,w}} \cdot ln(RH) \tag{18}$$

The idea is that due to the close vicinity of hydrate surfaces in cement paste, the adsorption of water is locally hindered. Disjoining pressure is supposed to be active in these locations to maintain equality of chemical potentials. Moreover, Setzer 2006 [10] proposes disjoining pressure to be the main factor determining the average distance h between opposing solid/liquid interfaces in the nanoscopic cement system. The volume stability and hygral properties of cement paste are then proposed to be exclusively governed by disjoining pressure:

$$p_{disj.}(h) = -\left(\frac{\partial G}{\partial h}\right)_{T,p;\mu_i} \tag{19}$$

and

$$\Delta p_{disj.}(h) = \frac{1}{h}\int_{\mu_1}^{\mu_1+\Delta\mu} \Gamma_W d\mu_W \tag{20}$$

where

- G: Gibbs free energy
- h: distance between surfaces
- μ_i: chemical potential of dissolved components
- μ_W: chemical potential of water
- Γ_W: surface concentration of water

It is important to note that Setzer [10] concludes that if pores empty in the course of drying, then, the repulsive contributions of the disjoining pressure vanish. The air filled pores then only have the attractive component of disjoining pressure, the dispersive force. Due to these strong attractive forces the pore volume decreases, which is macroscopically recognised as shrinkage. In contrast to this view, his former models incorporating disjoining pressure exclusively related shrinkage to the water filled fraction of partially saturated bodies.

The main difference between capillary and disjoining pressure approaches for modeling of cement paste shrinkage can be summarized as follows: Capillary pressure is assumed to act similar to hydrostatic pressure. In contrast, disjoining pressure acts perpendicular to solid/liquid interfaces and, according to [10], results from overlapping force fields of air filled pores in the partially saturated body.

In regard to mechanisms underlying the effects of SRA on shrinkage, the disjoining pressure view suggests that the shrinkage reduction may be a repulsive steric contribution to disjoining pressure related to the presence of non-ionic surfactants in wetting films (section 4.2.6).

Indeed, referring to the model recently introduced by Setzer [10], decreasing the disjoining pressure in the air filled pores causes shrinkage. Therefore, the incorporation of SRA that increases the disjoining pressure would reduce shrinkage.

3.1.4 The concept of average pore pressure

Modeling approaches for predicting shrinkage deformation usually refer to linear elasticity of the partially saturated body, where an average pressure acts on the bulk and the mechanical response, i.e. deformation, is calculated based on these characteristics.

Independent of the origin of the pressure acting on the solid body, the magnitude can be derived from standard thermodynamics of the open pore system. i.e. by Gibbs free energy considerations. In the following a short introduction on this subject is given.

Referring to cement systems, the drying state is usually defined with respect to its degree of saturation, i.e. fully saturated or partially saturated. The degree of saturation can be determined from the desorption isotherm of the sample. As shown by Coussy [11, 13], an overall energy balance for drying can be derived referring exclusively to the desorption isotherm or saturation curve respectively, as is shown below.

In the case of a non-rigid porous media, the pore fluid causes a certain deformation of the solid skeleton by acting on the pore walls. Let Φ be the total porosity and S the saturation of a unit volume of the porous material. In the saturated state (S_w=1) the amount of pore water will be given by

$$v_{water} = \Phi_0 S_w \tag{21}$$

where

Φ_0: initial porosity [m³/m³]

S_w: liquid saturation

The total increase in free energy along a measured desorption isotherm can now be expressed as a function of initial porosity and liquid saturation. As introduced by Bangham [1-4] and also used by Setzer [6]; Hansen [8] and Coussy [11], an overall energy balance of the open drying porous system can be calculated from:

$$G(RH) = RT \int_1^{RH} \Phi_0 \cdot \frac{1 - S_w}{v_{m,w}} \cdot \frac{dRH}{RH} \tag{22}$$

In regard to the implementation of SRA into the drying process it is of high interest to link the liquid saturation to the interfacial area exposed. This can be easily done by combining equations (12) and (22). The imposed relative humidity determines the chemical potentials of the coexisting phases and the surface tension at the liquid/vapour interface determines the saturation of the pore space, reading:

$$dG = \Delta p \cdot \Phi_0 dS_w = \gamma \cdot da \tag{23}$$

or

$$dS_W = \frac{\gamma \cdot da}{\Phi_0 \cdot \Delta p} \tag{24}$$

At this point one does not discriminate between the origins of pressure. The denomination Δp stands for either capillary or disjoining pressure (compare (18) and (11)) and in the following Δp is referred to as moisture potential, following Scherer’s notation [15].

For a constant surface tension and Δp exclusively determined by the imposed relative humidity, one can calculate the interfacial area exposed to the liquid/vapour interface. Moreover, the energy U utilized in the creation of liquid/vapour interfaces can be linked to liquid saturation according to:

$$U(S_w) = \int_{S_w}^{1} \Delta p dS_w = \Delta p \cdot (1 - S_w) \tag{25}$$

where the middle term is taken from Coussy [11, 13] and extended by the right term describing the water loss as a function of actual saturation and moisture potential.

As previously stated, capillary pressure often is supposed to act similar to hydrostatic pressure. For partially saturated cementitious system, authors usually refer to the degree of liquid saturation to define an average fluid pressure $\overline{p}$, active over the whole cross sectional area or unit volume of the system.

$$\overline{p} = S_w \cdot \Delta p \tag{26}$$

where

$\overline{p}$: average pressure

Coussy et al. [13] emphasise that letting $\overline{p}$ play the role of an equivalent pore pressure ignores the tensile stresses acting along the interfaces and their subsequent effects on the deformation of solids. Therefore they introduce an equivalent pore pressure π containing both, the average fluid pressure and the stresses exerted by the interfaces reading:

$$\pi = -\overline{p} - U \tag{27}$$

Note that the negative sign of U is to account for the tensile character of the capillary or average fluid pressure respectively.

In Figure 1 the equivalent pore pressure π and both its contributions are plotted against the liquid saturation. The graph was built from the set of equations given by Coussy et al. [11, 13] but using a sorption isotherm obtained from a well hydrated cement paste measured in the course of this study.

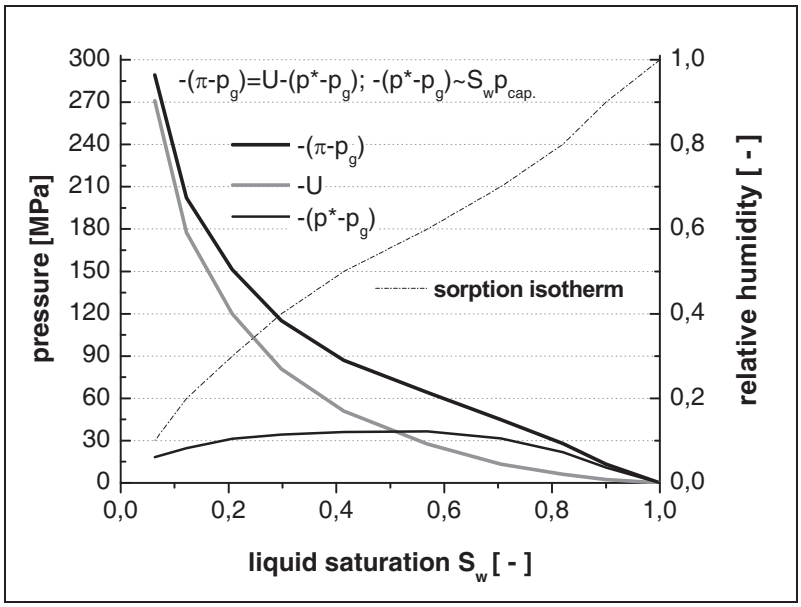

Figure 1: Contributions of average fluid pressure and surface energy to the equivalent pore pressure according Coussy [13], but constructed using a different sorption isotherm.

Figure 1 shows that the saturated porous body exposed to drying first experiences an increase of both contributions ($\overline{p}$, *U*) to the equivalent pore pressure. Due to the decrease in liquid saturation, the average fluid pressure decreases and, by definition, vanishes when liquid saturation reaches zero at the very dry boundary. Over the whole range of decreasing relative humidity, the work done in increasing the interfacial area increases. From 100% down to about 50% saturation, surface pressure is smaller than the capillary contribution. However, below that it increasingly exceeds the capillary contribution in magnitude.

Whereas this approach can distinguish between liquid and surface pressure, the following should be noted:

Referring to the set of equations given by Coussy et al. [11, 13] an slightly different approach can be followed that discriminates between hydrostatic liquid pressure and surface pressure. If equations (11), (25) and (26) are combined to express π more generally one obtains:

$$\pi = -\overline{p} - U = -(\Delta p S_w) - (\Delta p(1 - S_w) = -\Delta p \ = \frac{RT}{v_m} ln(RH) \qquad (28)$$

This demonstrates that Coussy just discriminated between two contributions to the overall moisture potential/stress, i.e. the accumulation of $\overline{p}$ and *U* returns that π is equivalent to the the moisture potential. The model itself brings up two main issues:

a) the question of the importance of capillary pressure and

b) the question of whether capillary pressure can still be applied for the low humidity range <50% RH

With respect to this, the literature on drying and shrinkage of cement paste presents several arguments on the importance of capillary pressure:

Ferraris et al. 1987 [19] take into account both, disjoining pressure and capillary forces. From surface separation measurements they could evaluate disjoining pressures and so were able to distinguish between repulsive forces due to changes in surface energy and disjoining pressure. They concluded that

a) Bangham’s law describes hygral length change up to about 40% RH

b) shrinkage due to disjoining pressure develops steadily from 100%RH to 40% RH

c) in case of swelling the disjoining pressure can not freely separate surfaces due to the constraint of the three dimensional coherent paste structure.

Beltzung et al. 2005 [9] investigated the dominant phenomenon for drying shrinkage. From surface separation experiments they concluded that disjoining pressure rather then capillary forces are the dominant mechanism for drying shrinkage above 50% RH. They additionally showed that the alkali content of cement pore solution increases hygral deformations, which they attributed to a decrease of disjoining pressure.

Based on the example given in Figure 1, Coussy´s model [11, 13] supports the idea that capillary pressure looses importance with decreasing humidity and that surface forces can be supposed to be the driving force for shrinkage. More specifically, referring to surface energy approaches as introduced by Bangham [1-4] and refined by Setzer [6] and Hansen [8] the presence of a coherent liquid phase below the bifurcation point of the sorption isotherm is more than questionable. Thereof, capillary pressure can not be active at such a low relative humidity.

3.1.5 Deformation upon drying induced pressure

Cementitious systems are known to show viscoelastic behaviour [22]. Drying shrinkage of cement paste can be discriminated into elastic and viscous deformation. These processes can be considered to decrease porosity only [10, 23] and leave the volume of the solid skeleton unaffected.
In the literature on drying cement paste, authors usually focus on the elastic properties. Moreover linear elastic approaches are usually applied. In the following a short derivation is outlined that exclusively deals with linear elastic properties of cement paste.

For a viscoelastic porous material a proper derivation of an energy balance is given by Coussy [23]. To implement viscoelasticity, the overall deformation has to be properly separated into an elastic and viscous fraction. For this it is important that during drying, the increase of excess Gibbs free energy is partly utilized in elastic deformation and that the rest is dissipated due to viscous deformation. Concerning cement paste, this viscous part is usually referred to as irreversible shrinkage (see subsection 3.3).

3.1.5.1 Non-rigid, deformable systems

We assume a non-rigid solid skeleton where the solid matter is incompressible so that the deformation of the skeleton decreases the pore space ($\Phi(d\varepsilon)$) only. Therefore, such deformations also impact the saturation S and exposed interfacial area $a_{liquid/vapour}$.
If the porous structure comprises ideally viscous property (bulk modulus K=O), evaporation of pore fluid causes a contraction of the solid skeleton while the system maintains full saturation. This means that water loss is compensated by an equivalent decrease in porosity Φ. Due to this; the porous system undergoes at least no increase of the area of the liquid/vapour interface. Moreover, most probably the liquid/vapour interfacial area decreases with overall volume reduction, so that $da \leq 0$).

A principal scheme indicating the change of pore space characteristic, i.e. saturation; porosity and interfacial area exposed at the liquid/vapour interface, is displayed in Figure 2. For sake of simplicity the change of the liquid/vapour interfacial area in Figure 2 is assumed to decrease with porosity. Furthermore it should be noted that the saturation S_W refers to the total porosity of the sample.

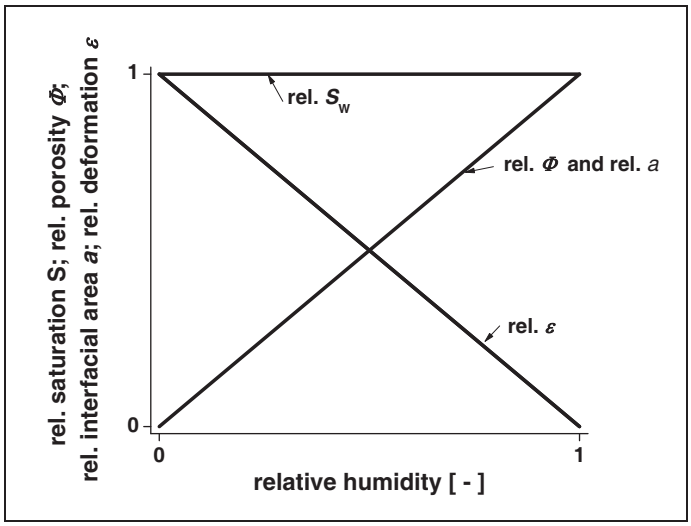

Figure 2: Schematic comparison of characteristic values of rigid/non-rigid porous matter subjected to drying - change of saturation; porosity and interfacial area for non rigid porous matter (*K*=0)

3.1.5.2 Non-deformable systems

The scheme given in Figure 3 shows that for infinite rigidity of the pore system, porosity remains constant during drying. This causes the saturation to decrease and the interfacial area of the liquid/vapour interface to increase. This comes from curved liquid interfaces and the wetting film at the pore walls.

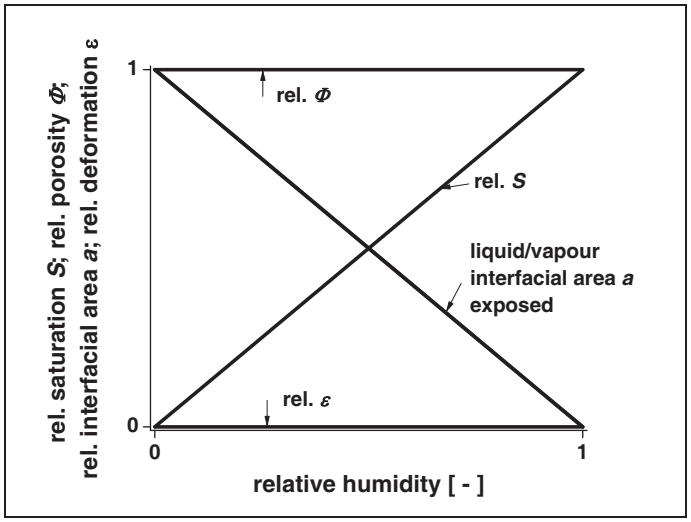

Figure 3: Schematic comparison of characteristic values of rigid/non-rigid porous matter subjected to drying - change of saturation; porosity and interfacial area for rigid porous matter (infinite K)

Figure 2 & Figure 3 point out the additive character of the Helmholtz free energy. Whilst free energy is utilised at the interfaces of rigid matter, the excess energy is dissipated by deforming the ideal viscous system.

3.1.5.3 Hygral deformation of cementitious material

As to cementitious materials, for non-rigid solid skeletons comprising a bulk modulus *K* the total free energy gained due to isothermal drying is utilized in creation of interface at the liquid/vapour interface and the deformation of the solid skeleton.

Coussy et al. 2004 [12] derived the following energy balance for partially saturated cementitious materials from standard thermodynamics of an open system:

$$\sigma d\varepsilon + \overline{p} d\varphi - \Phi p_{cap.} dS_w - d\Psi_S = 0 \tag{29}$$

and state equations reading:

$$\sigma = \frac{\partial \Psi_S}{\partial \varepsilon}; \overline{p} = \frac{\partial \Psi_S}{\partial \varphi}; \Phi p_{cap.} = \frac{\partial \Psi_S}{\partial S} \tag{30}$$

where $\partial \Psi_S$ stands for the Helmholtz free energy of the solid skeleton and the interfaces derived by removing the Helmholtz free energy of the fluid phase from the total Ψ according to:

$$\Psi_S = \Psi - n_w \mu_w - n_v \mu_v - n_a \mu_a \tag{31}$$

Substituting (27) into (29) the energy balance given by Coussy et al. reads:

$$\sigma d\varepsilon + \varphi d\pi - d\Psi_S = 0 \tag{32}$$

For an elastic porous body the volumetric strain ε is related to the volumetric mean stress σ and the fluid pore pressure p according to equations (33) and (34) [11]:

$$\varepsilon = \frac{\sigma + b \cdot p}{K} \tag{33}$$

$$b = 1 - \frac{K}{K_S} \tag{34}$$

where

b:	Biot coefficient
K:	bulk modulus of the porous matter
K_S:	bulk modulus of the solid part of the skeleton (matrix)

Assuming the absence of an external load and infinite K_S as well as substituting the fluid pressure by an equivalent pore pressure, we get [11, 13]:

$$d\varepsilon = \frac{b \cdot d\pi}{K} \tag{35}$$

Coussy et al. [11] successfully applied the concept of equivalent pore pressure for predicting the swelling of cellulose fibre composites down to 40% RH, but obtained disproportionally high deformations for relative humidity below that.

Other approaches relate the liquid saturation obtained from water vapour desorption isotherms to tensile stresses acting on the porous matter. Referring more or less to the Kelvin equation, they assess hypothetical pore space distributions. Within a given range of humidity, they relate the change of saturation to a change in capillary tension acting on the porous body [24].

For the response of the solid skeleton to capillary tension, the elastic properties of the cementitious skeleton are either described by the bulk modulus of the partially saturated porous material (Mackenzie1950 [25]; Granger 1997 [26] and Bentz 1998) or are treated as one dimensional property, where the Young’s modulus is used for calculating the systems deformation due to the action of the pore fluid [27-29].

For example Granger 1997 [26] proposes to use the following equation (36) for a humidity range above 50% RH.

$$\varepsilon_{shr} = \frac{\Phi \cdot S_w \cdot RT}{(1-\Phi) \cdot K_S \cdot v_m} \cdot ln\, RH \tag{36}$$

where

ε_{shr}:	linear deformation
S_W:	degree of saturation; ratio of actual volume of water to absolute pore volume
K_S:	bulk modulus of the material forming the skeleton

Comparing equation (36) and (11) / (28) / (35) one can see that Granger and Coussy account for similar average pressures but that the mechanical response of the solid is derived differently.

For the linear deformation of a partially saturated body, Bentz 1998 [24] proposed the following equation:

$$\varepsilon_{shr} = \frac{S_w \cdot p_{cap}}{3} \cdot \left(\frac{1}{K} + \frac{1}{K_S} \right) \tag{37}$$

The integer 3 accounts for the one-dimensional length change of the three-dimensional body, where only a third of the randomly distributed pores contribute to the considered dimensional change.

3.1.5.4 Summary

The different approaches to the drying and shrinkage of porous materials deliver expressions for the shrinkage strain where the saturation degree and sometimes the capillary pressure appear. For a fixed RH, SRAs can modify the first but not the second. This suggests that the SRA effects must be sought either in their effect on saturation or on disjoining pressure. However, given the high internal surface it is unlikely that SRA effect is to be found in a change of the disjoining pressure, at least in hydrated systems.

3.2 Impact of cement specificity on drying & shrinkage

3.2.1 Ionic strength of cement pore solution

The pore fluid of cementitious materials comprises a high ionic strength. According to Raoult’s law, the partial vapour pressure over cement pore solution is controlled by the activity of water.

$$p_{sat;solution} = a_{water} \cdot p_{sat,water} \tag{38}$$

where

$p_{sat;solution.}$:	water vapour saturation pressure over aqueous solution
$p_{sat;\,water}$:	water vapour saturation pressure over water
a_{water}:	activity of water in aqueous solution

The combination of Kelvin’s law and Raoult’s law leads to the so called Köhler-equation traditionally used for condensation phenomena in atmosphere science, aerosols etc. [30]. It was also applied by Lura 2003 [31] for the modeling of autogenous shrinkage of cement paste. For the afore mentioned cylindrical pore, the equilibrium relative humidity over a curved meniscus of an aqueous solution having a water activity a_{water} , is given by:

$$RH = a_{water} \cdot exp\left[-\frac{2\gamma \cos\alpha \cdot v_m}{r_{cyl.} \cdot RT} \right] \quad (39)$$

or more generally

$$RH = a_{water} \cdot exp\left[-\frac{\gamma da \cdot v_m}{dv \cdot RT} \right] \quad (40)$$

The activity of the water in pore solution decreases with increasing amount of dissolved salts. In equilibrium with an imposed relative humidity, the liquid saturation increases with decreasing water activity of the pore solution. This impacts the desorption isotherms or the saturation curves of cementitious materials. Concerning Coussy´s approach [11] for predicting shrinkage, we recognize that the activity of water impacts drying and shrinkage, however, this influence is covered by measuring sorption isotherms.

Concerning the impact of electrolyte concentration on the disjoining pressure, it can be said that it should decrease the thickness of double layers. This would reduce repulsion and mean that cementitious materials would be more subject to shrinkage. This would however not affect SRA performance.

Beltzung et al. [9] propose that the nature and concentration of dissolved cations in pore solution impacts disjoining pressure through ion hydration forces. This would explain that measurements of alkali enriched mortars indicated an increase of drying shrinkage with increasing monovalent ions in pore solution.

Concerning the interactions of SRAs in presence of electrolytes and in analogy to findings for non-ionic surfactants, the following can be taken into account (section 4.2.6):

a) According to Churaev [32] non-ionic surfactants weakly influence electrostatic interactions.

b) Concerning disjoining pressure a repulsive steric contribution from SRA can be thought of

Again, the question arises if the repulsive steric effect from SRA can be considered to reduce drying shrinkage.

3.2.2 Surface tension of cement pore solution

The calculation of capillary forces using the Kelvin-Laplace or the Köhler-equation usually accounts for the surface tension of plain water (γ_{SFT}~72.6mN/m). It is evident that cement pore solutions are strong electrolytes composed of ions of different valence and exhibiting high ionic strength and therefore comprise an increased surface tension compared to water.
The surface tension of electrolyte solutions increases with increasing concentration as shown by many authors (Langmuir 1917 [33]; Onsager et al. 1934 [34]; Jarvis et al. 1968 [35]; Ralston 1973 [36]; Aveyard et al. 1975/76 [37, 38]; Hey 1981 [39]; Stairs 1995 [40]; Weissenborn 1995/96 [41, 42] and Bostrom 2001 [43]).

The increase of surface tension at the liquid/solid interface was derived from the Gibbs-Duhem equation. For electrolytes, the excess surface concentration of ions at the liquid/vapour interface is decreased. Onsager et al. [34] proposed a first model involving electrostatic repulsion of ions at the interface due to the permittivity difference of water and air due to Coulomb image forces. The model was supposed to be a crude approximation up to a salt concentration of 0.2M. For more concentrated electrolytes an increase in surface tension can be observed, but its quantification is more delicate.

For quite a large number of electrolytes, Weissenborn et al. [42] could show that the increase of surface tension and the surface deficiency of electrolyte correlate very well with increasing electrolyte activity. The concentration dependant increase in surface tension furthermore depends on ion species

and increases with decreasing Debye-length (different salts); increasing entropy of hydration (cations) and increasing Jones-Dole viscosity coefficients (cations).

Bostrom [43] proposed a model where exclusively short range dispersion forces cause an increase of surface tension of electrolytes, thereby accounting for the specific ion effects in simple electrolytes.

Summarizing the results of surface tension studies in this subchapter an increase of surface tension in the range of 1 to 3mNm^{-1}mol^{-1}, dependent on the electrolyte composition, can be expected for cementitious systems. An increase of surface tension of the pore fluid increases the energy utilized for creating interfacial area at the liquid/vapour interface. Hence, for high electrolyte concentrations, the porous body experiences less desorption at an imposed relative humidity. Regarding Coussy´s model (3.1.4), the surface forces would decrease due to the electrolyte but the average capillary pressure would increase due to higher saturation. However, the magnitude of these changes is only small and can most probably be neglected.

For aqueous electrolyte solutions of non-ionic surfactants, Karaker et al. [44] developed a self-consistent model able to predict surface tensions of electrolyte solutions both with and without surfactant. This model handles high and low electrolyte concentrations (up to 4M potassium chloride solutions), significantly larger than the range of concentrations where the limiting law of Onsager applies. In principal, this makes it possible to calculate actual surface tensions of cement pore solution.

3.2.3 The microstructure of cement paste

The main structure-forming hydration phase in Portland cements is calcium-silicate-hydrate (C-S-H). Thomas and Jennings [45] came up with a structural model of C-S-H gel where the C-S-H phases precipitate in basic building blocks flocculating into clusters or globules with a unit diameter of about 2.5 nm [46]. They distinguish two different types of C-S-H, one with higher density (HD-C-S-H) comprising a denser packing of flocculated C-S-H globules and a lower density C-S-H (LD-CSH) where flocculated globules enclose a higher amount of pore fluid.
Environmental scanning electron microscopy revealed [47], that the microstructure of precipitated C-S-H in hydrated Portland cement can rather be compared with a haystack (Figure 4) enclosing other hydrates and unhydrated cement phases (Figure 5) as well as aggregates in case mortar or concrete are referred to. (Pictures taken from and provided by Roessler 2006 [47])

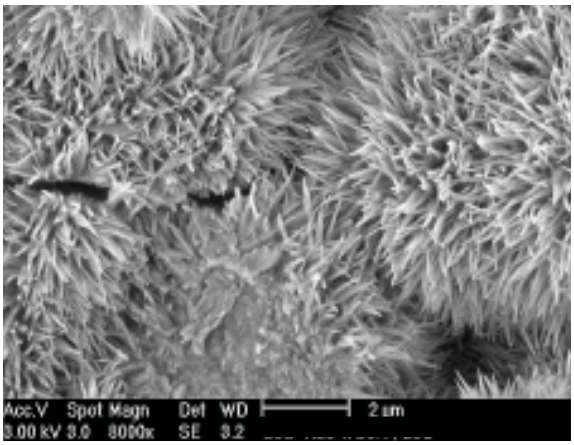

Figure 4: C-S-H after 28d of hydration from [47]

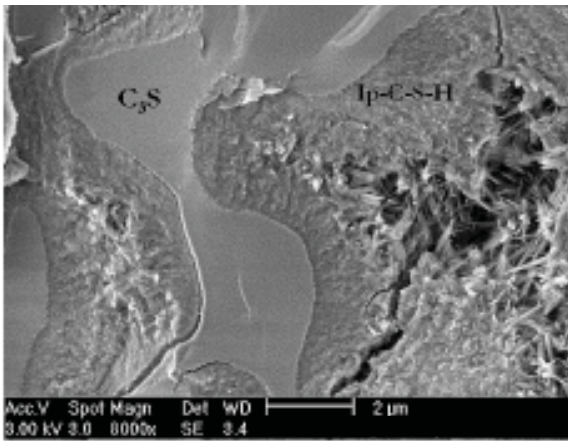

Figure 5: C-S-H around unhydrated C_3S from [47]

The microstructure of hydrated cement comprises a high specific surface area (SSA). Powers [48, 49] accounts for specific surface areas in the range of 200-300m²/g of dry hardened paste. Thomas et al. [50], comparing different techniques of surface measurement, report a SSA for dry hardened paste in the range of 200-600m²/g measured by small angle X-ray scattering, 70-150m²/g for small angle neutron scattering and 50m²/g (nitrogen) -200m²/g (H_2O) based on BET measurements using different

sportive gases. Because of this high internal surface area, cement paste is usually described and treated as a gel or, if it is dried, a xerogel respectively, although the “gel”-terminology is debated [51].

3.2.3.1 Formation of water adsorption layers

From water vapour adsorption isotherms of porous materials it determined that within the first, low humidity part of adsorption, a water mono layer is formed. With increasing relative humidity the statistical thickness increases and water is adsorbed in multi-layers. Based on measurements on various types of hydrated cement, Badmann, Stockhausen and Setzer 1981 [18] provided a general equation for the statistical water layer thickness ***t*** as a function of humidity:

$$t(RH) = 0.385 - 0.189\,ln(-ln(RH)) \tag{41}$$

where

t: statistical water layer thickness [nm]

Bentz et al. [24] modified (41) and applied:

$$t(RH) = 0.584 - 0.189\,ln(-ln(RH)) \tag{42}$$

for approximating absolute values of surface energy with the purpose of modeling drying shrinkage of reconstructed porous materials.

Above certain humidity, i.e. 45% to 50% RH for cementitious material, the adsorbed water volume disproportionally increases due to capillary condensation. The reverse is true for desorption. Indeed, the menisci formed by water are reported to break down within the mentioned range of humidity (Powers 1965 [52]), which corresponds to the bifurcation point of desorption and adsorption isotherms [53]. After this and because of the absence of capillary pressure, cement paste would be expected to expand. On the contrary, a steady shrinkage is observed for hydrated cement pastes and mortar as humidity continues to decrease [54, 55].

Fisher et al. [53, 56, 57] revealed that the actual surface tensions for small menisci are substantially lower than predicted by the macroscopic Kelvin-Laplace equation. From adhesion measurements between mica surfaces they found that hydrocarbon liquids can form menisci down to gap widths of one or two molecular diameters whereas for water a minimum of 10 -15 molecular diameters (r_m=5nm) are necessary before bulk thermodynamics are recovered. Contrary to a sharp breaking point, for gaps in the range of a few molecular diameters (water), they suggest that water menisci can exist but that surface tension is significantly decreased [53, 56]. The pressures in the low humidity range do therefore probably not disappear but are complex to quantify.

Another issue of concern is the assumed pore geometry. The images given in Figure 4 and Figure 5 are suggestive of how questionable the use of simplified models as cylindrical or slit shaped pore distributions might be for modeling of hygral deformations. As mentioned above, macroscopic thermodynamic approaches were however set up trying to overcome the dependencies on pore shape in particular.

Setzer [7] used water vapour sorption isotherms and could prove the applicability of Bangham’s law for hydrated cement paste in the humidity range of up to about 50% RH. This approach exclusively refers to the linear correlation between changes of free surface energy and length change. For the change in free energy per gram of cement paste Setzer gives:

$$\Delta\gamma_{SFE} = \frac{R \cdot T}{v_m} \int_{p_0}^{p} \left[\int_{(p')}^{(p_0)} a(p)dt(p) \right] \cdot d\,ln\left(\frac{p}{p_0}\right) \tag{43}$$

where

$\Delta\gamma_{SFE}$:	change in free surface energy (here referring to weight [J/g])
a:	internal surface area free for adsorption [m²/g]
t:	water layer thickness [m]

Note that *a(p)* denominates the internal surface area available for ad-/desorption of water at a given saturation state. At the very dry boundary this interfacial area can be related to the total specific surface. However, it seems that for overlapping adsorption layers and at least at the starting points of capillary condensation, this interfacial area must decrease drastically. As explicitly pointed out by the author, the approach can be applied for low humidity only.

Once capillary condensation starts, a fraction of the solid/adsorbed water interface is covered by condensed bulk water. Then, additionally the liquid/vapour interface has to be taken into account. Due to the nanoscopic microstructure of hydrated cement paste quantification is complex.

The new model for drying shrinkage recently introduced by Setzer [10] (see section 3.1.3) overcomes this issue. Over the whole range of relative humidity, the disjoining pressure in the air filled pores is proposed to cause shrinkage. Although Setzer explicitly mentions that for the low humidity range the interpretation of mechanisms is different, the results of the calculation, i.e. the linear correlation between deformation and changes in surface energy, remain valid.

Unfortunately, both appoaches based on interfacial area and on disjoining pressure have shortcomings in terms of quantification. In the first case this is due to the lack of proper quantification of the area of these interfaces. In the second case it is the estimate of equilibrium distances between solid surfaces in cement paste that poses problem.

Hansen 1987 [8] investigated drying mechanisms of cement paste using changes of free energy over the whole humidity range. For the change of free energy between two discrete points of relative humidity (RH_1 and RH_2) he postulates that:

$$\Delta\gamma_{SFE} = \frac{R \cdot T}{v_m} \int_{RH_1}^{RH_2} \frac{v_l}{a_{BET}} \cdot d\,ln(RH) \tag{44}$$

where

$\Delta\gamma_{SFE}$:	change in free surface energy [J/m²]
v_l:	volume of adsorbed liquid
a_{BET}:	internal surface area; N_2-BET

Note that Hansen exclusively referred to the *t*-curve developed by Cranston & Inkley in 1957 [58] for nitrogen adsorption. Despite the more or less questionable application of nitrogen *t*-curve for water vapour ad-/ desorption the approach returns a linear correlation between free surface energy and linear shrinkage strain for low humidity. However, it fails to return proper mechanical properties that are consistent with the shrinkage deformation measured.
Additionally the shrinkage deformations measured in the capillary range of the desorption isotherm were higher than predicted. Nevertheless, the results of Hansen [8] imply that shrinkage deformation comprises two contributions, the first one related to internal surface of cement paste and the second one occurring with the onset of capillary condensation. Hansen [8] however failed to implement the latter into his model. Comparing this approach to the set of equations given by Coussy [11] reveals that

indeed, the excess shrinkage deformation might have been captured (compare to 3.1.4). In contrast, whereas Coussy [11] overestimated shrinkage deformation below the onset of capillary condensation, Hansen achieved reasonable results in this particular range.

Summarizing the findings for shrinkage mechanisms related to microstructure of hydrated cement paste it can be said that thermodynamics of the drying open system have been applied to deformation predictions. So far the approaches try to overcome issues related to microstructure by applying *t*-curves obtained from measurements on even half planes. Microstructural models of cement paste indicate that due to the overlapping of adsorption layers and capillary condensation, the internal surface free for ad-/desorption must change with the degree of saturation but this has not yet been properly quantified. Due to this, the description of the drying progress based on changes of free energy of the interfaces (liquid/vapour and liquid/solid interfacial area) should probably still be seen as a rough approximation. For the purpose of this study, the evaluation of a model in which the SRA characteristics can be implemented is the subject of section 5.

3.3 Irreversible shrinkage of cement paste

Drying shrinkage of cement pastes incorporates two components, a reversible elastic part and an irreversible part, resulting from the viscoelastic character of hydrated cement. The so-called irreversible shrinkage of cement paste is the final length or volume change after the specimen has been dried and resaturated.

Roper 1966 [54] measured shrinkage isotherms of cement pastes and revealed irreversible shrinkage within cyclic drying and rewetting. Powers 1968 [5] reported that irreversible shrinkage already was described at the beginning of the 20th century. Mindess et al.1978 [59] and Bentur et al. [60, 61] studied irreversible shrinkage and creep deformation of C-S-H gel made from C_3S and blends of C_3S/ C_2S. They found that the irreversible part of the deformation is caused by microstructural changes of the C-S-H gel. From nitrogen adsorption measurements they identified a decrease of nitrogen accessible surface and related this to a densification of the gel structure accompanied by an enhanced polymerisation of the C-S-H phases. From their experiments it appears that elastic shrinkage is subsequently accompanied by irreversible deformation.
According to the C-S-H model of Jennings et al. [45, 46, 50, 62-67], drying of C-S-H gel involves phenomena similar to the ageing of gels, i.e. the enhanced polymerisation of C-S-H and irreversible shrinkage, which in this case is attributed to the collapse of LD-C-S-H.

The drying induced irreversible change of the C-S-H microstructure changes the overall pore size distribution depending on the type of constraint. This can come from unhydrated clinker particles or aggregates in case of mortar and concrete. In other words, if bulk shrinkage is hindered due to self restraint, the densification of LD C-S-H has to result in a coarsening of some of the pores.

For normal vibrated concrete, comprising a relatively high volume ratio of aggregate to cement paste, this phenomenon can be assumed to have a higher impact than for self consolidating mixtures.

Regarding standard thermodynamics, one has to take into account that irreversible shrinkage causes the drying porous system to relax. A certain amount of energy is dissipated by viscous deformation [23] and does not develop stress in the material.

Concerning the model proposed by Setzer [10], the question arises on the origin of LD C-S-H collapsing in the course of drying. Setzer suggests that the average distance *h* between surfaces would be just weakly influenced because the attractive disjoining pressure exclusively acts in empty pores. Therefore, if the collapsing is due to removal of interlayer water of LD C-S-H while keeping this space saturated, the effect on the driving force for shrinkage ought to be minor.

This can be the case as the pore sizes attributed to C-S-H are small and can be supposed to remain saturated until achieving very low humidity.

3.4 Impact of SRA on drying shrinkage

Regarding the working mechanism of SRA most authors [27-29, 68-71] refer to the decrease of capillary tension of the pore fluid acting on the porous body.
Sato [29] and Shoya [27] used the Kelvin-Laplace approach for cylindrical pores to model shrinkage of hydrated cement paste. Without considerations for adsorbed water layers or decreased activity of water in pore solutions, they determined linear correlations between shrinkage reduction and reduction of surface tension of aqueous solutions of the SRA used. For a humidity range from 10% RH or 20% RH up to 90% RH, they found that the moisture loss of SRA treated samples is systematically slightly higher than the untreated reference. These findings are in line with other studies showing similar results [68, 72]. Other authors [73-77] found however no effect of SRAs on weight loss.

The literature search done in this study revealed that drying shrinkage models incorporating surface activity of SRA explicitly refer to Kelvin-Laplace equation assuming cylindrical pore shapes.

So far a suitable approach for implementing SRAs into recent models for drying shrinkage could therefore not be found.

3.5 Summary

The state of the art review on drying and shrinkage of cement paste revealed the following main findings:

a) The drying and shrinkage of porous cementitious systems can be described using standard thermodynamics. The porous system can be treated as an open system exchanging water vapour and gas with its environment.

b) The forces induced upon drying can be derived from the excess Gibbs free energy independent of their origins.

c) Generally, the approaches discriminate between capillary forces acting similar to hydrostatic pressure and attractive contributions of disjoining pressure acting upon overlapping force fields.

d) Recent models for drying shrinkage indicate the importance of surface forces for shrinkage in the course of drying. Whereas Setzer [10] explicitly refers to disjoining pressure acting via overlapping force fields in empty pores, Coussy [11] indeterminately refers to surface forces acting along the surfaces.

e) Following Coussy´s [11] set of equations the concept of average pore pressure can be applied independent of nature of the force assumed to act on the solid porous body.

f) For low humidity Bangham’s law still is supposed to be valid and a linear relationship between changes of surface energy and length change can be found.

g) Modeling approaches for drying shrinkage mainly refer to linear elasticity of cement paste.

h) The impact of SRA on drying shrinkage still lacks a satisfying explanation. Up to now, authors exclusively refer to changes in capillary forces that, for severe reasons, can be supposed to be insufficient.

The above points imply that the following questions remain open:

1) What specific chemical behaviour of SRAs in cement paste can modify drying and shrinkage of cementitious material?

2) How to implement these specific SRA characteristics into models for shrinkage prediction?

The first question is dealt with in the next chapter, where the state of the art knowledge of SRA is reviewed. Concerning the second, this is the subject of chapter 5, in which the SRA nature and its impact on drying and shrinkage is considered from a theoretical point of view.

4 State of the art “Shrinkage Reducing Admixture (SRA)”

4.1 General introduction

Arguing about working mechanisms and material characterisation of shrinkage reducing admixtures authors usually refer to the “capillary force” shrinkage model. Within this simplifying model the formation of menisci in pores generates capillary forces pulling together the pore walls of the drying body, causing contraction or shrinkage deformation respectively.

Shrinkage reducing admixtures are composed of organic surfactants that decrease the surface tension of pore solution. With respect to the “capillary force” shrinkage model, a decrease of surface tension is supposed to decrease capillary forces acting on the porous body, which then would reduce drying shrinkage.

SRA were introduced in a study by Sato et al. in 1983 [29], in which shrinkage reduction due to SRA was suggested to come from a reduced surface tension of the cement pore solution. There, the capillary force approach was explicitly referred to and, indeed, a more or less good correlation between shrinkage reduction, SRA dosage in cement paste and the SRA concentration dependence of surface tension of aqueous solutions of SRA was obtained. Moreover, well before SRA were introduced in 1983 [29], already in 1965 Ostrikov et al.[78] obtained similar results with shrinkage of cement paste, subjected to solvent replacement prior to drying. Actually this study focused on the mechanism of drying shrinkage rather than on shrinkage reduction of concrete. By coincidence however, it revealed some very interesting results. Ostrikov tried to eliminate capillary forces by osmotically replacing the pore solution by several organic liquids with substantially lower surface tension. With hexan, that comprises a surface tension of about 25% compared to water (γ_{hexane} ~18mN/m, γ_{water} ~73mN/m), drying shrinkage deformation surprisingly was reduced to about 25% also. It is however not clear if this proportionality between the reduction of surface tension of the pore fluid and the reduction of drying shrinkage deformation is or not of broader relevance.

As to the nature of SRAs, a patent search on materials used as shrinkage reducing admixtures has been conducted and is presented in annex (A1). It reveals that two main groups of admixtures can be discriminated:

1. SRA containing one type of non-ionic surfactants
2. SRA containing mixtures of non-ionic surfactants

This non-ionic nature probably comes from the need to prevent the products from adsorbing onto cement phases. Furthermore, several SRAs may comprise additional components like dispersing agents, accelerators and/or air entrainers, which indicate that the surfactants may influence hydration as well as mechanical performance of cementitious material.

The non-ionic surfactants used in SRAs can be classified as:

a) monoalcohols, incorporating linear, branched and cyclic types,

b) glycols, incorporating alkandiols and oxyalkylene glycols,

c) alkylether oxyalkylene glycols, comprising a linear “hydrophobic tail – hydrophilic head” structure,

d) polymeric surfactants configured as dimeric, trimeric or multi-headed surfactants as well as grafted polymers having “hydrophilic head” side chains and hydrophobic spacer units.

Regarding mixtures of surfactants, it is explicitly pointed out that there is a synergistic effect that enhances drying shrinkage reduction [79-83].

It is important to note that the molecular design of several surfactants claimed as shrinkage reducing admixture limits their applicability in mortar and concrete. On the one hand some materials turn out to be too expensive to be used in concrete [79-82]. Other components have to be excluded from applica-

tion because their low molecular weight causes issues regarding low saturation vapour pressure (high-explosive) and/or low flaming points [79-81].
Several other important material characteristics concerning the use of surfactants in cementitious systems as well as basic working mechanisms should be derivable from the general knowledge on non-ionic surfactants. The broad spread of the non-ionic surfactant nature justifies a special examination of the properties of surfactant molecules. This is the objective of the next section. There the surface activity and self association are also discussed, i.e. the formation of micelles, which are essential properties of such molecules. In what follows possible implications concerning cementitious hydrated matter are lined out in bold characters.

4.2 Properties of non-ionic surfactants

4.2.1 General introduction

Surfactants constitute a variety of chemical substances that modify the surfaces or interfaces of the systems in which they are contained. Surfactant molecules traditionally comprise a non-polar hydrocarbon chain, the so called “hydrophobic tail”, and a polar functional group, the so called “hydrophilic head”. Because of their amphiphilic nature, surfactants show a strong affinity to adsorb onto liquid/liquid, liquid/solid interfaces or liquid/gas surfaces respectively. A simple scheme of a surfactant molecule is given in Figure 6.

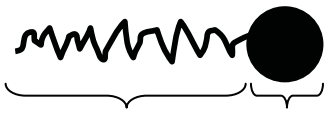

Figure 6: Schematic scetch of a surfactant molecule

The classification of surfactants follows the constitution of their hydrophilic heads. For non-ionic surfactants the simplest head would be the hydroxyl radical of a monoalcohol, but traditionally it consists of a poly-oxyalkylene chain. More complicated structures of surfactants were developed over time. Linear multiple head adducts or two-, three-headed configurations with branched or crossed tails can be found within the group of low molecular mass surfactants.
New generations of surfactants are the so called polymeric and oligomeric surfactants. Polymeric surfactants consist of amphiphilic block or graft copolymers. As to oligomeric surfactants, they are composed by tying (n-) linear surfactants (the oligomers) by hydrophobic (n-1) spacer-groups, resulting in dimers (n=2), trimers (n=3) etc. or poly-oligomers respectively. Both, polymeric and oligomeric surfactants provide a wide range of molecular architectures, enabling a tailoring to the systems in which they are supposed to perform [84].

4.2.2 Surface activity

Concerning drying and shrinkage of cement paste, the hygral properties of these nanoscopic systems are mainly determined by the properties of their interfaces. Therefore it is of high interest how these interfaces are impacted by the presence of non-ionic surfactants. In what follows a short excourse on the surface activity of non-ionic surfactants at the liquid/vapour interface of their aqueous solutions is given. For this type of interface, the surface activity of non-ionic surfactants refers to their ability to reduce the surface tension of the solvent in which they are contained. We start our examination focussing on the surface tension of water.

4.2.2.1 Surface tension of water

In addition to van der Waals forces water molecules interact through hydrogen bonds (due to strong dipole moments) forming a loose three-dimensional network. Molecules at the water surface cannot achieve the same level of molecular interactions as those in the bulk and therefore have an energy

excess. A consequence of this is, that to minimize the overall energy of the system, the liquid squeezes itself together to minimize surface area. An important term in that process is the “surface tension” (γ_{SFT} [J/m²; N/m]) that describes the energy per unit area required to expand the liquids surface. For water that is a very cohesive liquid, the surface tension is relatively high and about 72.6mN/m (or mJ/m²) at T=20°C.

4.2.2.2 Surface activity of non-ionic surfactants

Aqueous solutions of non-ionic surfactants exhibit a decreased surface tension. Hydrocarbon surfactants can reduce the surface tension down to about 30mN/m and fluorocarbon surfactants to about 20mN/m [85-87].

In the capillary force model, the impact of SRA on drying shrinkage would result from the reduction of surface tension at the water/air interface [27-29, 68-71]**.**
The same is expected to hold in cementitious materials. Therefore it is of high interest to know how non-ionic surfactants act in general and might impact interfacial properties of cementitious matter.

Due to their amphiphilic nature, surfactants adsorb at the water/air interface with the hydrophilic head pointed towards the water and the hydrophobic tail pointed towards the air. This adsorption behaviour can be described with the Gibbs adsorption isotherm [86, 87]. Moreover, using the Gibbs-Duhem equation (45) it is possible to obtain a definition of the surface tension or interfacial tension respectively [86].

$$dG^{\sigma} = -S^{\sigma}dT + ad\gamma + \gamma da + \sum n_i d\mu_i \tag{45}$$

where:

G^{σ}	surface free energy
S^{σ}	entropy
T	absolute temperature
a	area of interface
n_i	number of moles of component i
μ_i	chemical potential of component i at the interface

The interfacial tension at constant temperature and without adsorption is therefore defined by (46).

$$\gamma = \left(\frac{\partial G^{\sigma}}{\partial a} \right)_{T,n_i} \quad [\text{J/m}^2] \tag{46}$$

Gibbs derived a thermodynamic relationship between the interfacial tension γ and the excess surface adsorption Γ [mol/m²], the number of moles adsorbed per unit area. At constant temperature and fixed interfacial area, the condition of equilibrium in the presence of adsorption in equation (45) reduces to

$$d\gamma = -\sum \frac{n_i^{\sigma}}{a_i} d\mu_i = -\sum \Gamma_i \, d\mu_i \tag{47}$$

where:

Γ_i	excess surface concentration

For aqueous solutions of a single surfactant, equation (47) can be written as

$$-d\gamma = \sum \Gamma_1^{\sigma}\, d\mu_1 + \sum \Gamma_2^{\sigma}\, d\mu_2 \tag{48}$$

where integer i=1 denominates water and i=2 the surface active agent.

If the Gibbs dividing surface is used, where $\Gamma_{1,2}$ is the relative adsorption of surfactant (i=2) with respect to water (i=1) so that Γ_1= 0, then (49)

$$-d\gamma = \Gamma_{1,2}^{\sigma} d\mu_2 \tag{49}$$

Since,

$$\mu_2 = \mu_2^o + RT\, ln\, a_2^L \tag{50}$$

or,

$$d\mu_2 = RT d\, ln\, a_2^L \tag{51}$$

then,

$$-d\gamma = \Gamma_{1,2}^{\sigma} RT d\, ln\, a_2^L \tag{52}$$

or

$$\Gamma_{1,2}^{\sigma} = -\frac{1}{RT}\left(\frac{d\gamma}{d\, ln\, a_2^L}\right) \tag{53}$$

where:

a_2^L activity of the surfactant in bulk solution equal to C_2f_2 or x_2f_2; C_2 being the concentration of surfactant in bulk solution; x_2 the mole fraction of surfactant in bulk solution and f_2 the activity coefficient

R gas constant; R= 8.31 $Jmol^{-1}K^{-1}$

While activities and concentrations must be clearly distinguished, the derivative of the natural log of activity is much less affected by non-ideality. Therefore it is common to replace activity by concentration in the above expression.

$$d\, ln\, a_2 = \frac{da_2}{a_2} = \frac{c_2 df_2 + f_2 dc_2}{f_2 c_2} \cong \frac{dc_2}{c_2} \cong d\, ln\, c_2 \tag{54}$$

For aqueous solutions of surfactants the plot of surface tension versus the surfactants bulk concentration generally follows the scheme given in Figure 7.

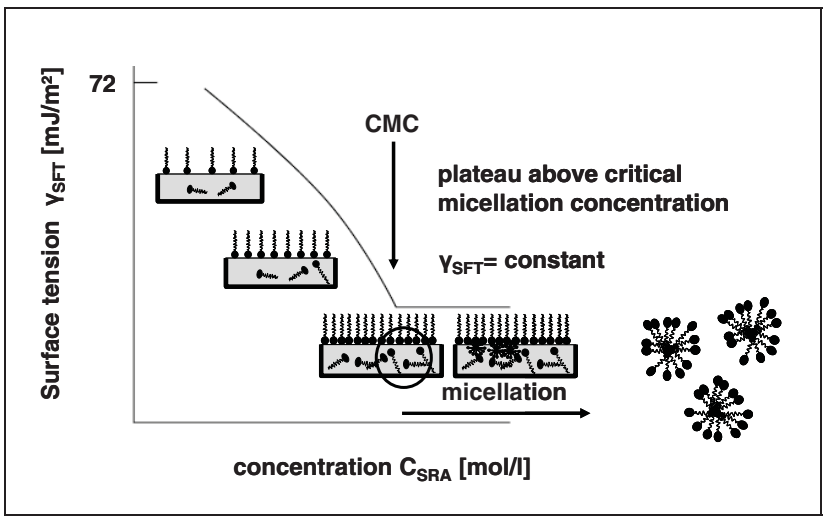

Figure 7: Surface tension of aqueous solutions of surfactant vs. bulk concentration of surfactant

With increasing bulk concentration, more surfactant molecules adsorb at the water/air interface and decrease the surface tension of the aqueous solution (52). This enables the system to reduce its free energy. At a critical bulk concentration, Figure 7 shows a sharp breaking point for the reduction of surface tension. Above this point, the surface tension virtually remains constant (55).

$$\left(\frac{\partial\gamma}{\partial ln c_2}\right) = 0 \text{ ; for } C_2 > \text{CMC} \qquad (55)$$

This break point is explained by a stop to the surfactant enrichment at the liquid/vapour interface. The reason for this is that above this specific bulk concentration there is a self-association of surfactant molecules to form micelles in the bulk. The surfactant bulk concentration at the break point is defined as Critical Micellation Concentration (CMC).

Regarding SRAs in cementitious materials, the decrease of surface tension is limited by the CMC. Moreover, in the course of hydration a fraction of mixing water is chemically bound into hydrates causing the bulk concentration of SRA to increase. At a certain degree of hydration the SRA concentration in the pore solution may exceed the CMC, defacto putting a limit to shrinkage reduction.
It is therefore of high interest to describe association and self-aggregation of non-ionic surfactants in cementitious materials.

This is done in the next sections. In particular, such phenomena are related to strong electrolytes which can be assumed to affect SRA in cement pore solution.

4.2.3 Association and self-aggregation of non-ionic surfactants in aqueous solution

At low bulk concentrations, surfactant molecules are first found as single molecules. Above the CMC they assemble into micelles, which are spontaneously formed clusters. The shape and size of the micelles are governed by geometric and energetic parameters.
The simplest cluster is a spherical micelle, formed by the assembly of the hydrophobic segments into an “oil-like” core with the hydrophilic heads in close proximity, forming the outer shell of the sphere.

4.2.3.1 The assembly of amphiphiles

Above the CMC this process is a mainly entropy driven [84-89]. Furthermore, the free energy of micellation ($\Delta G^{o}_{micellation}$) remains almost constant over a wide range of temperatures, which may seem surprising for an entropy driven process. The reason for this is not yet settled. The entropy increase upon micellation is indeed explained in two ways [86, 87].

a) Water entropy gain due to hydrophobic bonding:
   By forming micelles the hydrophobic tails of surfactant molecules assemble into the oil like cores and release water, previously structured around the hydrophobic segments. The system gains entropy because of the increased freedom of motion of these water molecules.

b) Surfactant entropy gain:
   The other view is to state that the hydrophobic chains of the surfactants increase their freedom in the non-polar core of the micelle. The entropy gain is therefore supposed to be due to fewer restrictions for orientations and bending of the organic chains.

4.2.3.2 The self assembly of micelles into liquid crystalline structures

The interactions between spherical micelles are repulsive [84]. With increasing surfactant concentration, the number of micelles increases. At a certain point the only way to reduce their mutual repulsion is to change the size and shape of these spherical micelles into geometries that provide a higher de-

gree of packing. For aqueous solutions of non-ionic surfactants above the CMC, the following mesophases or lyotropic liquid crystals can be observed [84-87, 90]:

a) cubic phase (abbreviation I_1), body centred, close packing of short prolate micelles

b) hexagonal phase (abbreviation H_1), close packed rod-like or worm-like cylindrical micelles

c) bi-continuous cubic phases (abbreviation V_1); three dimensional coherent structure

d) lamellar phase (abbreviation L); two dimensional bi-layers of water and surfactant

These transient networks can exhibit static properties comparable to semi-dilute polymer solutions [91]. For very high concentrations of surfactants in water or rather low concentrations of water in surfactant, micelles and mesophases form reverse. This leads to a separation between a water rich and a surfactant rich phase, where reversed micelles comprise water filled cores with the hydrophilic heads pointed towards the core and the hydrophobic tails pointed outwards.

Mesophases or liquid crystalline phases exhibit intermediate properties between liquid and solid structures and have at least one dimension of higher order. Some of these phases are detectable via X-ray diffraction, polarisation and electron microscopy [90].

An example of a binary phase between a surfactant and water is shown in Figure 8 (from [86]). The line between the domain of the solution and the micellar phase denotes the CMC temperature dependence.

As an illustration of the system behaviour, we note that one would observe various regimes as the temperature and bulk concentration of the surfactant is increased. One would pass from an isotropic micellar solution, to a hexagonal phase, to a bicontinuous phase, to a lamellar phase and finally to an isotropic reverse micellar solution.

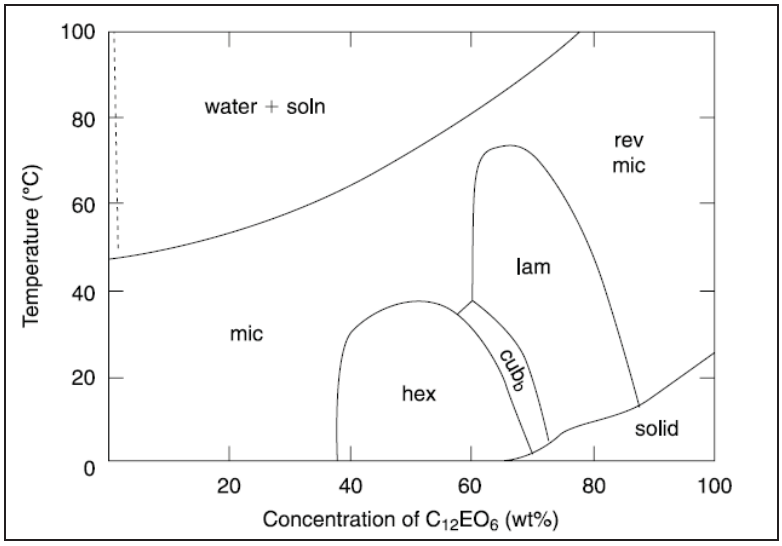

Figure 8: Binary phase diagram for dodecyl hexaoxyethylene glycol monoether–water mixture; from [86]

Legend:

soln:	Solution
mic:	micelles
hex:	hexagonal
cub:	cubic
lam:	lamellar
rev mic:	reverse micelles

Another important temperature dependent phenomenon can be pointed out. Above a certain temperature, often referred to as the “cloud point”, the isotropic micellar solution becomes turbid or cloudy and separates into two liquid layers, a phase rich in water (denom.: “water” in Figure 8) and a phase rich in surfactant (denom.: “soln.” in Figure 8). The separation of the two phases occurs because of the differences in density. This temperature is defined as the Lower Critical Temperature (LCT). The discontinuous line in Figure 8 that divides the two-phase (liquid/liquid) region from the isotropic micellar solution may be defined as the lower cloud point curve [86] or lower consolute boundary [92]. This cloud point or phase separation depends on temperature and bulk concentration of the surfactant. Depending on the molecular structure one can find closed miscibility gaps for non-ionic surfactants. This means that above a certain temperature the two liquid phases recover total miscibility due to increased entropy of the system.

The mechanism that underlies this phenomena is supposed to be driven by a very sensitive balance between attractive (enthalpic) and repulsive (entropic) interactions between micelles. Regarding these interactions, Tadros [86] summarizes two detailed studies on polyethylene oxide [93, 94] as follows:

At low temperatures and concentrations the micelle interactions are repulsive due to an enthalpic contribution. Then, depending on temperature and concentration various scenarios may develop:

Scenario 1: For low temperature and increasing bulk concentration the entropy term causes the formation of liquid crystals or mesophases. (Referring to Figure 8 this would be a horizontal line along increasing bulk concentration.)
Scenario 2: For rising temperature, the hydrophilic chains become less hydrophilic [94] and the repulsive enthalpic contribution decreases. (Referring to Figure 8 this scenario would follow a vertical line along temperature rise.). For example, a temperature rise can cause a micellar isotropic solution to turn into a solution of monomers.
Scenario 3: The phase separation at the LCT is due to an entropy gain that exceeds both, the enthalpic contribution and the loss in entropy due to the higher surfactant concentration in the more concentrated phase.
Scenario 4: With increasing temperature the entropy of mixing gains importance and the miscibility gap is closed.

The LCT or the miscibility gap depends on the molecular architecture of the surfactant. For a given hydrophobic tail the LCT increases with increasing hydrophilic chain length of the surfactant [95]. With decreasing length of the hydrophobic tail the LCT also increases, additionally widening the concentration range for the miscibility gap [86, 96].

4.2.3.3 Summary

The phase transitions of non-ionic surfactants in aqueous solution depend on three major parameters a) molecular structure, i.e. the ratio between length of hydrophobic tail and hydrophilic head group, b) temperature and c) bulk concentration of the surfactant. Studies on non-ionic surfactants mainly focus on molecules with high molecular weight, high if compared to the compounds that are claimed within the patents on SRA (see annex A1).

However, there is a strong indication that in cementitious systems, with temperature changes or drying, SRAs may exhibit phase transitions that influence their performance. In the next section the impact of electrolytes is specially examined because they are likely to enhance this behaviour in cementitious systems.

4.2.4 Association and self-aggregation of non-ionic surfactants in electrolyte solution

For non-ionic surfactants in electrolyte solutions the phenomenon of self-aggregation can be observed [92, 95, 97-101]. On the one hand there is a “salting-in” effect that promotes solubilisation or miscibility of the surfactant in aqueous electrolyte solution. On the other hand there is a “salting-out” effect that decreases critical micellation concentration and lowers the consolute boundary (phase separation-liquid/liquid). This increases the liquid-liquid miscibility gap or enhances self-organisation into mesophases or lyotropic liquid crystals respectively (see 4.2.3).

The terms salting-out and salting-in often refer to the work of Hofmeister 1888 [102, 103], i.e. the so-called Hofmeister series or lyotropic series. This relates the ability of ions to increase (“salting-in”) or decrease the solubility of a protein in water (“salting-out”). The Hofmeister series orders anions with increasing salting-in effect as:

$$SO_4^{2-} > HPO_4^{-} > OH^{-} > F^{-} > HCOO^{-} > CH_3OO^{-} > Cl^{-} > Br^{-} > NO_3^{-} > I^{-} > SCN^{-} > ClO_4^{-}$$

salting –out ***salting-in***

water structure makers *water structure breakers*

Ions left of Cl^{-} are called cosmotropic or water structure makers and promote the salting-out. The other ions are called chaotropic or water structure breakers and increase the solubility of proteins in water.

4.2.4.1 The mechanism of salting-in & salting-out

In aqueous solutions of non-ionic surfactants, water molecules are hydrogen bonded to ether oxygen bonds of the hydrophilic moieties or oxyalkyl-repeating-units respectively. The hydrophilic moiety of the surfactant is then surrounded by a second nearest neighbour water layer that is suggested to be considered as bulk water [101]. The presence of salts affects both the amount and the properties of the hydration water.
In [101] it is summarized that H^{+}; Ag^{+}, Li^{+}, as well as di- / trivalent cations salt-in polyoxyethylated surfactants by complexation with their ether groups so that the polyoxyethylene moiety of the amphiphiles acts as a polydentate ligand. The weak cation binding is suggested to impart a slight cationic character to the non-ionic surfactants micelles, which would promote salting in. The anions that cause salting-in are rather large polarisable ions, the so called water structure breakers. They increase the amount of water able to form hydrogen bonds with the ether groups. We recognize that for cement pore solution, the clinker phases release di- and trivalent cations ions as for instance Ca^{2+} and Al^{3+}. **This would imply that for cementitious systems salting-in may occure.**

The origin of the salting out phenomenon was studied by Bowron & Finney in 2003, 2004 [104, 105] using isotope substitution neutron scattering on mixtures of water - tertiary butanol - sodiumchlorid-solutions. The association of molecules in aqueous solution to form micelles dramatically changed in the presence of salt. They could show that the cation retains its normal hydration shell and only loosely interacts with the hydrated hydrophobic moiety of the alcohol, whereas the anion directly bridges the hydroxyl groups of two alcohol molecules. Due to the direct anion-bridging the alcohol reorganizes so that four polar groups point towards the polar group of a central alcohol molecule. **Concerning cementitious environmental conditions, this however implies that non-ionic surfactants are subjected to salting-out.** The question arises on whether salting-in or salting-out dominates the behaviour of non-ionic surfactants in cementitious systems.

The exposure of the hydrophobic moieties to the aqueous environment is less favourable thermodynamically. The polar interactions between hydroxyl groups or other polar moieties with the anions in solution are supposed to be one possible mechanism that promotes phase separation.
In Rosen 2004 [87], the influence of ions on the CMC in aqueous electrolyte solutions of non-ionic surfactant was found to generally follow the Hofmeister anion series:

$$SO_4^{2-} > F^{-} > BrO_3^{-} > Cl^{-} > Br^{-} > NO_3^{-} > I^{-} > SCN^{-}$$

Moreover the classification of cation salting out effect was found to be:

$$NH_4^{+} > K^{+} > Na^{+} > Li^{+} > {}^{1}/_{2}\, Ca^{2+}$$

For cementitious materials, the electrolyte nature of pore solution should enhance the salting-out of non-ionic surfactants, which may affect the shrinkage reduction achievable with SRA.

4.2.5 Adsorption of non-ionic surfactants on the solid/liquid interface

The efficiency of SRAs may be reduced if they adsorb at the solid/liquid interfaces. Indeed, it is assumed that the working mechanism of SRA is directly linked to its presence at the water/air interface, so that any losses to the solids would be highly undesired. Moreover, adsorption of surfactants onto hydrates may cause an undesired development of the properties of mortar and concrete containing SRA.

The adsorption isotherms of non-ionic surfactants generally show langmurian behaviour or two-stepped- (L2) or even four-step- (L4) langmurian behaviour. They reach a maximum of adsorption (plateau) near the critical micellation concentration (CMC) [86, 87, 106-118]. The different shapes of the adsorption isotherms are due to the adsorbate-adsorbate, adsorbate-adsorbent and adsorbate-solvent interactions. This is evidenced in various studies on the adsorption of non-ionic surfactants onto several solids as precipitated silica [106, 108, 110, 114], ground quartz [108, 112, 117], pyrogenic silica [108, 111], soils [109, 118], clay [107, 108, 112, 118] and activated carbon [107, 115]. Overall, the adsorption mechanism can be summarized as follows [86, 87, 106-118]:

Non-ionic surfactants are rather physically adsorbed than electrostatically or chemisorbed. Due to their amphiphilic nature they can adsorb onto either hydrophilic or hydrophobic surfaces. **With respect to cementitious materials, the adsorption onto hydrophilic surfaces would be expected to be due to hydrogen bonding of the polar moieties (hydrophilic heads) with the silanol groups (silica, amorphous quartz etc.) and/or aluminol groups (clay). However, at the elevated pHs of these systems most of these groups are deprotonated.**

At low bulk concentrations, the non-ionic surfactant monomers are anchored to the surface. With increasing concentration, the surface coverage increases and the adsorption isotherms show a rather low slope. Above a certain bulk concentration, adsorption increases because micellar aggregates form at the surface. The bulk concentration at which this starts can be defined as Critical Aggregation Concentration (CAC).
The formation of these aggregates is due to the same molecular interactions as for micellation and self-aggregation in the bulk (see 4.2.3). They are also responsible for the two- to four-stepped langmurian adsorption isotherms. The number of steps can be related to the formation of different types of aggregates.
Levitz 2002 [114] reports that at coverage of about 20% the surface aggregates have almost the same aggregation number (number of monomers forming an aggregate) as micelles formed well above the CMC. This implies that the free energy of aggregation on the surface is similar to the free micellation energy of bulk aggregates [108, 110, 114].
With increasing bulk concentrations above CAC, the monomers turn from flattened micelles into fragmented bilayers and further on into extended bilayers. Reaching the CMC of the bulk solution, the adsorption isotherms flatten out and exhibit a plateau.

Assuming this happens to SRAs in cementitious systems, the loss of surfactant would have to be discriminated into a fraction adsorbed onto hydrates and a fraction inactivated due to formation of micelles.

The question arises on how to measure a phenomenon like this. Heretofore we examine in the following how the molecular nature of non-ionic surfactants, the properties of the solid and the liquid phase impact the adsorption onto the solid/liquid interfaces.

4.2.5.1 Influence of hydrophilic chain length

Partyka 1984 [106] calculated the cross sectional occupation area onto precipitated silica by the repeating units within a homologues series of ethoxylated non-ionic surfactants, having similar hydrophobic tails with increasing hydrophilic chain length.
An almost linear correlation between number of repeating Polyethylene oxide-units (PEO-units) and

the molecular cross-sectional occupation area could be found. However, the linear regression did not pass through the origin but rather defined the “zero-area” of a PEO-unit-number of 4. From this it was concluded that the last four members of the hydrophilic chain take not part in covering the surface. Furthermore the rate of adsorption was shown to increase with increasing length of the hydrophilic moiety of the surfactant.

4.2.5.2 Influence of hydrophobic chain length

Within a homologous series of ethoxylated surfactants, having similar hydrophilic heads with different alkyl chain lengths, Partyka 1984 [106] observed that the maximum coverage was only slightly changed (adding one methyl unit) whereas the CMC drastically decreased.

4.2.5.3 Influence of pH

Investigations on silica and kaolin showed that the adsorption of non-ionic surfactants drastically decreases with increasing pH [108]. For silica sorbents at high pH it is suggested that either the dissolution of these minerals or the strong increase in surface charge may be responsible for the decreased adsorption. The maximum adsorption of ethoxylated non-ionic surfactants is at low pH near the point of zero-charge of silica [87]. It possibly relates to the protonation of ether bonds, causing a slight positive charge to the molecules and hence getting then attracted to the negatively charged surface [87].

4.2.5.4 Influence of temperature

The adsorption of non-ionic surfactants is temperature dependent and increases with temperature. This was observed for temperatures below the lower consolute temperature [87, 106]. Tadros 2005 [86] suggests that the increase in adsorption with raising temperature is due to the desolvation of the oxyalkyl repeating units, that reduces their size. Furthermore the increasing temperature reduces the solubility (see 4.2.4), which also enhances the adsorption at the liquid/solid interface.

4.2.5.5 Influence of aqueous electrolyte environment

In presence of salts the adsorption isotherm is displaced towards lower bulk concentrations and is accompanied by a slight increase of the adsorption plateau. This was at least reported for precipitated silica [106, 108] and for kaolin [112], using sodium chloride as salt. Therefore, in regard to the Hofmeister anion series, the salting-out effect (see 4.2.4) could be responsible for the adsorption increase. This is suggested to be analogous to the effect of raising temperature.

4.2.5.6 Influence of ζ-potential of the sorbent

Nevskaia et al.1998 [112] measured changes of ζ-potentials due to the adsorption of non-ionic surfactants. Kaolin and silica were immersed in aqueous electrolyte solutions and non-ionic surfactants were added. Results showed that for both sodium and calcium chloride solutions of different concentrations, the ζ-potential of both sorbents increased in relation to the adsorption isotherms. At the isotherm plateau the ζ-potential remained constant.

4.2.6 Influence of non-ionic surfactant on surface forces

An abundant literature can be found on the impact of surfactants on the stability of foam and wetting films. ***In regard to the drying of porous cement systems, wetting films or rather adsorbed water layers can be assumed to be important. This is particularly true if the concept of disjoining pressure is referred to.*** The concept of disjoining pressure was introduced by Derjaguin-Landau-Verwey-Overbeek (DLVO theory) and is nowadays recognized as the contemporary paradigm of colloidal stability [119]. Concerning this, the presence of water films at the solid interface determines the average interparticular distance by means of disjoining pressure and hence the volume stability of the nanoscopic cementitious system. ***It is therefore of high interest to know, if and to what extent non-ionic surfactants impact disjoining pressure.***

Concerning drying cementitious pore systems the following findings might be of interest:

a) The film thickness is determined by the presence and magnitude of disjoining pressure. For aqueous electrolyte solutions, it increases with increasing vapour pressure but this depends strongly on the nature of the solid substrate.

b) The thickness of wetting films from aqueous electrolyte solutions of non-ionic surfactant depends furthermore on electrolyte concentration and pH of the solution as well as the surfactant concentration [32, 44, 119-121]. It could be shown that with increasing electrolyte concentration the film thickness decreases (Churaev 2003 [32]).

c) Whereas ionic surfactants impact wetting film stability by changing electrostatic forces, non-ionic surfactants only weakly impact their stability. According to Churaev 2003 [32] the effect may rather be caused by structural forces. Exerowa et al. [121] identified a critical electrolyte concentration where the film thickness decrease reaches a plateau. They concluded that a transition from electrostatic to steric stabilisation takes place at this particular concentration. Moreover, Sedev [119] identified a steric contribution to the disjoining pressure in foam films due to the molecular nature of non-ionic surfactants and augmented the DLVO theory with a steric term Π_{ST} reading:

$$\Pi_{disj.} = \Pi_{EL} + \Pi_{VW} + \Pi_{ST} \tag{56}$$

where:

Π_{disj}	total disjoining pressure
Π_{EL}	electrostatic component of disjoining pressure
Π_{VW}	van der Waals component of disjoining pressure
Π_{ST}	steric component of disjoining pressure

This implies that in the course of the drying of cementitious materials, it may be necessary to consider a possible impact of an additional steric contribution of surfactant to total disjoining pressure.

4.2.7 Summary

In this section the behaviour of pure component non-ionic surfactants has been reviewed. They correspond to a class of molecules used in SRAs. It was shown that their concentration at the liquid/vapour interface, responsible for shrinkage reduction, can be affected by various factors as molecular structure, electrolyte nature & concentration, temperature, adsorption, etc. This must be taken into account when attempting to quantify the effects of SRAs in cementitious materials.

In the next section, the state of the art knowledge of mixtures of those surfactants with glycols is examined. It is shown how these mixtures can develop properties that are more beneficial to use as SRAs in cementitious materials.

4.3 Mixtures of non-ionic surfactants and glycols in aqueous solution

The patent search revealed that SRA often exploit a synergy between glycols or alkandiols and non-ionic surfactants. The reason for this positive interaction is not clear but we can note that the diols not only reduce the surface tension, but also change the interfacial properties of non-ionic surfactants. This is discussed in the following section.

4.3.1 Interfacial phenomena

In what follows the surface activity of glycols or rather co-surfactants is outlined and in regard to SRA products, the co-surfactant nature is given particular attention. Lunkenheimer 2004 [122] classifies this type of surface active molecules also as solvo-surfactants or hydrotropic detergents because they combine properties of solvents and surfactants. In the case of SRA glycols may enhance the molecular solubilisation for the main non-ionic surfactant, partly by organising the liquid structure. **It turns out that, beside a small direct contribution of glycols to lowering surface tension, their more important contribution to SRA performance comes from their ability to avoid undesired phase transitions of the non-ionic surfactants.**

4.3.1.1 Surface activity and phase behaviour of water-glycol mixtures

Tan et al. [123-126] extensively studied the surface activity of water-glycol mixtures using polypropylene and polyethylene glycols. Within the aqueous solutions of the homologue series of polypropylene glycols (PPG), comprising a molecular weight between 192 and 2000 g/mol, the presence of a sharp break point in the plots of surface tension versus the logarithm of concentration ($\log_C$) was absent, although the mixtures became turbid above a certain bulk concentration. The surface tensions of the aqueous solutions of PPG were reduced down to 40mN/m. For PPG with low molecular weight the surface tension could be shown to decrease to about 33mN/m (M_{PPG}=192 g/mol).
Compared to non-ionic surfactants, glycols decrease the surface tension of aqueous solutions to a comparable level but are less efficient with respect to the bulk concentrations required.
In contrast to non-ionic surfactants, Seguin [127] observed total miscibility of glycols with water. Also, the polyethylene glycols (PEG) up to a molecular weight of 600 g/mol are miscible with water. This was observed for ethylene glycol and diethylene glycol. Nagamune 1996 [128] observed the CMC of aqueous solution of PEG1000 (molecular weight; M=1000g/mol) to be about 0.02 mol/l and the solutions were exhibiting a surface tension of about 48 mN/m.
The surface activity of PEG turns out to be low compared to PPG [125], due to the lower polarity of PPG.

4.3.1.2 The co-surfactant nature of glycols

The ability of glycols to reduce the surface tension of their aqueous solutions makes them useful for the application as co-surfactant. For PPG the plots of surface tension versus logarithm of concentration (γ/ln$c$) are almost linear [123-126], so that

$$\left(\frac{\partial\gamma}{\partial ln c_{PPG}}\right) \approx const. \geq 0 \text{ ; for } c_{PPG,0} \text{ up to } C_{PPG;max} \qquad (57)$$

Also, in contrast to common non-ionic surfactants, there is no critical micellation concentration (CMC) to be found for low molecular glycols. The absence of a CMC implies that the excess surface concentration Γ_a at the liquid/vapour interface is still increasing even after the first bulk aggregates or droplets form [124-126].
The synergistic effect of the reduction of surface tension of ternary mixtures, i.e. non-ionic surfactant-glycol-water, can be derived from Gibbs adsorption equation for multicomponent systems (from [86]):

$$d\gamma = -\sum \Gamma_i \; d\mu_i = -\sum \Gamma_i \; RTd\ln c_i \tag{58}$$

where:

c_i concentration of each surfactant component

For two surfactants systems, the contributions of the main surfactant (sa) and the co-surfactant (co) sum up to decrease of surface tension in agreement with (58), so that

$$d\gamma = -\Gamma_{sa} RTd\ln c_{sa} - \Gamma_{co} RTd\ln c_{co} \tag{59}$$

Integrating (59) gives:

$$\gamma = \gamma_0 - \int_0^{C_{sa}} \Gamma_{sa} RTd\ln c_{sa} - \int_0^{C_{co}} \Gamma_{co} RTd\ln c_{co} \tag{60}$$

From this it can be seen that the surface tension of the aqueous solutions can be decreased by the contribution of both, the surfactant and the co-surfactant, if they do not interact and can adsorb independently one from the other.

4.3.1.3 Impact of Glycols on phase behaviour of aqueous solutions of non-ionic surfactants

Seguin 2006 [127], using mixtures of ethylene glycol and a poly ethoxylated alkyl ether as non-ionic surfactant in water as solvent, observed only a slight additional reduction of surface tension but a drastic increase of the CMC when applying the glycol as co-surfactant. This CMC increase in presence of glycols was also observed by Palepu et al. 1993 and Carnero Ruiz et al. 2007 [129, 130]. They suggested that the glycols act as water structure breakers around the surfactants, reducing the entropy gain resulting from micelle formation. Consequently, in presence of a glycol co-surfactant the micellation requires a higher surfactant bulk concentration [87].

It should also be noted that Martino 1995 [131] observed that the lamellar phases occurring at high bulk concentrations in the binary mixtures (water – surfactant) brake up when propylene glycol is added. The explanation was also given in terms of the water structure breaker character of glycols.

In summary, although glycols are less efficient in decreasing the surface tension they can drastically impact the phase behaviour of non-ionic surfactants in aqueous solution. In cementitious systems this may change the shrinkage reduction efficiency of some SRAs. This is the subject of the next section.

4.3.2 Implications on cementitious environmental conditions

The patent literature [79-83] explicitly mentions the synergy between glycols and surfactants in terms of enhanced shrinkage reduction. This raises the following question: If the co-surfactant is not significantly efficient in reducing surface tension what can be other possible benefits?

In hydrated cementitious systems, SRAs are exposed to strong electrolyte conditions (pore solution) as well as to high internal specific surface area of hydrophilic material (hydration products).

This can enhance surface absorption/aggregation of surfactant at the solid/liquid interface as well as the salting-out effects (see sections 4.2.4 and 4.2.5).

4.3.2.1 Loss of surfactant at the solid/liquid interface

For surfaces which onto surfactants can adsorb, it was shown that surface aggregation of non-ionic surfactant starts well below the critical micellation concentration (CAC<CMC) [86]. This would imply

that the cementitious surface area may be covered well before the bulk solution reaches the CMC. Moreover, the SRA dosage to reach the maximum shrinkage reduction (required to form a monolayer at the water/air interface) should increase. However, for a highly basic environment, as for Portland cement, non-ionic surfactants show a dramatic decrease in adsorption onto silica surfaces [108]. The synergy with glycols must therefore come from something else than a reduction of surface aggregation. This is only partly true since, even if the extent of adsorption or surface aggregation is low per unit surface, the internal surface area of hardened cementitious material is very large. Therefore, if the co-surfactant increases the monomer solubility (decreases the extent of self-assembly), the critical aggregation concentration will increase also and potentially affect the system significantly. From this point of view it is easier to explain the benefit of glycols.

4.3.2.2 Decrease of CMC in aqueous electrolyte environment

In section 4.2.4 it was shown that salts can drastically decrease the CMC of non-ionic surfactants. The high ionic strength and the type of ions in cement pore solution are susceptible to induce salting-out effects. Rajabipour 2008 [132] measured surface tension of a commercially available SRA in both water and synthetic pore solution, composed of potassium and sodium hydroxide. This revealed that the CMC was decreased for the aqueous electrolyte solution of SRA.
A decrease of CMC or rather a decrease of the monomer solubility could enhance adsorption onto the solid/liquid interface and bulk micellation.
Again, there would be benefit for cementitious material if the co-surfactant compensates for the salt-induced decrease of CMC.

4.3.2.3 Summary

This section has shown that glycols, through specific chemical interaction can modify the aggregation behaviour of non-ionic surfactant used in SRAs. It is expected that in one or another way this explains the synergistic benefit referred to in the patent literature.

In the next section we examine more specifically the literature dealing with the use of SRAs in cementitious systems.

4.4 SRAs in concrete – Phenomenological overview

The literature published on SRAs predominantly focuses on the influence of the admixture on concrete performance as shrinkage reduction in general, crack prevention, influence on mechanical properties and to a lesser extent on the durability of SRA modified concretes [27, 29, 68, 70-77, 133-183].

4.4.1 Characterisation of SRA used in scientific studies

In general, authors do not report the exact chemical compositions of the admixtures used in their studies. For authors that own a patent and are affiliated to a SRA-producing company, one can however guess the type of compounds used. For example Berke, N.S. listed as inventor/co-inventor of patents [184-190] (Assignee: W.R. Grace & Co.-Conn (US)) is involved in several publications [137, 140, 156, 160, 161, 191, 192]. In Balogh 1996 [193] it is explicitly pointed out, that the SRA used was developed within a corporation of W.R. Grace & Co. and ARCO Chemicals, entitled assignee of patents granted to Shawl [83, 194-199]. So it is not surprising that within the patent search (see annex A1) the general formulas of the compounds claimed by both inventors appear to be quite similar.

In very few studies the brand of the SRA used is pointed out. Hua 1997 [68] uses the brand eclipse^{TM} (ARCO) and determines dipropylene glycol ether as the efficient ingredient of the admixture. Cope 2001 [157] also used the brand eclipse^{TM} and refers to a data sheet provided by W.R. Grace & Co.-Conn (US).

From Shawl's examples within patents [83, 194, 195, 197, 199] one gathers that they used a mixture based on dipropylene tert-butyl ether (DPTB) as surfactant and dipropylene glycol (DPG). From the

material safety data sheets (MSDS) of two commercially available products carrying the brand “Eclipse Floor” [200] and “Eclipse Plus” [201] from W.R. Grace & Co.-Conn (US) one can also find a mixture of DBTB and DPG. In both cases DPTB is denominated with Propanol, [2-(1.1-dimethyl-ethoxy)methylethoxy] with the chemical abstract number CAS: 132739-31-2.

For a lot of other studies, authors refer to a generic term describing the chemical composition of the SRA used as polypropylene glycol derivates or blends of propylene glycol ethers [72, 136-138, 146, 158, 163, 171, 176, 180, 183, 192].

Another two authors Cerulli 2001 [72] and Maltese 2005 [171] are related to Mapai S.P.A. (It), of which the SRA brand is denoted “Mapecure SRA”. Maltese accounted for propylene glycol as chemical compound of the SRA used.

Nmai 1998 [202] and Holt 1999-2004 [75, 149, 167], using the brand Tetraguard from Masterbuilders (now BASF), also refer to polyoxyalkylene ether as chemical compound, with a minimum content of the efficient ingredient of about 60% [203].

Only a few investigations focus on more or less exotic compounds. For instance Kim 1997 [141] applied polyethylene glycols with a high molecular weight between 3000 and 8300 g/mol and Holt 1999-2004 [75, 149, 167] used Peramin SRA (Perstorp Specialty Chemicals AB; Sweden) with the main efficient ingredient described as “cyclo aliphatic alcohol ethers” or rather acetals. These are 1,3 dioxane of a trihydric alcohol or trimethylol-$C_{1\text{-}8}$-alkane or trihydric alcoxylated alcohol (see Engstrand [204] annex A1).

It can be summarized that for the majority of studies mentioned above propylene- or polypropylene ethers were most probably introduced as non-ionic surfactants and combined with glycols as co-surfactants in many cases.

4.4.2 Surface activity of SRA

4.4.2.1 Reduction of surface tension

Several authors measured the reduction of surface tension, caused by SRAs in aqueous solution, using the Wilhelmy plate or the du Noüy Ring method [27, 29, 68, 71, 72, 76, 173]. For dipropylene glycol tert-butyl ether (DPTB) Hua 1997 [68] measured a CMC at about 5wt.-% to 6wt.-% in water at a surface tension of about 35mN/m. Rajabipour et al. 2008 [132] using Tetraguard® AS20 (BASF) measured a CMC at about 15wt.-% SRA in deionised water (γ_{SFT} ~ 33mN/m). However, the same SRA in a synthetic pore solution (0.35M KOH plus 0.05M NaOH), showed a decrease of CMC down to about 8wt.-% accompanied by a further decrease in surface tension to about 30mN/m. The benefit of this additional surface tension effect is most probably marginal and a side effect.

4.4.2.2 Adsorption of SRA onto the solid/liquid interface

Hua et al. 1997 [68] found no evidence for the adsorption of DPTB onto hydrated cement phases from 1 hour to 3 days of hydration. Zhang et al. 2001 [205] and Merlin et al. 2005 [206] investigated the adsorption behaviour of short ethoxylated non-ionic surfactants onto hydrated cementitious material. For very low molecular weight the non-ionic surfactant did not adsorb at all [205] and Merlin identified adsorption of non-ionic surfactants onto C-S-H at the very detection limit.

4.4.3 Efficiency of SRA in shrinkage reduction

The main purpose for introducing shrinkage reducing admixtures is to combat drying shrinkage. It also turns out that plastic shrinkage as well as autogenous shrinkage can be efficiently decreased by SRA.

4.4.3.1 Plastic shrinkage

Holt et al. [75, 149, 167] observed a decrease in plastic shrinkage for SRA containing normal and high strength concrete up to 50% at equal rates of water evaporation. Due to SRA-modification, Engstrand 1997 [139] measured a reduction in plastic shrinkage up to 85% at 12 hours of hydration on standard

mortar according to EN 196-1. Lura et al. [71] observed a drastic decrease of settlement by introducing SRAs to mortars exposed to drying at early ages. Mora et al. [163] found a significant decrease in plastic shrinkage as well as crack prevention for concrete using restrained panels and restrained beams with a wedge.

4.4.3.2 Autogenous shrinkage

For high performance concrete with low water/cement ratios, self desiccation causes autogenous deformation and may induce early age cracking. Several authors [50, 69, 70, 135, 155, 159, 167, 168, 175, 179, 181, 207] describe a significant decrease of free autogenous deformations for paste, mortar and concrete containing SRAs. Under restrained conditions for SRA-modified cement pastes, i.e. the ring test with sealed specimen, Sant 2007 et al. [207] measured a significant decrease of the residual tensile stress during self desiccation.

4.4.3.3 Free drying shrinkage

The influence of SRA on free drying shrinkage usually is carried out by applying different amounts of SRA to paste, mortar and various types of concrete, where SRA replaces an equal amount of mixing water. The range of SRA-dosages is given either per weight of cement (up to 2wt.-%) or per amount of mixing water with an average maximum of 5wt.-%. These are similar dosages by assuming an average water/cement ratio of ~ 0.4 for high performance and self consolidating concretes. Tests have been performed on several specimen geometries within different curing regimes and exposure conditions.

For the short range, up to 28d of drying, authors report 50% up to about 80% reduction of free drying shrinkage. However, the values strongly depend on the shrinkage evolution of the reference specimen as shown in Figure 9.

Figure 9 displays shrinkage curves obtained by Eberhardt et al. 2006 [178] within a preliminary study on SRA efficiency for self consolidating mortars and concretes. There, self consolidating mortars were modified in SRA dosage and drying shrinkage was measured. Further details are given in [178].

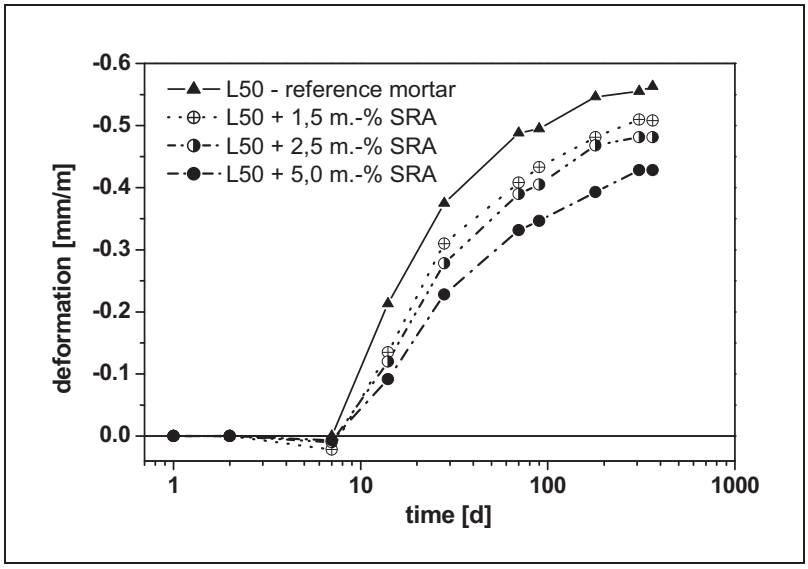

Figure 9: Free drying shrinkage of self consolidating mortars containing different amounts of SRA [178]

storage:

curing; t < 7d at 20°C / 95% R.H.

drying; t > 7d at 20°C / 70% R.H.

In the above figure, it can be seen that:

a) the major part of shrinkage reduction is gained within the first part of drying (~50days) well before drying equilibrium is reached (~ first 300 days)

b) after certain time (~ 30 days) of drying, the absolute increase in deformation proceeds independently of the SRA dosage.

Regarding the efficiency of SRAs in mortar and concrete, another important limitation can be derived from Figure 9. The evaluation of shrinkage reduction has to refer to the storage regime, time and shape of shrinkage curves. This becomes obvious when data are reported in relative terms with respect to the reference. For the data in Figure 9 the corresponding values are presented in Table 1 and show that the relative benefit in shrinkage reduction from SRAs decreases with time. This is because the SRA containing samples and the reference show a parallel evolution after about 30 days. It emphasises the care that must be taken in data interpretation.

Table 1: Shrinkage reduction of SRA modified mortars dependent on dosage and time of drying [178]

time	shrinkage reduction [%]		
14d	37	44	57
28d	17	26	39
70d	16	20	32
180d	12	14	28
364d	10	14	24
SRA*	**1.5%**	**2.5%**	**5.0%**

*wt.-% of mixing water

On the long term and near equilibrium (shrinkage curves show a plateau) Gettu et al. 2001/2002 [74, 158] report 30% to 50% after one year at 20°C/50%R.H., Videla et al. 2005 [176] up to 40% shrinkage reduction for concrete at 23°C/50%R.H. for a trial period of 1350d and Roncero et al. 2003 [165] give 26% to 51% shrinkage reduction after two years at 20°C/50% R.H. and for a dosage of 1wt.-% and 2wt.-% SRA by weight of cement respectively.

4.4.3.4 Restrained drying shrinkage

Crack prevention is the major reason for the introduction of shrinkage reducing admixtures. In the early 1990s researchers started restrained shrinkage performance tests on concrete using different devices as:

a) the restrained ring setup [76, 77, 136, 140, 146, 152, 153, 166, 169, 177, 178, 207-210];

b) restrained beams [27, 152, 154]

c) restrained slabs [144, 147, 157, 192, 211]

It can be summarized that the SRA-modified mixtures either cause a decrease in crack width of 30% to 80%, dependent on the SRA dosage, accompanied with delayed cracking times or even a complete prevention of cracking in some cases.

4.4.4 Influence of SRA on cement hydration and microstructure

4.4.4.1 Influence on hydration kinetics

The incorporation of SRAs causes an increase in both initial and final setting times. The phenomenon was mainly observed with penetration tests [139, 140, 157, 171, 172, 179]. Using isothermal heat flow calorimetry, Cerulli 2001 [72] measured a delay of the beginning of the acceleration period and a delay of the time of maximum heat release in presence of SRA. In their measurements, the heat release or heat of fusion (upon contact of cement and liquids) increased with increasing amount of SRA.

For high performance or self consolidating concretes containing higher amounts of superplasticizer and SRA several authors describe an increasing delay of setting with dosage [151, 177, 178]. Eberhardt et al. 2006 [177, 178] measured the heat release of cement pastes modified with poly carboxylate type superplasticizer (SP-PCE) and/or SRA using isothermal heat flow calorimetry. They could show that for both types of admixtures, SP-PCE and SRA alone, an extension of the induction period of cement hydration can be observed. Moreover, this was accompanied by a delay of the main heat release within the acceleration period. Superplasticizers were observed to have higher impact then SRAs. However, the combination of both admixtures causes a disproportionally high delay of cement hydration.

This has important practical implications for self consolidating mortars and concrete for which the use of superplasticizer is essential. Indeed, in such cases the application of SRA can cause an excess delay of setting that may not be tolerable and may have to be mitigated by some other means.

4.4.4.2 Influence on hydrated phase assembly and composition of pore solution

For SRA containing pastes, Cerulli et al. 2001 [72] and Maltese et al. 2005 [171] report a decreased amount of portlandite after 24 hours hydration related to a slow down in hydration kinetics observed by isothermal heat flow calorimetry [72]. Maltese et al. [171] furthermore observed a dramatic morphological change for cement paste containing a polypropylene based SRA. Using environmental scanning electron microscopy they found long prismatic crystals on the surface of the paste, which were interpreted as morphologically modified portlandite or ettringite. However, the X-ray powder diffraction provided no evidence for either portlandite or ettringite as the diffractograms for both pastes, with and without SRA, appeared to be almost congruent. Hua et al. 1997 [68] investigated the influence of dipropylene glycol tert-butyl ether on the hydrated phase composition of Portland cement. Their quantitative analysis showed no alteration in phase composition. Indeed, the XRD pattern for both 1 day and 28 days hydrated samples, with and without SRA, were essentially identical.
Engstrand 1997 [139] found that, in presence of SRA, a significant amount of potassium and sodium ions are depleted from the pore solution. Especially after 24 hours of hydration, the amount of potassium was reduced by 25% while the sodium content showed no change. After 28 days of hydration, potassium and sodium were depleted by 25% and 30% respectively. Engstrand relates the depletion of ions from pore solution to their enhanced fixation into C-S-H-phases. However no detailed explanation is given about how and why the SRA would cause this to happen.

4.4.4.3 Influence on microstructure

The results of mercury intrusion porosimetry performed by Shah et al. 1992 [76] and Hua et al. 1997 [68] revealed a minor influence of SRA on the pore size distribution of hydrated cement. The volume of pores in the range of 50nm to 10µm were slightly decreased in presence of SRA [76].
Several authors observed an increase of specific surface area measured with nitrogen adsorption (BET) [68, 72, 171]. For example after 28 days of hydration, Hua et al. 1997 [68] measured up to 25% and Cerulli et al. 2001 [72] up to 100% increase in specific surface area. The observed phenomenon was related to an enhanced amount of low density C-S-H forming in the presence of SRA [72]. Here again, this preposition remains very speculative and has only few solid facts to support it.

4.4.5 Influence of SRA on mechanical properties

In a lot of phenomenological studies, the influence of SRAs on the mechanical properties of mortar and concrete was evaluated, usually using homologue series with increasing SRA dosage. The properties reported in the following mainly refer to mature material ($\geq$28d). Note, that in regard to the findings on the impact of combined application of SRA and superplasticizer, early age mechanical properties can be less developed due to lower degrees of hydration.

4.4.5.1 Compressive strength

In presence of SRAs the compressive strength is reported to be decreased by up to 20% [76, 141, 147] but in average alternating between 5% and 10% [74, 138, 157, 158, 169, 176, 202].

4.4.5.2 Modulus of elasticity

There seems to be no significant change for the development of the modulus of elasticity in presence of SRAs (compressive setup).

4.4.5.3 Flexural strength

Dependent on the SRA dosage, a decrease of flexural strength up to 10%-15% was observed by [139] and up to 28% by [141].

4.4.5.4 Splitting tensile strength

Within a series involving 5 different SRAs, Videla et al. [176] observed no significant change for splitting tensile strength (7d; 28d; 90d).

4.4.5.5 Tensile strength

The direct tensile strength also can be influenced disadvantageously. It was reported to be deceased by SRA in the range of 8% to 34% [138, 157]. Within the study of Lam 2005 [169] the tensile strength was measured on specimen stored at 50% R.H., where one part of specimens had been submerged in water before being tested. This revealed that dry specimens containing SRA comprised higher strengths compared to the untreated reference whereas the saturated samples behave in the opposite way.

4.4.5.6 Creep

A major influence of SRA is the decrease of creep both in compression and in tension [27, 74, 133, 138, 154, 166]. Reductions up to 60% were measured in compression [133] and up to 29% in tension [154]. Roncero et al. [165] investigated basic and drying creep of SRA-modified concrete. The drying creep was decreased whereas the basic creep was not significantly influenced by SRA.

4.4.6 Influence of SRA on durability

SRA efficiently decrease the crack number and width or even prevent cracks from forming. This benefits durability in all cases, since cracks can be identified as damage inducing factors, for example by facilitating water sorption. This would explain the results of Ribeiro [182], Lam [169] and Berke [192] who measured a decrease in chloride penetration for concretes containing SRA.

Early studies revealed however that some SRAs were not compatible with air entraining admixtures and therefore induced low frost- and freeze/thaw resistance [134]. Berke [192] and Bae [160] could show that a good resistance can nevertheless be obtained with SRAs using compatible admixtures that provide a proper air void system in presence of SRAs.

4.5 Summary

The state of the art review on SRAs revealed that the commercial admixtures used in many studies are synergistic mixtures of non-ionic surfactants and glycols.
There is a strong indication that, due to the electrolyte nature of cement pore fluids, SRAs may exhibit phase transitions that influence their performance. From the state of the art knowledge on non-ionic surfactants it can be estimated that the electrolyte nature of cement pore solution might enhance the salting-out of non-ionic surfactants, which may affect the shrinkage reduction achievable with SRA.

Non-ionic surfactants are rather physically adsorbed than electrostatically or chemisorbed. Due to their amphiphilic nature they can adsorb onto either hydrophilic or hydrophobic surfaces. With respect to cementitious materials, the adsorption onto hydrophilic surfaces would be expected to be due to hydrogen bonding of the polar moieties (hydrophilic heads) with the silanol groups and/or aluminol groups. However, at the elevated pHs of these systems most of these groups are deprotonated.

Concerning the synergy effect described in the patent literature on SRAs, it turns out that, besides a small direct contribution of glycols to lowering surface tension, their more important contribution to SRA performance comes from their co-surfactant nature, i.e. their ability to avoid undesired phase transitions of the non-ionic surfactants.

With respect to models for drying and shrinkage that involve surface activity: Based on fundamentals of non-ionic surfactants and co-surfactants the surface activity of SRA can be described using the Gibbs-Duhem equation.
Concerning models that account for the disjoining pressure, governing the hygral properties of cementitious material, the molecular nature of non-ionic surfactants adsorbed on cement hydrates might in-

duce steric hindrance. This implies that in the course of the drying of cementitious materials, it may be necessary to consider a possible impact of an additional steric contribution of surfactant to total disjoining pressure.

The phenomenological overview on SRA in concrete revealed that despite the shrinkage reduction and improved crack resistance, some properties of concrete can be negatively affected to some extend.

Concerning the implementation of SRA characteristics into recent models for drying and shrinkage: The surface activity of SRAs was studied by several authors, however, the measurements performed (paste, mortar, concrete; synthetic pore solution) provide only few solid facts and results that may be used to derive the working mechanisms of these admixtures in terms of shrinkage reduction.

In the next chapter, in a first step a suitable model for drying and shrinkage is derived by theoretical considerations. Then, based on the findings of this chapter, surface activity of SRAs will be implemented therein.

5 Theoretical considerations

In this chapter the author wishes to derive a suitable model capturing the most important effects of SRAs during drying and shrinkage of cement paste. In a previous chapter, the review on drying shrinkage of cementitious materials identified that implementing surface activity of the pore fluid would be essential for this. This change in surface activity modifies the saturation degree at a fixed RH. In turn this affects the average pore pressure and the shrinkage that results. In chapter 4 it was also shown that for fixed surfactant dosage the surface activity depends on the volume to surface ratio. This changes during drying because of the formation of a liquid film on the internal surface. To assess the importance of these effects it was necessary to construct a model capable to deliver simple conceptual indications of which factors matter most. This is the ultimate object of this chapter, which also discusses relevant literature.

5.1 Thoughts about a suitable model for drying and shrinkage

As mentioned above, the state of the art review on drying shrinkage models brought up the question on the importance of capillary pressure in general and the question of the humidity range in which these forces are present. In particular Coussy [11, 13] applied capillary pressure to very low humidity, far below the bifurcation point of the sorption isotherms of cement paste. In this low humidity range, water is widely agreed to be exclusively present as adsorbed water layers. To address this issue, the total liquid saturation is now discriminated into two fractions:

1) liquid water fraction S_{bulk} or bulk water respectively and
2) adsorbed water associated with solids S_{ads}

so that

$$S_w = S_{bulk} + S_{ads.} \tag{61}$$

Based on this assumption Coussy´s [11, 13] approach can be modified and the results thereof are displayed in Figure 10.

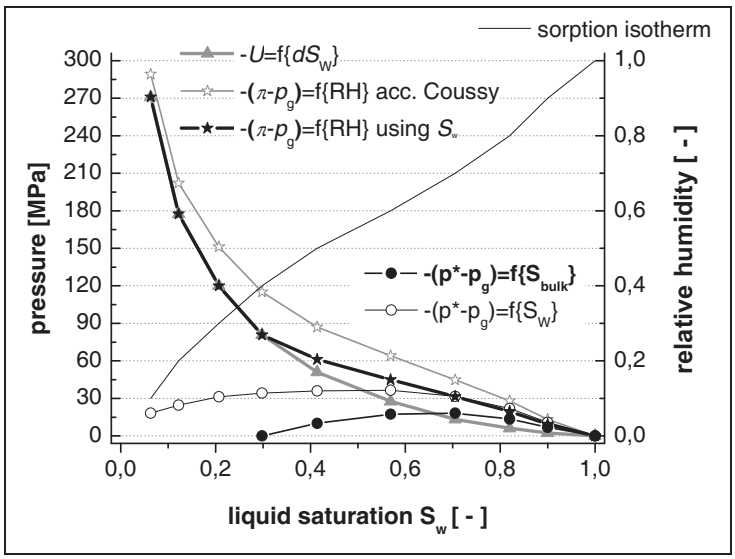

Figure 10: Modified contribution of capillary pressure to average pore pressure.

The figure is constructed with the concept of average pore pressure acc. Coussy [13], using a different sorption isotherm.

In Figure 10 it can be seen how a discrimination of bulk water saturation from total liquid saturation impacts the magnitude of the average capillary pressure (filled circles – $p^*=f(S_{bulk})$; hollow circles – $p^*=f(S_W)$) and the total average pore pressure (hollow stars according to Coussy´s model; filled stars – adjusted model). The magnitude of surface forces (filled triangles) remains unaffected because it is

exclusively calculated from water loss dS_W. Due to the discrimination between bulk and adsorbed water in the adjusted model, the total average pore pressure decreases because of the decreased contribution from average capillary pressure. As can be seen the surface forces gain in importance and now would exceed capillary contribution below 60% to 70% RH.

The modification used could also be applied to the findings of Hansen [8] who followed Bangham's approach for drying cement paste to predict shrinkage. In that work, the increase of excess Gibbs free energy was calculated from the desorption isotherm. The results of linear shrinkage deformation were drawn against increase in free surface energy. Figure 11 is taken from there. It shows that the measured length change of the different pastes follow Bangham's law at low RH.

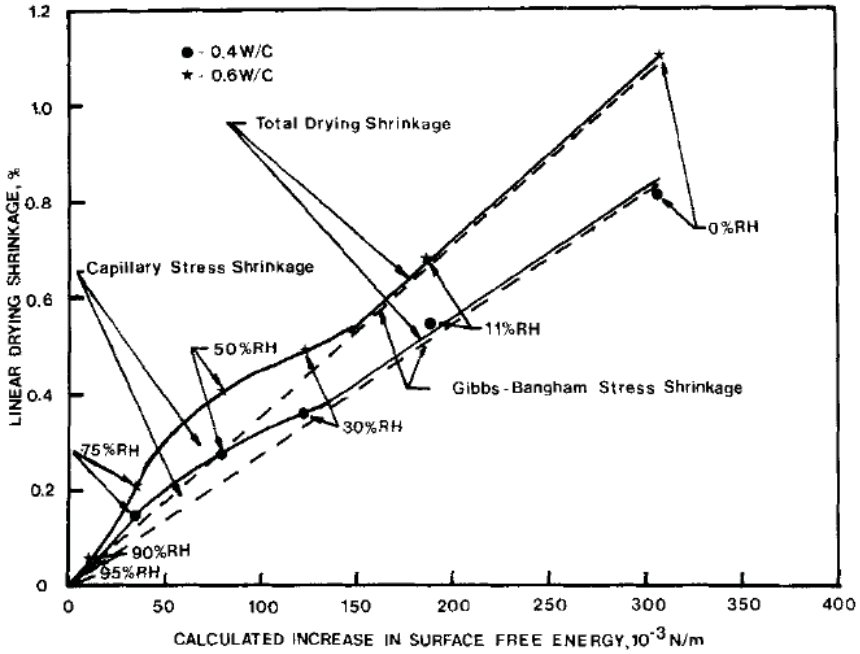

Figure 11: First drying shrinkage of 0.4 and 0.6 W/C ratio pastes vs calculated increase in surface free energy (Hansen 1987 [8])

In particular, for low humidity a linear correlation between length change and increase in surface energy can be found. Moreover, the dashed line, denominated „Gibbs-Bangham Stress shrinkage" goes through the origin, indicating that these surface forces act over the whole range of partial pressures. The notation „Gibbs Bangham stress" that Hansen [8] uses can be considered the direct equivalent to Coussy´s surface force contribution expressed in terms of excess Gibbs free energy per unit area (compare (6); (27); (44)). The solid lines are based on the measurement of shrinkage and desorption isotherms, for which water loss and shrinkage were measured at different relative humidity (filled circles). The measurements were taken from independent samples and are not successive. In so far the line is just suggesting a continuous progress. However, it reveals that the shrinkage deformation in the capillary range is increased. According to Hansen [8], in this range an additional stress is working along Gibbs-Bangham stress.

Comparing the approaches of Coussy [11, 13] and Hansen [8] we can state the following:

1) Different to Coussy, Hansen was exclusively referring to excess Gibbs free energy and did not take into account the capillary contribution proposed by Coussy. Therefore he underestimates deformation in the capillary range of humidity.
2) For predicting shrinkage Coussy obtains reasonable values in the capillary range but deformations in the lower humidity range are overestimated. A part of this can be directly linked to the overestimation of the water fraction he is allowing to exert hydrostatic pressure on the solid body.

3) Consequently, the discrimination of bulk water from total water content is a modification that seems beneficial for the shrinkage prediction for both approaches to reach better predictions for both, the low and high humidity range. Moreover, letting the capillary contribution vanish with the stability limit of menisci, which is widely agreed to happen for cement paste around 40% RH, would compensate for the specific short comings of each model.

5.2 Impacts of SRAs on mechanisms of drying & shrinkage

5.2.1 Impact of SRA on drying

Standard thermodynamics concerning the drying of porous materials describe how surface activity of the pore fluid controls liquid saturation. Usually this is done referring to rigid porous material. This simplifying boundary condition assures that the work done at the liquid/vapour interface can be exclusively related to changes of free energy, i.e. the sorption energy. For example, Brunauer 1967 [16] used this assumption to develop the “Modelless method” for pore size/distribution characterization from gas sorption measurements.

In the following, an artificial pore system is introduced that, despite some simplifications, can be used to describe how SRAs might impact the drying of porous matter. For the sake of simplicity, a pore system, in the following referred to as “normcube”, is used. It comprises a layered structure of cubic single end pores (Figure 12). This insures that in the course of drying and filling there will be no hysteresis to be found.

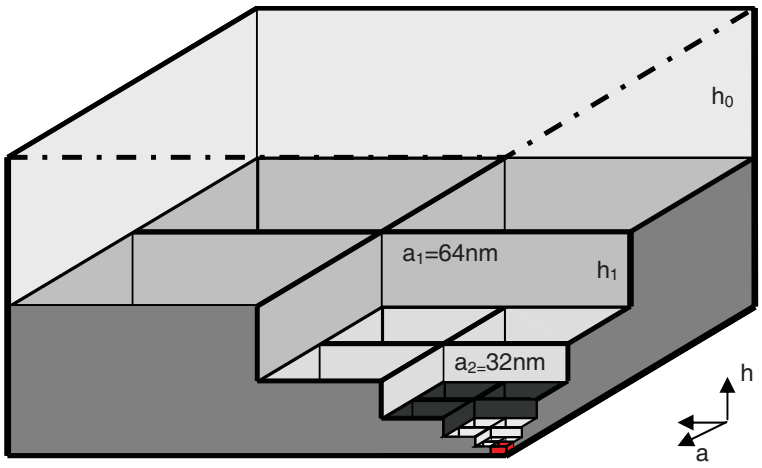

a_0=128nm; n_0=1 (max. pore size);
….
a_i= a_0*(1/2)^(i); n_i=4^(i);
…
a_6=2nm; n_6=4096 (min. pore size);

$h_i > a_i/2$; varying for each class

$V=\Sigma (n_i a_i^2 h_i)$; i=0,..,6 (volume);

$A=a_0^2+\Sigma (n_i 4 a_i h_i)$; i=0,..,6 (spec. area);

Figure 12: Normcube

Starting from a maximum pore size of a_0=128nm the drying of this pore enforces the next smaller class of pores to be exposed to the liquid/vapour interface and so on. The proposed pore system comprises the following advantages for sorption analysis:

a) the sorption proceeds in steps by pore class,

b) the pore size distribution is setup as a geometrical series following $a_i=2R_i$; $a_{i+1}=a_i/2$; i=0,…,6 so that the number of pores is $n_i=4^i$,

c) the overall geometry can easily be described enabling to discriminate between adsorbed layers (pore walls) and liquid phase,

d) the range of pore sizes can be adjusted similar to cementitious matter by varying the heights (h_i) of pores within each pore class with the only limitation that the $h_i > a_i/2$ so that a spherical meniscus can form before the pore class empties.

With this model, a sorption isotherm quite similar to cementitious material can be generated. Moreover, all along the sorption process the evolution of interfacial area can be described. This is true for all types of interfaces (liquid/vapour; solid/vapour; liquid/solid).

In a first attempt, the liquid phase considered is pure water. Using the t-curve for water vapour adsorption on cementitious matter provided by Badmann, Stockhausen and Setzer [18] one now can model the sorption process.

Starting from the very dry boundary, water vapour adsorbs at the pore walls thereby decreasing the actual interfacial area of the solid vapour interface. At certain humidity the smallest pores fill due to capillary condensation. This is determined over the whole sorption process by comparing the pore radius with the efficient Kelvin radius, calculated accounting for the thickness of the adsorbed water layer. Furthermore the volume of capillary condensed phase is calculated from the volume of the given class of pores and corrected for:

1) the volume of adsorbed water and
2) the volume of the spherical shaped meniscus.

The first correction is especially important for very small pores and the second is important if the length (h_i) of the pore is small.

Step by step, along the sorption isotherm one can follow how the normcube saturates. Most important: The evolution of interfacial area (area of menisci and pore walls with adsorbed layer) can be tracked along the sorption isotherm.

Concerning capillary condensation in small pores, it should be mentioned that for the smallest pore size, i.e. 2nm, there is no significant difference if either capillary condensation or the evolution of adsorbed multi layers is taken into account. In this work, capillary condensation was considered to proceed in pores of 2nm, which causes the sorption isotherm to comprise a sudden increase at the corresponding humidity.

In Figure 13 the hypothetical water vapour sorption isotherm of the normcube with minimum pore length can be seen (triangles). If the length of pores within each class is adjusted (normcube) a desorption isotherm of a hydrated cement paste (CEM I; w/c=0.4), measured in the course of this study (stars), can be approximated (circles). For these calculations a surface tension of γ=0.0726N/m was estimated. Figure 14 contains the cumulated surface area of the adjusted normcube versus the pore diameter. Additionally the appropriate surface plot of the chosen paste sample is shown. Results on paste are obtained from nitrogen adsorption and the model of Cranston & Inkley [58] for nitrogen desorption.

Figure 13: Hypothetical and measured sorption isotherms of CEM I, w/c=0.4

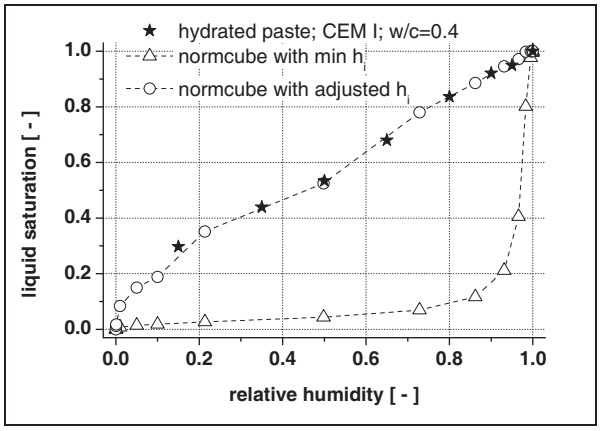

Figure 14: Surface area of adjusted normcube and paste from Figure 13 (measured N_2 desorption; Cranston & Inkley [58])

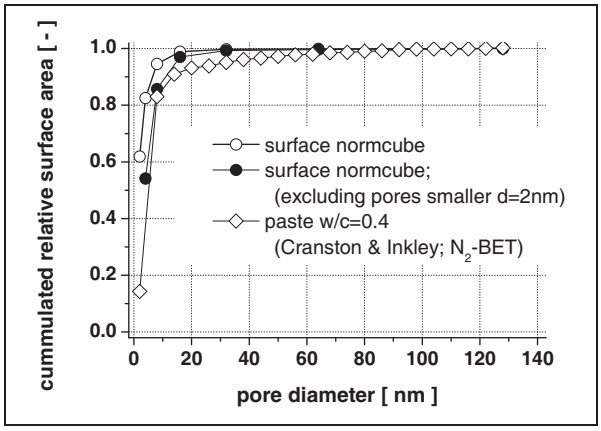

Taking into account that nitrogen ingress is supposed to be limited to pores smaller then 2-3nm, the cumulated normcube surface area excluding contribution from pores smaller 2nm is displayed. As can be seen, then, the modeled specific surface area contributions of the normcube pore classes gives

better correlation. Moreover, the actual volume/surface ratios are in reasonable correlation. In particular the model well captures the fact that about 85% of the internal surface area is to be found in pores smaller than 10nm. This is an important advantage for examining the behaviour of SRAs in cementitious materials.

To see if the assumption made for desorption of water vapour in this model are reasonable, we check if the energy of desorption and the work done at the liquid vapour interface are similar. For this, the energy of sorption is calculated using:

$$d^2G = dn_w \cdot d\mu_w \tag{62}$$

and the work done at the interfaces from:

$$dU = \gamma da \tag{63}$$

As can be seen in Figure 15, the plot of “energy of desorption” vs. “interfacial energy” gives a reasonable correlation. These results indicate that the normcube model performs reasonable well. Based on this, we now turn using this model to examine the (hypothetical) impact of SRA on drying.

Figure 15: Surface work vs. energy of sorption

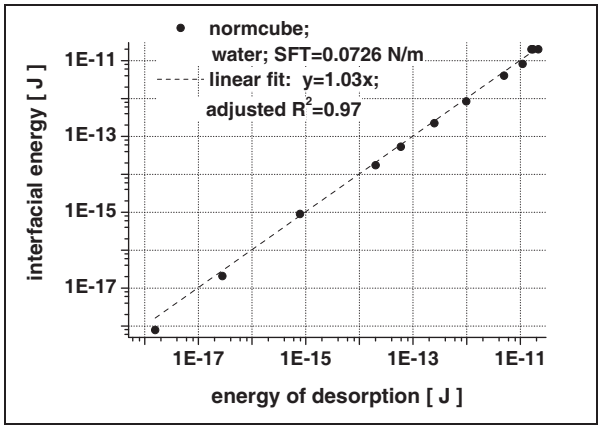

Figure 16: Influence of surface tension on water vapour sorption

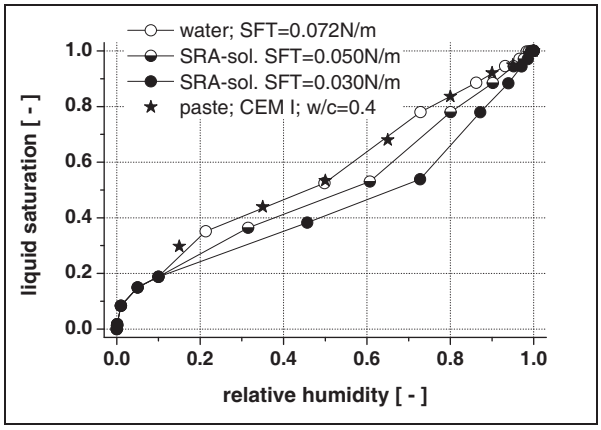

In Figure 16 the drying of the adjusted normcube is given for pore fluids comprising different surface tensions, starting from water down to γ=0.030N/m, which can be assumed to be the lower boundary for hydrocarbon surfactants (see section 4.2.2). For this, the *t*-curve used (Badmann, Stockhausen and Setzer [18]) was assumed to be unaffected by the presence of SRA. This is based on the review of Churaev 2003 [32] (subsection 4.2.6.), where non-ionic surfactants are identified to just weakly impact wetting film thickness.

A first observation is that the saturation curves merge at low humidity when the sorption is governed by pore wall adsorption only. More important, Figure 16 shows that for a fully rigid porous material a decrease in surface tension enhances water loss. In other words it reduces the saturation degree and hence the average pore pressure.

This is globally consistent with the literature observations reported in section 3.4. However, those results showed a much smaller increase of desorption along the isotherms or, for some, even none at all. To understand the reason for this, it proved beneficial to switch from a fully rigidity of porous material to a deformable one as outlined below.

5.2.2 Impact of surface tension on drying shrinkage of deformable systems

Based on the standard thermodynamics introduced above, the total gain of free energy of the partially saturated porous material can be described by the cumulative nature of the Helmholtz free energy, i.e. deformation energy and work done at the liquid/vapour interface.
In a first attempt, let us assume the desorption isotherms of porous deformable matter to be independent from the presence of SRA, so that the water loss of both systems dv_w is identical. This enforces the increase in Gibbs free energy to be similar for both systems all along the desorption proess. Because SRAs are proven to reduce shrinkage, the systems that contain them must comprise less deformation than the reference (so that $\varepsilon_{SRA} < \varepsilon_{plain}$). If the SRA system utilizes less energy in deformation of the solid, then the excess of energy has to be utilized to create additional interfacial area at the liquid solid interface. In the following we evaluate whether the water loss of the different systems can be similar in total, once this effect is taken into account.

For the sake of simplicity, the drying and shrinkage for a certain imposed humidity can be investigated using a single end cylindrical capillary as model system (Figure 17) instead of the normcube. Let R_0 be the initial radius of the cylindrical pore and ε_{plain} the equilibrium volumetric drying strain of the plain pore system, observed for an imposed relative humidity. Let furthermore the ratio of surface tensions of pore fluids with and without SRA be γ_w/γ_{SRA} and the shrinkage reduction due to the presence of SRA be a factor $f_{red} = \varepsilon_{SRA}/\varepsilon_{plain}$. For the saturated state the pore has a liquid/vapour interface with an area $a_0 = 2\pi R_0^2$.

Based on the pore geometry and shrinkage deformation, the water loss due to drying and shrinkage can be calculated using the Kelvin-Laplace equation (17).

Figure 17: Cylindrical single end “model” pore in equilibrium with imposed humidity of surrounding gas phase

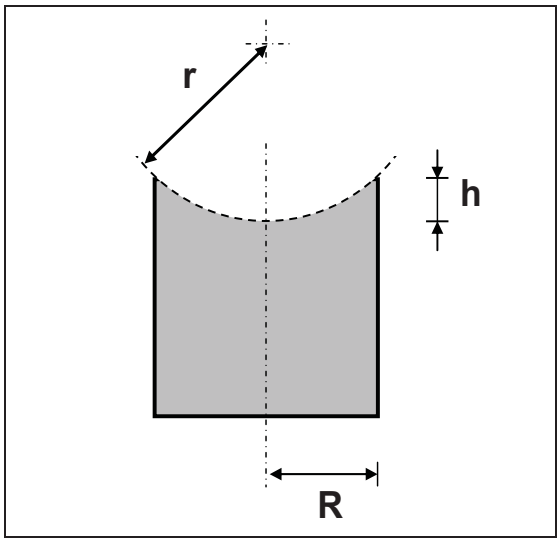

Surfaces exposed:

$a_0 = 2\pi R_0^2$ (saturated state);
$a_{curvatur} = 2\pi rh$ (partially saturated state);
$da = 2\pi rh - 2\pi R_0^2$;

Radii:

R_0 (saturated state)
$R_{plain} = R_0 (1-\varepsilon_{shr})$; (partially saturated state);
$R_{SRA} = R_0 (1-\varepsilon_{shr}) \gamma_{SRA}/\gamma_w$; (partially saturated state)

Volume:

$v_0 = 2\pi R_0^2 l$; (l – length of the pore)
$dv_\varepsilon \sim v_0 (\varepsilon_{shr})$; (due to pore shrinkage);
$dv_{cap} = \pi/3\, h^2 (3r-h)$; (due to meniscus)

Using the deformations defined for the pores (with/without SRA) one first can derive the water loss due to overall shrinkage of the pore $dv_W[\varepsilon]$ reading:

$$dv_W\{\varepsilon\} \sim v_0 \varepsilon \tag{64}$$

The water loss due to the formation of the meniscus $dv_{interface}$ at certain humidity can be derived using Kelvin-Laplace (17) for deriving the Kelvin-radius r_K and the volume of the cap formed by the meniscus then reads:

$$dv_{Interface}\{RH\} = \frac{\pi}{3} h^2 \left(3r_K - h\right) \tag{65}$$

The total water loss upon drying now can be defined reading

$$dv_{W\_tot.}\{RH;\varepsilon\} \sim v_0\varepsilon + \frac{\pi}{3} h^2 \left(3r_K - h\right) \tag{66}$$

Because the geometry of the cylindrical pore one can exactly discriminate between interfacial energy utilized at the liquid/vapour interface and energy utilized in deformation of the solid body. Moreover, the energy balance can be setup because the referring amounts of water, i.e. water loss upon formation of meniscus and water loss due to decrease of pore volume, can be calculated.

The volume loss due to overall shrinkage of the pore is smaller in presence of the SRA as indicated in Figure 18.

$$dv_{W\_SRA}\{\varepsilon\} = v_0\varepsilon_{shr\_plain} f_{red} < v_0\varepsilon_{shr\_plain} = dv_{W\_plain}\{\varepsilon\} \tag{67}$$

According to this, the energy utilized in deformation is lower for the SRA-modified pore.

The water loss due to formation of a meniscus at an imposed humidity can be calculated according (17). One obtains that the pore solution with the lower surface tension leads to a smaller Kelvin-radius r_K:

$$\frac{r_{K\_SRA}\{RH\}}{r_{K\_plain}\{RH\}} = \frac{\gamma_{SRA}}{\gamma_{plain}} \tag{68}$$

Let us assume that the smaller meniscus of the SRA-modified pore does not get smaller than the pore radius of the shrunken pore. For convenience of representation we however consider the meniscus forming to fully penetrate the pore (same radius). As can be taken from (68) the meniscus of the pore without SRA will comprise a larger radius as indicated in Figure 18. Because its penetration depth is always smaller, the volume of water lost due to formation of the meniscus has to be lower (compare to (65)).

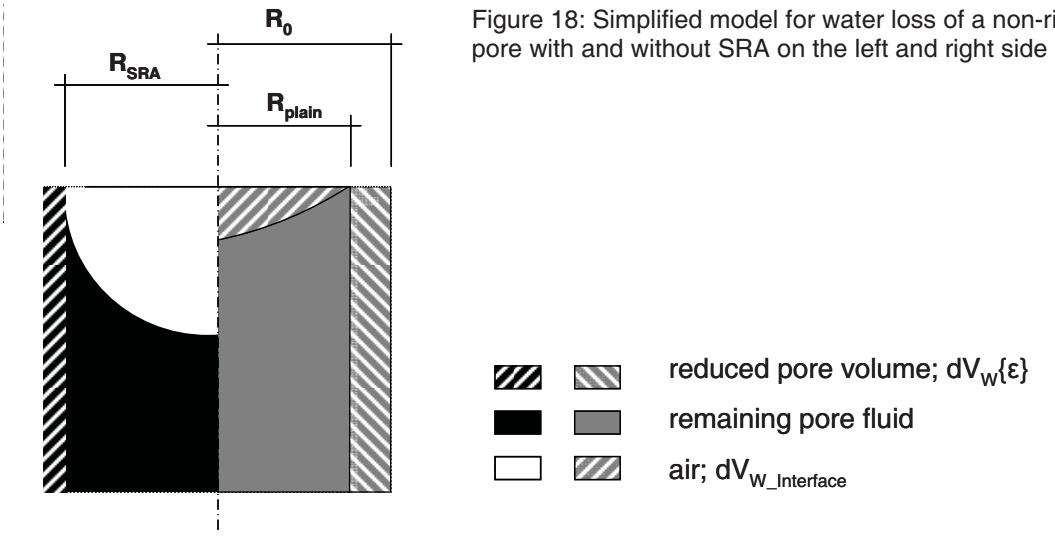

Figure 18: Simplified model for water loss of a non-rigid drying pore with and without SRA on the left and right side respectively

It can be summarized that the water loss due to the formation of the meniscus is higher for a decreased surface tension. However, the water loss due to deformation of the pore is lower with SRAs.

In a next step, the energy balance for each pore system is obtained from the change of excess Gibbs free energy. Moreover, because one can discriminate between water fractions lost either because of deformation or creation of liquid/vapour interfaces, the energy utilized for elastic deformation and for creating interfacial area can be obtained separately.

With this, it can be shown that for different combinations of:

a) relative humidity

b) pore lengths and initial pore radii

c) surface tensions (30mN/m to about 75mN/m)

d) shrinkage reduction (0.5 to 1)

the total water loss upon drying and shrinkage can be similar in presence or absence of SRA.

Therefore, the results of authors, who could not observe enhance drying due to SRA, are not contradictionary to the results obtained from normcube modeling.

Moreover, an important limitation referring to the application of models for shrinkage deformation prediction can now be evidenced:

From the total water loss one cannot discriminate between work utilized for deforming the material and work done to create interfacial area at the liquid/vapour interface. A proper description of the process always requires additional information over whole drying process concerning the evolution of:

a) interfacial area exposed

b) pore geometry

c) surface tension on the liquid/vapour interface

5.3 Conclusions

Based on the considerations of the above section, it appears that drying shrinkage of SRA treated systems most probably cannot be calculated just using desorption isotherms. The following considerations would help to overcome this:

1) Assumed that SRA treatment has minor impact on microstructure of cement paste, the geometry factor can be handled. Within comparative studies on systems comprising different dosages of SRAs, energy balances based on the measured shrinkage and desorption isotherms would enable a clear discrimination between water lost because of deformation and water lost due to the increase of interfacial area.

2) In case major differences in microstructure are obtained with SRA, porosity and internal surface area have to be examined in particular. Despite differences for these parameters, one still can obtain which fraction of Gibbs fee energy is utilized for deformation and address the residual amount to the creation of interfacial area.

3) For SRA treated systems, the evolution of surface tension during drying is unknown but takes strong impact on how the excess Gibbs free energy is utilized. In this chapter, it could be shown that in presence of SRA more liquid/vapour interfacial area is exposed for a given relative humidity. Moreover, this increases with the decrease of the surface tension.
   We recognize that both has to be properly described, the interfacial area, determined by the cement microstructure, and the evolution of surface tension, determined by the nature and the presence of SRA on these interfaces. The first is essential because the ability of the SRA to decrease the surface tension depends mainly on its concentration at these interfaces.

4) Eventually, based on the findings of 1) to 3), a relationship might be obtained that provides a clear view on how the excess free energy will be utilized and which microstructural features are responsible for that. Then, if such specific information can be obtained from a sorption isotherm, shrinkage may be predictable thereof.

5.4 Summary

In this chapter a suitable model capturing the most important effects of SRAs during drying and shrinkage of cement paste was obtained from a theoretical point of view. This model is mainly based on Coussy´s approach for shrinkage predictions but the major difference comes from the discrimination between bulk and adsorbed water, which may compensate for the specific short comings of his and other current models for shrinkage prediction.

Furthermore, an artificial pore system is introduced that, despite some simplifications, can be used to describe how SRAs might impact the drying of porous material. With this model, a sorption isotherm quite similar to cementitious material can be generated. Moreover, all along the sorption process the evolution of interfacial area can be described.

It revealed that SRA most probably reduce the saturation degree and hence, shrinkage is reduced because of the reduction of the average pore pressure. Assuming cementitious materials as deformable, this hypothesis then could be shown to be in line with data published in the literature on SRAs, which on a first look seemed to be contradictory.

Based on the theoretical findings in this chapter, the methodology required elaborating the mechnisms of SRAs for drying and shrinkage within the experimental part of this study can properly be developed and is the subject of the next chapter.

6 Materials and methods

6.1 Model systems

Regarding the application of SRA to self consolidating concretes, possible admixture interaction effects have to be taken into account. Therefore, a combination of both types of admixtures, SRA and SP, are investigated. To enable a more clear view on the mechanisms of SRA it was decided to study hydration mechanisms on hydrated Portland cement paste containing different amounts of SRA and SP alone as well as mixtures thereof.

To exclude influences from autogenous deformation and enable a high degree of hydration, the water content of paste is set to a water/cement ratio of w/c=0.4. Regarding Portland cement hydration, work published by Stark et al. 2000-2006 [212-214] as well as Lothenbach et al. 2006 [215] is used for plain cement pastes (without admixture/reference paste). With respect to self consolidating concretes a composite binder comprising 35wt.-% limestone is introduced as a second model system. Hydration mechanisms for this type of composite binder are well described and can be derived from Matschei et al. 2006-07 [216-220].

The investigation on shrinkage involves shrinkage and water vapour desorption isotherms on:

a) cement paste (two binder systems) containing different commercial SRA,

b) self consolidating mortars (two binder systems) containing SP (for adequate flow property) and different amounts of a representative SRA. and

c) standard mortar according EN 196-1 (without superplasticizer)

In general all substitutions concerning addition of admixtures or replacement of cement are executed on volume base, i.e. admixtures replaced mixing water and mineral additive replaced unhydrated cement.

With the focus on drying shrinkage all samples were allowed to hydrate at water vapour saturated condition for 28 days before being exposed to a dry climate.

6.2 Materials

Cement: In this study the investigations were carried out using a Normal Portland Cement CEM I 42.5N according European Standard EN197-1 with Blaine fineness of 2650cm²/g and density ρ_c=3.17g/cm³. The analysis of chemical and mineralogical composition of the commercially available cement was conducted using different methods on both, the commercial cement and its clinker raw material. The elemental oxide compositions are given in Tab.A2- 1. For adsorption measurements additionally tricalciumsilicate (C_3S); synthetic ettringite and synthetic calcium-silicate-hydrate (C-S-H) were used. The synthetic clinker and hydrate phases were produced and provided by Zingg [221].

Mineral additions: The binders for self consolidating mortars and concretes were prepared by replacing cement by an inert additive i.e. natural limestone containing more than 95wt.-% $CaCO_3$; density ρ_L=2.77g/cm³. The elemental oxide composition is given in Tab.A2- 1. This inert additive was chosen in such a way that the particle size distribution was close to that of the cement. Under this condition and at constant volume ratio of solids/liquids in paste, mortar suspensions were supposed to achieve similar flow properties.

Aggregates: Mortars were mainly composed containing 50vol.-% of CEN-reference-sand (0-2mm) / European Standard EN 196-1. For a selected series of self consolidating mortars, alluvial aggregate 0-4mm was incorporated (aggregate content about 45vol.-%).

Superplasticizer (SP): To adjust flow properties of mortars, a polycarboxylate type superplasticizer (SP-PCE; solid content 26 ±1wt.-%) was added at a maximum dosage of 2wt.-% of cement. For

the investigation on the interaction of superplasticizer and shrinkage reducing admixtures an additional polynaphthalene based plasticizer (SP-PNS) was incorporated.

Shrinkage reducing admixtures (SRA): For a comparative study on the performance and efficiency of different shrinkage reducing admixtures four commercially available products, three different raw materials for the production of SRA as well as two industrial cleaning agents/surfactants were applied to several self consolidating mortars (SCM). Hydration studies were executed mainly with SRA1 but also with SRA2 and SRA3. Table 2 contains the denomination, type of application and main ingredients of the admixtures used.

Table 2: Shrinkage Reducing Admixtures

Denom.	application	main ingredients	density [g/cm³]
SRA 1	concrete admixture	~ 80wt.-% dipropylene-tert-buthylether; M=190.3g/mol; ~15wt.-% dipropylenglykol; M=134.2g/mol; ~5wt.-% dipropylene-di-tert-buthylether	0.96
SRA 2	concrete admixture	~ 2.5-10wt.-% 2-butylaminoethanol;M=117.2g/mol; ~50-100wt.-% 2.2-dimethyl-1.3propandiol; M=104.2g/mol	1.00
SRA 3	concrete admixture	not available	0.91
SRA4	cleaning agent	not available	1.01
SRA5	cleaning agent	not available	0.98
SRA6	concrete admixture	not available	0.96
SRA7	surfactant	1.5 Pentanediol ($HOCH(CH_2)_3CHOH$)	0.99
SRA8	surfactant	Octanol ($CH_3(CH_2)_7OH$)	0.82
SRA9	surfactant	n-Nonanol ($CH_3(CH_2)_8OH$)	0.83

6.3 Methods

6.3.1 Preparation and curing of cement paste, mortar and concrete

6.3.1.1 Preparation of samples

Cement paste: Cement pastes were prepared with w/c=0.4; that is v_{water}/v_{solid}= 1.27. Pastes containing composite binder with 35vol.-% limestone also comprise v_{water}/v_{solid}= 1.27 and therefore have a water to binder ratio of w/b=0.42 and an efficient $w/c_{eff.}$=0.61.
As mentioned before, admixtures replaced mixing water by volume. For a minimum amount of 1l paste, the suspensions were premixed using a Hobart mixer prior to high-speed mixing in a static blender with blade guard at 1000rpm.
The total amount of mixing water was divided into two or three parts because organic admixtures were pre-dispersed in about 50ml of water (part of mixing water). Cement and two thirds of water were premixed for one minute. Then the aqueous solutions of admixtures were added. Total mixing time was set to 4 minutes.
To avoid bleeding and segregation before stiffening, especially when SP was introduced, pastes were poured in cylindrical polyethylene flasks (max. 0.5l) and homogenized on a roller block. Setting times were approximated from results of isothermal heat conduction calorimetry measurements. At the time the acceleration period of cement hydration started, the flasks were removed and stored in a water basin (T=20°C).

Mortars and Concrete: Mortars were mixed according to the European Standard EN 196-2 using a Hobart Mixer, mix capacity V= 2l. For concretes, cement and aggregates were dry-mixed for one minute. Then, the mixing water or aqueous solution of SRA was added. After an absolute mixing time of two minutes the SP was added as an aqueous solution (dilution of about 1:3; water as part of total amount of mixing water). The dosage of SP was adapted to reach self consolidation.

The flow properties of self consolidating mortars (SCM) and concrete (SCC) were adjusted using the slump flow and V-funnel test for mortars as well as the slump flow and L-box test for concrete. Criterions for self consolidating property are shown in Figure 19. Compositions of mortars and concretes are outlined in appendix, tables Tab.A2- 5 and Tab.A2- 6.

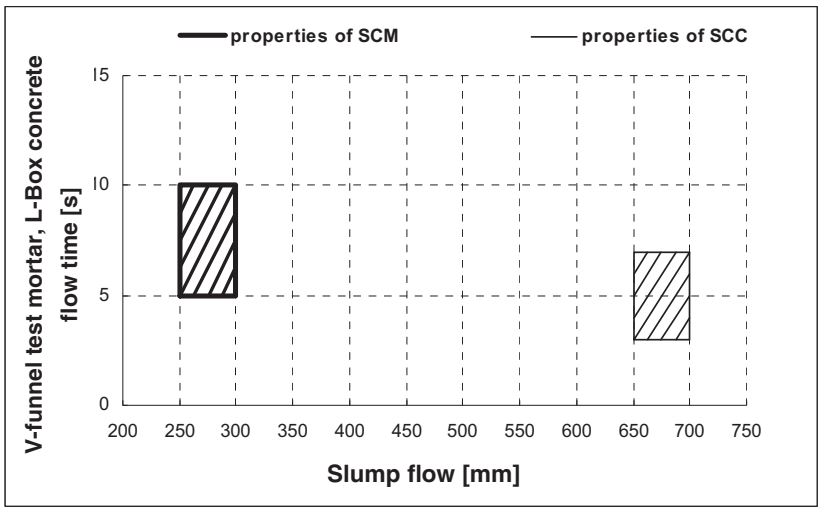

Figure 19: Criterions for self consolidating property of SCM and SCC

6.3.1.2 Curing of samples

Cement paste: Samples for the measurement of one dimensional drying or drying profiles were cast and stored at 20°C and 95%R.H and demolded after 16 hours of hydration. Before exposition into dry climate these samples were wet cured at 20°C/95% RH.
Prismatic samples for measurement of drying shrinkage or shrinkage isotherms were produced after seven days (demolding and sawing). Up to this time these samples hydrated under sealed conditions. After saw cutting, the specimens were stored in sealed containers at 20°C and >95%R.H. up to 28 days of hydration.
For series of specimens that did not show capillary condensation during wet curing the surface was wetted using a sprayer and deionised water (in the following referred to as “inert saturation”). By following this approach, a maximum degree of saturation was supposed to be ensured, thereby avoiding leaching effects that would have to be taken into account if specimen had been stored in water.

Mortar: The mortar samples were cast and stored at 20°C and 95%RH. Depending on the SP content of the different mortars, the samples were demolded after 16 hours (plain mixtures) and about 24 hours for mortars containing SP. After demolding, the mortars were wet cured/stored to at 20°C/95%R.H. until exposition to drying. A maximum degree of saturation was supposed to be achievable by applying inert saturation.

Concrete: Specimens were cast and stored at 20°C/95%RH. After 24 hours of hydration, the specimen were demolded and stored at 20°C/95%R.H. until exposition into dry climate.

6.3.2 Analytical methods

6.3.2.1 Surface activity and phase behaviour of SRA

The following measurements were carried out in 20°C/65%RH using material comprising ambient temperature.

The surface tension of aqueous solutions was measured using Wilhelmy-plate method [86] where the dosage of admixture was changed by titration with a stock solution.
For aqueous electrolyte solutions, i.e. synthetic pore solutions, the pendant drop [86] method was pre-

ferred due to rapid carbonation of the solution in presence of carbon dioxide when using the plate method.

Phase transition experiments of aqueous solutions of SRA were performed in 50ml polyethylene flasks. After shaking, the solutions were kept at rest at 20°C for 24h to achieve equilibrium conditions. In case of phase transition, the volume fractions were read out from the flask scale, matching a resolution of 0.1ml/50ml (= 0.2%).

6.3.2.2 Isothermal heat flow calorimetry

The heat release during cement hydration was measured on cement pastes by isothermal heat conduction calorimetry (conduction calorimeter - TAM Air; Thermometrics). The samples were equilibrated to a reference temperature of 20°C. To produce a homogeneous paste, the samples were stirred while injecting liquids (mixing water including admixture) into the reaction vessel.
The method was used to develop time schedules for sample preparation in case of hydration kinetics are impacted in presence of admixtures. In this way, it was possible to provide the comparison of paste properties at equal stages of hydration. Five stages of Portland cement hydration were distinguished a) first hour of induction period, b) end of induction period, c) acceleration period, d) deceleration period and e) final period. Sampling times for several different analyses were scheduled according to this characteristic heat release.

6.3.2.3 Phase analysis of unhydrated and hydrated cement

Elemental oxide distributions of unhydrated cement and clinker were obtained from Wavelength Dispersive X-ray Fluorescence Spectroscopy (WD-XRF).

Crystalline hydration products, unhydrated cement phases and crystalline organic compounds were identified by X-ray powder diffraction (XRPD) using a Philips PW2400. The CuK_α (λ=1.5418Å) radiation was generated at 40mA and 40kV. Data have been collected over a Bragg angle range of 5-80°2Θ, screening an angular range of 6°2Θmin^{-1}, resolution or angular step width of 0.017°2Θ respectively.
Thermogravimetric measurements were performed using a *Mettler Toledo TGA/SDTA851e*. An amount of about 10mg of the ground samples (<63µm) was weighed and inserted into the analyser. The temperature range covered was 30°C to 1100°C with a heating rate of 20Kmin^{-1} under steady flow of nitrogen as protective gas.

6.3.2.4 Adsorption of SRA onto solid/liquid interface of selected hydration phases

In addition to the measurement of SRA adsorption onto hydrating Portland cement, the adsorption onto selected hydrated phases was investigated. For this, synthetic ettringite and synthetic C-S-H phases were first analysed for their specific N_2-BET surfaces (see 6.3.3.4). A stock solution of synthetic cement pore solution was prepared comprising an electrolyte composition according the results obtained for the reference cement paste (CEM I, w/c=0.4) at the end of the induction period. An amount of solids providing a specific surface area of about 20m² and one litre of stock solution were poured into an Erlenmeyer flask and stirred using a magnetic stirrer. Within a titration regime, the dosage of organic admixture was increased step by step. After each titration step the mixture was stirred for 5 minutes and then left to rest until the solid content had settled down and the liquid phase appeared to be clear. In average and for each step this took about 20 minutes. After each cycle a volume of solution equal to the one added in the titration step was removed for analysis. It was filtered using a 0.4µm syringe filter before the total organic carbon content (TOC) was measured. These adsorption measurements were conducted at T=20°C.

6.3.2.5 Analysis of liquid phases

The pH-measurements on cement pore solution were carried out immediately after extraction using a pH-electrode (Knick SE pH7Pt1000 electrode) calibrated with 0.1M to 1M potassium hydroxide-solutions.

The total organic carbon content (TOC) was measured on eluate from leaching tests, extracted cement pore solutions and synthetic pore solutions with organic admixtures. The solutions were passed through a 0.4µm nylon filter and subsequently diluted using hydrochloric acid to a) achieve acid conditions or pH~2 for outgasing of carbon dioxide or inorganic carbon respectively and b) to avoid precipitation of solids. Further dilutions with respect to the measuring range of the used analysers (Shimadzu TOC-5000A; Sievers DataPro5310C) were prepared using purified water.

The ionic composition of solutions was measured by Inductively Coupled Plasma-Optical Emission Spectroscopy (ICP-OES) using a Varian VISTA Pro. The freshly extracted pore solution passed through a 0.4µm nylon filter and 1ml of it was diluted with 9ml nitric acid, i.e. 6.5% HNO_3 , sealed and stored at T=5°C until measurement.

To discriminate and quantify SRA and SP-PCE in aqueous solutions, Gas Chromatography (GC) was used. The measurement approach was developed for discriminating SRA1 in electrolyte solutions of SRA1 and SP-PCE (see 6.2).

To remove the ionic content and water from the eluate and extract SRA or SRA/SP-PCE, 1ml of the eluate was processed into an extraction column NT 1.0 (Merck). After 15 minutes, the organic residue was eluted and removed from the column using dichloromethane as liquid-liquid extractor. The extract was then poured into a rounded flask containing 0.7ml 2-propanol. At 50°C and 600mbar, the dichloromethane was removed using a rotary evaporator and the residue was filled into a 1ml volumetric flask. The gas phase chromatography was executed using a *Carlo Erba HRGC Mega 2* chromatograph with standard GC column 30m x 0.25 mm *Stabilwax@DB*, film thickness 0.25µm, carrier gas hydrogen, p_{H2} = 110kPa, make-up gas nitrogen, p_{N2}=80kPa. The injection was executed “on column”. The temperature regime was as follows: From 80°C to 110°C the heating rate was 30K*min^{-1}; from 110°C-200°C a rate of 10Kmin^{-1} was applied. After reaching 200°C, the temperature was kept constant for 10min.
Due to the different molecular masses of SRA ($M_{Ø}$~200g/mol) and SP used (M>1000g/mol), the SP-PCE fraction is non-volatile and hence not part of the gaseous phase.

Calibration curves for SRA1 quantification were constructed using dipropylene glycol-tert-butylether (Di(propylene glycol) tert-butyl ether, mixture of isomers; 90%; Sigma-Aldrich) as pure substance. Dipropylene glycol-tertbutylether is the main ingredient of SRA1 (compare to Table 2) and therefore chosen as reference. Note that the calibration regime directly started with gas chromatography and did not include the procedure for removing the ionic content. The calibration regime revealed an appropriate recovery degree for aqueous solutions of SRA1.

6.3.2.6 Preparative methods

Stopping of hydration reactions: Thermogravimetric measurements and solid phase analyses in the course of ongoing cement hydration required the precise stopping of the chemical reactions. The hydration of cement paste was stopped by adding 2-propanol to the paste and subsequently drying at 35 °C. For samples at hydration levels beyond setting, a slice was sawed and subsequently stored in 2-propanol. Later the slice was pre-ground and dried at 35°C. After drying, all samples were ground to a grain size below 45 µm.

Extraction of pore solution from hydrating cement paste and mortar: For hydrated cement pastes with low degrees of hydration the pore solution was extracted by pneumatic filtration (pressure). Pore solution from hardened cement pastes was extracted from cylindrical specimen by squeezing on a hydraulic press.

After extraction, the solutions were passed through a 0.4µm nylon filter using a syringe and stored in sealed tubes at a temperature of T=5°C.

6.3.3 Microstructural investigations

6.3.3.1 Chemical shrinkage of hydrating cement

The chemical shrinkage of cement paste and mortar was measured on cylindrical specimens (diameter 6cm; volume v_{sample}~ 260±10ml). In contrast to literature reports, the sample diameter was chosen that large to reduce the sample height. This facilitates the measurement if water movement upon self desiccation is impacted by the presence of SRA. Because low permeability or depercolation of capillary pores may retard the core hydration, the observation time had to be sufficiently long. Specimens were observed over a time range of one year.

For the production of theses samples a volume of about 260±10ml of fresh cement paste, w/c=0.4, and mortar were inserted by weight into a 300ml PE-LD bottle (known material density and weight of bottle including lid). After inserting paste or mortar the bottles were carefully filled with and closed under water. The amount of excess or curing water respectively was obtained by weighing the surface-dry bottle. The overall volume of the filled bottle was obtained by water displacement or hydrostatic weighting (Archimedes' principle) respectively.

Due to chemical shrinkage, the volume of paste is supposed to decrease. This internal volume reduction may deform the wall of the bottles and may generate tensile stress (bottle material) or depression (sample and excess water). To avoid this problem, prior to each hydrostatic measurement, the bottle was opened and subsequently closed under water to compensate any possible volume loss by an equivalent amount of entering excess water.

The refilling of bottles additionally provides two main advantages: On the one hand the excess water surrounds the shrinking body and so contributes to wet curing of the samples; on the other hand compensation of volume loss due to chemical shrinkage re-establishes atmospheric pressure inside the bottle and relaxes the wall material.

Furthermore, the closed bottle is stored in a water bath (T= 20°C) This provides an almost closed system or a semi permeable diffusion barrier at least. Assuming that the concentration of the sample's pore solution and excess water is much higher than that of the surrounding water, only an osmotically driven ingress of water into the bottle would be expected. The amount of water that osmotically enters is then included in the total amount of excess water from "refilling". The ingress of carbon dioxide through the walls of the bottle during storage can be neglected due to fact that the chosen water bath periodically was used for water curing of fresh mortar samples (leached portlandite serves as sacrifice material) and so provides active protection from carbonisation (measured pH in the range of 10<pH<12).

At each time step, the chemical shrinkage of the initial volume of paste or mortar sample was calculated from the following equations:

$$\Delta v_{sample;\,tx} = \left(\frac{m_{bottle;\,tx} - mu_{bottle;\,tx}}{\rho_{water}} \right) - v_{bottle} - v_{excess\_water;\,tx} - v_{sample;\,t0} \qquad (69)$$

$$v_{excess\_water;\,tx} = \left(\frac{m_{bottle;\,tx} - m_{bottle;\,empty} - m_{sample;\,t0}}{\rho_{water}} \right) \qquad (70)$$

where:

$m_{sample;\,to}$	initial weight of inserted sample	[g]
$m_{bottle;tx}$	total weight of blotted bottle (sample, excess water; bottle with lid)	[g]
$mu_{bottle;tx}$	under water weighing of the bottle	[g]

ρ_{water}	density of water at 20°C;	[g/cm³]
v_{bottle}	volume of bottle material including lid	[ml]
$v_{excess\_water;tx}$	volume of excess water at each measurement	[ml]
$v_{sample;\ to}$	calculated volume of unhydrated cement and liquid components	[ml]

After the final hydrostatic measurement the samples were removed from the bottles and the total volume of the sample could be obtained by hydrostatic measurement using equation (71).

$$v_{sample;\ t_{end}} = \left(\frac{m_{sample;\ t_{end}} - mu_{sample;\ t_{end}}}{\rho_{water}} \right) \quad (71)$$

From weight and volume measurements the amount and density of adsorbed and physically bound water can be calculated.

6.3.3.2 Environmental Scanning Electron Microscopy (ESEM)

The observation of early cement hydration was carried out with an Environmental SEM (FEI, Netherlands) equipped with a Field Emission Gun (ESEM-FEG). The operational parameters for the "Environmental" mode were the following: water vapour pressure in the chamber was set to 8.3 – 9.4 mbar and sample temperature to 12°C. Depending on pressure and temperature, the relative humidity was kept between 75 and 90% for the area of the cooled sample. Micrographs were taken at 25keV acceleration voltages.

For ESEM observations during early cement hydration it is crucial to avoid drying artefacts. Following the proven approach given in Roessler et al. 2008 [222] two adjustments were made to address this problem:

1. The residual pore solutions of fresh cement pastes were removed with filter paper. Then the sample immediately was inserted into the microscope chamber.
2. Inside the chamber a few millimetres of the sample surface were removed using a micromanipulator and generating a fresh fractured surface. This fresh surface is supposed to be free from drying artefacts or precipitates formed due to residues of pore solution evaporating in close vicinity to sample surface.

6.3.3.3 Mercury Intrusion Porosimetry (MIP)

Mercury intrusion porosimetry was measured on cement pastes and mortars. After an absolute hydration time of 28 days the samples were sawed into slices of about 5mm, stored for 2 days in 2-propanol (solvent exchange) and then oven dried at T= 50°C. The dried slices were broken into pieces of about 25mm³. The measurements were carried out on a mercury porosimeter Thermoelectron Pascal 140/440.

6.3.3.4 Measurement of specific surface (N_2-BET)

Samples of unhydrated cement; synthetic alite, hydrated cement and pure hydration products were ground to a maximum particle size smaller than 63µm. The drying regime for hydrated samples follows 6.3.3.3. Before measurement, the samples were evacuated for 3 hours at a temperature T=35°C. The measurements were executed in a Beckman Coulter SA 3100 versatile gas adsorption analyzer using nitrogen as sorptive gas.

6.3.4 Drying shrinkage and water vapour desorption isotherms

6.3.4.1 Sample preparation

Prismatic samples for measurement of drying shrinkage or desorption isotherms were produced and cured according to section 6.3.1.

6.3.4.2 Water vapour desorption isotherms

Water desorption isotherms were measured for pastes and mortars on specimens with different ratios of surface/volume (a/v). Table 3 contains an overview of the different specimen geometries as well as the different storage regimes. For the storage regimes 1 and 3 - “static” mass loss was documented until equilibrium saturation was achieved and sample weight was constant. For the storage regime 2 - “step by step” the mass loss of certain selected reference samples was monitored online. After mass equilibrium was approximately achieved, the specimen were weighed and climate conditions were changed. Measurement for regime 2 was carried out without protective gas environment so that impact of carbonation could be an issue.

Table 3: Geometries and drying regimes for paste and mortar specimen

regime	geometry	a/v	regime description
[nbr.]	[mm³]	[m^{-1}]	[-]
1	25.4 x 25.4 x 12.7***	315	“static”; storage till equilibrium humidity is achieved; at different RH (87%; 80%; 70%; 50%; 40%; 30%) under N_2
2	a) 10 x 40 x 160 * b) 10 x 40 x 100 **	263 270	“step by step” from 100%; 90%; 80%; 65%; 50% to 35% RH; static at 88%; 70% and 35% RH; ~equilibrium humidity between each step
3	Ø12.7 x 101.6 ***	335	“static”; storage till equilibrium humidity is achieved; at different RH (87%; 80%; 70%; 50%; 40%; 30%) under N_2

*) mortar; **) cement paste; ***) mortar and cement paste

In Figure 20 it can be seen that the paste sample achieves equilibrium after about 56 days of exposition. Moreover, the time to equilibrium increases with decreasing relative humidity. The duration of drying steps for the “step by step” regime therefore increased with decreasing relative humidity.

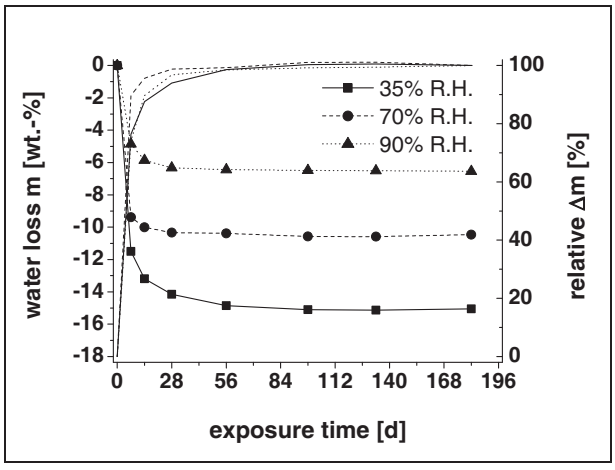

Figure 20: Example for measuring weight loss of saturated paste sample exposed to defined climates

lines with symbols: water loss

dashed lines: relative water loss

6.3.4.3 Shrinkage isotherms

Length change was measured using a digital comparator with a resolution of 1µm. The measurements were taken along the measurements of water vapour desorption isotherms on cement paste and mortar samples regime-nbr. 2a, 2b and 3 (see above). At the end of each desorption regime specimens were resaturated and the irreversible shrinkage strain was calculated from final length change.
In Figure 21 the length change of the sample introduced via Figure 20 is shown. It can be seen that

the length still changes whilst moisture equilibrium is already achieved. This is due to either drying creep or carbonation shrinkage. Because of this, absolute values for shrinkage isotherms were taken once moisture equilibrium was achieved.

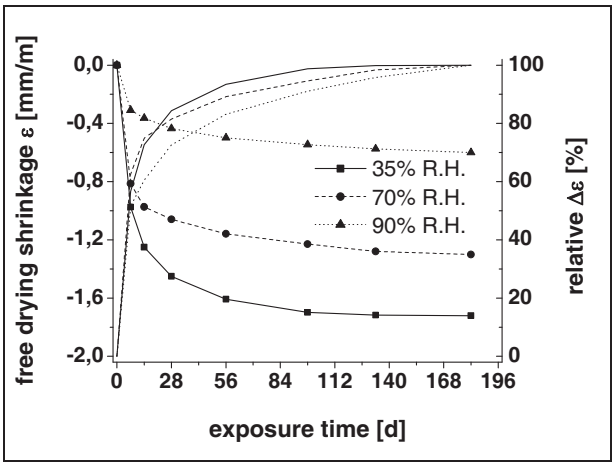

Figure 21: Example for measuring free drying shrinkage of saturated paste sample exposed to defined climates

lines with symbols: shrinkage strain

dashed lines: relative shrinkage strain

6.3.5 Leaching of SRA

6.3.5.1 Introduction

In this section a short overview on diffusion terminology is given [223-235]. This is later used for data treatment of the leaching tests. Furthermore material characteristics and the sample preparation as well as the tank test specifications are outlined.

6.3.5.2 Evaluation of effective Diffusion coefficients using tank tests

In the above mentioned studies the evaluation of effective diffusion coefficients is based on Ficks second law (72) in which the concentration of species c(x;t) changes due to diffusion.

$$\frac{dc}{dt} = D\frac{d^2c}{d^2x} \tag{72}$$

where:

***c*:**	concentration of diffusing species	[mol/m ³]
***D*:**	diffusion coefficient	[m²/s]
***t*:**	time	[s]
***x*:**	diffusion length	[m]

The binary diffusion coefficient $D_{i,j}$ describes the diffusion of the species "*i*" in a solvent "*j*". For cementitious systems, SRA diffusion can be assumed to proceed in the water saturated pores and the binary diffusion coefficient for SRA would then refer to an aqueous electrolyte solution. Dependent on the tortuosity of the pore systems, the effective diffusion length significantly increases. Moreover, interactions of the freely diffusing molecules with the pore walls may additionally increase the effective diffusion length. For porous systems, all factors enhancing the diffusion length can be described using the overall impedance factor "*y*" of the porous system. Regarding this, the effective diffusion coefficient D_e of the species "*i*" in the pore fluid "*j*" of a given pore system is:

$$D_e = yD_0 \tag{73}$$

where:

***D₀*:**	binary diffusion coefficient of species i in solvent j	[m²/s]

***y*:**	impedance factor	[-]
***D_e*:**	effective diffusion coefficient	[m²/s]

For diffusing species that additionally comprise interactions with the solids forming the porous system, the effective diffusion coefficient D_e can be obtained from the apparent diffusion coefficient D_a by introducing the retardation term *R*. The *R*-term accounts for the distribution of the diffusing species, i.e. the fraction which is part of the liquid phase (solvent) and the fraction associated to solid interfaces [227, 234].

$$D_a = \frac{D_e}{R} = \frac{yD_0}{R} \tag{74}$$

where:

***D_a*:**	apparent diffusion coefficient	[m²/s]
***R*:**	retardation term	[-]

For a given saturated pore system the impedance factor *y* can experimentally be obtained using a tracer comprising no interaction with the solid interfaces. This requires that the binary diffusion coefficient of this tracer in the specific pore fluid is known. The effective diffusion coefficient is obtained from the measurements and the impedance factor can be calculated therefrom.
Once the impedance of a given pore system is obtained, the diffusion of species comprising certain interaction with the solid interface can be properly described.

The evaluation of effective diffusion coefficients strongly depends on the geometric boundaries ot the tank test setup. Concerning tank tests used in this study, the one dimensional solution to Fick´s second law will be used.

6.3.5.3 Determination of the dominating leaching mechanism by tank tests

In Hohberg [233] the solution to Fick's second law for various geometric setups of tank tests is described. As limiting factors, the volume to surface ratio and the amount of eluate are chosen so that the leached species can be properly detected. One possible tank test procedure is given as follows:

Within several cycles, the sample is placed in a defined amount of eluent and the leached species are quantitatively determined. After each cycle the eluent is replaced. For mortar and concrete, Hohberg [233] recommends using deionised water as eluent. The cycles or rather intervals of eluent replacement are adjusted to account for the detection limit of the analytical methods at hand but intervals should be kept as short as possible.
Hohberg [233] distinguishes between three main mechanisms of leaching, displayed in Figure 22.

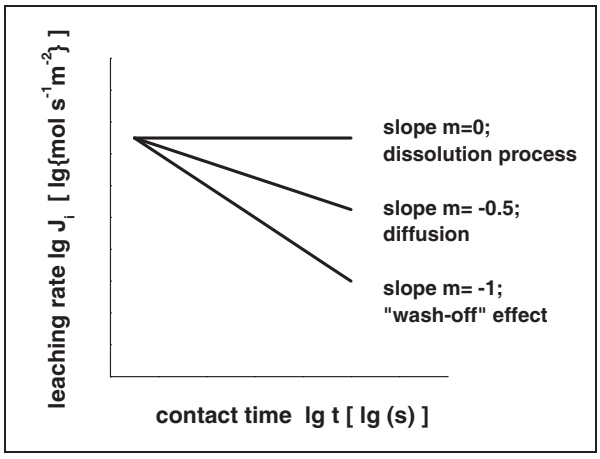

Figure 22: Determination of leaching mechanism according to Hohberg 2003 [233]

For the distinction of the different mechanisms, the leaching rate J_i (t) is defined as the quantity of leached species from the solid/liquid external surface over time. It is then plotted on a double logarithmic scale versus time. The leaching mechanisms are then determined from the slope of leaching rate versus time.

If the SRA would be totally incorporated into hydration phases, the leaching rate would follow the steady dissolution process of inorganic matter and show a slope m~0.
A slope in the range of about -0.55<m<-0.4 would describe a diffusion dominating process, most likely to be anticipated for cementitious materials with a depercolated pore system.
The "wash-off" effect would describe the leaching of species located at very surface of the material, leached within the first contact between material and eluate.

For practical leaching tests on mortar Blachnik [235] and Hohberg [233] suggest to approximate the leaching rate using (75)

$$J_i = \sum_{n=1}^{N} (c_{n;i} - c_{0;i}) \cdot \frac{v_E}{a \cdot t}; n = 1,..., N \qquad (75)$$

where:

J_i:	leaching rate of species i	[mol m^{-2} s^{-1}]
a:	surface of specimen in contact with eluate, interfacial area	[m^2]
$c_{n;i}$:	bulk concentration of species i in eluate within cycle n	[mol m^{-3}]
$c_{n;0}$:	bulk concentration of species i in eluate within cycle n=0 (blank)	[mol m^{-3}]
v_E:	volume of eluate	[m^3]
t:	time of contact in interval	[s]
n:	integer; number of cycles n=1,…, N	[-]

Note that according to Hohberg [233], the different mechanisms may superimpose but the wash-off effect usually disappears within the first cycles.

According to Hohberg [233] the cumulated amount of leached species reads

$$\sum E(t) = 2ac_{mob}\sqrt{\frac{D_e t}{\pi}} \qquad (76)$$

where:

E:	leached amount of species	[mol m^{-2} s^{-1}]
C_{mob}:	mobile fraction of species	[mol m^{-3}]

Using (76), the evaluation of the above leaching tests on cementitious systems reveals apparent diffusion coefficients smaller than the true diffusion coefficients [233].

Concerning the application of the one-dimensional solution of Fick's second law we recognize that by adjusting the geometry of samples according to the tank used might enhance the ability of the measuring setup to meet "one-dimensional" conditions for the diffusing species. Such a measuring setup is the subject of the next section.

6.3.5.4 Diffusion model „infinite slab"

The model describes the one-dimensional diffusion from an infinite slab into two adjacent semi-infinite spaces (Figure 23). According to Kriegel et al. [228], the one dimensional solution can be applied for practical tests if the leaching sample comprises a ratio of lateral dimension [y;z] / sample thickness [h] of [y;z]/[h] > 8 :1.

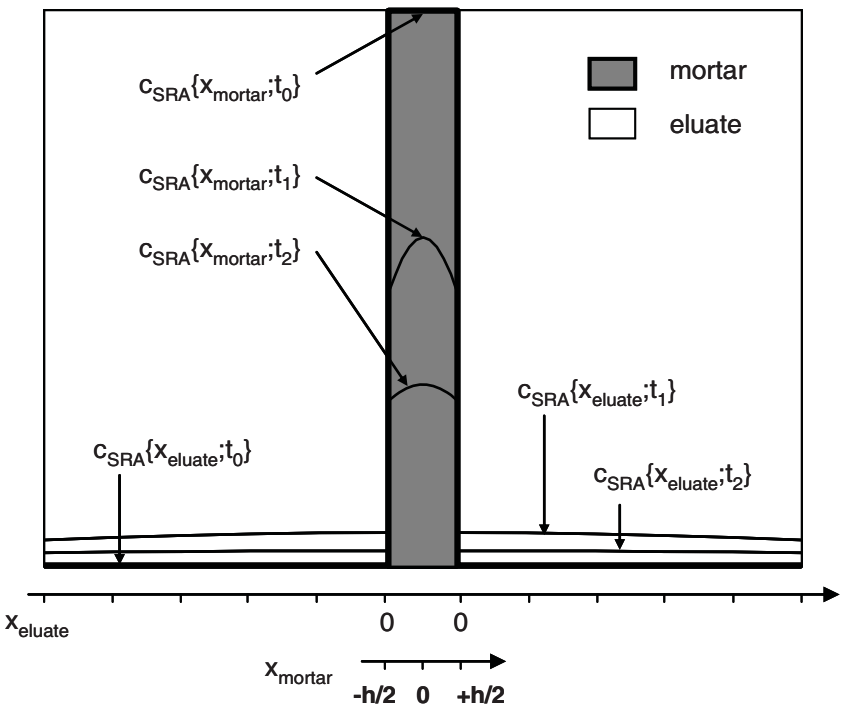

Figure 23: Diffusion model „infinite slab“ according [228]

This diffusion model was applied in several studies [228, 229, 236-238]. The solution of Fick's second law for a constant diffusion coefficient for this model was taken from the above publications.

In the special case of the infinite slab, the solution to Fick's second law is based on the evolution of an infinite series, in which the concentration of the species c(x,t) is expressed as an average concentration $c_m(t)$.

$$c_m(t) = \int_{-h/2}^{h/2} c(x,t)\,dx \tag{77}$$

where:

c_m:	average concentration of species over slab thickness	[mol/m³]

In a next step, the absolute average concentration $C_m(t)$ is converted into a relative concentration, reading

$$c_r(t) = \frac{c_m - c_e}{c_a - c_e} \tag{78}$$

where:

c_r:	relative concentration of species	[-]
c_a:	initial concentration of species in slab	[mol/m³]
c_e:	end concentration of species in slab	[mol/m³]

We recognize that for the determining the end concentration c_e **,** an estimate of the immobile fraction of the species is required. With $c=c_a$ for $-h/2 < x < h/2$ at $t=0$ and c_e =constant for $x=-h/2$ and $x=h/2$ for $t<0$ the infinite series reads:

$$c_r(t) = \frac{c_m - c_e}{c_a - c_e} = \frac{8}{\pi^2} \sum_{\upsilon=0}^{\infty} \frac{1}{(2\upsilon+1)^2} exp\left(-\left(\frac{(2\upsilon+1)\pi}{h} \right)^2 Dt \right) \quad (79)$$

According to [228, 229, 237], the first member of the infinite series sufficiently describes the diffusion process if the values for *t* are sufficiently large, which leads to

$$c_r(t) \approx \frac{8}{\pi^2} exp\left(-\left(\frac{\pi}{h} \right)^2 Dt \right) \quad (80)$$

Using natural logarithm, (80) can be linearized, given a constant *D*. Therefore; the diffusion coefficient is obtained as a function of slab thickness *h*, reading

$$ln(c_r(t)) \approx ln\left(\frac{8}{\pi^2} \right) - \left(\frac{\pi^2 D}{h^2} \right) t = a - bt \quad (81)$$

and

$$D = \frac{bh^2}{\pi^2} \quad (82)$$

where

b: slope of the linearized equation (80) [-]

6.3.5.5 Tank test conditions used in this study

Materials: Mortar specimens that were exposed to leaching are a subset of samples prepared for measurement of shrinkage isotherms and desorption isotherms. Hence they were prepared following the procedure given in sub-section 6.3.1. Eluate of the leaching tests was only tested for organic matter. The leaching of inorganic matter, i.e. predominantly portlandite, was estimated by pH-measurements using indicator stripes.

Permanent leaching: Specimens exposed to permanent leaching were wet cured (inert saturation, see 6.3.1.2) until immersion into a defined quantity of deionised water (0.007m³). In half height of the tank and with the lowest joint space possible, the mortar specimens (10x40x160mm³) were placed side by side on a stainless steel grid to ensure that leaching can proceed “one-dimensionally”.
The sealed polyethylene containers were stored at 20°C/90%RH. Additionally, a so-called “blank” container containing deionised water was introduced along the several leaching series to obtain the amount of total organic carbon that might be leached from the container material. For every series exposed to leaching, a parallel series was kept wet and sealed for comparison after completion of leaching cycles.
Every month the eluate was drawn from the containers and TOC as well as GC were carried out to quantify absolute depletion of organic admixtures and more specifically the quantity of SRA and SP (in case that both admixtures were applied). After weighing the leached specimen, the containers were refilled with deionised water. After eight leaching cycles, the specimens were exposed to drying regime nbr. 2a) “static” (see Table 3).
For the evaluation of efficient diffusion coefficients from this test, equations given in 6.3.5.4 are to be applied.

Cyclic drying/rewetting In the course of cyclic drying and rewetting, every type of mortar (references and modified mixtures) was subjected to one of the different regimes described below.

Regime 1: Mortar series were exposed to drying at 20°C/35%RH for 3 weeks and then immersed in water for 1 week. After resaturation, the total organic content of eluate was measured. Evaluation of SRA leaching follows the approach mentioned above.
Regime 2: Mortar series were exposed to drying at 20°C/35%RH for 3 weeks and then "inert saturation" (see 6.3.1.2) was applied for 1 week.

In the development of this procedure, it was tested that both drying and rewetting times are sufficient to approximately achieve equilibrium conditions. Along the several cycles, length change and weight loss/gain were measured to ensure that drying equilibrium/resaturation had been sufficiently approached. Specifications concerning the modified tank test are given in Table 4.

The evaluation of efficient diffusion coefficients for this tank test configuration does not meet the requirements of the "infinite sheet" model and is therefore to be obtained from the set of equations given in 6.3.5.3.

Table 4: Specifications tank test/modified tank test

tank test					
v_{mortar}	[m³]	7.4E-04	v_{eluent}	[m³]	7.0E-03
a_{mortar}/v_{mortar}	[m^{-1}]	100	v_{eluent}/v_{mortar}	[-]	10
contact time	[d]	28	number of cycles	[-]	8
sample height				[-]	0.01
modified tank test (cyclic drying/rewetting)					
v_{mortar}	[m³]	6.1E-04	v_{eluent}	[m³]	7.0E-03
a_{mortar}/v_{mortar}	[m^{-1}]	250	v_{eluent}/v_{mortar}	[-]	12
sample height				[-]	0.01
contact time (tank test)				[d]	7
drying at 20°C/35%R.H.				[d]	21
			cycle time	[d]	28
			number of cycles	[-]	8 *

* 8th cycle: contact time t=56d

6.3.6 Thermodynamic modelling of cement hydration using GEMS-PSI

6.3.6.1 Introduction

For the thermodynamic modeling of solid/liquid interactions in the course of cement hydration the geochemical speciation code GEMS-PSI (Gibbs Energy Minimization Selector) provided by Paul Scherrer Institute/Villingen/Switzerland was used (provided at public domain: http://gems.web.psi.ch).
The software package includes a solver for chemical equilibrium and an integrated data base. For a given initial bulk composition the liquid and solid phase composition in equilibrium state are calculated within a certain range of temperature and pressure. The calculation method implemented into the solver works on the base of minimization of Gibbs free energy of the whole system. Therefore, for any given temperature and pressure of interest, the database has to provide standard molar energies for components of interest. Regarding Portland cement hydration, this preferably includes all constituents of unhydrated and hydrated cement as well as gases and components of the liquid phase.
Within recent years, the thermodynamic database for cementitious systems was expanded due to the contribution of several scientists working on several thermodynamic cement models.
Recent extensive studies on thermodynamics of cement hydration also using GEMS-PSI can be found elsewhere (Matschei 2007 [220] and Möschner 2007 [239]).
The kinetic model used in this study was developed by Lothenbach and Winnefeld 2006 [215]. It is based on dissolution kinetics of the clinker phases provided by Parrot et al. 1984 [240]. This approach can approximate the time dependent composition of both, cement pore solution and solid phases of the plain paste, i.e. paste without organic admixtures as used in this study (SRA; SP).

6.3.6.2 Input data

The thermodynamic modeling of cement hydration after Lothenbach et al. [215] requires a particular approximation of the initial bulk constitution of the unhydrated cement as well as the specific surface of material subjected to the initial chemical reactions, i.e. the Blaine specific surface area and the mineralogical phase composition. The modified Bogue calculation, given in detail in Taylor 1997 [241], was used to calculate the initial mineralogical composition of the cement. Furthermore the oxide element distributions of the mineral additions were calculated by comparing the WD-XRF results for both, the commercial cement and its clinker (annex; Tab.A2- 1).
For an approximation of the distribution of foreign oxides within the four main clinker phases the crystallite modification of the aluminate phase had to be estimated. Using Taylor's [241] approach the siliceous clinker phases were removed from bulk composition of the clinker material by salicylic acid pulping (SAP). Results of the XRD analysis revealed that the aluminate phase of the cement is a mixture of cubic and orthorhombic aluminate (Fig.A2- 1). The elemental oxide distribution used is given in Tab.A2- 2.
The calculation of the minerals that are not part of the four major clinker phases was done using data from several supporting methods as

a) TGA for the amount and distribution of calcium sulphates (gypsum; bassanite; anhydrite),
b) free lime according to Franke 1941 [242];
c) rapidly soluble alkali sulphates from pore solution using ICP-OES etc.,

Details are given in the appendix Tab.A2- 1 and Tab.A2- 3, where the latter contains the overall mineral composition of the Portland cement used.

The thermodynamic database used in this study contained pure clinker phases. Foreign oxides present in these phases are not taken into account. Therefore, based on the modified Bogue calculations the elemental distributions of the main clinker phases were calculated (given in Tab.A2- 4) and implemented into the thermodynamic modeling.

6.3.6.3 Simulation

The process simulation of Portland cement hydration is taken from Lothenbach [215]. Some important features are given in the following. Starting from the initial mineral bulk composition and taking into account the dissolution kinetics of Parrot et al. [240] for the major clinker phases, in a first time step, the minerals dissolve to certain extent. The GEM-solver calculates thermodynamic chemical equilibrium and returns the new bulk composition (liquid and solid) for the next calculation step and so on.
Note that free lime and rapidly dissolving alkalis are dissolved within the first iteration which may cause a slight overestimation of pH and secondary gypsum content etc.
The modeling process accounts for a linear relationship of C_3S- and C_2S-dissolution after one hour of hydration (~85% C_3S and ~15% C_2S). Note that GEMS accounts for HD-C-S-H [66] with the general formula $C_{1.67}SH_{2.1}$, see Lothenbach et al. 2008 [243]

Generally it has to be pointed out that the predicted hydration kinetics are rather estimates. For that reason the hydration kinetics are corrected by using isothermal heat flow calorimetry data, especially for the early stages of hydration.

7 Surface activity of SRA/SP and Phase transitions of SRA in aqueous and aqueous electrolyte solution

7.1 General introduction

The drying shrinkage of cementitious porous material is significantly decreased due to the action of SRA. According to the Kelvin-Laplace approach for modeling drying shrinkage, the surface activity of SRA is anticipated to be the dominating mechanism for reducing drying induced stress acting on the porous body.
However, SRA in analogy to common non-ionic surfactants, may exhibit several phase transitions dependent on bulk concentration and temperature. Also, because water is consumed during hydration and lost in the course of drying, the SRA concentration in the liquid phase of hardened cement paste will be much increased. Therefore and in regard to what was presented in chapter 3, one now wishes to know if and to what extent phase transitions of SRA may affect their performance.

7.2 Specific materials and methods

In a first step, the surface activity of different SRAs (SRA1, ..., SRA5) at the liquid/vapour interface of aqueous solution was evaluated by measuring surface tension.
It is well known that the surface activity and phase behaviour of SRA may significantly be influenced by the presence of dissolved salts. Therefore in a second step, the interaction of SRA (SRA1; SRA2) and synthetic cement pore solution was investigated and a representative synthetic pore solution composition was chosen. It was prepared to have an electrolyte of almost similar composition to the one of the reference pastes, determined by extraction at the end of the induction period and measured by ICP-OES. The extracted reference pore solution comprised over-saturation for several minerals and therefore it was necessary to reduce the content of several ion species to achieve saturated conditions and avoid mineral precipitation in its synthetic analogue. The composition given in Table 5 exhibits almost no precipitation. Using thermodynamic modeling (GEMS) it is suggested that on long term about 7mmol/l (~0.5g/l) portlandite should precipitate.

Table 5: Composition of saturated synthetic pore solution

mineral phase	quantity	
	[mol/l]	[g/l]
KOH	0.123	6.9
K_2SO_4	0.156	27.2
Na_2SO_4	0.024	3.4
$Ca(OH)_2$	0.015	1.1

To reveal information about the influence of the electrolyte composition on surface tension, a concentration series using KOH was studied. Starting with plain deionised water, the content of KOH was increased by titration of 2M KOH-stock solution and surface tension was measured..
Regarding the use of both admixture types, SRA and SP, surface tension measurements on each admixture alone and mixtures thereof were performed. The composition of SRA- and SP-stock solutions as well as the specification of their mixtures and raw data are given in Tab.A3- 1/Tab.A3- 2 (aqueous solutions) and Tab.A3- 3/ (synthetic pore solution) respectively.

The phase behaviour of SRA1, SRA2 and SRA3 was tested within miscibility experiments. Several concentration steps were introduced to reveal potential phase separation using deionised water or synthetic pore solution. The volumes of different phases formed were determined from the volume scale of the 50ml flasks. The resolution was 0.1ml/50ml or 0.2% respectively.
The procedure was carried out as follows: In a first step, a defined volume of the component compris-

ing the higher density was poured into the flask and the second component was carefully added to avoid early mixing. The flasks were sealed and shaken for about one minute. The mixtures were kept at rest for 24 hours at T=20°C and then the change of bulk volume due to mixing as well as the volume of phases were read out from the flasks scale. Solids that precipitated from the bulk solution were analysed using TGA and XRD. Liquid phases were analysed using TOC and ICP-OES (for electrolyte aqueous solutions).

7.3 Results and discussion

7.3.1 Surface activity of SRA, SP-PCE and SRA/SP-PCE

7.3.1.1 SRA/SP in aqueous solution

In Figure 24 the surface tension of aqueous solutions of SP-PCE and different SRAs is shown. Data were obtained using Wilhelmy plate method. This method and the pendant drop method provide almost similar results for SRA1 in aqueous solution (Fig.A3- 1).

Except for SRA2 and SRA5 the admixtures show very similar performance. With increasing bulk concentration the adsorption of molecules at the liquid/vapour interface causes a decrease in surface tension until reaching a plateau. This is expected to be associated to the CMC at about 10 to 20wt.-% of SRA in solution.

The cleaning agent designated SRA5 exhibits the highest surface activity with a CMC at a bulk concentration of about 0.06wt.-%. For SRA2 containing a relatively high amount of glycol, i.e. neopentylglycol (see chapter 6), the evaluation of CMC is difficult because the γ_{SFT}-C_{SRA}-plot shows no discrete break point.

The surface tension of aqueous solutions of the different admixtures is decreased towards 30mN/m at the CMC. In the same range of bulk concentrations the solution of SRA2 still shows a surface tension of 40 to 45mN/m. The superplasticizer SP-PCE used in this study surprisingly exhibits a surface activity comparable to the performance of a commercial shrinkage reducing admixtures (compare to SRA1 and SRA 3).

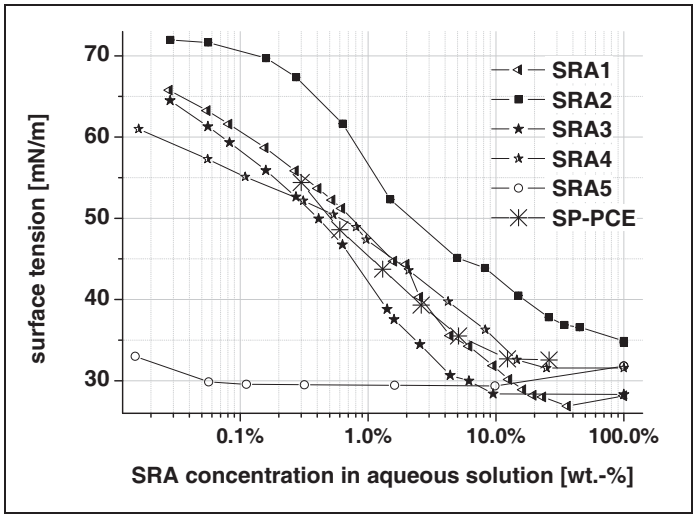

Figure 24: Surface tension of different SRA and SP-PCE in aqueous solution

measuring conditions:

- deionised water
- Wilhelmy-plate method
- T=20°C
- dosages of SRA refer to wt.-% of solution
- dosage of SP-PCE refers to solid content of SP-PCE in solution

Surprisingly the performance of these SRAs in mortars appears to be almost similar. Fig.A3- 2 (appendix) displays the drying shrinkage of a homologues series of self consolidating mortar containing 5wt.-% of admixture (by weight of mixing water). The samples containing SRA, all cured for seven days at 20°C/95%RH and then dried at 20°C/70% RH, show no significant differences in shrinkage. Neither from the maximum reduction of surface tension nor from the CMC is it possible to rationalize the observed shrinkage behaviour. Especially SRA2 with the lowest activity is well in between the range of shrinkage reduction observed in the performance test.

The question arises about whether the comparison of surface activity by weight of SRA is relevant. Due to different molecular weights of SRAs and probably different cross sectional occupation areas, the excess SRA concentration at the liquid/vapour interface can vary.
Additionally, in the course of drying, the SRA would adsorb increasingly because of the increase of the liquid/vapour interface. The excess interface concentration at the CMC would provide information about the extent to which the available SRA is able to "cover" this increasing interfacial area.
To address this issue, the bulk concentration of SRA was expressed in mole fractions (x_2) and the excess surface concentration at the CMC was calculated using Gibbs adsorption isotherm (see (53)).

The cross sectional occupation area $a_{n,SRA}$ [Å²/molecule] at the liquid/vapour interface was derived from the excess interface concentration Γ [mol/m²] using equation (83) according [86].

$$a_{n,SRA} = \frac{1}{\Gamma \cdot N_A} \tag{83}$$

where:

N_A: Avogadro's constant; N_A=6.022x10^{23}mol^{-1}

Several limitations for this type of approximation have to be pointed out. First of all the ingredients of SRA and the molecular weight of these ingredients have to be known. Unfortunately only the composition of SRA1 is given in the material data sheet. For SRA2 it is known that 2.5 -10wt.-% of 2-tert-butylamino ethanol (surfactant) and 50-100wt.-% of Neopentylglycol (co- or solvo-surfactant) are part of the compound. For SRA 3 to 5 the composition is not known. According to Zingg 2008 [221] the superplasticizer can be expected to comprise a molecular weight between $M_{SP\text{-}PCE}$=1E4 to 1E5 g/mol. It can be assumed that all commercial products used in this study are mixtures of components and in a first step SRA and SP-PCE are treated as single components. This is acceptable in so far, that we assume average molecular weights and only one ingredient active on the liquid/vapour interface. In a second step a possible impact of a mixture of ingredients with different molecular structures and weight is taken into account.

The dependence of SRA surface activity on its mole fractions in solution is displayed in Figure 25. Note that for SRA1 and 2 the molecular weights of the non-ionic surfactants according to Table 2 were used and for SRA3 to 5 an average weight of 200g/mol was estimated.

Figure 25: Plot of surface tension versus mol fraction of SRA in aqueous solution

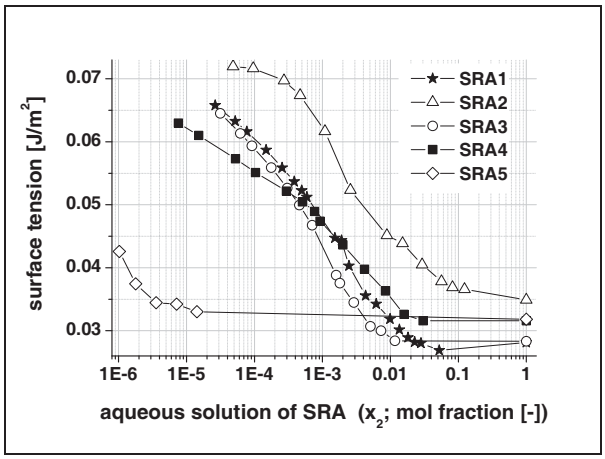

Figure 26: Plot of surface tension versus mol fraction of SP-PCE in aqueous solution – impact of molecular weight

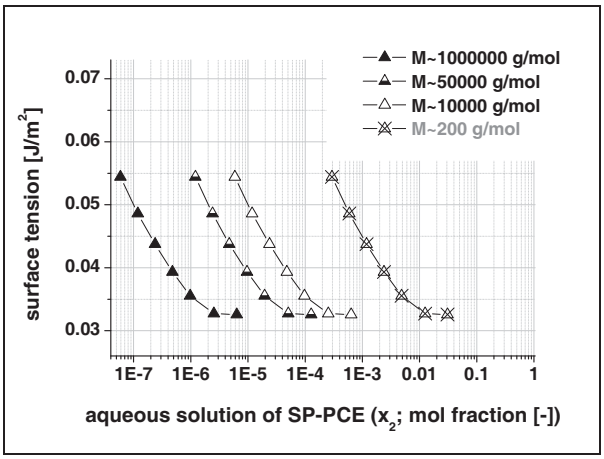

In Figure 25 it can be seen that except for SRA2 and SRA5 a discrete breaking point for the evolution of surface tension versus molar fraction of SRA can be obtained. Hence, a CMC can clearly be determined.

For the superplasticizer SP-PCE the average molecular weight was not known. Therefore, different average molecular weights were estimated. Most probably an appropriate range can be assumed to be 10´000 g/mol < $\varnothing M_{SP\text{-}PCE}$ < 100´000 g/mol. Additionally, a fictitious value of $M_{SP\text{-}PCE}$ ~ 200 g/mol and 1000´000g/mol was assumed. Plots of surface tension versus mol fraction of SP-PCE were constructed and are displayed in Figure 26. It can be seen that any change in molecular weight causes a horizontal displacement of the plot of surface tension versus superplasticizer molar fraction.

In a next step the cross-sectional occupation of the surfactant monomers areas are calculated from the slope of the γ_{SFT}-x_2-plot near the CMC (see (9) & (10) chapter 4.2.2). The results are displayed in Table 6.

Table 6: Calculated cross sectional occupation area per molecule and influence of molecular weight variation

admixture	assumed occupation area	average molecular weight	change of occupation area with Ø M	
			range of Ø M [g/mol]	ΔA_n [Å²]
[denom.]	A_n [Å²]	Ø M [g/mol]		
SRA1	85 ± 9	190	-	-
SRA2	96 ± 16	117	-	-
SRA3	83 ± 12	n.a.	50, … , 1-E5	± 0.5
SRA4	85 ± 6	n.a.	50, … , 1-E5	± 0.9
SRA5	89 ± 25	n.a.	50, … , 1-E5	0
SP-PCE	140	n.a.	1-E4, 1-E5; 1-E6	0

The calculations reveal that the molecular weight of the admixture has no significant impact on the obtained cross-sectional occupation area. Especially for the γ_{SFT}-x_2-plots of SP-PCE in Figure 26 this can be clearly derived. Whilst the molecular weight enforces a horizontal shift of the curves, the slope near the CMC remains unaffected because $\partial\gamma/\partial\ln(x_2)$ remains constant (compare to equation (53)).

It has to be pointed out, that the evaluation of the cross-sectional area is very sensitive to estimates of the slope of the surface tension plot. For SRA1, 3 and 4 however this slope does not change significantly for bulk concentrations towards and near the breaking point (CMC). The results for cross-sectional areas given in Table 6 include deviations that account for errors related to slope estimates.

The figures shown above indicate that a discrete breaking point or rather a CMC can hardly be determined for SRA2; SRA5 and SP-PCE.

The SP-PCE is a commercially available liquid admixture and comprises a solid content of about 26wt.-%. The last measuring point of the surface tension measurement was carried out using the pure, liquid admixture. For SP-PCE it is not clear if the second last measuring point can be assumed to be close to CMC. If this is the case, then the cross sectional occupation area calculated is about 140 Å². For SP-PCE it could be shown that the assumed molecular weight has no impact on the slope of the surface tension plot. Referring to the molecular size of the SRA, the SP-PCE molecules are some orders of magnitude larger then SRA. For that reason an occupation area of about 140Å² seems much too low.
If, however, the SP-PCE is thought to be polydisperse, its low molecular weight fraction could be confessing the surfactant character. Hence, the evaluated bulk composition remains unknown but the “true” cross-sectional occupation area of this surfactant was evaluated. Errors can however result from the difficult determination of a plateau for the γ_{SFT}-plots of SP-PCE.

For SRA2 and SRA5 a more or less bi-linear evolution of surface tension can be found for higher bulk concentrations. In a first attempt, the cross sectional occupation areas given in Table 6 are calculated from the slope of the surface tension plot near the intersection of this “quasi” bi-linear region. Most probably for these SRAs, the combined impact of surfactant and co-surfactant has to be taken into account. This will be discussed in the following using SRA2 that is one of the SRA containing a surfactant (2-tert-butyl-amino ethanol) and a co-surfactant (Neopentylglycol).

From the theory on these combined systems (see 4.3) we can infer the following:

a) The bulk activity of the non-ionic surfactant drastically decreases after reaching the CMC and the surface tension of the solution further on shows a plateau.

b) For glycols, Tan et al. [123-126] found that the surface tension of aqueous solutions of glycol show steady decrease with increasing glycol concentration. From their surface tension measurements one can see that the γ_{SFT}-c_{glycol}-plots show almost constant slope, i.e. $\Delta\gamma_{SFT}/\Delta ln(x_2)$, over the whole range.

c) Furthermore, according to the Gibbs adsorption equation for multi-component adsorption at the liquid/vapour interface, the decrease of surface tension is a superimposition from the action of surfactant and co-surfactant.

For SRA2 in aqueous solution, the surface tension well above x_2=0.1 (mole fraction) still shows a steady decrease (compare to Figure 25). This probably comes from the glycol that continues to enrich the interface after the surfactant has reached CMC. This supports the idea that the reduction of surface tension in Figure 27 should be divided into two parts. One coming from the contribution of the co-surfactant, extrapolated to “zero bulk concentration” using the assumption of constant slope $\Delta\gamma_{SFT}/\Delta ln(x_2)$ [123-126], and the other one resulting from the contribution of the surfactant.

From the material data sheet of SRA2 several compositions of surfactant and co-surfactant have to be taken into account if the molar fractions of the ingredients have to be calculated (compare to Table 2). In a first attempt the possible range of compositions was covered by assuming a composition with a minimum content of both ingredients (SRA2 –composition “min”) and a maximum (SRA2 –composition “max”), given in Table 7.

Table 7: Range of possible compositions of SRA2

ingredients		**content**	**SRA 2 composition "min"**	**SRA 2 composition "max"**
[substance]	[effect]	[wt.-%]	[wt.-%]	[wt.-%]
2-butyl-aminoethanol	surfactant	2.5 - 10	**2.5**	**10**
Neopentylglycol	co-surfactant	50 - 100	**50**	**90**
water	solvent	0 - 47.5	**47.5**	**0**

According to the compositions given in Table 7 the mole fractions of surfactant and co-surfactant were calculated for each composition assumed. The corresponding surface tension plots are given in Figure 27.

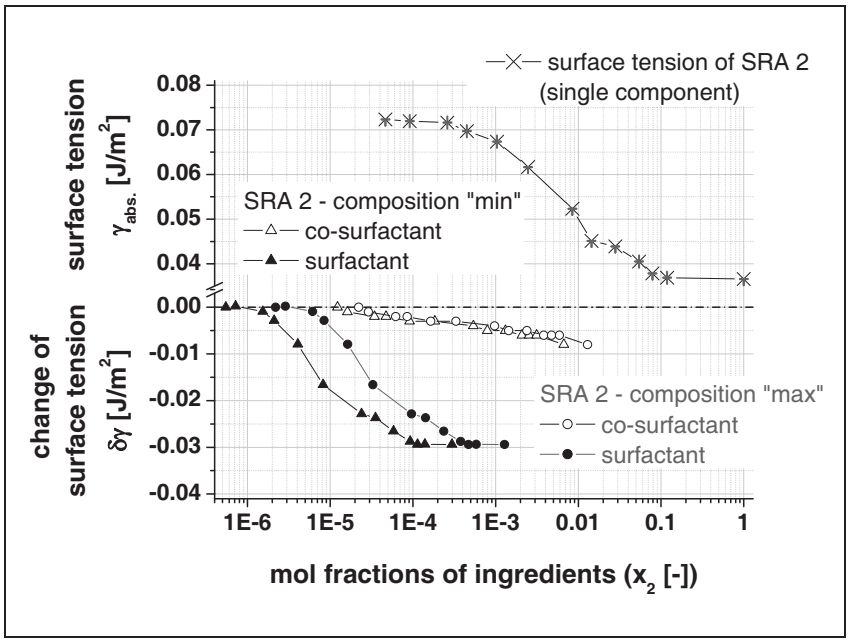

Figure 27: Overall surface tension of SRA2 and contributions from surfactant and co-surfactant

The upper plot shows the surface tension of SRA2 solution versus mole fraction of SRA2. The lower plots show how much each component changes that surface tension when its own molar fraction is changed. Calculating the cross sectional occupation area by accounting for the contribution of non-ionic surfactant one now obtains an area of about 85 Å² independent of the composition of SRA2 assumed (compare to Table 7). This is a reasonable result for two reasons:

1) As already shown for SP-PCE, the cross-sectional area depends on the slope of the surface tension plot near the CMC. For both assumed SRA2 compositions, this slope is unaffected from surfactant content.
2) The surfactants tail moiety of SRA1 and SRA2 is a tert-butyl (C_4H_9-). The occupation areas evaluated for both surfactants are about 85 Å², which is in the range of what is found for other SRA having a similar tail moiety (compare to Table 6).

Moreover, based on the findings in chapter 4.4.1, SRA3 can be assumed to contain a propylene glycol based surfactant. The cross-sectional area evaluated is about 83Å², which suggests that the non-ionic surfactant used in SRA3 comprises a tert-butyl group as tail moiety.

Summary: SRAs used in this study decrease the surface tension to about 30mN/m. SRA2 comprises a relatively high amount of neopentyl glycol and therefore is less surface-active. The calculations of cross sectional occupation areas of the surfactants are reasonable, at least for SRA1 and SRA2 given their similar tail moieties.

However, the calculated occupational area of the superplasticizer appears to be quite low. This may be due to polydispersity or to the product containing a mixture of components with lower molecular weight, which may therefore be preferentially adsorbed onto the liquid/vapour interface. The calculated cross sectional occupation area then most probably refers to such a low molecular weight fraction.

7.3.1.2 SRA/SP in synthetic cement pore solution

The influence of the ionic content of aqueous solution on surface tension was measured using the Wilhelmy plate method. In Figure 28 it is shown that with increasing concentration of potassium ions the surface tension increases. Black stars are measured values for titration of 2M-potassium hydroxide stock solution. Hollow symbols indicate cement pore solutions extracted from hydrated cement paste without admixtures.

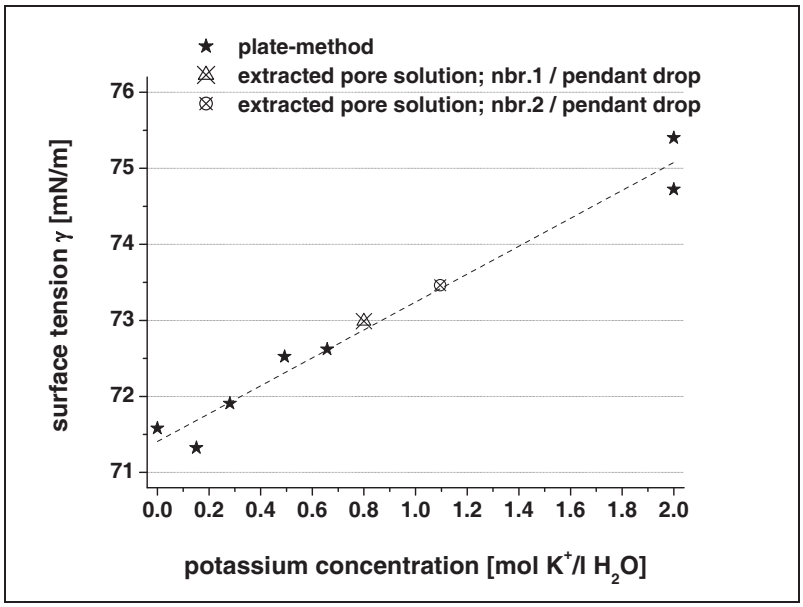

linear fit:

$$\Delta\gamma_{SFT} = 1.83 \cdot x_{M;K^+} + 71.5;$$

[mN m^{-1} mol$_{(K^+)}^{-1}$]; R^2=0.99

Figure 28: Influence of potassium hydroxide on surface tension of aqueous solution

According to previous studies mentioned in chapter 3.2.2, surface tension increases with the electrolyte concentration. There an average increase between 1 to 3mNm^{-1}mol^{-1} could be pointed out. Regarding to potassium ion content, a linear regression, given in the legend of Figure 28, reveals an increase in surface tension by ~1.8 mNm^{-1}mol^{-1}. The synthetic cement pore solution measured with pendant drop method, composition given in Table 5, comprises a surface tension of 75.2 ± 0.1mN/m (see Tab.A3-4).It does not lie in the regression, which indicates that KOH alone cannot account for the change in surface tension.

As could be shown in a previous section, the superplasticizer used in this study exhibits a surface activity at the liquid/vapour interface comparable to a SRA. With respect to the combined application of both admixtures in self consolidating concretes, aqueous solutions and aqueous electrolyte solutions carrying both admixtures, i.e. SRA1 and SP-PCE, were investigated.

In a first step, the surface activity of each admixture in water and in synthetic cement pore solutions was studied. Further on, surface tension measurements on mixes of stock solutions with different total dosages of each admixture were performed. Details on composition and raw data are given in appendix A2 (Tab.A3- 1 and Tab.A3- 2 for aqueous solution; Tab.A3- 3, Tab.A3- 4 for synthetic cement pore solution).

In Figure 29 and Figure 30 the results of these surface tension measurements are displayed. For aqueous solutions of admixtures, the superplasticizer shows the largest surface activity. In synthetic cement pore solution the performance of the 1-component solutions appears to be almost similar, except for dilute solutions.

Concerning the influence of ion species on the performance of SRA1 and SP-PCE it can be stated that the surface tension in cement pore solution is slightly more decreased. Note that the initial surface tension of the plain electrolyte was 75.2mN/m instead of water with 71.6mN/m. Referring to initial values, the performance of both admixtures improves for dilute solutions in the electrolyte solution. The CMC of SRA1 seems to be only slightly influenced by the electrolyte, but due to insufficient number of measuring points in this range no further statement can be given. The maximum decrease of surface tension appears to be independent from ion species content of the solution.

From the surface tension measurements on solutions comprising different fractions of both admixtures, the following can be taken. The measuring points (stars) of these mixes fall right between the curves obtained for the single admixture solutions. Although the admixture fractions are different, the accumulated amount of admixture determines the overall surface tension. From this, it can be seen

that the contributions from each compound superimpose, indicating that both species can adsorb at the liquid/vapour interface independent from each other.

Figure 29: SRA1; SP-PCE and mixes of admixtures in aqueous solution

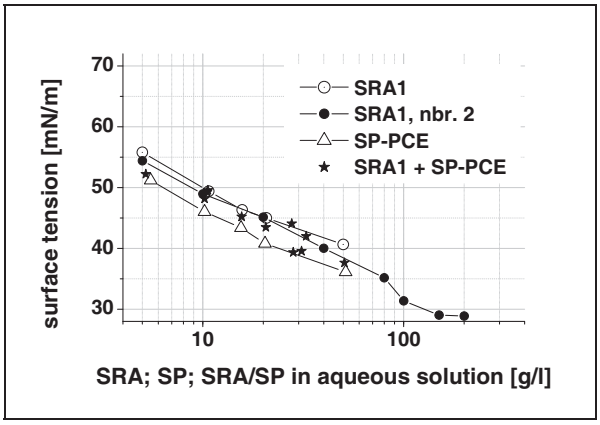

Figure 30: SRA1; SP-PCE and mixes of admixtures in synthetic cement pore solution

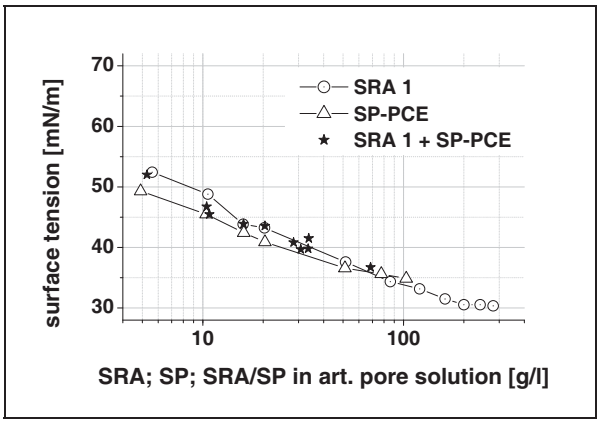

Using the results displayed in Figure 30, fit functions for the decrease of surface tension of electrolyte solutions of SRA and SP-PCE were developed. An exponential decay of third order was found to describe the data well (parameters shown in appendix A2; Tab.A-3). As a first attempt towards shrinkage modeling, these fit-functions might be used for estimating the surface tension of mortar and paste in the course of drying. This constitutes a progress with respect to approaches that use a constant surface tension, neglecting changes due to water loss.

7.3.2 Phase transitions of SRA

The phase behaviour of SRA1, 2 and 3 was examined by means of miscibility tests. Phase separation was quantified by reading out the volumetric scale of the 50ml test tubes used.

7.3.2.1 SRA in aqueous solution

SRA1: The study on phase behaviour of SRA1 covered 31 different compositions over the whole range of bulk concentrations. In the range of observed phase boundaries the density of measuring points was increased. Additionally several repetitions were performed. The results of the miscibility series of SRA1 in water are shown in Figure 31.

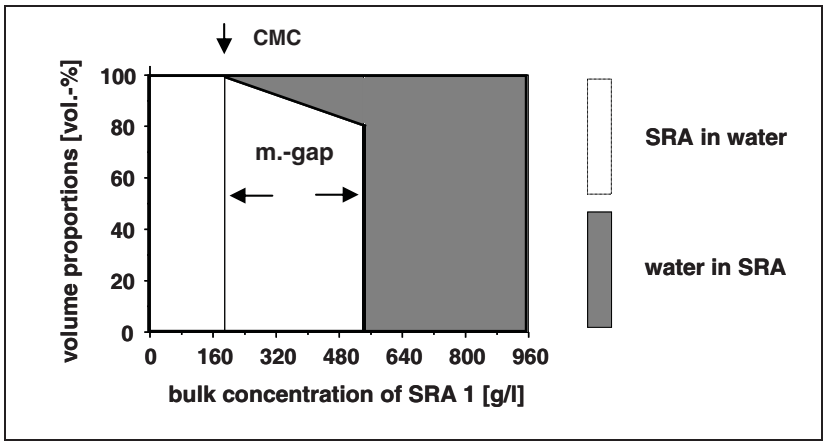

Figure 31: Phase behaviour of SRA1 in water

SRA1 appears to be an isotropic solution for bulk concentrations up to a CMC of about 200g/l. Above this concentration, the mixture turns cloudy, which reflects the logical link between the cloud point and the CMC. After a while, phase separation occurs and two clear solutions appear, separated due to dif-

ferences in density. This behaviour follows the general phase transition properties introduced in sub-chapter 4.2.3. Crossing a bulk concentration of about 560g/l the solution appears to be isotropic again. This corresponds to a reverse micellization (see sub chapter 4.2). Thereof, for SRA1 in aqueous solution a miscibility gap between 200g/l and 560g/l of SRA1 was found (indicated “m-gap” in Figure 31).

The question arises about what happens in the 2-phase region. From theory on non-ionic surfactants, it is known that the cloudy solution separates into a water rich isotropic liquid comprising a SRA1 bulk concentration near the CMC (phase 1) and a second phase rich in surfactant (phase 2).
From the thermodynamics of miscibility gaps, the 2-phase region should provide two phases with constant bulk concentrations where only the volume ratio phase1/phase2 changes with increasing SRA bulk concentration of phase 2. Furthermore, applying the “law of the lever” one can derive the bulk concentrations of phase 1 and phase 2 from the invariant points or the phase boundaries respectively. For the water rich phase1 a bulk concentration of approximately ~200g/l equivalent to the CMC can be estimated. According to this, the bulk concentration of water in the reverse solution (phase 2) should be about 417 g/l.

SRA2: The investigation on SRA2 revealed that this admixture exhibits unlimited solubility in water without showing phase transition.

SRA3: Generally SRA3 shows a similar phase transition as observed for SRA1 but its miscibility gap appears to be wider. At a bulk concentration of ~ 60g/l (CMC almost similar to the concentration obtained from surface tension measurements) the cloud point is achieved. With increasing bulk concentration, a miscibility gap up to about 820g/l can be observed (T=20°C). Above this, the isotropic liquid can be characterised as reverse micellar solution (water in SRA3).

7.3.2.2 Aqueous electrolyte solutions of SRA

SRA1: In comparison to SRA1 in pure water, the electrolytes cause the precipitation of solids for dilute SRA1-solutions. In Figure 32 some selected samples of aqueous electrolyte solutions of SRA1 are displayed. Samples 1 to 3 are mixtures with bulk concentrations of SRA1 below the CMC (sample1-very dilute, increasing SRA content with increasing sample number). Below the CMC the precipitates appear to be dispersed right after mixing, later they settle down without consolidation at the very bottom of the flask. For samples where liquid/liquid phase separation occurs (samples 4; 5; 6 in Figure 32) the solid precipitate appears to be more densified. Moreover, by moving or shaking the flask one observes the *precipitate dispersion* to have a higher viscosity.

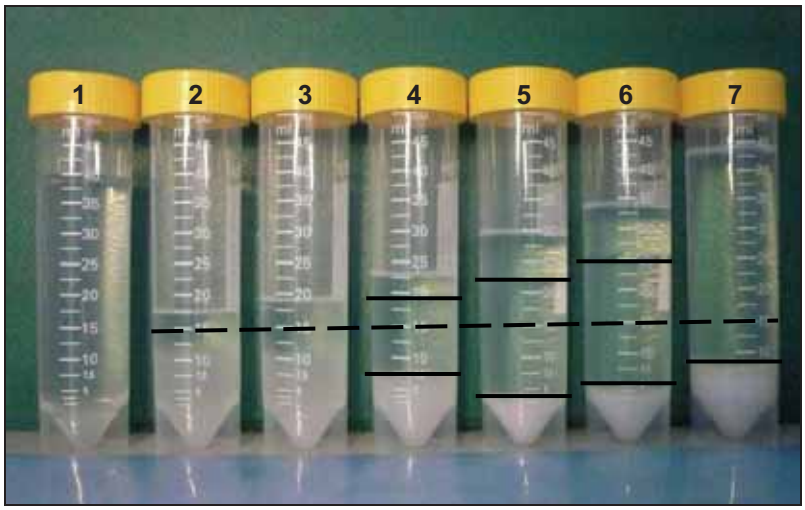

Figure 32: Phase separation of SRA1 in synthetic pore solution

dashed line: initial amount of pore solution

1: dilute electrolyte solution of SRA

2 and 3: isotropic solution and precipitates

4, 5 and 6: liquid/liquid/solid phase separation

7: reverse micellar solution of pore solution in SRA1; liquid/solid phase separation

solid lines: phase boundaries

From theory on non-ionic surfactants one can conclude that self aggregation of SRAs separates liquid crystals from the liquid phase (chapter 4.2.3). For higher dosages of SRA one observes reverse micel-

lation (sample 7 in Figure 32) where an isotropic liquid of pore solution in SRA1 is separated from a solid precipitate, composed of liquid crystal most probably.

In comparison to aqueous solutions of SRA1, the liquid/liquid phase boundaries in synthetic cement pore solutions are shifted towards lower bulk concentrations, as shown in Figure 33.

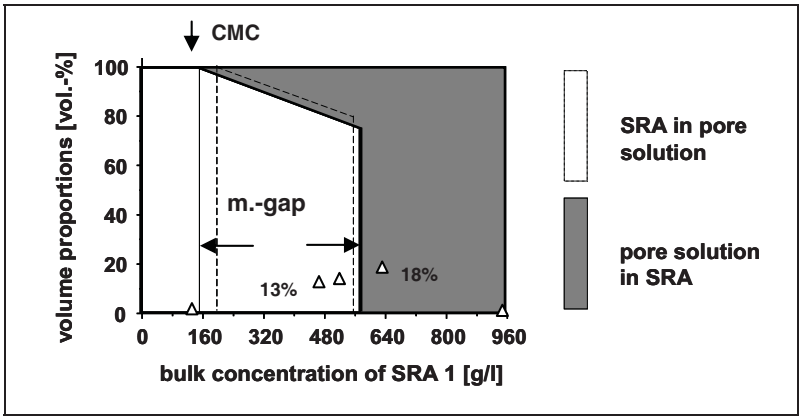

Figure 33: Phase behaviour of SRA1 in synthetic cement pore solution

Solid lines: liquid/liquid phase boundaries in synthetic pore solution

dashed lines: liquid/liquid phase boundaries in aqueous solution

triangles: volume captured by liquid crystal and precipitations

Note that in Figure 33 the volume of the precipitates or liquid crystal is included in the overall volume of phase 1. For dilute SRA1 solutions, the volume captured by the solid phase cannot be estimated because it is dispersed. For higher bulk concentrations, it is quite uncertain if and to what extend liquid and solid form a coherent phase. Because of this, Figure 33 can only account for deviation of CMC and volume fraction of the liquid phase rich in SRA. Later on, the volume part of the solid phase is evaluated.
However, both the decrease of CMC and the enhanced self aggregation are due to the electrolytic nature of the synthetic pore solution. This is in agreement with predictions of phase behaviour derived from theory of non-ionic surfactants (4.2.4).

The question we now have is whether salting-out takes place in cementitious systems in the course of drying. So far the following can be said.

The measuring tubes comprise a rather low ratio liquid/vapour interfacial area to bulk volume. The ability of the solution to deposit surfactant at this interface is rather small. For high bulk concentrations of SRA, the liquid phase finds a low energy state by reordering the remaining (bulk) fraction of SRA by phase transition (see sub chapter 4.2.3).

Concerning cementitious systems, this specific ratio of liquid/vapour interfacial area to liquid volume can be expected to be magnitudes higher. Thereof, in drying cementitious systems the ability of the liquid phase to deposit surfactant at the interface will be significantly higher. Hence, the SRA monomers or micelles in the bulk volume might still be sufficiently separated and not subjected to phase transition. The CMC would therefore be reached at higher SRA bulk concentrations. This will be investigated later on.

SRA2: As observed for its behaviour in pure water, SRA2 shows unlimited miscibility with synthetic pore solution in so far, that no liquid/liquid phase separation occurs. However it does form a precipitate in presence of electrolytes. Nevertheless, in comparison to SRA1 the volume occupied by the “solid” phase or liquid crystal is similar over the whole range of SRA2 dosages and within this range the amount of pore solution seems to determine the amount of salt-outs (Figure 34).

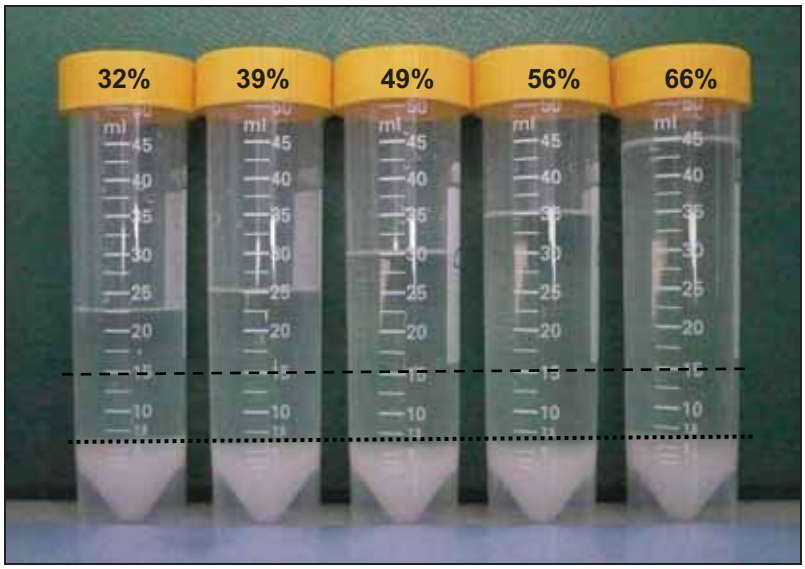

Figure 34: Liquid/solid phase separation of SRA2 in synthetic pore solution

dashed line: volume of synthetic pore solution

dotted line: phase boundary

SRA3: The studies on SRA3 revealed that the CMC of the electrolyte solution is shifted towards lower bulk concentrations and the miscibility gap widens ($8g/l_{electrolyte} < c_{SRA3} < 840g/l_{electrolyte}$ instead of $60g/l_{water} < c_{SRA3} < 820g/l_{water}$) due to the presence of electrolytes. In comparison to SRA1, for dilute solutions of SRA3 a relatively small amount of precipitates is observed.

7.3.2.3 Analysis of the solid phases

The solid phases, separated from the liquid bulk solution, were filtered using a 0.4µm nylon filter, glass frit and pneumatic pressure. The solid residue was weighed and subsequently analysed using XRD and TGA. With SRA3 there was not sufficient material to prepare proper samples. Therefore, only solid residues from SRA1 and SRA2 solutions were analysed.

SRA1: The qualitative XRD evaluation reveals that syngenite, mirabilite, arcanite and thenardite are possible compounds of the residue. The diffractogram is shown in appendix A2; Fig.A3-3. Thermo-gravimetric measurements on such filtered residues of the phase separation experiments show two general mass loss curves displayed in Figure 35.

Below the CMC, residues contain exclusively inorganic matter (black solid lines). The main product that could be identified is the double salt "syngenite" (K_2SO_4-$CaSO_4xH_2O$; molar mass M=328.4g/mol). Additionally portlandite and calcite were observed. It can be assumed that the calcite formed during sample preparation (carbonation of portlandite). Note that the composition of the synthetic pore solution was known, so the inorganic matter precipitated from bulk solution could be easily identified.

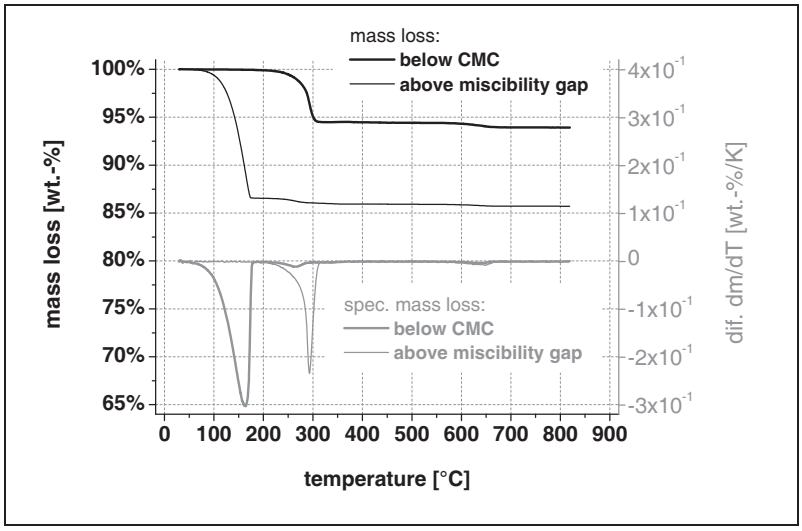

Figure 35: TGA curves of filtered residuals of SRA1 solutions

<u>TG-analysis/phase identification:</u>

Organic matter: < 200°C

Syngenite: 200°C to 350°C

Portlandite: 420°C to 480°C

Carbonated portlandite from calcite: 530°C to 730°C

For bulk concentrations well above the miscibility gap, the residue contains organic matter. Fortunately, as can be seen in Figure 35, one finds well separated peaks, enabling to distinguish between organic and inorganic matter. Results of the TG-analysis are given in appendix A2; Tab.A3- 6.

Figure 36 contains the absolute amounts of inorganic precipitates separated from solution by pneumatic filtration (cycles with dashed line). Additionally the following data are given:

a) total inorganic content of the synthetic pore solution (solid line)

b) theoretical (stoichiometric) maximum of syngenite (dashed-dotted line)

c) syngenite measured (squares)

d) portlandite measured (triangles – solid line)

According to the data given in Figure 36, the presence of SRA in solution seems to cause depletion of calcium from the aqueous phase by precipitating syngenite. Moreover, the precipitates formed below the CMC mainly are syngenite accompanied by a small amount of portlandite. Above the CMC and with increasing bulk concentration of SRA1, there is an additional precipitation of potassium and sodium sulphates. For sodium sulphate the precipitate would be mirabilite or thenardite depending on water activity. It should however be noted that after separation, samples containing mirabilite could easily dehydrate before the TG or XRD measurements in the course of preparation.

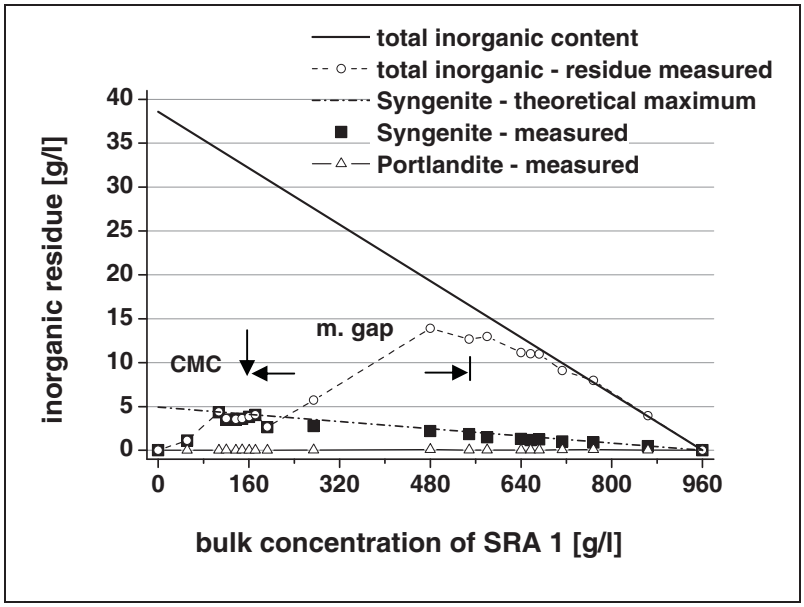

Figure 36: Absolute amounts of inorganic precipitates from electrolyte solution of SRA1

For the reverse micellar solution of SRA1 and especially for SRA concentration above 640 g/l it can be seen that the whole salt content is removed from solution and separated from bulk by precipitation (total inorganic content equal to measured inorganic residue).

The organic residues obtained by pneumatic filtration and analysed by TG are shown in Figure 37. It can be seen that below the CMC, the amount of organic residues is negligible. Above the CMC the amount of residue increases. Moreover, with increasing concentration of SRA1 in the reverse micellar solution (> ~560g/l), the amount of organic solids separated from solution shows a steep increase, achieves a maximum and then decreases. This evolution most probably can be attributed to a dilution effect concerning the electrolyte concentration in the bulk solution.

The values given in Figure 37 are residues after filtration, an operation that would have drawn liquid crystals through the filter. For that reason, the total amount of aggregated surfactant could not be determined from this method. The amount of SRA that self-assembled into liquid crystals is however estimated later by using the TOC-data obtained from the liquid phases.

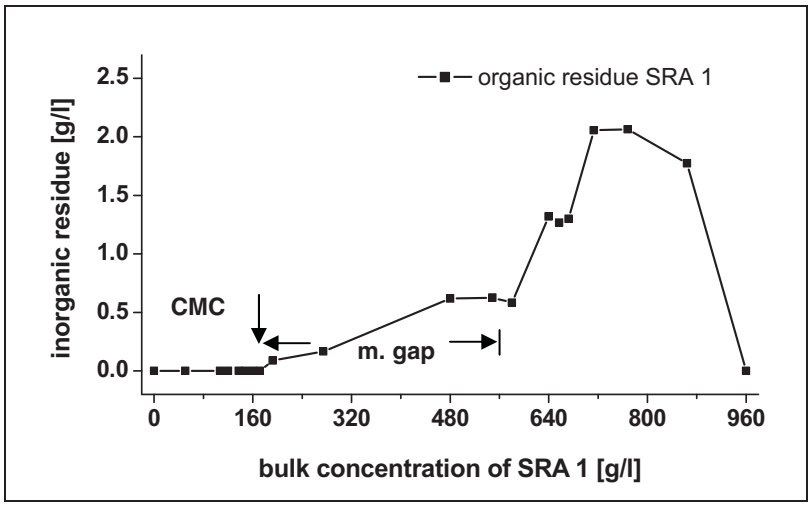

Figure 37: Filtrated organic residue of SRA1 in synthetic pore solution

SRA2: The qualitative XRD analysis of the residue of a 1:1 mixture of SRA2 and pore solution revealed that syngenite, mirabilite, thenardite and potassium sulphate are precipitated from bulk solution. Additionally an organic crystalline compound could be identified; 2.2 dimethyl-1.3 propandiol, the co-surfactant of SRA2. The diffractogram is shown in appendix A3; Fig.A3- 4.

The relative composition of the residue was derived from TG analysis and is displayed in Table 8.

Table 8: Phase composition of residue, SRA2

phase	composition [wt.-%]
2.2 dimethyl-1.3 propan diol	~ 32
Syngenite	~ 20
Portlandite	~ 1
Arcanite	~ 47
Thenardite	

Most probably mirabilite dehydrated during sample preparation forming thenardite.

It can be said that for both SRA1 and SRA2 in synthetic pore solution

a) salt-out effects (compare to sub-chapter 4.2.4) and

b) mineral precipitations

can be observed. Moreover, for reverse micellar solutions of SRA1 the electrolyte is completely removed.

7.3.2.4 Analysis of the liquid phases

The analysis of the liquid phase was executed on the miscibility series of SRA1 in synthetic cement pore solution. The results of TOC measurements are given in Figure 38. For bulk concentrations near the CMC, where exclusively small amounts of inorganic precipitates could be detected by TGA, the organic content of the isotropic micellar solution is approximately similar to the bulk concentration. Therefore no organic self assemblies seem to form below the CMC.

In the two phase region the TOC samples were extracted using a syringe. According to the theory on non-ionic surfactants, the SRA content of the water rich phase 1 should slightly increase after the bulk concentration crosses the CMC. This phenomenon is due to the so-called solubilisation where micelles grow slightly. Surprisingly the SRA content of the SRA rich phase 2 is higher than expected. It implies that above the CMC the micellar solution expels an almost pure SRA phase. With increasing SRA bulk concentration, the water content of the SRA rich phase increases. Figure 38 implies that the concentrations of the two phases converge at the upper boundary of the miscibility gap.

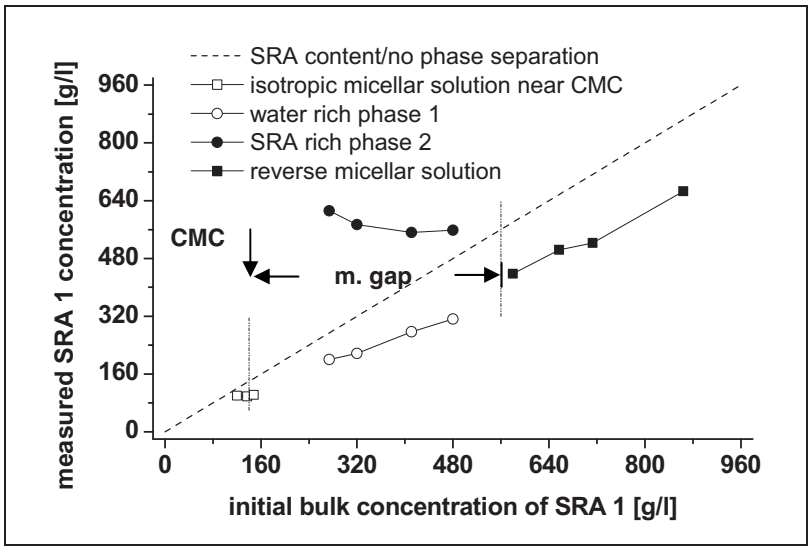

Figure 38: TOC analysis of liquid phases

Comments:

dashed line: theoretical SRA1 content for isotropic solution without phase separation

dash-dotted, vertical lines: boundaries of miscibility gap

The isotropic reverse micellar solution that forms above the miscibility gap shows a SRA-content lower than the bulk concentration. This seems reasonable since the liquid crystal separated from the bulk depletes the liquid phase of organic matter. From the results of TOC analysis the total amount of these liquid crystals can be estimated (mass balance), values are given in Table 9.

Table 9: Approximated amount of SRA1 in different phases

bulk concentration of SRA 1	SRA 1 in liquid phase	SRA 1 in liquid crystal	SRA 1 solid residue	comments
[g/l]	[g/l]	[g/l]	[g/l]	
120	104	16	0.0	isotropic; near CMC
139	103	36	0.0	
148	106	42	0.0	
274	239	35	0.2	two liquid phase region; m.-gap
320	266	54	~0.2	
411	338	73	~0.2	
480	380	100	0.2	
580	458	122	0.2	isotropic, reverse micellar solution
657	527	128	1.7	
713	547	164	1.7	
864	696	166	2.0	

The TOC measurements reveal that already below the CMC, SRA1 salts out from the isotropic solution (rows 1-3 in Table 9). It can be assumed that this is due to the formation of surfactant aggregates in the presence, at the surface or in vicinity of the mineral phases precipitated from bulk solution and that these may be *precursors*.

The ionic composition of selected mixes (rows 7 & 9 in Table 9) and the corresponding liquid phases was analysed by ICP-OES. Composition of the phases and results are displayed in Tab.A3- 7.
The results of the ICP-OES measurements show that SRA1 causes a significant depletion of ion species from the liquid phases. In particular, Ca is rapidly and completely depleted. This is in line with Figure 36 showing that maximum syngenite precipitation is reached already at low concentrations of SRA1. Moreover, within the miscibility gap, the reverse micellar solutions are almost totally depleted.

In a second step it was checked whether mass equilibrium exists between precipitated minerals and the referring composition of the solid residue obtained by pneumatic filtration (analysed by TGA).

The equilibrium between the pore solution and mineral precipitates was analysed on the same mixes (rows 7 & 9 in Table 9). The first one shows a liquid-liquid-solid phase separation (bulk concentration

of 480g/l SRA1) and second one a reverse micellar solution with liquid-solid phase separation (bulk concentration of 657g/l SRA1).

The bulk ion content of the SRA solutions was calculated from the SRA bulk concentration of the mix (third columns of Table 10 and Table 11) and the composition of the plain electrolyte (second columns of Table 10 and Table 11).

The measured ion concentrations are displayed in column 4 of Table 10 and Table 11. They serve to calculate the total amount of depleted ion species (column 5 of Table 10 and Table 11).

Note that for the reverse micellar phases (phase 2) within the miscibility gap the amounts of ions in solution were all below the detection limit (b.d.l.) and therefore are assumed to be totally depleted.
Furthermore it has to be pointed out that the amount of water being part of the liquid crystal structure was not accounted for. Thereof, the effective water content of the water rich phases (within the miscibility gap) must be slightly too low and as a result the amount of mineral phases precipitated from bulk solution is probably underestimated. Based on this, we calculate the distribution of ions in the precipitated phases previously determined (7.3.2.3).

The calculation was done as follows:

a) for ion species contents below detection limit (b.d.l.) the depletion was assumed to correlate directly to the ones still detectable;

b) from TGA the relative amounts of mineral phases were already known and in a first step the total amount of calcium was distributed between portlandite and syngenite;

c) all sodium formed thenardite;

d) the residual of potassium ions were assigned to arcanite.

The results of these mass balance calculations in Table 10 and Table 11 are in reasonable agreement with TGA, although in general slightly lower. This can be due to the previously mentioned error on the effective water content, which results from not accounting for the amount of water that is part of liquid crystal.

Table 10: Calculated amount of inorganic precipitates formed from isotropic micellar solution

ion species obtained from ICP-OES	composition of plain pore solution	dilution with SRA; f=0.620*	measured composition	depleted from liquid phase	calculated mineral phase composition from ICP-OES			mineral phases in solid residue from TGA	
[-]	[mmol/l]	[mmol/l]	[mmol/l]	[mmol/l]	[-]	[g/l]	[wt.-%]	[g/l]	[wt.-%]
K^+	435	270	159	**111**	**Syngenite**	1.94	**16.7%**	2.20	**15.9%**
Na^+	48	30	17*	**12**	**Arcanite**	8.71	**75.1%**	11.60	**83.4%**
Ca^{2+}	11	7	0*	**7**	**Thenardite**	0.90	**7.8%**		
SO_4^{2-}	175	108	37	**71**	**Portlandite**	0.06	**0.5%**	0.11	**0.8%**
* estimated, value below detection limit					**sum**	**11.61**	**100%**	**13.90**	**100%**

Table 11: Calculated amount of inorganic precipitates formed from reverse micellar solution

ion species obtained from ICP-OES	composition of plain pore solution	dilution with SRA; f=0.338	measured composition	depleted from liquid phase	calculated mineral phase composition from ICP-OES			mineral phases in solid residue from TGA	
[-]	[mmol/l]	[mmol/l]	[mmol/l]	[mmol/l]	[-]	[g/l]	[wt.-%]	[g/l]	[wt.-%]
K^+	435	138	46	**92**	**Syngenite**	1.02	**10.6%**	1.17	**10.7%**
Na^+	48	15	5*	**10**	**Arcanite**	7.77	**81.2%**	9.79	**88.9%**
Ca^{2+}	11	3	0*	**3**	**Thenardite**	0.75	**7.8%**		
SO_4^{2-}	175	56	1*	**54**	**Portlandite**	0.03	**0.3%**	0.05	**0.4%**
* estimated, value below detection limit					**sum**	**9.57**	**100%**	**11.00**	**100%**

The issue is now to know the role of the SRA in the formation of these precipitates. Therefore, the GEM-solver was used to model the precipitation of minerals from bulk by assuming the synthetic cement pore solution is hypothetically constricted. This however evaluates purely the water removal effect. The result of this modelling is displayed in Figure 39.

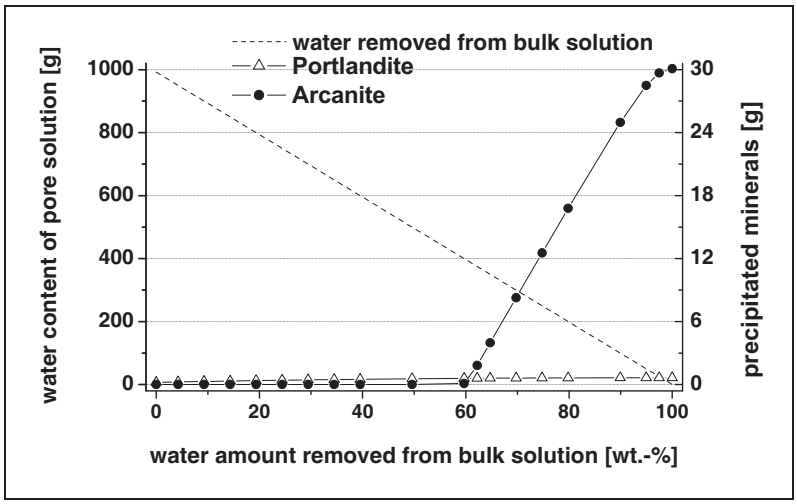

Figure 39: Modeled precipitation of minerals due to the constriction of synthetic pore solution

Results in Figure 39 show two major differences with respect to the observations previously discussed. First, the modelling code predicts the precipitation of portlandite and potassium sulphate (arcanite) instead of syngenite, second potassium sulphate starts to precipitate when the water content is reduced to 40% of the initial amount instead of about 80%, as previously observed. Concerning the first, there is only a small difference in energy of formation that decides between syngenite and arcanite but the second is surprising.

The measurements on aqueous electrolyte solutions of SRA show, that syngenite precipitates even for very small amounts of SRA below the CMC. Let us assume a CMC of 120 to 140g/l for SRA1, where a significant amount of syngenite is detected. The actual amount of aqueous solution in the isotropic micellar solution then is approximately 890 g/l. To constrict the pore solution and to enforce precipitation of potassium sulphate, the SRA would have to physically bind or remove about 530g plain water from the bulk. This corresponds to 4times the SRA amount, which appears much too much. Simple water binding is therefore a questionable explanation.
Additionally the analysis of the inorganic solid residues (from filtration) shows that syngenite precipitates at a SRA1 bulk concentration of only 51g/l. In this case the SRA in the dilute solution would have to inactivate water by factor 11 of the SRA amount.

The more probable explanation is therefore, that in presence of SRA, the solubility (or rather solubilisation capacity) of salts decreases. Currently however, the GEM-solver cannot capture this and is therefore not adequate for systems containing SRAs. Concerning the solubility change, the reason might be that water activity is decreased by SRAs.

7.3.3 Impact of volume-interface ratio on efficient surface activity

In the previous chapters it could be shown that surface activity and phase behaviour strongly depend on the admixture bulk concentration. At the CMC the liquid/vapour interface is occupied by a maximum amount of molecules, which also corresponds to the point where they start to assemble into micelles. The presence of these micelles can play the role of a buffer, maintaining the surface tension if the interfacial area is increased. This could for instance be the case in the course of drying, if a liquid film develops on the pore walls. An increase in the interface area would therefore not result in a decrease of surface tension as long as micelles can dissolve and supply molecules to the interface, occupying the voids created.

To examine this, surface tension measurements with varying volume/surface-ratios (v/a) were conducted. This was done on aqueous electrolyte solutions of SRA1 using the pendant drop method.

In the course of these measurements, the maximum drop size for obtaining a stable drop was iteratively determined for each SRA dosage investigated. In Table 12 these drop volumes are displayed in the third column. The appropriate drop surface areas are given in the fourth column.
From this, the v/a-ratios were calculated and are displayed in the fifth column. It can be seen that the maximum drop size decreases with increasing SRA bulk concentration. Hence different v/a-ratios could be introduced to the evaluation regime. The surface tensions measured are displayed in the first column of Table 12. The corresponding surface tension – bulk concentration plot for SRA1 was already displayed in Figure 30. From this plot, the excess surface concentration Γ of SRA versus its bulk concentration was calculated using equation (53) and is displayed in columns 6 and 7 of Table 12.

Table 12: Evaluation of core concentration of SRA1 by pendant drop surface tension measurement

measured surface tension		drop volume	drop surface area	v/a	Γ_{excess}*		bulk concentration	core concentration**
avg [mN/m]	sd [mN/m]	[1E-6m²]	[1E-9m³]	[m]	[mol/m²]	[kg/m²]	[wt.-%]	[wt.-%]
74.76	0.01	27.5	43.6	6.30E-04	0	0	**0.00%**	**0.00%**
61.76	0.21	20.1	34.5	5.83E-04	1.85E-06	3.51E-07	**0.13%**	**0.06%**
57.8	0.15	18.1	32.0	5.65E-04	2.03E-06	3.85E-07	**0.25%**	**0.18%**
54.41	0.32	20.5	35.7	5.74E-04	2.17E-06	4.12E-07	**0.50%**	**0.43%**
48.96	0.31	16.1	29.7	5.44E-04	2.38E-06	4.53E-07	**1.00%**	**0.92%**
45.13	0.52	16.6	30.6	5.42E-04	2.52E-06	4.79E-07	**2.00%**	**1.91%**
40.02	0.42	12.6	24.8	5.10E-04	2.69E-06	5.11E-07	**4.00%**	**3.90%**
35.16	0.14	12.1	24.2	4.98E-04	2.83E-06	5.38E-07	**8.00%**	**7.89%**
31.37	0.26	9.6	20.3	4.75E-04	2.93E-06	5.57E-07	**10.00%**	**9.88%**
29.03	0.40	8.9	19.1	4.64E-04	2.99E-06	5.67E-07	**15.00%**	**14.88%**
27.88	0.03	7.4	16.7	4.45E-04	3.01E-06	5.72E-07	**20.00%**	**19.87%**

* calculated from the γ_{SFT}-plot of SRA1 in artificial pore solution

** calculated, assuming core volume equal total volume of solution

We now proceed to calculate the distribution of SRA molecules in the drops generated. For this, the following mass balance can be used:
The total number of molecules present in the drop is calculated from SRA bulk concentration and drop volume (84). It is considered that one fraction of these SRA molecules is adsorbed at the liquid/vapour interface and that the rest remains distributed within the drop core (85). From the excess surface concentration, the bulk concentration and v/a-ratio (here drop geometry), one obtains the core concentration of SRA as follows (86).

$$c_{SRA\_bulk} = \frac{n_{SRA}}{v_{solution}} \tag{84}$$

$$n_{SRA} = \Gamma_{SRA} \times a_{exposed} + n_{SRA\_core} \tag{85}$$

$$c_{SRA\_core} = c_{SRA\_bulk} - \Gamma_{SRA} / \frac{v_{solution}}{a_{exposed}} \tag{86}$$

where:

$c_{bulk:}$	bulk concentration	[mol/m³]
$n_{SRA:}$	moles SRA	[mol]
$v_{solution:}$	volume of solution	[m³]
$\Gamma_{SRA:}$	excess surface concentration	[mol/m²]
$a_{exposed:}$	actual liquid/vapour interfacial area	[m²]

From the equations above, we now derive a very useful relationship between the admixture distributions in solution and deposition at the interface. For every given geometry or v/a-ratio respectively the surface tension of the liquid/vapour interface can be calculated from total bulk concentration and the equilibrium characteristics between core and excess surface concentration (86). From this, the CMC for the pure solvent, i.e. the solvent without interface, can be obtained independent of the geometric boundary conditions the measuring device comprises.

For each measurement carried out, the calculated distribution of SRA1 in the drop is displayed in Table 12. As can be seen, for the tests performed, the v/a-ratios cause negligible difference between bulk and core concentration of SRA1 however from (86) it can be deduced that this difference increases if the system comprises lower v/a-ratios.

The question arises if and to what extend this might influence the surface tension present at the liquid/vapour interface of the drying porous matter. To get an impression on that, we examine the case of a well hydrated cement paste with a water/cement ratio of *w/c*=0.4 during drying:

The saturated state: Given a sample with a water saturated porosity of about 20vol.-% and a cubic geometry, we obtain a *v/a*-ratio of ~3.3 E-02m for its saturated state. For a SRA dosage of about 5wt.-% of the mixing water, the SRA bulk concentration after hydration would be in the range of 16wt.-%. According to Table 12 the surface tension hence achieves a value in the range of 30mN/m, i.e. at the very minimum.

The dried out state: Upon drying, water evaporates, causing constriction of the pore fluid. The SRA bulk concentration therefore increases, if no adsorption at any solid/liquid interface is assumed. We let the very limit of the evaporation regime be the presence of the non-evaporable SRA with a given volume of about 30l/m³.
Regarding the liquid/vapour interfacial area, a limiting value of about 50m²/g to 200m²/g, referring to N_2 or H_2O adsorption data, may be taken for the dried out state. If water layers are considered to be present at this state, the liquid volume increases by about 10l/m³ per molecular layer. According to this, for cement paste the v/a ratio could go down to values v/a <1E-8m. The 30l of SRA1 then are to cover an interfacial area larger than ~1E8m². As a result of this, the excess surface concentration is low (about 1.5E-6 to 3.8E-7mol/m²). According to Table 12, due to drying the initial surface tension increases from a minimum of 30mN/m to higher than about 60mN/m.

Based on these theoretical considerations, it reveals that the exposure of more and more interfacial area in the course of drying may significantly affect the surface tension of the liquid phase in cement systems. It is therefore of high interest to describe this evolution in particular.

Using (86) and the results of pendant drop measurements displayed in Table 12, the specific relationship between SRA1 bulk concentration, v/a-ratio and surface activity for SRA1 in aqueous electrolyte solution is displayed in Figure 40. It shows how, at a given bulk concentration of SRA, a decreasing v/a-ratio reduces the surface tension of the liquid/vapour interface. The plateau forming at high bulk concentrations and rather high v/a-ratios indicates the range where micellization occurs. Furthermore it can be seen for which bulk concentrations and v/a-ratio this would happen.

The main information that Figure 40 reveals is, that starting from a v/a-ratio of 1E-6 the surface tension significantly decreases for a given bulk concentration. As could be shown previously, the v/a-ratios of drying cement paste can be expected to be one or two orders of magnitude lower than this.

For a drying cementitious system the exposed surface area increases due to the evaporation of the pore solution, i.e. the v/a-ratio decreases while the SRA bulk concentration in the pore solution increases. These phenomena are expected to have exactly opposite impact on the surface tension of the liquid/vapour interface. The question now arises about how much surface tension ultimately changes as a result of increasing bulk concentration (that would decrease it) and increase in interfacial area (that would increase it).

The evolution of surface tension of cement paste and mortar in the course of drying will be discussed later on in chapter 11.

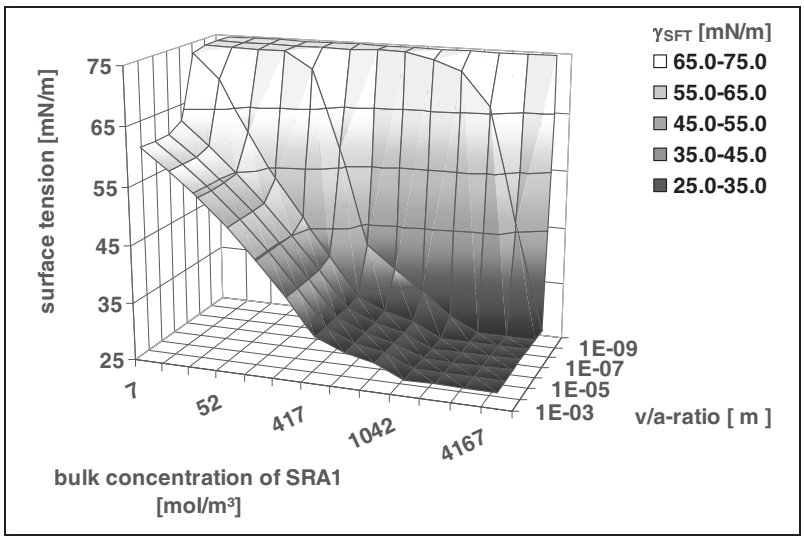

Figure 40: Impact of volume /interface ratio on surface activity of SRA1

At this stage, the model pore system “adjusted normcube” (sub chapter 5.2) is used to visualize the impact of v/a-ratio on the desorption isotherm. Indeed, as drying proceeds, we can use this model to determine the ratio of liquid volume to the area of the liquid/vapour interface.

We start with initial SRA bulk concentrations of 2.5, 5 and 10%, and initial surface tensions of about 41mN/m; 35mN/m and 31mN/m respectively. We can also determine the variation of surfactant bulk concentration. Then, together with Figure 40, desorption isotherms for the infinite rigid “adjusted normcube” can be calculated.
The calculations lead to v/a-ratios in the range of 1E-5 to1E-10m. As a result, the surface tension is significantly affected (compare to Figure 40).

As a result of the simulations, the evolution of surface tension of the pore fluids is displayed in Figure 41, while the corresponding desorption isotherms are given in Figure 42.

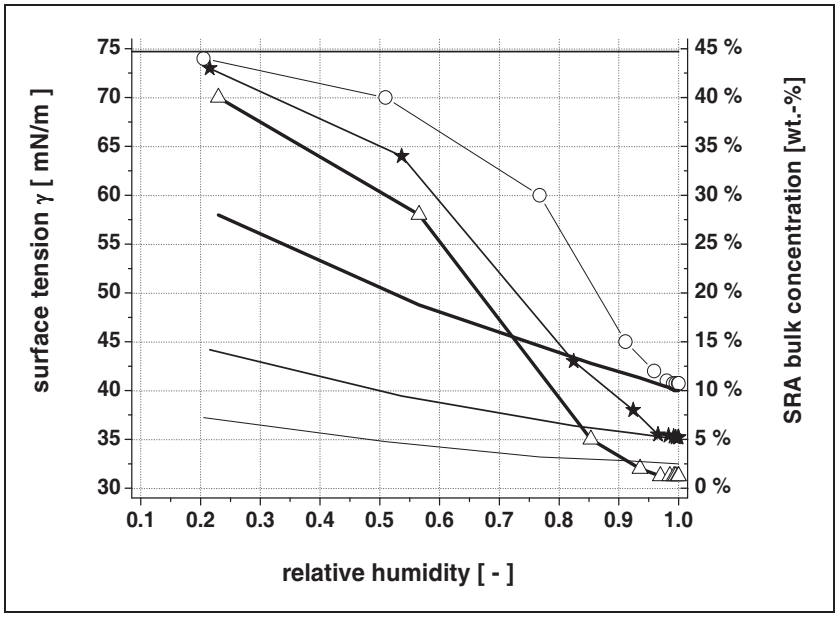

Figure 41: Evolution of surface tension of pore fluids with different initial bulk concentrations of SRA1 upon drying of norm-cube

Legend:

surface tension of plain pore solution

surface tension:
C_{SRA_ini}=2.5 wt.-% o.w
C_{SRA_ini}=5.0 wt.-% o.w
C_{SRA_ini}=10 wt.-% o.w

bulk concentration:
C_{SRA_ini}=2.5 wt.-% o.w
C_{SRA_ini}=5.0 wt.-% o.w
C_{SRA_ini}=10 wt.-% o.w

Depending on the initial bulk concentration, the surface tension increases upon drying (lines with symbols) whilst the SRA bulk concentration increases due to evaporation.

This answers the question on the dominating impact on surface tension in the course of drying. Indeed, this simple modeling approach indicates that the increase of interfacial area determines the surface tension evolution.

The scenario given in the introduction of this chapter can now be described more in detail:

Due to the increase of interfacial area, more SRA molecules can adsorb at the interface and these are provided from bulk. When these are no more present in sufficient amounts the surface tension decreases. This overrides the increase of SRA bulk concentration that acts in the opposite sense.

For the pore fluid with high initial SRA concentration this effect can be described well. Due to drying induced water loss, the bulk concentration increases. At about 70% relative humidity the bulk concentration approaches what was formerly found to be the CMC in macroscopic surface tension measurements (about 16wt.-% ; see sub chapter 7.3.1.2). For a low interfacial area the solution now would be expected to show micellation. However, due the enormous increase in interfacial area, a huge number of molecules adsorbs at the interface, thereby decreasing the SRA core concentration.
The new equilibrium that establishes between surface and liquid core raises the surface tension from about 30mN/m to 45mN/m.

For all the modelled drying scenarios the initial surface tension of the pore fluid increases upon the increase in interfacial area. Systems with lower initial SRA bulk concentration show an increase of surface tension for lower extents of drying. The curves for surface tension shown in Figure 41 appear to converge for the very dry boundary conditions. However, this strictly depends on the interfacial area and the amount of SRA introduced to the model pore system.

In Figure 42, the modelled sorption isotherms are given. The solid lines indicate a) the desorption isotherm for the plain electrolyte (grey) and b) a pore fluid with a minimum, constant surface tension of 30mN/m (black).

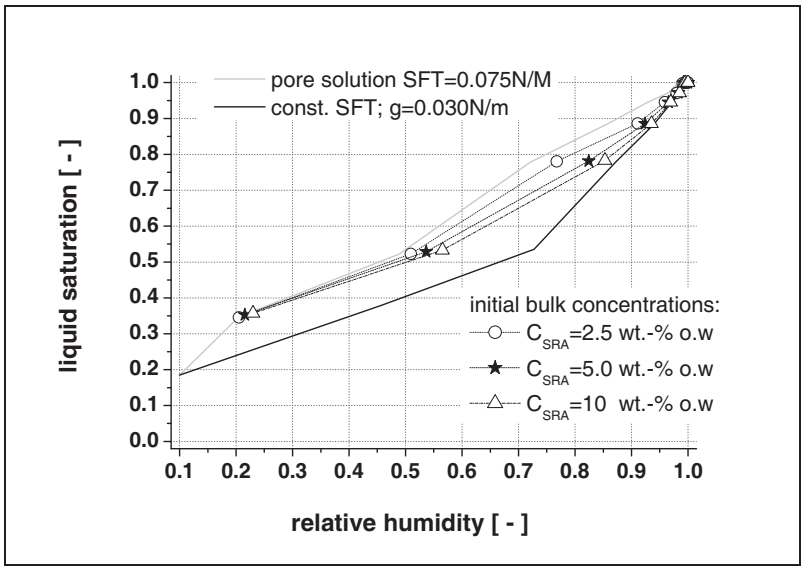

Figure 42: Impact of v/a ratio on the water vapour desorption isotherms of normcube comprising pore fluids with different initial bulk concentrations of SRA1

The effect of drying on surface tension can clearly be seen to impact the desorption isotherms. This directly impacts the capillary condensation equilibrium (5.2.2).

It can be seen that for high humidity and low surface tension the curves are in close vicinity of the isotherm of the “low tension liquid”. As introduced in chapter 5.2, low surface tensions cause the pore system to loose more water.

In contrast, for lower humidity the curves move towards the one of the plain electrolyte solution. This is due to the evolution of surface tension that increases with increasing interfacial area. As this increase causes the surface tension of the SRA pore fluids to approach that of the plain electrolyte, the desorp-

tion isotherms converge. Of course, the initial bulk concentration of SRA determines at which saturation level this happens.

It is to be noted that there is no significant difference in the evolution of desorption isotherms calculated for medium and high SRA dosages. Moreover, the relative humidity at which the isotherms merge with the reference are similar. This is due to a resolution issue of normcube, which is limited by its structure that comprises only 6 discrete pore classes. Increasing the number of classes for the normcube improves the resolution of calculation. If the pore classes are chosen in a sufficient number one could exactly determine at which point these isotherms merge, i.e. at which point the surface tension of the pore fluid is no longer impacted by the presence of SRA.

The results of this chapter make an important contribution towards the understanding of the role of SRA for drying of cement systems. It can be said that the evolution of interfacial area and the efficient amount of SRA present in the system determine the drying behaviour.

From this we conclude that a predictive model of drying shrinkage must incorporate the dependence of surface tension on the extent of drying. This depends not only on the initial dosage and surfactant type but also on the pore structure of the drying material.

7.4 Concluding remarks

The investigation of surface activity and phase behaviour of SRA in aqueous and aqueous electrolyte solution lead to the following conclusions:

7.4.1 Surface activity in aqueous solution

SRAs exhibit a surface activity comparable to the one observed with common non-ionic surfactants. Like common hydrocarbon non-ionic surfactants, SRAs can reduce the surface tension of aqueous solution down to about 30mN/m.

For SRA2, containing a relatively high amount of co-surfactant, an unlimited miscibility with water was observed. This is in line with the findings of subchapter 4.3. The presence of glycol inhibits the phase transition of the surfactant. For SRA1 comprising a significantly lower amount of co-surfactant, a miscibility gap could be found between the CMC and a high bulk concentration at which the two liquid phases turn into a reverse micellar solution (water in SRA).

Due to higher co-surfactant content, SRA2 is less efficient in reducing the macroscopic measured surface tension (compared to SRA1). However, admixture performance tests on mortars reveal that the shrinkage reducing effect of both SRA types is similar.

For all the SRAs investigated and despite differences in overall surface activity, CMC and maximum reduction of surface tension, performance tests on self-consolidating mortars do not show any significant differences in drying shrinkage.

The polycarboxylate type superplasticizer (SP-PCE) used in this study showed a surface activity comparable to the commercially available SRA's. So far, it can be said that this probably comes from a low molecular weight fraction of this poly-disperse admixture. The result with SP-PCE is most surprisingly and deserves further investigation.

For mixtures of SRA1 and SP-PCE it was found that the surface active species of both admixtures contribute to the reduction of surface tension. Moreover, measurements incorporating different fractions of these admixtures show an additive effect.

The cross-sectional occupation areas of the surfactants at the liquid/vapour interface are similar for SRAs with similar tail moieties. This result further on can be used to estimate the total fraction of interfacial area occupied by SRA molecules.

7.4.2 Surface activity in aqueous electrolyte solution

In synthetic pore solutions surface tension was found to increase due to the dissolved salts. However, the surface activity of SRA1 does not seem to be significantly altered by this. The CMC of two commercially available SRAs (SRA1 and SRA3) were slightly decreased towards lower bulk concentrations. As for aqueous solutions of SRA, SP-PCE and mixtures thereof, the contribution of SRA1 and SP-PCE can be superimposed.

7.4.3 Phase behaviour of SRA

SRAs can exhibit a miscibility gap in aqueous solutions, where initially turbid solutions separate into a water rich micellar solution and a reverse micellar phase rich in SRA. Above a certain SRA concentration, the aqueous solution forms an isotropic reverse micellar solution, where water is separated from bulk by reverse micelles. The lower phase boundary of the miscibility gap was observed at the CMC. In aqueous electrolyte solutions, SRAs exhibit phase behaviour comparable to common non-ionic surfactants. For low SRA bulk concentrations, mineral phases precipitate. Moreover, above the CMC, liquid crystal structures separate from the bulk solution. The underlying mechanism is related to the impact of the salting out effects described in literature on common non-ionic surfactants. The enhanced self aggregation in presence of dissolved salts goes inpair with the solubility of SRA molecules that decreases the CMC.
Additionally, SRAs cause a depletion of ionic species from the liquid phase. Despite the salting-out of organic matter, the solubility of inorganic salts is decreased. For bulk concentrations below the CMC, the isotropic solution precipitates calcium, potassium and sulphate ions as syngenite. For higher concentrations, when all calcium is removed from bulk, additionally sodium and potassium sulphates precipitate.

7.4.4 Impact of the interfacial area on surface activity

The surface activity of SRAs could be related to both the SRA bulk concentration and the area of the liquid/vapour interface. Moreover, using pendant drop experiments, a relationship was derived to calculate excess surface concentrations for systems comprising variable interfacial areas. Generally summarized one can distinguish between two basic states:

a) For bulk concentrations above the CMC, an increase of interfacial area would consume SRA molecules from liquid crystal structure and micelles maintaining a constant surface tension as long as this SRA supply is guaranteed.

b) For bulk concentrations below the CMC the increase in interfacial area effectively reduces the number of SRA molecules per unit area, which results in an increase of surface tension.

Results indicate that measurements of surface tensions on extracted pore solutions of cement pastes are often not representative of the actual conditions within the porous system because the measurement drastically changes the volume to surface ratio.

7.4.5 Possible impact on the hydration of Portland cement

Common dosages for SRA can be found to be in the range of up to 2wt.-% of cement or 5wt.-% as part of mixing water. This concentration steadily increases with the degree of hydration because water is consumed by hydration. This is especially true for mixtures comprising a w/c ratio near or lower than w/c=0.4 for which all the water can be bound (chemically and physically). Therefore, SRAs may possibly exhibit the whole range of phase transitions previously described.
The question then arises whether the formation of liquid crystal structures that comprise high viscosity impacts diffusion controlled processes as for instance hydration kinetics.

Furthermore the presence of SRA may enhance depletion of potassium, calcium and sodium from the pore solution. This phenomenon was already observed by Engstrand 1997 [139], Maltese 2005 [171]

and Rajabipour 2008 [132]. One may therefore wonder whether this impacts hydration kinetics of cement in one way or another.

7.4.6 Implications for modeling of shrinkage

Regarding predictive models for drying shrinkage of cementitious materials, the results presented in this chapter clearly emphasise the importance of including the evolution of interfacial area as well of surface tension. For this, the adsorption behaviour of SRA at the solid/liquid interface must be known. Second, the evolution of the liquid/vapour interfacial area needs to be known as well as its impact on surface tension.

A lot of parameters assumed to be essential for a predictive shrinkage model can be obtained from the investigation of Portland cement hydration in presence of SRAs, as for instance microstructure, admixture adsorption and bulk water content. This will be the subject of the next section.

8 Influence of SRA on the hydration of normal Portland cement

8.1 General introduction

The investigation on the hydration of normal Portland cement was carried out to determine: If and to what extent hydration kinetics, mineral phase composition and microstructure are affected by the application of SRA. Moreover, we examine whether there are interactions between SRA; SP and cement hydration that must to be taken into account if SRAs are introduced to self consolidating mortars and concretes.

The primary aim of this chapter therefore is

a) to reveal possible risks concerning the overall durability that may result from changes in hydrated phase composition and microstructure and

b) to identify SRA induced changes that may impact shrinkage modeling

8.2 Specific materials and working approach

The hydration of two different binders was studied, first on a normal Portland cement (NPC) and second, a composite binder containing 80% of the aforementioned Portland cement and 20 % limestone. The geochemical modeling code GEMS was used to model the hydration of the two binders.
It is well known that superplasticizers can delay the hydration kinetics of normal Portland cement. It is also known that especially mixtures of SRA and SP retard hydration kinetics of Portland cement paste [177, 178]. In this study, isothermal heat flow calorimetry was used to measure and compare the hydration kinetics of cement pastes with SRAs, SP and mixtures thereof. Using the results of this method, the hydration kinetics of pastes can be compared using a normalization approach, which will be introduced later on.
Thermo-gravimetric analysis was performed according the above mentioned normalization approach that enables to compare cement pastes at comparable stages of hydration. By this method, selected mineral phases as well as the degree of hydration were approximated.
The microstructure of hydrating cement pastes was qualitatively described by environmental scanning microscopy. Additionally, mercury intrusion porosimetry and nitrogen adsorption were applied to obtain pore size distributions and internal surface areas of hydrated pastes.
The adsorption behaviour of admixtures onto the solid/liquid interface was studied on hydrating Portland cement paste and some selected synthetic hydrate phases, i.e. synthetic C-S-H-phases and ettringite (material provided by Zingg [221]).

8.3 Results and discussion

8.3.1 Influence of SRA on the hydration kinetics of Portland cement

Isothermal heat conduction calorimetry: The methodical approach of sample preparation is given in detail in subchapter 6.3. The results of measurements of isothermal heat conduction calorimetry on the set cement pastes (w/c=0.4) is displayed in appendix A3, Tab.A4- 1. The table additionally contains remarks on the denomination of the system examined. For the main series as the reference and the outer boundaries of the sets, the heat release was measured up to the seventh day of hydration. Other samples were investigated during three days by when the majority of pastes had entered the final period of hydration.

In Figure 43 the heat flow of cement pastes with relatively low dosage (0.5wt.-% of cement) of different SRAs are displayed. It can be seen that none of the SRAs (SRA1; …; SRA 6) significantly influence hydration kinetics for such low dosages. In contrast, a low dosage of SP-PCE displaces the onset of the acceleration period and the time of maximum heat release for several hours.

Figure 43: Heat release of cement paste w/c=0.4 with different SRAs or SP-PCE at low dosage (0.5wt.-% of binder)

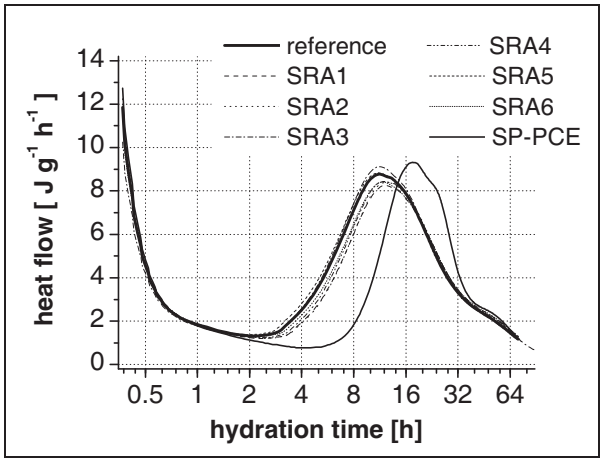

Figure 44: Heat release of cement paste w/c=0.4 with different SRAs or SP-PCE at high dosage (2.0wt.-% of binder)

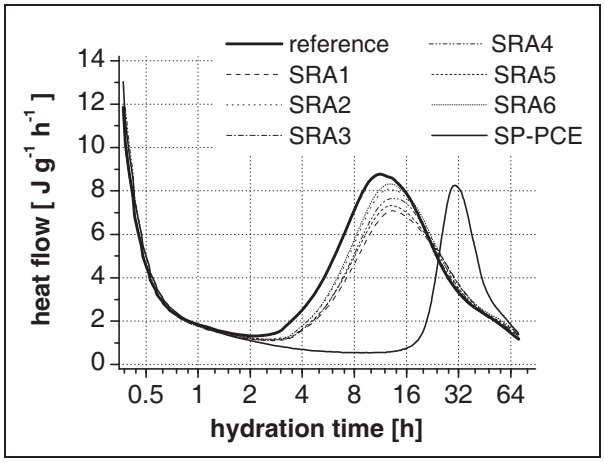

For higher dosages of SRAs (Figure 44), the induction period of cement hydration is slightly expanded and the time of maximum heat release is displaced by several hours. Additionally, the same data show that the SP-PCE admixture retards cement hydration to a much higher extent.

The hydration kinetics of the two different binder systems (with and without limestone) are not significantly different (Fig.A4- 3 and Fig.A4- 4). Both show the characteristic heat release (temporary minima, maxima and inflection points), however the absolute heat release of the pure Portland cement binder CP is higher than that of the limestone composite binder LP. For that reason, one can assume that the difference in heat release of the system is mainly due to a dilution effect referring to the substitution of 20wt.-% NPC by limestone.

In what follows the hydration kinetics are evaluated using the relative degree of hydration $rel\alpha_{hyd.;i}(t)$, which accounts for the differences in degree of hydration between the reference paste and pastes that contain admixture. The expression is obtained by comparing the total heat release at any point in time to the one released by the reference paste at the same time, reading.

$$rel\alpha_{hyd.;i}(t) = \frac{Q_i(t)}{Q_{ref.}(t)} \tag{87}$$

where:

$rel\alpha_{hyd.;i}(t)$:	relative degree of hydration	[-]
t:	time	[h]
$Q_i(t)$:	heat of hydration of sample i at time t	[Jg^{-1}]
$Q_{ref.}(t)$:	heat of hydration of the reference sample at time t	[Jg^{-1}]

Values smaller than unity indicate a retardation with respect to the reference, values larger than unity indicate acceleration.

Based on this, one can better compare the binder systems in general and pastes containing different type of SRA. In Tab.A4- 2, the relative degrees of hydration are given with respect to the absolute heat release of the plain reference paste at the designated point in time.

8.3.1.1 Influence of dosage and type of SRA on hydration kinetics

In a first step, the influence of SRA on hydration kinetics is estimated qualitatively. The plain Portland cement paste exhibits a heat release of about 293J/g after 72 hours and 339J/g after seven days respectively. The calculated relative degrees of hydration $rel.\alpha_{hyd.;i}(t)$ are displayed in Table 13.

The SRA modified pastes containing 0.5wt.-% SRA all show relative degrees of hydration of about relα_{hyd}=1, which means the hydration is unchanged. For the maximum dosage of 2wt.-% of SRA one can find relative degrees of hydration of 0.95 to 0.97 after 72 hours, indicating some retardation.

After seven days of hydration pastes containing SRA1 as well as SRA2 comprise relative degrees of hydration higher than unity independent from admixture dosage. This result is most important as these two SRA are quite different concerning their main ingredients.

Table 13: relative degrees of hydration of pastes containing SRAs

cement paste w/c=0.4		t=72 h	t=72 h	t = 168 h
		rel. $\alpha_{hyd\_CEM\ I}$	rel. $\alpha_{hyd\_CEM\ II}$	rel. $\alpha_{hyd\_CEM\ I}$
reference	-	1.00	1.00	1.00
SRA 1 [wt.-% o.b.]	0.5	1.00	0.99	1.01
	1.0	0.99	0.97	1.02
	2.0	0.95	0.94	1.00
SRA 2 [wt.-% o.b.]	0.5	1.01	0.99	1.02
	1.0	1.00	-	1.03
	2.0	0.97	0.93	1.02
SRA 3 [wt.-% o.b.]	0.5	1.02	-	-
	2.0	1.00	1.01	-
SRA 4 [wt.-% o.b.]	0.5	1.00		-
	2.0	0.96	0.94	-
SRA 5 [wt.-% o.b.]	0.5	1.02	-	-
	2.0	1.03	0.99	-
SRA 6 [wt.-% o.b.]	0.5	1.02	-	-
	2.0	0.97	0.94	-

Also in the composite binder, one finds no significant change in hydration kinetics for the low dosage of SRA1 and SRA2. For the 2wt.-% dosage the relative degree of hydration is almost similar to the NPC paste (Table 13).

The results show that depending on their composition, SRAs only have a minor effect on the degree of hydration at three days. They do however cause a slight but significant delay of the acceleration period as well as of the time of main heat release. The total cumulated heat release at the seventh day of hydration is unaffected or slightly increased.

8.3.1.2 Influence of admixture combinations (SRA&SP) on hydration kinetics

As described earlier and found in literature, the combined use of SRA and SP-PCE disproportionally delays the cement hydration of blended and pure NPC pastes. Indeed, one can find relative degrees of hydration of ~0.8 after three days and ~0.9 after seven days, for high dosages. An overview is given in Table 14.

Table 14: Relative degrees of hydration of pastes containing SRAs ,SP-PCE and mixtures thereof

cement paste w/b~0.4			t=72 h	t=72 h	t = 168 h
admixture	SRA [wt.-% o.b.]	SP-PCE [wt.-% o.b.]	rel. $\alpha_{hyd\_CEM\ I}$	rel. $\alpha_{hyd\_CEM\ II}$	rel. $\alpha_{hyd\_CEM\ I}$
SRA 1	2.00	-	0.95	0.94	1.00
SRA 1 + SP-PCE	2.00	2.00	0.81	0.82	0.93
SP-PCE	-	2.00	0.89	0.89	0.94
SRA 2 + SP-PCE	2.00	2.00	0.82	0.82	0.92
SRA 2	2.00	-	0.97	0.93	1.02

From the data given in Table 14 it can be seen that after three days and for both binder systems the degree of hydration is decreased for pastes containing both admixtures. The type of SRA does not influence the result. At that time, an interaction effect exists because the reduction of $rel\alpha_{hyd.;i}(t)$ with respect to the reference is larger for the combination of both admixtures than the sum of the two individual mixes. After seven days however, the pastes containing both admixtures show a hydration progress that is similar to the sum of the progress of the individual mixes. This suggests that between three days and seven days neither admixture depresses hydration. Reactions are proceeding normally but the initial delay is not yet caught up.

8.3.1.3 Thoughts about the influence of SRA on the hydration kinetics of Portland cement

In this section we examine the influence of SRAs on the hydration kinetics of the different binder types investigated. This seems necessary because of the following reason: The composite binder used in this study was produced by replacing 20wt.-% of the Portland cement by limestone comprising an almost similar particle size distribution. In pastes, the dosage of SRA applied referred to the binder content, i.e. the absolute amounts of admixture used in both types of binder were identical. As a result of this, in the composite binder the dosages of SRAs relative to the clinker content are larger by factor 1.25. As previously stated; for both binder types the delaying impact increase with the admixture dosage. One now would expect that the composite binder experiences an enhanced retardation due to its higher relative dosage of SRA per Portland cement content but this is not the case.

Assuming a simple dilution effect, the heat release of the limestone containing pastes should be in the range of 80% of the CEM I pastes. However, for the whole range of measurements the heat release of the composite binder after 72 hour is found to be in the range of 88.3%± 1.4% (Tab.A4- 2) This covers six different types of SRA, SP and combinations thereof.
From this it appears that the Portland cement reacts faster in presence of limestone. This is especially true for the early hydration for which the induction period reduced in presence of fine limestone. These results are in line with the findings of other authors showing that, in presence of limestone the hydration of Portland cement is accelerated. A fundamental study on this accelerating effect was recently published by Bellmann et al. [244].

In Figure 45 & Figure 46 the heat release of corresponding pastes types carrying high dosages of the six SRAs investigated are displayed. The corresponding pastes (LP – composite binder; CP – pure cement paste) contain similar absolute amounts of water as well as admixture.

Figure 45: Heat release of pastes with similar absolute amounts of different SRA

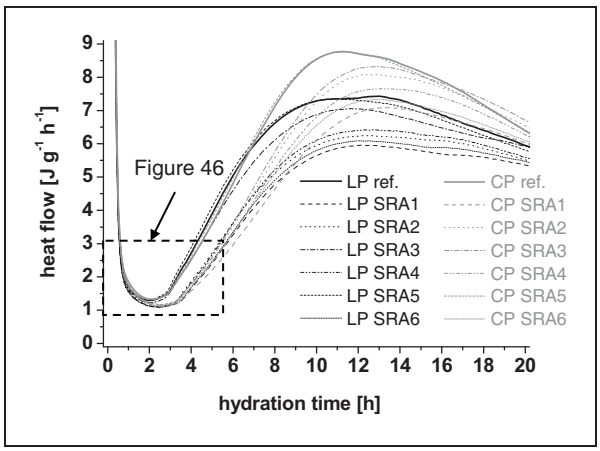

Figure 46: Detail of Figure 45

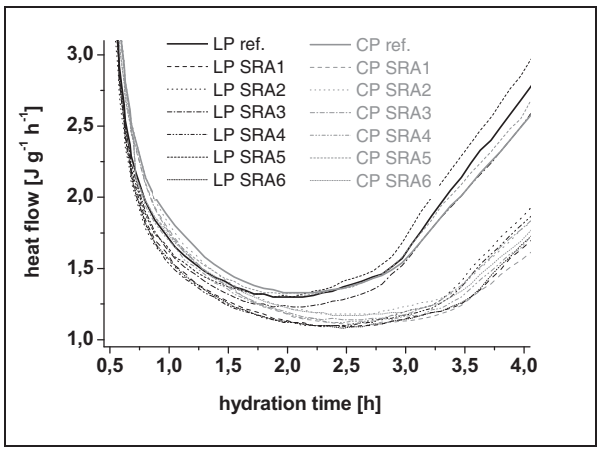

Figure 45 focuses on the time of maximum heat release and Figure 46 provides a closer view on the transition from induction to acceleration period of hydration. A significant difference in delay of hydration for one or the other binder type is hardly to define.

For this reason the following two characteristics are viewed for each binder: a) minimum of heat flow during induction period and b) time of maximum heat release (Table 15). The time displacement of the characteristic heat flow minimum as well as of the heat flow maximum is expressed as $dt[q_{min}]$ or $dt[q_{max}]$. The difference *dt* reflects the effect of the binder type (limestone composite binder LP or Portland cement CP).

The results in Table 15 show that the effect of binder type on both the time of minimum heat release ($dt[q_{min}]$ <0.25h) and the time of maximum heat release ($dt[q_{max}]$.< 1.2h) is smaller than 10%.

Table 15: Impact of SRA on hydration kinetics of different binder systems

w/b=0.4; SRA dosage 2wt.-% o.b.	dormant period			time of main heat release		
	LP	CP	dt [q_{min}]	LP	CP	dt [q_{max}]
	t[q_{min}]	t[q_{min}]		t[q_{max}]	t[q_{max}]	
	[h]	[h]	[h]	[h]	[h]	[h]
reference	2.00	2.13	0.13	11.00	11.33	0.33
SRA 1	2.50	2.75	0.25	12.17	13.33	1.16
SRA 2	2.38	2.50	0.13	12.50	12.50	0.00
SRA 3	2.25	2.50	0.25	11.67	12.83	1.16
SRA 4	2.38	2.50	0.13	12.67	13.17	0.50
SRA 5	2.00	2.13	0.13	11.00	11.33	0.33
SRA 6	2.50	2.50	0.00	12.17	12.83	0.66
		min dt	**0.00**		min dt	**0.00**
		max dt	**0.25**		max dt	**1.16**

This is somewhat surprising. Because of the higher relative admixture dosage in the composite binder (factor 1.25), one expects to see these pastes subjected to an enhanced delay. In contrast, it can be seen, that despite the lower relative dosage of SRA, the Portland cement binder is slightly more retarded. This is shown by the minimum and maximum values of *dt* given in the last row of Table 15.

We recognize that the dosage of SRA relative to the clinker content of the binder does not reflect the extent of retardation. The question now arises about the reason for this.

Retardation from superplasticizers can be assumed to be linked to adsorption []. However, from theory on non-ionic surfactants it can be taken that SRA might not adsorb much, given the high pH-cementitious environment. Anyway, if adsorption of SRA would impact hydration kinetics, the composite binder pastes should be more affected / delayed due to a higher relative admixture load.

On the other hand, a preferred adsorption of SRA onto the limestone may occur but is very unlikely.

However, if the SRA induced delay is not related to admixture/solids interaction, its interaction with the electrolyte solution may explain the retardation.

In subchapter 7.3.2.2 the interactions of SRA in aqueous electrolyte solution were studied. It revealed that SRAs have an impact on the amount of ionic species soluble in the bulk solution. Indeed, the phenomenon could be observed for SRA concentrations even lower than the one used in the calorimetric measurements on paste.
Furthermore, enhanced self-assembly of SRA was observed for synthetic pore solutions with a composition similar to the one of the Portland cement paste used here, i.e. a composition similar to the one during the induction period. However, the salting out effect was not observed before the CMC was achieved.

8.3.1.4 Hydration kinetics normalization approach for liquid and solid phase analysis

To develop a suitable time schedule to compare results from hydrated phase analysis, the different hydration kinetics observed by isothermal heat conduction calorimetry were normalized. Figure 47

shows how this was done for different pastes independent of type or amount of admixture introduced.

All the following measurements were executed according to the schedule derived from this approach. Further on, for phase analysis we exclusively refer to the 8 stages defined in the legend of Figure 47.

The absolute values of hydration time versus stage of hydration of the set of pastes investigated are given in appendix, Tab.A4- 3.

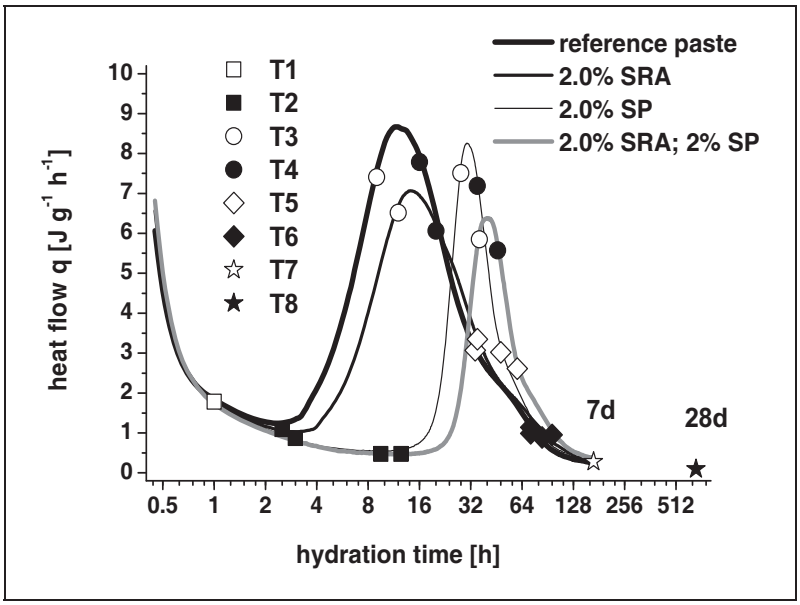

Figure 47: Normalisation of hydration progress of CEM I pastes carrying different dosages and combinations of SRA1 and SP-PCE and SRA/SP-PCE

T1: 1 hour

T2: minimum of heat flow during induction period

T3: start of acceleration period

T4: end of acceleration period

T5: change of slope within deceleration period

T6: end of deceleration period

T7: start of final period (7d)

T8: 28 days of hydration

8.3.1.5 Thermo-gravimetric analysis

The methodical approaches for sample preparation and handling are to be found in subchapter 6.3. For the 8 characteristic stages of hydration, water loss of

a) the plain reference paste (CP 00.00) as well as of

b) pastes carrying high dosages of SRA; SP-PCE and SRA/SP

is displayed in appendix, Fig.A4- 7, Fig.A4- 8, Fig.A4- 9, Fig.A4- 10.
Note that concerning the drying procedure applied, ettringite was assumed to comprise a water content of 20 rather than 26 mole water per mole ettringite. Other hydrate phases additionally may have lost some water before the start of thermal analysis. For that matter an absolute amount of chemically and physically bound water cannot be derived from these measurements.

A comparison of the degree of hydration obtained from thermo-gravimetric measurements is given in Table 16. Here a degree of hydration of $\alpha_{hyd.}$=1 refers to 26g water chemically bound into cement. The columns in Table 16 contain values for pastes carrying SRA and SP-PCE in different dosages as well as mixtures thereof.

Table 16 shows that for all pastes the bound water content increases with stage of hydration. For SRA1 no significant impact on degree of hydration can be found. For pastes carrying only SP-PCE (columns 4 and 5 in Table 16) and mixtures of SP-PCE and SRA1 (last two columns in Table 16) differences can be obtained up to the start of the final period. For these pastes, up to stage T6 the evaluated degree of hydration is higher. This comes from the normalization schedule. For example, the pastes with high dosage of SP-PCE and SP-PCE + SRA1 comprise a significant extension of the induction period. As the start of main silicate phase reactions determines the beginning of the acceleration period, the increased degree of hydration at this stage is due to the ongoing aluminate phase reaction during the induction period.

Table 16: Relative degree of hydration derived from thermo analysis

stage of hydration		degree of hydration [-]*						
		reference	min. SRA1	max. SRA 1	-	-	max. SRA 1	max. SRA 1
			-	-	min. SP	max. SP	min. SP	max. SP
[T X]	[-]	CP 00.00	CP 11.00	CP 13.00	CP 00.11	CP 00.13	CP 13.11	CP 13.13
T1	1 hour	7%	5%	5%	7%	9%	7%	9%
T2	end of induction period	8%	6%	6%	7%	11%	8%	18%
T3	end of acceleration period	22%	27%	26%	36%	45%	29%	52%
T4	start of deceleration period	32%	37%	41%	50%	56%	56%	66%
T5	mid of deceleration period	55%	57%	57%	57%	67%	64%	66%
T6	start of final period	70%	69%	79%	73%	73%	75%	75%
T7	7 days	74%	75%	78%	82%	77%	81%	80%
T8	28 days	82%	84%	85%	-	84%	80%	77%

* referring to 26g water chemically bound to 100g cement for complete hydration

From this it can be assumed in a first attempt that the enhanced degree of hydration at T2 for

a) the paste with high SP-PCE content and

b) the paste containing high dosages of SRA1 and SP-PCE

may be due to a suppression of the silicate phase hydration. By the end of final period (T6) these differences vanish.

Concerning the suppression of silicate phase reactions, we now use the mass loss curves of thermo gravimetric measurements to examine the nature of phases present at the different stages of hydration.

Figure 48 contains the mass loss curves of different pastes at the end of the induction period. From their derivatives the phase composition can be determined within limits.

What can be seen in Figure 48 is that for the derivatives

a) in the range up to 200°C and

b) between 500°C and 720°C as well as

c) between 750°C and 900°C

discrete peaks can be obtained of which a) refers to the dehydration of aluminate phases, b) refers to decalcination of $MgCO_3$ and $CaCO_3$ and c) might refer to a decomposition of organic residues under of reducing conditions (N_2 –carrier gas). Note that losses above 750°C were mainly found for hydrated pastes containing admixture. Concerning the decalcination of $MgCO_3$ and $CaCO_3$, for the temperature regime applied the unhydrated cement showed decalcination in that specific temperature range.

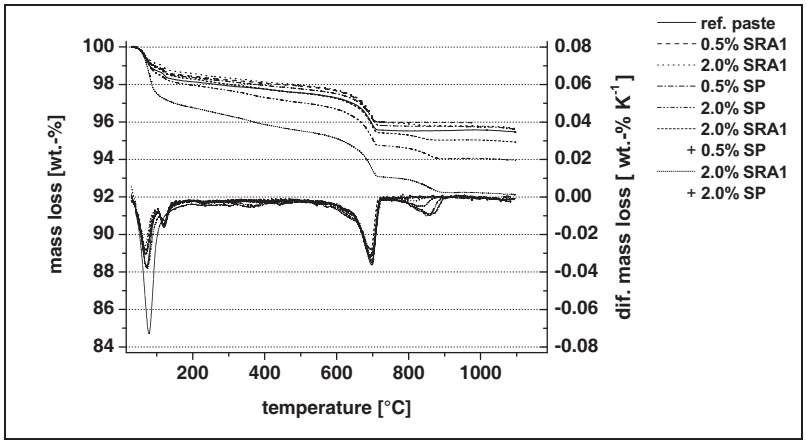

Figure 48: Thermo analysis of different cement pastes at the end of the induction period of cement hydration (T2)

The main silicate clinker reactions are accompanied by the precipitation of portlandite, which shows a characteristic water loss between 400°C and 500°C. As expected, at stages T1 and T2 such a charac-

teristic peak cannot be found, which indicates that portlandite is not yet formed and the main silicate hydration has not started yet.

The mass loss referring to decalcination can be found to be similar for all pastes investigated and directly related to the $MgCO_3$ and $CaCO_3$ content of the unhydrated cement.

The mass losses of the pastes up to a temperature of 200°C are displayed in Table 17. Additionally the absolute time of hydration is given. From this table it can be seen that also the aluminate phase hydration is impacted by SRA1 because the amount of water bound is decreased.

Table 17: Water loss of cement pastes at the end of the induction period

T2 - end of induction period	amount of chemically bound water [g/100g unhydrated cement]*						
	reference	min. SRA1	max. SRA 1	-	-	max. SRA 1	max. SRA 1
		-	-	min. SP	max. SP	min. SP	max. SP
paste [CP xx.xx]	CP 00.00	CP 11.00	CP 13.00	CP 00.11	CP 00.13	CP 13.11	CP 13.13
water loss [g]	2.0	1.5	1.6	1.7	2.9	2.1	4.7
absolute time [h]	2.5	2.5	3.0	4.0	9.5	5.0	12.5

*referring to

For pastes containing high dosages of SP-PCE and additional SRA1 the following can be pointed out. Both, the time entering the acceleration period and the amount of aluminate hydrates are heavily increased. Furthermore, referring to the paste with high admixture dosages, the start of the acceleration period is displaced an additional three hours if both admixtures are present. Due to this one concludes that it is the amount of aluminate hydrates that increases upon the ongoing hydration.
It now can be said that SRA1 causes a slight delay of aluminate reactions. However, the main impact on the hydration kinetics concerns the silicate hydration, i.e. the time C-S-H phases start to precipitate.

Within the main period of cement hydration, thermal analysis reveals, that the silicate phase hydration increasingly contributes to the binding of water. Well after the maximum heat release (at T4; Figure 49), the peak of the mass loss derivatives at 100°C (indicator 1) broadens due to water loss of C-S-H gel. Moreover, the characteristic portlandite peak appears (indicator 2). Similar trends can be observed at hydration stage T3, displayed in annex, Fig.A4- 12..

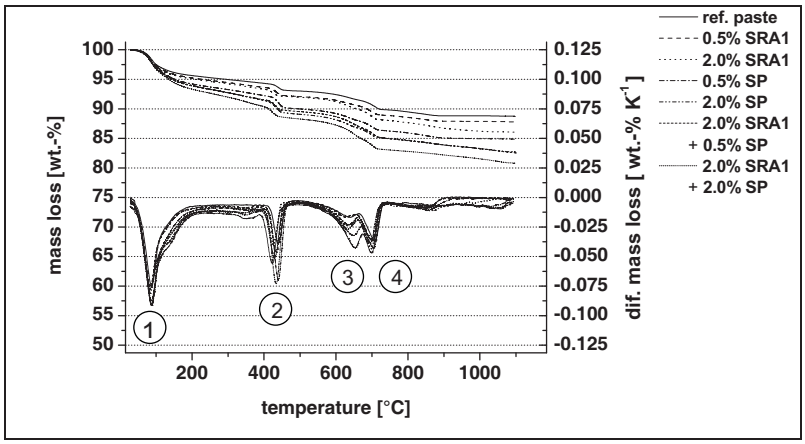

Figure 49: Thermo analysis of pastes after main heat release (T4)

Another feature of Figure 49 is that the amount of portlandite seems to be enhanced for pastes containing both, SRA and SP and increases with increasing dosage of admixture. Furthermore an additional peak in the temperature range of around 600°C (indicator 3), well before decalcination of calcite (indicator 4; ~700°C) appears. It has an increasing height with increasing admixture dosage and appears independent from the type of admixture.
According to [217] this peak is due to the presence of Monocarbonates. Seeing this development is somewhat surprising. To understand this we first need a proper phase analysis by XRD.

At the end of the deceleration period (hydration stage T5; Fig.A4- 13) the weight loss within the temperature range characteristic for portlandite dehydration increases steadily.

Up to the 28th day of hydration, weight loss due to portlandite decomposition is always higher for the plain cement paste. For pastes containing admixtures; the portlandite content decreases with increasing dosage of both admixtures alone or in the combination of SRA and SP-PCE. The results of portlandite quantification are displayed in Table 18.

In Table 18, data for high dosages of SRA and/or SP-PCE show comparably low amounts of portlandite. This can indicate either a delay of the silicate hydration or a change in the composition of hydration products. Especially the results for 28 days of hydration are surprising. Data show that all pastes comprise almost similar amounts of bound water (see

Table 19) but different portlandite contents (compare to Table 18). To solve this, it is necessary to conduct appropriate phase analysis.

Table 18: Amount of portlandite derived from weight loss between 420°C and 500°C

stage of hydration		approximated amount of Portlandite [g/100g unhydrated cement]						
		reference	min. SRA1	max. SRA 1	-	-	max. SRA 1	max. SRA 1
			-	-	min. SP	max. SP	min. SP	max. SP
[T X]	[-]	CP 00.00	CP 11.00	CP 13.00	CP 00.11	CP 00.13	CP 13.11	CP 13.13
T1	1 hour	-	-	-	-	-	-	-
T2	end of induction period	-	-	-	-	-	-	-
T3	end of acceleration period	2.5	2.6	1.3	4.3	4.4	1.8	5.6
T4	start of deceleration period	4.4	5.5	3.5	6.9	8.6	5.6	4.6
T5	mid of deceleration period	11.3	10.0	6.6	10.4	10.8	7.2	5.7
T6	start of final period	13.8	11.9	8.7	13.3	11.7	8.3	7.9
T7	7 days	14.8	14.2	10.2	14.5	12.6	9.4	7.0
T8	28 days	16.3	15.6	11.0	15.9	14.1	9.6	8.1

Table 19: Water loss of pastes after 28 days of hydration

T8 - 28 days	amount of chemically bound water [g/100g unhydrated cement]*						
	reference	min. SRA1	max. SRA 1	-	-	max. SRA 1	max. SRA 1
		-	-	min. SP	max. SP	min. SP	max. SP
paste [CP xx.xx]	CP 00.00	CP 11.00	CP 13.00	CP 00.11	CP 00.13	CP 13.11	CP 13.13
water loss [g]	21.4	21.8	22.0	21.0	21.7	20.8	20.1

* referring to drying at 37°C/13±3%R.H.

8.3.1.6 Concluding remarks

Using isothermal heat conduction calorimetry, the delaying impact of SRA1, SP-PCE and their combinations on hydration kinetics was studied. Based on the characteristic heat flow curves, the hydration progress of admixture containing pastes was normalized to select discrete times/stages at which pastes would be expected to show comparable hydration. Those stages were the ones at which thermal analysis and pore solution extraction was performed.

Thermal analysis revealed that SRA and SP seem to cause a depression of the silicate phase hydration indicated by a significant extension of the induction period of cement hydration, whilst the aluminate phase hydration proceeds almost unaltered.
During the main hydration period, the silicate phase hydration continues to be depressed. Taking portlandite as an indicator of the silicate phase hydration, thermo-analysis reveals that for high dosages of both admixture types, alone and in combination, the degree of silicate hydration is reduced to about 70% for SRA1 (c_{SRA}=2wt.-% o.c.) and about 50wt.-% for SP-PCE (c_{SP_PCE}=2wt.-% o.c.) after 28 days of hydration.

In contrast, the amount of water bound to cement after 28 days of hydration appeared to be almost similar and independent from admixture addition (about 20.5 ±0.5g water per100g unhydrated ce-

ment). This may indicate that the phase composition of hydrates could be changed due to the presence of SRA1 and/or SP-PCE. This possibility is examined in the next section.

8.3.2 Influence of SRA/SP-PCE on hydrated phase composition

8.3.2.1 Hydration of the reference cement paste

Based on the mineralogical composition and fineness of the Portland cement used, the hydration process was modelled using the GEM-Solver. Results are given in Figure 50. The phase evolution displayed should be seen as an approximation since other important cement or clinker characteristics are not implemented into the calculation routine.

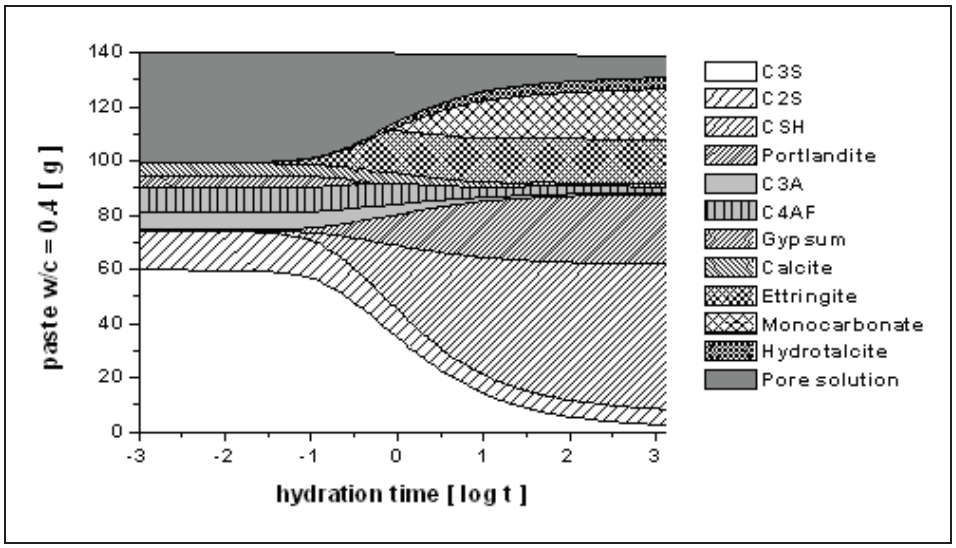

Figure 50: GEMS process modeling - hydration of plain paste (CP 00.00)

The cement used comprises about 4wt.-% calcite and therefore monocarbonate preferably precipitates instead of monosulphate (compared to Portland cement without calcite). Syngenite is also predicted to precipitate but only as a minor phase (<0.25g/100g unhydrated cement) and therefore is not shown in Figure 50. Its maximum content occurs right before gypsum is depleted from bulk and then diminishes.

In what follows GEMS results are used for semi-quantitative assessment of solid phase composition of the hydrated reference paste. For this however, the main outcome is first summarized.

a) Concerning the silicate hydration, after hydration stage T2 the proportions of the following phases:
"C_3S + C_2S : C-S-H-phases : portlandite" were found to meet approximately **1 : 0.81 : 0.38** independent from time.

b) After depletion of gypsum, the amount of ettringite remains almost constant and further on mainly monocarbonate is formed during the ongoing aluminate hydration.

c) If the TGA data are corrected for ettringite carrying 20 mole water instead of 26 (effect of sample preparation) the amount of chemically bound water predicted by GEMS is in very good agreement. Note that this correction only was executed for samples totally depleted from gypsum, i.e. after the end of the induction period of cement hydration.

Based on the above, the TGA data were used to produce a semi-quantitative analysis of the solid phases. Additionally, this was supported by the data set obtained from X-ray powder diffraction. (The set of these samples is given in appendix, Tab.A4- 6.)

For semi-quantitative analysis of the XRD data, the appropriate peak locations of the main clinker phases had to be determined. This was done as follows: The silicate phases of the unhydrated ce-

ment and clinker were removed by salicylic acid hydrolysis (SAH) according to Taylor 1997 [241]. In Figure 51 a selected part of the diffractograms of the unhydrated cement and of the residue of the clinker after SAH are displayed.

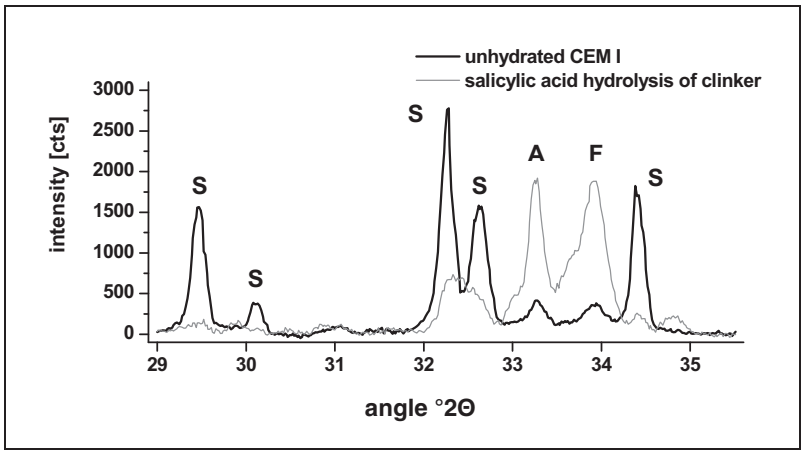

Figure 51: X-ray diffractograms of NPC and appropriate clinker after salicylic acid hydrolysis

A: aluminate phase
F: ferrite phase
S: silicate phases

It can be seen that the silicate phases indicated by the characteristic peak between 32° and 33°2Θ are removed by selective hydrolysis. Hence, in the SAH residue the aluminate phases, i.e. aluminate and ferrite between 33° and 34°2Θ, give higher peaks due to the enrichment effect. In the course of semi-quantitative analysis the areas under the peaks in this 2Θ-range should be used for approximation for the hydration/conversion of clinker phases.

8.3.2.2 Numerical approach for semi-quantitative XRD-analysis

The set of pastes investigated contained samples carrying different dosages of SRA (SRA1; SRA2; SRA3; SRA5) as well as several combinations of SRA1 and SP-PCE. According the previously described time schedule, the hydration of these pastes was stopped and samples were prepared for X-ray powder diffraction (subchapter 6.3.2.3). The range of these samples is given in appendix, Tab.A4-6.

The comparison between the reference samples and the set of SRA-modified pastes reveals that the diffractograms are approximately congruent (Fig.A4- 17, Fig.A4- 18, Fig.A4- 19, Fig.A4- 20 and Fig.A4- 21). To prove that no significant changes exist, a numerical procedure was applied screening the diffractograms for characteristic changes in either peak area or peak location.
For all of the different hydration stages (T1, …, T8) neither new mineral phases nor changes in phase proportions could be derived from XRD (Tab.A4- 7 and Tab.A4- 8). This indicates that the normalized time schedule worked out well.
The issue of how preferred orientation of portlandite can affect results is referred to later on.

8.3.2.3 Semi-quantitative XRD-analysis of the main clinker phase dissolution

As expected, up to the end of the induction period, the amount of silicate clinker phases is not significantly changed in presence of SRAs (Tab.A4- 7; changes lower then standard deviation of the reference). For the ferrite and aluminate clinker phases, no significant change referring a) to the unhydrated reference and b) in between the homologues series can be observed. This is due to the low initial diffraction intensities that reduce the accuracy on these phases.
At the beginning of the final hydration period (T6) and after 28 days of hydration (T8), the progress in hydration more or less leads to a significant decrease of all of the main clinker phases (Tab.A4- 8). A significant difference between the series cannot be reliable determined, since the standard deviation is too large.

8.3.2.4 Semi-quantitative XRD-analysis of the sulphate regulator consumption

The results concerning gypsum and anhydrite are displayed in Table 20. Compared to the unhydrated cement, due to the initial hydration of the calcium sulphate hemihydrates, the amount of gypsum (initial content plus secondary phase) after 10min and 1hour of hydration (stage T1) is increased for the whole range of the investigation. Later on, gypsum diminishes and can no longer be detected by XRD. One exception is paste CP13.13, comprising high amounts of both, SP-PCE and SRA1. Because of a very large retardation (silicate phases), gypsum is depleted between hydration stage T1 and T2 before hydrates of the silicate phase reactions appear. This does not come from the admixture accelerating gypsum consumption, but from the silicates being so much retarded that stage T2 has not begun by the time all gypsum has been consumed. This is further confined by the absolute hydration times in Table 20 showing that, independent from admixture treatment, gypsum is depleted between about 9 and 12 hours. The aluminate reactions therefore proceed approximately independent from admixture presence.

Table 20: Depletion of sulphate regulator

sulphat regulator consumption		**paste [CP xx.xx]**						
		CP 00.00	CP 11.00	CP 13.00	CP 00.11	CP 00.13	CP 13.11	CP 13.13
		reference	min. SRA1	max. SRA 1	-	-	max. SRA 1	max. SRA 1
			-	-	min. SP	max. SP	min. SP	max. SP
gypsum	*time frame [h]*	2.5 - 9	2.5 - 11	3 - 12	4 - 15	9.5 - 28	5 - 16	1 - 12.5
	hydration stage [T_i]	T2 - T3	T2 - T3	T2 - T3	T2 - T3	T2 - T3	T2 - T3	T1 - T2
anhydrite	*time frame [h]*	34 - 72	34 - 72	35 - 72	35 - 72	48 - 84	40 - 72	36 - 46
	hydration stage [T_i]	T5 - T6	T5 - T6	T5 - T6	T5 - T6	T5 - T6	T5 - T6	T3 - T4

The characteristic times obtained for the depletion of the slowly soluble anhydrite are also displayed in Table 20. Despite a resolution issue (time frame), this phase also diminishes within a time of about 40 hours of hydration, which also suggests that aluminate reactions proceed more or less independently of admixtures used. XRD analysis further shows that monocarbonate is always detected right after anhydrite is depleted.

So far, results obtained by X-ray powder diffraction and thermo gravimetric analysis indicate that SRA, SP-PCE and their combinations cause a delay in hydration that rather impacts the silicate than the aluminate phases.

8.3.2.5 Semi-quantitative XRD-analysis of the hydrate phases

The results of semi quantitative XRD-analysis of hydrates are given appendix, Tab.A4- 7 and Tab.A4-8 (ettringite; monocarbonate; portlandite). Up to one hour of hydration, results show that the amount of ettringite in pastes containing high dosages of SRA seems to be increased. However, it is hard to say whether by the end of the induction period there is an additional difference for the ettringite content between SRA containing sample and the reference without SRA.

In NPC the depletion of sulphate regulator most probably causes the formation of monocarbonate instead of monosulphate [217, 218, 243]. For the whole range of samples investigated, no monosulphate appeared and monocarbonate was not found before the beginning of the final period of hydration. This can be due to the fact that AFm-phases may comprise low cristallinity and hence might not be detected by common X-ray diffraction [243].

A particularly intense peak referring to portlandite at 18.7°2Θ was found for paste containing 2wt.-% SRA5 (CP 53.00) at hydration stage T6 as well as for hydration stage T8 (Fig.A4- 20, Fig.A4- 21 and Tab.A4- 8). The calculated area under the peak is almost double the value that was found for the reference samples and all the other samples within the homologue series. This is most probably due to an artefact for more than one reason: First, the amount of silicate phases in this paste was evaluated not to be significantly different for the whole set. Thermo-gravimetric analysis contributes to this assumption, since results in Table 21 show similar portlandite contents for all samples.

Table 21: Portlandite quantification in cement paste CP at hydration stage T6 and T8

stage T6 start of final period		reference paste	pastes containing 2wt.-% SRA or SP-PCE					2 wt.-% SRA1 + 1wt.-% SP-PCE	2wt.-% SRA1 + 2wt.-% SP-PCE
			SRA1	SRA2	SRA3	**SRA5**	SP-PCE		
TGA	**[g/100g]**	18	14	16	16	**17**	16	14	13
XRD	**peak area [Cts°2T]**	551	361	603	656	**1319**	542	224	338

stage T8 28 d of hydration		reference paste	pastes containing 2wt.-% SRA or SP-PCE					2 wt.-% SRA1 + 1wt.-% SP-PCE	2wt.-% SRA1 + 2wt.-% SP-PCE
			SRA1	SRA2	SRA3	**SRA5**	SP-PCE		
TGA	**[g/100g]**	22	17	18	20	**21**	20	16	14
XRD	**peak area [Cts°2T]**	793	552	688	835	**1492**	756	382	303

In Figure 52 the results of TGA are plotted against the portlandite quantification by XRD.

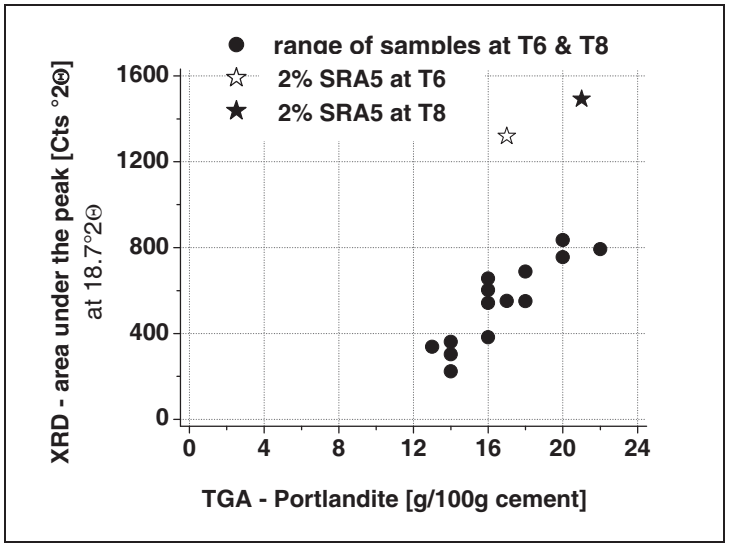

Figure 52: Portlandite quantification in hydrated cement paste CP – semi-quantitative XRD vs. TGA

Obviously the XRD-quantification of portlandite in the paste with 2wt.-% SRA5 can be assumed to suffer an artefact and may be related to preferred orientation. It cannot be excluded, that other pastes carrying admixtures may also but to a lesser extent be affected by this.

So far it can be stated that the XRD analysis led to the following conclusions:

a) With the resolution of the method at hand SRA, SP-PCE and their combinations seem to have no impact on the hydrate phase composition.

b) The methodical setup turned out to be insufficient for semi-quantitative analysis of the hydrated samples by XRD. For hydrates of the aluminate and ferrite clinker phase diffraction patterns are insufficient for quantification due to either undesired drying of Aft or poorly crystalline AFm. For portlandite in pastes carrying SRA a statistical over representation due to preferred orientation cannot be excluded.

8.3.2.6 Combination of semi-quantitative XRD-analysis and thermo-gravimetry

Combining the results of thermo gravimetric analysis, XRD analysis and isothermal heat conduction calorimetry, an overview on the whole hydration process can be obtained based on the following assumptions and is displayed in Table 22:

a) Results from XRD analysis indicate no significant changes in hydrated phase composition at normalized times. Therefore, only differences in hydration kinetics can be taken into account.

b) The depletion of the sulphate regulator, independent of the type of SRA, indicates that the aluminate clinker phase hydration is not significantly influenced and the delay observed by isothermal heat conduction calorimetry refers to retardation of silicate clinker phase hydration.

c) From thermo-gravimetric analysis portlandite can be quantified. From portlandite content and the results obtained from thermodynamic modelling (GEM solver), the amount of silicate phase dissolved as well as the quantity of C-S-H phases can be estimated.

d) The amount of chemically bound water can be derived from TGA and the amount of free water can be distinguished.

e) The results derived from isothermal heat conduction calorimetry show that at hydration stage T7 (after 7 days of hydration) the heat conduction curves of all of the admixture treated pastes merge (see Figure 47), indicating that the main reactions took place and further progress can be assumed to be not significantly impacted by the presence of SRA.

f) After a hydration of 28 days, the reaction rates for the aluminate clinker phases in pastes with and without SRAs are assumed to be similar. The amounts of the hydrates and remaining clinker phases were derived from GEMS process modelling of the plain reference paste.

Table 22: Calculated main phase composition of hydrated cement pastes after 28 days of hydration

main phases	reference	pastes containg 2wt.-% SRA or SP-PCE					2 wt.-% SRA + 1wt.-% SP-PCE	2wt.-% SRA1 + 2wt.-% SP-PCE
		SRA 1	SRA 2	SRA 3	SRA 5	SP-PCE		
	[g / 100g cement]							
C_3A+C_4AF	3							
AFt; Afm; Calcite	41							
Portlandite *	**22**	17	18	20	21	20	16	14
C-S-H	**46**	37	39	43	46	42	34	30
C_3S+C_2S	**17**	28	26	21	18	23	32	37
free water	**10**	10	10	8	8	10	12	13
balance	**1**	3	3	3	3	2	2	2

(* from TGA)

According to Table 22, SRAs suppress the C_3S hydration to different extents. SRA1 followed by SRA2 and SRA3 lead to a decreased degree of hydration of the silicate clinker phases. SRA5 seems to have almost no impact. The combination of SRA1 and SP-PCE drastically reduces C_3S hydration and this increases with the amount of superplasticizer. We however note that the impact of the superplasticizer alone can rather be described as a minor influence.

Another important fact can be obtained from Table 22: Even though the amounts of hydrates of C_3S differ, the amounts of free water, derived from TGA measurements, are quite similar. Accounting for a water content of C-S-H phases as implemented into GEMS ($C_{1.67}SH_{2.1}$), a maximal difference of about 15g C-S-H between the reference and pastes with admixtures (row C-S-H in Table 22) should result in a free water difference of about 3g (compare reference paste to last column in Table 22). Furthermore, the amount of free water increases to about 5g if the maximum difference in portlandite content (as a by-product of C_3S hydration) is additionally referred to (compare reference paste to last row in Table 22). As can be seen, the values given in Table 22 approximately meet this condition.

So far, as a result of the solid phase analysis, it can be summarized that SRAs differently influence the hydration kinetics.
SRA1 and SRA2 strongly suppress the silicate clinker phase hydration. For pastes containing 2wt.-% of admixture (maximum dosage used in this study) the degree of silicate hydration after 28 days is decreased from 77% to about 64%.
For SRA3 and 5 the degree of hydration was observed to decrease only to 72% or 76% respectively.

The superplasticizer used in this study also causes a reduction of silicate hydration. The degree of hydration decreases with increasing amount of superplasticizer.

Combinations of SRA1 and SP-PCE led to particularly high delays of hydration. After 28 days the degree of hydration was decreased to 50% when both admixtures were added with initial concentrations of 2wt.-% of cement each.

The question arises as to whether

- these pastes continue to hydrate and achieve a higher degree of hydration at later stages or
- the water identified as “free water” (see Table 22) is “inactivated” for some reason (physically bound) and so may not be available to keep reactions running.

The latter would imply that in presence of SRA and SP-PCE the final degree of hydration would always be reduced. However, we note, that for the composite binder, carrying 20% of lime stone and therefore comprising a higher efficient w/c ratio, the degree of hydration for every referring cement binder paste was always increased (evaluated by isothermal calorimetry). One could wonder if SRAs inactivate huge amounts of free water, which then would no more be available for hydration.
Alternatively, a preferred adsorption on the limestone could be invoked, resulting in the higher degrees of hydration observed for the composite binder pastes. This issue deserves further investigation and is of clear practical relevance.
These effects appeared to be a reasonable explanation for the decreased performance of SRA treated mortars and concretes tested for mechanical properties (see subchapter 4.4.5).
We recognize, that answering the above question would reveal, whether by wet curing of SRA containing concretes a higher degree of hydration can be achieved and whether this improves the mechanical properties of mortar and concretes.

8.3.3 Properties of pore solution during hydration progress

The analysis of pore solution was mainly executed on extracted cement pore solution. The measurements all were scheduled according the normalized hydration stages defined above. The methodical approaches for measurement of ionic content by ICP-OES and total carbon content (TOC) are given in chapter 6.3.2.5. Note that all samples hydrated under sealed conditions.

8.3.3.1 Admixture content of pore solution

For every admixture compound, the average total carbon content was determined (Tab.A4- 9). Especially the commercial products most probably comprise a mix of ingredients. For that reason, TOC measurements are rather rough estimates. For example, SRA1 comprises three main ingredients of varying molecular weight and their carbon contents are different. In Table 23 a potential range of compositions was calculated using the average carbon load of SRA1 evaluated from TOC measurements of aqueous solutions (measured c_{SRA1}=0.62g_C/g).

Table 23: Possible composition of SRA1 calculated from TOC measurements

mass fraction	ingredient	molar mass	C - fraction
range [-]	[-]	[g/mol]	[-]
0.10 _ 0.15	$C_6 H_{14} O_3$	134	0.54
0.85 _ 0.75	$C_{10} H_{22} O_3$	190	0.63
0.05 _ 0.10	$C_{14} H_{30} O_3$	246	0.68
	avg. C_{SRA1} [g/g]		**0.62**

In the first column of Table 23 the range of compositions for SRA1 is given, which theoretically leads to an average carbon content of c_{SRA1}=0.62g_C/g. However, from this example one can also derive that specific adsorption of the ingredients would mean that an average value for total organic content would lead to incomplete interpretations.

In Table 24, the raw data from TOC measurements on extracted pore solutions are displayed. Additionally, the amount of liquid phase evaluated by TGA for every stage of hydration is given. The column denominated “initial” contains the organic carbon load carried by the mixing water. Note that the

values for pastes containing both SRA and SP-PCE are calculated from the samples containing only one of the admixtures in the appropriate dosage. From Table 24, one can see that the admixtures exhibit different behaviours.

For SRA1 the concentration of organic carbon in pore solution increases from the very beginning up to the 28th day of hydration. For SRA2; 3 and 5 as well for the SP-PCE treated paste the concentration of organic carbon content decreases up to the end of the induction period (T2 in Table 24).

The pastes containing both SRA1 and SP-PCE to comprise only small changes of the organic carbon content up to hydration stage T2.

For whole range of paste samples investigated, it can be stated that from hydration stage T3 on, close to the time of maximum heat flow, all pore solutions comprise an admixture load higher than the initial bulk concentration. This covers different types of SRA, SP-PCE as well as mixtures thereof.

From the second part of Table 24 it can be seen that at stage T2, the amount of liquid phase in the paste is decreased (calculated from thermo-gravimetric analysis). Using data from the upper part of Table 24, the total amount of admixture which is part of the pore solution can be calculated. To determine the amount of admixture that was subjected either to adsorption or formed liquid crystals, the following calculation was performed:

a) The raw data obtained from TOC were transferred into admixture content using its average organic carbon load (Tab.A4- 11).

b) Taking into account that the pore solution is constricted in the course of hydration, the actual water content was obtained from TGA measurements (Tab.A4- 12).

c) Assuming that no admixture is expelled from pore solution the theoretical maximum bulk concentrations of admixtures could be obtained (Tab.A4- 13).

d) For each stage of hydration, the absolute amounts of admixture lost in the course of hydration were then calculated from the actual recovery degree of the admixture (Tab.A4- 14).

Table 24: Total organic content of extracted pore solutions and absolute amount of bulk solution in paste

pastes	hydration stages								
	initial	T1	T2	T3	T4	T5	T6	T7	T8
	carbon content of extracted pore solution [mg/l]								
reference	11	145	156	88	112	81	95	102	233
0.5% SRA1	6809	8168	8052	8615	9731	14560	18780	21480	24420
2.0% SRA1	31190	31360	31730	34010	41900	51370	61420	73660	77900
2.0% SRA2	24350	24030	23200						
2.0% SRA3	28240	21110	22910						
2.0% SRA5	19220	14400	13360						
0.5% SP-PCE	1700	1340	1387	1767	2305	3822	4125	4604	4971
2.0% SP-PCE	7700	6155	5434	7790	10040	12700	16720	19250	19880
2% SRA1 + 0.5% SP	32890*	32970	33620	35620	52610	56090	67920	75800	79030
2% SRA1 + 2% SP	38890*	37830	40250	57900	64520	74960	76860	87450	91800

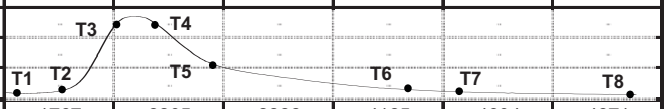

*calculated from CP13.00; CP00.11 & CP00.13

pastes	initial	T1	T2	T3	T4	T5	T6	T7	T8
	absolute amount of liquid phase [g/100g unhydrated cement]								
reference	40	37	36	31	27	20	14	13	9
0.5% SRA1	40	37	36	29	26	18	14	13	9
2.0% SRA1	40	37	36	28	23	18	13	11	9
2.0% SRA2	40	37	36	-	-	-	13	-	9
2.0% SRA3	40	37	36	-	-	-	12	-	8
2.0% SRA5	40	37	36	-	-	-	13	-	7
0.5% SP-PCE	40	37	36	26	22	21	12	10	9
2.0% SP-PCE	40	36	34	23	19	15	12	11	9
2% SRA1 + 0.5% SP	40	36	35	27	18	16	12	11	11
2% SRA1 + 2% SP	40	35	31	20	15	16	13	11	12

The values given in Table 25 are relative losses that refer to the initial bulk concentration of the admixture. They show that admixtures are at least partially depleted from pore solution.

For the superplasticizer used in this study, depletion from bulk solution must be due to adsorption and possibly also intercalation into the first hydration products [245].

Table 25: Loss of admixture in the course of hydration – relative amounts

hydration stage	T1	T2	T3	T4	T5	T6	T7	T8
	relative loss of admixture [wt.-%]							
reference	-	-	-	-	-	-	-	-
0.5% SRA1	5%	8%	21%	21%	16%	19%	15%	33%
2.0% SRA1	8%	9%	23%	22%	28%	35%	33%	45%
2.0% SRA2	9%	14%	-	-	-	-	-	-
2.0% SRA3	31%	27%	-	-	-	-	-	-
2.0% SRA5	29%	36%	-	-	-	-	-	-
0.5% SP-PCE	37%	36%	37%	32%	-	28%	33%	39%
2.0% SP-PCE	20%	32%	34%	31%	29%	25%	22%	33%
2% SRA1 & 0.5% SP-PCE	9%	10%	26%	28%	35%	37%	40%	36%
	37%	36%	37%	32%	-	28%	33%	39%
2% SRA1 & 2% SP-PCE	12%	15%	24%	35%	21%	37%	41%	27%
	20%	32%	34%	31%	29%	25%	22%	33%

For SRA1 the loss only loosely correlates with initial dosage. Pastes containing SRA1 and SRA2 comprise almost similar behaviour up to the end of the induction period (T2). The amount of admixture depleted from solution is significantly lower than for superplasticizer. In contrast, SRA3 and SRA5 comprise depletion from bulk solution at early stages comparable to the SP-PCE modified pastes.

The description given above is restricted to the term depletion of admixture from bulk solution because the methodical approach cannot provide information about whether the admixtures either adsorb, intercalate or assemble into liquid crystals. In what follows, we nevertheless attempt to determine whether the phase transitions of SRA observed in synthetic pore solutions impact consumption here either by the formation of liquid crystals and/or adsorption at the liquid/solid interface.

In Figure 53, the measured bulk concentration of SRA1 was plotted versus its theoretical concentration “without losses”. The data shown come from different hydration stages (initial; T1, …, T8). They suggest that the measured concentration asymptotically approaches a maximum value. This could correspond to the CMC determined in synthetic pore solution as indicated by the solid line.

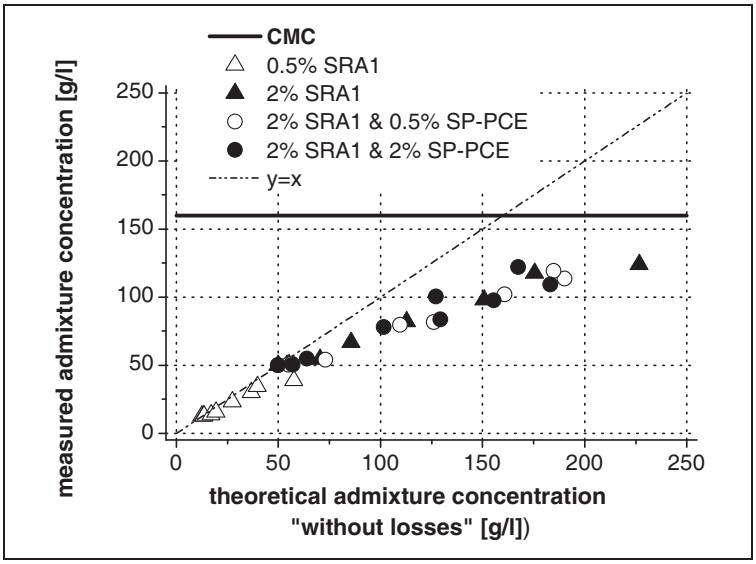

Figure 53: Admixture losses for SRA1 pastes with different dosages, at different hydration stages

* For each series the measured concentration increases with increasing hydration time.

Concerning the findings in subchapter 4.2.5, this behaviour underlies adsorption of SRA1 onto the solid/liquid interface. A critical aggregation concentration (CAC) here could be determined for a bulk concentration of about 50g/l at which the measured curve diverges from the y=x line (dash-dotted). From the theory of non-ionic surfactants, the CAC usually is lower than CMC. Furthermore, it determines the start of adsorption that reaches a plateau when CMC is reached (see 4.2.5).

Moreover, in subchapter 7.3.2.2 a salting out effect that separates liquid crystals from bulk solution was not observed below the CMC. From this, the behaviour shown in Figure 53 can be interpreted as adsorption of SRA1 at the solid/liquid interface. However, the CMC obtained in miscibility tests (subchapter 7.3.2) refers to a synthetic pore solution at stage T2 and therefore may not be representative concerning later stages of hydration. Furthermore, the area of this interface can be expected to exhibit a huge increase in the course of hydration because the solid/liquid interfacial area increases with the amount of hydrates.
From GEMS modeling for the plain paste, the ionic strength of the pore fluid increases over time from about 0.54 mol/kg at the end of the induction period (T2) to about 0.69 mol/kg after 28 days (T8). The question arises about whether this impacts the CMC and causes self aggregation at lower bulk concentrations. This deserves further investigation.

The following conclusion can be drawn from the results obtained:

In contrast to the findings for the adsorption of non-ionic surfactants onto cementitious matter, an adsorption of SRA1 onto the solid interface can be observed for concentration below CMC. As a reminder, Hua et al. 1997 [68] (28d hydrated paste), Zhang et al. 2001 [205] (early age) and Merlin et al. 2005 [206] (synthetic C-S-H) hardly could detect adsorption of non-ionic surfactants onto cement/hydrated cement compounds.
Adsorption of SRA can be assumed to impact hydration kinetics. However, calorimetric measurements show, that this effect is rather small (see 8.3.1). For mixtures of SRA1 and SP-PCE, the losses of SRA1 from the pore solution of hydrated paste were similar to those of the paste with SRA1 only. However, a disproportionally high delay of hydration was observed. From this we conclude that the additional coverage of reactive sites by SRA enhances retardation if SRA and SP-PCE are present.

Concerning the overall SRA distribution in saturated hydrated paste, the question arises about how much admixture is removed from solution before the CMC is reached and whether this solid adsorption competes with self-aggregation of SRA in the pore fluid.

8.3.3.2 Ionic content of cement pore solutions

Another important phenomenon was observed in studies on SRA-phase behaviour. It is that SRA1, 2 and 3 in mixture with synthetic pore solution cause an almost complete depletion of ions from the aqueous electrolyte solutions (appendix, Tab.A4- 15). Except for the sodium content of the superplasticizer used, all other ion species were below detection limit in the starting solution.

In pore solutions extracted from hydrated cement paste, it can be seen that the presence of both SRA and/or SP-PCE mainly changes the relative amounts of calcium, potassium, sulphate and sodium (annex; Fig.A4- 22; Fig.A4- 23; Fig.A4- 24 and Fig.A4- 25).

From TOC measurements it was found that the organic content of pore solution, especially in the later stages of hydration, increases dramatically for the whole range of pastes investigated. To exclude possible dilution effects coming from the organic load of the solutions, the water content of pore solution was back-calculated using the data for total amount of liquid phase and TOC measurements.

In a next step, the measured ion content of pore solutions was related to the actual water content of the pore solutions (Tab.A4- 16 and Tab.A4- 17). The SRA-induced changes in ion content relative to the reference pore solution show that the calcium, potassium and sulphate ion content decreases with increasing dosage of SRA1 (Tab.A4- 18).
In contrast to pastes with SRA1, the addition of superplasticizer (SP-PCE) leads to an increase of cal-

cium and sulphate ions, probably due to the retarded aluminate phase hydration. For a combination of admixtures (SRA1 and SP-PCE), calcium and sulphate ion contents decrease with respect to pastes containing superplasticizer alone.

The liquid phase composition of the reference paste (CP 00.00) can be predicted in good approximation by GEMS as shown in Figure 54. However, this software cannot account for possible impacts and interaction of the organic admixtures used in this study.

In a rather crude approach, the modeling process was done using either the measured amounts of water or an amount based on the efficient w/c ratio that was decreased to account for the related dosage of admixture applied to the referring paste.
In a next step HBr, supposed to be inert regarding the ongoing cement hydrations, was added into the modeling process to occupy the space elsewise occupied by admixture.
However, none of these approaches to use the GEM-solver lead to the observed decrease of the ion species mentioned above. The adjustments of efficient w/c within the modeling process always lead to a further increase of the alkali ion content as well as to a related depression of calcium ions.

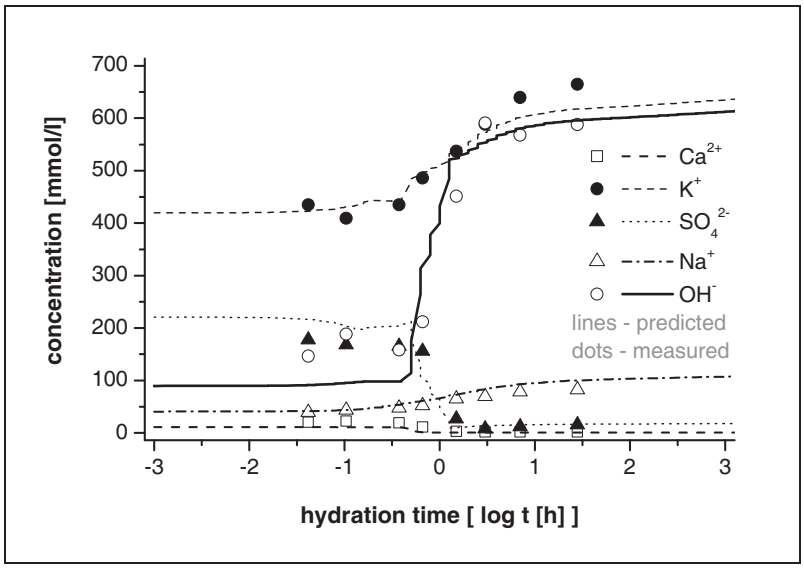

Figure 54: Ionic content of pore solution – measurements and prediction by GEMS

From the measurements performed, it can be stated that SRA1 causes a significant decrease of calcium, sulphate and potassium ions, independent of the presence of the superplasticizer used. Regarding the maximum dosage (2%), one can account for an overall reduction of the ionic content of about 10-20% at early hydration stages. At later stages, calcium ions are depleted by about 30% for SRA1 alone and 50% to 20% in the presence of additional superplasticizer.

For SRA2 one observes a similar behaviour but the impact is not as high. SRA3 only slightly influences the ionic composition of pore solution.

As a reminder, for aqueous electrolyte solutions of SRA1 and 2, significant amounts of syngenite precipitated. SRA3 showed precipitation also, but to significantly lower extent (7.3.2.2).

The question arises if the precipitation of syngenite, composed of calcium, potassium and sulphate, occurred in these pastes. Unfortunately neither by XRD nor thermo-gravimetric analysis syngenite was detected, which is consistent with the detection limits of these instruments. Fortunately even minor amounts of syngenite are known to be detectable by environmental scanning electron microscopy [47, 222] and this is exploited in the next section.

8.3.3.3 Salting out of organic and inorganic compounds

Environmental scanning electron microscopy (ESEM-wet mode) was applied to determine whether minor phases, related to salting out and inorganic precipitations, can be detected directly in pastes. The methodical approach for sample preparation and observation is given in chapter 6.3.3.2.

In Figure 55 a) the microstructure of the reference cement paste without admixture after 1 hour of hydration is displayed. The micrograph shows that the surfaces are covered with compact ettringite crystals. The few larger, plate-like crystals are supposed to be syngenite, predicted by GEMS to form in minor amounts up to the depletion of gypsum.

According to Roessler 2006 the detection limit for XRD is supposed to be about 2wt.-% of the bulk. The GEMS process modeling predicts a maximum content of syngenite right before gypsum depletion of about 0.25% which is well below this limit.

In Figure 55 b), c) and d) the micrographs of pastes containing respectively SRA1; SRA2; SRA3, at a 2%-dosage are displayed. An enhanced amount of lager crystals is apparently observable.
Especially for SRA1 and SRA3, the habitus of these crystals indicates syngenite as the most probable precipitate. For SRA2, the appearance of the microstructure is a little bit different. Compared to Figures a), c) and d), the edges of the crystals apparently are not that sharp. Additionally, the morphology appears to be a little bit more compact.

Figure 55: Enhanced precipitation of syngenite in presence of SRA

a) reference cement paste; 1 h of hydration

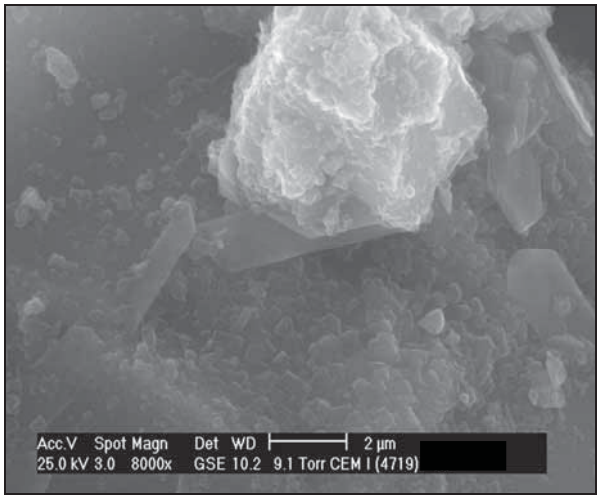

b) paste containing 2wt.-% SRA1; 1 h of hydration

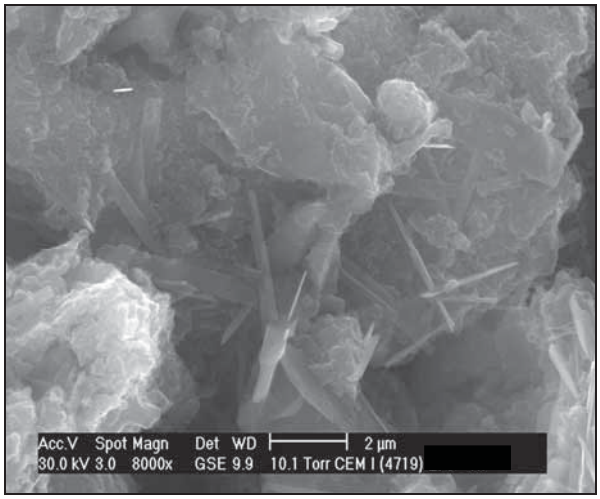

c) paste containing 2wt.-% SRA2; 10min of hydration

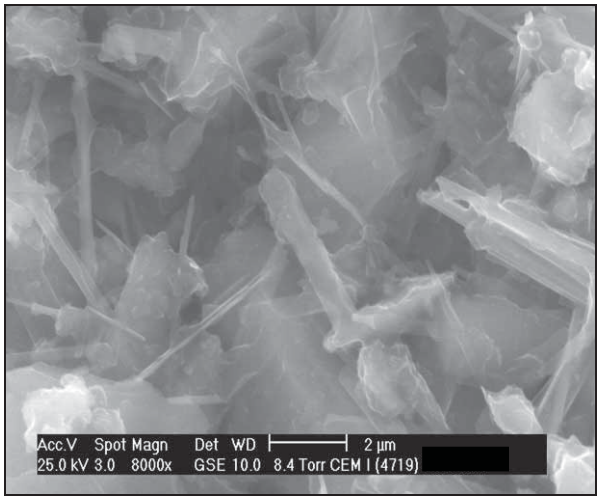

d) paste containing 2wt.-% SRA3; 10min of hydration

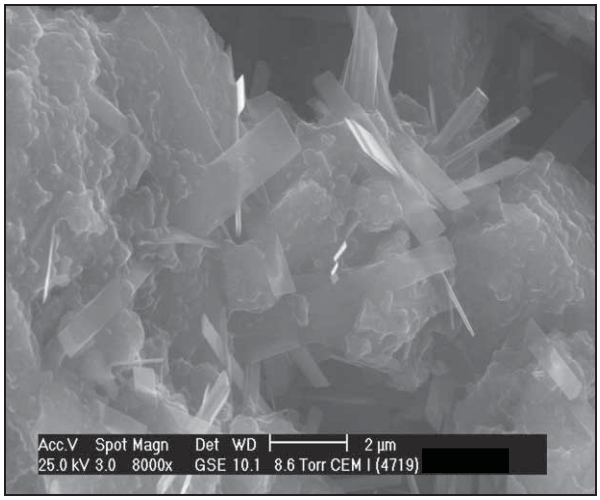

The enhanced formation of syngenite observed in pastes containing SRA is consistent with the ICP-OES results which revealed that the syngenite forming ions are significantly depleted from pore solution.

In addition, XRD analysis revealed that gypsum is depleted between the end of the induction period (T2) and well before the maximum heat release (T3). Syngenite is therefore expected to be observed up to T2 as is the case for Figure 55. Moreover, it ought to have converted after the maximum heat release (T3; T4).

To examine this, we now consider Figure 56 where micrographs of SRA modified pastes were collected after 12 hours of hydration. In comparison with Figure 55, the surfaces of clinker particles are now covered with C-S-H precipitates (needle like phases). For the pastes carrying SRA2, the large plate like crystal is assumed to be Portlandite, the second hydration product of the silicate clinker phase. For all the pictures shown in Figure 56, it can be stated that, syngenite has indeed totally disappeared.

Figure 56: Micrographs at hydration stage T3 (12 hours of hydration)

a) reference paste after 12 hours of hydration

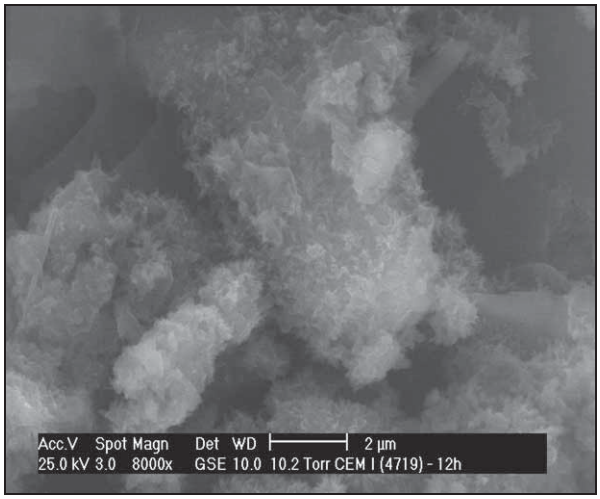

b) paste containing 2wt.-% SRA1 after 12 hours of hydration

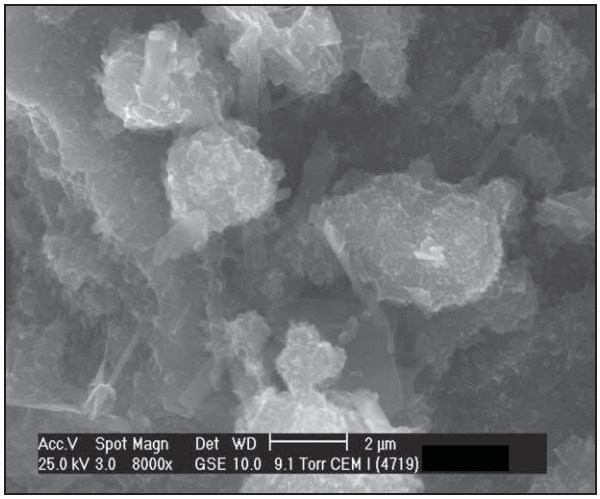

c) paste containing 2wt.-% SRA2 after 12 hours of hydration

d) paste containing 2wt.-% SRA3 after 12 hours of hydration

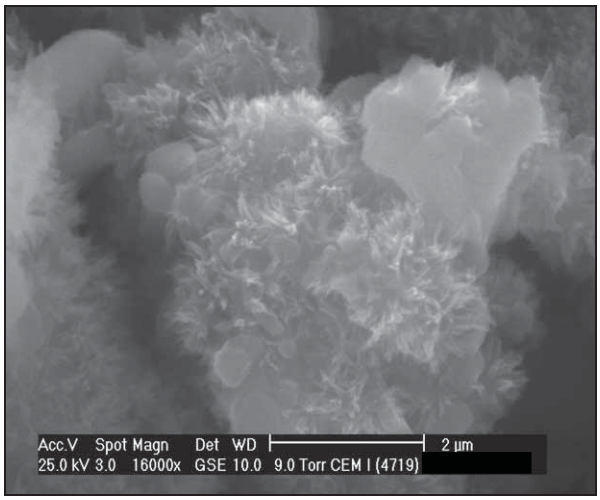

Regarding the salting-out phenomenon, the cement paste containing 2wt.-% SRA2 showed a significant result. An additional organic phase was observed after 1 hour of hydration. Figure 57a) gives an

overview on the microstructure. It shows large crystals that are not homogenously distributed and that show unusual features. In the centre of Figure 57b), one of these large crystals was focused for EDX-measurement. Figure 57c) contains the EDX spectrum taken and Figure 57d) shows the EDX target that melted in the course of measurement.

From the EDX spectrum it can be concluded that these precipitates are mainly composed of carbon and oxygen, indicating organic matter. Referring to the results of XRD on salted out residuals of SRA2 in phase behaviour studies (7.3.2.3), the compound most likely can be assumed to be Neopentylglycol. Also, TOC measurements revealed a depletion of this admixture from pore solution of about 9% at the corresponding hydration stage.

Figure 57: Organic salt-outs precipitating from bulk solution of CP23.00

a) paste containing 2wt.-% SRA2 hydrated for 1h

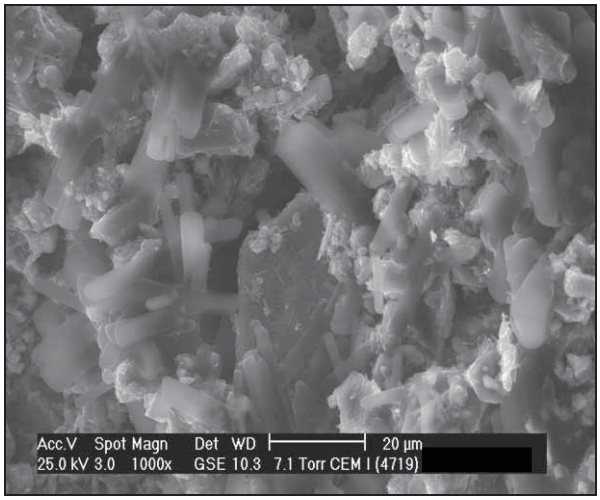

b) target before EDX-measurement

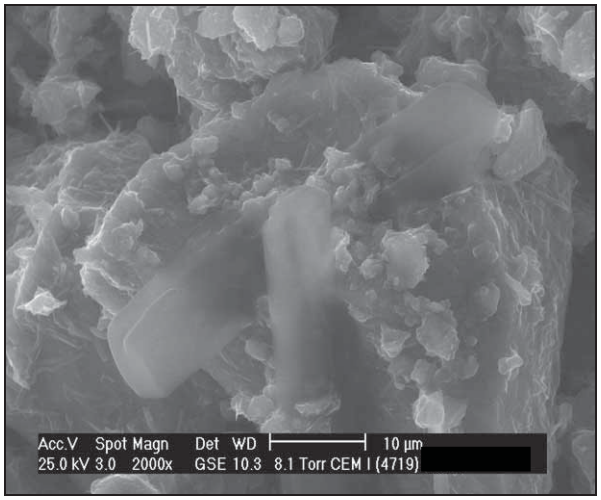

c) appropriate EDX-spectrum

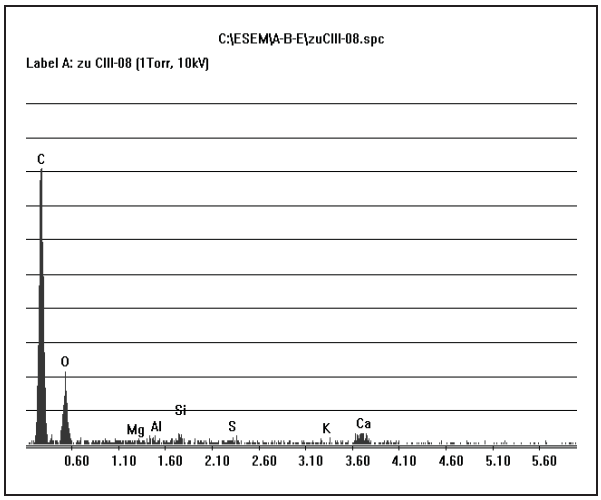

c) target after EDX-measurement

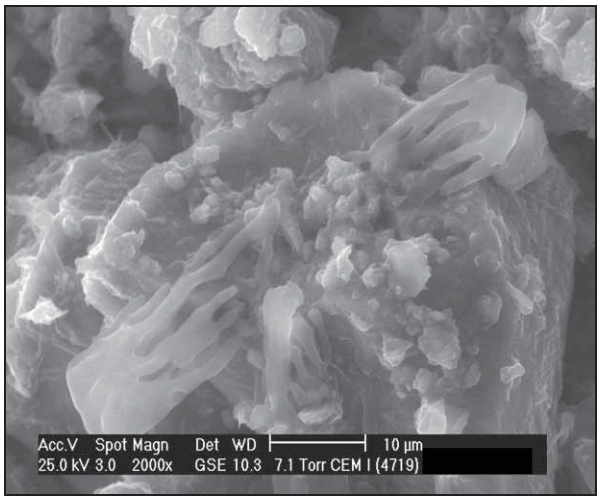

According to this, and at least for SRA2, self assembly into crystal or liquid crystal does take place. However, this can be a specific property due to the composition of SRA2. Concerning the findings in chapter 7.3.2.2, the amount of liquid crystal forming from SRA2 was independent from the bulk concentration.

In contrast, for SRA1 it was strictly related to bulk concentration and started above the CMC. Furthermore the measured concentration of SRA1 in extracted cement pore solution up to hydration stage T8 was found to be below CMC and the depletion from pore solution due to adsorption.

If the admixture depletion from pore solution at hydration stage T2 is considered, SRA2 shows a significantly higher loss than SRA1 (compare to Table 25). However, according to Table 15 retardation was found to be slightly lower for paste with SRA2 (dt_{T2_SRA2}=0.5 h; dt_{T2_SRA1}=0.75 h).
The question arises about whether the self-assembly of SRA2 reduces the adsorption and if hydration kinetics are then less impacted.

Still the question remains open about why the hydration retarding effect of SRA is lower than for SP_PCE. The retardation of SP-PCE is often explained by invoking specific adsorption either onto hydrates (blocking growth) or onto anhydrous phase (hindering dissolution). This would suggest that the comparably low retarding effect of SRA means that their depletion from solution comes rather from self-assembly than from adsorption onto solid interfaces.

Vice versa, the adsorption of SRA, calculated from admixture depletion, might not be representative for the problem at stake. Assuming that liquid crystals separate in the vicinity of solid matter, the macroscopic outcome might be similar to adsorption. Furthermore the extraction of pore solutions might cause such liquid crystals to be squeezed out.

To put the microscopy results in the right context, the absence of organic precipitates, as observed for SRA2 paste, does not ensure that other types of self-assemblage are not present, but just, that they are not detected with this method.

In this study only one firm evidence supporting the adsorption theory can be found. It is, that the hydration kinetics of SRA2 pastes are less affected and that salting-out effects could be identified.

Still an answer on the different impacts of SP-PCE and SRA on retardation is lacking, in particular whether the type of adsorption is responsible for this. From theory of SP-PCE we can state that adsorption is electrostatically driven. In contrast, from theory on non-ionic surfactants, we can gather that adsorption force is weak and preferably works through hydrogen bonding, entropic effects or the more or less the dipole character of ether bonds. This different type of interaction with the surface could also explain the different impact on hydration kinetics.
In section 8.3.4 the adsorption characteristics are studied further in detail. There, we examine whether SRAs show selective adsorption onto solid phases. Moreover, it is examined whether a proper discrimination between self-assembly and solid adsorption can be obtained.

8.3.3.4 Surface tension of extracted pore solution

In the literature on shrinkage reducing admixtures, authors proved that autogenous shrinkage significantly decreases in presence of SRAs. Lura 2003 [31] exclusively refers to the capillary force model and modelled autogenous shrinkage in presence of SRA. This states that the surface tension of the pore fluid determines the magnitude of capillary forces acting on the pore walls. In this regard, it is of interest to know how the surface tension of the pore solution evolves in the course of hydration, particularly since we found that the amount of admixture depleted from pore solution was significant. For example for SRA1 probably 45% of the initial amount of admixture is “lost”.
In Figure 58, results of surface tension measurements (pendant drop method) are displayed for samples hydrated under sealed conditions. For the whole range of samples, the surface tension of the extracted pore solution decreases slightly throughout the hydration process. This is probably the result of a balancing effect. On the one hand the amount of pore water decreases due to hydration and causes an increase of admixture concentration. On the other hand admixture is lost due to adsorption or self assembly. The decrease in surface tension means that the first factor dominates, which is in good agreement with the increase of admixture bulk concentration in the extracted pore solutions.

The hydrated samples comprise a high liquid saturation. Therefore, in regard to the findings in subchapter 7.3.3 the interfacial area exposed to the liquid/vapour interface is low and pendant drop method returns reasonable results with respect to the conditions of the pastes pore system. From the samples containing high dosages (2%) of SRA1, SRA3 and SRA5 it can be seen that the minimum surface tension, which is about 0.03N/m for hydrocarbon non-ionic surfactants (chapter 4.2), can be

reached also for the real cement pore solution. From the samples containing a mixture of SRA1 and SP-PCE it furthermore can be seen that the SRA determines the surface tension of the pore solution. Thereof, we conclude that SP-PCE does not contribute to the evolution of surface tension in cement paste. This must come from the depletion of SP-PCE from pore solution due to adsorption onto solid phases.

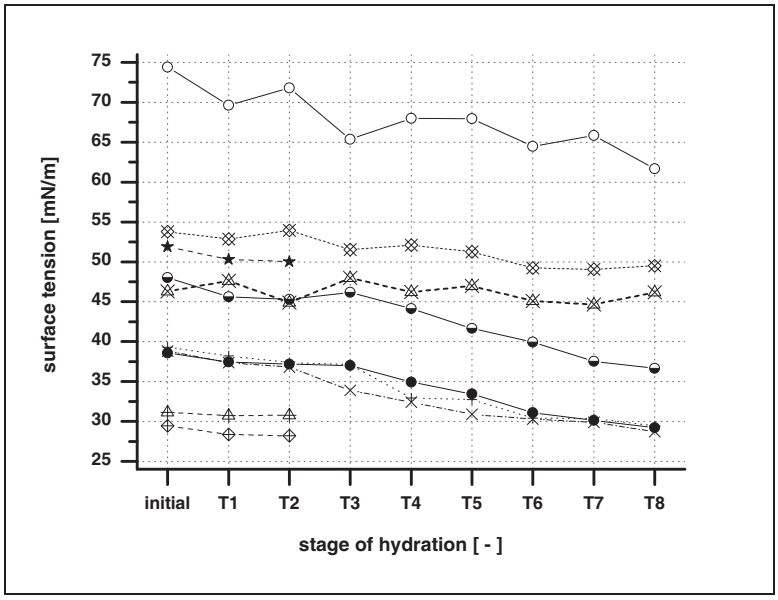

Figure 58: Surface tension of extracted cement pore solution from pastes with and without SRAs at different stages of hydration

Legend:

- plain paste
- 0.5 wt.-% SRA1
- 2.0 wt.-% SRA1
- 2.0 wt.-% SRA2
- 2.0 wt.-% SRA3
- 2.0 wt.-% SRA5
- 0.5 wt.-% SP-PCE
- 2.0 wt.-% SP-PCE
- 2.0 wt.-% SRA2 + 0.5 wt.-% SP-PCE
- 2.0 wt.-% SRA2 + 2.0 wt.-% SP-PCE

Surprisingly the surface tension of the plain paste also decreases with hydration progress. One could argue that this could be due to the presence of grinding aids in the unhydrated cement. According to [246] glycols and triethanolamine are possible compounds for grinding aids used at dosages lower then 0.1wt.-% of cement. Referring to the results from patent search polyhydric compounds are also efficient in the reduction of surface tension [198]. Glycols explicitly are recommended as co-surfactants for SRA [79-83]. The above mentioned grinding aids are supposed to be bound onto the clinker material by chemisorptions but are probably released upon contact with water. According to Duez 2006 [247] the group of grinding aids consisting of ethanolamine, triethanolamine, glycerine (or glycerol), sorbitol, and glycols comprises a surface tension of greater than 40mN/m. Taking into account that the initial dosage of grinding aid is about 0.1wt.-% of the cement and therefore quite low, it is quite questionable that the amount of this admixture is sufficiently high to cover the surface of the liquid/vapour interface and thus reduce surface tension.

As a reminder, the findings of chapter 7.3.3 show that the surface activity of the surfactant is determined by bulk concentration and interfacial area. As could be shown for high dosages of SRA, magnitudes higher than the amount of grinding aid, the increase of interfacial area most probably depletes the grinding aid in this interfacial area. This may not be the case for well saturated cement systems. However, at least for the drying induced increase of the liquid/vapour interface, the grinding aid concentration is too low to impact surface tension significantly.

8.3.4 Influence of SRA on the hydration of C_3S and adsorption measurements on pure hydrates

In this section we examine whether one can distinguish between SRA adsorption onto the solid/liquid interface and self-assemblies like liquid crystal structures. Furthermore it is investigated if SRA exhibits its preferred adsorption onto hydrates.

8.3.4.1 Adsorption onto the solid/liquid interface and self-assembly

Concerning the differentiation between adsorption of SRA onto the solid/liquid interface and self-assembly, the measurements were performed as follows: From the studies of phase behaviour of SRA in synthetic pore solution it was established that with increasing bulk concentration of the organic admixture the amount of organic salt outs and mineral precipitates increases. The phenomenon is more pronounced when the critical micellation concentration (CMC) is exceeded. To avoid liquid/liquid phase separation the measurements were all conducted well below CMC, i.e. below 160g/l for SRA1.

To distinguish between self-assembly into liquid crystals and adsorption onto solids the measurements were splitt into two parts.

1. First, the depletion of admixture due to self-assembly was measured on electrolyte solutions of SRA1 (synthetic cement pore solution with SRA1). The depletion dependence on bulk concentration was obtained from TOC measurements.
2. Then, in a second step, a defined amount of solids was introduced into the same solutions as described above. The excess depletion of admixture now indicates which fraction adsorbed onto the solid interface. Thereof, one can discriminate between adsorption and self-assembly.

For the above measurements, synthetic pore solution according to subchapter 7.2, Table 5 was prepared. All experiments were executed at 20°C, materials comprised ambient temperature and heat of hydration of SRA was not taken into account because of the rather low dosages applied. The concentration series were conducted by stepwise titration of admixture to the synthetic cement pore solution. After each titration step, the Erlenmeyer flask was closed and the solution was homogenized for about 2 minutes using a magnetic stirrer. After 15 minutes, a sample of the solution was taken for TOC measurement. Note that titration and sampling were executed in volume-equivalents.

For the adsorption measurements, synthetic ettringite and C-S-H phases with known N_2-BET surfaces were used as sorbents (a_{ETT}~9m^2/g and $a_{C\text{-}S\text{-}H}$~19m^2/g; material provided by Zingg [221]). A defined amount of solid was introduced to the synthetic cement pore solution and the titration regime was started as follows: For the measurement of a first reference point, the dilute suspension was homogenized for about 1 hour in a closed Erlenmeyer flask and then kept at rest. After about one minute without motion, the solids settled to the bottom of the flask and a clear solution appeared. The equilibration time was kept at 15 minutes. Sampling for TOC measurement was executed using a pipette and a 0.4µm syringe filter.

In Figure 59 it can be seen that SRA1 exhibits phase separation in the synthetic cement pore solution, which is consistent with the miscibility tests. In fact, the amount of SRA lost is proportional to the amount dosed and of about 24%.

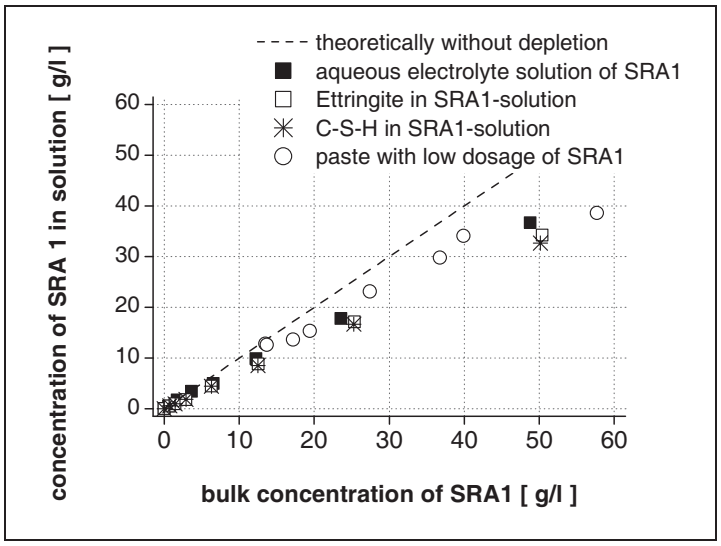

Figure 59: Depletion of admixtures in synthetic pore solution with and without synthetic hydrate phases

Amount of sorbents:

SRA1-solution:
- Ettringite: 25g/l => 225m^2/l
- C-S-H: 20g/l => 380m^2/l

SRA1- extracted pore solution:
- paste with C_{SRA1} = 0.5wt.-% o.c.
- hydration stages T1, …, T8

Figure 59 shows that with respect to the plain electrolyte, the introduction of both sorbents (ettringite and C-S-H) only slightly impacts the SRA concentration in solution. The differences of SRA loss with respect to the solution without sorbents were determined and the adsorption onto ettringite and C-S-H was calculated. The admixture loss due to adsorption onto ettringite is ~8% and the loss onto C-S-H ~10%.

Additionally in Figure 59, the results for the SRA content in extracted pore solution of hydrated paste are shown (hollow circles in Figure 59). For cement paste with a SRA1 dosage of 0.5wt.-% of cement, the amount of admixture depleted from cement pore solution during hydration is approximately similar to what is found for the synthetic sorbents in synthetic pore solution. This is somewhat surprising because despite similar bulk concentrations of SRA1 the amount of solution and the solid surface available for adsorption in cement paste are quite different. Accounting for the N_2-BET surface areas used in subchapter 8.3.3, the ratio of solid surface provided per litre of pore solution in hydrated paste is significantly higher (for about 30 times for early hydration up to 1000 times at 28 days). This is implying that it is the constitution of the liquid phase that mainly determines how much SRA remains in solution. The amount of solid surface available therefore can be assumed to have only a low impact on the solid adsorption isotherm. This is examined in the following.

In Figure 60, the self assembly of SRA in synthetic pore solution is shown. With increasing bulk concentration of SRA1 self-assembly increases, which is in line with the findings in subchapter 7.3.2.2. However, the term self-assembly has to be reconsidered: From theory of non-ionic surfactants, micelles are supposed to form above the CMC. The dosages applied for these tests are much lower than this but a loss of admixture can be detected. Moreover, even if micelles are formed, the measurement of an admixture loss then requires a sufficient phase separation so that the separated phase is excluded from sampling. For this measuring approach, such phases would have to separate due to enhanced density, i.e. settled down to the very bottom of the flask.

The question arises on whether the SRA loss comes along with the precipitation of minerals that are separated from solution below the CMC (compare to 7.3.2.2). Such minerals can be thought to provide solid surface for SRA adsorption. On the other hand, SRA could be thought to act as a nucleation agent for these minerals. In this context, the term self-assembly might not be suitable and the admixture loss rather has to be referred to “solid adsorption”. Anyway, the increase in admixture loss can most probably be related to the increasing solid interface provided by the increasing amount of minerals precipitated.

Figure 60: Self-assembly of SRA1 in synthetic pore solution

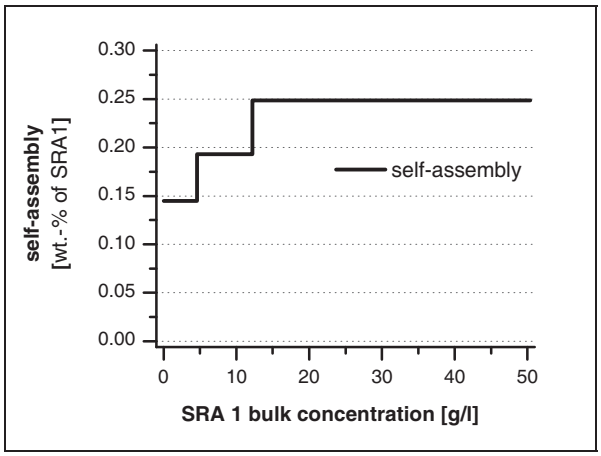

Figure 61: SRA1 adsorption onto synthetic hydrates

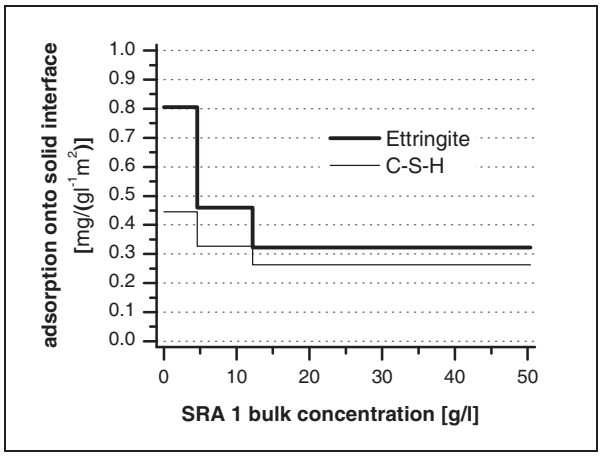

In Figure 61, the adsorption degrees of SRA1 onto ettringite and C-S-H are given. It can be seen that for both sorbents, the adsorption is significantly higher for low bulk concentrations. With increasing

dosage of SRA1 this decreases and remains constant above C_{SRA}~15g/l. This behaviour is somewhat surprising, but we note that it could be due to a resolution issue. The absolute difference of the TOC values obtained for the plain synthetic pore solution and the dilute suspension were rather small for low SRA bulk concentrations and errors therefore have high impact. Moreover, these results are directly influenced by the results of admixture loss for the solution without solids (see Figure 60). For that matter just the results for higher bulk concentrations can be discussed. According to this, adsorption of SRA1 onto the solid/liquid interface are about 0.26mg $m^{-2}/(g_{SRA1}l^{-1})$ for C-S-H and 0.34mg $m^{-2}/(g_{SRA1}l^{-1})$ for ettringite.

The issue to clarify is whether this result is either due to the difference of interfacial area available for adsorption or it depends on the nature of the sorbent used. Indeed, for these tests the degree of admixture loss was different for the sorbents used (99mg/$(g_{SRA1}l^{-1}$ for C-S-H and 77mg/$(g_{SRA1}l^{-1}$ for ettringite). However, the interfacial area referred to was obtained from nitrogen adsorption measurements on dry powder. In aqueous suspension this interface may be different so that these adsorption differences are probably not significant.

Again, the constitution of the electrolyte solution seems to determine how much SRA is expelled from solution. For the synthetic hydrates used, it is not known whether the solids themselves impact the electrolyte concentration of the suspension through dissolution or by physically binding of water.

Based on the results of this chapter it is not clear whether SRA1 shows preferred adsorption onto hydrates. Moreover, the term self-assembly now has to be reconsidered because the admixture loss in electrolyte solution started far below the CMC. Additionally, a liquid/liquid phase separation and liquid crystals were not observed below CMC (compare to 7.3.2.2). Because of this, the admixture loss seems to be directly related to the precipitation of mineral phases, which was observed to start even at low SRA dosages (7.3.2.2), i.e. below CMC. This may come from an enhance nucleation for these minerals in vicinity of SRA molecules or from adsorption onto the additional interfacial area provided by the precipitates. In any case, the term self-assembly then does not fit. However, the phenomenon can macroscopically be described using the term adsorption.

From theory on adsorption of non-ionic surfactants [86, 87, 106-118] described in subchapter 4.2.5, it can be stated that these surfactants are adsorbed through dispersion forces and not through electrostatic ones or chemical bonds. It was also pointed out that, due to their amphiphilic nature, they can adsorb onto hydrophilic and hydrophobic surfaces. With respect to the elevated pHs of cementitious materials, adsorption through hydrogen bonding of the hydrophilic heads with the silanol groups and/or aluminol groups is unlikely because these then are deprotonated.

The concentration at which surfactant adsorption onto the solid surface starts is defined as “the critical aggregation concentration (CAC)” and can be found well below CMC [86, 87, 106-118]. Therefore, the admixture loss below the CMC, for both synthetic hydrates and hydrated paste, is in line with the theory on non-ionic surfactants.

As a reminder, the SRA concentrations used for the adsorption measurements were rather low with respect to what was found in hydrated pastes in the course of hydration. Using the findings of the both experimental sets (sections 8.3.3 & 8.3.4) the following can be stated:

For cementitious environments, SRA is separated from solution. For SRA bulk concentrations below CMC, the admixture loss comes along with the precipitation of mineral phases. In presence of solid interfaces a slightly enhanced removal of SRA1 is detectable for bulk concentrations below 50g/l but a critical aggregation concentration (CAC) could not be determined for this range.
However, for hydrated cement paste samples, the measurements on pore solution in section 8.3.3 clearly show a steep increase in admixture loss above bulk concentrations of 50g/l (compare to Figure 53). Accounting for those significant losses of SRA1 the CAC might be defined for this specific concentration.

8.3.4.2 Influence of SRA1 on the hydration of C_3S

In this section we examine the impact of SRA1 on the silicate phase hydration in further detail. This seems especially important since the hydration kinetics of these phases were found to be impacted by SRA (sub-sections 8.3.1 & 8.3.2).

For the tests, synthetic C_3S was hydrated in synthetic pore solution containing different dosages of SRA1. The dilute suspensions were mixed by hand. The samples were sealed and kept at 20°C on a shaker. Except for the sample without SRA this procedure ensured that the suspensions did not segregate before setting. Unfortunately the reference pastes without SRA segregated and excess water was separated from the solid body. Therefore, this sample most probably suffered from self desiccation and could not achieve a high degree of hydration.

After 14 days, the C_3S-hydration was stopped. Sampling for TOC measurement was conducted using a filter syringe. Thermo-gravimetric analysis was carried out according subchapter 6.3 and the results can be found in Fig.A4- 26. The amounts of portlandite precipitated in the course of C_3S-hydration were evaluated from the characteristic mass loss (TGA). The degree of C_3S hydration was calculated from equation (69), where C_3S was assumed to hydrate into C-S-H with a composition already used for GEMS-process modeling, i.e. $C_{1.67}SH_{2.1}$

$$C_3S + 3.43H \rightarrow C_{1.67}SH_{2.1} + 1.33CH \tag{88}$$

where the mass ratios of product/educt are

$$CH / C_3S = 0.43 \tag{89}$$

and

$$C-S-H / C_3S = 0.803 \tag{90}$$

respectively.

The above water content of C-S-H was chosen because samples for TGA measurement were dried in an oven at 37°C on a metal plate for about 10 minutes. This temperature causes a drop of humidity inside the drying oven from 20°C/~50%RH (room) down towards 37°C/ ~15%RH. Based on this, it was decided to account for 2.1mole instead of 4 moles of chemically bound water in C-S-H [66].
The results of calculations for the degree of C_3S hydration after 14 days are displayed in Table 26 and details are to be found in Tab.A4- 19.

Table 26: Degree of C_3S-hydration and specific surface

C_{SRA}		degree of hydration	specific surface
* [g/l]	** [mg/g C_3S]	[-]	[m²/g]
0	0	54%	7,8
3,2	10	71%	14,0
6,4	19	67%	13,6
16	48	48%	9,9
32	96	48%	16,7
64	192	38%	14,0
128	384	24%	10,7

* C_{SRA} ref. to liquid phase
** C_{SRA} ref. to solid phase

The data show a decreasing degree of hydration as the dosage of SRA1 increases. However, the reference paste is an outlier to this trend. As mentioned before, the reference sample segregated despite continuous shaking. This might have caused densification and insufficient supply of water for proper hydration.

From the TG analysis, the amount of fixed water is known and the actual amount of “free” water can be calculated by difference with the initial amount. This is then used to obtain depletion of admixture

from bulk solution (Fig.A4- 27). Within the range of admixture added, a linear regression reveals that about 20% of the admixture is depleted from bulk solution. Assuming a bilinear progress of admixture depletion as indicated in Figure 62, the CAC can be found at SRA bulk concentration of about 50g/l.

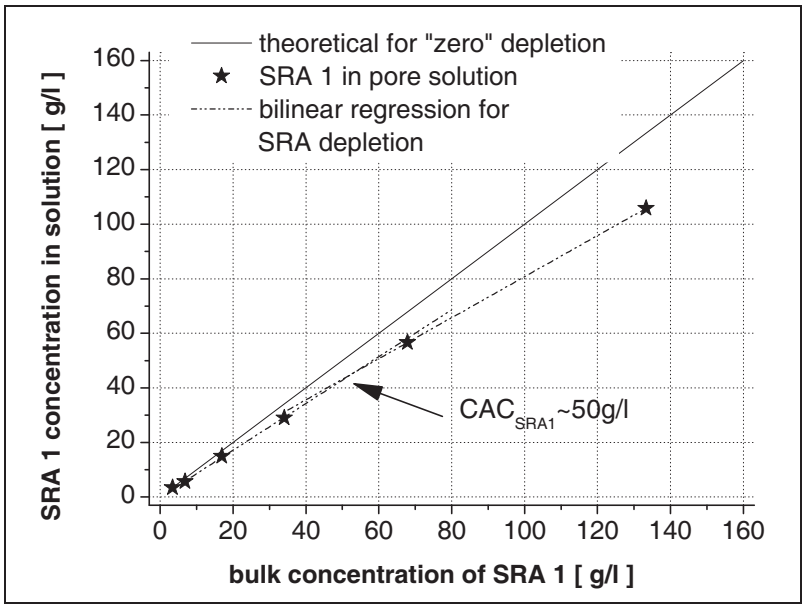

Figure 62: Depletion of SRA1 from pore solution of hydrating C_3S

From Figure 62 it can be deduced that the SRA depletion found in these tests is less than observed for hydrating Portland cement but this however can be due to differences in the solid content or the effective electrolyte concentration of the suspension. However, accounting for a more or less bilinear progress for the SRA depletion, the results obtained are in line with what was found for hydrating paste (Figure 53).

8.3.4.3 Influence of SRA1 on the specific surface area

The paste samples obtained after 14 days of hydration were dried at 35°C and N_2-adsorption was measured. In Table 26 the specific surface areas of dried paste samples are displayed along with the calculated degree of hydration. This is shown also in Figure 63.

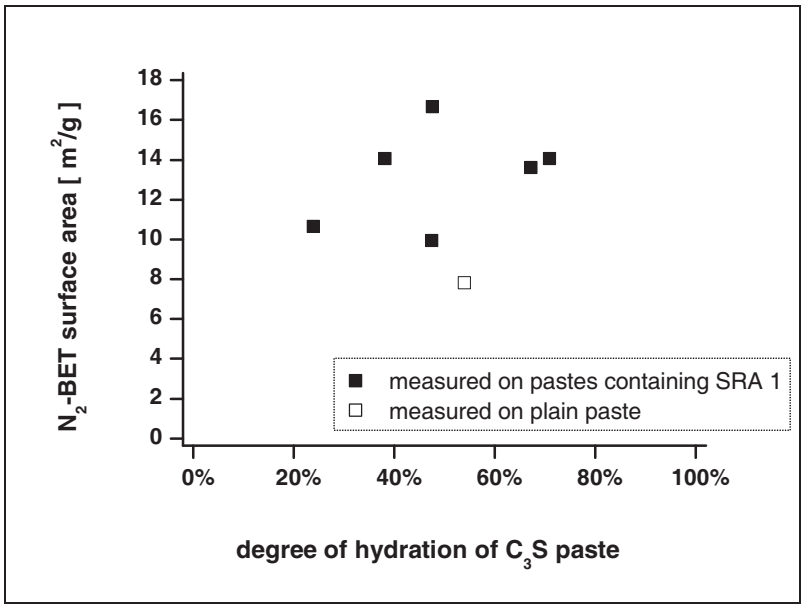

Figure 63: Surface area of hydrated C_3S-pastes

Results show that samples with SRA1 all have a higher specific surface than the plain paste independent on the degree of hydration (Figure 63). Moreover, SRA1 samples show little increase in specific surface with degree of hydration. This suggests an effect on the hydrate growth morphology.

8.3.4.4 Influence of SRA1 on hydrate morphology

Environmental scanning electron microscopy was used to investigate fractured surfaces of wet samples. Sample preparation and measuring conditions are given in subchapter 6.3.3.2. Selected images are displayed in Figure 64 (a - d). They show that the reference paste comprises portlandite with a rather compact habit. The thickness of the hexagonal plate shown in Figure 64 a) is about 10µm whereas the thin portlandite plates in subfigure Figure 64 b) comprise a thickness below 1µm (upper right). Other thinner and foil like crystals can be seen in the lower left of the same figure.

Figure 64: Microstructure of portlandite in plain paste (C0) compared to paste containing a high dosage of SRA1 (C6 = 384mg/g C_3S)

a) plain paste C0: compact portlandite crystal

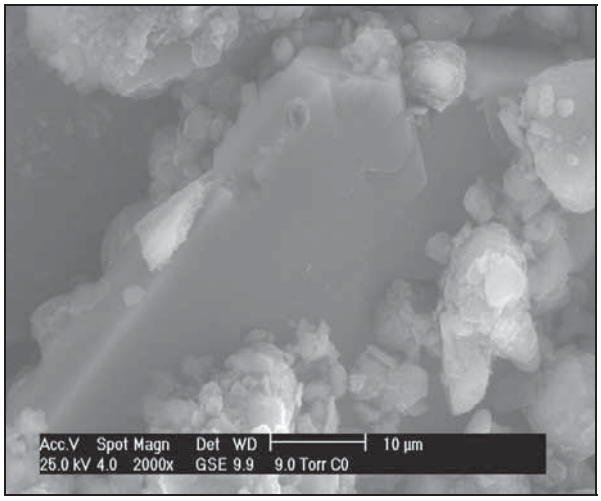

b) paste C6: rather plate/foil like portlandite

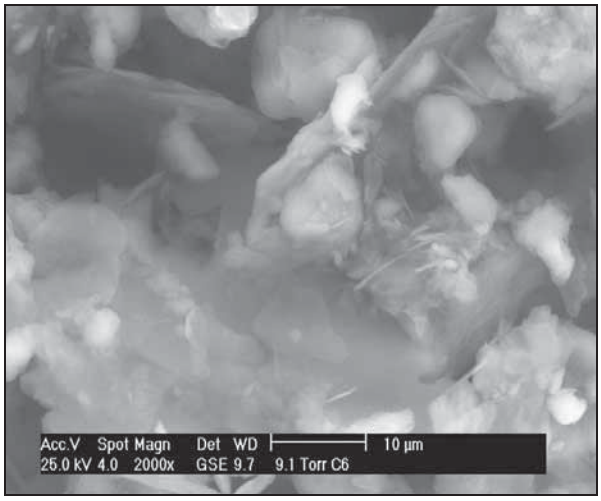

c) plain paste C0: compact portlandite crystal

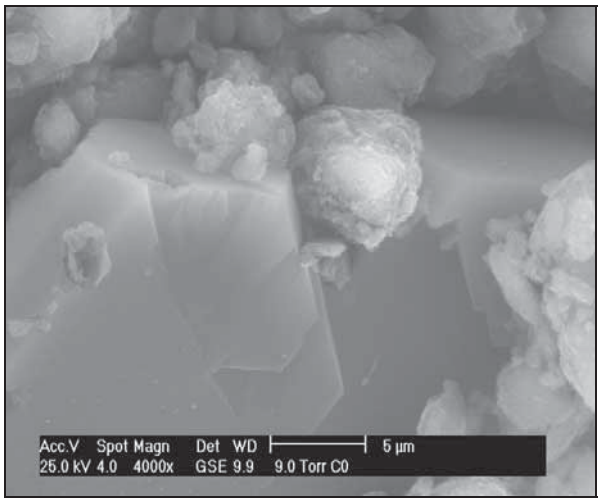

d) paste C6: layered portlandite crystals

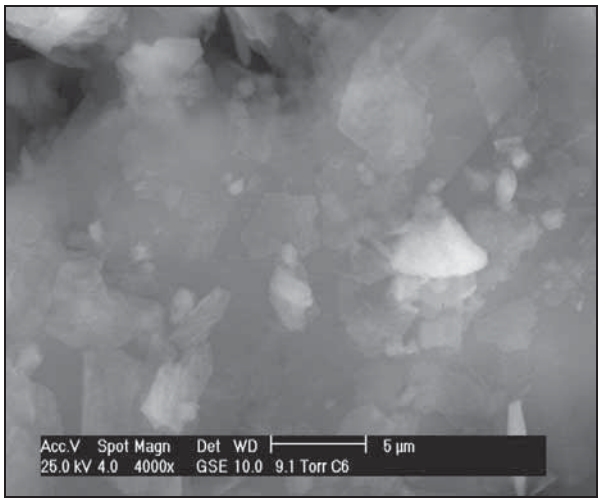

A comparison of the microstructure at higher magnification (Figure 64 c) and d)) also indicates that portlandite seems to be significantly layered in presence of SRA1. Although appearing only very dimly, the hexagonal habit of the foils indicative of portlandite can nevertheless be identified as for example in the upper right and centre of frame d).

Figure 65: C-S-H phases in plain paste (C0) compared to paste containing a high dosage of SRA1 (C6 = 384mg/g C_3S)

a) plain paste C0: C-S-H covering surfaces

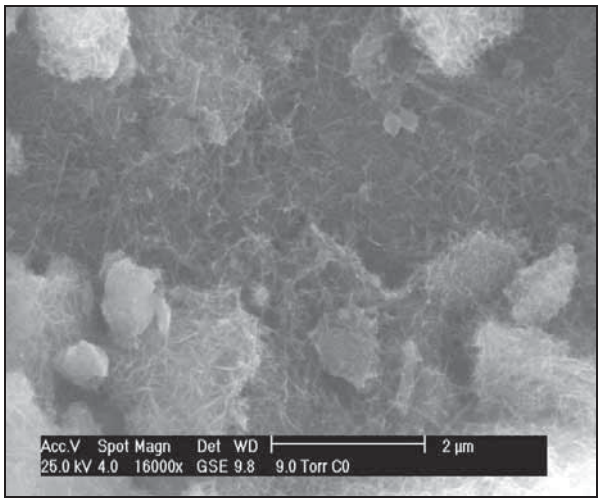

b) paste C6: layered structures, portlandite surrounded by C-S-H phases

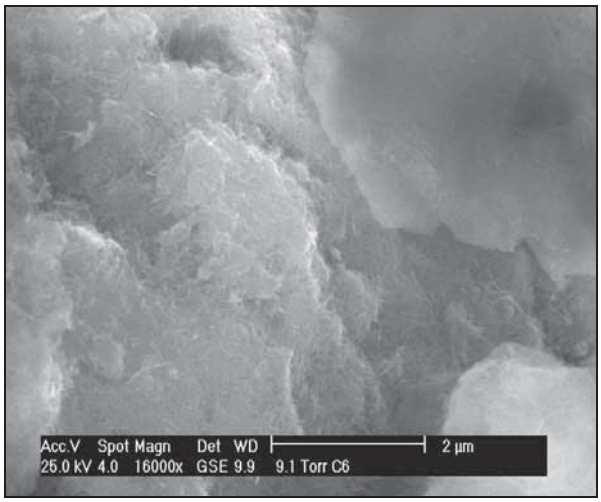

c) plain paste C0: C-S-H phases covering surfaces

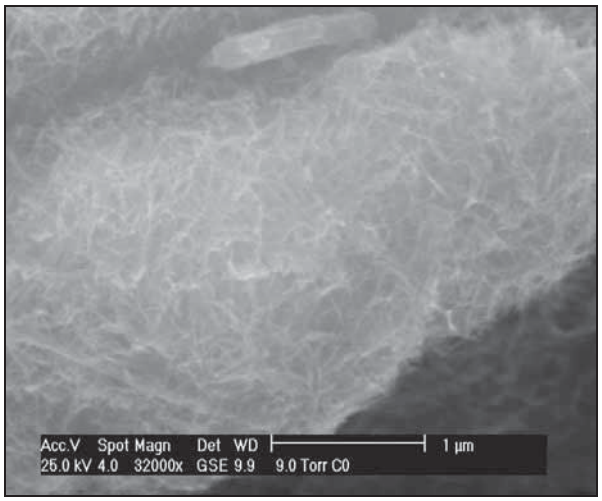

d) paste C6: zoom of subfigure f); C-S-H in-between layers of Portlandite

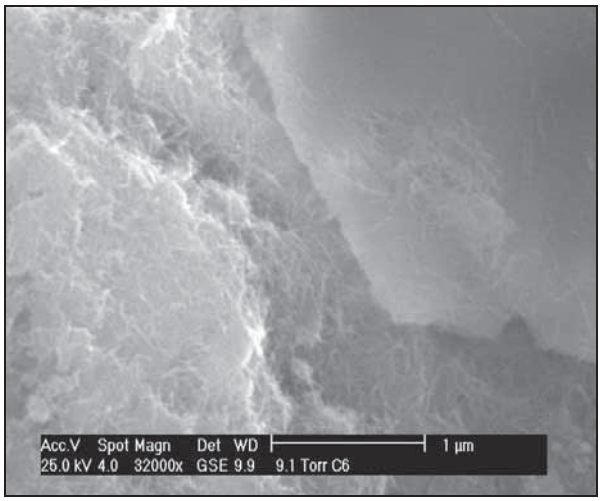

The images for Figure 65 were chosen to support the findings by showing that SRA1 most probably leads to thin portlandite layers intermixed with C-S-H phases. The formation of this strongly layered Portlandite, instead of compact crystals, could explain the increase in BET specific surface in presence of SRAs.

To match the BET surfaces measured in presence of SRA1, a rough calculation suggests that the specific surface of portlandite would have to increase by factor of about 35 (70m²/g instead of 2m²/g). Let us assume that the crystals lateral dimensions are conserved while their thickness changes from 10 µm to about 0.5 µm as suggested by Figure 64. This on its own would increase the specific surface of portlandite in paste by a factor 20, which is in the right range.

BET measurements of cement pastes hydrated for 28 days, all containing high dosages of different SRAs, show an increase in surface compared to the plain paste (Table 27)

Table 27: Measured N_2-BET surfaces on cement pastes with 2wt.-% SRA hydrated for 28 days

cement paste	N_2-BET surface [m²/g]
reference	9.7
SRA1	10.8
SRA2	11.7
SRA3	10.8
SRA4	10.6

Let us also recall that the cement paste sample containing 2wt.-% SRA5 that showed a disproportional intensity within XRD. The interpretation that this is due to preferred orientation of the crystals is consistent with the change in portlandite morphology.

Microscopic observations also show portlandite separated or intermixed with C-S-H. For example, in Figure 66a, the layered structure to be seen is most probably portlandite surrounded by C-S-H phases. In subfigure b) an EDX-analysis reveals mainly calcium and oxygen, indicating portlandite, if one takes into account that the surrounding C-S-H is part of the volume excited in the course of EDX analysis.

Figure 66: Microstructure of CP13.00 (SRA1 at initial 2wt.-% o.c.) after 7days of hydration

a) layered structure surrounded by C-S-H phases

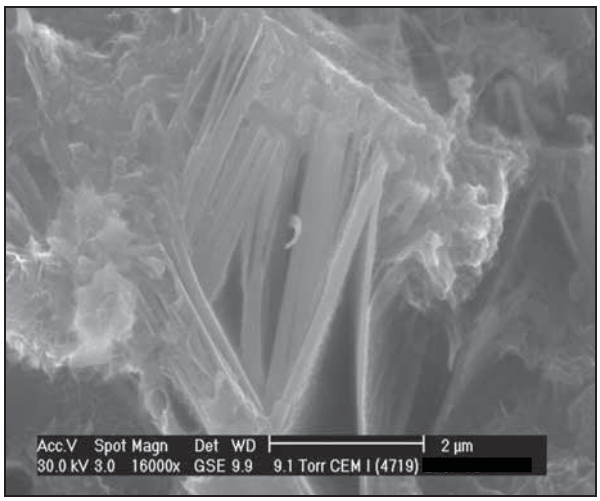

b) EDX-analysis of subfigure a)

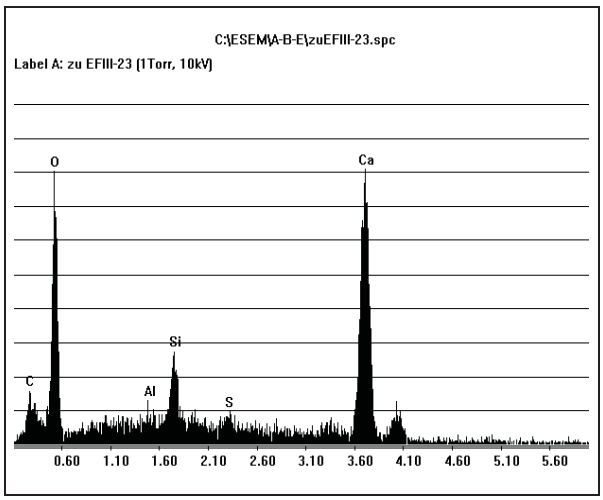

c) Ettringite, C-S-H and C-S-H – portlandite layers

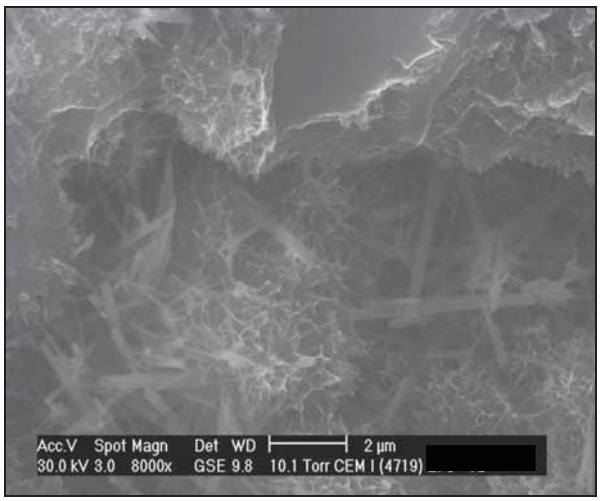

d) Portlandite with C-S-H grown on individual portlandite layers

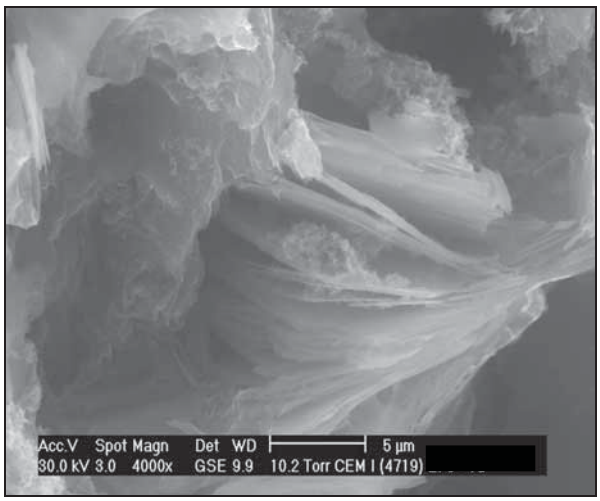

In Figure 66c, one can see that ettringite (rod like crystals) is present in the microstructure too. More important, in the upper part of this picture, growth of C-S-H can be seen to have taken place between portlandite layers (Figure 66d)

One now wonders how SRA molecules influence crystal growth of portlandite. From theory on adsorption of non-ionic surfactants onto the solid/liquid interface it is known (see subchapter 4.2.5) that non-ionic surfactants are only physically linked to the solid surface, where silanol groups and/or aluminol groups can hydrogen bond to ether groups of alkylene groups. ***Because of its high isoelectric point, portlandite can provide hydroxyl groups that do not get deprotonated in the high pH of cementitious materials. Contrary to other minerals, it can therefore be expected to adsorb these surfactants. This appears the most probable explanation of the effect that SRAs have on portlandite morphology.***

8.3.5 Concluding remarks

Within a descriptive approach, the hydration of Portland cement in presence of SRA and/or SP-PCE was investigated. Using isothermal heat conduction calorimetry, SRAs were shown to cause a detectable delay of hydration kinetics, increasing with the dosage of this admixture. Compared to similar dosages of SP-PCE, retardation is significantly lower for SRA treated pastes. A disproportional delay of the hydration process was however measured for pastes containing both types of admixtures.

The retardation caused by SRA and/or SP-PCE was independent of the binder type used in this study.

Results from TGA and XRD analysis indicate that SRAs do not cause significant differences in hydrated phase assembly at equivalent hydration stages. However, they do increase the precipitation of syngenite up to the end of acceleration period. Most probably the same mechanisms responsible for the depletion of ions when SRA is present in aqueous electrolyte solution can be invoked to explain this.

In contrast to the aluminate phase hydration, the silicate clinker phase hydration is significantly reduced in presence of SRAs. This is consistent with the observation that the depletion of gypsum and anhydrite happened independently of SRA presence. After 28 days of hydration SRA treated pastes comprise a significantly lower degree of silicate phase hydration (determined by on portlandite quantification). Surprisingly the amount of bound water was disproportionally high for SRA treated pastes, suggesting that the microstructure of hydrated phases is influenced by SRAs. This results in uncertainty on the real degree of hydration and makes any relation to mechanical performance delicate. It is therefore still an open question, whether the degree of hydration, decreased by SRA, can explain the slight decrease of mechanical performance of SRA treated mortars and concretes described in the literature (compare to section 4.4.5).

Investigations of microstructural development on cement and C_3S pastes revealed that the specific surface area of the hydrates formed is significantly increased in presence of SRAs. This probably means that the increased amounts of bound water determined from TGA probably include an enhanced amount of physically bound water. Using electron microscopy it could indeed be shown that portlandite morphology is strongly influenced by SRA (drastic decrease of plate thickness).

Contributing to the working hypothesis of preferred precipitation of layer–like portlandite crystals it should be mentioned that XRD patterns on cement paste showed a disproportionally high intensity for portlandite, most probably caused by preferred orientation of these crystals in the course of sample preparation.

The composition of the pore solutions extracted from hydrating cement pastes indicates that SRAs mainly self assemble due to the electrolyte nature of the liquid phase. The salting-out of SRAs comes along with mineral precipitation. It remains open whether this is either induced by the SRA that might act as a nucleation agent for the mineral precipitates or whether the precipitates provide surface for SRA adsorption.

Adsorption experiments using synthetic pore solutions with and without addition of synthetic hydrates revealed that SRA adsorption onto the solid/liquid interface, i.e. ettringite and C-S-H phases, is significantly lower than losses by liquid/solid phase separation in aqueous electrolyte solution. It can therefore be assumed that mainly the electrolyte concentration determines the the phase behaviour of the SRA therein, so that losses onto solids can be assumed to depend mainly on that.

In regard to the retarding effect of SRA on cement Portland cement hydration, it is overall concluded that adsorption takes place on the 001 plane of portlandite. This can take place because of hydroxyl groups that do not get hydrolysed at high pH of cementitious systems. This explains the thin platelets, the increase of specific surface and the higher amount of bound water at a given degree of hydration. Assuming that the adsorbed SRAs limit growth rates of portlandite, this then rises the calcium concentration in solution and penalizes dissolution [248].

Concerning parameters that are essential for predictive models for drying and shrinkage, some important results and their implications are given in the following:

1. Due to the electrolyte nature of the cement pore fluid, SRA is expelled from bulk solution. Whether this impacts its availability to adsorb at the liquid/vapour interface in one or another way is not known, but the extent of these losses can be taken into account.
2. In presence of SRA the specific surface area of cement paste is increased. We recognize that this increases the interfacial area and hence, during drying, the energy to be utilized at these interfaces increases. Moreover, this certainly impacts the evolution of surface tension in the course of drying.

Concerning the first, this will be examined in chapter 10. Concerning the second, the impact of SRA on microstructure of cement paste and mortar is the subject of the following chapter.

9 Impact of SRA on microstructure

9.1 General introduction

In this chapter the impact of SRA on microstructure is examined. In case such changes can be detected, the main question is, whether drying shrinkage is affected. From the literature research on drying shrinkage mechanisms presented in chapter 3 and 5, it turned out that regardless the mechanism, the major material properties determining the magnitude of drying shrinkage were:

a) pore structure and pore space distribution

b) initial pore saturation

c) constitution of the pore solution.

This chapter focuses, on the one hand, on the evolution of porosity during hydration and on the other hand, on the porosity and internal surface area of well hydrated cementitious material, which is later on used for the drying and shrinkage measurements.

9.2 Specific materials and working approach

In general two types of material were investigated. On the one hand cement pastes with similar compositions as used for investigating the hydration mechanisms. Details are given in subchapter 6.3.1, denomination in Tab.A4- 2. On the other hand three series of mortars were also investigated. In each series, the dosage of SRA was varied. In the first mortar series, denominated “CM 00”, the binder was 100% Portland cement, while in the second, denominated “LM00”, it was a limestone composite binder, containing 35% of limestone and 65% Portland cement. Both mortar series comprised self consolidating properties (50vol.-% of aggregates < 2mm grain size). The third mortar, denominated “SM00”, introduced in this studies was a standard mortar according to EN 196, with w/c=0.5. The composition of these base mortars is given in Tab.A2- 5. The referring homologue series of SRA treated self consolidating mortars were composed using similar absolute amounts of SRA in the mixing water respectively. All mixtures were composed to comprise similar ratios of solids/liquids, and the SRA was part of the mixing water. The denomination of the mortars followed the system introduced for cement pastes (see above) and is displayed in Table 28.

Table 28: Denomination and SRA dosages of mortars

denomination		binder			aggregates		liquids/admixtures				
series	mortar	cement	limestone	volume	CEN-sand		water	SP-PCE	SRA 1		liquids
[lfd. Nr.]	[-]	[kg/m³]	[kg/m³]	[l/m³]	[kg/m³]	[l/m³]	[kg/m³]	[kg/m³]	[wt.-% o.c]	[kg/m³]	[l/m³]
01	CM 00	743.5	-	234*	1324	504	251	12.3	0.0	**0.0**	259
02	CM 11						247	12.3	0.5	**3.7**	
03	CM 12						243	12.3	1.0	**7.4**	
04	CM 13						235	12.3	2.0	**14.9**	
05	CM 14						220	12.3	4.0	**29.7**	
11	LM 00	487.3	229.3	236*			256	4.4	**adjusted according series CM**	**0.0**	
12	LM 11						252	4.4		**3.7**	
13	LM 12						248	4.4		**7.4**	
14	LM 13						241	4.4		**14.9**	
15	LM 14						225	4.4		**29.7**	
21	SM 00	512.0	-	161	1533	583	256	0.0	0.0	0.0	256
22	SM 11						253	0.0	0.5	2.6	
23	SM 12						250	0.0	1.0	5.1	
24	SM 13						245	0.0	2.0	10.2	
25	SM 14						234	0.0	4.0	20.4	

* solid content of SP~25m.-% was assumed to be part of solids

In a first step, the chemical shrinkage of mortars and paste was investigated using the method described in subchapter 6.3.3.1. Additionally, after these measurements, the actual bulk volumes as well

as the evaporable and non-evaporable water content were measured in order to evaluate pore space and further on to distinguish between capillary and gel porosity.

Samples produced for measurement of drying shrinkage were prepared and cured according the approach given in subchapter 6.3. These samples were wet cured to achieve a high degree of hydration while approximately maintaining saturated conditions. Doing so, it was assumed to exclude autogenous shrinkage due to self desiccation, so that the strain measured exclusively refers to drying shrinkage. Measurement of drying shrinkage was performed until specimen approximately achieved equilibrium in the climate they were exposed to. Then, the specimens were resaturated to determine the irreversible part of drying shrinkage (drying induced creep). Additionally the pore system was described by measuring content of evaporable and non-evaporable water. With the purpose of modeling drying shrinkage according the “capillary force” model, a series of pastes and mortars were used to extract pore solution right after wet curing and before exposition to a dry environment.
The porosity of paste and mortar of selected samples was additionally investigated by mercury intrusion porosimetry as well as nitrogen sorption.

9.3 Impact of SRA on microstructure of cement paste during wet curing

One major issue in comparing material properties often is choosing a suitable point in time when the materials of interest actually comprise comparable condition. For the material at hand, i.e. cementitious paste and mortar with and without organic admixtures, the chapter on hydration mechanics (chapter 8.3.2) showed a strong hydration retardation, when SRA and SP-PCE were added. Furthermore the increase of specific surface was found to increase the amount of bound water, so that self desiccation may additionally lower the degree of hydration at certain point in time. Moreover, the experiments on hydration were all conducted under autogenous boundary conditions, i.e. closed systems, so that the actual amount of water available for hydration might have been insufficient. Whether this can be compensated by wet curing is of interest.

It is well known that cementitious materials may compensate bulk shrinkage (due to chemical shrinkage) by adsorbing water from the exterior. This water then occupies space that is generated in the course of chemical shrinkage. Hence, compensating bulk shrinkage by water suction increases gel porosity, which was to impact drying shrinkage.

In the next section chemical shrinkage of the binders is measured using pastes and mortars. The measurement approach allows to additionally obtaining bulk volumes and the extent of water ingress during hydration. From these results the impact of SRA on gel porosity can be obtained.

9.3.1 Chemical shrinkage of cement paste and mortars

Using GEMS, the chemical shrinkage of the reference paste CP00.00 (w/c=0.4) could be predicted. From Figure 67 it can be seen that the initial volume of educts is predicted to increase very slightly just after mixing. This is due to a GEM solver issue, i.e. the sulphate regulator initially is hydrated and all easily soluble compounds are dissolved. In the course of hydration of the reference cement paste CP00.00 the bulk volume decreases. The simulation reveals that this paste, comprising a w/c of 0.4, still contains a certain amount of “free” water at long hydration times. From Figure 67, the total chemical shrinkage can be obtained from the volume of “educts & products” (medium thick solid line) whereas the bulk shrinkage is derived from the decrease of bulk volume (thick solid line). The volume of chemically bound water can be obtained from the decrease of the total amount of liquids (thin solid line). The residual water is supposed to be present as bulk water or physically adsorbed water.

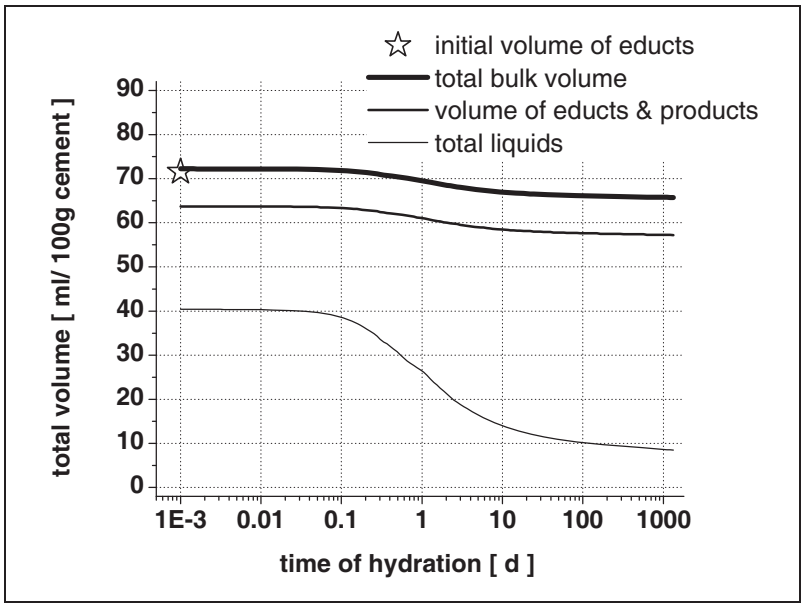

Figure 67: Modeled chemical shrinkage of cement paste (reference CP.00.00)

In Figure 68, the result of an actual measurement of reference paste CP00.00 is displayed. The stars give the measured bulk shrinkage and the solid line is the results of the GEMS simulation.

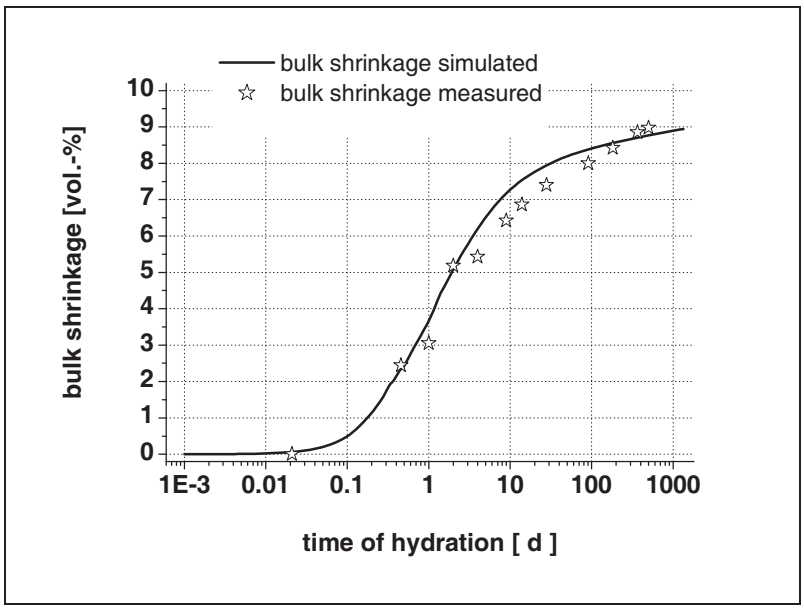

Figure 68: Modeled and measured chemical shrinkage of reference paste CP 00.00

It can be seen that the results derived from experiment generally follow the predictions derived from GEMS modeling. Differences between modeling and experiment most probably are due to hydration kinetics, since the measured paste seems to be slightly delayed.

The results of chemical shrinkage measurements of the main series of paste and mortars are given in figures Fig.A5- 1 to Fig.A5- 4. Results show that with increasing dosage of SRA, chemical shrinkage generally is delayed. Furthermore it can be seen that SRA3 has almost no impact on the progress of chemical shrinkage.

Whereas for SRA treated pastes the hydration progress is suppressed in the beginning, the shrinkage curves seem to merge with the reference at later stages. This seems reasonable since in chapter 8.3.2 we found that SRAs do not change the hydrates phase assemblage but cause the silicate phase hydration to be delayed. Whereas similar phase composition implies that the extent of chemical shrinkage remains unaffected, a change in hydration kinetics is expected to directly impact the shrink-

age evolution. Moreover, because of excess water available, the degree of hydration for SRA containing samples is theoretically not limited as for the sealed samples used in the hydration studies. This accounts for the observation that the curves merge for long hydration times.

Figure 69 displays the shrinkage curves of pastes and mortars without SRA and with an SRA dosage of 2wt.-% of cement. Two major phenomena can be deduced from this graph. First, it points out the impact of different SRAs on pastes hydration progress (CP samples). Second, the different mortars exhibit different behaviour. Also, with SRA1 they show almost no differences in shrinkage progress up to 28 days of hydration and later on chemical shrinkage is enhanced in CM and LM.

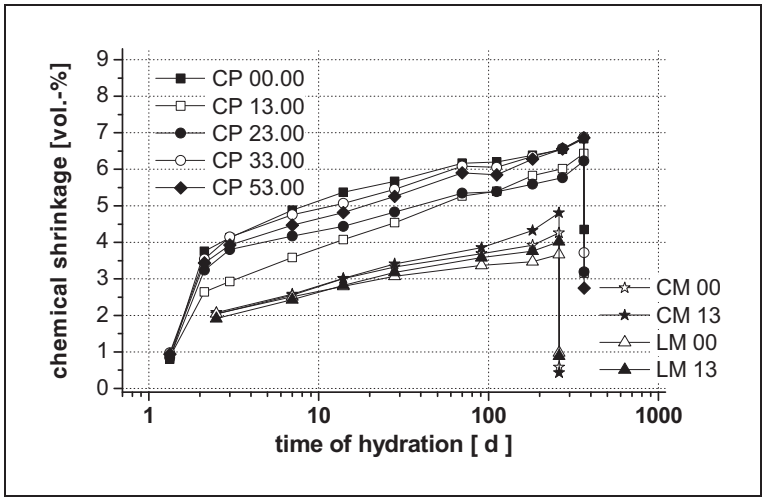

Figure 69: Chemical shrinkage of cement paste and mortars containing different SRA

- References: CP 00.00 (paste); CM 00; LM 00 (mortars)
- SRA dosage 2wt.-% of cement;
  SRA1: CP13.00; CM13; LM 13
  SRA2: CP23.00
  SRA3: CP33.00
  SRA5: CP53.00
- Last point of measurement displays sample volume after measurement

After finishing the measurements of chemical shrinkage the bulk volume of the specimen was measured. It revealed that the samples containing SRA show a higher total bulk volume (see Figure 69). Whereas the reference cement paste CP 00.00 shows total bulk shrinkage of about 4.3vol.-%, the SRA treated pastes comprise a bulk volume clearly below 4vol.-%.

For mortars, a significant difference in total bulk shrinkage can not be observed. Most probably the aggregates (50vol.-%) act as a restraint and suppress the macroscopic shrinkage of the bulk. As a result, the self-restraint prevents the sample from reducing its size so that continued hydration causes the formation of porosity. Depending on pore structure, this allows water ingress. Overall, these processes reduce bulk shrinkage.

In Figure 70, the water sorption of cement paste and mortar samples is drawn against porosity created by hydration. This is obtained from the volume difference between educts and hydrates on the one hand and final bulk volume on the other.

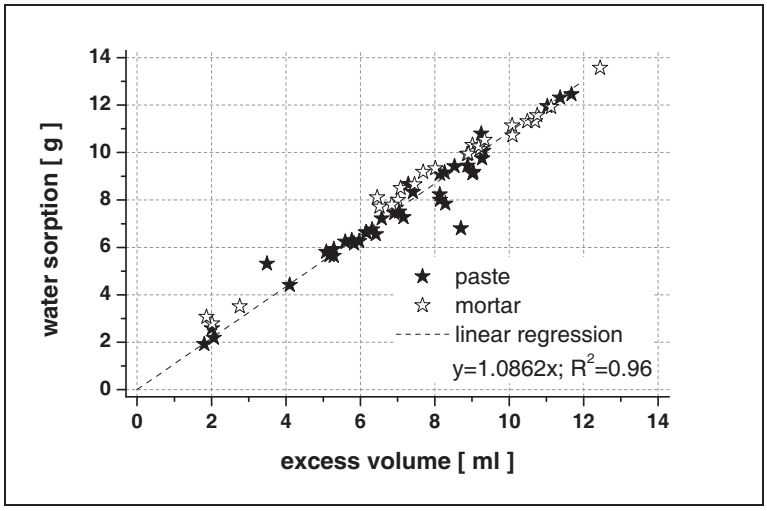

Figure 70: Water sorption and excess volume of cement paste and mortar samples after saturated curing

It can be seen how pastes and mortars, independent from SRA type and load, completely fill this porosity by water sorption. Moreover, a linear regression reveals that the excess water comprises a density of about 1.09 g/cm³, which suggests that this water is partly associated to solids (physically bound to hydration products). This is in line with the findings of Powers et al. [249] who found the density of physically bound water to be about 1.15 g/cm³.

So far, no significant impact of SRA on the magnitude of chemical shrinkage was found. Although they slow down hydration kinetics, they do not change the hydrated phase composition.

We can observe that the adsorbed amount of water at the end of chemical shrinkage increases with the dosage of SRA and this independent of the type of SRA (Tab.A5- 1 and Tab.A5- 2). The question now arises about what mechanism causes this. As outlined above, pastes and mortars are designed to comprise similar volume ratios of liquids/solids and therefore admixtures replace mixing water by volume. Obviously this strategy causes the water to cement ratio to slightly decrease with increasing admixture content. When water suction after measurement of chemical shrinkage is used to calculate an effective water/cement ratio w/c_{eff} , it is found that for both, paste and mortar, have similar values of w/c_{eff_paste} =0.41±0.01 or w/c_{eff_mortar} =0.40±0.01 respectively. Note that for mortar type LM, carrying 35wt.-% inert limestone filler in binder, the initial ratios are w/c_{LM00}=0.59 and therefore w/b_{LM00}=0.36. Accounting for water suction during wet curing, the effective initial water/binder ratio increases towards w/b_{LMXX}~0.40±0.01 also. From this we conclude that the systems targets complete hydration, which can be achieved by water sorption.

As mentioned above, the enhanced water sorption impacts porosity of the samples containing SRA. This is the subject of the next section.

9.3.2 Porosity of cement paste and mortar

9.3.2.1 Water porosimetry

The porosity of paste and mortar series containing different dosages of SRA was obtained by measuring evaporable and non-evaporable water content. The results show that the volume ratios of gel porosity to capillary porosity increase with the amount of SRA (Tab.A5- 1 and Tab.A5- 2). This is illustrated in Figure 71 that outlines the pores space and the differentiation between capillary and gel porosity of cement paste carrying different dosages of SRA1.

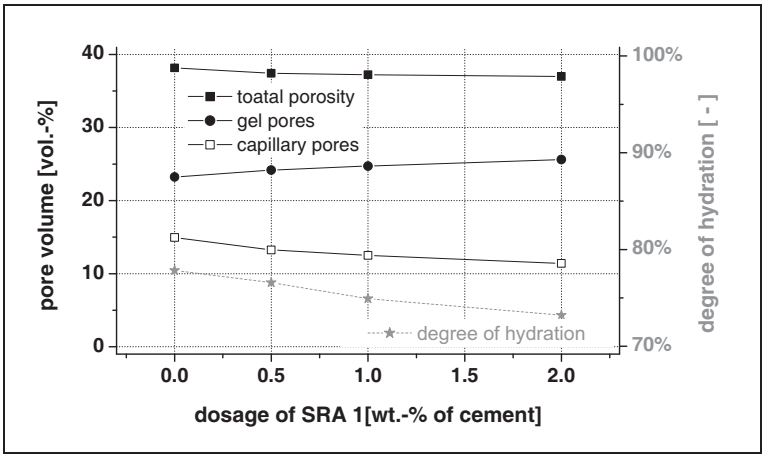

Figure 71: Pore volume and distribution according to evap./non-evaporable water content of cement paste with/without SRA1

It reveals that the ratio of gel porosity to capillary porosity significantly increases with increasing amount of SRA. Surprisingly, the samples comprising low bulk shrinkage due to SRA treatment show almost similar total pore space. However, this could be related to the differences in the degree of hydration but if so, paste with a higher degree of hydration should comprise the lower amount of capillary pores. Indeed, SRA were found to retard hydration but Figure 71 clearly shows that the plain paste comprises enhanced capillary porosity despite a higher degree of hydration. This is in fact misleading.

The data really show that for a given porosity the distribution between capillary and gel pores is changed. More specifically, an increase of SRA dosage appears to refine the microstructure by reducing capillary porosity on the expense of gel porosity. This is confirmed in the next section.

9.3.2.2 Mercury Intrusion Porosimetry

The phenomenon of increased gel porosity in presence of SRA, relative to the amount of capillary pore space, could also be derived from mercury intrusion porosimetry measurements (MIP) on paste and mortar. The obtained pore size distributions measured on specimen hydrated for 28days in wet conditions are displayed in Figure 72 (cement paste with SRA1) and Figure 73 (cement mortar series CM). Results of MIP on mortar series SM; LM as well as cement paste series with SRA3 and SRA5 are displayed in appendix, Fig.A5- 5 to Fig.A5- 8.

Both figures below show that with increasing amount of SRA1 the average pore radius of the different series (paste and mortar) shifts from about 40nm towards 10 to 20nm. Due to this, the width of the distribution seems to decrease. The cumulative plots of series CM and CP show that the overall amount of pore space evaluated by MIP is approximately unaffected as could be also concluded from Figure 71.

Figure 72: Mercury intrusion porosimetry of cement paste with increasing amount of SRA1 after 28days of wet curing

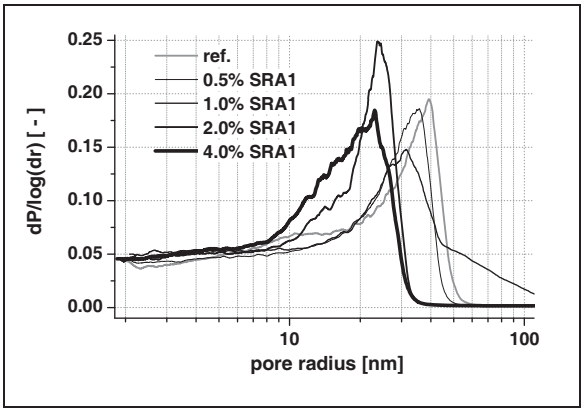

Figure 73: Mercury intrusion porosimetry of cement mortar with increasing amount of SRA1 after 28days of wet curing

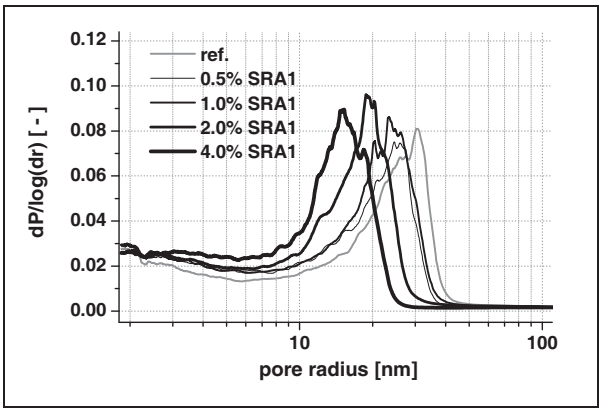

9.3.2.3 Nitrogen sorption measurements

To take the porosity analysis further, nitrogen adsorption/desorption was also performed. Measurements on mortar series CM, LM and SM reveal sorption isotherms of type IV according [250], i.e. type H3 according IUPAC recommendations/Sing 1985 [251]. Figure 74 displays the sorption hysteresis of mortar CM00 and the hysteresis of mortar CM14, containing 4wt.-% SRA1 (by weight of cement). Graphs for mortar series LM and SM are given in appendix, Fig.A5- 9 (LM) Fig.A5- 10 (SM).

In Figure 74, the x-y projection plane shows the adsorption/desorption isotherms of the mortars CM00 and CM14. In the x-z projection, the *t*-curve for nitrogen at T=77K is given. The y-z plane shows the appropriate *t*-plots of the mortars.

The nitrogen ad-/desorption isotherms measured on the three different mortar series reveal that SRA1 increases the total volume of nitrogen adsorbed over the measured range of partial pressures (x-y projection). The hysteresis formed is slightly increased due to SRA1. This is especially true for mortar CM, containing Portland cement as binder.

The differences in nitrogen adsorption of SRA containing mortars comes from an enhanced adsorption at partial pressures below the bifurcation point, indicating an enhanced amount of smaller pores or rather increased specific surface area. In this regard, the t-plots displayed in the y-z-projection of

Figure 74 shows that the SRA treated samples exhibit a larger slope up to the corresponding partial pressures. As explained in subchapter 8.3.4, this is related to a larger specific surface.

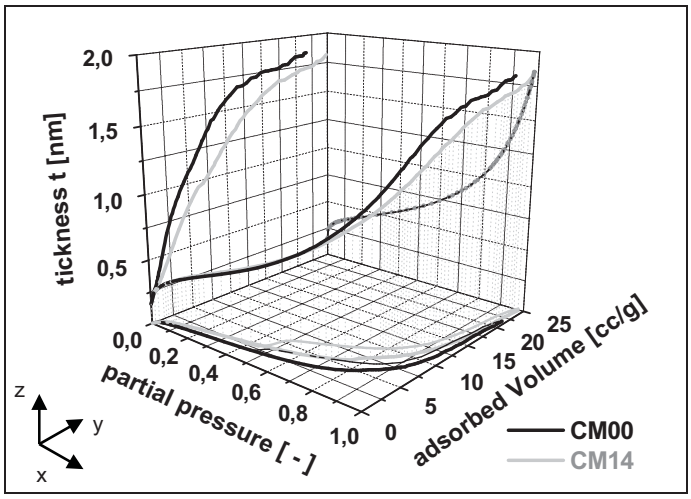

Figure 74: Nitrogen sorption hysteresis of mortar CM00 and CM14

legend

x-y projection: sorption isotherms

x-z projection: t-curve; nitrogen at 77K

y-z projection: t-plot

thick solid lines: adsorption

thin solid lines: desorption

The same conclusion is reached with the BET specific surface areas. They show that, independent of the type of mortar, SRA1 treated mortar samples have a larger surface area (Table 29).

Table 29: Increase of specific surface of different mortar types without SRA and with 4wt.-% SRA1

mortar	SRA	A_{BET}	$A_{t\text{-plot}}$	$A_{BET}/A_{t\text{-plot}}$
[denom.]	[yes/no]	[m²/g]	[m²/g]	[-]
CM00	no	5.0	6.3	1.26
CM14	yes	8.1	10.9	1.34
LM00	no	7.1	9.0	1.26
LM14	yes	9.3	12.4	1.33
SM00	no	5.2	6.6	1.27
SM14	yes	6.1	8.1	1.34

As expected, the specific surface area derived from the t-plot is higher than the BET surface. This is due to a slight underestimation of adsorption of nitrogen in micro-pores within the BET method, which uses the adsorption data at partial pressures above 0.05 whereas the linear regression used in the *t*-plot method goes down to zero. Surprisingly the ratio of BET/*t*-plot surface is quite similar for all the mortar types investigated. This would suggest that the surface of pores measured below the BET limit is proportional to the BET surface.

The pore space distribution of the mortars was evaluated using the corrected modeless-method developed by Brunauer et al 1967 [16, 17]. It uses an algorithm where the pore volume distributions are not derived from the Kelvin equation for specific pore geometries like cylindrical or plate shaped pores, but as functions of the hydraulic radii, i.e. the ratio of volume/surface area within classified pore ranges.

In Figure 75 and Figure 76 the cumulative pore size distributions and the corresponding internal surface areas of mortars according this Modelless-method are given. The absolute contributions of specific surface areas over pore size are displayed also. Data on mortar series SM are displayed in appendix, Fig.A5- 11.

Figure 75: Influence of SRA1 on specific surface area of mortar series CM according Modelless-method (nitrogen desorption)

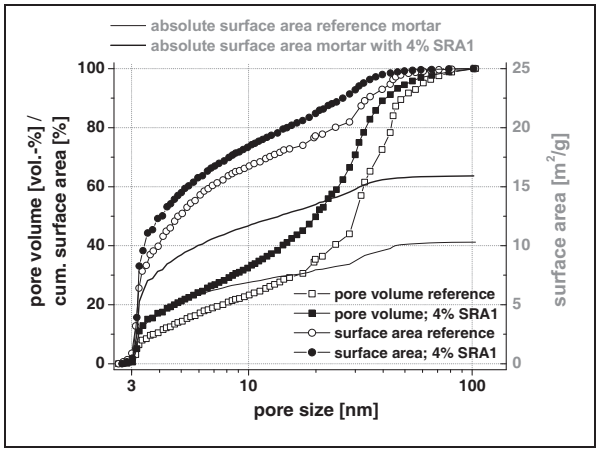

Figure 76: Influence of SRA1 on specific surface area of mortar series LM according Modelless-method (nitrogen desorption)

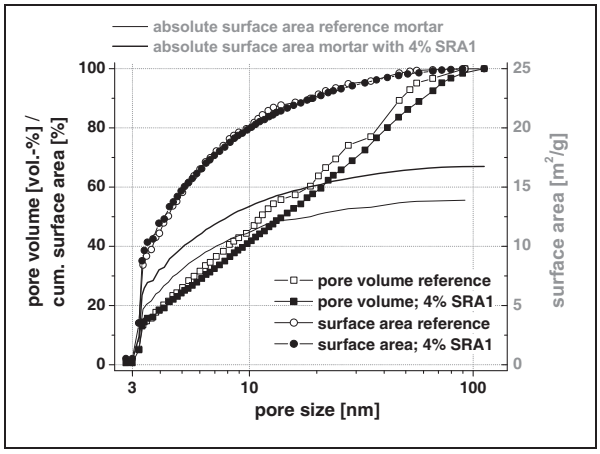

The above figures reveal that independent of the type of the mortar series, the increased specific surface area in presence of SRA1 is due to an increase in the amount of small pores mainly between 3nm and 20nm. Above this threshold size, the incremental increase in surface area seems to be similar and independent from SRA treatment.

In Figure 77 the differential pore size distributions of reference mortar CM00 and mortar CM14 (4wt.-% SRA1) are displayed. Figure 78 shows the contribution of pore size to the surface. The pictures show that the increase of surface area indeed has to be related to pores smaller then 4nm. This is true since above this size the mortars comprise different pore size distribution but these pores do not significantly contribute to the overall specific surface, i.e. the plots in are almost congruent.

Figure 77: Differential pore size distribution of mortars CM00 and CM14

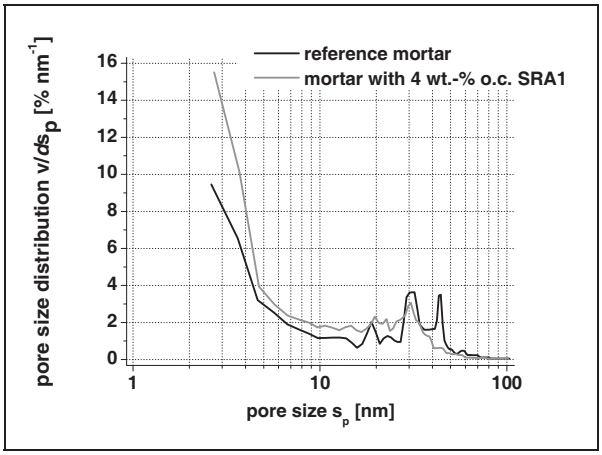

Figure 78: Differential surface contribution vs. pore size of mortars CM00 and CM14

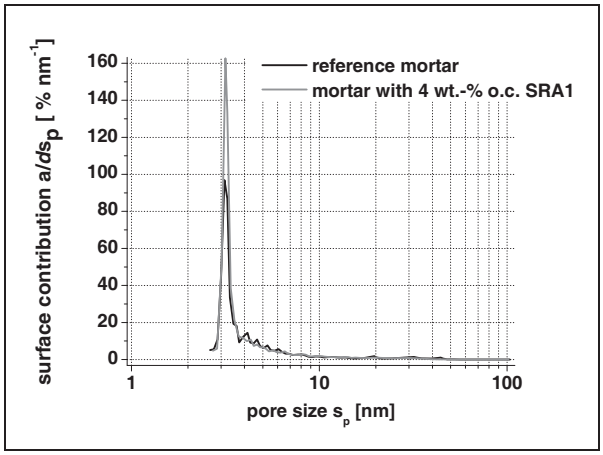

Regarding what was found by MIP, the question does however arise if the results of MIP and nitrogen desorption mismatch in terms of mesoporosity. Midgley et al. 1983 [252] investigated pastes and applied MIP and nitrogen sorption and found good agreement in a pore size region of 5 to100nm.

As a reminder, the results of MIP revealed that SRA1 caused the pore size distribution in the range from 2nm to 50nm to be shifted towards smaller pore sizes with increasing dosage (Figure 73). Moreover, MIP returns that due to SRA1, pores in the region of about 25-50nm totally vanish. The results displayed in Figure 77 are globally consistent with that. In contrast to MIP data, nitrogen adsorption

obtained that the sharp peak in the range of 40 to 50nm, occurring for the reference mortar CM00, vanishes in mortar CM14 that contains SRA1.

Nevertheless, both methods indicate a refinement of pores on the expense of capillary porosity. This is consistent with the results from evaporable/non evaporable water content.

9.3.3 Summary

In this chapter the impact of SRA on porosity of paste and mortar was examined. It can be said that for well cured material, the presence of SRA causes an increase of gel porosity on expense of capillary porosity. Along with that, pastes and mortars containing SRA comprise an increased specific surface area which is due to an enhanced amount of pores smaller then 4nm. The increase in specific area is in line with the findings of subchapter 8.3.4 where this was suggested to come from a change in portlandite morphology.
The question arises on whether the increase of pores smaller then 4nm in presence of SRA1 can be related to portlandite interlayer space. With respect to the increase in specific area, layered portlandite seems the most probable explanation.

Concerning the impact of an altered microstructure on drying and shrinkage the following can be said. In chapter 5, the drying in presence of SRA was shown to depend on the interfacial area exposed and the actual bulk concentration of the surfactant. This will determine how drying proceeds or how a specific desorption isotherm will look like. However, with respect to the findings in this chapter and the previous one, the synthetic pore system used to model drying in presence of SRA (chapter 5) now can be evaluated to comprise two main issues. The model does neither account for

a) impact of SRA on the pore structure nor
b) specific distribution of SRA within the pore structure, i.e. the presence of SRA in the portlandite interlayer space.

The first one might be of minor importance as the pore size distribution of the normcube can be adjusted.

For a given imposed relative humidity we conclude the following: In presence of SRA the absolute water loss will be slightly decreased but the largest water filled pore will comprise a smaller size. Furthermore, the interactions between SRA bulk concentration, v/a-ratio and excess surface concentration of SRA may cause differences for the sorption isotherms predicted to some extent.

However, the huge increase in gel porosity and the findings on SRA associated to layered portlandite might have significant impact on drying and shrinkage. Most important, if SRA is partly associated to solid interfaces, the question arises on whether this fraction can be accounted for to be surface active. This is especially important for determining the properties of the interfaces in the course of drying, i.e. an estimation of the surface tension.

This is partly the topic of the next section that deals with the leachability of SRA. From this it can also be obtained how strong SRA are associated to the solid surfaces and whether this SRA fraction may desorb if an excess of interfacial area or aqueous solution is provided.

10 Sustainability of SRA application for self compacting mortars and concretes – How long will concrete benefit from SRA addition?

10.1 General introduction

The efficiency of SRAs for surface tension reduction is directly related to their presence at the liquid/vapour interface of the drying material. Therefore, enhanced leachability of SRAs may be a severe issue and the questions arises about if and to what extent it might influence long-term performance of SRA treated mortars.
In this chapter, the dominating leaching mechanism for SRA is evaluated using results from tank tests (6.3.5). One might argue that tank tests probably do not reflect actual field exposure conditions of SRA-treated mortars. For that reason, a cyclic drying/rewetting regime was also set up to evaluate the impact of leaching on the long term shrinkage behaviour of these mortars.

To clearly distinguish between ageing phenomena and alterations due to leaching, two sets of identical samples were prepared. The first set was submitted to cyclic tank test. The second served as a reference sealed under wet conditions.

After finishing tank tests, the shrinkage isotherms of both types of specimen were measured. From this, the impact of SRA leaching on shrinkage reduction is obtained.

The quantification of leached amounts of SRA and the shrinkage measurements should enable estimations of long term performance of SRA-treated mortars and concretes. This contributes to answering the question about how long concrete can benefit from SRA application.

10.2 Specific materials and methods

10.2.1 Materials

The leaching tests were performed on three mortar series introduced in chapter 9. The standard mortar (SM) according EN-196 represents cementitious material comprising a high water/cement ratio. Mortar types CM and LM were introduced as representative mixes for self-consolidation mortar. Especially mortar type LM has a binder rich design, typical for self consolidating mixtures with moderate amounts of inert additives. Samples of the three main mortar types were prepared, cured and stored as described in subchapter 6.3. SRA dosages used and denominations applied follow the system introduced in subchapter 9.2 (Table 28: Denomination and SRA dosages of mortars).
The SRA used in samples exposed to leaching tests was SRA1 and was chosen for more than one reason: (a) for SRA1 most detailed information on composition is known; (b) as indicated in subchapter 4.4.1, SRA1 represents a main ingredient, i.e. a tail moiety (tert-butyl group) most probably often used in commercial products and described in a lot of performance tests published so far.

10.2.2 Methods

Investigation on the dominating leaching mechanism was conducted using the tank test described in subchapter 6.3.5.5.

The impact of cyclic drying and rewetting was studied following two different exposure regimes:

Regime 1: In this case, a slightly modified tank test was used to discriminate between leaching and ageing. It comprises two subcycles; the first consists in three weeks drying at 20°C/35% RH, while the second is a one week resaturation in deionized water (subcycle tank test).

Regime 2: In this case, the same drying conditions are used, but the resaturation followed the procedure of “inert resaturation” to prevent loss of SRA. This is done by spraying deionized water on the surfaces for several times while specimens are stored at 20°C/>97%RH. Regime 2 therefore isolates ageing phenomena related to cyclic drying/rewetting and is unaffected by SRA leaching.

The quantification of leached amounts of admixtures was conducted using a mass balance. Before starting the tests all mortars were wet cured for 28days. During this period they experienced water suction as outlined in chapter 9. Accounting for this mass change, the initial phase composition was recalculated (Tab.A6- 1).

In general the leached amounts of admixtures were quantified using TOC. To distinguish between SRA and SP-PCE for self-consolidating mortar types (CM; LM), the eluate was additionally analyzed using gas chromatography (subchapter 6.3.2.5).

The impact of SRA leaching on shrinkage performance was investigated as follows:

a) The initial shrinkage behaviour of the mortars was evaluated by measuring shrinkage isotherms (subchapter 6.3.4).

b) Deformation of prisms subjected to cyclic drying & rewetting was measured after each subcycle. Weighing after each subcycle served to determine, whether drying/saturation was complete.

c) After completing tank test & cyclic drying/rewetting, shrinkage isotherms were measured on the corresponding samples.

d) Shrinkage isotherms of mortars aged but not leached (wet; sealed) were measured to distinguish changes purely due to ageing.

10.3 Permanent leaching

10.3.1 Results – tank test

The raw data collected during tank tests are displayed in appendix, Tab.A6- 1. These are summarized in Figure 79 where the cumulated amount of organic carbon leached is given relative to the amount initially present in the samples. Values are corrected for organic carbon load introduced a) by the tanks themselves (tank blank sample) and b) by sample manipulation (blind measurement).

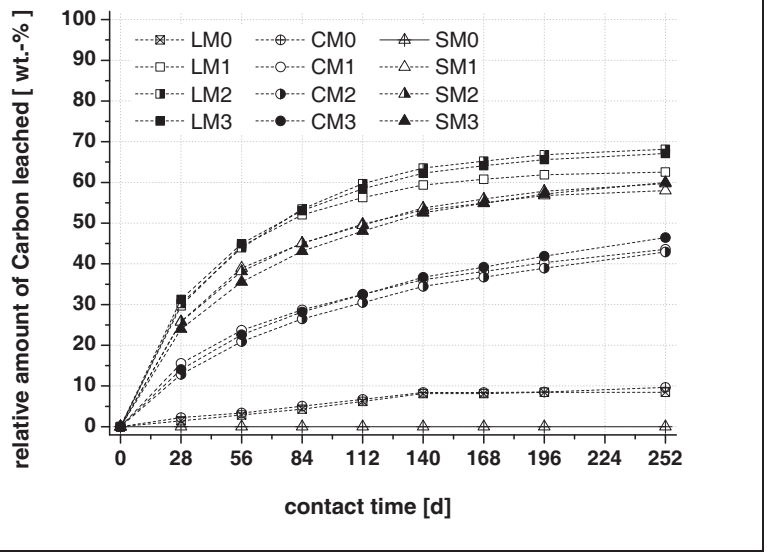

Figure 79: Relative amounts of organic carbon leached from mortar (TOC) in tank tests

SRA dosage:

xM0 (0.0% SRA1);

xM1 (0.5% SRA1);

xM2 (1.0% SRA1)

xM3 (2.0% SRA1)

For standard mortar series SM 1-3 the relative amounts of carbon leached are exclusively due to SRA1. In this case, the leaching extent is independent of the SRA dosage, when values are given relative to the initial dosage. This strongly suggests that equilibrium between SRA in eluate and SRA in pore solution is achieved by the end of each leaching cycle.

For mortars containing SRA1 and SP-PCE the relative amounts of carbon leached are also similar but slightly less congruent in comparison to SP-PCE mortars CM0 & LM0. However, in these mortars we must be more careful because two products can be leached: SRA & SP-PCE. To this end it is useful to examine mortars containing SP-PCE only (CM0; LM0). For these, it can be seen that the organic carbon leached out follows a linear trend up to the fifth cycle and then approximately reaches a plateau. Independent of mortar type, the relative amount leached is approximately similar (see Fig.A6- 1 for detail).

Since mortar series LM1-3 and CM1-3 comprised an admixture mix, the individual admixture fractions (SRA vs. SP-PCE) have to be distinguished.

10.3.2 Differentiated analysis of leached SRA & SP-PCE

In a first attempt, it was assumed that SP-PCE was leached out independently of the SRA content. Based on this, the cumulated amount of SRA leached was calculated using the TOC data obtained from CM0 or LM0 respectively. In the following, this is referred to as “leached SRA1 quantified by TOC”.

In a second stage, gas chromatography (GC) was used on these samples. Results in Figure 80 & Figure 81 show that, independent of the mortar type and initial dosage of SRA1, the average ratio of leached SRA1 quantified by GC vs. TOC was GC/TOC=0.66. This ratio is constant, but clearly different from the expected value of one. The reason for this is discussed below.

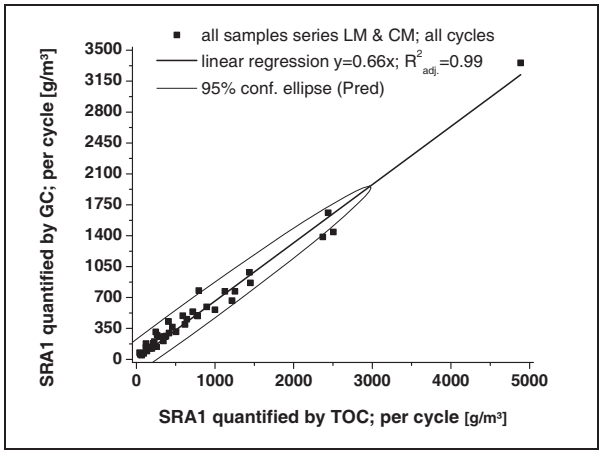

Figure 80: Comparison of SRA1 quantification by different methods (GC vs. TOC) - incremental approach

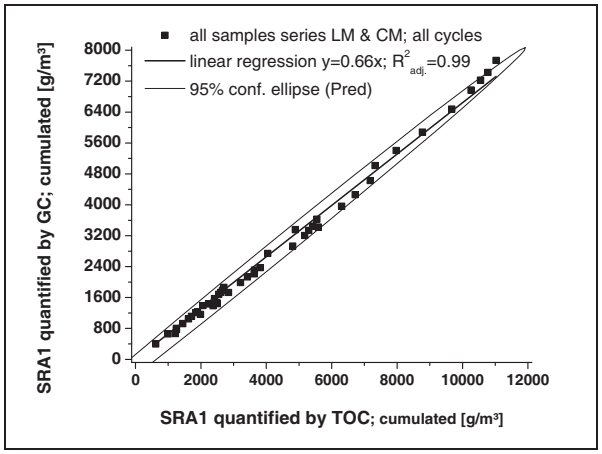

Figure 81: Comparison of SRA1 quantification by different method (GC vs. TOC) - cumulative approach

The first thing that was checked was whether this difference comes from favoured leaching of SP-PCE in presence of SRA. To examine this possibility a mass balance according (91) was applied to each member of the admixture using the data displayed in Figure 80 & Figure 81. Using the initial content of SP-PCE in mortar, the remaining amount after each cycle was calculated. For this, the amount of organic carbon from SRA (GC) was subtracted from the total amount of organic carbon leached (TOC).

$$C_{SP\_remaining} = C_{SP\_initial} - \sum_{i=1}^{n} \frac{C_{C\_tot.} - C_{C\_SRA\_GC}}{C_{C\_SP}} \qquad (91)$$

where:

$C_{SP\_remaining}$:	bulk concentration of SP-PCE in mortar after leaching cycle i	[g/m³]
$C_{SP\_initial}$:	initial bulk concentration of SP-PCE in mortar	[g/m³]
C_{C_tot}:	total amount of organic carbon leached in cycle i from TOC	[g/m³]
$C_{C\_SRA\_GC}$:	leached amount of SRA-carbon from GC measurement	[g/m³]

C_{C_SP}:	carbon content of SP-PCE admixture	[g_C/g]
i:	cycle number	[-]
n:	number of cycles	[-]

From (91) it can be deduced that an underestimation of the leached amount of SRA leads to an overestimation of leached SP-PCE. Using the data on SRA leaching from GC, we find that, for the limestone binder series (LM), SP-PCE is completely removed

a) after the first leaching cycle for mortars containing high dosages of SRA1

b) independent from SRA dosage after the second leaching cycle.

This conclusion is erroneous because, after the second cycle, the the mass balance in (91) would still imply that SP-PCE is leached out. Therefore, the discrepancy between GC & TOC cannot come from SP-PCE-leaching.

The same conclusion is reached for mortars containing pure Portland cement as binder. There, the SP-PCE leaching would be calculated to be disproportionally high in presence of SRA if the GC data are referred to (50% to 100% after the 8th cycle). For both types of mortar containing SP-PCE, this is most unlikely.

Moreover, the evaluated amounts of SRA leached from mortar samples carrying both admixtures would then be very different from those of the SM series (no SP-PCE), which also seems poorly credible.

The linear regression curves found for the correlation between quantification of SRA determined by TOC and GC (Figure 80 & Figure 81) are statistically reliable, because that correleation is found independent of mortar type, initial SRA dosage and cycle number.

For all these reasons we conclude that the results of GC systematically underestimate SRA leaching, for a reason that still has to be determined.

In what follows we assume that “SP-PCE is leached out independently of the presence and dosage of SRA.” This hypothesis does not change much the leached amounts but narrows the curves for different SRA dosages as shown in Figure 82. The results for the individual mortar types are displayed in appendix (Fig.A6- 2; Fig.A6- 3; Fig.A6- 4).

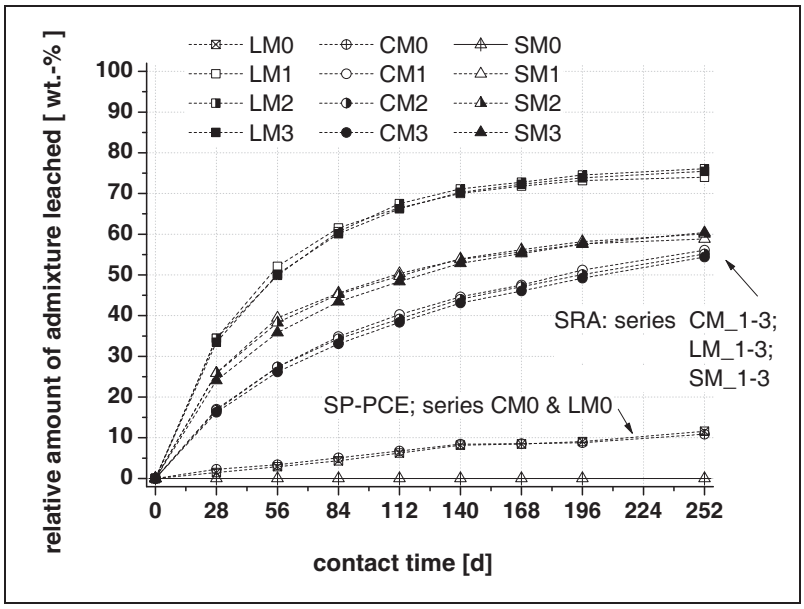

Figure 82: Relative amounts of SRA and SP-PCE leached from different mortar types - Leached amount refers to initial admixture content.

SRA dosage:

xM1 (0.5% SRA1);

xM2 (1.0% SRA1)

xM3 (2.0% SRA1)

An additional step in cross checking GC and TOC can be taken. This however first requires determining the difference between the mobile and immobile fraction of SRA in these mortars. This is done in the next section.

10.3.3 Discrimination between the mobile and the immobile fraction of SRA

In what follows the discrimination between these fractions is mainly based on three observations:

a) For series SM, there is firm evidence that the amounts of SRA leached relative to the initial dosage are independent of admixture dosage.

b) As described in literature, the amount of SRA leached during the first cycle is relatively high and might be due to wash off effects. With increasing time and cycle number the leaching decreases and the cumulated plots tend towards a plateau. For cycles (2-7) the cumulated plots in Figure 82 indicate that the leaching process can be assumed to be based on diffusion since the cumulated leaching over time seem to follow a $\sqrt{t}$-correlation. As mentioned in Hohberg [233], the species of interest might however not be fully leachable by diffusion if a fraction is inactivated and associated to the binder. For that fraction, the leaching rate is determined by dissolution of the cementitious matrix itself or by an organo-mineral phase contained therein.

c) For each mortar type, a master curve is obtained when the leached amount is plotted relative to the initial SRA dosage. This implies that a certain equilibrium between SRA in eluate (leached out) and in pore solution (remaining) has to establish during each leaching cycle.

To prove the above equilibrium hypothesis, the SRA starting and ending concentrations were compared for each cycle. Using a mass balance, the remaining SRA concentration for the following cycle could be calculated from the measured SRA loss. The results of this incremental approach for mortar series LM are displayed in Figure 83. The results for mortar series CM & SM are similar and can be found in appendix Fig.A6- 5 & Fig.A6- 6 respectively.

Figure 83 shows that independent of initial dosage, a linear correlation between SRA remaining in the sample ($C_{tot,ti}$) and measured in the eluate ($C_{eluate,ti}$) can be found. The slope of this linear regression is independent of initial admixture dosage, which supports the equilibrium hypothesis. However, the intercepts correlate with the initial SRA dosage. Higher dosages lead to larger intercepts.

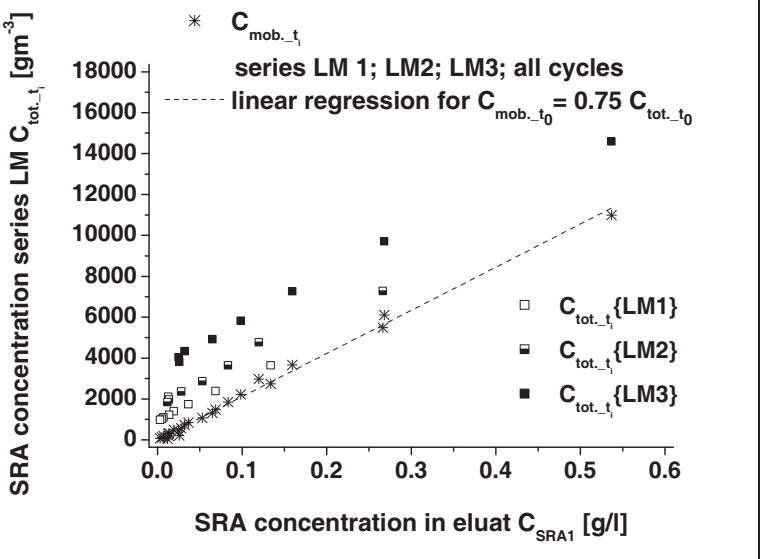

Figure 83: Direct linear correlation between remaining SRA concentration in series of typ LM and admixture content in eluate

Surface response optimization delivers best fit if intercept of linear regression is at zero and $C_{mob._t0}$=75% $C_{tot._t0}$

SRA dosage:

LM1 (0.5% SRA1);

LM2 (1.0% SRA1)

LM3 (2.0% SRA1)

The linear behaviour with non-zero intercepts indicates that SRA can be distributed between mobile and immobile fractions. As already indicated in Figure 82, mortar series LM comprises a leachable SRA portion of about 75%.
For mortar series CM and SM, the incremental approach delivers similar results (Fig.A6- 5 & Fig.A6-6). Both mortars types comprise a pure Portland cement as binder and the mobile fraction of SRA is ~60% of the total. We can therefore wonder why mortar types SM and CM comprise an approximately similar leachable portion of SRA (60%), whereas it is higher for mortar type LM (75%).

In Table 30, the binder compositions of the three mortar types are displayed. For mortar type LM, 35% of NPC were replaced by limestone. It turns out that the immobile fraction of SRA can be directly related to the actual fraction of Portland cement in binder, which therefore has a fixed capacity of immobilizing SRAs. For these mixes it is 40% of the initial dosage for all types of mortar independent of the initial dosage of SRA1. Mix designs with more cement would immobilize more SRA, and vice versa.

Table 30: Binder composition of mortar types and mobile/immobile fractions of SRA1

mortar type	binder composition			C_{SRA_mobile}	$C_{SRA\_immobile}$ with error	
	NPC	limestone	clinker			
[-]	[wt.-%]	[wt.-%]	[wt.-%]	[%]	[C_{SRA_tot}/C_{NPC} in %]	[$C_{SRA\_tot}/C_{clinker}$ in %]
CM	100	0	95	60	40	42
SM	100	0	95	60	40	42
LM	65	35	62	75	38	40
				avg	**39**	**42**
				rel. sd	**2%**	**2%**

As a reminder, for mortars that contain both admixtures, the results on the mobile and the immobile fractions of SRA are based on the assumption that for the GC a systematic error is involved and that SRAs are leached independently of the presence of SP-PCE.

To cross check the results obtained above, a second step can be taken. Heretofore, the role of the SRA multicomponent nature is examined.

According to Table 2, the 3 main ingredients of SRA1 consist of 80% DPTB; 15% DPG and 5% DPDTB.

Let us assume that the immobile fraction is correct but that only one component adsorbs onto hydrates. This would be DPTB, because it is the only one present in large enough amounts to account for the 40% loss.

If the immobile fraction can be attributed to DPTB, the new composition of the SRA that remains to be potentially be leached, would comprise a composition of **66.6 % DPTB**, 25 % DPG and 8.4 % DPDTB. This is, provided that the immobile fraction is fixed by the time the first cycle starts.

The above composition change is an important result. Indeed it explains that the GC measurement was indentifying only the DPTB. More important, it now leads to a quantitative agreement with TOC that determines the whole leachate.

We now examine how this influences the results outlined above. The quantification of leachable admixtures was performed using the average carbon loads. We recognize that these have to be adjusted according to their altered composition in the eluate.

In Table 31 the carbon loads of the initial SRA1 compound and the compositions for the leached residuals are given. We have to take into accounts that, for mortars with Portland cement as binder, 40wt.-% of the SRA1 are removed from the liquid phase. For the mortar containing limestone binder an efficient amount of 25wt.-% of SRA1 is effectively removed. Attributing those amounts to DPTB, the composition of SRA1 in the eluates can be calculated (columns 4 and 5 in Table 31). On this basis, the average carbon load of these new compositions is calculated (last row in Table 31).

Table 31: Calculated carbon load of initial SRA1 composition and composition of the leached admixture

ingredients		molar mass	carbon fraction	fractions in product	fractions in eluate for CM & SM	fractions in eluate for LM
[abrev.]	[-]	[g/mol]	[g_C/g]	[wt.-%]	[wt.-%]	[wt.-%]
DPTB	$C_{10}H_{22}O_3$	190	0.631	80	66	73
DPG	$C_6H_{14}O_3$	134	0.537	15	25	20
DPDTB	$C_{14}H_{30}O_3$	246	0.682	5	9	7
average carbon content [g_C/g]				**0.62**	**0.61**	**0.62**

From Table 31 we deduce that the carbon load does not change significantly. Especially for the mortar type LM (last column of Table 31) an adjusted recalculation is not necessary. For the other mortar types (CM, SM), it reveals that the leached amounts are underestimated by 2%. This causes all values concerning the leached amount of SRA1 to be underestimated by about 2% relative to the initial dosage. Regarding this, the immobile fractions given in Table 30 have to be corrected. This is outlined in Table 32.

Table 32: Corrected values for leachable and immobile fraction of SRA1

mortar type	binder composition			C_{SRA_mobile}	$C_{SRA\_immobile}$	
	NPC	limestone	clinker			
[-]	[wt.-%]	[wt.-%]	[wt.-%]	[%]	[C_{SRA_tot}/C_{NPC} in %]	[$C_{SRA\_tot}/C_{clinker}$ in %]
CM	100	0	95	**62**	38	40
SM	100	0	95	**62**	38	40
LM	65	35	62	**75**	38	40
				avg	**38**	**40**
				rel. sd	**1%**	**1%**

The data given in the above table show that due to the adjustment of the calculation the results improve with respect to the independence of the fixed fraction with respect to the mortar type and admixture dosage.

Based on these findings, it can be assumed that SRA is initially distributed homogeneously within the cement paste. In the course of hydration, about 40% of it gets associated to hydration products. In regard to chapters 8.3.3 and 8.3.4, these could be layered portlandite crystals. SRA1 could however also be immobilized in gel pores.

Concerning the amount of immobile SRA, in chapter 8.3.3 the loss of SRA after 28 days of hydration was in the range of about 33-45% (Table 25). Although, this was measured on samples hydrated under sealed conditions and comprising different degrees of hydration, these specific losses are in line with what was found in this chapter and may therefore be attributed to the immobile fraction of SRA.

More important, based on the above, the hypothesis of SP-PCE being leached independently of the SRA can be confirmed. This further implies that the immobile fraction of SRA1 can even more reliably be exclusively attributed to DPTB. This also means that the adsorption of SRA1 onto portlandite is most probably due to a selective adsorption of DPTB.

10.3.4 Successive equilibrium hypothesis

The hypothesis brought up on the equilibrium between SRA in eluate (leached out) and in pore solution has to be looked at in more detail. To do this, in Figure 84 the concentration of SRA1 in the eluate at the end of each cycle is plotted against the corresponding SRA content of the pore solution at the same time. For this, the capillary pore space of the mortars was calculated from evaporable/non-evaporable water content (Tab.A5- 2). Assuming full saturation and the remaining mobile fraction, the SRA concentration of the pore fluid was calculated for each sample. In Figure 84 this is outlined for mortar series CM (squares) and LM (circles). It shows that for both mortar types, the average SRA concentration in pore solution exceeds the one in the eluate by about two orders of magnitude. The

trend lines in Figure 84 indicate that independent of SRA dosage, a linear correlation (factor) can be found for each mortar type.

Figure 84: Relationship between SRA concentration in pore solution and eluate

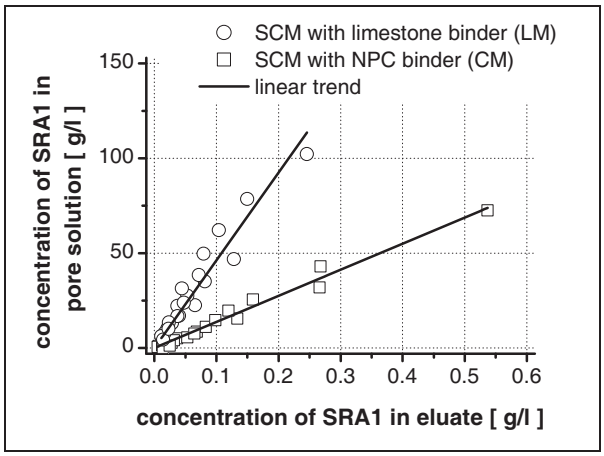

Figure 85: Relationship between concentration gradient ($C_{SRA\_eluate}/C_{SRA\_pore\ solution}$) and capillary porosity

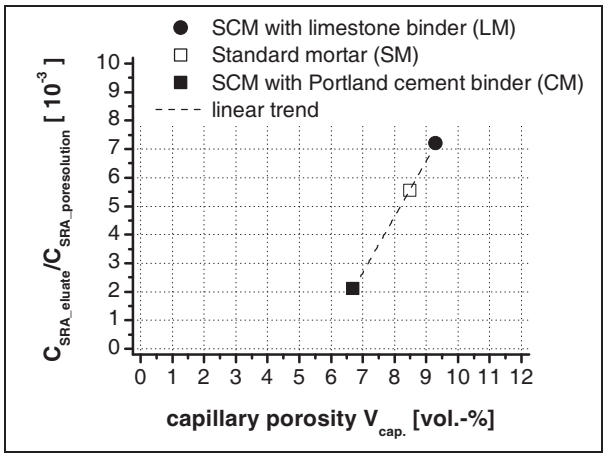

The difference in average concentrations between pore fluid and eluate implies the presence of a concentration gradient. These gradients can establish in the mortars and/or in the eluate. Whether gradients form and where they establish is determined by the effective diffusion coefficients of SRA in the liquid phase of the pore system and in the eluate.

We get a first clue about this by plotting the ratio of SRA concentration in eluate and pore solution against average capillary porosity of the mortar series. Figure 85 shows that this leads to a linear relationship. This suggests that the porosity determines the value of this ratio. Most probably this comes from the tortuosity and percolation of the pore system through which the SRA migrates. This would support a transport limited process.
In contrast, the average SRA concentration in the pore solution and the eluate comprise a specific correlation factor, which would support the equilibrium hypothesis. The evaluation of this will be the subject of the next section.

10.3.5 Determination of effective diffusion coefficients

In this section, effective diffusion coefficients are approximated using the results of the tank tests and the appropriate solutions of Fick's 2nd law according to subchapter 6.3.5. However, based on the above findings the boundary conditions outlined in 6.3.5.5 are first refined.

We recognize that the relative mass flow of SRA is similar and proceeds independently of the initial dosage of SRA (Figure 82). This means that, the starting concentration of a sample with low SRA dosage can be found at a higher cycle number of a sample with a higher initial dosage.

As an example, we consider the mortar type LM: From Figure 82 it can be deduced that after the second cycle ~50% of the initial dosage of SRA is removed. Consequently, sample LM03, that had a starting concentration of 2% SRA, comprises 1% of it at the start of the third cycle. This is similar to the initial dosage of LM02 (C_{SRA_ini}=1wt.-% o.b). Moreover, the mortar LM02 (C_{SRA_ini}=1wt.-% o.b) comprises an average SRA dosage at the the start of the third cycle similar to the initial dosage of mortar LM01 (C_{SRA_ini}=0.5wt.-% o.b.).
Based on this, the effective diffusion coefficient should be a constant for each type of mortar and independent of admixture concentration. Therefore, the evaluation of diffusion coefficients can be performed for each mortar type referring to the average relative amount of SRA leached, which facilitates the problem.

Concerning the evaluation of the diffusion coefficients according to the “infinite slab model” (6.3.5.4), the discrimination of SRA fractions, obtained in the previous chapter, is used to define the starting concentration C_a and the end concentration C_e of SRA for each leaching cycle. In particular, the starting concentration C_a refers to the mobile SRA fraction present before starting leaching tests whereas C_e can be attributed to the immobile fraction. The calculation of diffusion coefficients in the infinite slab model requires the determination of the average SRA concentration $C_m(t)$ present in the slab at discrete times. In this study, this refers to the remaining amount present at the end of each leaching cycle. Furthermore, the relative average concentration $C_r(t)$ accounts for the fraction of mobile SRA that is present after each cycle and can be calculated from $C_m(t)$ because the distribution of SRA between mobile and immobile fraction is already known (for details see 6.3.5.4).

Because the eluate was changed after each cycle one now has to treat these cycles independent of each other. For each cycle, the average relative concentration $C_r(t)$ is calculated according to (78). Then, the linearization approach outlined in 6.3.5.4 can be applied and the diffusion coefficient can be obtained thereof (for details see 6.3.5.4). As an example, the calculations for mortar series LM are outlined in Table 33.

Table 33: Calculation of diffusion coefficients according to the infinite slab model; mortar series LM

cycle	time	C_m	C_r	ln (C_r)	b(n)	D_a
[-]	[s]	[-]	[-]	[-]	[-]	[m²/s]
1	2419200	65%	55%	-0.60	-2.5E-07	-2.7E-12
2	2419200	48%	33%	-1.10	-2.1E-07	-2.3E-12
3	2419200	38%	20%	-1.60	-2.1E-07	-2.3E-12
4	2419200	32%	12%	-2.10	-2.0E-07	-2.3E-12
5	2419200	28%	7%	-2.61	-2.1E-07	-2.4E-12
6	2419200	27%	5%	-3.00	-1.6E-07	-1.8E-12
7	2419200	25%	3%	-3.54	-2.2E-07	-2.5E-12
8	2419200	24%	1%	-4.45	-3.8E-07	-4.2E-12
			average		-2.1E-07	-2.3E-12
			sd		2.5E-08	2.8E-13
			rel sd		12%	12%

In this table, the average SRA concentration C_m accounts for the amount of SRA relative to initial dosage and shows how much of the initial SRA is remaining at the end of the cycles (third column). The relative amount C_r denominates how much of the mobile fraction is remaining at the end of the cycle, where it refers to the total mobile fraction of SRA present at t=0.
In the sixth column of Table 33 b_n is the slope of ln(C_r) over cycle time of each cycle, from which the diffusion coefficient can be calculated using (82) in chapter 6.3.5.4 reading

$$b_n = \frac{ln\left(C_r\left(n-1\right)\right) - ln\left(C_r\left(n-1\right)\right)}{t_n} \tag{92}$$

and

$$D_n = \frac{b_n h^2}{\pi^2} \tag{93}$$

where:

b_n:	slope of ln(C_r) in cycle n	[-]
n:	cycle number	[-]
t:	cycle time	[s]
D_n:	diffusion coefficient of cycle n	[m²/s]

h: thickness of the infinite slab [m]

From Table 33 one can see that over the whole leaching test we find the diffusion coefficient to be approximately identical. An exception is the last leaching cycle 8 in which the evaluated coefficient is increased. This phenomenon occurred also for mortar type SM and will be discussed later on.

For all mortars investigated the diffusion coefficient can be found to be a constant and independent of initial SRA1 dosage. This is shown in Figure 86. Note that the linear trends shown in this figure is just to indicate the average values of the individual b_n evaluated. The graphs must not be confused with a continuous treatment of the individual leaching cycles.

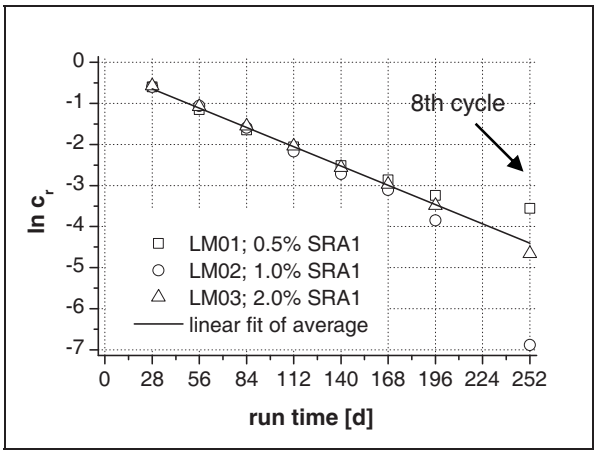

Figure 86: Evaluation of apparent diffusion coefficients according the „infinite slab“ model

apparent diffusion coefficient D_a:

$D_{a,LM}$=2.23 E-12 [m²/s]

$D_{a,SM}$=1.91 E-12 [m²/s]

$D_{a,CM}$=1.09 E-12 [m²/s]

a) mortar series LM

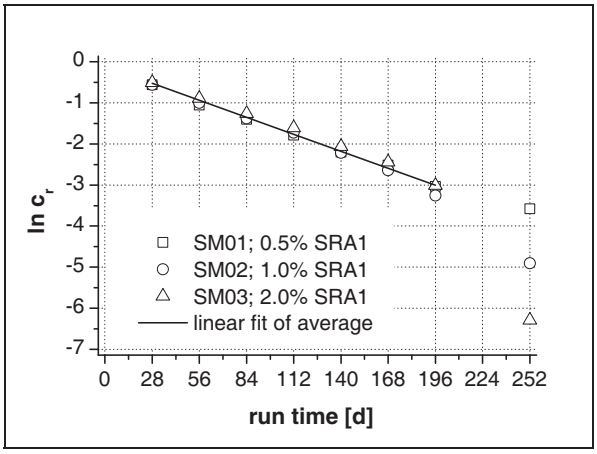

b) mortar series SM

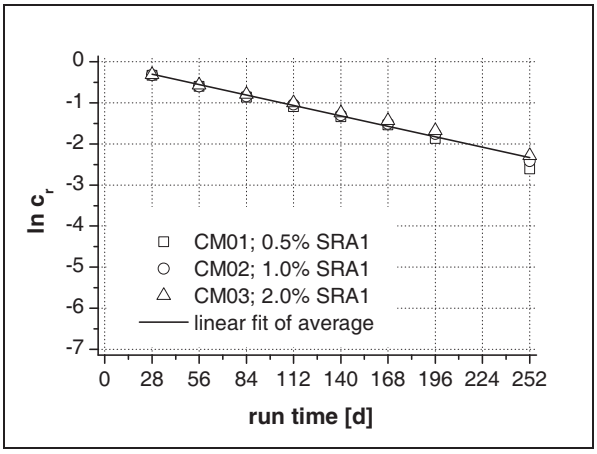

c) mortar series CM

In Figure 86 a)-c) it is shown that, indeed for all mortars, an approximately constant diffusion coefficient is obtained. As mentioned above, for the eights cycle, mortar types LM and SM show a deviation from this. This is most probably due to the fact that for these mortars at the end of cycle number 7 the mobile fraction of SRA is almost depleted (compared to Figure 82). In contrast, mortar type CM still comprises a significant amount of mobile SRA after cycle 7.

The diffusion coefficients evaluated using the “infinite slab” model are to be referred to as apparent diffusion coefficients. In a previous chapter, the investigation of SRA losses due to solid adsorption and phase transformation were examined (chapter 8.3.3 for high bulk concentrations of SRA; chapter 8.3.4 for low bulk concentrations of SRA in pore solution). According to the findings of chapter 6.3.5.2, we recognize that due to the interaction of SRA with the solids, the effective diffusion coefficient is different from the apparent one evaluated above.

We now conclude that the distribution of SRA has to be reconsidered upon this to provide a better estimate of the effective diffusion coefficient. About 40% of the SRA dosages are to be found strongly associated to solids and cannot be removed by diffusion. The other fraction is mobile and can be discriminated into an isotropic solution of monomers or micelles and a fraction that is subject to self-aggregation in vicinity of solids and/or solid adsorption.

The immobile fraction of SRA is most probably only released along the dissolution of the cementitious skeleton.

In contrast, the fraction of the mobile SRA that undergoes self-assembly or solid adsorption can be assumed to be leachable by diffusion as long as it is part of the capillary pore system. However, its reference concentration in solution that is pertinent for diffusion is changed.

Based on the findings in chapter 8.3.4, we can assume that about 33% of the mobile fraction is expelled from pore solution and may be subjected to aggregation at the internal surface of the capillary pore space. This directly impacts the retardation term *R*, which is the ratio between apparent and effective diffusion coefficient according to equation (74). In the course of leaching, self-assemblies vanish and/or SRA molecules desorb if the pore solution depletes from SRA.

We now can think of the following scenarios.

a) The fraction of mobile SRA which is not part of the pore solution serves as a buffer. The effective SRA concentration of the pore solution can be assumed to be constant until this reservoir is depleted. After that, the concentration of SRA in pore solution decreases. This would enforce Fick's first law to be applicable up to this specific point in time. We can reject this hypothesis because the leaching process does not follow a simple $\sqrt{t}$-law.

b) A constant ratio between concentration of SRA in bulk and in pore solution (as observed in 8.3.4, compare to Figure 59) establishes. Therefore, the values used for the starting concentration in the infinite slab model are too high. This causes the assumed concentration gradient to be overestimated and hence the diffusion coefficient to be underestimated.

It is of high interest how the effective diffusion coefficient can be derived from the results obtained. For this we refer to the solution of Fick's second law (76) given by Hohberg [233], introduced in subchapter 6.3.5.3. This equation can be used to estimate the effective diffusion coefficient as follows:

The amount of SRA in the eluate is considered to be accurate. However, the concentration in the pore solution is assumed to be overestimated due to the 33% of the mobile SRA associated to self-assemblies and/or solid adsorption (chapter 8.3.4). Using (76) we now can write

$$\sum E(t) = 2ac_{mob}\sqrt{\frac{D_a t}{\pi}} = 2ac^*_{mob}\sqrt{\frac{D_e t}{\pi}} \tag{94}$$

and

$$c^*_{mob} = (1 - 0.33)c_{mob} \tag{95}$$

where:

c^*_{mob}: mobile fraction of SRA in pore solution [mol m^{-3}]

Because time of contact and exposed surface remain unaffected we obtain (96)

$$D_e = \frac{1}{(1 - 0.33)^2} D_a \tag{96}$$

From (96) we get a better estimate on the effective diffusion coefficients of each mortar type ($D_{e,LM}$=5.0 E-12 m²/s; $D_{e,SM}$=4.3 E-12 m²/s; $D_{e,LM}$=2.4 E-12 m²/s).

10.3.6 Diffusion in sample and in eluate

Still, the evaluation of the effective diffusion coefficient faces a severe issue, which is the equilibrium hypothesis made in regard to the discrimination of the immobile fraction of SRA in subchapter 10.3.3. There, we found the ratio between average SRA concentration in pore solution and in the eluate to be a constant for each mortar type (compare to Figure 84 & Figure 85). Indeed, this seems to be a contradiction concerning an equilibrium condition. Let us assume to have derived a good approximation of the apparent diffusion coefficient. Using the one-dimensional solution of Fick's second law for the tank test and virtually increasing the cycle time, we find that the leached amount of SRA steadily increases with contact time.

However, the diffusion length for SRA in the eluate might lead to a concentration gradient if the binary diffusion coefficient $D_{0,SRA}$ is sufficiently low. The question arises whether a lower limit for binary diffusion coefficients exists, so that the diffusion mechanism in the eluate decelerates the transport or mass flow in the mortar. In what follows, this will be the subject of examination. Unfortunately the binary diffusion coefficient of SRA1 is not known and has to be approximated.

If a gradient establishes in the eluate, the effective concentration gradient for the mortar interior is reduced and the effective diffusion coefficients evaluated so far may be underestimated. To solve this issue, the concentration gradients in the mortar slab as well as in the eluate have to be described. Once this is properly done, a binary diffusion coefficient can be found that enables the equilibrium between the SRA concentration in pore solution and in the eluate to establish.

In a first attempt, the mortar/eluate interface is examined focusing on the mortar phase. We assume a diffusion coefficient $D_{eq,\,mortar}$. Moreover, the measured amount of SRA is taken equal to the maximum that can be mobilized during the leaching cycle. This requires the mass flow to reach zero up to the end of this cycle, reading

$$J(t_n) \cong 0 \tag{97}$$

Using (97) as a governing boundary condition the system of equations (98) has to be solved.

$$0 = \begin{bmatrix} E_{LM,j,n} \\ E_{SM,k,n} \\ E_{CM,l,n} \end{bmatrix} - 2A_{mortar} \cdot \begin{bmatrix} c_{LM,j,n} \\ c_{SM,k,n} \\ c_{CM,l,n} \end{bmatrix} \cdot \sqrt{\frac{t_n}{\pi}} \cdot \begin{bmatrix} \sqrt{D_{eq,LM}} \\ \sqrt{D_{eq,SM}} \\ \sqrt{D_{eq,CM}} \end{bmatrix} \tag{98}$$

where:

***E*:**	amount of SRA leached from mortar in cycle n	[mol m^{-3}]
***c*:**	concentration of mobile SRA in cycle n	[mol m^{-3}]
***j*:**	index for the initial dosage of SRA for series LM; j=1, 2, 3	
***k*:**	index for the initial dosage of SRA for series SM; j=1, 2, 3	
***l*:**	index for the initial dosage of SRA for series CM; j=1, 2, 3	

We now obtain the diffusion coefficients D_{eq} that account for the presence of a certain SRA concentration at the interface between mortar and eluate. This causes the mass flow out of the mortar to reach zero at the end of each leaching cycle. However, due to the change of eluent, the diffusion can continue in the next cycle.

The results of the calculation are displayed in Table 34, where the average values for D_{eq} for each mortar type are given.

Table 34: Average efficient diffusion coefficients of mortar series

mortar type	LM	SM	CM
$D_{eq.}$ [m²s^{-1}]	1.47E-11	1.38E-11	1.36E-11

In Figure 87, the simulated leaching (lines) and the measured cumulated leached amount of SRA are displayed (symbols). The simulations for mortar types LM and SM are displayed in annex (Fig.A6- 7 & Fig.A6- 8). From these graphs it can be deduced that the diffusion coefficients obtained for each mortar type are quite similar and account for the data well.

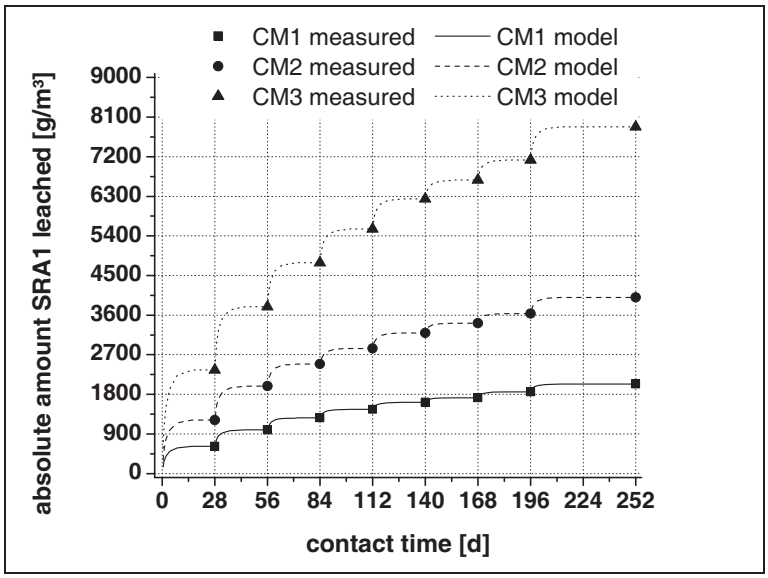

Figure 87: Evaluation of the diffusion coefficients $D_{eq.}$ for mortar type CM

SRA dosage:

CM1 (0.5% SRA1);

CM2 (1.0% SRA1)

CM3 (2.0% SRA1)

Diffusion coefficients

CM1: $D_{eq.\_28d}$ = 1.36 1E-11 m²/s

CM2: $D_{eq.\_28d}$ = 1.33 1E-11 m²/s

CM3: $D_{eq.\_28d}$ = 1.37 1E-11 m²/s

In the next step of our examination, the approximated diffusion coefficients are used to calculate the concentration gradients for the pore solution in the mortar slabs. To obtain such a concentration profile we use a special solution of Fick's second law assuming a temporary plane-source of SRA so that at t_0 all SRA molecules are located in the y-z-plane at x_{mortar}=0 and $C_{SRA}(0,0)$=>∞ reading

$$c(x,t) = \alpha t^{-\frac{1}{2}} exp\left(-\frac{x^2}{4D_{eq.}t}\right) \tag{99}$$

where:

***α*:** constant that accounts for the power of the source [g l^{-1}s$^{1/2}$]

With this, we can now calculate the concentration of pore solution for all cycles over the whole leaching test by accounting for the cumulated leached amount of SRA and the saturated capillary porosity of the mortars. Furthermore, based on the assumption on the effective concentration of pore solution made above, we can evaluate α using

$$\int_{-\frac{h}{2}}^{\frac{h}{2}} c_{poresolution}(x,t_n)\partial x = \int_{-\frac{h}{2}}^{\frac{h}{2}} \alpha t^{-\frac{1}{2}} exp\left(-\frac{x^2}{4D_{eq.}t}\right)\partial x = \overline{c}_{poresolution}(t_n) \tag{100}$$

where:

$\bar{c}_{poresolution}$: average concentration of SRA in pore solution at the end of cycle [g l^{-1}]

h: slab thickness [m]

Based on the findings in chapter 8.3.4, we can assume that 33% of the mobile SRA fraction is associated to self assemblies and/or solid surfaces so that the average pore solution concentrations are:

$$\bar{c}_{poresolution}(t_n) = \frac{c^*_{mob.}(t_n)}{\phi_{cap.}} = (1-0.33)\frac{c_{mob.}(t_n)}{\phi_{cap.}} \quad (101)$$

The values for $c_{mob.}(t_n)$ are given in Figure 83 (for mortar type LM) as well as Fig.A6- 5 & Fig.A6- 6 (for CM & SM). Using them in equations (100) & (101), the concentration gradients of pore solution for each mortar type and each leaching cycle are obtained. The analysis of variation on the simulated average pore concentrations versus the measured average values is displayed in Table 35. The concentration gradients of mortar SM03 are displayed in Figure 88.

Table 35: Analysis of variation for the leaching simulation

model:	C(t)_measured=C(t)_simulated		
mortar type	**Adj. R²**	**F**	**Prob>F**
LM	0.998	12389	0
SM	0.996	4656	0
CM	0.998	12515	0

In a next step, the evolution of the concentration gradient in the eluate is examined focusing on the interface. There, the mass flow through the open porosity of the mortar experiences a sudden dilution because the area fraction of the open pores can be assumed to be much lower than the total surface that the mortar exposes to the eluate. To factor this in, we first introduce an area ratio that accounts for this specific surface fraction, which is then used as a dilution factor for the SRA concentration at the interface. Assuming that this surface fraction depends on capillary porosity and a factor f_{open} that accounts for the pore necks at the exposed mortar surface, reading

$$a_{porosity} = f_{open}\phi_{cap.}a_{mortar} \quad (102)$$

so that the dilution factor f_d is

$$f_d = \frac{a_{porosity}}{a_{mortar}} = f_{open}\phi_{cap.} \quad (103)$$

and

$$c_{eluate}(0, t_{2n-1}) = f_{open}\phi_{cap.}c_{poresolution}(|h/2|, t_{2n-1}) \quad (104)$$

where:

n: cycle number; n=1, ...,7

From (100) & (101) we already have the interfacial concentration $c_{poresolution}(l^h/_2 l, t_n)$. Using the dilution factor introduced above (103), the effective concentration of the eluate at the interface can be calculated with (104). However, the factor accounting for the open fraction of capillary porosity is unknown and has to be approximated. Moreover, the binary diffusion coefficient for SRA in the eluate $D_{0;SRA}$ is not available.

To solve these issues, we modify (100) to express c_{eluat} (x,t) as a function of the binary diffusion coefficient and maintain mass balance concerning the measured average SRA concentration of the eluate, reading

$$\int_{-x}^{x} c_{eluat}(x,t_n)\partial x = \int_{-x}^{x} \alpha t^{-\frac{1}{2}} exp\left(-\frac{x^2}{4D_{eq.}t}\right)\partial x = \bar{c}_{eluate}(t_n) \qquad (105)$$

where:

$\bar{c}_{eluate}$: average concentration of SRA in eluate at the end of cycle n [g l^{-1}]

x: length of the adjacent semi-infinite half space; -0.05 < *x* < 0.05 [m]

For the tank test setup, the semi-infinite adjacent spaces comprise a length of *x*=±0.05m (see chapter 6.3.5.4).

To solve this system of equations, the porosity factor and the binary diffusion coefficient remain variable. However, the following constrictions can be set up:

a) $0< f_{open} < 1$

b) $D_{0,SRA} > D_{eq.}$

c) $c_{eluate(0,tn)} = c_{poresolution(h/2, tn)}$

For each mortar type, a least square regression was performed using variable pairs of [f_{open}; $D_{0,SRA}$]. For the values (f_{open}; $D_{0,SRA}$) given in Table 36 a local minimum of the residual square sum is obtained. The results of analysis of variation on the model are given in columns 4-6 of Table 36 and indicate a good fit.

Table 36: Analysis of variation for modeling the dilution factor and the binary diffusion coefficient

model:	$C(t)_{measured}=C(t)_{simulated}$; $C_{mortar}(h/2,t_n)=C_{eluate}(0,t_n)$				
mortar type	$D_{0,SRA}$	f_{open}	**Adj. R^2**	**F**	**Prob>F**
LM	3.3 E-8	0.7	0.9998	258130	0
SM	3.3 E-8	0.6	0.9996	103846	0
CM	3.4 E-8	0.3	0.9994	69788	0

From Table 36 we can see that the binary diffusion coefficient evaluated is independent of the mortar type and is about 3.3E-8 m²/s. The factor accounting for open porosity is different for each mortar type. However, the model was tested for the whole range of possible values of f_{open} but for each type of mortar only one local minimum could be found. This is a strong indication that the results are reliable.

As an example of these calculations, the simulated concentration gradients of mortar series SM03 (2% SRA1) are displayed in Figure 88.

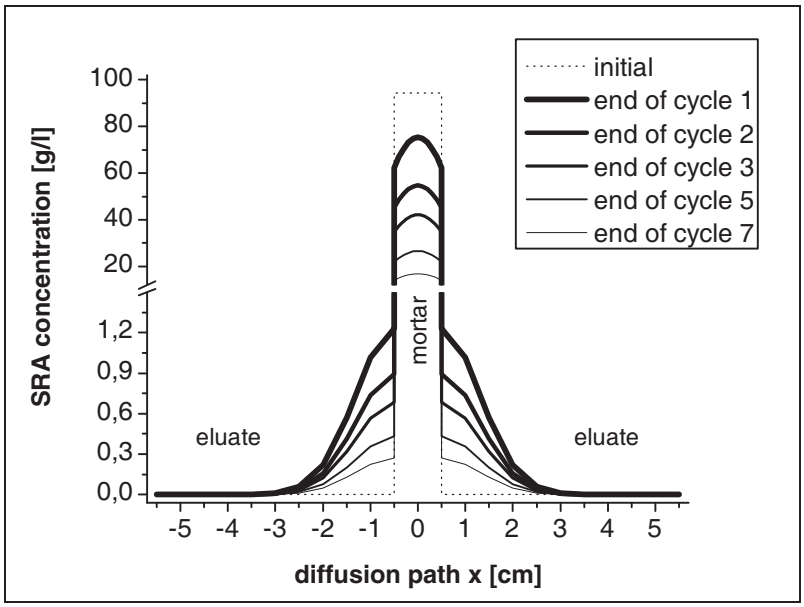

Figure 88: Concentration gradients of SRA in mortar SM03 (2% SRA1) and eluate at the end of leaching cycles; plot for D=3.3 E-8m²/s and f_{open}= 0.6

From the simulations above the following can be deduced. The binary diffusion coefficient evaluated has a small but non neglible impact on the diffusion process in the mortar. For larger values of $D_{0,SRA}$ the interface would be depleted from SRA and the leaching somewhat faster. However the overall rate would quickly be limited by the mass flow from the interior which is comparably low.

Still, this binary diffusion coefficient is unknown and has to be approximated. For that matter, values of other organic, non-ionic species are given in Table 37 (values for 20°C or 25°C).

Table 37: Binary diffusion coefficients for monoalcohols* and non-ionic surfactants**

species x	$D_{0,x}$	source	molar mass
	10^{-9} [m²/s]	[-]	[g/mol]
* ethanol	1.24	[253]	46.1
* 1-pentanol	0.794	[254]	60.1
* 2,2-dimethyl-1-propanol	0.789	[254]	88.2
** $C_{12}E_6$	0.05	[255]	450
** Triton X 100	0.47	[256]	624

We can see that those diffusion coefficients are rather low compared to the values estimated for SRA1 (3.3E-8 m²/s). Furthermore, at least for monoalcohols the binary diffusion coefficient decreases with increasing molecular weight. This is however not the case for the non-ionic surfactants displayed in Table 37.

Based on the above, it appears that the diffusion coefficient must be in the range of 0.5 < $D_{0,SRA}$ < 0.8 E-09 m²/s, rather than 3.3 E-08 m²/s.

For such a range of diffusion coefficients, the diffusion of SRA in the eluate decelerates the mass flow from the mortar interior, leading to a significant decrease of the mass flow rate at the end of the leaching cycle. The system would not reach a true equilibrium but the drastic mass transfer decrease would macroscopically give the impression that this was the case.

10.3.7 Summary

The analysis of the tank test led to the conclusion that transport in the eluate is rate limiting towards the end of each leaching cycle. It causes the systems to give the impression that it reached equilibrium, but it is not the case. Because of this, the periodic refreshing of the water was a good choice to "reactivate" the leaching. Performing the test with a stirred solution would however have been better.

Apart from this we could finally establish that the SRA is split between a mobile and an immobile fraction. The amount of the latter depends on the clinker content.

10.4 Cyclic leaching and drying

10.4.1 Results

The quantification of SRA leached due to cyclic leaching and drying is displayed in Figure 89 and expressed relative to the initial dosage. Additionally, the relative loss of the mortar series subjected to permanent leaching in tank tests is given.

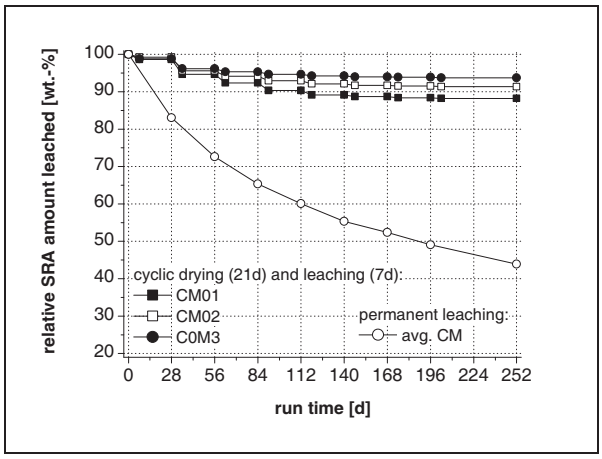

Figure 89: Leaching of mortars subjected to cyclic leaching and drying

SRA dosage:

xM1 (0.5% SRA1);

xM2 (1.0% SRA1)

xM3 (2.0% SRA1)

a) mortar series CM

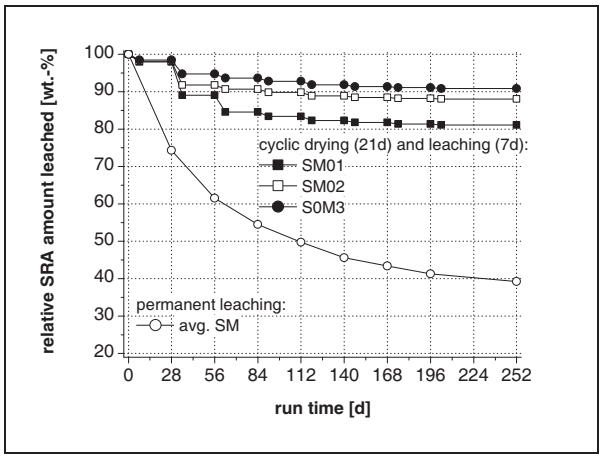

b) mortar series SM

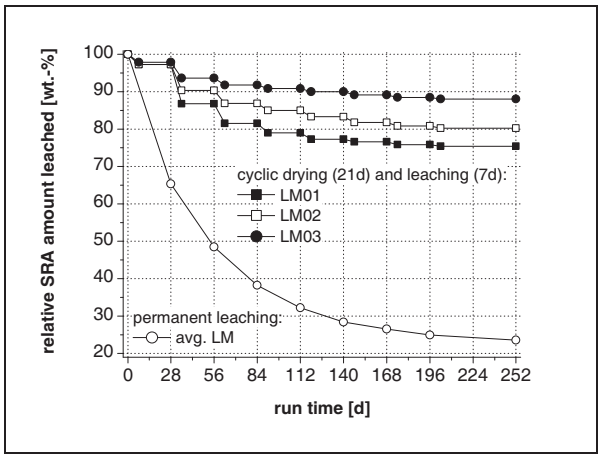

c) mortar series LM

Although, not comparable due to different absolute contact time with the eluate, the amount of SRA leached in the cyclic regime is significantly decreased. Note that for cyclic drying and rewetting the tests started with a drying cycle. For this reason the losses in the first leaching cycle is different from that of the tank tests with permanent leaching, for which leaching of mortars started with full saturation (solid lines with hollow circles in the above figure).

It can be seen that, in contrast to permanent leaching, the relative amounts leached per cycle depend on the initial dosage of SRA. The lower the dosage, the higher the relative amount of SRA leached. One can furthermore take from Figure 89 that with increasing cycle number, the amount of SRA leached decreases drastically. As an example, after the fourth cycle, more than 80% of the SRA leached throughout the test are removed from the samples independent of the mortar type and the initial dosage.

10.4.2 Discussion

In a first step, for each mortar type the diffusion coefficients, that were obtained previously, are used to simulate the leaching sub cycle. The results show that the leached amounts predicted are far too high. This comes from the drying sub-cycle. Indeed, at the beginning of each leaching cycle the samples are partially saturated. Once immersed into the eluent, the partially saturated samples first saturate and then the diffusion based leaching starts. Moreover, it can be assumed that the ingressing water from the exterior may cause a transport of some SRA towards the mortar interior during the saturation process. As a result, the effective diffusion length for the SRA to reach the eluate increases drastically. This may explain that the leaching rates for the higher cycle number are substantially lower than calculated.

From the results obtained in this section, we conclude that for practical applications, leaching of SRA can proceed, but that its extent is low. In comparison to the permanent leaching in tank tests, in which these mortars loose almost the total amount of their mobile SRA fraction, losses here are only of about 10% for the low porosity mortar series with Portland cement binder (CM), and 10-20% for the mortars comprising higher porosity (SM; LM). It is important to mention that, for these mortars, the relative amounts leached are lower for higher initial SRA dosages.

One now wonders how shrinkage reduction is impacted by the loss of SRA. This is the subject of the next section.

10.5 Impact of leaching on shrinkage reduction

10.5.1 Results - permanent leaching

In Figure 90, shrinkage isotherms of the mortars CM0 without SRA and CM3 with 2% SRA are displayed. The shrinkage isotherms of these mortars after 28days of hydration and wet curing are given by triangles.

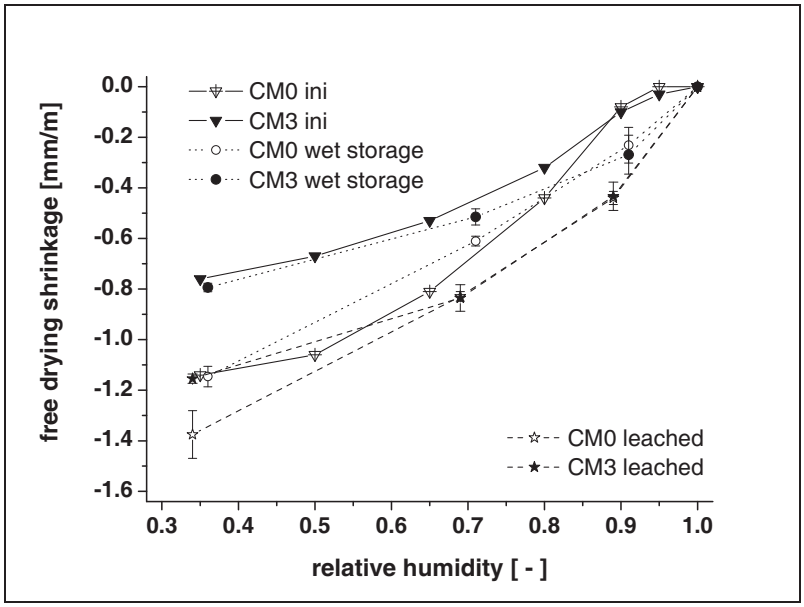

Figure 90: Shrinkage isotherms of mortar series CM0 and CM3 initially, after wet storage (252days) and after tank test (252days & mobile fraction of SRA completely removed);

Filled symbols indicate samples with SRA and open ones samples without.

In the above figure, it can be seen that the deformations in presence of SRA are significantly reduced (filled triangles versus open ones). Moreover, the plots indicate that SRA effectively reduces deformations in the humidity range from 50 to 90% RH. No effect is seen for higher relative humidity. The same is true from 50% to 35% RH, where deformations evolve independently of SRA presence. Therefore, for mortar series CM, SRA1 does not contribute to additional shrinkage reduction below 50% RH.

During the tank tests, the duplicate series of mortar type CM were stored at 20°C/>95%RH. After completing the tank tests the shrinkage isotherms were measured. The series were split and stored at different relative humidity. From Figure 90 it can be seen that the duplicate samples, that were wet stored, comprise similar total deformation at 35% RH, whilst at higher relative humidity the deformations are slightly enhanced with respect to their non-aged references. Because no SRA was removed during wet storage, this must come from structural changes due to the slight but ongoing hydration or ageing phenomena.

From data on mortar CM0 we can deduce that permanent leaching impacts drying shrinkage (hollow stars). Over the whole range of humidity the total deformations are increased. More important, after completing the tank tests, the mobile fraction of SRA in mortar CM3 is completely removed. In the capillary range of humidity (> 50%RH) the drying deformation of CM3 (black stars) is similar to the samples without SRA. However, at low relative humidity the deformation of the mortar containing SRA is nevertheless reduced. This is also true for mortar series CM1 and CM2.

In Figure 91 the shrinkage isotherms of mortars LM0 and LM3 are displayed. The shrinkage isotherms measured initially show that SRA effectively reduces drying deformations. Again, the humidity range, in which SRA1 is active, can be said to be 50 to 90%RH, which is in line with mortar type CM.

In contrast to mortar CM, the duplicate samples of LM (wet stored) comprise no difference in deformation in the capillary range of humidity (> 50% RH) but the shrinkage reduction for the SRA containing mortar remains at low humidity (35% RH). The altered shrinkage behaviour of the wet stored samples must come from ageing phenomena because no SRA was removed. The most probable explanation is that microstructural changes in LM3 compensate the shrinkage reduction from SRA1. Unfortunately this issue cannot be tackled further because of lacking data.

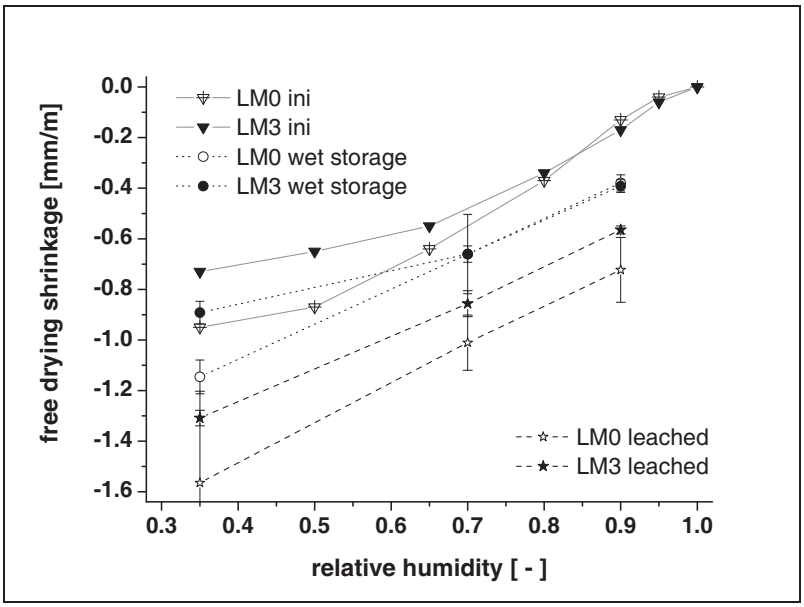

Figure 91: Shrinkage isotherms of mortar series LM0 and LM3 initially, after wet storage (252days) and after tank test (252days & mobile fraction of SRA completely removed) ;

Filled symbols indicate samples with SRA and open ones samples without.

In contrast to mortar type CM, after the complete removal of the mobile fraction of SRA in LM3, the SRA containing samples still seem to comprise the lower deformations over the whole range of humid-

ity. However, the increments of the drying strain between 90 and 70%RH are approximately identical or, in regard to the error bars given, not significantly different. This may indicate that the measurement suffered from an error that may have been a gauge displacement. From this similar strain increment in this humidity range, one concludes that the SRA effect has vanished with the complete removal of the mobile SRA fraction. In contrast, between 70 and 35%RH the strain increment of the SRA containing samples is lower than that of the reference SM0. From this one can conclude that, again, the immobile fraction of SRA seems to contribute to shrinkage reduction.

In Figure 92 the shrinkage isotherms of mortars SM0 and SM3 are displayed. The ones measured initially show that SRA effectively reduces drying deformations. Again, this concerns the humidity range from 50 to 90%RH, which is in line with mortar types CM and LM.
In contrast to LM and CM, the wet stored duplicates that contain SRA comprise higher shrinkage deformations in the capillary range of humidity. However, a closer look on the evolution of deformation between the adjacent relative humidity reveals that the increase in deformation between 90 and 70% RH as well as between 70 and 35% RH is lower for the SRA containing sample. This, again, is indicating that the measurement suffered from an error that concerns the reference length. Again, the drying strain increments indicate, that the SRA effect vanishes in the capillary range of humidity with the removal of the mobile SRA fraction, whilst it remains for low humidity.

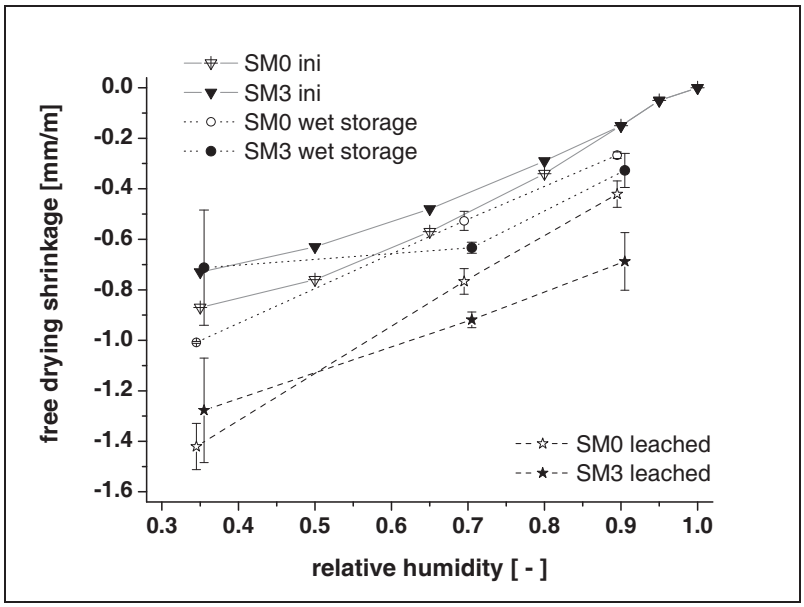

Figure 92: Shrinkage isotherms of mortar series SM0 and SM3 initially, after wet storage (252days) and after tank test (252days & mobile fraction of SRA completely removed) ;

Filled symbols indicate samples with SRA and open ones samples without.

As concluded for the mortar types CM and LM, the results on mortar series SM indicate that the immobile fraction of SRA1 contributes to shrinkage reduction.

10.5.2 Discussions on permanent leaching

The drying shrinkage of samples subjected to permanent leaching was measured. The results show that after permanent leaching, in which the mobile fraction of SRA is completely removed, the SRA containing samples still comprise a shrinkage reduction at 35%RH. This result was found for the whole set of mortars investigated and is therefore independent of the mortar type and the initial SRA dosage. It implies that the immobile fraction of SRA contributes to drying shrinkage reduction. The question now arises about why the shrinkage isotherms measured before leaching do not show this also.

For all mortars shown above, the shrinkage between 50% and 35%RH was similar for each mortar type, hence independent of the presence of SRA1. Unfortunately, for the samples exposed to leaching

the data points at 50% RH are lacking. Due to this, a clear distinction of impacts from either SRA fraction can so far not be discussed in detail.

From the leached series of mortar type CM it could be deduced that the shrinkage reducing effect in the capillary range of humidity vanishes with the complete removal of the mobile fraction of SRA1. This is true for all series of this type (CM1; CM2; CM3). Moreover, the wet stored duplicates indicate that the shrinkage due to storage/ageing increases but the SRA effect remains. Based on this, one concludes that the mobile fraction reduces the average capillary pressure, whilst the immobile fraction increases disjoining pressure.
However, the results obtained from mortar types LM and SM are somewhat different concerning the capillary range of humidity. Although an error for the measurement was considered, for those samples the SRA might have remained to some extend, which then would imply that the immobile fraction contributes to shrinkage reduction over the whole range of humidity.

Concerning the shrinkage reduction that remained, the immobile fraction of SRA might contribute to this by another phenomenon that has been found to be altered in presence of SRA. For example if drying creep were reduced in presence of SRA at least the results found for low humidity could be explained.

At this stage and due to lacking data on microstructural changes caused by leaching, the issue of discriminating these impacts cannot be taken further. Concerning a possible contribution of creep to the overall deformations observed the impact of cyclic drying and rewetting or leaching is the subject of the next section, in which this phenomenon is covered by the measurements performed.

10.5.3 Results on cyclic leaching and drying

The results on deformation during cyclic leaching and drying for mortar types CM, LM and SM all show similar trends. Because of this, the mortar type CM is taken as “representative” and discussed in the following. Data for mortar types SM and LM are given in the annex (A6).

In Figure 93 the deformations of mortars CM0 and CM3 during the cyclic regimes are given. The sub-figures are arranged in such a way that a comparison from left to right enables to discriminate between the impact of SRA. The differences between impact of leaching and the impact of inert resaturation can be discriminated vertically.

For all the sub-figures given, hollow squares indicate the total drying deformation at the end of the drying sub-cycle. The black squares indicate how much the samples recovered in the course of resaturation. Over the whole tests, these black squares also express the cumulated drying creep.

In the upper part of those figures, the filled circles indicate total deformation per cycle. The hollow circles indicate the absolute creep per cycle and the half-filled circles indicate the reversible or elastic sample deformation per cycle.

a) CM0 – cyclic leaching (without SRA)

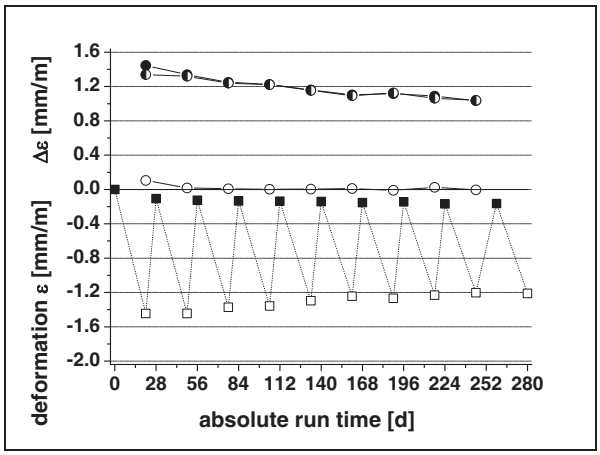

b) CM3 – cyclic leaching (with 2% SRA)

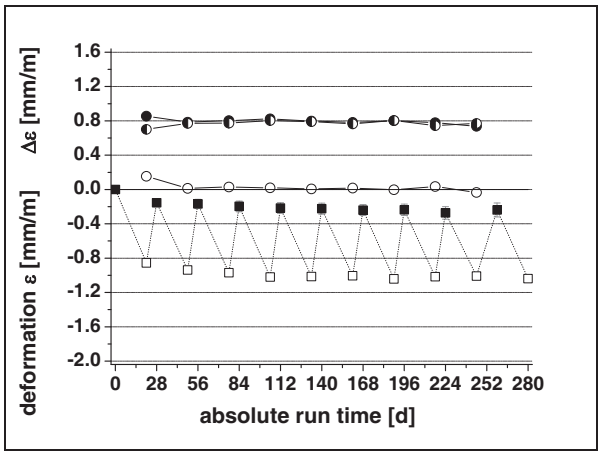

c) CM0 – inert resaturation (without SRA)

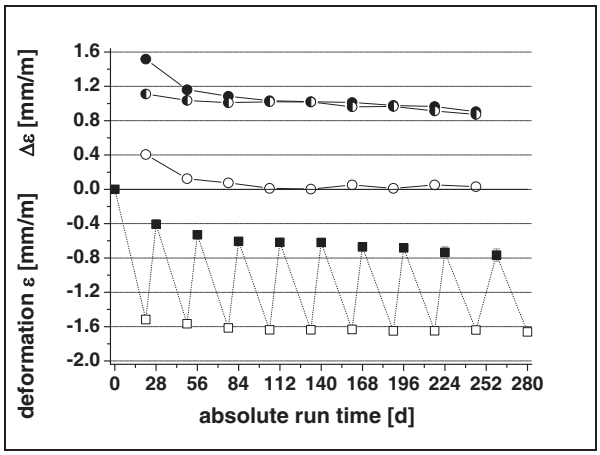

d) CM3 – inert resaturation (with 2% SRA)

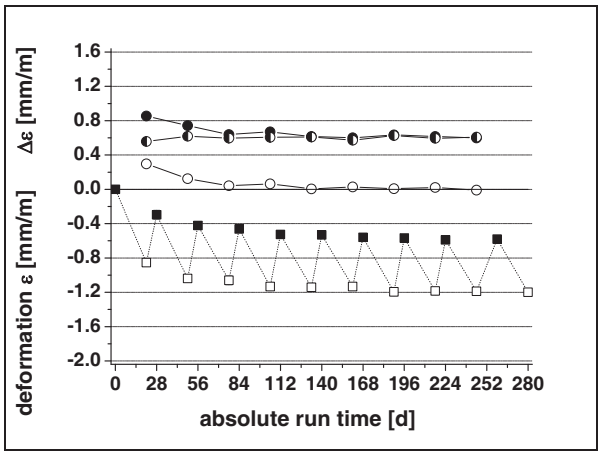

Figure 93: Shrinkage of mortar series CM during cyclic leaching / drying and cyclic rewetting / drying

Legend:

- absolute deformation per cycle
- absolute elastic deformation per cycle
- absolute creep deformation per cycle
- dry at 35% RH
- wet, cumulated creep

10.5.3.1 Impact of cyclic leaching on shrinkage reduction

From Figure 93 it can be seen that due to SRA, the shrinkage of CM3 for the first drying cycle is significantly reduced from about -1.5mm/m to 0.8mm/m or 47% respectively.

For the reference without SRA in Figure 93a, the first resaturation reveals that the total drying deformation is mainly reversible but is also accompanied by creep (10%). During cyclic drying and leaching both the elastic and the irreversible deformations decrease. Moreover, this leads to a slight decrease of the total deformation if the initial sample size is referred to (trumpet shape in Figure 93a).

In contrast, in presence of SRA (Figure 93b) the first drying cycle reveals that creep also accompanies elastic deformation. However, the elastic deformations over the whole test remain constant and are almost unaffected by leaching (Figure 93b). This is not surprising because in the previous section the amount of SRA leached from CM3 was found to be about 6% of the initial dosage at the end of the tests.

The fraction of irreversible deformation of these samples is about 25% of the total. However, if the absolute values of creep in Figure 93a and Figure 93b are referred to, the drying creep in presence of SRA1 is only slightly increased. Independent of the presence of SRA, creep vanishes after the first few drying cycles.

The irreversible shrinkage (or drying creep) results were obtained from length measurement after resaturation. In Figure 94 the average values of mass change of the specimens of mortar series CM0 and CM3 are displayed. On the right side of Figure 94 this is given for cyclic leaching and drying. The right subfigure contains data for cyclic drying and rewetting. In this figure, data displayed using lines and symbols indicate the mass change in the course of cyclic drying and resaturation. Filled squares on solid line indicate the adsorption/desorption process of reference mortar CM0 without SRA, hollow circles on dashed line indicate the mass change of the mortar containing the high dosage of SRA1 (2wt.-% of cement). In the upper part of the graphs, black squares indicate cumulated drying creep of CM0, hollow circles show the cumulated drying creep of the SRA mortar.

From this figure it can be seen that for the SRA containing mortar CM3, independent of the cyclic regime, the time for the resaturation subcycle was not sufficient. Indeed, in contrast to mortar without SRA, these samples are not able to achieve their initial degree of saturation. This comes from the reduced surface tension of the pore fluid in presence of SRA. As described in literature, water sorption of mortars and concretes containing SRA is decelerated [182].
For samples exposed to cyclic leaching and drying this proceeds up to cycle number 7. After this cycle the initial saturation is reached. After the 8th cycle the mass gain due to resaturation exceeds the initial water content. The question now arises about how this impacts the results of drying creep.

a) cyclic drying and leaching

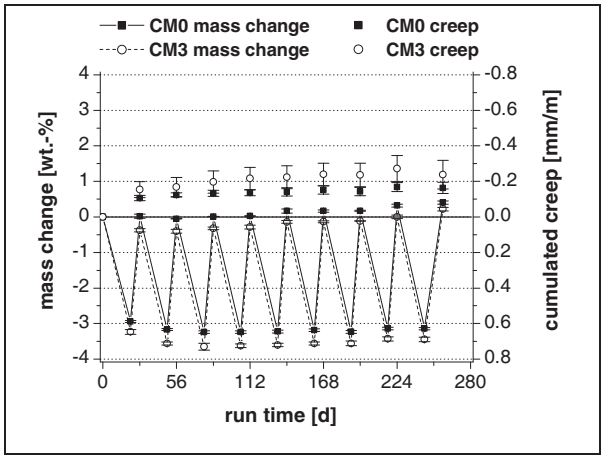

b) cyclic drying and rewetting

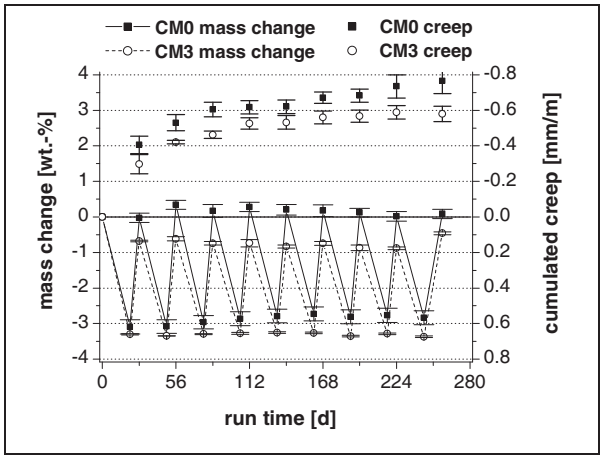

Figure 94: Adsorption/desorption and cumulated creep in the cyclic regimes of mortars CM0 and CM3

Cyclic leaching and drying: In case of cyclic leaching and drying (Figure 94a) the drying creep of the SRA containing mortar seems to be slightly increased. The error bars however indicate no significant difference. If nevertheless a trend is assumed, an increased drying creep of the SRA containing mortar is obtained. In a first attempt, this could be related to the insufficient resaturation of these samples. But this seems unlikely as the drying creep increases with increasing degree of saturation (after resaturation). Moreover, from the last few cycles, where saturation is complete, there is no significant impact on irreversible deformation.

In a next attempt, from Figure 94a one can see that the water loss of the SRA containing specimen is higher throughout the test and that the difference is almost constant. This comes from the enhanced drying of the porous system in presence of SRA and is in line with the findings of subchapter 5. Because the relative humidity imposed was low (35%RH), the increased drying creep in presence of SRA may come from the removal of adsorbed water that might have caused a collapsing of some LD-C-S-H (chapter 3.3).

Surprisingly, despite a constant value for water loss, with increasing cycle number the amount of water sorbed in the resaturation cycle increases independently of the presence of SRA. This could imply that leaching of easily soluble minerals is superimposed to carbonation. The first would cause a steady increase of the mass loss in the dry state. Samples are loosing more than just water. The second would cause a mass increase by the reaction of portlandite (74g/mol) with carbon dioxide into calcium carbonate (100g/mol) and water. Samples then gain more mass than by water sorption.

Cyclic drying and rewetting: Within this regime (Figure 94b), the effect of insufficient resaturation for the SRA containing mortar is even more pronounced. However, despite full saturation of the plain reference mortar CM0, the cumulated drying creep is higher than that of CM3. Here, the observed drying creep cannot only be related to enhanced drying in presence of SRA.

For this cyclic regime, the impact of carbonation can be supposed to be high. The effects of carbonation are later on discussed in subchapter 10.5.4.

10.5.3.2 Impact of SRA on cyclic drying and rewetting

Deformation of mortars CM0 and CM3 (2%SRA1) are displayed in Figure 93c and Figure 93d. It can be seen that the drying creep drastically decreases after the third cycle. Also, whereas the elastic deformations of the plain mortar slightly decrease with time, those of the SRA containing mortar remain constant over the whole test. Finally, it should be emphasised that the reduction of elastic deformations due to the SRA is unaffected by pure ageing phenomena.

10.5.4 Discrimination between ageing and leaching phenomena

10.5.4.1 Ageing and leaching of the reference mortar CM0 without SRA

Comparing Figure 93a and Figure 93c the effects of leaching and ageing can be discriminated. It can be seen that the major differences lie in the evolution of total drying deformation and the drying creep. Additionally the elastic deformations of the samples subjected to cyclic leaching are slightly higher but they decrease over time more than those in inert saturation.

The total deformation for the samples subjected to cyclic leaching decreases throughout the test. This most probably comes from leaching during which the dissolution of solids may cause a coarsening of the pore structure. As a result the average pore pressure would decrease, causing decreasing the elastic deformations and irreversible drying deformations. In contrast, samples which are subjected to cyclic drying and rewetting show a slight increase in both.

As a reminder, in the previous section the mass gain during saturation was found to increase with cycle number. The phenomenon was related to carbonation, which causes a mass gain. In what follows the impact of carbonation on shrinkage is focused on.

Concerning carbonation shrinkage (details can be found elsewhere [257-261]), portlandite and C-S-H which are part of the capillary pore system can react with carbon dioxide during the drying subcycles. Depending on the modification of the calcium carbonate forming this causes a volume increase of the reaction product in the range of 3 to 19vol.-%. For cementitious materials this results in a refinement of the pore space and at a given relative humidity the shrinkage strain increases thereof.

Let us assume that the portlandite fraction that is leached in the leaching tests carbonates in the case of the samples that are subjected to inert saturation. In the first case, the portlandite leaching leads to pore coarsening, whilst in the second case the chemical reactions cause a pore refinement.

In the first case, at a given relative humidity the average pore pressure decreases because the pore widening will drastically decrease the degree of saturation. This causes the energy to be utilized at the interfaces and the solid skeleton to be decreased, hence shrinkage deformation decreases.

In the second case the opposite behaviour is obtained, causing pore refinement. With the finer pores, the interfacial area that has to be created as well as the energy to be utilized at the solid skeleton increase. Therefore, shrinkage deformation increases. Because the carbonation is irreversible, a progress in carbonation leads to an increase in irreversible deformations.

For the mortars subjected to leaching, both the leaching (tank) and carbonation (drying) superimpose and a clear distinction can hardly be derived from the data at hand. Whilst leaching may decrease drying shrinkage, the carbonation during the drying cycle has the opposite effect. However, the increased irreversible deformations of the mortars subjected to cyclic drying and rewetting can be attributed to carbonation shrinkage.

10.5.4.2 Ageing and leaching of the SRA containing mortars

Concerning drying creep, the differences between ageing and cyclic leaching (Figure 93b and Figure 93d) are similar for samples with SRA as those without reported in the previous section. The samples subjected to cyclic leaching comprise the lowest extent of drying creep and the lowest elastic deformation.

For SRA containing mortars and cyclic leaching, the solid surfaces can be assumed to be covered with adsorbed SRA. This is supported by the findings of chapters 8.3.3 & 8.3.4 in which the solid adsorption was found to be about 33% of the mobile fraction of SRA. Also, from the quantification of the leached amounts of SRA in the previous chapter we obtained that during cyclic leaching the relative loss for mortars with high initial dosage was about 10% (Figure 89).
Based on this, the leaching of portlandite may be retarded by the presence of SRA adsorbed on the solid surface of the capillary pore system. In comparison to the SRA free reference, less portlandite is leached from the SRA sample, which then may carbonate during the drying subcycle. This could explain why the SRA containing samples show an increase in total shrinkage deformation throughout the leaching test, whilst the SRA free reference does not. In other words, the portlandite fraction that is not leached from the samples then may cause carbonation shrinkage in the drying subcycles.

Comparing the deformation of the mortars subjected to inert saturation in Figure 93c and Figure 93d it can be seen that overall the deformations in presence of SRA are reduced. In comparison to the corresponding samples subjected to leaching, the irreversible deformations are significantly higher. This most likely is due to enhanced carbonation shrinkage, because no portlandite was leached in these tests.

A comparison between deformations obtained with SRA but for the different regimes (Figure 93b and Figure 93d) reveals that the reversible deformations of the non-leached series are slightly lower. With the data at hand this can be attributed to the SRA loss of the mortar subjected to leaching. As a reminder, the main loss of SRA happened during the first cycles of the leaching series. From that, one concludes that, the increased elastic deformation of the leaching samples comes from the SRA lost in these cycles.

From the above findings, the impacts of leaching and ageing of SRA containing mortars can be better understood. The leaching of SRA to a low but significant amount increases the elastic deformations to some extent. Apart from that, the irreversible deformations are only remotely dependent on SRA and seem mainly determined by ageing phenomena and carbonation shrinkage in particular.

10.6 Concluding remarks

In this chapter, the dominating leaching mechanism for SRA1 was evaluated using tank tests. Based on the findings, this SRA can be discriminated into a mobile faction, which can be removed by diffusion, and an immobile fraction that cannot. In the course of hydration, about 40% of SRA1 gets associated to hydration products. The immobile fraction was found to be DPTB. That part of this compound would only be released with the dissolution of the solid matrix itself. In regard to chapters 8.3.3 and 8.3.4, DPTB could be associated to layered portlandite or could however also be immobilized in gel pores.

Concerning the most likely presence of SRA and SP-PCE in SCC, the hypothesis of SP-PCE being leached independently of the SRA could be confirmed.

A detailed study of the diffusion process showed that the low binary diffusion coefficient of SRA1 in the eluate decreased the diffusion of SRA from the mortar interior. This leads to a significant decrease of the mass flow rate at the end of the leaching cycle. Macroscopically this gives the impression that equilibrium conditions have been reached, but it is not the case.

The impact of the complete removal of the mobile SRA completely or almost completely eliminates the shrinkage reduction in the capillary range of humidity. However, for all mortars some shrinkage reducing effect remains for low relative humidity, which implies that the immobile fraction of SRA contributes to shrinkage reduction via disjoining pressure.

For cyclic leaching it can be seen that, in contrast to permanent leaching, the relative amounts leached per cycle depend on the initial dosage of SRA. The amount of admixture leached during the cycles however is drastically decreased. For these tests, the removal of about 10 to 20% SRA1 seems to have only minor effect on the shrinkage reduction.

More important, from cyclic drying and rewetting tests the main impact on strain evolution could be shown to come from the ageing of the cement matrix itself. Carbonation shrinkage was found to be enhanced for the non-leached specimen and this clearly determines the magnitude of irreversible deformations. For leached mortars this is less pronounced because readily soluble phases that tend to carbonate are removed prior to drying in the course of the leaching subcycles.

Concerning the impact of SRA on drying and shrinkage, the most important findings of this chapter are summarized and discussed below.

1. A main contribution to the question at hand can be seen in the discrimination of SRA into a mobile and an immobile fraction. Concerning the evolution of surface tension in the course of drying the relationship between bulk concentration, interfacial area and surface tension can be refined. The distinction of these fractions allows determining the effective amount of SRA able to diffuse to the liquid/vapour interfaces created in the course of drying. For this however, we assume that the immobile fraction does not participate in covering interfacial area created during drying. Based on this, Figure 40 can be used to calculate surface tension if the bulk concentration of SRA is corrected for the immobile fraction of SRA1.
2. Concerning the mobile fraction of SRA, together with the findings of subchapters 8.3.3 and 8.3.4, it can be stated the process of self-assemblage and/or surface aggregation/adsorption that SRA underwent in cement paste is completely reversible. In terms of diffusion, this part of the mobile SRA fraction can be assumed to be able to diffuse to the interfaces created in the course of drying. Therefrom, we conclude that the complete mobile fraction of SRA must be accounted for when calculating surface tensions.

3. Concerning the immobile fraction of SRA, the results imply a statistical, homogeneous distribution of SRA in the paste. Moreover, in regard to the findings of chapter 8.3.4, DPTB may be associated to portlandite or captured in gel porosity. This may impact both, disjoining pressure and water sorption isotherms.
4. DPTB is the non-ionic surfactant in SRA1 and can be supposed to be its main active component, whilst the DPG just serves as a co-surfactant. The reduced content of DBTB in the mobile fraction of SRA impacts its capacity to reduce surface tension. With the purpose of predicting surface tension of the pore fluid of drying cementitious material, this has to be accounted for. In this study, this will be factored in assuming a dilution effect that accounts for the DPTB concentarion in the mobile SRA fraction relative to the initial DPTB content of SRA1.
5. Concerning irreversible deformations, one finds that it is carbonation that matters most and which can be attributed to be an ageing phenomenon. However, we recognize that in presence of SRA, carbonation and hence, carbonation shrinkage are reduced. This most probably comes from SRA that reduces the amount of solid phases available to react with carbon dioxide in the course of drying. For the cycle times applied in our tests, drying creep is to some extent determined by the enhanced drying in presence of SRA. However, the basic creep related to the extent of average pore pressure in mortars with or without SRA remains unknown because it cannot be distinguished in the measurement setup used.

Summarizing the findings of this chapter, essential contributions concerning the implementation of SRA into recent models for predicting drying and shrinkage of cementitious systems could be obtained. In the next chapter these results and the findings of previous chapters are synthesised and then used to examine shrinkage and drying of SRA containing cement paste and mortar in particular.

11 Physical impact of SRA on drying and shrinkage

11.1 General introduction

In this chapter the main target is to derive the mechanisms of SRA in drying and shrinkage of cementitious systems. Based on the theoretical consideration of chapter 5 and the findings of the experimental work introduced previously, the drying and shrinkage of different cement pastes and mortars shall be examined in particular.
In a first step, the theoretical and experimental findings obtained so far are synthesised. This allows to obtain a clear overview concerning the open questions of the theory laid out and the answers obtained from experimental work. Based on this, the most promising approach can be developed towards clearly distinguishing main and side effects that come from the presence of SRA.

In a next section, the results of drying and shrinkage measurements are given and then adequately discussed. This sets the basis needed for the critical discussion of the results presented in this chapter.

11.2 Synthesis of theoretical and experimental results that matter dyring and shrinkage

Based on the state of the art review in chapter 3 and the theoretical considerations of chapter 5, drying and shrinkage of cementitious material can be described using the standard thermodynamics of the drying open pore system. From this, overall energy balances for drying and shrinkage can be obtained. In particular, for the isothermal drying of these systems the free energy of desorption can be separated into two fractions. The first is utilized in the deformation (drying shrinkage) of the solid skeleton and the second is utilized in creating interfacial area at the liquid/vapour interface. Using the set of equations given in the above mentioned chapters, these energy balances can be obtained from measuring drying and shrinkage isotherms of cementitious materials. The first of these allows calculating the increase of the Gibbs free excess energy with drying and the second enables to separate the fraction of energy utilized in the deformation of the solid skeleton. Concerning the latter, the viscoelastic properties of these systems are of high interest. From the elastic or reversible part of the deformation one can deduce how much energy effectively is stored in the solids, whereas the viscous part of deformation reveals how much energy is dissipated over time. Regarding drying induced cracking, the elastic stress can lead to cracking, whilst the viscous part does not or at least not completely. In a first attempt however, the cementitious systems examined are treated as linear elastic material [262, 263]. The implications of this rather crude assumption will be discussed later on. For this, measurements of length change after drying and resaturation are used as an estimate of the viscoelastic properties of these materials.

As a result of the approach introduced above, the distinction of both energy fractions is obtained as well as their relation, over the whole humidity range and for each reference system. Concerning the impact of SRAs on drying and shrinkage, one reveals if and to what extent this specific property is affected.

Using the artificial pore system normcube (chapter 5), the simulations suggested that a decreased surface tension of the pore fluid causes an enhanced drying of the pore system. Furthermore, the literature on SRAs shows that the admixtures reduce shrinkage of cementitious material. Based on this, one concludes that SRAs must increase the ratio of energy utilized at the interfaces with respect to the energy of deformation. This is especially true since elastic properties of SRA treated materials are not significantly altered and that creep is reported to be decreased (chapter 4.4.5).
We recognize that a predictive model for drying shrinkage requires a proper description of how SRAs affect the energy balances in general and the ratio of energies (creation of interfacial area over deformation) in particular.

The findings of chapter 5 unravelled another issue. This concerns the evolution of the pore fluids surface tension in the course of drying and how this affects drying and shrinkage. From the experimental work of chapter 7.3.3, the surface tension of the pore fluid can be expressed as a function of the surfactant bulk concentration and of the interfacial area that the surfactant is supposed to be active at. This allows estimating the evolution of surface tension in the course of drying in which the surfactant bulk concentration increases due to evaporation whilst more and more interfaces are exposed to the vapour phase. Whilst this can be conceptually well described, the actual interfacial area and its evolution during the drying process are to be assessed quantitatively. Only then can one deduce a relation ship between the properties of these interfaces and the energy fraction obtained from shrinkage and desorption isotherms.

This requirement leaves two main questions open. The first one concerns the pore structure, which determines the solid interfacial area and how to describe its evolution in the drying process. The second question addresses the distribution of SRAs in the cementitious system, which determines their potential activity at interfaces.

Concerning the first, nitrogen sorption measurements revealed that, in presence of SRA, the interfacial area in pores smaller than 2-3nm is drastically increased. Based on the analysis of these sorption data, the internal surface area available for nitrogen was obtained for the mortars investigated. Assuming that this specific surface area can be attributed to the capillary pore system; one now gets an estimate of the interfacial area exposed when capillaries are emptied in the course of drying.
Concerning the internal surface area not available for nitrogen, the t-curve provided by Badmann, Stockhausen and Setzer [18] for water adsorption onto cementitious materials can be used estimating the specific surface area attributed to C-S-H. For this, data on the water desorption at relative humidity below the bifurcation point can be used.
Both contributions to total specific surface of the cement system are of high interest because the findings of chapter 10.3 clearly show that about 40% of the SRA are associated to portlandite or at least C-S-H. That part of the SRA is therefore supposed to be immobile, whereas the rest is mobile and distributed in the capillary pore space. The knowledge of these two fractions of internal specific surface area together with the known distribution of the SRA fractions allows approximating effective excess surface concentrations of SRA at interfaces. From this, estimates on the reduction of surface tension or surface energy may be enabled. Considering this, the mobile fraction of SRA can be assumed to alter interfaces that are attributed to the capillary pore space, whilst the immobile fraction may impact the interactions between solid surfaces of the hydrates or effective disjoining pressure respectively.

More specifically, the mobile fraction can be discriminated into a fraction subjected to surface aggregation and a fraction that is part of the pore solution. This helps to describe the evolution of the interface in the course of empting the capillary pore space. In particular, at the bifurcation point of the sorption isotherm of cementitious materials one now can use nitrogen sorption data as an estimate of the exposed interfacial area. With this, the excess surface concentration of the SRA that determines surface tension can be estimated.

Another important finding comes from the leaching tests and contributes to the estimation of actual surface tension. It is the association of the non-ionic surfactant to hydrates. For SRA1, this decreases its capacity to reduce surface tension of the liquid phase. Concerning the cement pastes and mortars examined in this study, the effective surfactant content of mobile SRA1 reduces to 66% for systems with cement binders and 73% in case of limestone composite binders. Based on these results and neglecting minor contributions to surface tension from the co-surfactant, the effective surface tensions of the liquid/vapour interface can be estimated.

In what follows, the results collected on drying and shrinkage of mortar and paste containing differents SRAs in different dosages are shown. Data on mechanical properties as well as irreversible deformation are introduced and shortly discussed.

In a next step the overall energy balances are derived from shrinkage and desorption isotherms. The distinction of the energy utilized in deformation is then used to approximate the drying induced stresses, which are separated into surface induced and capillary stresses according to the findings of chapter 5.

11.3 Results

11.3.1 Drying

In Figure 95 the saturation isotherms of pastes with different binder and different amounts of SRA are displayed. The dosage of SRA refers to the binder content. The corresponding desorption isotherms of these pastes are given in annex (Fig.A7- 1). The saturation and desorption isotherms of cement pastes with different types of SRA (SRA2; SRA3; SRA5) are given in the annex (Fig.A7- 2; Fig.A7- 3; Fig.A7- 4). Note that the point of zero saturation refers to oven drying at 100°C. Furthermore, 8% RH corresponds to drying at T=50°C in an open oven and an ambient room climate of 20°C/40%RH.

a) cement paste CP; w/b=0.4

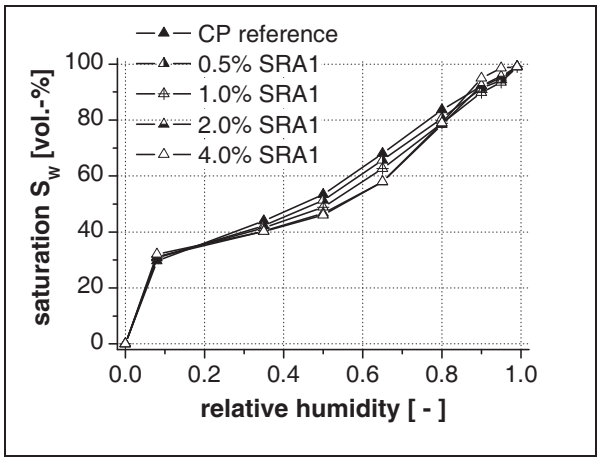

b) lime stone composite binder LP; w/b=0.4

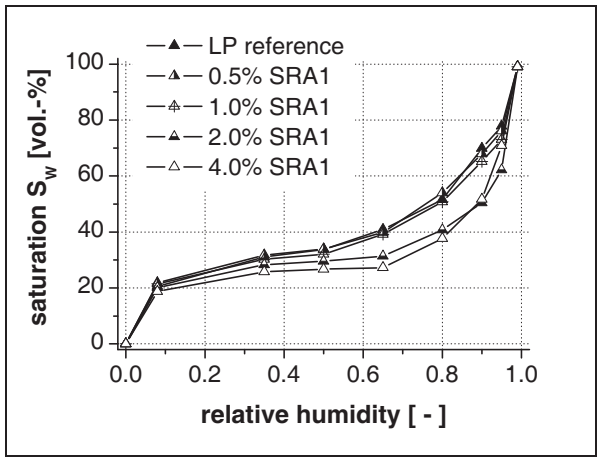

Figure 95: Saturation isotherms of paste with SRA1

In the above graphs it can be seen how, with increasing SRA dosage, the drying increases in the upper range of humidity. On the other hand the isotherms merge for low relative humidity.

The results obtained for drying of pastes in presence of SRA are clearly in line with the results of modeling using the artificial pore system “normcube”, which was developed in chapter 5. As a reminder, based on the evaluation approach for predicting surface tension in dependence of actual SRA bulk concentration and interfacial area (chapter 7.3.3), saturation isotherms for the adjusted normcube with aqueous solutions of SRA1 could be obtained: More specifically, results in Figure 42 are in line with the isotherms given in Figure 95a. This is especially important since the normcube was adjusted for the plain cement paste CP in the above figure. Based on the simulation in these previous chapters, it can be said that the surface tension decreases in the course of drying. This can be deduced separately from the fact that the isotherms merge at low relative humidity.

For the composite binder paste LP in Figure 95b, one can see that for high dosages of SRA1 the saturation isotherm reaches a plateau at 65% RH. The amount of water lost in the following steps (50% RH and 35% RH) is low. Most probably this is because menisci have already vanished at 65% RH. This is most likely since (68) implies that due to the reduced surface tension the so-called Kelvin radius decreases. It is therefore credible that, for these mortars, the capillary pore system is emptied at 65% RH already and that water loss in the following drying steps must be due to water desorbing from adsorbed water layers.

In Figure 96 the saturation isotherms of the mortars containing SRA1 are displayed. The corresponding graphs, giving the absolute values of pore space, can be found in annex (Fig.A7- 5; Fig.A7- 6; Fig.A7- 7).

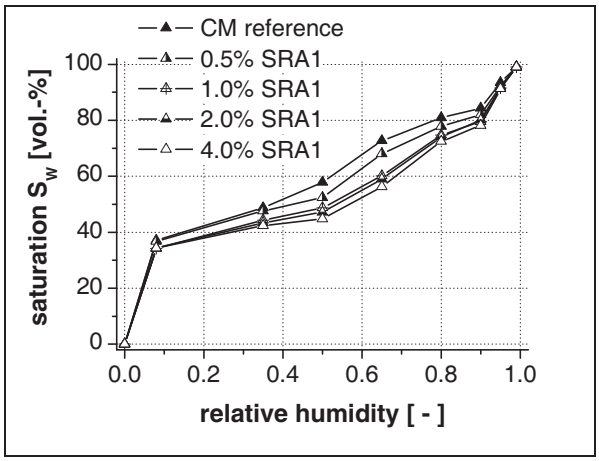

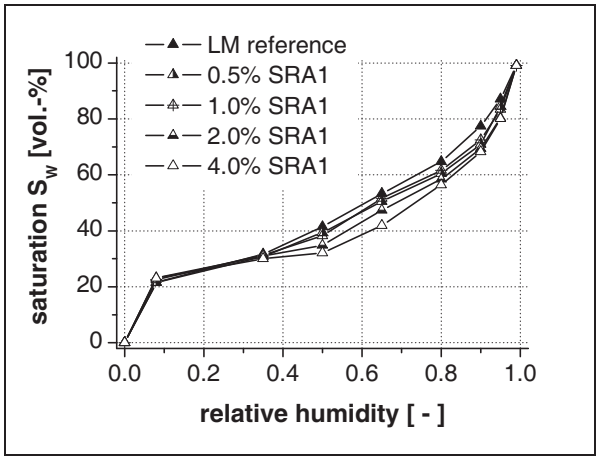

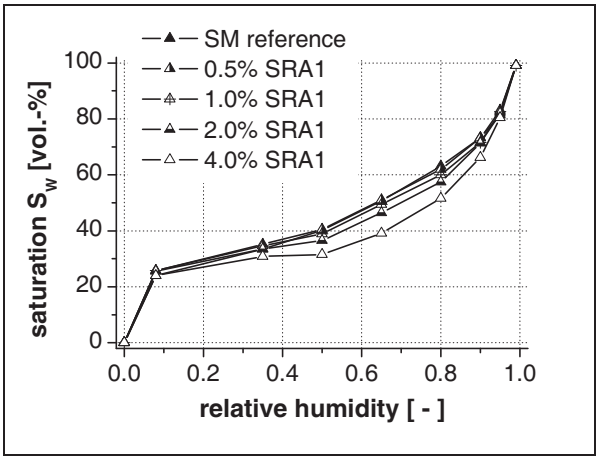

Figure 96: Saturation isotherms of mortars with SRA1

upper left: cement mortar CM

lower left: mortar with lime stone comp. binder LM

lower right: standard mortar SM

In these figures, the drying behaviour of mortars is analogue to their corresponding pastes. Again, with increasing dosage of SRA the saturation decreases for a given relative humidity in the upper range. The saturation isotherms merge for low humidity.

For the mortars comprising high porosity (LM & SM), the saturation isotherms of pastes containing a high dosage of SRA1 comprise a plateau between 50% RH and 35% RH, similar to the LP paste. Here also, this indicates that menisci have vanished and that capillary porosity is emptied. The water loss for the following drying steps most probably again corresponds to water desorbed from adsorbed water layers.

11.3.2 Free drying shrinkage

In Figure 97 the shrinkage isotherms of pastes are displayed.

a) cement paste CP with SRA1

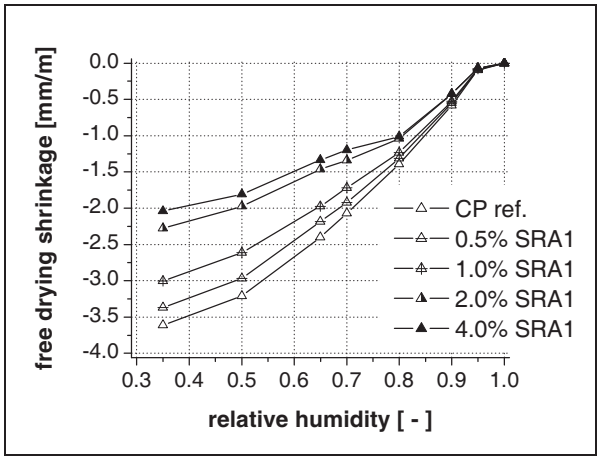

b) paste with composite binder LP and SRA1

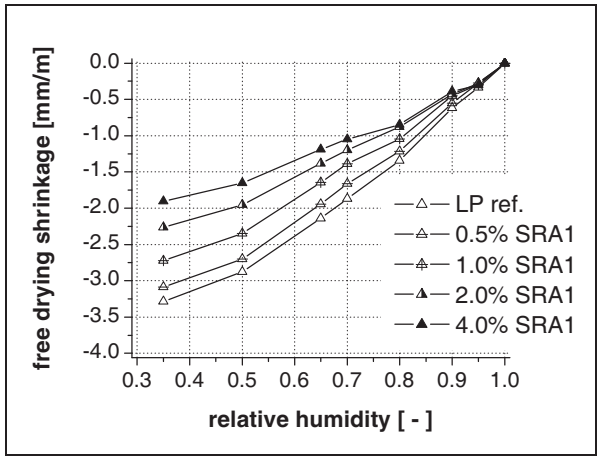

c) cement paste CP with SRA2

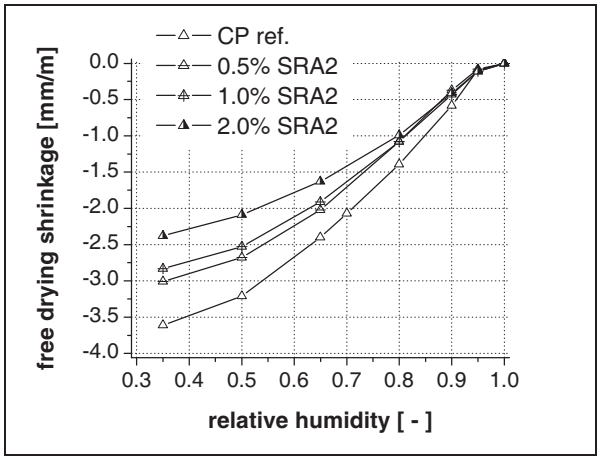

d) cement paste CP with SRA3

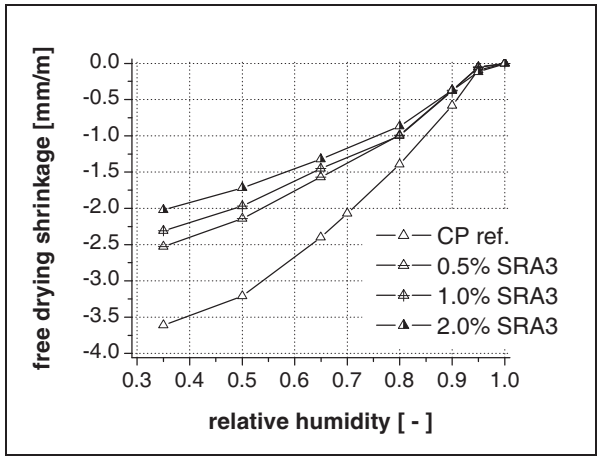

Figure 97: Shrinkage isotherms of paste containing different SRAs

In subfigures a) and b) the impact of SRA1 on the free drying shrinkage of cement paste CP (Figure 97a) and the limestone composite binder LP (Figure 97b) is shown. Subfigures c) and d) contain the shrinkage isotherms of cement paste CP with different dosages of SRA2 and SRA3.

From these graphs it can be seen that with increasing dosage of SRA, shrinkage is effectively reduced. More interesting, one can clearly distinguish in what range SRAs are active. Concerning high relative humidity, the shrinkage reduction starts below 95% RH. For humidity lower than 50%RH however, SRAs no longer seem to contribute to the reduction of drying strains. Indeed, the strain increments between 50% RH and 35% RH are almost identical, independent of the mortar type and the SRA dosage.

There is one exception to this observation and it is found for the pastes CP and LP with an initial SRA dosage of 4%. However, such a high dosage significantly exceeds the application limit by factor 2 (2% usually is the maximum recommended by producers) and is therefore not of practical relevance.

In Figure 98 the shrinkage isotherms of different mortars are given. As previously observed for paste; the shrinkage reduction increases with SRA dosage. Again, SRA can be seen to be active in the humidity range between 95% and 50% RH.

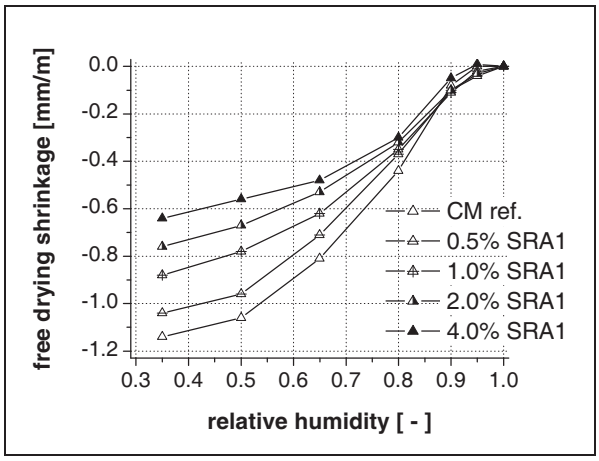

Figure 98: Shrinkage isotherms of mortars with SRA1

upper left: cement mortar CM

lower left: mortar with lime stone comp. binder LM

lower right: standard mortar SM

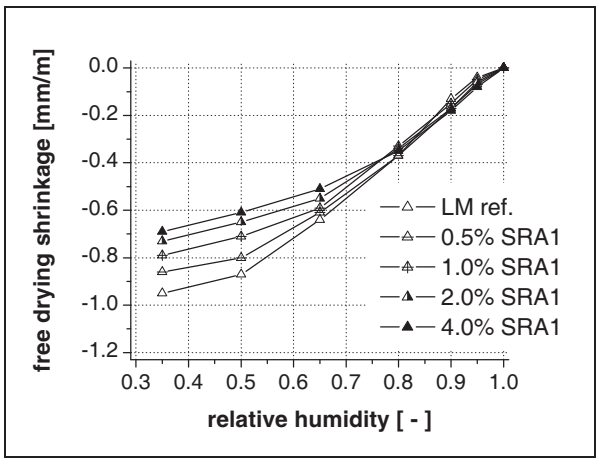

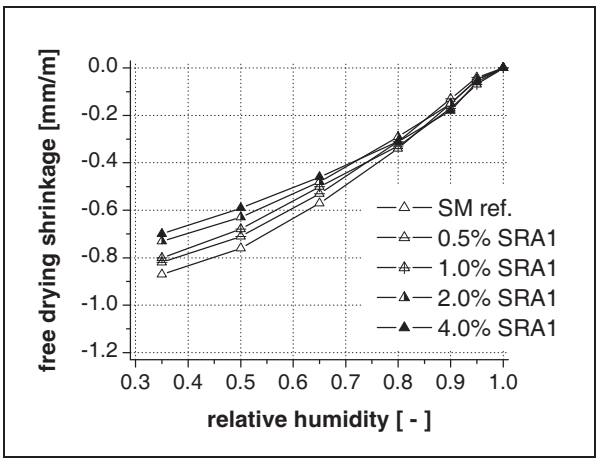

Similar to the findings on cement pastes, the mortar strain increment measured between 50%RH and 35% RH is unaffected by the presence of SRA.

11.3.3 Irreversible shrinkage

The irreversible shrinkage was examined on mortars. Different to the data set obtained in the previous chapter, shrinkage and drying isotherms were measured using cylindrical specimens comprising a slightly higher surface to volume ratio (see Table 3 in chapter 6.3.4). The majority of specimen was dried over 64 days after which moisture equilibrium had been sufficiently obtained. A part of the series was dried for only 44days and then exposed to lower relative humidity. After 64 days drying, the specimens were submerged into deionized water for seven days. After that, mass and length change were measured. The resaturation was successful, because for all specimens the initial weight recovered. This can be seen in the results for mortar type CM containing different dosages of SRA1 (0.5; 1; 2%) as well as 2% of SRA2; SRA3 and SRA6 displayed in annex (Tab.A7- 2; Tab.A7- 3; Tab.A7- 4).

In Table 38 the results of these measurements are summarized. In the second column the irreversible fraction of shrinkage of the plain mortars exposed to different relative humidity is displayed. In the third column, the corresponding average values for mortars containing 2% of different SRA are shown. Data displayed without *-indicator are the results for mortars stored in climate chambers fed with nitrogene to minimize carbonation and carbonation shrinkage. They remained at this climate throughout the test. It can be seen that, the irreversible farction of shrinkage increases with humidity.

In contrast to these samples, the specimens stored at 65% RH and 80% RH (***) were exposed to carbon dioxide over the test duration (climate chamber without protective gas). This caused the total shrinkage strain to disproportionally increase. Indeed, this shrinkage strain in 65% RH was compara-

ble to the ones obtained for samples exposed to 30% RH. Moreover, the irreversible fraction of shrinkage rose to about 78% for the plain mortar and about 65% for the SRA containing ones.

Table 38: Irreversible fraction of drying shrinkage obtained from length measurement after resaturation

humidity	plain mortar	with 2% SRA
[% RH]	[-]	average [-]
*** 20**	26%	21%
30	56%	32%
50	43%	43%
**** 50**	44%	41%
***** 65**	78%	64%
70	63%	63%
***** 80**	68%	66%

* 44 days at 40% RH, then 20 days at 20% RH

** 44 days at 87% RH, then 20days at 50% RH

*** 64 days without protective environment (carbonated)

Most important information can be deduced from the specimen that were first stored at 40% RH (44days) and then exposed to 20% RH for the rest of the drying regime (20days). For these samples (indicated with* in Table 38) the impact of carbonation should be low because of the low water saturation. The average irreversible fraction of strain is about 26% for the reference mortar without SRA. As a comparison, the samples exposed to 30% RH for the whole test duration comprise a higher irreversible deformation of about 56% for the reference and 32% for SRA containing mortars. From this, one concludes that not only relative humidity but also exposure time significantly impacts the irreversible deformations. This would explain why the samples stored at 30%RH for 64days to comprise double the irreversible strain than the ones first stored at 40%RH (44days) and then exposed to 20%RH (20days).

In the following the results of the samples exposed to cyclic drying and resaturation (subchapter 10.5) are examined.
As a reminder, those specimen were resaturated for 7 days and then exposed to 35% RH for 21 days. The measurements covered weight loss and length change over 9 cycles (cycle time 28days). The results for cumulated creep of the three mortar types investigated are shown in Table 39.

Based on this data set, the extent of creep can be estimated dependent on exposure time. It is important to mention that mortar types LM and CM are self-consolidating mortars with high paste volume, in which the aggregates are discretely distributed; whereas mortar SM comprises a lower binder content. This may have caused the macroscopical irreversible strains of SM types to decrease because of the higher order of elastic contacts between aggregates. However, for this mortar type the presence of SRA causes the irreversible strains to decrease drastically.

Table 39: Cumulated creep of mortars exposed to cyclic drying (35% RH) and rewetting

cycle nbr.	mortar type CM			mortar type LM			mortar type SM		
* [-]	*reference*	*1% SRA*	*2% SRA*	*reference*	*1% SRA*	*2% SRA*	*reference*	*1% SRA*	*2% SRA*
1	27%	23%	35%	23%	0%	5%	15%	2%	0%
2	34%	30%	40%	29%	17%	26%	22%	11%	3%
3	37%	34%	44%	34%	19%	27%	26%	17%	6%
4	38%	38%	46%	39%	24%	28%	30%	20%	11%
5	38%	38%	47%	40%	28%	32%	30%	22%	12%
6	41%	42%	49%	44%	31%	34%	36%	26%	16%
7	41%	40%	48%	45%	33%	35%	35%	24%	16%
8	45%	43%	50%	48%	35%	38%	38%	27%	19%
9	47%	37%	49%	49%	37%	40%	41%	25%	24%

* cycle time 21d

11.3.4 Mechanical properties of paste and mortars

The elastic modulus of the different mortar types was measured after 7, 28 and 91days. For all mortar types, the moduli is unaffected by the presence of SRA (Tab.A7- 1): Furthermore, after 28 days samples were stored at different relative humidity up to 91 days (35; 70; 90%RH) prior to measurement.

These mechanical tests revealed that the modulus of elasticity changes slightly, but that this does not correlate with storage conditions or humidity respectively. Because the deviations obtained remain in the range of ± 5%, the elastic moduli of the mortars are assumed to be a constant in the humidity range between 35 and 90% RH.

For cement pastes the elastic modulus was assumed to be in the range of about 20GPa for Portland cements and 16.8 GPA in case of the limestone composite binders. The elastic properties of the limestone composite binder were assumed to be proportional to the ratio that was found for the mortars containing either binder.

The bulk moduli of pastes and mortars were calculated assuming Poisson's ratio to be about 0.2 (Tab.A7- 1).

11.4 Energy balances for drying and shrinkage

In this chapter, energy balances of the drying and shrinkage of paste and mortars are derived from desorption and shrinkage isotherms. In what follows, the overall energy excess due to evaporation of water *dG* is calculated using the set of equations given in chapter 3, in particular (22). Because of isothermal conditions the Gibbs free energy can be attributed free Helmholtz energy $\Psi_{tot.}$. To separate the deformation energy $\Psi_{def.}$ from $\Psi_{tot.}$. the cementitious material was assumed to comprise linear elastic properties according Tab.A7- 1. Based on these data, the energy utilized in deformation of the solid skeleton can be calculated from the shrinkage isotherm.

$$\Psi_{def.} = \frac{K}{2} \int d^2\varepsilon \tag{106}$$

The difference between $\Psi_{def.}$ and $\Psi_{tot.}$ gives the energy utilized in the creation of interfacial area $\Psi_{int.}$, reading

$$\Psi_{tot.} = \Psi_{def.} + \Psi_{int.} \tag{107}$$

Such energy balances were carried out for all pastes and mortars investigated.

11.4.1 Separation of the energy of deformation

As an example, in Figure 99 and Figure 100 the Gibbs free energy and the energy of deformation are given for the cement paste (CP) and mortar series (CM) containing different dosages of SRA1. Data for other pastes and mortars are given in annex A7. Note that these energy balances were calculated from shrinkage and desorption isotherms that are obtained at discrete relative humidity (35; 50; 65; 80; 90; 95%RH). With the purpose of numerical integration these isotherms were interpolated.

In the same figures it can be seen that, due to enhanced water loss, the SRA containing samples have an excess free energy that increases more as the relative humidity decreases to about 50%RH. This is true for both, cement paste and mortar. Then, the slope of these curves changes and they merge at about 35%RH.

Another important result that can be taken from these figures is that the ratios between energy of desorption and the energy of deformation are large. This is true for the SRA containing specimen and independent of either paste or mortar. Especially in the capillary range of humidity (>50%RH) the energy of desorption is high for specimen with high SRA dosages. In addition, due to shrinkage reduction, the energy of deformation of these samples is low.

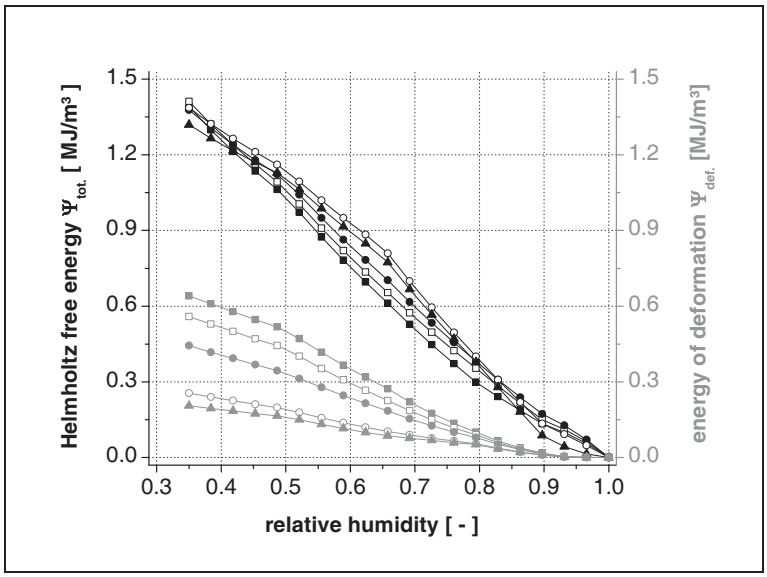

Figure 99: Energy balance for cement paste containing SRA1

From these figures one can also deduce that, in the course of drying of cementitious porous systems, a main part of the excess free energy is utilized as interfacial energy, independent of the presence of SRA. Nevertheless, concerning all mortars and pastes examined, in presence of SRAs this energy fraction increases with dosages. It can be summarized that this is a characteristic feature of SRAs.

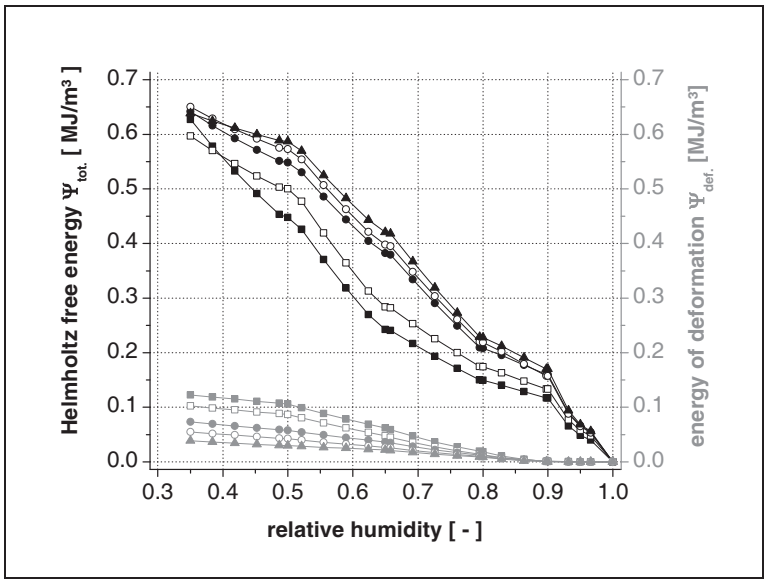

Figure 100: Energy balance for mortar type CM with SRA1

As mentioned in the above introduction, concerning a predictive model for drying shrinkage, the knowledge of the distribution of energy between deformation and creation of interfaces is therefore a must. We now proceed in having a closer look at this.

11.4.2 Specific energy of deformation

In this section it is examined how SRAs impact the distribution of energy between deformation and creation of interfacial area. Heretofore, we derive the specific energy of deformation from the first derivative of energy of deformation versus total Helmholtz energy, reading

$$\Psi_{def.}{}^{\bullet} = \frac{\partial \Psi_{def.}}{\partial \Psi_{tot.}} \tag{108}$$

In addition, the specific deformation ε* can be expressed in a similar way. This can support the discussions in case the assumption on the mechanical properties of pastes and mortars is inaccurate (non-linear elastic behaviour) and would hence perturb the overall picture.

$$\varepsilon^{\bullet} = \frac{\partial \varepsilon}{\partial \Psi_{tot.}} \tag{109}$$

As a reminder, the specific relationship between surface free energy and deformation was found by Bangham [2-4] and became known as the Bangham shrinkage that governs deformations for low humidity. But also for higher humidity this can be applied as formerly done by Setzer [7, 10] and Hansen [8] as well as Duckheim & Setzer [264].

One now can use either the specific energy of deformation or the specific deformation to discuss the impact of SRAs on the distribution of the energy fraction utilized in the course of drying and shrinkage. It is important to note that the specific deformation is derived from actual measurements and may therefore be assumed to provide the more solid facts.

11.4.2.1 Cement paste with SRA1

In Figure 101a, the energy of deformation versus total Helmholtz free energy is displayed for cement paste with and without SRA1. From this, the specific energy of deformation was obtained and is displayed in Figure 101b. In Figure 101c the measured specific deformations of the reference paste without SRA and paste containing SRA1 are given.

a) energy of deformation versus total free energy

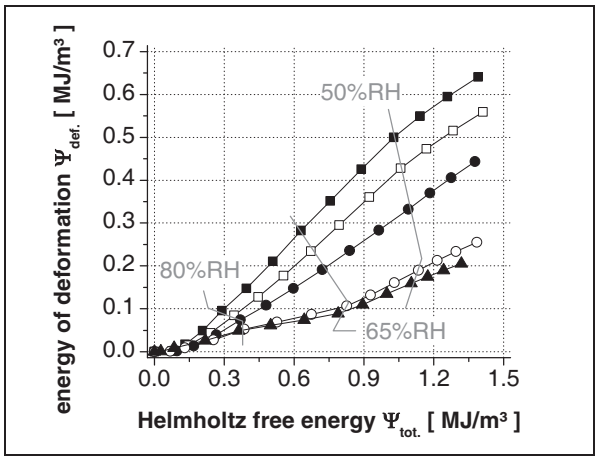

Figure 101: Energy of deformation versus total Helmholtz free energy, specific deformation energy and specific deformation of cement paste CP with SRA1

Legend:

- reference
- 0.5% SRA1
- 1.0% SRA1
- 2.0% SRA1
- 4.0% SRA1

light lines indicate fixed RH

b) specific energy of deformation

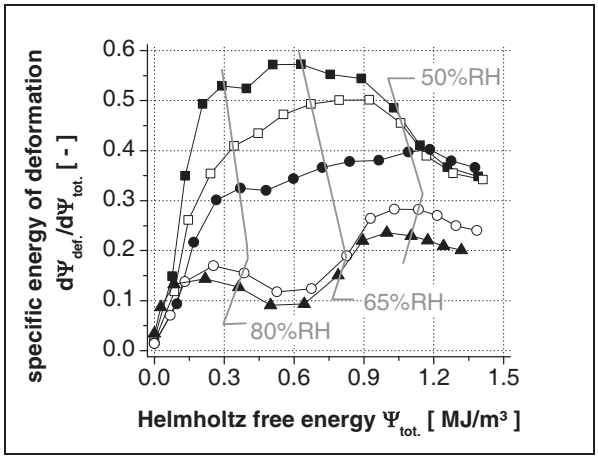

b) specific deformation

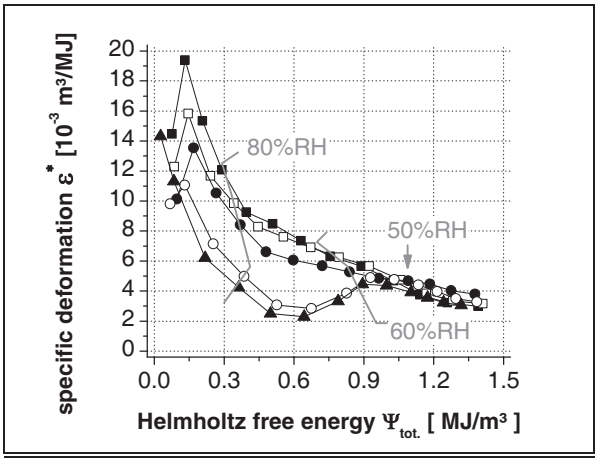

From Figure 101b one can see that the specific deformation energy decreases with increasing dosage of SRA1. This is especially true for the humidity range between 90%RH and about 50%RH. More spe-

cifically, one finds large differences for the distribution of the energy fractions in the capillary range of humidity. For pastes containing 0.5 and 1% SRA1, the specific energy of deformation merges the curve of the reference without SRA1 below 50%RH. In contrast, the pastes with higher dosage of SRA1 comprise lower specific energy of deformation for the whole humidity range. However, after showing a local minimum at about 70% RH the specific energy of deformation comprises a local maximum between 60% and 50% RH. For lower humidity, the evolution of specific energy of deformation seems to be unaffected by the presence of SRA.
The difference in the absolute values of the specific energy of deformation can come from deviations from linear elastic behaviour. Indeed, from Figure 101c one can see that, for low humidity, the specific deformation of is unaffected by the presence of SRA1. More specifically, the pastes containing SRA1 merge the curve of the reference paste at different relative humidity and this depends on the dosage of SRA1. For pastes with high dosage of SRA1 this can be assumed to have been achieved with the emptying of the capillaries.

From the data set obtained with paste containing SRA, it be concluded that SRA1 is mainly efficient in the capillary range of humidity (>50%). For lower humidity, the admixture does not contribute to shrinkage reduction because the specific deformation $d\varepsilon/d\Psi_{tot.}$ Is unaffected by its presence.

Concerning the working mechanism of SRA1 it reveals that the admixture causes a decrease of the ratio between energy of deformation and energy for creating interfacial area. From the results on the specific deformation in presence of SRA1, an impact of SRA1 on disjoining pressure cannot be distinguished. This is especially true for the low range of humidity. There, the specific deformation should be decreased if disjoining pressure was increased, but it is not the case. The lower specific energy of deformation of pastes with high SRA1 dosage (Figure 101b) would support such an assumption; however, the curves might be perturbed, because linear elastic behaviour was assumed.

11.4.2.2 Cement paste with SRA2

In Figure 102 the specific energy of deformation and the specific deformation of pastes containing SRA2 are displayed. There, it can be seen that an analogue behaviour to the pastes containing SRA1 can be observed. With increasing SRA2 dosage, the fraction of energy, utilized in creation of interfacial area, increases. Again, this is especially true for the capillary range of humidity (>50% RH). Here also, the evolution of specific energy of deformation at low humidity is unaffected by the presence of SRA2. The results for specific deformation in Figure 102b imply that the curves merge at low humidity. As concluded for SRA1, SRA2 is mainly active in the capillary range of humidity (> 50% RH).

a) specific energy of deformation

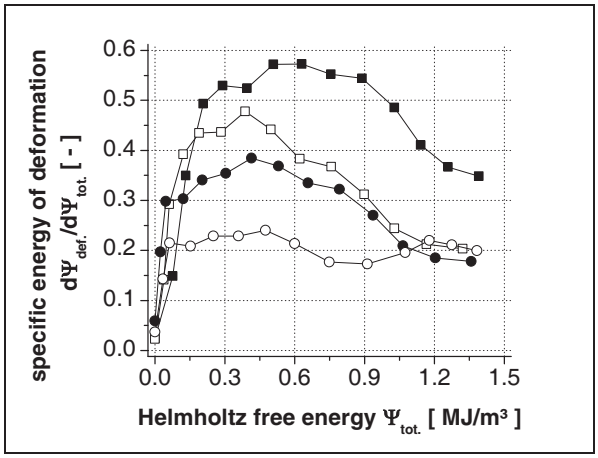

b) specific deformation

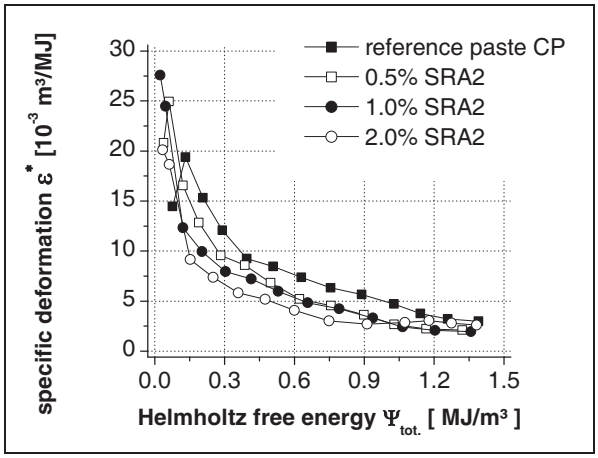

Figure 102: Specific energy of deformation and specific deformation of cement paste with SRA2

11.4.2.3 Cement paste with SRA3 and SRA5

The specific deformations of pastes containing SRA3 and SRA5 are displayed in Figure 103. Additionally their corresponding shrinkage isotherms are given.

a) specific deformation of pastes with SRA3

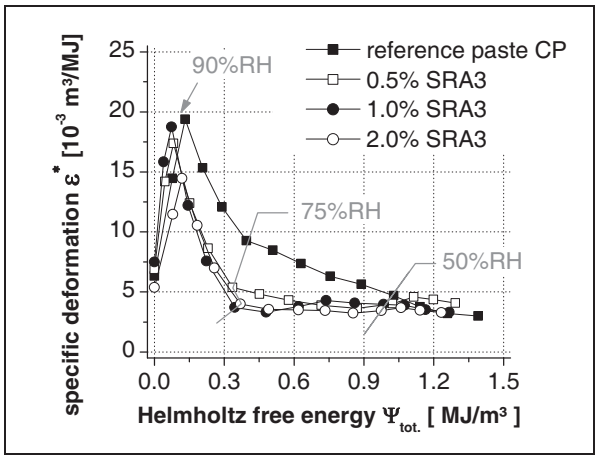

b) specific deformation of pastes with SRA5

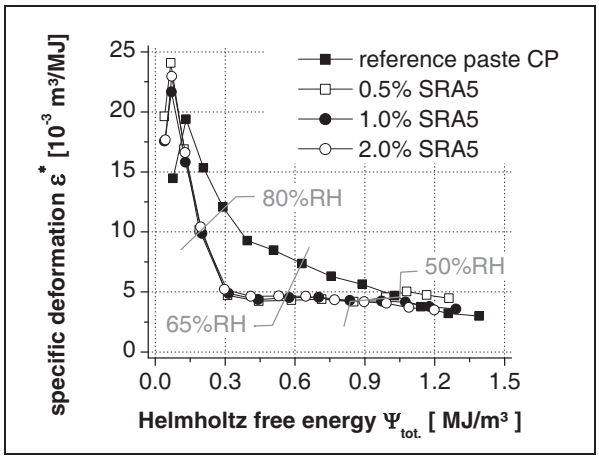

c) Shrinkage isotherm of pastes with SRA3

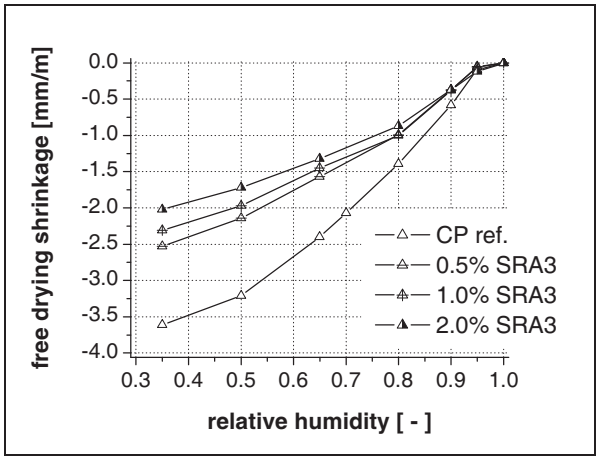

d) Shrinkage isotherm of pastes with SRA5

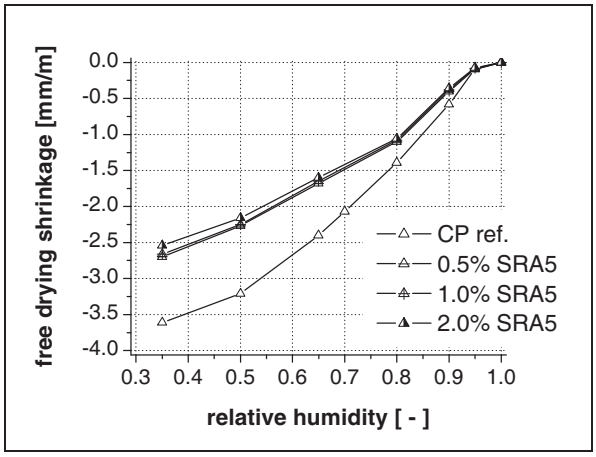

Figure 103: Specific deformation and saturation isotherms of pastes containing SRA3 and SRA5

From the above figures, the following can be deduced: Similar to what was observed with SRA1 and SRA2, the specific deformation of the pastes containing SRA3 and SRA5 is lower than that of the reference paste without SRA. Moreover, the specific deformation at low humidity is independent of the presence of SRAs. However, two major differences occur: First, the specific deformation of the SRA containing pastes reaches a plateau at about 75%RH. Second, this can be found independent of the dosage of SRA.

For pastes containing SRA5 (Figure 103b), the identical specific deformation is independent of the initial SRA dosage. This can be explained when the drying strains of these pastes are considered, which are displayed in Figure 103d. There, it can be seen that, for SRA5, dosages higher 0.5% do not contribute to further shrinkage reduction. Because of this, the specific deformation remains unaffected and is identical for all the dosages applied.

In contrast, for pastes containing SRA3 the shrinkage reduction depends on dosage (Figure 103c), however, the differences in specific deformation are less pronounced with respect to the results obtained with SRA1 and SRA2. Comparing the drying strains of those pastes (Figure 97 & Figure 103c) it can be seen that, here also, the dosage dependence of strains is more pronounced for pastes containing SRA1 and SRA2.

11.4.2.4 Mortars with SRA1

The specific deformations of the different mortar types containing SRA1 are displayed in Figure 104.

Figure 104: Drying shrinkage of mortars CM and SM and LM with SRA1 over energy of desorption

a) cement mortar CM with SRA1

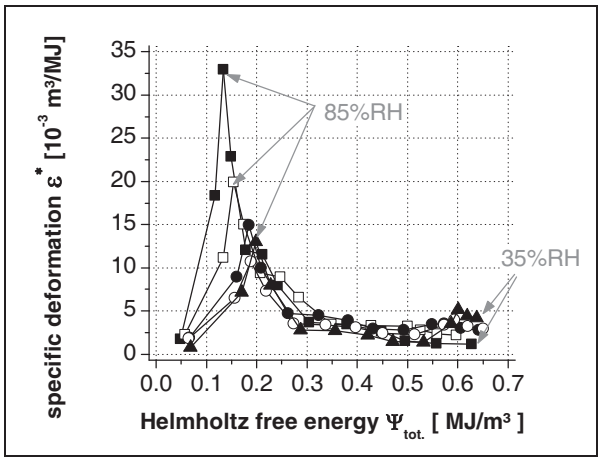

b) limestone composite mortar LM with SRA1

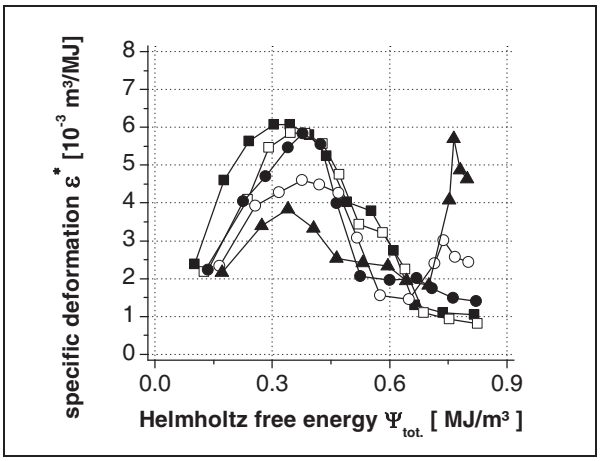

c) standard mortar SM with SRA1

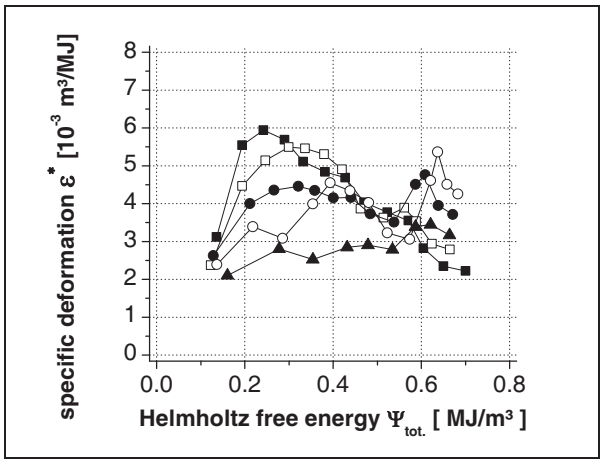

There, it can be seen that, for higher relative humidity, the SRA containing samples comprise a lower specific deformation than the reference mortar without SRA. At certain humidity however, their curves merge the one of the reference. In particular, this seems to go in pair with the emptying of the capillaries. Then, for lower humidity, the specific deformation of the SRA containing samples exceeds the one of the reference without SRA. This is, indeed, different from what was observed with cement paste. There, no significant difference in specific deformation occurred for relative humidity lower than 50% RH. Moreover, the specific deformation of SRA containing pastes merged the one of the reference paste without SRA at low humidity.

11.4.3 Concluding remarks

In this chapter, the evolution of the Helmholtz free energy was determined from the Gibbs free energy of the drying material. SRA containing materials comprise an increased Helmholtz free energy for moderate relative humidity. For lower relative humidity however, the curves merge (chapter 11.4.1). The separation of energy of deformation obtained on pastes and mortar are based on the assumption of a constant bulk modulus and linear elastic behaviour of the drying material. Due to a reduced shrinkage with increasing dosage of SRA the energy of deformation determined is also decreasing in presence of SRA. One now faces two main problems. The first is the question on whether the bulk

modulus, which was derived from measurements of modulus of elasticity and assuming a Poisson's ratio of 0.2, is an adequate measure. The second issue concerns the assumption of linear elastic behaviour in the course of drying and shrinkage. Concerning the first, we recognize that the absolute values of energy of deformation may be different for different bulk moduli assumed. For a higher bulk modulus the ratio of energy of deformation over energy utilized for the creation of interfacial area increases and vice versa. However, the relative differences between samples with different SRA dosage will not be affected. It remains valid that the enhanced utilization of energy for creating interfacial area is a characteristic feature of SRA.

In chapter 11.4.2, the results on specific deformation show that SRA containing samples always comprise less specific deformation for higher relative humidity before their curves of specific deformation merge on the one of their reference without SRA. This is especially true for cement pastes containing different SRAs in different dosages. For the mortars investigated this is similar in the capillary range of humidity. However, right after the emptying of the capillary pore space the SRA containing samples show an increased specific deformation prior to the collapse of their appropriate curves on the one of the reference without SRA.

Whilst the results obtained on energy of deformation as well as on specific energy of deformation may be perturbed by inappropriate assumptions, which concern the mechanical properties, the evaluation of specific deformation delivers solid evidence that supports the hypothesis of the enhanced utilization of energy for the creation of exposed interface in presence of SRA. Moreover, the collapse of the curves of specific deformation of the SRA containing samples on the one of the neat reference, implies that, indeed, the impact of SRA, i.e. its working mechanism, requires the presence of a liquid/vapour interface. This means that with the vanishing of the menisci or rather the emptying of the capillary pore space the SRA looses its impact on drying shrinkage.

The issue now is to know whether the enhanced fraction of energy utilized in the creation of interfacial area in the course of drying of the SRA containing samples can be attributed to surface activity. Heretofore, the evolution of surface tension in the course of drying has to be properly described. Moreover, the target of this examination is whether the properties of the liquid/vapour interface can be described at the point when the desorption isotherm of the SRA containing samples merge the one of the reference without SRA. This is the subject of the next section.

11.5 Evolution of interfacial area and surface tension in the course of drying

In this section, the evolution of surface tension in mortars and paste containing SRA1 is examined. In a first step the model predicting surface tension of cement pore solution containing SRA1 is adjusted. Then, within an iterative approach, the interfacial area exposed during drying is estimated.

With respect to internal specific surface area the vanishing of the liquid/vapour interface uncovers the vapour/adsorbed water interface that is orders of magnitudes larger. In a first attempt the ratio between these different types of interface can be roughly approximated. The liquid/vapour interfacial area should reach its maximum with the emptying of the capillary pore space. This interfacial area can be assumed to be approximately the nitrogen accessible internal surface area derivable from nitrogen adsorption measurements. According to the results of such measurements on paste in chapter 8.3.4, this maximum is about $10 m^2 g^{-1}$. The internal surface area of paste obtained from water vapour adsorption exceeds this value in orders of magnitude, because in these measurements the adsorbed water that is part of C-S-H phases is additionally accounted for. Though not measured in this study, in literature one can find, that this specific internal surface area is in the range of 200-300m²/g for dry hardened paste (Powers [48, 49]) up to 200-600m²/g (Thomas et al. [50]). From these data the ratio of interfacial area between the vapour phase/liquid and vapour/adsorbed water can be up to 30. With this, one now can evaluate, whether the interfacial area exposed is in the range of the liquid/vapour interface or can be attributed to the adsorbed water/vapour interface. This requires a proper description of the evolution of surface tension in the course of drying.

11.5.1 Surface activity of SRA1 in hydrated mortars and paste

In previous chapters the surface activity of SRA1 was measured and these results could be transferred into a relationship that predicts surface tension as a function of SRA bulk concentration and interfacial area at which the surfactant is supposed to be active at (7.3.3). Based on the leaching studies, this model can be refined because the non-ionic surfactant in SRA1 was found to partially show specific adsorption onto hydrates in the course of hydration (chapter 10). Since this fraction and the active components of SRA1 are known, the surface activity of SRA1 can roughly approximated by accounting for a dilution effect that concerns the non-ionic surfactant (DPTB) in the mobile fraction of SRA.

11.5.2 Interfacial area exposed in the course of drying

In a previous section (chapter 11.4) the interfacial energy of the drying cement samples could be separated from the total excess free energy $\Psi_{tot.}$ by calculating the energy of deformation $\Psi_{def.}$ from the measured shrinkage isotherms.

With this, the area exposed at the liquid/vapour interface $a_{cap.}$ can be roughly approximated using

$$a_{cap.} = \frac{\Psi_{tot.} - \Psi_{def.}}{\gamma_{SFT}} \tag{110}$$

where:

$a_{cap.}$:	exposed interfacial area of capillary pore space	[m²/m³]
$\Psi_{tot.}$:	Helmholtz free energy	[J/m³]
$\Psi_{def.}$:	energy of deformation	[J/m³]
γ_{SFT}:	surface tension of pore fluid	[J/m²]

and

$$\gamma_{SFT} = f\left(a_{cap.}; C_{SRA}\right) \tag{111}$$

where:

$C_{SRA.}$:	effective SRA concentration	[mol/m³]

From (111) it can be deduced that an iterative approach must be taken as the extent of interfacial area exposed affects the surfactant excess surface concentration, which in turn determines surface tension.

In the following figures (Figure 105; Figure 106 & Figure 107) the evolution of interfacial area exposed and the evolution of surface tension are displayed for the different mortars investigated. There it can be seen, how the presence of SRA impacts the evolution of the interfacial area exposed in the course of drying, whilst it is getting diluted, causing the surface tension of the pore fluid to increase in that process. These results are obtained from the above mentioned iterative approach in which for each given drying state equilibrium between SRA concentration, SRA excess surface concentration and exposed interfacial area was determined. Note that the order of exposed interfacial area calculated according (111) requires that the complete mobile fraction is evenly distributed within the capillary pore space. Furthermore, it is assumed that, again, the complete mobile fraction of SRA contributes to the reduction of surface tension, i.e. self-assembly and micellation are attributed metastable states. Such assemblies are assumed to disintegrate in the process of creating accessible interfacial area due to drying, in which surfactant monomers diffuse towards the liquid/vapour interface to adsorb and occupy the voids. The calculations can therefore be seen as a rough approximation on the maximum interfa-

cial area the drying pore system is able to expose in presence of certain amount of SRA. In case the fraction of mobile SRA (that determines surface activity) is overestimated, the interfacial area is being overestimated also.

In Figure 105 the data of mortar type CM are given. The plain reference comprises a surface tension of 75mN/m. This value was taken from surface tension measurements of synthetic pore solution and is assumed to be constant. For the mortars containing small dosages of SRA1 it can be seen that the surface tension increases due to the increase of the interfacial area. For the high dosage of SRA the surfactant gets slightly depleted at low relative humidity.

a) interfacial area exposed in the course of drying b) evolution of surface tension

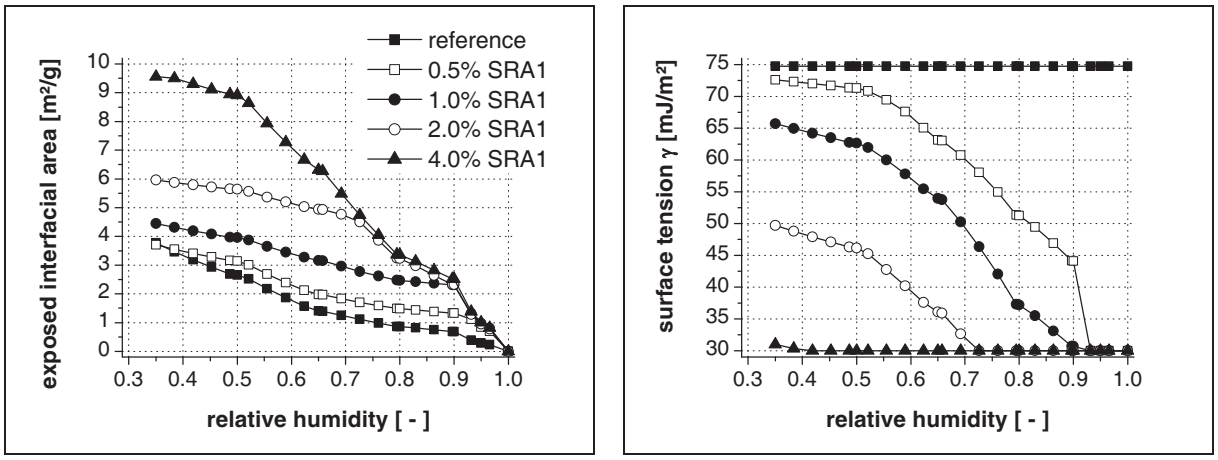

Figure 105: Interfacial area exposed to the liquid/vapour interface and evolution of surface tension in pore fluid of mortar CM

In Figure 106 & Figure 107 the data for mortars LM with limestone composite binder and the standard mortar SM containing SRA1 are shown. Both types of mortar show similar trends to what was observed for mortar CM. Differences are to be found in the extent of surface area exposed in the course of drying. For all mortar types investigated, the most important finding concerns the interfacial area exposed, which scales with the dosage of SRA1 added. This is more pronounced for high dosages of SRA1 where a doubling of the area is seen with respect to the reference without SRA.

a) interfacial area exposed in the course of drying b) evolution of surface tension

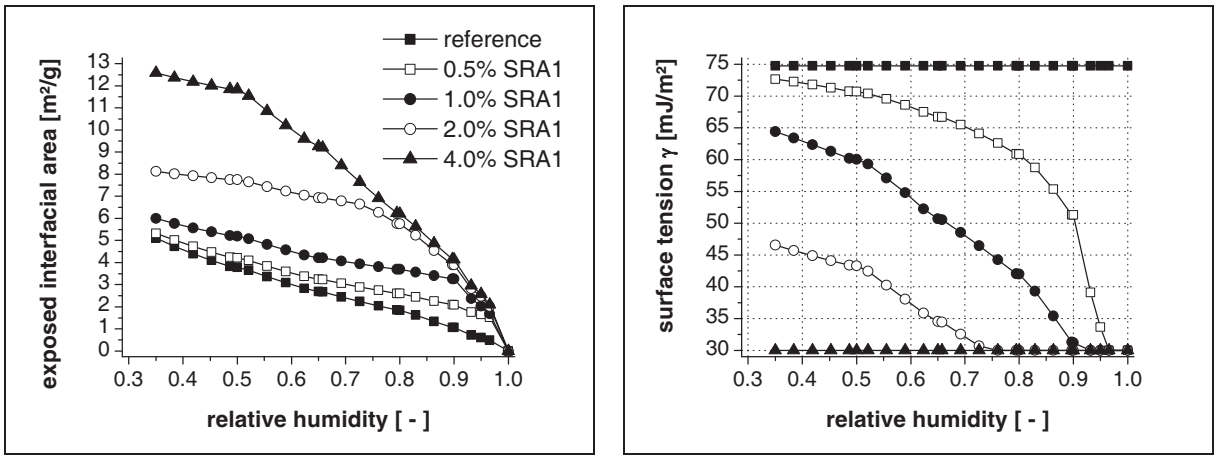

Figure 106: Interfacial area exposed to the liquid/vapour interface and evolution of surface tension in pore fluid of mortar LM

a) interfacial area exposed in the course of drying b) evolution of surface tension

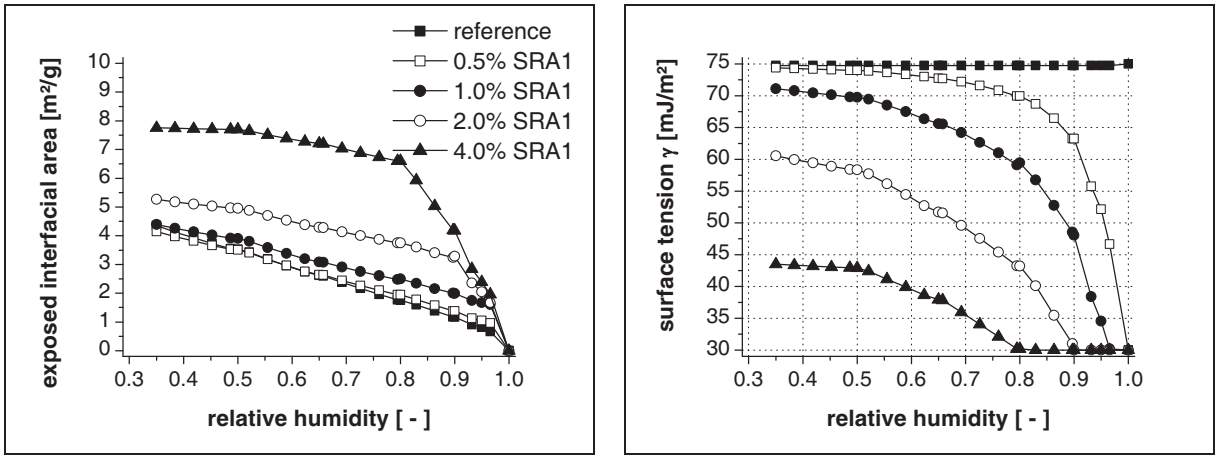

Figure 107: Interfacial area exposed to the liquid/vapour interface and evolution of surface tension in pore fluid of mortar SM

The above results involved a number of hypotheses, so that the results must be evaluated very critically. For this matter the specific surface area obtained from nitrogen sorption measurements is given in Table 40. There the values for the specific surface area evaluated according the BJH [265] and the modeless method [16, 17] are given. In this table the contributions of pores smaller and larger than 4nm can be distinguished.

In the last three columns of Table 40 an overview is given on how much interfacial area the different mortars expose to the liquid vapour interface (reference and mortars containing 4% SRA1). Moreover this is shown for different relative humidity.

Table 40: Specific surface of mortars from nitrogen sorption measurements and exposed interfacial area dependent on relative humidity

mortar	specific surface (nitrogen)							A exp. [m²/g]		
	BJH [m²/g]			modelless [m²/g]			average [m²/g]	RH [-]		
[-]	< 4nm	> 4nm	sum	< 4nm	> 4nm	sum	> 4nm	**50%**	65%	80%
CM ref	5	8	13	4	6	10	**7**	2.7	1.4	0.9
CM 4%SRA1	9	11	20	8	8	16	**10**	**8.9**	6.3	3.4
LM ref	4	11	15	6	8	14	**9**	3.8	3.8	2.7
LM 4%SRA1	9	12	21	8	9	17	**10**	**11.8**	11.8	9.3
SM ref	5	8	13	4	6	10	**7**	3.5	2.6	1.8
SM 4%SRA1	5	9	14	4	7	11	**8**	**7.7**	7.2	6.6

From the above table, the interfacial areas calculated based on surface tension are in good agreement with the surface contribution of pores larger then 4nm in all cases of the high SRA dosage and a relative humidity of 50%RH. This is due to the fact that for these conditions, the desorption isotherms, given in a previous section (11.3.1; Figure 96), indicate that then the capillaries have already emptied. Because of this we consider the results of the iterative approach for deriving surface tension and exposed interfacial area (liquid/vapour interface) as reasonable.

In contrast to the SRA containing samples, the interfacial area of the reference mortars is about half of the specific surface area of the capillary pore system. This result is in good agreement considering that due to higher surface tension of the liquid/vapour interface

a) deformation impacts a lot in minimizing the systems free energy and
b) the interface itself can be assumed to be less curved, which additionally decreases the interfacial are exposed.

The above findings are an important result. Finding the maximum of exposed interfacial area of the liquid/vapour interface of SRA containing mortars to be in good agreement with the specific surface are obtained from nitrogen adsorption, supports the assumptions made on the order of energy utilized in deformation $\Psi_{def.}$, which in turn was used to derive the interfacial energy $\Psi_{int.}$ from the total energy of desorption ΔG or the total Helmholtz free energy $\Psi_{def.}$ respectively. From this one can derive that the Helmholtz free energy approach can be used to describe drying and shrinkage with or without SRA.

Concerning the impact of SRA on drying of cementitious matter the results on both the evolution of interfacial area and surface tension of the liquid/vapour interface in the course of drying are in line with the simulations performed using the artificial pore system normcube. This is in particular true for the simulations with evolving surface tension due to the increase of the interfacial area (chapter 7.3.3). With respect to this, the measurements verify the simulations.

Concerning the SRA mechanism for shrinkage reduction, the energy balance approach supports the idea of the importance of the surface tension of the liquid/vapour interface. This however supports the view that it might be a reduced average pore pressure in presence of SRA that contributes to shrinkage reduction. Moreover, the results obtained on pastes, for which the specific deformation revealed to be independent of the presence of SRA once capillaries are emptied, suggest that average pore pressure is important.

According to the model introduced by Coussy [11, 13] (chapter 3.1.4) the degreased degree of saturation in presence of SRA would cause this pressure to be decreased relative to a reference system without SRA. In particular, it is the reduction of average capillary pressure that reduces the overall average pore pressure. In principle and allowing simplifications to some extent, this mechanism can be viewed as the analogue to the model accounting for capillary forces to be the origin of drying induced deformation. However, as could be derived from the state of the art review in chapter 3, there are severe doubts on the importance of capillary forces for drying shrinkage. To tackle this issue is the objective of the next section. There, the role of capillary pressure for drying cementitious material with and without SRA is examined in particular. The ultimate objective is to determine if the change that SRAs cause on this property is or not the main reason for the shrinkage reduction that they also cause.

11.6 The role of average capillary pressure for drying shrinkage

In this section, the contribution of average capillary pressure to overall deformation is discussed. In chapter 5 the theoretical considerations led to the conclusion that different to Coussy´s model of average pore pressure [11, 13], the pore fluid would preferably be separated into a liquid and adsorbed fraction. For each series of mortars and pastes, desorption isotherms can be used to obtain an estimate on the liquid fraction of the bulk water content. In particular, at about 40 to 50%RH the menisci are supposed to break down in hydrated cementitious materials. Then, water in the pore system is supposed to be present as adsorbed water exclusively.
In a first attempt, we consider this to hold for cementitious materials independent of the presence of SRAs. Based on this, we assume that water evaporation down to about 40%RH is mainly due to evaporation of the liquid fraction. We recognize that this leads to an overestimation because of neglecting a possible water loss from gel porosity. Due to this, we furthermore recognize that the contribution of average capillary pressure is overestimated. The impact of this is discussed later on.

The average capillary pore pressure can be calculated according to

$$\overline{p}_{cap.} = \Delta p \cdot \Phi_0 S_{bulk} \tag{112}$$

where:

$\overline{p}_{cap.}$:	average capillary pressure	[Pa]
Δp:	moisture potential	[Pa]
Φ_0:	porosity	[m³/m³]
S_{bulk}:	liquid water saturation	[m³/m³]

Concerning Coussy´s model [11, 13] outlined in chapter 3.1.4, the second contribution to average pore pressure π is the surface force induced tension *U* which can be calculated from overall water loss according to

$$U(S_w) = \int_{S_w}^{1} \Delta p dS_w = \Delta p \cdot (1 - S_w) \tag{113}$$

where

S_W:	total water saturation	[m³/m³]

so that

$$\pi = -\overline{p} - U \tag{114}$$

For our examinations, we use an estimate of the average pore pressure π, derived from bulk modulus *K* of the cementitious material and its measured drying strains. Thus, the elastic mechanical properties (11.3.4) and the shrinkage isotherms are accounted for, by writing:

$$\pi = \varepsilon K \tag{115}$$

where:

:	shrinkage strain	[-]
K:	bulk modulus	[-]

With this one obtains an estimate of the extent to which the capillary pressure contributes to overall drying shrinkage.

As an example, in Figure 108 the average capillary pressure and the surface force induced pressure are displayed for the mortar CM with different dosages of SRA1. In this figure it can be seen that the contribution of average capillary pressure to overall deformation is low (note the different scales in Figure 108). Although, between 60 and 80%RH it reaches a maximum, its contribution to overall effective pressure is then only in the range of 4% for the reference mortar without SRA and about 10% for the one containing the high dosage of SRA1.

The curves presented in Figure 108 are representative of all mortars and pastes, including paste containing different SRAs and different dosages.

From this we conclude that in general, the contribution of average capillary pressure according Coussy´s model [11, 13] to drying shrinkage is low. This is in line with the findings in chapter 3, in which the literature review revealed severedoubts on the importance of capillary pressure in drying shrinkage of cementitious material.

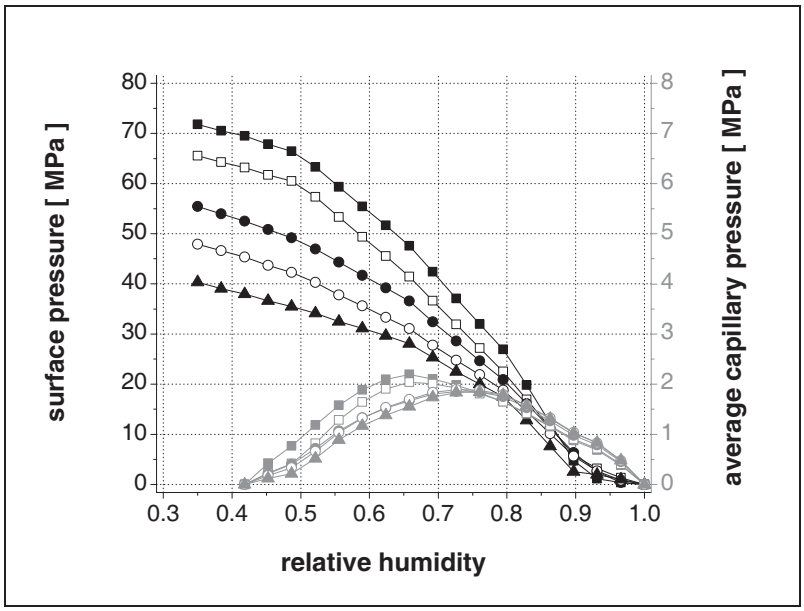

Figure 108: Contribution of average capillary pressure to average pore pressure, mortar CM

Thus, as an overall conclusion of this chapter, concerning Coussy´s model for drying shrinkage [11, 13] we consider the SRA impact on the average capillary pore pressure is a minor effect that cannot account for the overall shrinkage reduction.

Therefore, the SRA effect must concern the role of disjoining pressure or another contribution that is impacted by the reduced interfacial energy of the pore fluid. The latter so far lacks a reasonable explanation but, as a reminder, the role of increased disjoining pressure due to steric repulsion alone can also not account for the sudden increase of deformation once the capillary pore space has emptied upon drying. It is the topic of the next section to tackle this issue.

11.7 The role of SRA in drying and shrinkage of cementitious material

11.7.1 Basic concept for drying and shrinkage of cementitious material

In the previous sections the role of average capillary pressure according Coussy´s model [11, 13] for drying shrinkage was found to be only of minor impact. Although SRAs reduce this average capillary pressure, their main impact on shrinkage appears to come from something else. The objective of this section is to examine which other mechanism is responsible for shrinkage of cementitious material and how it is affected by the presence of SRA.

The state of the art knowledge on drying and shrinkage of cementitious systems leads us to consider the role of disjoining pressure on shrinkage and how surface activity of SRA can impact this. According to Setzer [6, 10], the disjoining pressure governs the overall volume stability and with this the hygral deformations of cementitious material. In the course of drying, the average distance between solid surfaces *h* enters in this balance and contributes to keeping surfaces apart. We reconsider Setzer´s definition of disjoining pressure [6, 10], reading:

$$p_{disj.}(h) = -\left(\frac{\partial G}{\partial h}\right)_{T,p;\mu_i} \tag{116}$$

where

***G*:** Gibbs free energy

***h*:** distance between surfaces

There, the extent of disjoining pressure is determined by the Gibbs free energy of the system and the distance between solid surfaces. Furthermore, Setzer [6, 10] defines:

$$\Delta p_{disj.} = (h) = \frac{1}{h} \int_{\mu_1}^{\mu_1 + \Delta\mu} \Gamma_w d\mu_w \tag{117}$$

where

μ_W: chemical potential of water

Γ_W: surface concentration of water

From the above equation, one can take that disjoining pressure is a function of average surface-to-surface distance, of the surface concentration and of the chemical potential of water. Most important, the Gibbs free energy defined in (116) refers to the adsorbed water, as (117) exclusively refers to the surface concentration of water, i.e. the water between solid surfaces.

Because of this, the disjoining pressure cannot be derived from the total water loss. Again, the liquid (capillary water) and the adsorbed water fractions have to be discriminated. This is a complex task that cannot be fulfilled with the measurements performed in this study. However, a macroscopic thermodynamic dimensional approach offers a useful working approximation.

Using the concept that the disjoining pressure governs the hygral volume stability of cementitious materials, the drying deformation ε can be assumed to be proportional to the average distance h between solid surfaces, reading:

$$\partial h \approx \partial \varepsilon \tag{118}$$

With respect to our Helmholtz free energy approach (section 11.4), this links energy of deformation $\Psi_{def.}$ and disjoining pressure, reading

$$p_{disj.} = \frac{\partial \Psi_{def.}}{\partial h} \tag{119}$$

With

$$\partial \Psi_{def.} \approx K\varepsilon\partial\varepsilon \tag{120}$$

and the combination of equations (118) and (119):

$$p_{disj.} = \frac{\partial \Psi_{def.}}{\partial \varepsilon} \tag{121}$$

one obtaines

$$p_{disj.} \approx \frac{K\varepsilon\partial\varepsilon}{\partial\varepsilon} \approx K\varepsilon \tag{122}$$

so that

$$p_{disj.} \approx \varepsilon \tag{123}$$

Based on the above equations, one concludes that, for a given relative humidity and a reduced drying strain due to the presence of SRA, the disjoining pressure of the SRA containing system must be lower than that of the reference system without SRA, so that for

$$\varepsilon_{SRA}(RH) < \varepsilon_{reference}(RH) \tag{124}$$

$$p_{disj.\_SRA}(RH) < p_{disj.\_reference}(RH) \tag{125}$$

The assumption on the proportionality of shrinkage deformation and decrease of the average distance *h* between solid surfaces also requires the surface concentration of water between these solid surfaces to decrease with shrinkage. This means that with increasing shrinkage deformation ε the amount of adsorbed water Γ_W is decreasing, reading

$$\partial\varepsilon \approx \partial h \approx \partial\Gamma_w \tag{126}$$

With (126) one derives a relationship that scales shrinkage deformation with energy of deformation, because the change in the surface concentration of adsorbed water Γ_W can be expressed as the water loss of adsorbed water layers, i.e. the adsorbed water fraction $v_{W\_ads.}$. Reconsidering the Helmholtz free energy approach introduced in section 11.4 reading

$$\Psi_{tot.} = \Psi_{def.} + \Psi_{int.} \tag{127}$$

and the discrimination of adsorbed and liquid water fractions

$$v_w = v_{w\_ads.} + v_{w\_bulk} \tag{128}$$

one obtains

$$\begin{aligned} \Psi_{tot.} &= \frac{RT}{v_m}\int v_w d\,ln(RH) \\ &= \Psi_{def.} + \Psi_{int.} \\ &= \frac{RT}{v_m}\int\left(v_{w\_ads.} + v_{w\_bulk.}\right) d\,ln(RH) \end{aligned} \tag{129}$$

where

v_w :	total water loss	[m³/m³]
v_{w_ads} .:	loss of adsorbed water	[m³/m³]
v_{w_bulk} .:	loss of liquid water	[m³/m³]
v_m :	molar volume of water	[m³/mol]

As mentioned above, the discrimination between adsorbed and liquid water fractions is delicate, so that the total Helmholtz free energy can be quantified from the desorption isotherm of cementitious

material, whilst the energy fractions cannot be separated. However, the concept of disjoining pressure allows a second derivation of the energy of deformation independent of the mechanical properties, reading

$$d\Psi_{def.} = p_{disj.}dh + hdp_{disj.} \tag{130}$$

in which the energy of deformation is determined by the energy needed to approach solid surfaces and in which this approaching causes the concentration of adsorbed water between solid surfaces to decrease. Furthermore, the energy utilized in creating interfacial area ($\Psi_{int.}$) can be expressed as a function of surface energy γ and interfacial area *a*, so that the total Helmholtz free energy ($\Psi_{tot.}$) of the open drying cementitious material can be written

$$d\Psi_{tot.} = p_{disj.}dh + hdp_{disj.} + \gamma da + ad\gamma \tag{131}$$

With (131) we derive a simple conceptual base from which the mechanism of SRA in shrinkage can be explained. Moreover, with (131) one derives a general expression that can also be applied once the bulk liquid/vapour interface vanishes in the course of drying. Then, the interfacial area of interest is between the vapour and the adsorbed water. Its surface energy is noted γ_{SFE}. An increase of the energy fraction utilized in creating interfaces or an increase of this interfacial area can be described as follows: On the one hand, the surface energy of this interface increases with decreasing relative humidity [24]. On the other hand, after vanishing of the bulk liquid/vapour interface, the area of the vapour/adsorbed water interface may be equated to the internal specific surface of the capillary pore space a_{cap}. This interfacial area would therefore also increase if further drying induces microcracking of the C-S-H-gel structure. However, unless this happens and down to extremely low humidity when the adsorbed water film would become discontinuous, the area of this interface should remain constant.

This conceptual view is different from the models on drying and shrinkage given by recent authors. In particular, Setzer[10] explicitly relates the total Helmholtz free energy ($\Psi_{tot.}$) to disjoining pressure (compare to (116)), whilst (131) accounts for an additional surface term. With this we can distinguish energy fractions with an approximation that is acceptable for our purpose of comparing systems with and without SRAs. This allows simplifications that are otherwise not possible, but they here help us to gain insight into SRA behaviour, which is the subject of the next section.

11.7.2 The shrinkage reducing mechanism of SRAs

In a first attempt to derive the shrinkage reduction mechanism of SRAs let us reconsider a fundamental statement of Scherer [15], in which the formation of menisci in the drying porous system is explained. Scherer suggests that because the exposure of low energy liquid/vapour interface is preferred over the exposure of a high energy solid/vapour interface, the pore fluid tends to cover the solids by forming menisci, i.e. a curved liquid/vapour interface. In that way the system minimizes its free energy.

Let us now reconsider the findings of chapter 5.2. There, based on theoretical considerations, it could be simulated that, the deformable drying pore system can contribute to reducing exposed interfacial area by deformation. We recognize that, to minimize its energy, the drying cementitious system must reduce its exposed interfacial area and that deformation can contribute to this. However, for deformation itself energy has to be utilized. From this one can take, that drying and shrinkage of cementitious material can be generally described macroscopically by an overall free energy minimization approach, reading:

$$min\,\Psi_{tot.} = min\left(\Psi_{def.} + \Psi_{int.}\right) \tag{132}$$

in which the macroscopically measured drying shrinkage is a result of a minimum of exposed interfacial area, which is determined

a) by the systems microstructure that determines the magnitude of interfacial area to be exposed

b) by the surface tension of the liquid/vapour interface and

c) to some extent by deformation, for which energy can be utilized ($\Psi_{def.}$) to reduce the interfacial energy ($\Psi_{int.}$).

The first and the second property mentioned above determine the energy that must be utilized at the interfacial area. In chapter 11.5 it was shown that the evolution of surface tension and of the exposed interfacial area could be described well for the range of relative humidity that the samples were exposed to.

In chapter 11.7.1, the deformation of the cementitious material was linked to the change of the average distance *h* between solid surfaces of the solid/liquid gel system. In particular, the change of the average solid interspace h was scaled with the change in deformation *ε*. Moreover, energy of deformation was expressed as an energy equivalent for changing this average interspaces distance against the action of disjoining pressure (130).

Just like the name implies, SRA reduce drying shrinkage of cementitious materials. With this and also supported by own results on drying shrinkage (section 11.3.2), there is solid evidence that the deformation energy ($\Psi_{def.}$) is decreased in presence of SRA at any given relative humidity (chapter 11.4).

Furthermore, shrinkage reduction increases with dosage (chapter 11.3.2) so that energy of deformation also decreases with SRA dosage (chapter 11.4). How deformation energy of cement paste CP is impacted in presence of different dosages of SRA1 is displayed in Figure 109. There, the total Helmholtz free energy ($\Psi_{tot.}$), deformation energy ($\Psi_{def.}$) and energy utilized at interfaces ($\Psi_{int.}$) for cement past CP without SRA and with different dosages of SRA1 at different relative humidity are displayed by means of stacked columns.

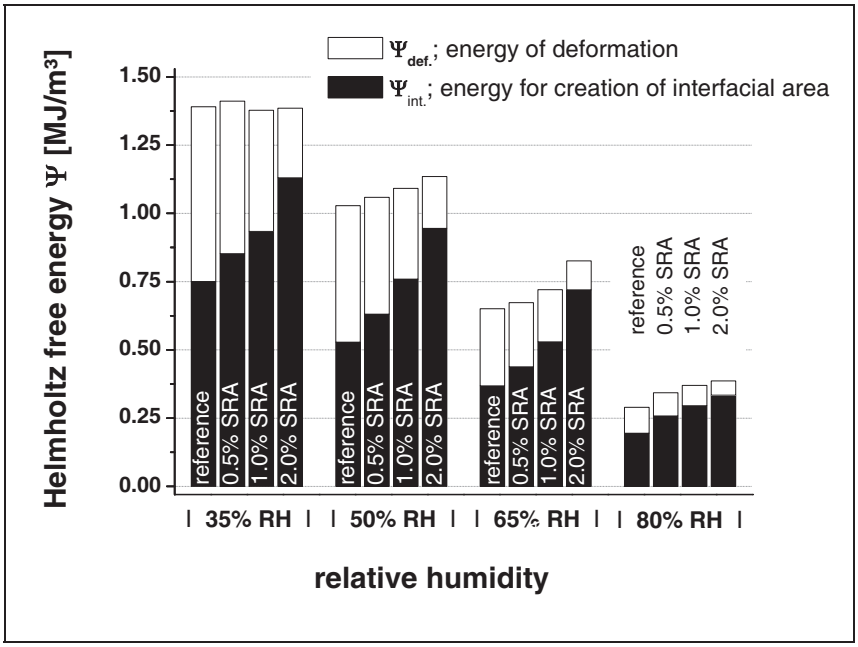

Figure 109: Total Helmholtz free energy , deformation energy and energy utilized at interfaces for cement paste CP without SRA and with different dosages of SRA1 at different relative humidity

Concerning the deformation energy ($\Psi_{def.}$), one can see that indeed, energy of deformation decreases with the dosage of SRA1 whatever the relative humidity. In contrast, the energy utilized for creating interfacial area ($\Psi_{int.}$) increases with SRA dosage at each relative humidity.

The total Helmholtz free energy ($\Psi_{tot.}$) in Figure 109 is calculated using the desorption isotherms measured on samples with and without SRA. One can see that $\Psi_{tot.}$ is slightly increased in presence of SRA.

From Figure 109 one can take that in presence of SRA, the energy balance of drying cementitious material is affected mainly in two different ways. First, the total Helmholtz energy ($\Psi_{tot.}$) increased with dosage. Second, the energy fraction utilized in the creation of interfacial area increases with dosage. The importance of this can be better seen on the following graph (Figure 110) in which the energy fractions (normalized to $\Psi_{tot.}$ at different RH) of the cement paste samples without and with different dosages of SRA1 are displayed. In particular, it shows that, with increasing dosage of SRA1, the fraction of energy used for deformation increases with SRA dosage in a way that is more or less independent of relative humidity.

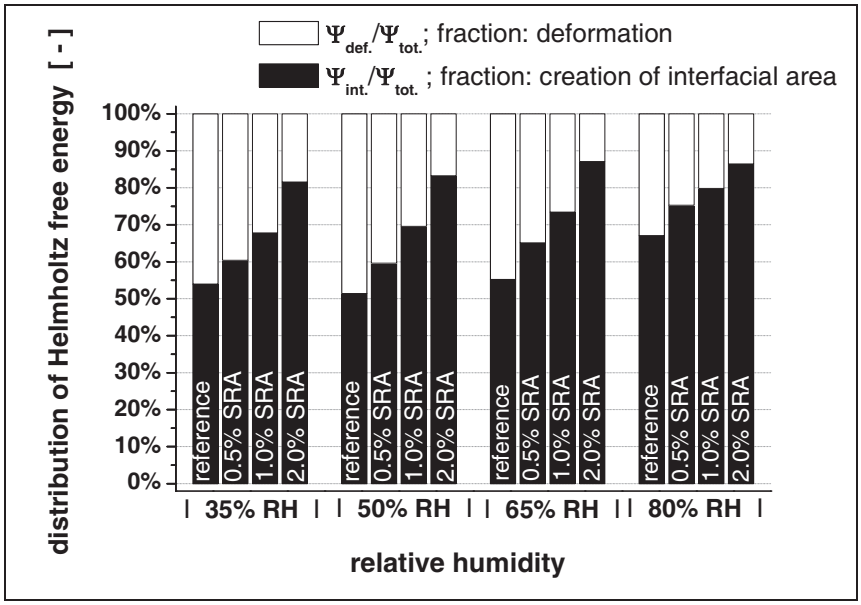

Figure 110: Energy fractions for deformation energy and energy utilized at interfaces for cement past CP without SRA and with different dosages of SRA1 at different relative humidity

Summarizing these results, it can be said the enhanced utilization of Helmholtz free energy for creating interfacial area ($\Psi_{int.}$) with increasing dosage of SRA1 is due to the surface activity of SRA1.

An important point here is that the measurement of desorption isotherms reveal a decreasing partial water saturation with increasing SRA dosage (section 11.3.1), which is found to be a characteristic feature of SRA. The enhanced water loss increases the total Helmholtz free energy.

Because shrinkage in presence of SRA is reduced and the reduction scales with SRA dosage (11.3.2), the loss of adsorbed water at/between solid surfaces decreases with the dosage of SRA. This means, that the enhanced water loss in presence of SRA must be due to enhanced loss of liquid water (bulk liquid), which increases the energy for creation of interfacial area $\Psi_{int.}$. This appears paradoxical, but is not the case as explained below.

The simulations using the artificial pore system “normcube” in chapter 5.2.2. clearly show that the enhanced water loss in presence of SRA is due to the reduced surface tension that decreases with SRA dosage. Moreover, based on the relationship between SRA dosage, surface excess concentration and

exposed interfacial area, developed in chapter 7.3.3 and the results obtained in chapter 10 (leaching), the evolution of surface tension and exposed interfacial area of cement pastes and mortars investigated in this study could be properly approximated (section 11.5). Based on these results it is now possible to explain that both the increase in total Helmholtz free energy and the enhanced utilization of energy at interfaces is due to the surface activity of non-ionic surfactant in SRA1. Moreover, these phenomena could be found to be a characteristic feature of SRAs (section 11.4.1).

From the above, the shrinkage reduction mechanism of SRA in a first attempt can be said to come from the pore system's ability to minimize its free energy more efficiently by creating interfacial area at the liquid/vapour interface than by deforming the solid matrix and that this is facilitated by the reduction in surface tension due to the presence of SRA

While the above explanation is generally coherent, a number of questions subsist. In particular, it is not sufficiently clear how SRAs in general and their surface activity in particular cause the disjoining pressure to decrease. While the results gained in this study do not allow examining this question in detail, some hypotheses nevertheless deserve to be examined. This is done in the next section with the objectives of suggestions directioned in which our simplifying basic concept about the SRA working mechanism may be further developed.

11.7.3 Perspectives on the SRA mechanism

The measurements of desorption and shrinkage isotherms of cementitious material, without and with SRA in different dosages, allow to draw energy balances according to the Helmholtz free energy approach in which energy of deformation and interfacial energy are separated. While this separation, with more or less accuracy, reveals that in presence of SRA the fraction of energy utilized in creating interfacial area significantly increases with dosage, it is not clear what the specific reason for this may be.

In a first attempt one might assume that it comes from a force balance. To take this further one needs to know how the evolution of the liquid/vapour interface impacts the narrowing of the solid interspaces. In particular, a parameter is required that links energy of deformation and energy of the liquid/vapour interface. Because deriving a mechanical model incorporating interparticular forces, microstructure and surface forces is far beyond the scope of this thesis, a simple conceptual approach is selected, suitable to be implemented in the Helmholtz fee energy approach used in this thesis.

In a first step let us reconsider Setzer´s definition on how disjoining pressure governs the hygral volume stability of cementitious material [6, 10]. There it is stated that the average distance *h* between solid surfaces is governed by said disjoining pressure. In particular, the hygral equilibrium conditions can be attributed to be a force balance between repulsive and attractive components of the disjoining pressure. More specifically, for a given material in equilibrium with an imposed relative humidity the overall disjoining pressure or net force is zero because repulsive and attractive components are in equilibrium. One now wonders how the surface tension of the liquid/vapour interface can impact this equilibrium. For this, the repulsive and attractive components are examined in what follows.

According to Setzer´s model for how disjoining pressure governs the hygral volume stability of cementitious material in [10], the disjoining pressure is mainly a function of the distance *h* between the solid surfaces. The attractive contributions to the overall disjoining pressure are dispersive or molecular interaction forces (p_m), whilst the repulsive components are electrostatic (p_e) and structural forces (p_s) (within limits [10]) so that

$$p_{disj.} = p_m + p_e + p_s \tag{133}$$

where

p_m: dispersive or molecular interaction force; attractive

p_e: electrostatic interaction force; repulsive

p_s: structural interaction force; repulsive

Referring to Horn [266] and for the sake of simplicity, the repulsive and attractive components of disjoining pressure can be thought to be a combination of a repulsive exponential function of separation and an attractive power law function, for which attraction decreases with increasing separation.

Assuming moisture equilibrium, in which the net disjoining pressure is zero, one writes

$$-p_m = p_e + p_s \tag{134}$$

From (134) one can take that surface tension of the liquid/ vapour interface must either impact the dispersive interaction between solid surfaces (attractive forces) or the electrostatic/structural interaction (repulsion). Because an impact of surface tension on dispersion forces cannot be seen, one may assume that it is the the repulsive component of disjoining pressure that is affected.

Let us examine the repulsive contribution to overall disjoining pressure in cementitious material more in detail. According to Scherer [15] this electrostatic repulsive contribution may be assumed to be of osmotic nature. Dependent on the imposed relative humidity, or more specifically the moisture potential (see equation (11)), the electrolyte nature of the pore fluid in the interspaces between solid surfaces determines separation force (p_e). For cementitious material the ionic strength is high and the average distance h is low, so that electric double layers superimpose, which causes repulsion. The system tends to attract water from the surrounding to separate these overlapping layers. However, this is governed by the imposed relative humidity. For cementitious material Badmann, Stockhausen and Setzer et al. [18] measured the statistical adsorbed water layer thickness t as a function of relative humidity. From their measurements one can take that t decreases with decreasing relative humidity. Based on the above, we recognize that the imposed relative humidity not only determines the evolution of the liquid/vapour interface but also the amount of the adsorbed water, which in turn determines the average distance h and with that the drying deformation.

The question now arises on how this can happen if the vapour phase is separated from the main part of the C-S-H gel by the liquid/vapour interface. One now concludes that it must be a property of the liquid/vapour interface that impacts the amount of adsorbed water between the C-S-H solid surfaces.

The question is now how this can happen if the vapour is separated from the main part of the C-S-H gel by the liquid/vapour interface. What can be said is that this must lie in a property of the liquid/vapour interface that impacts the amount of adsorbed water between the C-S-H solid surfaces.

An insight into this comes from disjoining pressure measurements carried out using atomic force microscopy (AFM) [267-271]. There, the force measured between the AFM tip and a flat surface is said to originate from the liquid bridge that builds between both surfaces. This formation of this bridge comes from the condensation of water from the ambient humidity [267, 269]. Moreover, we can infer that once such a water bridge forms between AFM tip and the opposing surface, then the surface tension of the liquid/vapour interface determines the magnitude of the disjoining pressure.

In cementitious materials, the C-S-H binding phase is composed of “nano building blocks” between which such liquid bridges can establish. We can therefore assume that owing to its surface tension, the liquid/ vapour interface exerts a negative pressure on the water that is part of the C-S-H-gel. This would tend to cause attraction of opposing surfaces and is opposed by a repulsive or separation pressure acting between the C-S-H interspaces. Equilibrium is found at the separation distance where both attraction and repulsion balance each other.

Assuming in a next step that a reduced surface tension of the liquid/vapour interface develops less attraction, the cementitious material will find its hygral equilibrium with a larger average distance h between solid interspaces and deforms less respectively.

If such a force or rather pressure balance is accounted for, the energy balances drawn in the previous sections can be better explained. In particular, in can be explained why, in presence of SRA, less shrinkage occurs and why an increased energy fraction of the total Helmholtz free energy can be utilized in the creation of interfacial area at the liquid/vapour interface.

As on overall statement on the SRA mechanism it can be said that, due to a reduced surface tension, the pressure exerted by the liquid/vapour interface is reduced. Therefore, less water can be drawn from the gel porosity. However due to the reduced surface tension the creation of interfacial area is facilitated and the loss of liquid water increases thereof.

In case the surface tension increases in the course of drying, as was shown to be the case for some SRA dosage in chapter 11.5, the pressure exerted on the C-S-H-gel should increase too. With an increasing pressure working against the repulsive osmotic pressure, water is drawn from the gel and the cementitious material shrinks. At low humidity, the solid-vapour interfacial properties of the SRA containing material should no more be much different from those of the system without SRA. The differences in the specific deformation therefore vanish as is observed experimentally (chapter 11.4.2).

As a concluding remark, it is has to be noted that the above thoughts refer to a model involving a reduced capillary pressure. However, this must not be confused with the traditional “capillary force model” which assumes capillary pressure to act as a hydrostatic pressure, exerting tensile stress on the pore walls and causing contraction of the porous matter or drying shrinkage respectively. In what was discussed above, the reduced interfacial tension of the liquid/vapour interface induces a reduced capillary pressure that, in turn, causes the repulsive contribution to disjoining pressure to be reduced since equilibrium is reached at a larger separation distance. Hence, in presence of SRA drying shrinkage is reduced.

Although the above is a simplifying view on the working mechanisms of SRA, which of course cannot account for changes of the microstructure in presence of SRA and other side effects, it reflects well enough the main phenomena of how drying and shrinkage of cementitious material is affected by SRAs.

A more detailed study of how SRA affects the equilibrium between the interfacial properties of the liquid/vapour interface and disjoining pressure would be a complement to this. Moreover, a closer view on the behaviour of surfactants in cementitious materials and their ability to reduce surface tension is also required. Based on such investigations, the thoughts about the force balance introduced above, may be developed further and might be put on a more solid base.

12 Overall conclusions

The present theses tried to shed light on the role of SRAs in self consolidating concrete focusing on the three main subjects:

1. the mechanisms of cement hydration
2. the sustainability of SRA application
3. physical impact on shrinkage

The main findings for each of these areas are summarised in individual subsections of this chapter. Before this however, two more general contributions that this thesis makes to the literature on SRAs are summarized.

The first of these is that in the course of this thesis the patent search provided important information on the ingredients of SRA products. It was found that these are most often synergistic mixtures of non-ionic surfactants as main active component and glycols which act as co-surfactants. This fact is generally overlooked by the scientific literature dealing with these products. It is something rather unfortunate since it is responsible for many aspects of SRA performance. Indications about this could be gathered by exploring the abundant literature that focuses on the properties of non-ionic surfactants, the co-surfactant nature of glycols as well as mixtures of both types of these ingredients found in commercial SRAs. This rich pool of information proved beneficial for proper discussion of the results obtained from cement hydration studies.
The second broad implication came from the work on SRA leaching that showed that under conditions of practical relevance, the sustainability of SRAs is guaranteed. This part of the work turned out to be of utmost importance for understanding the physical impact of SRA on drying and shrinkage. In particular, it was shown that the added SRA must be discriminated into mobile and immobile fractions. Thus not all the added SRA is effective. This finding together with shrinkage measurements on leached mortar samples impacts the quantitative interpretation of the performance of SRAs in cementitious systems. It is something that further research on SRAs cannot overlook.

12.1 Cement hydration in presence of SRA

How SRAs affect cement hydration was the subject of chapter 8. It was found that whilst hydration is to some extent retarded by SRAs alone, their combination with superplasticizers can lead to a disproportional extension of the induction period. Concerning the more detailed analysis of hydration, the solid phase analysis revealed that the silicate hydration is retarded in presence of SRA, whilst the aluminate clinker phase reactions proceed rather unaffected.
A first important result on how hydration kinetics are impacted by SRA came from the comparative investigation of paste with different binder types but similar SRA dosages. These results implied that, in contrast to the case of superplasticizers, the retardation of cement hydration is not due to admixture adsorption.

This conclusion is supported by the work of Zhang et al. 2001 [205] as well as Merlin et al. 2005 [206] who investigated the adsorption behaviour of short ethoxylated non-ionic surfactants onto hydrated cementitious material. Indeed, they found that for very low molecular weight compounds, the non-ionic surfactant did not adsorb at all [205] and Merlin identified adsorption of non-ionic surfactants onto C-S-H only on the verge of the detection limit. This is consistent with own results obtained on the hydration of synthetic C_3S in presence of SRA1. Indeed, in this part of the work, it could be shown that the main ingredient of SRA1 is dipropylene tert-butyl ether (DPTB) that shows a specific adsorption onto portlandite, but not on C_3S or C-S-H.

This interaction of SRAs with Portlandite is something new and would deserve to be further investigated in the context of more detailed studies of cement hydration. While this was beyond the scope of this thesis, some time effort was spent to better understand this interesting phenomenon. For exam-

ple, it was found that in presence of SRA the specific surface can be found to be increased. This phenomenon was already described in literature and was also observed for cement pastes and mortars investigated in the course of this study. Investigations in this thesis could prove that this comes from the increased contribution of portlandite surface, resulting from the SRA blocking the 001 crystal plane of portlandite and causing portlandite crystals to mainly grow in their lateral dimensions. Therefore, in mature cement pastes, portlandite can be found as thin platelets or even layered sheets. The increased specific surface area of SRA containing cement pastes increases the amount of water associated to solid surfaces. For pastes, mortar and concrete with rather low water binder ratios this can reduce the amount of water available for cement hydration and, might thereof compromise the degree of hydration achievable. This might explain the reduced mechanical properties of SRA modified concretes reported in literature (see chapter 4.4.5). Whether sufficient wet curing of these concretes can remedy this, is still pending. In this context it is worth commenting on the fact that the chemical shrinkage measurements in chapter 9.3 showed that during “under water” storage the amount of adsorbed water increased with the SRA dosage. In particular, SRA containing pastes and mortars with initial w/c≥0.36 tended to achieve an effective water/cement ratio of w/c=0.41±0.01. This is an important result since it shows that SRA containing systems do benefit from curing. If and to what extent this can be used to compensate the mechanical performance decrease of SRA containing concretes deserves further investigation.

Concerning the preferential adsorption of SRA1 onto portlandite, it is concluded that this takes place on the 001 plane. This is possible because of hydroxyl groups that do not get hydrolysed at high pH of cementitious systems and explains the thin platelets morphology, the increased specific surface and the higher amount of bound water at a given degree of hydration. Assuming that the adsorbed SRAs limit growth rates of portlandite, this would be accompanied by an increase of the calcium concentration in solution that penalizes dissolution [248]. Furthermore, the disproportional retardation observed for the combined application of SRA and SP-PCE can now be explained better. Whilst retardation from superplasticizer seems to come from the specific interaction with the silicate clinker phase and C-S-H (Pourchet et al. 2007 [272]), the retarding effect from SRA concerns portlandite growth. As a simple conceptual explanation, one concludes that both effects are independent of each other and just accumulate when both admixtures are used together.

12.2 Sustainability of the SRA application

Whether SRAs are leachable and how this affects the long term shrinkage reduction was the subject of chapter 10. In this context, one objective was to clarify how strongly SRAs are associated to the solid surfaces and whether they may desorb if an excess of interfacial area or aqueous solution is provided.

A first important finding of the leaching studies is that SRA is initially distributed homogeneously within the cement paste. In the course of hydration, about 40% of it gets associated to hydration products. In regard to chapters 8.3.3 and 8.3.4, these could be layered portlandite crystals. SRA1 could however also be immobilized in gel pores.

The knowledge on how SRAs are distributed in the porous cementitious system impacts both the shrinkage reduction effect and its sustainability. Concerning shrinkage reduction, it was shown that the mobile fraction of SRA determines to what extent the surface tension of the liquid/vapour interface can be reduced in the course of drying. However, it is the same mobile fraction of SRA that can be released upon contact with water.

The complete removal of the mobile SRA almost completely eliminates the shrinkage reduction in the capillary range of humidity. However, for all mortars some shrinkage reducing effect remains for low relative humidity, which implies that the immobile fraction of SRA contributes to shrinkage reduction via steric repulsive contributions to disjoining pressure. While as such effects have been speculated in the literature, this is to the author’s best knowledge the first set of data showing this with some ex-

perimental clarity.
Concerning the shrinkage reduction that remained after leaching, the immobile fraction of SRA might contribute to this through its effect on another mechanical property. For example if drying creep were reduced in presence of SRA at least the results found for low humidity could be explained.

It has to be emphasised that the results from tank tests might not be of practical relevance and that cyclic leaching and drying can be assumed to better meet the exposure conditions of concrete in field. From cyclic leaching it was shown that, in contrast to permanent leaching, the relative amounts leached per cycle depend on the initial dosage of SRA. The amount of admixture leached during the cycles however is drastically decreased. For these tests, the removal of about 10 to 20% SRA1 seems to have only minor effect on the shrinkage reduction.
More importantly, from cyclic drying and rewetting tests the main impact on strain evolution could be shown to come from the aging of the cement matrix itself. Carbonation shrinkage was found to be enhanced for the non-leached specimen. This clearly has a big impact on the magnitude of irreversible deformations, but is not something that SRAs can act upon. For leached mortars this is less pronounced because readily soluble phases that tend to carbonate are removed prior to drying in the course of the leaching sub-cycles.
As an overall conclusion, it can be said that the shrinkage reduction from SRA is sufficiently sustainable as long as the concrete is not exposed to extreme volume of running water. Based on this, the application of SRA can be especially recommended for the long term reduction of drying shrinkage of concrete. However, it may become delicate in cases aiming at the reduction of early age shrinkage and cracking of concrete which is later on in contact with much water. For such concretes, drying and drying induced shrinkage are of course of interest but the release of SRA may become an environmental issue.

12.3 Drying and shrinkage of cementitious material in presence of SRA

How SRAs impact drying and shrinkage was the subject of chapter 11. In particular, their shrinkage reduction mechanism was of interest.

The different approaches to the drying and shrinkage of porous materials described in literature deliver expressions for the shrinkage strain where the saturation degree and sometimes the capillary pressure appear. For a fixed relative humidity, SRAs can modify the first but not the second. From a theoretical point of view it was concluded that the SRA effects must be sought either in their effect on the saturation degree or on the disjoining pressure. Concerning the interactions of SRAs in presence of electrolytes and in analogy to findings for non-ionic surfactants it was inferred that non-ionic surfactants weakly influence electrostatic interactions and, secondly, that they might induce a repulsive steric contribution to disjoining pressure.
Concerning the latter, the answer is still pendent whether the repulsive steric effect from SRAs contributes to reducing drying shrinkage. However, the leaching studies in general and the results from tank tests reveal that the shrinkage reduction from SRAs almost completely vanishes with the removal of the mobile fraction of SRAs, which is one of the most important result of this thesis.

The idea that the SRA effect on shrinkage is directly related to the surface tension and the presence of the liquid/vapour interface is supported by the results of the energy balances set up to describe drying and shrinkage of cement paste and mortar. In particular, from the specific distribution of the energy fractions, one can conclude that, in presence of SRAs, less energy is utilized for deformation, whilst the creation of interfacial area is facilitated by the reduced surface tension of the liquid/vapour interface. While some authors have talked about these different contributions to the overall Helmholtz free energy, no publications were found with numerical estimations derived from experimental measurement. It is therefore a contribution of this thesis to do this, and more specifically in the case of systems containing SRAs. The specific change of the energy distribution in presence of SRA was observed for

different types of SRA and was also found to correlate with dosage. It can therefore be attributed a characteristic feature of SRA containing cementitious material.

More specifically, the fact that the total water loss, and with that, the total Helmholtz free energy is barely affected by the presence of SRA is of greatest importance. It implies that, in presence of the non-ionic surfactant, more liquid water is evaporated while less adsorbed water is drawn from the interspaces of solids, i.e. from gel porosity. In the course of drying, this causes less narrowing of the gaps between solid surfaces, which macroscopically is recognised as shrinkage reduction.

This simple conceptual view on the surface tension of the liquid/vapour interface as the determining factor for the shrinkage reducing mechanism of SRA however leaves us with an unresolved issue. This is whether the shrinkage reduction mechanism of SRA is directly related to surface tension or whether it is a result of the decreased liquid saturation, which itself results from the decreased surface tension.
Concerning the latter, a decreased liquid saturation decreases the average capillary pressure. As a result, less water is drawn from the interspaces of solid surfaces. In this scenario, the view of average capillary pressure acting on the solid/liquid gel system must not be confused with the traditional capillary force model for drying shrinkage. In this thesis it could be clearly shown that the assumption of average capillary pressure acting as hydrostatic pressure on the solid skeleton of the porous cementitious material cannot explain the shrinkage reducing effect of SRA.

As an overall conclusion, the results of this thesis provide solid evidence that surface tension is of broad relevance for the shrinkage reducing effect of SRAs in general and of non-ionic surfactants in particular. However, it cannot be related to the traditional explanation of average capillary pressure.

Such results are important not only for the understanding but also the design of alternative admixtures, one that for example may be of less environmental concern in terms of leachability.

13 References

1. Bangham: "*The Gibbs adsorption equation and adsorption on solids"* Transactions of the Faraday Society 1937. **33**: p. 805-811.
2. Bangham and Fakhoury: "*The Swelling of Charcoal. Part I. Preliminary Experiments with Water Vapour, Carbon Dioxide, Ammonia, and Sulphur Dioxide"* Proceedings of the Royal Society of London. Series A, Containing Papers of a Mathematical and Physical Character, 1930. **130**(812): p. 81-89.
3. Bangham, Fakhoury and Mohamed: "*The Swelling of Charcoal. Part II. Some Factors Controlling the Expansion Caused by Water, Benzene and Pyridine Vapours"* Proceedings of the Royal Society of London. Series A, Containing Papers of a Mathematical and Physical Character, 1932. **138**(834): p. 162-183.
4. Bangham, Fakhoury and Mohamed: "*The Swelling of Charcoal. Part III. Experiments with the Lower Alcohols"* Proceedings of the Royal Society of London. Series A, Mathematical and Physical Sciences, 1934. **147**(860): p. 152-175.
5. Powers: "*The thermodynamics of volume change and creep"* Materials and Structures, 1968. **1**(6): p. 487-507.
6. Setzer, *Modified method to calculate pore size distributions from water vapour adsorption data*, in *RILEM/IUPAC International Symposium "Pore Structure and Properties of Materials"*. 1973, Academia (Prague): Prague.
7. Setzer and Wittmann: "*Surface energy and mechanical behaviour of hardened cement paste"* Applied Physics A: Materials Science & Processing, 1974. **3**(5): p. 403-409.
8. Hansen: "*Drying Shrinkage Mechanisms in Portland Cement Paste"* Journal of the American Ceramic Society, 1987. **70**(5): p. 323-328.
9. Beltzung and Wittmann: "*Role of disjoining pressure in cement based materials"* Cement and Concrete Research, 2005. **35**(12): p. 2364-2370.
10. Setzer: "*The solid-liquid gel-system of hardened cement paste"*. in *2nd International RILEM Symposium on Advances in Concrete through Science and Engineering*. 2006. Quebec City, Canada: RILEM Publications SARL.
11. Coussy, Dangla, Lassabatère, and Baroghel-Bouny: "*The equivalent pore pressure and the swelling and shrinkage of cement-based materials"* Materials and Structures, 2004. **37**(1): p. 15-20.
12. Coussy, Eymard and Lassabatere: "*Constitutive Modeling of Unsaturated Drying Deformable Materials"* Journal of Engineering Mechanics, 1998. **124**(6): p. 658-667.
13. Olivier Coussy: "*Unsaturated Thermoporoelasticity"*, in *Poromechanics*. 2004. p. 151-187.
14. Landau and Lifshits: "*Theory of elasticity"*. 4 ed. Course of theoretical physics. Vol. 7. 1987, Moscow: Izd. Nauka.
15. Scherer: "*Theory of Drying"* Journal of the American Ceramic Society, 1990. **73**(1): p. 3-14.
16. Brunauer, Mikhail and Bodor: "*Pore structure analysis without a pore shape model"* Journal of Colloid and Interface Science, 1967. **24**(4): p. 451-463.
17. Brunauer, Mikhail and Bodor: "*Some remarks about capillary condensation and pore structure analysis"* Journal of Colloid and Interface Science, 1967. **25**(3): p. 353-358.
18. Badmann, Stockhausen and Setzer: "*The statistical thickness and the chemical potential of adsorbed water films"* Journal of Colloid and Interface Science, 1981. **82**(2): p. 534-542.
19. Ferraris and Wittmann: "*Shrinkage mechanisms of hardened cement paste"* Cement and Concrete Research, 1987. **17**(3): p. 453-464.
20. Setzer: "*Interaction of water with hardened cement paste"*. in *Conf. Advances in cementitious materials*. 1991: Ceramic Transactions Vol. 16. Westerville Amer. Cer. Soc.
21. Wittmann: "*Interaction of Hardened Cement Paste and Water"* Journal of the American Ceramic Society, 1973. **56**(8): p. 409-415.
22. Nielsen: "*Rheologische eigenschaften für isotrope linear-viskoelastische kompositmaterialien"* Cement and Concrete Research, 1973. **3**(6): p. 751-766.
23. Olivier Coussy: "*Poroviscoelasticity"*, in *Poromechanics*. 2004. p. 261-277.
24. Bentz, Garboczi and Quenard: "*Modelling drying shrinkage in reconstructed porous materials: application to porous Vycor glass"* Modelling and Simulation in Materials Science and Engineering, 1998. **6**(3): p. 211-236.

25. Mackenzie: "*The Elastic Constants of a Solid containing Spherical Holes"* Proceedings of the Physical Society. Section B, 1950(1): p. 2.
26. Granger and Acker: "*Thoughts about drying shrinkage: Scale effects and modelling"* Materials and Structures 1997. **30**(2): p. 96-105.
27. Shoya: "*Improvement of drying shrinkage and shrinkage cracking of concrete by special surfactants"*. in *Admixtures for concrete / Improvement of properties*. 1990. Barcelona: Rilem, London.
28. Hua, Acker and Ehrlacher: "*Analyses and models of the autogenous shrinkage of hardening cement paste: 1. Modeling at macroscopic scale"* Cement and Concrete Research, 1995. **25**(7): p. 1457-1468.
29. Sato, *"Mechanism for reducing drying shrinkage of hardened cement by organic additives"*, C. Review, Editor. 1983, Cement Association of Japan CAJ. p. 52-54.
30. Bundke; Thesis: "Über die Variabilität der physikalischen Eigenschaften atmosphärischer Aerosolpartikel"; Fachbereich Geowissenschaften / Geographie; Johann Wolfgang Goethe-Universität; 2002
31. Lura; Thesis: "Autogenous Deformation and Internal Curing of Concrete"; Technical University Delft; 2003
32. Churaev: "*Surface forces in wetting films"* Advances in Colloid and Interface Science, 2003. **103**(3): p. 197-218.
33. Langmuir: "*The constitution and fundamental properties of solids and liquids. Part II. Liquids"* J. Am. Chem. Soc., 1917. **39**(9): p. 1848-1906.
34. Onsager and Samaras: "*The Surface Tension of Debye-Hückel Electrolytes"* The Journal of Chemical Physics, 1934. **2**(8): p. 528-536.
35. Jarvis and Scheiman: "*Surface potentials of aqueous electrolyte solutions"* J. Phys. Chem., 1968. **72**(1): p. 74-78.
36. Ralston and Healy: "*Specific cation effects on water structure at the air-water and air-octadecanol monolayer-water interfaces"* Journal of Colloid and Interface Science, 1973. **42**(3): p. 629-644.
37. Aveyard and Heselden: "*Salting-out of alkanols by inorganic electrolytes"* J. Chem. Soc., Faraday Trans. 1, 1975. **71**: p. 312-321.
38. Aveyard and Saleem: "*Interfacial tensions at alkane-aqueous electrolyte interfaces"* J. Chem. Soc., Faraday Trans. 1, 1976. **72**: p. 1609-1617.
39. Hey and David W. Shield: "*Surface tensions of aqueous solutions of some 1:1 electrolytes"* J. Chem. Soc., Faraday Trans. 1, 1981. **77**(1): p. 123-128.
40. Stairs: "*Calculation of surface tension of salt solutions: effective polarizability of solvated ions"* Can. J. Chem., 1995. **73**(6): p. 781.
41. Weissenborn and Pugh: "*Surface Tension and Bubble Coalescence Phenomena of Aqueous Solutions of Electrolytes"* Langmuir, 1995. **11**(5): p. 1422-1426.
42. Weissenborn and Pugh: "*Surface Tension of Aqueous Solutions of Electrolytes: Relationship with Ion Hydration, Oxygen Solubility, and Bubble Coalescence"* Journal of Colloid and Interface Science, 1996. **184**(2): p. 550-563.
43. Bostrom, Williams and Ninham: "*Surface Tension of Electrolytes: Specific Ion Effects Explained by Dispersion Forces"* Langmuir, 2001. **17**(15): p. 4475-4478.
44. Karraker and Radke: "*Disjoining pressures, zeta potentials and surface tensions of aqueous non-ionic surfactant/electrolyte solutions: theory and comparison to experiment"* Advances in Colloid and Interface Science, 2002. **96**(1-3): p. 231-264.
45. Tennis and Jennings: "*A model for two types of calcium silicate hydrate in the microstructure of Portland cement pastes"* Cement and Concrete Research, 2000. **30**(6): p. 855-863.
46. Jennings: "*A model for the microstructure of calcium silicate hydrate in cement paste"* Cement and Concrete Research, 2000. **30**(1): p. 101-116.
47. Roessler; Thesis: "Hydratation, Fließfähigkeit und Festigkeitsentwicklung von Portlandzement – Einfluss von Fließmitteln, Alkalisulfaten und des Abbindereglers"; F.A. Finger Institut für Baustoffkunde; Bauhaus-Universität Weimar; 2006
48. Powers: "*Physical Properties of Cement Paste"*. in *4th Int. Symposium on the Chemistries of Cement*. 1960. Washington.
49. Powers: "*Structure and Physical Properties of Hardened Portland Cement Paste"* Journal of the American Ceramic Society, 1958. **41**(1): p. 1-6.

50. Thomas: "*The surface area of hardened cement paste as measured by various techniques"* Concrete Science and Engineering, 1999. **1**(1): p. 45 - 64.
51. Scherer: "*Structure and properties of gels"* Cement and Concrete Research, 1999. **29**(8): p. 1149-1157.
52. Powers: "*Mechanisms of shrinkage and reversible creep of hardened cement paste"* Cement and Concrete Association, London, 1965: p. 319 – 344.
53. Fisher and Israelachvili: "*Direct measurement of the effect of meniscus forces on adhesion: A study of the applicability of macroscopic thermodynamics to microscopic liquid interfaces"* Colloids and Surfaces, 1981. **3**(4): p. 303-319.
54. Roper: "*Dimensional Change and water Sorption Studies of Cement Paste "*. in *Symposium on Structure of Portland Cement Paste and Concrete*. 1966. Washington D.C.
55. Daimon, Abo-El-Enein, Rosara, Goto, and Kondo: "*Pore Structure of Calcium Silicate Hydrate in Hydrated Tricalcium Silicate"* Journal of the American Ceramic Society, 1977. **60**(3-4): p. 110-114.
56. Fisher: "*Forces due to capillary-condensed liquids: Limits of calculations from thermodynamics"* Advances in Colloid and Interface Science, 1982. **16**(1): p. 117-125.
57. Fisher and Israelachvili: "*Determination of the Capillary pressure in menisci of molecular dimensions"* Chemical Physics Letters, 1980. **76**(2): p. 325-328.
58. Cranston, Inkley and Adalbert: "*17 The Determination of Pore Structures from Nitrogen Adsorption Isotherms"*, in *Advances in Catalysis*. 1957, Academic Press. p. 143-154.
59. Mindess, Young and Lawrence: "*Creep and drying shrinkage of calcium silicate pastes I. Specimen preparation and mechanical properties"* Cement and Concrete Research, 1978. **8**(5): p. 591-600.
60. Bentur, Milestone and Young: "*Creep and drying shrinkage of calcium silicate pastes II. Induced microstructural and chemical changes"* Cement and Concrete Research, 1978. **8**(6): p. 721-732.
61. Bentur, Berger, Lawrence, Milestone, Mindess, and Young: "*Creep and drying shrinkage of calcium silicate pastes III. A hypothesis of irreversible strains"* Cement and Concrete Research, 1979. **9**(1): p. 83-95.
62. Thomas, Jennings and Allen: "*The surface area of cement paste as measured by neutron scattering: Evidence for two C-S-H morphologies"* Cement and Concrete Research, 1998. **28**(6): p. 897-905.
63. Garci Juenger and Jennings: "*Examining the relationship between the microstructure of calcium silicate hydrate and drying shrinkage of cement pastes"* Cement and Concrete Research, 2002. **32**(2): p. 289-296.
64. Thomas and Jennings: "*Changes in the size of pores during shrinkage (or expansion) of cement paste and concrete"* Cement and Concrete Research, 2003. **33**(11): p. 1897-1900.
65. Jennings: "*Colloid model of C-S-H and implications to the problem of creep and shrinkage"* Materials and Structures, 2004. **37**(265): p. 59-70.
66. Thomas and Jennings: "*A colloidal interpretation of chemical aging of the C-S-H gel and its effects on the properties of cement paste"* Cement and Concrete Research, 2006. **36**(1): p. 30-38.
67. Jennings, Thomas, Gevrenov, Constantinides, and Ulm: "*A multi-technique investigation of the nanoporosity of cement paste"* Cement and Concrete Research, 2007. **37**(3): p. 329-336.
68. Hua: "*Mechanism of shrinkage reduction using a chemical admixture"*. in *Proceedings of the 10th International Conference on the Chemistry of Cement*. 1997. Göteborg, Sweden.
69. Bentz and Jensen: "*Mitigation strategies for autogenous shrinkage cracking"* Cement and Concrete Composites, 2004. **26**(6): p. 677-685.
70. Bentz: "*Influence of Shrinkage-Reducing Admixtures on Early-Age Properties of Cement Pastes"* Journal of Advanced Concrete Technology, 2006. **4**(3): p. 423-429.
71. Lura, Pease, Mazzotta, Rajabipour, and Weiss: "*Influence of shrinkage-reducing admixtures on development of plastic shrinkage cracks"* Aci Materials Journal, 2007. **104**(2): p. 187-194.
72. Cerulli, Pistolesi, Maltese, and Salvioni: "*Effects of shrinkage reducing admixtures on the physical mechanical properties of mortars"*. in *ICMA International Conference on Cement Microscopy*. 2001. New Mexico.
73. Collepardi, Borsoi, Collepardi, Olagot, and Troli: "*Effects of shrinkage reducing admixture in shrinkage compensating concrete under non-wet curing conditions"* Cement & Concrete Composites, 2005. **27**(6): p. 704-708.

74. Gettu: "*Long-term behaviour of concrete incorporating a shrinkage-reducing admixture"* Indian-Concrete-Journal, 2002. **76**(9): p. 586-592.
75. Holt: "*Methods of reducing early-age shrinkage "*. in *Shrinkage 2000*. 2000. Paris: RILEM.
76. Shah, Karaguler and Sarigaphuti: "*Effects of shrinkage-reducing admixtures on restrained shrinkage cracking of concrete"* Aci Materials Journal, 1992. **89**(3): p. Winterthur289-295.
77. Weiss and Shah: "*Restrained shrinkage cracking: the role of shrinkage reducing admixtures and specimen geometry"* Materials and Structures, 2002. **35**(246): p. 85-91.
78. Ostrikov: "*Deforming effect of osmotically dehydrating liquid media"* Kolloidnyi Zhurnal, 1965. **27**(1): p. 82-86.
79. Patent: U.P. Office: US 6712900; Wombacher, Bürge and Mäder (2004); "Method for the reduction of the degree of shrinkage of hydraulic binders"; Sika AG, Vorm, Kasper Winkler & Co. (Zurich, CH)
80. Patent: U.P. Office: US 6398866; Wombacher, Bürge and Mäder (2002); "Method for the reduction of the degree of shrinkage of hydraulic binders"; Sika AG, vorm. Kaspar Winkler & Co. (Zurich, CH)
81. Patent: E.P. Office: EP1024120 (A1); Wombacher, Buerge and Maeder (2000); "Method of reducing the shrinkage of hydraulic binders"; SIKA AG (CH)
82. Patent: E.P. Office: EP1914211 (A1); Gartner (2008); "Cement shrinkage reducing agent and method for obtaining cement based articles having reduced shrinkage"; Lafarge (FR)
83. Patent: E.P. Office: EP0643022 (A1); Shawl and Kesling Jr. (1995); "Cement composition"; Arco Chemical Technology, L.P. (US)
84. Wattebled; Thesis: "Oligomeric Surfactants as Novel Type of Amphiphiles: Structure – Property Relationships and Behaviour with Additives"; Mathematisch-Naturwissenschaftliche Fakultät; Universität Potsdam; 2006
85. Garnier; Thesis: "Novel Amphiphilic Diblock Copolymers by RAFT-Polymerisation, Their Self-Organization and Surfactant Properties"; Mathematisch-Naturwissenschaftliche Fakultät; Universität potsdam; 2005
86. Tadros: "*Applied surfactants : principles and applications"*, ed. Tadros. 2005, Weinheim: Wiley-VCH Verlag GmbH & Co. KGaA.
87. Rosen: "*Surfactants and Interfacial Phenomena (Third Edition)"*. 2004: John Wiley & Sons, Inc.
88. Evans: "*Self-organization of amphiphiles"* Langmuir, 1988. **4**(1): p. 3-12.
89. Molyneux, Rhodes and Swarbrick: "*Thermodynamics of micellization of N-alkyl betaines"* Transactions of the Faraday Society 1965. **61**: p. 1043-1052.
90. Schulz; Thesis: "The Phase Behavior of Amphiphilic Surfactants and Polymers: A Dissipative Particles Dynamics Study"; Fachbereich Chemie; Universität Duisburg-Essen; 2004
91. Schurtenberger, Cavaco, Tiberg, and Regev: "*Enormous Concentration-Induced Growth of Polymer-like Micelles"* Langmuir, 1996. **12**(12): p. 2894-2899.
92. Weckström and Zulauf: "*Lower consolute boundaries of a poly(oxyethylene) surfactant in aqueous solutions of monovalent salts"* J. Chem. Soc., Faraday Trans. 1, 1985. **81**: p. 2947-2958.
93. Kjellander: "*Phase Separation of Non-ionic Surf actant Solutions: A Treatment of the Micellar Interaction and Form"* J. Chem. Soc., Faraday Trans. 2, 1982. **78**: p. 2025-2042.
94. Claesson, Kjellander, Stenius, and Christenson: "*Direct measurement of temperature-dependent interactions between non-ionic surfactant layers"* Journal of the Chemical Society, Faraday Transactions 1: Physical Chemistry in Condensed Phases, 1986. **82**(9): p. 2735-2746.
95. Sharma, Patil and Rakshit: "*Study of the cloud point of C12En nonionic surfactants: effect of additives"* Colloids and Surfaces A: Physicochemical and Engineering Aspects, 2003. **219**(1-3): p. 67-74.
96. Mitchell: "*Phase Behaviour of Polyoxyethylene Surfactants with Water: Mesophase Structures and Partial Miscibility (Cloud Points)"* J. Chem. SOC., Faraday Trans. I 1983. **79**: p. 975-1000.
97. Kabalnov, Olsson and Wennerstroem: "*Salt Effects on Nonionic Microemulsions Are Driven by Adsorption/Depletion at the Surfactant Monolayer"* J. Phys. Chem., 1995. **99**(16): p. 6220-6230.
98. Alexandridis and Holzwarth: "*Differential Scanning Calorimetry Investigation of the Effect of Salts on Aqueous Solution Properties of an Amphiphilic Block Copolymer (Poloxamer)"* Langmuir, 1997. **13**(23): p. 6074-6082.
99. Leontidis: "*Hofmeister anion effects on surfactant self-assembly and the formation of mesoporous solids"* Current Opinion in Colloid & Interface Science, 2002. **7**(1-2): p. 81-91.

100. Bauduin, Wattebled, Touraud, and Kunz: "*Hofmeister Ion Effects on the Phase Diagrams of Water-Propylene Glycol Propyl Ethers"* Zeitschrift für Physikalische Chemie, 2004. **218**(6): p. 631-641.
101. Morini, Messina and Schulz: "*The interaction of electrolytes with non-ionic surfactant micelles"* Colloid & Polymer Science, 2005. **283**(11): p. 1206-1218.
102. Hofmeister: "*Zur Lehre von der Wirkung der Salze: Zweite Mittheilung"* Naunyn-Schmiedeberg's Archives of Pharmacology, 1888. **24**(4): p. 247-260.
103. Hofmeister: "*Zur Lehre von der Wirkung der Salze: Dritte Mittheilung"* Naunyn-Schmiedeberg's Archives of Pharmacology, 1888. **25**(1): p. 1-30.
104. Bowron and Finney: "*Structure of a salt--amphiphile--water solution and the mechanism of salting out"* The Journal of Chemical Physics, 2003. **118**(18): p. 8357-8372.
105. Finney and Bowron: "*Anion bridges and salting out"* Current Opinion in Colloid & Interface Science, 2004. **9**(1-2): p. 59-63.
106. Partyka, Zaini, Lindheimer, and Brun: "*The adsorption of non-ionic surfactants on a silica gel"* Colloids and Surfaces, 1984. **12**: p. 255-270.
107. Narkis and Ben-David: "*Adsorption of non-ionic surfactants on activated carbon and mineral clay"* Water Research, 1985. **19**(7): p. 815-824.
108. Denoyel and Rouquerol: "*Thermodynamic (including microcalorimetry) study of the adsorption of nonionic and anionic surfactants onto silica, kaolin, and alumina"* Journal of Colloid and Interface Science, 1991. **143**(2): p. 555-572.
109. Liu, Edwards and Luthy: "*Sorption of non-ionic surfactants onto soil"* Water Research, 1992. **26**(10): p. 1337-1345.
110. Narkiewicz-Michalek, Rudzinski, Keh, and Partyka: "*A combined calorimetric--thermodynamic study of non-ionic surfactant adsorption from aqueous solutions onto silica surface"* Colloids and Surfaces, 1992. **62**(4): p. 273-288.
111. Portet, Desbène and Treiner: "*Adsorption Isotherms at a Silica/Water Interface of the Oligomers of Polydispersed Nonionic Surfactants of the Alkylpolyoxyethylated Series"* Journal of Colloid and Interface Science, 1997. **194**(2): p. 379-391.
112. Nevskaia, Guerrero-Ruíz and de D. López-González: "*Adsorption of Polyoxyethylenic Nonionic and Anionic Surfactants from Aqueous Solution: Effects Induced by the Addition of NaCl and CaCl2"* Journal of Colloid and Interface Science, 1998. **205**(1): p. 97-105.
113. Kjellin, Claesson and Linse: "*Surface Properties of Tetra(ethylene oxide) Dodecyl Amide Compared with Poly(ethylene oxide) Surfactants. 1. Effect of the Headgroup on Adsorption"* Langmuir, 2002. **18**(18): p. 6745-6753.
114. Levitz: "*Non-ionic surfactants adsorption: structure and thermodynamics"* Comptes Rendus Geosciences, 2002. **334**(9): p. 665-673.
115. Gonzalez-Garcia, Gonzalez-Martin, Gonzalez, Sabio, Ramiro, and Ganan: "*Nonionic surfactants adsorption onto activated carbon. Influence of the polar chain length"* Powder Technology, 2004. **148**(1): p. 32-37.
116. Paria and Khilar: "*A review on experimental studies of surfactant adsorption at the hydrophilic solid-water interface"* Advances in Colloid and Interface Science, 2004. **110**(3): p. 75-95.
117. Kharitonova, Ivanova and Summ: "*Adsorption of cationic and nonionic surfactants on a SiO2 surface from aqueous solutions: 1. Adsorption of dodecylpyridinium bromide and Triton X-100 from individual solutions"* Colloid Journal, 2005. **67**(2): p. 242-248.
118. Chao, Chang, Lee, Lee, and Chen: "*Selective adsorption and partitioning of nonionic surfactants onto solids via liquid chromatograph mass spectra analysis"* Journal of Hazardous Materials, 2008. **152**(1): p. 330-336.
119. Sedev and Exerowa: "*DLVO and non-DLVO surface forces in foam films from amphiphilic block copolymers"* Advances in Colloid and Interface Science, 1999. **83**(1-3): p. 111-136.
120. Diakova, Plantikanov, Atanassov, and Kaisheva: "*Thin wetting films from aqueous solutions of a polyoxyethylene-polyoxypropylene block copolymer on silicon carbide surface"* Advances in Colloid and Interface Science, 2003. **104**(1-3): p. 25-36.
121. Exerowa, Sedev, Ivanova, Kolarov, and Tadros: "*Transition from electrostatic to steric stabilization in foam films from ABA triblock copolymers of poly(ethylene oxide) and poly(propylene oxide)"* Colloids and Surfaces A: Physicochemical and Engineering Aspects, 1997. **123-124**: p. 277-282.

122. Lunkenheimer, Schrödle and Kunz: "*Dowanol DPnB in water as an example of a solvo-surfactant system: adsorption and foam properties*", in *Trends in Colloid and Interface Science XVII*. 2004. p. 14-20.
123. Tan, Pugh, Fornasiero, Sedev, and Ralston: "*Foaming of polypropylene glycols and glycol/MIBC mixtures"* Minerals Engineering, 2005. **18**(2): p. 179-188.
124. Tan, Fornasiero, Sedev, and Ralston: "*The interfacial conformation of polypropylene glycols and their foam properties"* Minerals Engineering, 2006. **19**(6-8): p. 703-712.
125. Tan, Fornasiero, Sedev, and Ralston: "*The role of surfactant structure on foam behaviour"* Colloids and Surfaces A: Physicochemical and Engineering Aspects, 2005. **263**(1-3): p. 233-238.
126. Tan, Fornasiero, Sedev, and Ralston: "*The interfacial conformation of polypropylene glycols and foam behaviour"* Colloids and Surfaces A: Physicochemical and Engineering Aspects, 2004. **250**(1-3): p. 307-315.
127. Seguin, Eastoe, Clapperton, Heenan, and Grillo: "*Alternative non-aqueous water-miscible solvents for surfactants"* Colloids and Surfaces A: Physicochemical and Engineering Aspects, 2006. **282-283**: p. 134-142.
128. Nagamune, UEDA and NAGAI: "*Synthesis of (AB),-Type Block Copolymers Employing Surface-Active Macro-Azo Initiators"* Journal of Applied Polymer Science, 1996. **62**(2): p. 359-365.
129. Palepu, Gharibi, Bloor, and Wyn-Jones: "*Electrochemical studies associated with the micellization of cationic surfactants in aqueous mixtures of ethylene glycol and glycerol"* Langmuir, 1993. **9**(1): p. 110-112.
130. Carnero Ruiz, Díaz-López and Aguiar: "*Self-assembly of tetradecyltrimethylammonium bromide in glycerol aqueous mixtures: A thermodynamic and structural study"* Journal of Colloid and Interface Science, 2007. **305**(2): p. 293-300.
131. Martino and Kaler: "*The stability of lamellar phases in water, propylene glycol, and surfactant mixtures"* Colloids and Surfaces A: Physicochemical and Engineering Aspects, 1995. **99**(2-3): p. 91-99.
132. Rajabipour, Sant and Weiss: "*Interactions between shrinkage reducing admixtures (SRA) and cement paste's pore solution"* Cement and Concrete Research, 2008. **38**(5): p. 606-615.
133. Shoya: "*Effective Use of Shrinkage Reducing Admixture to Control Shrinkage Cracking of Concrete"*. in *Proceedings of the First International RILEM Congress*. 1987.
134. Fujiwara and R. Tomita: "*A Study of Frost Resistance of Concrete Using an Organic Shrinkage-Reducing Agent"*. in *Proceedings of the third CANMET-ACI International Conference on Durability of Concrete*. 1994. Nice: ACI.
135. Tazawa and Miyazawa: "*Influence of cement and admixture on autogenous shrinkage of cement paste"* Cement and Concrete Research, 1995. **25**(2): p. 281-287.
136. Shah: "*Control of cracking with shrinkage-reducing admixtures"* Transportation-Research-Record 1996. **1574**: p. 25-36.
137. Berke, Dallaire, Durning , Folliard, and Kerkar: "*Effects of shrinkage-reducing additives on concrete properties"* JOURNAL OF MATERIALS IN CIVIL ENGINEERING, 1997. **9**(1): p. 4-6.
138. Brooks: "*The influence of chemical admixtures on restrained drying shrinkage of concrete"*. in *Proceedings of the 5th International Conference on Superplasticizers and Other Chemical Admixtures in Concrete*. 1997. Rom: Am. Concr. Inst.
139. Engstrand: "*Shrinkage reducing admixture for cementious composition"* ConChem Journal - Verlag für Chemische Industrie H.Ziolkowsky GmbH, 1997. **5**(4): p. 149–151.
140. Folliard and Berke: "*Properties of high-performance concrete containing shrinkage-reducing admixture"* Cement and Concrete Research, 1997. **27**(9): p. 1357-1364.
141. Kim: "*Drying shrinkage reduction of polymer-modified mortars using redispersible polymer powder by use of shrinkage-reducing agents"* Zairyo-Journal-of-the-Society-of-Materials-Science, Japan 1997. **46**(1): p. 84-88.
142. N.S. Berke: "*New developments in shrinkage-reducing admixtures"*. in *Supplementary Papers of the CANMET/ACI 5th International Conference on Superplasticizers and Other Chemical Admixtures in Concrete*. 1997. Rom.
143. C.K. Nmai: "*Shrinkage reducing admixtures"* Concrete International, 1998. **20**(4): p. 31-37.
144. Leikauf and Oppliger: "*Durability of concrete. New admixtures for quality and durability improvement of concrete"* Chimia, 1998. **52**(5): p. 218-221.

145. Montani: "*Possibilities to control concrete shrinkage by means of chemical admixtures"* Chimia, 1998. **52**(5): p. 208-211.
146. Shah: "*Shrinkage cracking-Can it be prevented?"* Concrete International, 1998. **20**(4): p. 51-55.
147. Weiss, Yang and Shah: "*Shrinkage cracking of restrained concrete slabs"* JOURNAL OF ENGINEERING MECHANICS-ASCE, 1998. **124**(7): p. 765-774.
148. Holland: "*Using shrinkage-reducing admixtures"* Concr Constr., 1999. **44**(3): p. 15-18.
149. Holt: "*Reducing early-age concrete shrinkage with the use of shrinkage reducing admixtures "*. in *Nordic Concrete Research Meeting*. 1999. Reykjavik, IS.
150. Weiss: "*The influence of a Shrinkage Reducing Admixture on the Early-Age Shrinkage of High Performance Concrete"*. in *Utilization of High Strength/High Performance Concrete*. 1999. Sandefjord Norway.
151. Brooks: "*Effect of admixtures on the setting times of high-strength concrete"* Cement & Concrete Composites, 2000. **22**(4): p. 293-301.
152. Collins and Sanjayan: "*Cracking tendency of alkali-activated slag concrete subjected to restrained shrinkage"* Cement and Concrete Research, 2000. **30**(5): p. 791-798.
153. Weiss: "*Influence of specimen size and geometry on shrinkage cracking"* J. of Engrg. Mechanics Div., ASCE, 2000. **126**(1): p. 93-101.
154. Altoubat: "*Early-Age Tensile Creep and Shrinkage of Concrete with SRA"*. in *Creep, shrinkage and durability mechanics of concrete and other quasi-brittle materials : proceedings of the sixth international conference / CONCREEP-6; 20-22 August 2001,* . 2001. Cambridge (MA), USA: Elsevier Science Ltd.
155. Bentz, Geiker and Hansen: "*Shrinkage-reducing admixtures and early-age desiccation in cement pastes and mortars"* Cement and Concrete Research, 2001. **31**(7): p. 1075-1085.
156. Berke: "*Effects of Shrinkage Reducing Admixtures on Shrinkage and Cracking of Concrete"*. in *Creep, Shrinkage and Durability Mechanics of Concrete and other Quasi-Brittle Materials, Proceedings of the sixth International Conference*. 2001: Elsevier Science.
157. Cope and Ramey: "*Reducing Drying Shrinkage of Bridge-Deck Concrete"* Concrete International, 2001. **23**(8): p. 76-82.
158. Gettu: "*Evaluation of the Performance of Concrete Incorporating a Shrinkage Reducing Chemical Admixture"*. in *Creep, shrinkage and durability mechanics of concrete and other quasi-brittle materials : proceedings of the sixth international conference / CONCREEP-6; 20-22 August 2001,* . 2001. Cambridge (MA), USA: Elsevier Science Ltd.
159. Seigneur: "*Influence of the curing regime and of a shrinkage reducing admixture on shrinkage"* Concrete Science and Engineering, 2001. **3**(9): p. 47-52.
160. Bae, Berke, Hoopes, and Malone: "*Freezing ans Thawing Resistance of Concretes with Shrinkage reducing Admixtures"*. in *Frost Resistance of Concrete: From Nano-Structure and Pore Solution to Macroscopic Behaviour and Testing*. 2002: RILEM Publications S.A.R.L.
161. Berke, Li, Hicks, and Bal: "*Improving Concrete Performance with Shrinkage-Reducing Admixtures"*. in *Proceedings of the Seventh CANMET/ACI International Conference on Superplasticizers and Other Chemical Admixtures in Concrete*. 2003. Berlin.
162. Mohammed and Hamada: "*Durability of concrete made with different water-reducing chemical admixtures in tidal environment"* Aci Materials Journal, 2003. **100**(3): p. 194-202.
163. Mora, Aguado and Gettu: "*The influence of shrinkage reducing admixtures on plastic shrinkage"* Materiales De Construccion, 2003. **53**(271-72): p. 71-80.
164. Ribeiro: "*Effectiveness of shrinkage-reducing admixtures on different concrete mixtures"*. in *Seventh CANMET/ACI International Conference on Superplasticizers and Other Chemical Admixtures in Concrete* 2003. Berlin, Germany: American Concrete Institute; Canada Centre for Mineral and Energy Technology.
165. Roncero, Gettu and Martin: "*Evaluation of the influence of a shrinkage reducing admixture on the microstructure and long-term behaviour of concrete"*. in *Supplementary Papers of the Seventh CANMET/ACI international conference on superplasticizers and other chemical admixture in concrete*. 2003. Berlin.
166. See, Attiogbe and Miltenberger: "*Shrinkage cracking characteristics of concrete using ring specimens"* Aci Materials Journal, 2003. **100**(3): p. 239-245.
167. Holt and Leivo: "*Cracking risks associated with early age shrinkage"* Cement and Concrete Composites, 2004. **26**(5): p. 521-530.

168. Bentz: "*Capitalizing on self-desiccation for autogenous distrubution of chemical admixtures"*. in *Proceedings of the Fourth International Research Seminar: Self-Desiccation and its Importance in Concrete Technology*. 2005. Gaithersburg, Maryland, USA: Lund Institute of Technology; Division of Building Materials.

169. Hoa Lam and Hooton: "*Effects of internal curing methods on restrained shrinkage and permeability"*. in *Proceedings of the Fourth International Research Seminar: Self-Desiccation and its Importance in Concrete Technology*. 2005. Gaithersburg, Maryland, USA: Lund Institute of Technology; Division of Building Materials.

170. Holt: "*Contribution of mixture design to chemical and autogenous shrinkage of concrete at early ages"* Cement and Concrete Research, 2005. **35**(3): p. 464-472.

171. Maltese, Pistolesi, Lolli, Bravo, Cerulli, and Salvioni: "*Combined effect of expansive and shrinkage reducing admixtures to obtain stable and durable mortars"* Cement and Concrete Research, 2005. **35**(12): p. 2244-2251.

172. Palacios and Puertas: "*Effect of superplasticizer and shrinkage-reducing admixtures on alkali-activated slag pastes and mortars"* Cement and Concrete Research, 2005. **35**(7): p. 1358-1367.

173. Rongbing and Jian: "*Synthesis and evaluation of shrinkage-reducing admixture for cementitious materials"* Cement and Concrete Research, 2005. **35**(3): p. 445-448.

174. Suzuki, Tanimura and Sato: "*The effect of autogenous shrinkage on flexural cracking behaviour of reinforced HSC beams and improvement by using low shrinkage HSC"*. in *Proceedings of the Fourth International Research Seminar: Self-Desiccation and its Importance in Concrete Technology*. 2005. Gaithersburg, Maryland, USA: Lund Institute of Technology; Division of Building Materials.

175. Tanimura and Mitani: "*An investigation of prediction model for autogenous shrinkage/expansion strain of low-shrinkage-HSC"*. in *Proceedings of the Fourth International Research Seminar: Self-Desiccation and its Importance in Concrete Technology*. 2005. Gaithersburg, Maryland, USA: Lund Institute of Technology; Division of Building Materials.

176. Videla and Aguilar: "*Effectiveness of shrinkage-reducing admixtures on Portland pozzolan cement concrete"* Materiales De Construccion, 2005. **55**(278): p. 13-28.

177. Eberhardt and Kaufmann: "*Schwindreduzierter Selbstverdichtender Beton"*. in *Proceedings of the 16th International Conference on Building Materials in Weimar*. 2006. Weimar: F.A. Finger - Institut für Baustoffkunde.

178. Eberhardt and Kaufmann: "*Development of shrinkage reduced self compacting concrete"*. in *CANMET/ACI International Conference on Recent Advances in Concrete Technology*. 2006. Montreal: ACI.

179. Han and Yan: "*The effect of shrinkage-reducing admixture on mechanical properties and volume stability of concrete"* Environmental Ecology and Technology of Concrete, 2006. **302-303**: p. 230-234.

180. He, Li, Chen, and Liang: "*Properties of shrinkage-reducing admixture-modified pastes and mortar"* Materials and Structures, 2006. **39**(4): p. 445-453.

181. Qian, Meng, Zhan, and Fang: "*Influence of shrinkage reduce agent on early age autogenous shrinkage of concrete"*, in *Environmental Ecology and Technology of Concrete*. 2006. p. 211-217.

182. Ribeiro, Goncalves and Carrajola: "*Effect of shrinkage reducing admixtures on the pore structure properties of mortars"* Materials and Structures, 2006. **39**(2): p. 179-187.

183. Palacios and Puertas: "*Effect of shrinkage-reducing admixtures on the properties of alkali-activated slag mortars and pastes"* Cement and Concrete Research, 2007. **37**(5): p. 691-702.

184. Patent: U.S.P.a.T. Office: US 5556460; Berke, Dallaire, Gartner, Kerkar, and Martin (1996); "Drying shrinkage cement admixture"; W.R. Grace & Co.-Conn (US)

185. Patent: U.S.P.a.T. Office: US 5603760; Berke, Dallaire and Abelleira (1997); "Cement admixture capable of inhibiting drying shrinkage and method of using same "; W.R. Grace & Co.-Conn (US)

186. Patent: U.S.P.a.T. Office: US 5618344; Kerkar, Berke and Dallaire (1997); "Cement composition "; W.R. Grace & Co.-Conn (US)

187. Patent: U.S.P.a.T. Office: US 5622558; Berke and Dallaire (1997); "Drying shrinkage cement admixture "; W.R. Grace & Co.-Conn (US)

188. Patent: E.P. Office: EP0813506 (A1); Berke, Dallaire and Kerkar (1997); "Cement composition"; W.R. Grace & Co.-Conn (US)

189. Patent: E.P. Office: EP0813507 (B1); Kerkar, Berke and Dallaire (2000); "Cement composition"; W.R. Grace & Co.-Conn (US)
190. Patent: E.P. Office: EP0777635 (B1); Berke, Dallaire and Kerkar (2000); "Shrinkage reduction cement composition"; W.R. Grace & Co.-Conn (US)
191. Schließl: "*Assessing the moisture profile of drying concrete using impedance spectroscopy"* Concrete Science and Engineering, 2000. **2**(6): p. 106 - 116.
192. Berke and M.P. Dallaire: "*New developments in shrinkage-reducing admixtures"*. in *Supplementary Papers of the CANMET/ACI 5th International Conference on Superplasticizers and Other Chemical Admixtures in Concrete*. 1997. Rom.
193. Balogh: "*New admixture combats concrete shrinkage"* Aberdeen's Concrete Construction, 1996. **41**(7): p. 546-551.
194. Patent: U.S.P.a.T. Office: US 5938835; Shawl and Kesling Jr. (1999); "Cement composition"; Arco Chemical Technology, L.P. (US)
195. Patent: U.S.P.a.T. Office: US 5413634; Shawl and Kesling Jr. (1995); "Cement composition"; Arco Chemical Technology, L.P. (US)
196. Patent: E.P. Office: EP0758309 (A1); Shawl and Kesling Jr. (1997); "Cement composition"; Arco Chemical Technology, L.P. (US)
197. Patent: E.P. Office: EP0637574 (A1); Shawl and Kesling Jr. (1995); "Cement composition"; Arco Chemical Technology, L.P. (US)
198. Patent: E.P. Office: EP0758309 (B1); Shawl and Kesling Jr. (2001); "Cement Composition"; Arco Chemical Technology, L.P. (US)
199. Patent: E.P. Office: EP0643022 (B1); Shawl and Kesling Jr. (1997); "Cement composition"; Arco Chemical Technology, L.P. (US)
200. Chatterji: "*A discussion of the paper "percolation of phases in a three-dimensional cement paste microstructural model" by D.P. Bentz and E.J. Garboczi"* Cement and Concrete Research, 1991. **21**(6): p. 1185-1186.
201. Chatterji: "*A discussion of the paper "Percolation and pore structure in mortars and concrete" by D.N. Winslow, M.D. Cohen, D.P. Bentz, K.A. Snyder and E.J. Garboczi"* Cement and Concrete Research, 1994. **24**(8): p. 1567-1568.
202. Nmai and R. Romita: "*Shrinkage reducing admixtures"* Concrete International, 1998. **20**(4): p. 31-37.
203. MATERIAL SAFETY DATA SHEET: Tetraguard AS 20 (Version 1,3); BASF Corporation; 2006
204. Patent: U.S.P.a.T. Office: US 6251180 B1; Engstrand and Sjogreen (2001); "Shrinkage-reducing agent for cement compositions "; Perstorp AB (Perstorp, SE)
205. Zhang, Shang, Yin, Aishah, Salmiah, and Ooi: "*Adsorptive behavior of surfactants on surface of Portland cement"* Cement and Concrete Research, 2001. **31**(7): p. 1009-1015.
206. Merlin, Guitouni, Mouhoubi, Mariot, Vallée, and Van Damme: "*Adsorption and heterocoagulation of nonionic surfactants and latex particles on cement hydrates"* Journal of Colloid and Interface Science, 2005. **281**(1): p. 1-10.
207. Sant, Rajabipour, Lura, and Weiss: "*Examining Residual Stress Development in Cementitious Materials Experiencing an Early-age Expansion"*. in *Proceedings of the 9th CANMET-ACI Int. Conf. – T.C. Holland Symposium*. 2007. Warsaw, Poland.
208. Karaguler and Shah: "*Test method to evaluate shrinkage cracking of concrete"*. in *Serviceability and Durability of Construction Materials - Proceedings of the First Materials Engineering Congress*. 1990: ASCE, Boston Society of Civil Engineers Sect, Boston, MA.
209. He and Li: "*Influence of alkali on restrained shrinkage behavior of cement-based materials"* Cement and Concrete Research, 2005. **35**(3): p. 457-463.
210. Hossain and Weiss: "*The role of specimen geometry and boundary conditions on stress development and cracking in the restrained ring test"* Cement and Concrete Research, 2006. **36**(1): p. 189-199.
211. Ogawa and Tomita: "*Crack control of reinforced concrete structures"*. in *International Conference: Concrete 2000 - Economical and Durable Construction Trough Excellence*. 1993. Dundee.
212. Stark and Möser: "*Neue Aspekte der Zementhydratation"*. in *Proceedings of the 14th International Conference on Building Materials - ibausil*. 2000. Weimar: F.A. Finger-Institut für Baustoffkunde.

213. Stark, Möser and Bellmann: "*Ein neues Modell der Zementhydratation"*. in *Proceedings of the 15th International Conference on Building Materials - ibausil*. 2003. Weimar: F.A. Finger-Institut für Baustoffkunde.

214. Stark, Möser, Bellmann, and Rößler: "*Quantitative Characterisierung der Zementhydratation"*. in *Proceedings of the 16th International Conference on Building Materials - ibausil*. 2006. Weimar: F.A. Finger-Institut für Baustoffkunde.

215. Lothenbach and Winnefeld: "*Thermodynamic modelling of the hydration of Portland cement"* Cement and Concrete Research, 2006. **36**(2): p. 209-226.

216. Matschei and Glasser: "*The influence of limestone on cement hydration"* ZKG International, 2006. **59**(12): p. 78-86.

217. Matschei, Lothenbach and Glasser: "*The AFm phase in Portland cement"* Cement and Concrete Research, 2007. **37**(2): p. 118-130.

218. Matschei, Lothenbach and Glasser: "*The role of calcium carbonate in cement hydration"* Cement and Concrete Research, 2007. **37**(4): p. 551-558.

219. Matschei, Lothenbach and Glasser: "*Thermodynamic properties of Portland cement hydrates in the system CaO-Al2O3-SiO2-CaSO4-CaCO3-H2O"* Cement and Concrete Research, 2007. **37**(10): p. 1379-1410.

220. Matschei; Thesis: "Thermodynamics of cement hydration"; Department of Chemistry; University of Aberdeen; 2007

221. Zingg; Thesis: "Cement-superplasticizer interaction: link between macroscopic phenomena and microstructural data of the early cement hydration."; Swiss Federal Institute of Technology Zurich; 2008

222. Rößler, Eberhardt, Kucerová, and Möser: "*Influence of hydration on the fluidity of normal Portland cement pastes"* Cement and Concrete Research, 2008. **38**(7): p. 897-906.

223. Hebatpuria, ARAFAT, BISHOP, and PINTO: "*Leaching Behavior of Selected Aromatics in Cement-Based Solidification/Stabilization under Different Leaching Tests"* Environmental Engineering Science, 1999. **16**(6): p. 451-463.

224. Godbee, Compere, Joy, Kibbey, Moore, Nestor Jr, Anders, and Neilson Jr: "*Application of mass transport theory to the leaching of radionuclides from waste solids"* Nuclear and Chemical Waste Management, 1980. **1**(1): p. 29-35.

225. Parapar, de Elvira Francoy, Rodriguez-Pinero, Salvador Martinez, and Fernandez Pereira: "*Stabilization/solidification of hazardous metallic wastes: prediction of leach test performance to optimize S/S mixtures"* Waste Management Research, 1998. **16**(2): p. 175-182.

226. Pescatore: "*Leach rate expressions for performance assessment of solidified, low-level radioactive waste"* Waste Management, 1991. **11**(4): p. 223-229.

227. Wienberg: "*Diffusionsuntersuchungen und Transportberechnungen zum Schadstoffrückhaltevermögen mineralischer Dichtwandmassen"* Altlasten Spektrum, 1998(5/98): p. 274-280.

228. Kriegel, Buchwald and Kaps: "*Werkstoffaufbau und diffusiver Stofftransport aufgezeigt an ausgewählten Beispielen"* Internationale Zeitung für Bauinstandsetzten und Baudenkmalpflege, 2000. **6**(4): p. 429-450.

229. Buchwald and Kaps: "*Zur Diffusion des Ionenpaares Na+ und SO4+ in wassergesättigten Ziegelmaterialien - Modellexperimente zur Mauerwerksentsalzung"*. in *2. GDCh-Tagung Bauchemie; Siegen 1999; GDCh-Monographie Bd. 15; 46-51*.

230. Tiruta-Barna, Fantozzi-Merle, de Brauer, and Barna: "*Leaching behaviour of low level organic pollutants contained in cement-based materials: Experimental methodology and modelling approach"* Journal of Hazardous Materials, 2006. **138**(2): p. 331-342.

231. Saltzman and Langer: "*Transport rates of proteins in porous materials with known microgeometry."* Biophys J., 1989. **55**(1): p. 163-171.

232. Schieferstein and Heinrich: "*Diffusion Coefficients Calculated for Microporous Solids from Structural Parameters Evaluated by Fractal Geometry"* Langmuir, 1997. **13**(6): p. 1723-1728.

233. Hohberg: "*Charakterisierung, Modellierung und Bewertung des Auslaugungsverhaltens umweltrelevanter, anorganischer Stoffe aus zementgebundenen Baustoffen"* Deutscher Ausschuss für Stahlbeton, 2003. **Heft 542**.

234. Dietrich; Thesis: "Einfluss bauchemisch relevanter Schadstoffe auf Mineralphasen und mechanisch-hydraulische Eigenschaften werksfertiger Einphasen-Dichtwandmassen"; Mathematisch-Naturwissenschaftliche Fakultät; Christian-Albrechts-Universität zu Kiel; 2005

235. Blachnik; Thesis: "Zusatzmittel in Putzmörteln: Wirksamkeit, Dauerhaftigkeit und Auslaugung"; Fachbereich 8; Universität-Gesamthochschule Siegen; 2001
236. Buchwald, Kriegel, Kohl, and Kaps: "*Kompressenentsalzung an einer Modellmauer"*. in *Proceedings of the 14th International Conference on Building Materials - ibausil*. 2000. Weimar: F.A. Finger-Institut für Baustoffkunde.
237. Kriegel and Kaps: "*Determination of the Oxygen Ion Diffusion Coefficients in SrMnO3-y Mixed Conductor by the Reoxidation Kinetics"*, in *Functional Materials*, P.D.E.T.P.D.G.W.P.D.J.H.P.D.H.H. Dr. K. Grassie, Editor. 2006. p. 206-211.
238. Kriegel, Terheiden and Kaps: "*Simulation verfahrenstechnischer Grenzfälle der Kompressenentsalzung - Vergleich der numerischen Simulation mit experimentellen Daten von Laboruntersuchungen"*. in *WTA-Colloqium 2002: Erhalten, Umnutzen, Ertüchtigen*. 2002. Braunschweig: Aedificato Verlag, D-79110 Freiburg.
239. Möschner; Thesis: "A thermodynamic approach to cement hydration: The role of retarding admixtures and Fe-minerals during the hydration of cements"; Inst.f.Biogeochemie u.Schadstoffdynamik; ETH Zürich; 2007
240. Parrot and Killoh: "*Prediction of cement hydration"*. in *British Ceramic Proceedings*. 1984. London, Engl: British Ceramic Soc.
241. Taylor: "*Cement chemistry H. F. W. Taylor"*. 1997, London: Thomas Telford Publishing.
242. Franke: "*Determination of calcium oxide and calcium hydroxide also on water-free and watery calcium silicate"* Zeitschrift für anorganische und allgemeine Chemie, 1941. **247**(1/2): p. 180-184.
243. Lothenbach, Le Saout, Gallucci, and Scrivener: "*Influence of limestone on the hydration of Portland cements"* Cement and Concrete Research, 2008. **38**(6): p. 848-860.
244. Bellmann, Damidot, Skibstedt, and Möser, *Improved evidence for the existence of an intermediate phase during hydration of tricalcium silicate*, in *The Fred Glasser Cement Science Symposium*. 17. - 19. June 2009: Kings College Conference Centre, Aberdeen, Scotland, UK.
245. Flatt and Houst: "*A simplified view on chemical effects perturbing the action of superplasticizers"* Cement and Concrete Research, 2001. **31**(8): p. 1169-1176.
246. "*Zement-Taschenbuch 2000"*, ed. V.D.Z. e.V. 2000, Düsseldorf: Verlag Bau + Technik GmbH.
247. Patent: U.S.P.a.T. Office: US 7118618; Duez and Bethouart (2001); "Colored liquid composition for editing pen";
248. Bullard and Flatt: "*New insights into the effect of calcium hydroxide precipitation on the kinetics of tricalcium silicate hydrate"*; accepted by Journal of the American Ceramic Society, 2010.
249. Powers and Helmuth: "*Theory of volume changes in hardened Portland-cement paste during freezing"* Highway Research Board Proceedings, 1953. **Vol. 32**: p. 285-297.
250. Brunauer, Deming, Deming, and Teller: "*On a Theory of the van der Waals Adsorption of Gases"* Journal of the American Chemical Society, 1940. **62**(7): p. 1723-1732.
251. Sing, Everett and Haul: "*Reporting physisorption data for gas/solid systems with special reference to the determination of surface area and porosity"* Pure and Applied Chemistry, 1985. **57**(4): p. 603-619.
252. Midgley and Illston: "*Some comments on the microstructure of hardened cement pastes"* Cement and Concrete Research, 1983. **13**(2): p. 197-206.
253. "*CRC Handbook of Chemistry and Physics; 90th Edition "*. David R. Lide, National Institute of Standards & Technology (Retired), Gaithersburg, Maryland, USA. 2009.
254. Funazukuri and Nishio: "*Infinite Dilution Binary Diffusion Coefficients of C5-Monoalcohols in Water in the Temperature Range from 273.2 K to 353.2 K at 0.1 MPa"* Journal of Chemical & Engineering Data, 1998. **44**(1): p. 73-76.
255. Ning, Kita, Kriegs, Luettmer-Strathmann, and Wiegand: "*Thermal Diffusion Behavior of Nonionic Surfactants in Water"* The Journal of Physical Chemistry B, 2006. **110**(22): p. 10746-10756.
256. Qiao and Easteal: "*Mass transport in Triton X series nonionic surfactant solutions: a new approach to solute-solvent interactions"* Colloid & Polymer Science, 1996. **274**(10): p. 974-980.
257. Stark: "*Dauerhaftigkeit von Beton - Der Baustoff als Werkstoff"*, ed. F.A.F.-I.f.B.d.B.-U. Weimar. 2001, Basel; Boston; Berlin: Baupraxis Birkhäuser.
258. Johannesson and Utgenannt: "*Microstructural changes caused by carbonation of cement mortar"* Cement and Concrete Research, 2001. **31**(6): p. 925-931.

259. Chen, Thomas and Jennings: "*Decalcification shrinkage of cement paste"* Cement and Concrete Research, 2006. **36**(5): p. 801-809.
260. Castellote, Fernandez, Andrade, and Alonso: "*Chemical changes and phase analysis of OPC pastes carbonated at different CO2 concentrations"* Materials and Structures, 2009. **42**(4): p. 515-525.
261. Groves, Brough, Richardson, and Dobson: "*Progressive Changes in the Structure of Hardened C₃S Cement Pastes due to Carbonation"* Journal of the American Ceramic Society, 1991. **74**(11): p. 2891-2896.
262. Haecker, Garboczi, Bullard, Bohn, Sun, Shah, and Voigt: "*Modeling the linear elastic properties of Portland cement paste"* Cement and Concrete Research, 2005. **35**(10): p. 1948-1960.
263. Meyer; Thesis: "Influence of the interfacial transition zone when modelling the modulus of elasticity of concrete"; 03 Fakultät für Bauingenieurwesen; RWTH Aachen; 2007
264. Duckheim and Setzer: "*Ein lasergestütztes Messverfahren zur Ermittlung des Trocknungsschwindens von Zementstein"*. in *Proceedings of the 16th International Conference on Building Materials in Weimar*. 2006. Weimar: F.A. Finger - Institut für Baustoffkunde.
265. Barrett, Joyner and Halenda: "*The Determination of Pore Volume and Area Distributions in Porous Substances. I. Computations from Nitrogen Isotherms"* Journal of the American Chemical Society, 1951. **73**(1): p. 373-380.
266. Horn: "*Surface Forces and Their Action in Ceramic Materials"* Journal of the American Ceramic Society, 1990. **73**(5): p. 1117-1135.
267. Wei and Zhao: "*Growth of liquid bridge in AFM"* Journal of Physics D-Applied Physics, 2007. **40**(14): p. 4368-4375.
268. Bowles, Hsia, Jones, Schneider, and White: "*Quasi-Equilibrium AFM Measurement of Disjoining Pressure in Lubricant Nano-Films I:â€‰ Fomblin Z03 on Silica"* Langmuir, 2006. **22**(26): p. 11436-11446.
269. Bowles, Hsia, Jones, White, and Schneider: "*Quasi-Equilibrium AFM Measurement of Disjoining Pressure in Lubricant Nanofilms II: Effect of Substrate Materials"* Langmuir, 2009. **25**(4): p. 2101-2106.
270. Dutka and NapiÃ³rkowski: "*The influence of line tension on the formation of liquid bridges in atomic force microscope-like geometry"* Journal of Physics: Condensed Matter, 2007. **19**(46): p. 466104.
271. Lubarsky, Davidson and Bradley: "*Particle-surface capillary forces with disjoining pressure"* Physical Chemistry Chemical Physics, 2006. **8**: p. 2525-2530.
272. Pourchet, Comparet, Nicoleau, and Nonat: "*Influence of PC superplasticizers on tricalcium silicate hydration"*. in *Proceeding of the 12th International Congress on the Chemistry of Cement*. 2007. Montreal, Canada.
273. Patent: U.S.P.a.T. Office: Goto, Sato, Sakai, and Motohiko II (1985); "Cement-shrinkage-reducing agent and cement composition"; Nihon Cement Co., Ltd. (Kyoto, JP)
274. Patent: U.P. Office: Umaki, Tomita, Hondo, and Okada (1993); "Cement composition "; Nihon Cement Co., Ltd. (Tokyo, JP); Sanyo Chemical Industries, Ltd. (Kyoto, JP)
275. Patent: E.P. Office: EP0291073 (A2); Akimoto, Honda and Yasukohchi (1988); "Additives for cement"; Nippon Oil and Fats Co., Ltd. (Tokyo, JP)
276. Patent: E.P. Office: EP0291073 B1; Akimoto, Honda and Yasukohchi (1992); "Additives for cement"; Nippon Oil and Fats Co., Ltd. (Tokyo, JP)
277. Patent: U.S.P.a.T. Office: US 4946904; Akimoto, Honda and Yasukohchi (1990); "Additives for cement"; Nippon Oil and Fats Co., Ltd. (Tokyo, JP)
278. Patent: U.S.P.a.T. Office: US 5142036; Akimoto, Honda and Yasukohchi (1992); "Polyoxyalkylene alkenyl ether-maleic ester copolymer and use thereof"; Nippon Oil and Fats Co., Ltd. (Tokyo, JP)
279. Patent: E.P. Office: EP0308950 (A1); Schulze and Baumgartl (1989); "Shrinkage-reducing agent for cement"; Wacker Chemie GmbH (DE)
280. Patent: D.P.-u. Markenamt: DE 3732114 (A1); Schulze and Baumgartl (1989); "Mittel zur Reduzierung des Schwundmaßes von Zement "; Wacker Chemie GmbH (DE)
281. Patent: E.P. Office: EP0350904 (A2); Sakuta, Saito and Yanagibashi (1990); "Durability improving agent for cement-hydraulic-set substances, method of improving same, and cement-hydraulic-set substances improved in durability."; Fujisawa Pharmaceutical Co., Ltd. (Osaka, JP); Takenaka Corporation (Osaka, JP); Nippon Nyukazai Co., Ltd. (Tokyo, JP)

282. Patent: E.P. Office: EP0350904 (B1); Sakuta, Saito and Yanagibashi (1993); "Durability improving agent for cement-hydraulic-set substances, method of improving same, and cement-hydraulic-set substances improved in durability."; Fujisawa Pharmaceutical Co., Ltd. (Osaka, JP); Takenaka Corporation (Osaka, JP); Nippon Nyukazai Co., Ltd. (Tokyo, JP)
283. Patent: U.S.P.a.T. Office: US 5174820; Sakuta, Saito and Yanagibashi (1992); "Durability improving agent for cement-hydraulic-set substances, method of improving same, and cement-hydraulic-set substances improved in durability"; Fujisawa Pharmaceutical Co., Ltd. (Osaka, JP); Takenaka Corporation (Osaka, JP); Nippon Nyukazai Co., Ltd. (Tokyo, JP)
284. Patent: W.I.P. Organization: WO 9504010; Abdelrazig , Gartner and Myers (1994); "Low shrinkage cement composition"; W.R. Grace & Co.-Conn (US)
285. Patent: U.S.P.a.T. Office: US 5326396; Abdelrazig , Gartner and Myers (1994); "Low shrinkage cement composition"; W.R. Grace & Co.-Conn (US)
286. Patent: U.S.P.a.T. Office: US 5389143; Abdelrazig and Scheiner (1995); "Low shrinkage cement composition"; W.R. Grace & Co.-Conn (US)
287. Patent: U.S.P.a.T. Office: US 5604273; Kerkar and Gilbert (1997); "Drying shrinkage cement admixture"; W.R. Grace & Co.-Conn (US)
288. Patent: E.P. Office: EP1714949 (A1); Collepardi (2006); "Concrete composition with reduced drying shrinkage"; General Admixtures S.p.A. (IT)
289. Bensted: "*Structure and performance of cements"*. 2002, London: Spon Press.

14 List of tables

Table 1: Shrinkage reduction of SRA modified mortars dependent on dosage and time of drying [178] 43

Table 2: Shrinkage Reducing Admixtures 58

Table 3: Geometries and drying regimes for paste and mortar specimen 64

Table 4: Specifications tank test/modified tank test 70

Table 5: Composition of saturated synthetic pore solution 73

Table 6: Calculated cross sectional occupation area per molecule and influence of molecular weight variation 76

Table 7: Range of possible compositions of SRA2 77

Table 8: Phase composition of residue, SRA2 85

Table 9: Approximated amount of SRA1 in different phases 86

Table 10: Calculated amount of inorganic precipitates formed from isotropic micellar solution 87

Table 11: Calculated amount of inorganic precipitates formed from reverse micellar solution 87

Table 12: Evaluation of core concentration of SRA1 by pendant drop surface tension measurement 89

Table 13: relative degrees of hydration of pastes containing SRAs 99

Table 14: Relative degrees of hydration of pastes containing SRAs ,SP-PCE and mixtures thereof .. 99

Table 15: Impact of SRA on hydration kinetics of different binder systems 101

Table 16: Relative degree of hydration derived from thermo analysis 103

Table 17: Water loss of cement pastes at the end of the induction period 104

Table 18: Amount of portlandite derived from weight loss between 420°C and 500°C 105

Table 19: Water loss of pastes after 28 days of hydration 105

Table 20: Depletion of sulphate regulator 108

Table 21: Portlandite quantification in cement paste CP at hydration stage T6 and T8 109

Table 22: Calculated main phase composition of hydrated cement pastes after 28 days of hydration 110

Table 23: Possible composition of SRA1 calculated from TOC measurements 111

Table 24: Total organic content of extracted pore solutions and absolute amount of bulk solution in paste 112

Table 25: Loss of admixture in the course of hydration – relative amounts 113

Table 26: Degree of C_3S-hydration and specific surface 124

Table 27: Measured N_2-BET surfaces on cement pastes with 2wt.-% SRA hydrated for 28 days 128

Table 28: Denomination and SRA dosages of mortars 131

Table 29: Increase of specific surface of different mortar types without SRA and with 4wt.-% SRA1 137

Table 30: Binder composition of mortar types and mobile/immobile fractions of SRA1 146

Table 31: Calculated carbon load of initial SRA1 composition and composition of the leached admixture 147

Table 32: Corrected values for leachable and immobile fraction of SRA1 147

Table 33: Calculation of diffusion coefficients according to the infinite slab model; mortar series LM 149

Table 34: Average efficient diffusion coefficients of mortar series 153

Table 35: Analysis of variation for the leaching simulation 154

Table 36: Analysis of variation for modeling the dilution factor and the binary diffusion coefficient ... 155

Table 37: Binary diffusion coefficients for monoalcohols* and non-ionic surfactants** 156

Table 38: Irreversible fraction of drying shrinkage obtained from length measurement after resaturation 175

Table 39: Cumulated creep of mortars exposed to cyclic drying (35% RH) and rewetting 175

Table 40: Specific surface of mortars from nitrogen sorption measurements and exposed interfacial area dependent on relative humidity 185

15 List of figures

Figure 1: Contributions of average fluid pressure and surface energy to the equivalent pore pressure according Coussy [13], but constructed using a different sorption isotherm. 16

Figure 2: Schematic comparison of characteristic values of rigid/non-rigid porous matter subjected to drying - change of saturation; porosity and interfacial area for non rigid porous matter (*K*=0)..... 18

Figure 3: Schematic comparison of characteristic values of rigid/non-rigid porous matter subjected to drying - change of saturation; porosity and interfacial area for rigid porous matter (infinite K) 18

Figure 4: C-S-H after 28d of hydration from [47]..... 22

Figure 5: C-S-H around unhydrated C_3S from [47] 22

Figure 6: Schematic scetch of a surfactant molecule..... 28

Figure 7: Surface tension of aqueous solutions of surfactant vs. bulk concentration of surfactant 30

Figure 8: Binary phase diagram for dodecyl hexaoxyethylene glycol monoether–water mixture; from [86]..... 32

Figure 9: Free drying shrinkage of self consolidating mortars containing different amounts of SRA [178]..... 42

Figure 10: Modified contribution of capillary pressure to average pore pressure. 47

Figure 11: First drying shrinkage of 0.4 and 0.6 W/C ratio pastes vs calculated increase in surface free energy (Hansen 1987 [8])..... 48

Figure 12: Normcube..... 49

Figure 13: Hypothetical and measured sorption isotherms of CEM I, w/c=0.4 50

Figure 14: Surface area of adjusted normcube and paste from Figure 13 (measured N_2 desorption; Cranston & Inkley [58]) 50

Figure 15: Surface work vs. energy of sorption..... 51

Figure 16: Influence of surface tension on water vapour sorption 51

Figure 17: Cylindrical single end “model” pore in equilibrium with imposed humidity of surrounding gas phase..... 52

Figure 18: Simplified model for water loss of a non-rigid drying pore with and without SRA on the left and right side respectively..... 53

Figure 19: Criterions for self consolidating property of SCM and SCC..... 59

Figure 20: Example for measuring weight loss of saturated paste sample exposed to defined climates 64

Figure 21: Example for measuring free drying shrinkage of saturated paste sample exposed to defined climates 65

Figure 22: Determination of leaching mechanism according to Hohberg 2003 [233] 66

Figure 23: Diffusion model „infinite slab“ according [228] 68

Figure 24: Surface tension of different SRA and SP-PCE in aqueous solution..... 74

Figure 25: Plot of surface tension versus mol fraction of SRA in aqueous solution 75

Figure 26: Plot of surface tension versus mol fraction of SP-PCE in aqueous solution – impact of molecular weight 75

Figure 27: Overall surface tension of SRA2 and contributions from surfactant and co-surfactant 78

Figure 28: Influence of potassium hydroxide on surface tension of aqueous solution 79

Figure 29: SRA1; SP-PCE and mixes of admixtures in aqueous solution 80

Figure 30: SRA1; SP-PCE and mixes of admixtures in synthetic cement pore solution 80

Figure 31: Phase behaviour of SRA1 in water 80

Figure 32: Phase separation of SRA1 in synthetic pore solution 81

Figure 33: Phase behaviour of SRA1 in synthetic cement pore solution 82

Figure 34: Liquid/solid phase separation of SRA2 in synthetic pore solution 83

Figure 35: TGA curves of filtered residuals of SRA1 solutions 83

Figure 36: Absolute amounts of inorganic precipitates from electrolyte solution of SRA1 84

Figure 37: Filtrated organic residue of SRA1 in synthetic pore solution 85

Figure 38: TOC analysis of liquid phases 86

Figure 39: Modeled precipitation of minerals due to the constriction of synthetic pore solution 88

Figure 40: Impact of volume /interface ratio on surface activity of SRA1 91

Figure 41: Evolution of surface tension of pore fluids with different initial bulk concentrations of SRA1 upon drying of normcube 91

Figure 42: Impact of v/a ratio on the water vapour desorption isotherms of normcube comprising pore fluids with different initial bulk concentrations of SRA1 92

Figure 43: Heat release of cement paste w/c=0.4 with different SRAs or SP-PCE at low dosage (0.5wt.-% of binder) 98

Figure 44: Heat release of cement paste w/c=0.4 with different SRAs or SP-PCE at high dosage (2.0wt.-% of binder) 98

Figure 45: Heat release of pastes with similar absolute amounts of different SRA 100

Figure 46: Detail of Figure 45 100

Figure 47: Normalisation of hydration progress of CEM I pastes carrying different dosages and combinations of SRA1 and SP-PCE and SRA/SP-PCE 102

Figure 48: Thermo analysis of different cement pastes at the end of the induction period of cement hydration (T2) 103

Figure 49: Thermo analysis of pastes after main heat release (T4) 104

Figure 50: GEMS process modeling - hydration of plain paste (CP 00.00) 106

Figure 51: X-ray diffractograms of NPC and appropriate clinker after salicylic acid hydrolysis 107

Figure 52: Portlandite quantification in hydrated cement paste CP – semi-quantitative XRD vs. TGA 109

Figure 53: Admixture losses for SRA1 pastes with different dosages, at different hydration stages .. 113

Figure 54: Ionic content of pore solution – measurements and prediction by GEMS 115

Figure 55: Enhanced precipitation of syngenite in presence of SRA 116

Figure 56: Micrographs at hydration stage T3 (12 hours of hydration) 117

Figure 57: Organic salt-outs precipitating from bulk solution of CP23.00 118

Figure 58: Surface tension of extracted cement pore solution from pastes with and without SRAs at different stages of hydration 120

Figure 59: Depletion of admixtures in synthetic pore solution with and without synthetic hydrate phases 121

Figure 60: Self-assembly of SRA1 in synthetic pore solution 122

Figure 61: SRA1 adsorption onto synthetic hydrates 122

Figure 62: Depletion of SRA1 from pore solution of hydrating C_3S 125

Figure 63: Surface area of hydrated C_3S-pastes 125

Figure 64: Microstructure of portlandite in plain paste (C0) compared to paste containing a high dosage of SRA1 (C6 = 384mg/g C_3S) 126

Figure 65: C-S-H phases in plain paste (C0) compared to paste containing a high dosage of SRA1 (C6 = 384mg/g C_3S) 127

Figure 66: Microstructure of CP13.00 (SRA1 at initial 2wt.-% o.c.) after 7days of hydration 128

Figure 67: Modeled chemical shrinkage of cement paste (reference CP.00.00) 133

Figure 68: Modeled and measured chemical shrinkage of reference paste CP 00.00 133

Figure 69: Chemical shrinkage of cement paste and mortars containing different SRA 134

Figure 70: Water sorption and excess volume of cement paste and mortar samples after saturated curing 134

Figure 71: Pore volume and distribution according to evap./non-evaporable water content of cement paste with/without SRA1 135

Figure 72: Mercury intrusion porosimetry of cement paste with increasing amount of SRA1 after 28days of wet curing 136

Figure 73: Mercury intrusion porosimetry of cement mortar with increasing amount of SRA1 after 28days of wet curing 136

Figure 74: Nitrogen sorption hysteresis of mortar CM00 and CM14 137

Figure 75: Influence of SRA1 on specific surface area of mortar series CM according Modelless-method (nitrogen desorption) 138

Figure 76: Influence of SRA1 on specific surface area of mortar series LM according Modelless-method (nitrogen desorption) 138

Figure 77: Differential pore size distribution of mortars CM00 and CM14 138

Figure 78: Differential surface contribution vs. pore size of mortars CM00 and CM14 138

Figure 79: Relative amounts of organic carbon leached from mortar (TOC) in tank tests 142

Figure 80: Comparison of SRA1 quantification by different methods (GC vs. TOC) - incremental approach 143

Figure 81: Comparison of SRA1 quantification by different method (GC vs. TOC) - cumulative approach 143

Figure 82: Relative amounts of SRA and SP-PCE leached from different mortar types - Leached amount refers to initial admixture content 144

Figure 83: Direct linear correlation between remaining SRA concentration in series of typ LM and admixture content in eluate 145

Figure 84: Relationship between SRA concentration in pore solution and eluate 148

Figure 85: Relationship between concentration gradient ($C_{SRA\_eluate}/C_{SRA\_pore\ solution}$) and capillary porosity 148

Figure 86: Evaluation of apparent diffusion coefficients according the „infinite slab“ model 150

Figure 87: Evaluation of the diffusion coefficients $D_{eq.}$ for mortar type CM 153

Figure 88: Concentration gradients of SRA in mortar SM03 (2% SRA1) and eluate at the end of leaching cycles; plot for D=3.3 E-8m²/s and f_{open}= 0.6 156

Figure 89: Leaching of mortars subjected to cyclic leaching and drying 157

Figure 90: Shrinkage isotherms of mortar series CM0 and CM3 initially, after wet storage (252days) and after tank test (252days & mobile fraction of SRA completely removed); 158

Figure 91: Shrinkage isotherms of mortar series LM0 and LM3 initially, after wet storage (252days) and after tank test (252days & mobile fraction of SRA completely removed) ; 159

Figure 92: Shrinkage isotherms of mortar series SM0 and SM3 initially, after wet storage (252days) and after tank test (252days & mobile fraction of SRA completely removed) ; 160

Figure 93: Shrinkage of mortar series CM during cyclic leaching / drying and cyclic rewetting / drying 162

Figure 94: Adsorption/desorption and cumulated creep in the cyclic regimes of mortars CM0 and CM3 163

Figure 95: Saturation isotherms of paste with SRA1 171

Figure 96: Saturation isotherms of mortars with SRA1 172

Figure 97: Shrinkage isotherms of paste containing different SRAs 173

Figure 98: Shrinkage isotherms of mortars with SRA1 174

Figure 99: Energy balance for cement paste containing SRA1 177

Figure 100: Energy balance for mortar type CM with SRA1 177

Figure 101: Energy of deformation versus total Helmholtz free energy, specific deformation energy and specific deformation of cement paste CP with SRA1 178

Figure 102: Specific energy of deformation and specific deformation of cement paste with SRA2 179

Figure 103: Specific deformation and saturation isotherms of pastes containing SRA3 and SRA5 ... 180

Figure 104: Drying shrinkage of mortars CM and SM and LM with SRA1 over energy of desorption 181

Figure 105: Interfacial area exposed to the liquid/vapour interface and evolution of surface tension in pore fluid of mortar CM 184

Figure 106: Interfacial area exposed to the liquid/vapour interface and evolution of surface tension in pore fluid of mortar LM 184

Figure 107: Interfacial area exposed to the liquid/vapour interface and evolution of surface tension in pore fluid of mortar SM 185

Figure 108: Contribution of average capillary pressure to average pore pressure, mortar CM 188

Figure 109: Total Helmholtz free energy , deformation energy and energy utilized at interfaces for cement paste CP without SRA and with different dosages of SRA1 at different relative humidity 192

Figure 110: Energy fractions for deformation energy and energy utilized at interfaces for cement past CP without SRA and with different dosages of SRA1 at different relative humidity 193

16 Abbreviations

BET	Method for determination of specific surface area
C_2S	Dicalciumsilicate
C_3S	Tricalciumsilicate
CAC	Critical Aggregation Concentration
CEM I	Portland cement
CEM II	Portland-composite cement
CM	Mortar with Portland cement binder
CMC	Critical Micellation Concentration
CP	Paste containing Portland cement binder
C-S-H	Calciumsilicatehydrate
DPG	Dipropylene glycol
DPTB	Dipropylene tert-butyl ether
EDX	Energy dispersive X-ray spectroscopy
EN	European standard
ESEM	Environmental scanning electron microscopy
GC	Gas chromatography
GEMS-PSI	Gibbs energy minimization selector; (Paul Scherrer Institute/Villlingen/Switzerland)
HD-C-S-H	High density calciumsilicatehydrate
i.e.	That is
ICP-OES	Inductively coupled plasma-optical emission spectroscopy
LCT	Lower critical temperature
LD-C-S-H	Low density calciumsilicatehydrate
LM	Mortar with Portland-Limestone composite binder
LP	Paste containing Portland-Limestone composite binder
MIP	Mercury intrusion porosimetry
PE-LD	Polyethylene with low density
PEO	Polyethylene oxide
PPG	Polypropylene glycol
SAH	Salicylic acid hydrolysis
SCC	Self consolidating concrete
SCM	Self consolidating mortars
SM	Mortar according to european standard
soln.	Solution
SP	Superplasticizer
SP-PCE	Polycarboxylate type superplasticizer
SP-PNS	Polynaphthalene based plasticizer
SRA	Shrinkage reducing admixtures

SSA	specific surface area
TG	Thermogravimetry
TGA	Thermogravimetric analysis
TOC	Total organic carbon content
w/b	Water to binder ratio
w/c	Water to cement ratio
WD-XRF	Wavelength dispersive X-ray fluorescence spectroscopy
XRD	X-ray powder diffraction

17 Appendix

Table of content

A1 - Identification of SRA ingredients by patent search 226

A2 - Materials 232

A3 - Surface activity and phase behavior 234

A4 - Hydration of Portland cement 238

A5 - Microstructure of cement paste and mortar 256

A6 - Leaching 259

A7 - Drying and shrinkage of cement paste and mortar 264

A1 - Identification of SRA ingredients by patent search

The first publications explicitly using the term “cement shrinkage reducing agent” go back to Sato et al. released on different platforms around 1983 in Japan and the United States [29]. The reduction of drying shrinkage of up to 50% was derived using the capillary force shrinkage model or the reduction of surface tension respectively. In 1985 a US patent [273] was granted to this group of authors (Assignee: Nihon Cement Co. Ltd.; (JP)). They account for alkyl ether oxyalkylene glycol as the surface active compound given by the general formula F 1):

$$\mathbf{R - O - (AO)_n - H} \qquad \text{F 1}$$

where

R: a) $C_{1\text{-}7}$ alkyl alcohol radicals incl. the n- or iso- formations) or
b) $C_{5\text{-}6}$ cyclo-alkyl radicals

A: $C_{2\text{-}3}$ alkylene radicals

n: integer, $1 \leq n \leq 10$

The material can be classified as non-ionic surfactant carrying a hydrophobic tail (R) and a hydrophilic head formed by the hydrated oxyalkylene chain. Further details and specifications are to be found within the claims of [273] where tert-butyl ether is preferred as hydrophobic tail. Preferences for the molecular design of the hydrophobic tail are given in (F 2;F 3;F 4):

$$\mathbf{R - O - (C_2H_4O)_{1\text{-}5} - H} \qquad \text{F 2}$$

$$\mathbf{R - O - (C_3H_6O)_1 - H} \qquad \text{F 3}$$

$$\mathbf{R - O - (A_1O)_{2\text{-}10} - H} \qquad \text{F 4}$$

with

$\mathbf{R_{pref.}}$: $C_{1\text{-}5}$ alkyl or cyclohexyl radicals desirable, in particular tert-butyl radicals are preferred for the shrinkage reduction effect

$\mathbf{(AO)_{n;\,pref.}}$: a) ethylene oxide unit $(EO)_{1\text{-}5}$; propylene oxide unit (PO) or
b) $(EO,PO)_{1\text{-}5}$ with $0.2 < EO/PO < 5$; random configuration preferred for low foamibility

Lunkenheimer 2004 [122] classifies this type of surface active molecules as solvo-surfactants or hydrotropic detergents because they combine properties of solvents and surfactants.

In 1993 Umaki [274] (Assignee: Nihon Cement Co. Ltd.; (JP)) claimed lower alcohols to be efficient in shrinkage reduction. Compounds given by the general formula (F 5) turned out to be a special case of formula (F 1). Note that tert-butyl group forming the hydrophobic tail is preferred too.

$$\mathbf{R - OH} \qquad \text{F 5}$$

where

R: a) $C_{4\text{-}6}$ alkyl group; tert-butyl group preferred
b) $C_{5\text{-}6}$ cycloalkyl group

Starting from 1988 Akimoto et al. [275-277] claimed a cement admixture efficient in shrinkage reduction being copolymerized from a polyoxyalkylene derivative given by the general formula (F 6) and maleic anhydride, a hydrolyzed product of the copolymer, or a salt of the hydrolyzed product, using a peroxide catalyst. It seems to be important to mention that for Akimoto et al. another US patent [278] is filed in 1989 which claims a dispersant compound comprising a component familiar with the structure given in (F 6).

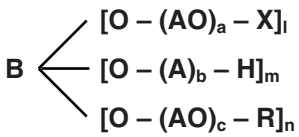

F 6

where:

B:	residue of a compound having 2 to 8 hydroxyl groups
AO:	C_{2-18} oxyalkylenes; C_{2-4} preferred
X:	C_{2-5} unsaturated hydrocarbon group or acyl group; C_{2-5} alkylene preferred
R:	C_{1-40} hydrocarbon group; C_{1-24} preferred
a; b; c:	$1 \leq a; b; c \leq 1000$
l; n:	$1 \leq l; n \leq 7$
m:	$0 \leq m \leq 2$
and	a) $2 < l + m + n < 8$; $m/(l+n) < 0.5$; $al + bm + cn \geq 1$; b) average molecular weight of the copolymer between 1000 and 200000

The polymer can be classified as polymeric non-ionic surfactant. In comparison to monoalcohols and alkylether oxyalkylene glycols the surfactant can be rendered a two or three headed. Concerning the effect of preventing slump loss and providing drying shrinkage reduction a copolymer which is soluble in water to some extent is pointed out to exhibit best performance [277].

In 1989 Schulze et al. [279, 280] (Assignee: Wacker Chemie GmbH (DE)) claim a group of alkanediols given by the general formula $C_nH_{2n}(OH)_2$; $5 < n < 10$, where 2,2 Dimethyl 1,3 Propanediol (Neopentylglycol) is preferred as a efficient compound for shrinkage reduction.

Starting in 1990 Sakuta et al. [281-283] claim a compound given with the general formula (F 7), almost similar to formula (F 1) in [273].

$$\mathbf{R - O - Z - H} \qquad \text{F 7}$$

where:

R:	C_{9-18} alkyl alcohol or alkanoyl radicals
Z:	single adduct $(EO)_{1-4}$; $(PO)_{1-30}$ or block or random copolymer containing EO and PO; $n_{tot.}<30$; EO/PO < 1

In comparison to (F 1) the radical R is formed by a branched alkyl, i.e. (2 tert butyl ethyl) ethyl-group.

Abdelrazig et al. [284-286] (Assignee: W.R. grace & Co.-Conn (US)) developed admixtures composed from amides or formyl compounds claiming compounds given by the general formula (F 8) in [284, 285] and amino alcohols (F 9) in [286]:

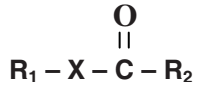

F 8

where:

$\mathbf{R_1}$:	C_{9-18} alkyl alcohol or alkanoyl radicals, preferred butyl group
X:	a) oxygen atom b) secondary nitrogen group –(NH)-
$\mathbf{R_2}$:	a) primary nitrogen group $–NH_2$ b) $–CH_2C(O)CH_3$ group; if X is an oxygen atom

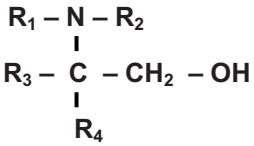

F 9

where:

R_1/R_2:	hydrogen atoms; linear or branched C_{1-3} alkyl group
R_3/R_4:	hydrogen atom; linear or branched C_{1-8} alkyl group; R_3+R_4 contain at least two carbon atoms
preferred:	a) 2-amino-butanol; b) 2-amino-2-methyl-propanol

Starting in 1995 Shawl et al. started to claim compounds comprising mixtures of glycols and oxyalkylene glycols [83, 194, 199] (F 10) or mixtures of alkyl ether derivates of glycerine as well as alkyl ether derivates of aliphatic polyhydroxy-compounds [195-198] (Assignee: Arco Chemical Technology, L.P. (US); (F 11).

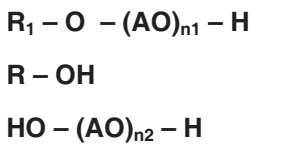

F 10

where:

R:	C_{4-10} alkyl or cycloalkyl group
R_1:	C_{1-10} alkyl or cycloalkyl group
A:	C_{2-4} alkylene group, or mixture of alkylenes
n1:	integer; $1 \leq n \leq 10$
n2:	integer; $1 \leq n \leq 8$

It has to be pointed out that general formulas (F 10 a, b) are similar to the compounds given by Sato et al. [273] and Umaki [274] or (F 1) and (F 5) respectively.
Regarding the shrinkage reduction efficiency the examples given in [83] explicitly show a synergistic effect by combining glycols (F 10 c) and alkyl ether oxyalkylene glycols (F 10 a).

Another efficient compound or mixture is given by the general formulas (F 11) in [198]:

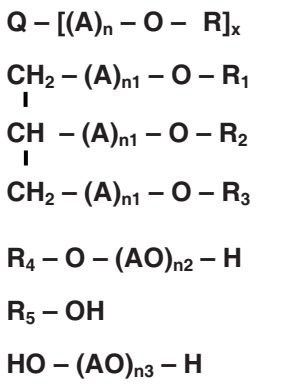

F 11

where:

Q:	C_{3-12} aliphatic hydrocarbon group
R:	hydrogen or C_{1-16} alkyl group
n:	integer; $0 \leq n \leq 10$
x:	integer; $3 \leq n \leq 5$

A:	C_{2-4} oxyalkylene group; preferred 2-methyletoxy group for (F8b)
R_{1-3}:	hydrogen or C_{1-16} alkyl group; at least one R_x is C_{1-16} alkyl group; tertiary butyl group preferred for R_1 and R_3 for (F8b)
R_4:	C_{1-7} alkyl or C_{5-6} cycloalkyl group
R_5:	C_{4-6} alkyl group
n_1:	integer; $0 \leq n \leq 10$
n_2:	integer; $1 \leq n \leq 8$
n_3:	no specifications, molecular weight between $200 \leq M \leq 1000$

Another type of surfactant introduced is represented by general formula (F 11a). The hydrophilic head (-chain) is formed by repeating units of oxyalkylene ethers in case of R as an alkyl group. One may assume that the increased number of oxygen within the head chain is permitting a higher amount of hydrogen bonds within aqueous solution, i.e. better miscibility. The surfactant represented by the general formula (F 11b) can be classified as polyol ($n_{1;\,2;\,3}$=0) or two headed (n_2=0) and three headed ($n_{1;\,2;\,3}$>0) polymeric surfactant.

Starting from 1996 Berke, Kerkar et al. [184-190, 287] (Assignee: W.R. Grace & Co.-Conn. (US)) mainly claim bicomponent admixtures containing a shrinkage reducing component A and a second component B, i.e. dispersing admixture.
Berke 1997 [184]:

Component A, the surfactants, comprising at least one component of

- oxyalkylene glycols similar to (F 10c) and (F 11e)
- alkyl ether oxyalkylene glycols similar to (F 10a) and (F 11c)
- oxyalkylene adducts of polyols similar to (F 11a)

Component B, the dispersant, a comb-polymer having free carboxylic acid groups (incl. salts thereof) and unit given by the general formula (F 12)

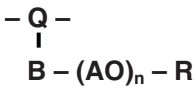

F 12

where:

Q:	ethylene group (part of chain or backbone polymer)
B:	tying group; carboxylic acid ester or amide group; alkylene ether or ether group
A:	C_{2-10} alkylene group, or mixtures thereof
R:	hydrogen or C_{1-10} various hydrocarbon groups
n:	integer, $25 \leq n \leq 100$

Kerkar 1997 [287] claims a copolymer as dispersing component B given by the general formula (F 13):

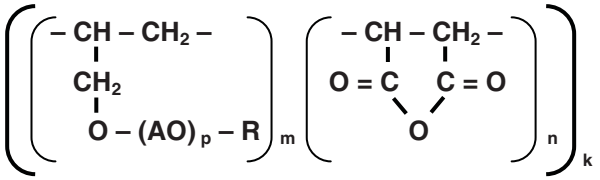

F 13

where:

A:	**C_{2-4}** oxyalkylene groups; in mixture
p:	integer, $25 \leq n \leq 75$
R:	C_{1-4} alkyl group

m, n: m/n = 1

k: integer, $1 \leq n \leq 100$

Regarding the invention of Akimoto [275-277] it has to be mentioned that dispersants may be able to contribute to shrinkage reduction. The molecular structure of the dispersant compound given by the general formula (F 13) can be classified as a polymeric macro-surfactant, in which the hydrophilic heads are formed by the grafted chains and the maleic unit serves as “head spacer”. The overall macromolecule constitutes the amphiphile or surfactant respectively.

In 1997 Berke claimed another multicomponent shrinkage reducing admixture using alkyl ether oxyalkylene adducts in combination with conventional cement admixtures, as pointed out in [188]: naphthalene sulfonate formaldehyde condensate and melamine sulfonate formaldehyde condensate.

This incorporation of dispersants into shrinkage reducing admixtures raises the question wheter SRA decrease fluidity of paste, mortar and concrete.

In another patent from 1997 Berke et al. claimed a cement admixture capable to counteract drying shrinkage by use of alkylene glycol, i.e. 2-methyl 2.4 pentanediol, or oxyalkylene glycols and maintain compressive strength of concrete using silica fume and a stabilizer as a second component.
Does one can conclude thereof that SRA might cause significant decrease of compressive strength?

Because of the defoaming property of this shrinkage reducing compound and to provide proper air entrainment for concrete Berke [185] and Kerkar [186] combine a shrinkage reducing compound similar to the composition given in (F8) and an organic amine salt of tall oil fatty acid [185] or an air entraining agent [186] respectively.

In 2000 Wombacher et al. [79-81] (Assignee: SIKA AG (CH)) claimed a composition of amino alcohols as surfactants and diols, glycols or alkylether glycols or neopentyl glycol adducts respectively. The amino ethanol surfactant claimed is given by the general formula (F 14):

$$\mathbf{R - NH - (AOH)} \qquad \text{F 14}$$

where:

R: $\mathbf{C_{1\text{-}6}}$ alkyl group, linear, branched, cyclic

A: ethyl (C_2H_4) or propyl (C_3H_6) group

Compared to other patents where the actual surfactant is an alkyl ether oxyalkylene glycol the ether bond is substituted by a secondary amine group.
Shrinkage measurements on mortars modified by using different compositions of amino alcohols, glycols and/or alkyl ether glycols, alone and in combination reveal a synergistic effect regarding the enhancement of shrinkage reduction [79-81]. A similar phenomenon could be shown earlier by Shawl et al. [83] for alkyl ether oxyalkylene glycols and glycols or diols respectively.

In 2001 Engstrand [204] (Assignee: Perstorp AB (SE)) claimed a powderous SRA comprising an acetal of a tri- or polyhydric alcohol, having at least a water solubility of 0.5%, and amorphous silicic acid. For further specification the acetal is a 1,3 dioxane of a trihydric alcohol or trimethylol-$C_{1\text{-}8}$-alkane or trihydric alcoxylated alcohol respectively.

Collepardi [288] (Assignee: General Admixtures S.p.A. (IT)) claims a bicomponent compound efficient in shrinkage reduction even in the absence of proper curing comprising a polycarboxylate-based superplasticizer and 2(2 alkoxy-ethoxy) ethanol given by the general formula (F 15). The compound turns out to be quite similar to the alkyl ether oxyalkylene glycols given in (F 1; F 10a; F 11c).

$$\mathbf{R - O - CH_2 - CH_2 - O - CH_2 - CH_2 - OH} \qquad \text{F 15}$$

where:

R: $\mathbf{C_{1\text{-}4}}$ linear or branched alkyl group

In 2008 Gartner [82] (Assignee: Lafarge (FR)), also involved in [184, 284, 285], claims a compound comprising a glycol with the general formula (F12) and a surfactant capable to reduce the surface tension of water down to below 30mN/m at a concentration below 1% (no further specifications).

$$C_nH_{2n}(OH)_2 \qquad \text{F 16}$$

where

n: integer; 1 < n < 10; preferred hexylene glycol

The surfactants that can be used are anionic, amphoteric or non-ionic surfactants, most preferred: a non-ionic fluorinated surfactant, as pointed out in [82], fluorinated polyester sold by 3M under the trade name Flourad FC-4430. The synergistic effect on enhancing shrinkage reduction by combining glycol and surfactant is explicitly pointed out.

A2 - Materials

A2.1 Tables

Tab.A2- 1: Element oxide composition of raw materials

element oxides	cement [wt.-%]	clinker [wt.-%]	limestone [wt.-%]	method
CaO	63.40	65.50	53.70	WD-XRF
SiO_2	19.90	21.60	0.50	WD-XRF
Al_2O_3	4.90	5.20	0.20	WD-XRF
Fe_2O_3	2.80	2.90	0.10	WD-XRF
MgO	1.80	2.00	0.80	WD-XRF
K_2O	1.00	0.68	-	WD-XRF
Na_2O	0.12	0.12	-	WD-XRF
P_2O_5	0.34	0.38	-	WD-XRF
TiO_2	0.29	0.31	-	WD-XRF
SrO	0.08	0.06	-	WD-XRF
Mn_2O_3	0.04	0.05	-	WD-XRF
SO_3	2.90 / 3.02	0.56 / 0.57	-	WD-XRF / C/S Determinator/LECO CS 400
LOI 975°C	2.18 / 2.50	0.13 / 0.14	42.89	TGA
sum	~ 100	~ 99.4	98.19	
CaO_{free}	0.40	0.35	-	Franke 1941 [242]
insoluble residue	0.45	-	1.60	EN 196-2
CO_2	1.76	0.26	-	C/S Determinator/LECO CS 400
	1.82	0.08	-	TGA; loss between 480°C-730°C

Tab.A2- 2: overall oxide distribution of the main clinker phases

overall oxide distribution		Na_2O	MgO	Al_2O_3	SiO_2	P_2O_5	SO_3	K_2O	CaO	TiO_2	Mn_2O_3	Fe_2O_3	sum
Alite	**[wt.-%]**	0.0	1.8	1.0	24.8	0.5	0.1	0.1	71.0	0.0	0.0	0.7	100.0
Belite	**[wt.-%]**	0.0	0.8	2.1	31.1	0.5	0.2	0.6	63.5	0.3	0.0	0.8	100.0
Aluminate	**[wt.-%]**	0.4	2.2	30.8	3.8	0.0	0.0	1.0	56.1	0.4	0.0	5.3	100.0
Ferrite	**[wt.-%]**	0.0	4.8	21.9	3.6	0.0	0.0	0.1	45.8	2.4	0.4	20.9	100.0

Tab.A2- 3: Mineral phase composition of cement and clinker

mineral components		clinker	clinker in cement	mineral additions	cement	supporting fixpoints / methods	
		100 wt.-%	91 wt.-%	9 wt.-%	100 wt.-%	[wt.-%]	methods /assumptions
C_3S	[wt.-%]	68.9	62.7	-	62.7		aluminate modification: ratio of cubic/orthorhombic ~ 80/20
C_2S	[wt.-%]	12.8	11.6	-	11.6		
C_3A	[wt.-%]	7.2	6.6	-	6.6		
C_4AF	[wt.-%]	9.3	8.5	-	8.5		
CaO_{free}	[wt.-%]	0.4	0.3	0.1	0.4	0.4	Franke [242]
$CaCO_3$	[wt.-%]	0.1	0.1	4.1	4.2		TGA; calcination
$MgCO_3$	[wt.-%]	0.1	0.1	0.0	0.1		TGA; calcination
K_2SO_4	[wt.-%]	0.9	0.8	0.7	1.5	1.5	ICP-OES
Na_2SO_4	[wt.-%]	0.1	0.1	0.0	0.1	0.1	ICP-OES
Ca_2SO_4 x 2 H_2O	[wt.-%]	0.0	0.0	1.7	1.7	1.7	TGA; water loss
Ca_2SO_4 x $^1/_2$ H_2O	[wt.-%]	0.0	0.0	1.2	1.2	1.2	TGA; water loss
$CaSO_4$	[wt.-%]	0.0	0.0	0.9	0.9		
insol. Residue	[wt.-%]	0.0	0.0	0.4	0.5	0.45	measured acc. to EN 196-2
sum	**[wt.-%]**	**100**	**91**	**9**	**100**		

Tab.A2- 4: Element distribution of the main clinker phases

overall element distribution		Na	Mg	Al	Si	P	S	K	Ca	Ti	Mn	Fe	O	sum
Alite	**[wt.-%]**	0.0	1.1	0.5	11.6	0.2	0.0	0.1	50.8	0.0	0.0	0.5	35.2	100.0
Belite	**[wt.-%]**	0.0	0.5	1.1	14.6	0.2	0.1	0.5	45.4	0.2	0.0	0.6	36.9	100.0
Aluminate	**[wt.-%]**	0.3	1.3	16.3	1.8	0.0	0.0	0.8	40.1	0.2	0.0	3.7	35.4	100.0
Ferrite	**[wt.-%]**	0.0	2.9	11.6	1.7	0.0	0.0	0.1	32.7	1.4	0.3	14.6	34.6	100.0

Tab.A2- 5: mixdesign for self consolidating mortars (SCM) with/without cement replacement

denom.			SM	SCM1	SCM1_L35	SCM48_L38	SCM46	SCM46_L50	SCM53	SCC B8_L38
aggregates	**grading curve**	[-]	CEN-sand	CEN-sand	CEN-sand	C2	B4	B4	C4	B8
	max. grain size	[mm]	2	2	2	2	4	4	4	8
	fractionated g.c.*	[nbrs./no]	no	no	no	1	5	5	5	1
paste	**paste volume**	[vol.-%]	41.7	50.0	50.0	48.1	46.7	46.7	52.6	41.9
	V_{liquid}/V_{solid}	[-]	1.58	1.10	1.10	0.98	0.98	0.98	0.98	0.98
	replacement	[vol.-%]	-	-	35	38	-	-	-	
	w/b	[-]	0.5	0.35	0.36	0.32	0.31	0.33	0.31	0.33
	$w/c_{efficient}$**	[-]	0.5	0.35	0.54	0.50	0.31	0.62	0.31	0.50
	m_{cement}	[kg/m³]	512	744	487	476	744	372	838	412
	$m_{additive}$	[kg/m³]	-	-	229	256	0	325	0	222
	m_{water}	[kg/m³]	256	249	257	231	223	226	247	201
	m_{SP}	[kg/m³]	0	12.6	4.8	8.1	10.4	7.4	16.8	7.0

Tab.A2- 6: mixdesign for self consolidating concretes (SCC) with/without cement replacement

denom.			SCC 1	SCC1_L50	SCC2	SCC2_L50	SCC2_L38	SCC3	SCC3_L38	SCC3_L50
aggregates	**grading curve**	[-]	A16	A16	AB16	AB16	~ AB16	B16	~B16	B16
	max. grain size	[mm]	16	16	16	16	16	16	16	16
	fractionated g.c.*	[nbrs./no]	7	7	7	7	1	7	1	7
paste	**paste volume**	[vol.-%]	32.8	32.8	35.7	35.7	34.9	38.5	37.2	38.6
	V_{liquid}/V_{solid}	[-]	0.98	0.98	0.98	0.98	0.98	0.98	0.98	0.98
	replacement	[vol.-%]	-	50	-	50	38	-	38	50
	w/b	[-]	0.31	0.33	0.31	0.33	0.32	0.31	0.32	0.33
	$w/c_{efficient}$**	[-]	0.31	0.62	0.31	0.62	0.50	0.31	0.50	0.61
	m_{cement}	[kg/m³]	522	261	570	285	344	612	370	311
	$m_{additive}$	[kg/m³]	0	229	0	248	186	0	201	269
	m_{water}	[kg/m³]	156	158	170	172	167	184	180	186
	m_{SP}	[kg/m³]	7.35	5.2	7.952	5.7	5.8	8.6	6.3	6.2

A2.1 Figures

Fig.A2- 1: aluminate modifications of cement

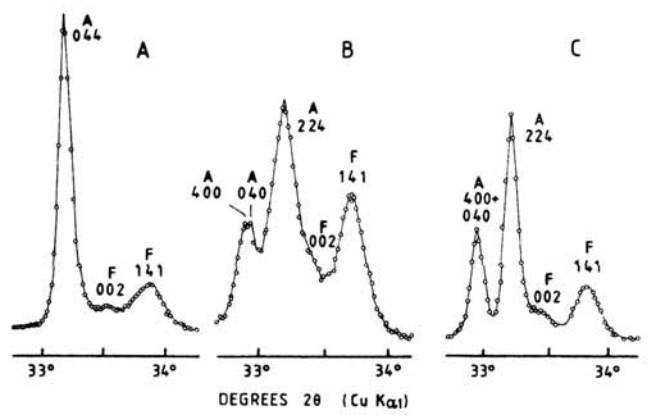

aluminate (A-peak)

A – cubic

B – orthorhombic

C – pseudotetragonal

D – SAP/CEM II 42.5 N

ferrite (F-peak)

XRD-peaks of different aluminate modifications A; B; C taken from [289]

A3 - Surface activity and phase behavior

A3.1 tables

Surface tension of aqueous solutions of SRA; SP-PCE and mixtures of SRA 1 and SP-PCE

Tab.A3- 1: Measuring regime-aqueous solutions

aqua_d.	Conc. of SRA		SRA_C1	SRA_C2	SRA_C3	SRA_C4	SRA_C5	SRA_C6	SRA_C7	SRA_C8	SRA_C9	SRA_C10	SRA_C11
Conc. of SP-PCE	[g/l]	0	5	11	16	21	50	-	-	-	-	-	-
	0	0	1	2	3	4	5						
SP_C1	5	6	1-6		3-6		5-6						
SP_C2	10	7		2-7									
SP_C3	15	8	1-8		3-8		5-8						
SP_C4	20	9		2-10		4-9							
SP_C5	51	10	1-10				5-10						

x — measurment_nbr. and stock solution_nbr.

x_x — measurment_nbr. of 1:1 mixes of stock solutions

Tab.A3- 2: Surface tension of aqueous solutions

measurement	C_SRA	C_SP-PCE	C_mix	SFT	Dev.
[Nbr.]	[g/l]	[g/l]	[g/l]	[mN/m]	[mN/m]
0	0.0	-	-	72.7	0.3
1	5.0	-	-	55.8	0.3
2	10.7	-	-	49.4	0.3
3	15.7	-	-	46.3	0.1
4	20.7	-	-	45.0	0.1
5	50.0	-	-	40.7	0.2
6	-	5.5	-	51.2	0.2
7	-	10.2	-	46.0	0.2
8	-	15.5	-	43.4	0.1
9	-	20.4	-	40.8	0.3
10	-	51.4	-	36.1	0.2
1-6	5.0	5.5	5.2	52.2	0.2
1-8	5.0	15.5	10.2	48.2	0.1
1-10	5.0	51.4	28.2	39.4	0.2
2-7	10.7	10.2	10.5	49.3	0.1
2-10	10.7	51.4	31.0	39.6	0.3
3-6	15.7	5.5	10.6	49.6	0.1
3-8	15.7	15.5	15.6	45.2	0.1
4-9	20.7	20.4	20.6	43.5	0.0
5-6	50.0	5.5	27.7	44.1	0.1
5-8	50.0	15.5	32.7	42.0	0.0
5-10	50.0	51.4	50.7	37.6	0.1

1:1 mixtures

Surface tension of aqueous electrolyte solutions of SRA1; SP-PCE and mixtures of SRA1 and SP-PCE

Tab.A3- 3: Measuring regime-synthetic pore solutions

p.-soln.	Conc. of SRA		SRA_C1	SRA_C2	SRA_C3	SRA_C4	SRA_C5	SRA_C6	SRA_C7	SRA_C8	SRA_C9	SRA_C10	SRA_C11
Conc. of SP-PCE	[g/l]	0	6	11	16	20	51	86	120	161	200	241	280
	0	0	1	2	3	4	5	6	7	8	9	10	11
SP_C1	5	12	1-12		3-12		5-12	6-12					
SP_C2	10	13		2-13			5-13						
SP_C3	16	14	1-14		3-14		5-14	6-14					
SP_C4	20	15				4-15							
SP_C5	51	16	1-16	2-16	3-16		5-16	6-16					
SP_C6	78	17											
SP_C7	103	18											

x — measurment_nbr. and stock solution_nbr.

x_x — measurment_nbr. of 1:1 mixes of stock solutions

Tab.A3- 4: Surface tension of synthetic pore solutions

measurement	C_SRA	C_SP-PCE	C_mix	SFT	dev.
[Nbr.]	[g/l]	[g/l]	[g/l]	[mN/m]	[mN/m]
0	0.0	-	-	75.2	0.1
1	5.6	-	-	52.4	0.1
2	10.6	-	-	48.8	0.1
3	15.9	-	-	43.8	0.1
4	20.3	-	-	43.3	0.1
5	51.5	-	-	37.6	0.4
6	86.0	-	-	34.4	0.1
7	120.3	-	-	33.2	0.1
8	161.1	-	-	31.5	0.0
9	200.0	-	-	30.5	0.1
10	240.9	-	-	30.5	0.1
11	280.0	-	-	30.4	0.0
12	-	4.9	-	49.3	0.1
13	-	10.4	-	45.5	0.1
14	-	16.0	-	42.4	0.2
15	-	20.4	-	40.9	0.1
16	-	51.1	-	36.6	0.0
17	-	77.5	-	35.6	0.1
18	-	103.2	-	34.9	0.1
1-12	5.6	4.9	5.3	52.0	0.1
1-14	5.6	16.0	10.8	45.5	0.2
1-16	5.6	51.1	28.3	40.8	0.1
2-13	10.6	10.4	10.5	46.7	0.1
2-16	10.6	51.1	30.8	39.7	0.1
3-12	15.9	4.9	10.4	49.3	0.2
3-14	15.9	16.0	16.0	43.9	0.0
3-16	15.9	51.1	33.5	39.8	0.1
4-15	20.3	20.4	20.4	43.6	0.0
5-12	51.5	4.9	28.2	43.5	0.1
5-13	51.5	10.4	30.9	42.8	0.0
5-14	51.5	16.0	33.7	42.2	0.1
5-16	51.5	51.1	51.3	39.5	0.1
6-12	86.0	4.9	45.5	40.9	0.1
6-14	86.0	16.0	51.0	39.7	0.1
6-16	86.0	51.1	68.5	36.7	0.0

1:1 mixtures

Tab.A3- 5: Fit functions for surface activity of SRA and SP-PCE and critical micellation concentration (CMC)

admixture	fit function: $\gamma_{SFT} = f\{C_{SRA}\}$; exponential decay of 3rd degree $\gamma_{SFT} = \gamma_{CMC} + A_1e^{(-C_{SRA}/t1)} + A2e^{(-C_{SRA}/t2)} + A3e^{(-C_{SRA}/t3)}$							CMC
[denom.]	γ_{CMC} [mN/m]	A1	t1	A2	t2	A3	t3	[g/l]
SRA1	28	12.9	0.6	14.6	12.0	16.8	60.9	~ 200
SRA2	34	13.0	182.9	24.9	10.5	0.7	-7.E+96	300 ± 50*
SRA3	30	14.2	0.4	28.7	12.6	-	-	80 ± 20*
SRA4	32	12.2	0.1	7.4	2.3	19.7	4.E+01	200 ± 50*
SRA5	30	-	-	-	-	-	-	~ 0.1
SP-PCE	31	22.7	2.5	17.9	27.5	2.4	-7.E+81	~ 135

* uncertain because of low density of measuring points

Tab.A3- 6: TGA-analysis on solid phases separated from electrolyte solutions of SRA1

nbr. of measurement	[C_X]	C 1	C 2	C 3	C 4	C 5	C 6	C 7	C 8	C 9	C 10	C 11
bulk conc. SRA 1	[g/l]	51	107	120	137	148	161	172	192	274	480	549
organic matter	[g/g]	0.0%	0.0%	0.0%	0.0%	0.0%	0.0%	0.0%	0.0%	3.0%	1.2%	8.0%
Syngenit	[g/g]	97.3%	98.9%	97.4%	99.6%	99.1%	99.8%	99.5%	99.3%	47.0%	15.6%	13.5%
Portlandit	[g/g]	0.5%	0.3%	0.2%	0.2%	0.1%	0.1%	0.1%	0.0%	0.4%	0.5%	0.0%
carb. Portlandit	[g/g]	1.0%	0.2%	0.8%	0.4%	0.8%	0.3%	0.3%	0.3%	0.2%	0.2%	0.2%
residue	[g/g]	0.0%	0.0%	0.0%	0.0%	0.0%	0.0%	0.0%	0.0%	49.0%	82.0%	78.0%
sum	[g/g]	99%	99%	98%	100%	100%	100%	100%	100%	100%	100%	100%
remarks	[-]	bulk concentration below CMC					liquid/liquid miscibility gap					

nbr. of measurement	[C_X]	C 12	C 13	C 14	C 15	C 16	C 17	C 18
bulk conc. SRA 1	[g/l]	580	640	657	672	713	768	864
organic matter	[g/g]	1.6%	7.8%	13.5%	8.0%	16.0%	24.0%	34.0%
Syngenit	[g/g]	11.3%	10.7%	9.2%	10.5%	9.1%	8.4%	7.8%
Portlandit	[g/g]	0.1%	0.0%	0.0%	0.2%	0.0%	0.1%	0.1%
carb. Portlandit	[g/g]	0.2%	0.3%	0.3%	0.2%	0.5%	0.9%	0.5%
residue	[g/g]	87.0%	81.0%	77.0%	81.0%	74.0%	67.0%	58.0%
sum	[g/g]	100%	100%	100%	100%	100%	100%	100%
remarks	[-]	isotropic liquid phase and solids						

TGA-analysis; species identified by weight loss

- organic material; < 200°C
- Syngenit; 200°C-350°C
- Portlandit; 420°C-480°C
- carb. Portlandit from Calcit; 530°C-730°C

Tab.A3- 7: Analysis of the liquid phases

composition of SRA1 - pore solutions		pore solution	Mix 1	Mix 2		Mix 3		Mix 4	SRA 1
			mic. Solution	phase 1	phase 2	phase 1	phase 2	reverse mic. Solution	plain admixture
bulk concentration of SRA 1 [g/l]		0	120	274		480		657	960
pore solution [g/l]		1030	901	736		515		325	0
SRA content of liquid phase [g/l] *		-	104	209	639	327	583	527	-
actual water content*		-	918	806	344	679	404	465	-
volume content of phase in bulk [vol.%]**		-	-	88%	7%	63%	21%	-	-
ion species obtained from ICP-OES	K^+ [mmol/l]	435	409	358	b.d.l	158	b.d.l	46	b.d.l
	Na^+ [mmol/l]	48	48	42	b.d.l	b.d.l	b.d.l	b.d.l	b.d.l
	Ca^{2+} [mmol/l]	11	4	b.d.l	b.d.l	b.d.l	b.d.l	b.d.l	b.d.l
	SO_4^{2-} [mmol/l]	175	153	131	b.d.l	37	b.d.l	b.d.l	b.d.l
dilution factor		1,000	0,901	0,762	-	0,620	-	0,325	0

* results from TOC on liquid phases and calculated referring water content

** volume of Phase 2 measured; volume of phase 1 calculated assuming that residual water is exclusively part of phase 1

A3.2 Figures

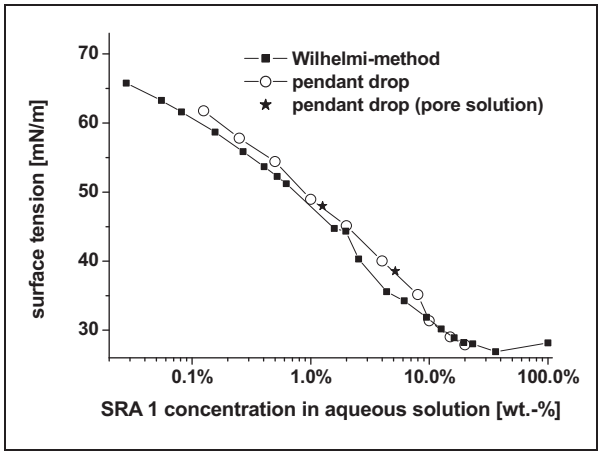

Fig.A3- 1: Results from Wilhelmy-plate method and pendant drop

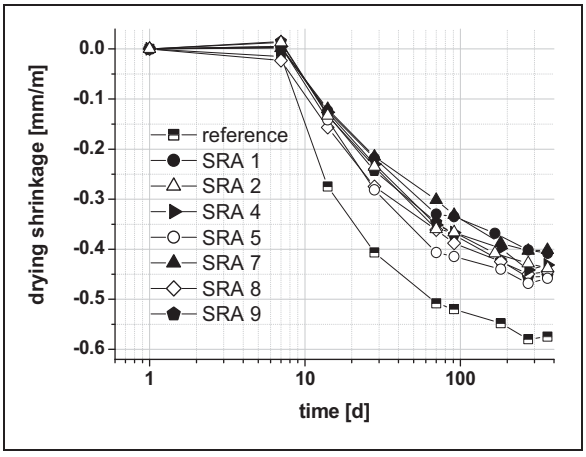

Fig.A3- 2: Performance of SRA in self consolidating mortar

regime:

- 7d wet cured at 20°C/95% RH, then stored at 20°C/70% RH
- dosage of SRA: 5wt.-% of mixing water
- SRA replaced water by volume

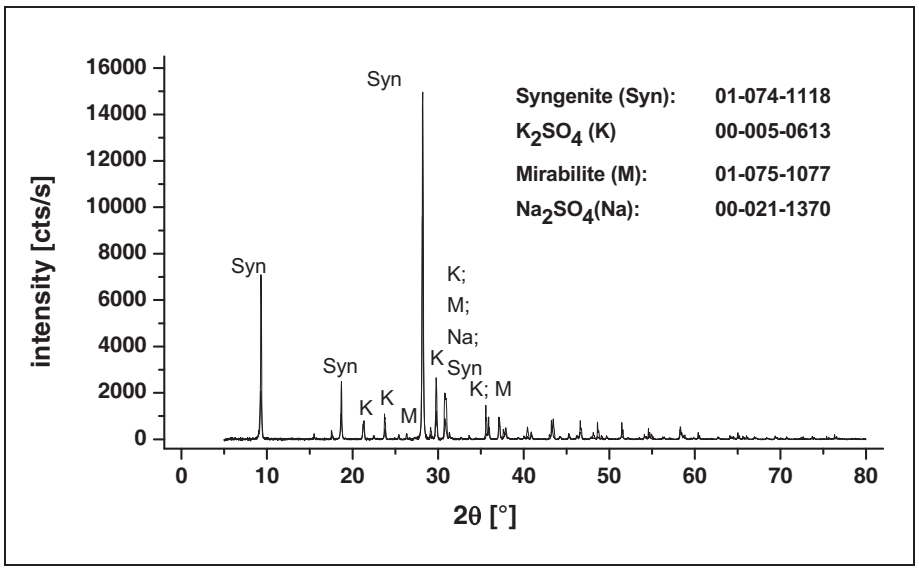

Fig.A3- 3: qualitative XRD analysis of SRA1 residue

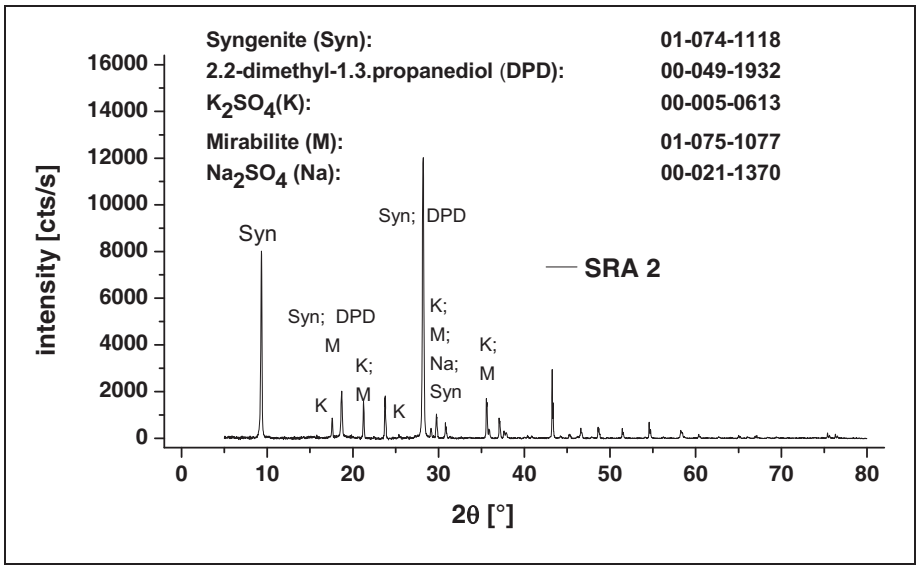

Fig.A3- 4: qualitative XRD analysis of SRA2 residue

A4 - Hydration of Portland cement

A4.1 Tables

Tab.A4- 1: Isothermal heatflow calorimetry on pastes– range of investigation and denomination

CEM I (CP)			SRA1			SRA2			SRA3			SRA4			SRA5			SRA6		
		Ref.	C1	C2	C3	C1	C2	C3	C1	C2	C3	C1	C2	C3	C1	C2	C3	C1	C2	C3
Ref.		00.00	11.00	12.00	13.00	21.00	22.00	23.00	31.00	32.00	33.00	41.00	42.00	43.00	51.00	52.00	53.00	61.00	62.00	63.00
SP1	C1	00.11	11.11	12.11	13.11	21.11		23.11			33.11			43.11			53.11			63.11
	C2	00.12																		
	C3	00.13	11.13		13.13	21.13		23.13			33.13			43.13			53.13			63.13
CEM II A-L (LP)			SRA1			SRA2			SRA3			SRA4			SRA5			SRA6		
		Ref.	C1	C2	C3	C1	C2	C3	C1	C2	C3	C1	C2	C3	C1	C2	C3	C1	C2	C3
Ref.		00.00	11.00	12.00	13.00	21.00		23.00			33.00			43.00			53.00			63.00
SP1	C1	00.11	11.11		13.11			23.11												
	C2																			
	C3	00.13	11.13		13.13			23.13			33.13			43.13			53.13			63.13

repetitions: 1 2 3

admixture dosages: C1 **0.5 wt.-%** C2 **1.0 wt.-%** C3 **2.0 wt.-%** of solid content

denomination: XY . $I_1 I_2$. $I_3 I_4$

letter X: C for CEM I-paste; L for CEM II_A (80% CEM I + 20% limestone)
letter Y: P for paste
integer I_1: nbr. of SRA according to Table 2
integer I_2: Concentration of SRA; 1=0.5 wt.-% ; 2=1 wt.-%; 3=2 wt.-% of cement, referring to CEM I)
integer I_3: nbr. 1 for SP-PCE
integer I_4: Concentration of SP-PCE; 1=0.5 wt.-% ; 2=1 wt.-%; 3=2 wt.-% of cement, referring to CEM I)

example: **LP 13.13**
- composite binder 80% CEM I/20% limestone (CEM II-A)
- paste
- SRA 1
- C_{SRA}=2 wt.-% of cement
- SP-PCE 1
- $C_{SP\text{-}PCE\ 1}$=2 wt.-% of cement

!!! Note that the absolute amount of admixture of corresponding composite binder pastes always refers to the amount of cement in the appropriate Portland cement paste!!!

Tab.A4- 2: Heat release of pastes at particular times

ad-mixture	denomination*			Q {t=72h}	rel. $\alpha_{hyd\_CEM\ I}$	Q {t=7d}	rel. $\alpha_{hyd\_CEM\ I}$	denomination			Q {t=72h}	rel. $\alpha_{hyd\_CEM\ II\text{-}}$	dilution effect + eff. w/c
	CEM I	C_{SRA}	C_{SP}	[J/g]	[-]	[J/g]	[-]	CEM II-A	C_{SRA}	C_{SP}	[J/g]	[-]	[-]
-	CP	00.	00	293	-	339	1	LP	00.	00	262	1	89%
SRA 1	CP	11.	00	292	1,00	343	1,01	LP	11.	00	260	0,99	89%
	CP	12.	00	291	0,99	345	1,02	LP	12.	00	255	0,97	88%
	CP	13.	00	278	0,95	338	1,00	LP	13.	00	245	0,94	88%
SRA 2	CP	21.	00	295	1,01	347	1,02	LP	21.	00	259	0,99	88%
	CP	22.	00	293	1,00	348	1,03	LP	22.	00	-	-	-
	CP	23.	00	283	0,97	345	1,02	LP	23.	00	243	0,93	86%
SRA 3	CP	31.	00	300	1,02	-	-	LP	31.	00	-	-	-
	CP	32.	00	-	-	-	-	LP	32.	00	-	-	-
	CP	33.	00	294	1,00	-	-	LP	33.	00	265	1,01	90%
SRA 4	CP	41.	00	292	1,00	-	-	LP	41.	00	-	-	-
	CP	42.	00	-	-	-	-	LP	42.	00	-	-	-
	CP	43.	00	282	0,96	-	-	LP	43.	00	247	0,94	88%
SRA 5	CP	51.	00	299	1,02	-	-	LP	51.	00	-	-	-
	CP	52.	00	-	-	-	-	LP	52.	00	-	-	-
	CP	53.	00	301	1,03	-	-	LP	53.	00	260	0,99	86%
SRA 6	CP	61.	00	299	1,02	-	-	LP	61.	00	-	-	-
	CP	62.	00	-	-	-	-	LP	62.	00	-	-	-
	CP	63.	00	285	0,97	-	-	LP	63.	00	247	0,94	87%
SP	CP	00.	13	262	0,89	317	0,94	LP	00.	13	232	0,89	89%
SRA + SP	CP	13.	13	238	0,81	316	0,93	LP	13.	13	215	0,82	90%
	CP	23.	13	241	0,82	312	0,92	LP	23.	13	216	0,82	90%

Tab.A4- 3: Hydration stages T X - normalized according heat conduction calorimetry

pastes	T1	T2	T3	T4	T5	T6	T7	T8
	[h]	[h]	[h]	[h]	[h]	[h]	[h]	[h]
CP 00.00	1	2,5	9	16	34	72	168	672
CP 11.00	1	2,5	11	16	34	72	168	672
CP 13.00	1	3	12	20	35	72	168	672
CP 00.11	1	4	15	24	35	72	168	672
CP 00.13	1	9,5	28	35	48	84	168	672
CP 13.11	1	5	16	30	40	72	168	672
CP 13.13	1	12,5	36	46	60	96	168	672

Tab.A4- 4: chemically bound water at different stages of hydration - without correction for undesired water loss of ettringite

stage of hydration		amount of chemically bound water [g/100g unhydrated cement]*						
		reference	min. SRA1	max. SRA 1	-	-	max. SRA 1	max. SRA 1
			-	-	min. SP	max. SP	min. SP	max. SP
[T X]	[-]	**CP 00.00**	**CP 11.00**	**CP 13.00**	**CP 00.11**	**CP 00.13**	**CP 13.11**	**CP 13.13**
T1	**1 hour**	**1,7**	**1,4**	**1,4**	**1,7**	**2,4**	**1,8**	**2,4**
T2	**end of dormant period**	**2,0**	**1,5**	**1,6**	**1,7**	**2,9**	**2,1**	**4,7**
T3	**end of acceleration period**	**5,6**	**7,0**	**6,6**	**9,4**	**11,6**	**7,6**	**13,5**
T4	**start of deceleration period**	**8,4**	**9,6**	**10,6**	**12,9**	**14,5**	**14,6**	**17,2**
T5	**mid of deceleration period**	**14,3**	**14,7**	**14,9**	**14,7**	**17,3**	**16,8**	**17,1**
T6	**start of final period**	**18,3**	**17,8**	**20,5**	**19,0**	**19,1**	**19,5**	**19,4**
T7	**7 days**	**18,3**	**19,5**	**20,2**	**21,2**	**20,1**	**21,2**	**20,8**
T8	**28 days**	**21,4**	**21,8**	**22,0**	**21,0**	**21,7**	**20,8**	**20,1**

* referring to drying at 37°C/13±3%R.H.

Tab.A4- 5: Phase composition of plain cement paste CP 00.00 according to GEMS process modeling

phases	C_3S	C_2S	C_3A	C_4AF	C-S-H	Ett-ringite	Port-landite	Gyp-sum	Calcite	Hydro-talcite	Mono-carbo-nate	Pore solu-tion
mass	**[g / 100 g unhydrated cement]**											
unhydrated	59,7	14,5	6,4	9,2	0,0	0,0	0,3	4,7	4,4	0,0	0,0	40,8
T1	35,2	10,5	3,9	7,6	23,1	15,5	11,2	0	3,9	1,8	1,3	25,5
T2	26,8	9,0	3,0	6,2	31,3	16,0	14,9	0,0	3,1	2,5	6,0	20,8
T3	14,4	6,8	1,5	3,9	43,2	16,2	20,4	0,0	1,7	3,5	13,6	13,8
T4	11,3	6,6	1,2	3,6	46,0	16,2	21,8	0,0	1,5	3,7	15,0	12,4
T5	8,2	6,3	1,0	3,3	48,6	16,2	23,2	0,0	1,3	3,9	16,0	11,0
T6	6,2	6,2	0,9	3,1	50,3	16,3	24,1	0,0	1,2	4,0	16,7	10,1
T7	4,6	6,1	0,7	2,9	51,7	16,3	24,7	0,0	1,1	4,1	17,4	9,4
T8	2,9	5,9	0,5	2,5	53,2	16,3	25,5	0,0	0,9	4,3	18,6	8,4

Tab.A4- 6: X-ray powder diffraction - range of investigation

unhydrated references									
CEM I ; clinker of CEM I & appropriate samples after salicylic hydrolysis									
pastes w/c=0,4									
hydration time / stage	10 min	T1	T2	T3	T4	T5	T6	T7	T8
reference paste	CP 00.00								
SRA 1; C_{SRA}=0.5wt.-%	CP 11.00								
SRA 1; C_{SRA}=2.0wtm.-%	CP 13.00								
SRA 2; C_{SRA}=2.0wt.-%	CP 23.00						CP 23.00		CP 23.00
SRA 3; C_{SRA}=2.0wt.-%	CP 33.00						CP 33.00		CP 33.00
SRA 5; C_{SRA}=2.0wt.-%	CP 53.00						CP 53.00		CP 53.00
SP-PCE; C_{SP}=2.0wt.-%		CP 00.11							
SP-PCE; C_{SP}=2.0wt.-%		CP 00.13							
SRA1 + SP-PCE		CP 13.11							
SRA1 + SP-PCE		CP 13.13							

Tab.A4- 7: characteristic peak areas of hydrated cement pastes from powder XRD_early hydration up to end of the induction period

pastes at 10min	reference values unhyd.			area under the peak					
mineral phase	**peak**	**ref.**	**s.d.**	**CP00.00**	**CP11.00**	**CP13.00**	**CP23.00**	**CP33.00**	**CP53.00**
[-]	[°2T]	[Cts*2T]	[Cts*2T]	[Cts*2T]	[Cts*2T]	[Cts*2T]	[Cts*2T]	[Cts*2T]	[Cts*2T]
Ettringite	9,0	**-**	-	0	0	35	34	28	22
Gypsum	11,7	**-**	-	90	64	71	76	130	77
Ferrit	12,2	**37**	**9**	28	38	33	33	53	47
Ettringite	15,9	**-**	-	0	0	0	0	0	1
Portlandite	18,1	**-**	-	0	0	0	0	0	0
Gypsum	20,7	**-**	-	23	17	22	24	20	19
Anhydrite	25,5	**-**	-	22	37	21	23	22	33
C_3S	29,5	**330**	**31,1**	389	334	371	284	342	301
C_3S	30,1	**68**	**6,2**	69	59	74	65	62	65
C_3S; C_2S	32,2	**477**	**45,2**	497	498	481	513	557	462
C_3S; C_2S	32,6	**401**	**37,9**	381	436	386	405	376	367
Aluminate	33,3	**73**	**8**	73	63	78	79	73	61
Ferrite / Portlandite	33,9	**99**	**21**	111	118	68	89	103	124
C_3S	34,4	**281**	**39,7**	234	284	276	263	231	250
total area under the curve; range: 5°2T; 80°2T			blender	3351	3602	3545	3277	3388	3124
			spatula	-	-	-	-	-	-

pastes at T1	reference values unhyd.			area under the peak									
mineral phase	**peak**	**ref.**	**s.d.**	**CP00.00**	**CP11.00**		**CP13.00**		**CP23.00**	**CP33.00**	**CP53.00**	**CP00.13**	**CP13.13**
[-]	[°2T]	[Cts*2T]	[Cts*2T]	[Cts*2T]	[Cts*2T]	[Cts*2T]	[Cts*2T]	[Cts*2T]	[Cts*2T]	[Cts*2T]	[Cts*2T]	[Cts*2T]	[Cts*2T]
Ettringite	9,0	**-**	-	0	30	29	40	31	33	51	25	28	27
Gypsum	11,7	**-**	-	84	90	60	78	74	80	81	100	67	38
Ferrit	12,2	**37**	**9**	27	29	35	27	42	32	38	35	31	23
Ettringite	15,9	**-**	-	7	0	1	0	21	10	32	23	33	34
Portlandite	18,1	**-**	-	0	0	0	0	0	0	1	0	0	1
Gypsum	20,7	**-**	-	22	21	15	16	21	17	23	19	15	10
Anhydrite	25,5	**-**	-	26	29	32	33	18	24	32	19	29	29
C_3S	29,5	**330**	**31,1**	350	322	346	345	387	415	325	296	327	348
C_3S	30,1	**68**	**6,2**	75	67	64	72	71	60	69	65	61	55
C_3S; C_2S	32,2	**477**	**45,2**	499	421	448	444	429	532	460	451	503	478
C_3S; C_2S	32,6	**401**	**37,9**	380	460	404	394	501	423	432	354	506	393
Aluminate	33,3	**73**	**8**	69	82	68	94	85	87	89	78	78	75
Ferrite / Portlandite	33,9	**99**	**21**	116	80	117	120	103	92	125	119	87	95
C_3S	34,4	**281**	**39,7**	272	307	276	401	261	243	278	318	286	304
total area under the curve; range: 5°2T; 80°2T			blender	3040	3115	-	3530	-	-	-	-	3463	3476
			spatula	3529	-	3290	-	3478	3188	3848	3162	-	-

pastes at T2	reference values unhyd.			area under the peak									
mineral phase	**peak**	**ref.**	**s.d.**	**CP00.00**	**CP11.00**		**CP13.00**		**CP23.00**	**CP33.00**	**CP53.00**	**CP00.13**	**CP13.13**
[-]	[°2T]	[Cts*2T]	[Cts*2T]	[Cts*2T]	[Cts*2T]	[Cts*2T]	[Cts*2T]	[Cts*2T]	[Cts*2T]	[Cts*2T]	[Cts*2T]	[Cts*2T]	[Cts*2T]
Ettringite	9,0	**-**	-	45	45	24	46	62	33	39	54	34	57
Gypsum	11,7	**-**	-	64	54	84	69	84	86	95	88	65	0
Ferrit	12,2	**37**	**9**	42	23	29	27	30	27	34	33	31	20
Ettringite	15,9	**-**	-	32	27	0	22	0	22	29	1	14	25
Portlandite	18,1	**-**	-	0	0	0	0	1	0	0	0	1	1
Gypsum	20,7	**-**	-	17	16	17	21	21	25	22	19	12	0
Anhydrite	25,5	**-**	-	34	23	17	44	30	36	31	37	17	12
C_3S	29,5	**330**	**31,1**	305	327	298	323	335	345	332	319	294	260
C_3S	30,1	**68**	**6,2**	71	62	68	64	82	85	72	64	74	63
C_3S; C_2S	32,2	**477**	**45,2**	413	401	539	424	577	489	529	499	507	453
C_3S; C_2S	32,6	**401**	**37,9**	477	334	406	414	378	359	379	389	408	379
Aluminate	33,3	**73**	**8**	68	72	80	57	67	67	73	88	75	76
Ferrite / Portlandite	33,9	**99**	**21**	87	61	84	89	80	75	93	64	118	85
C_3S	34,4	**281**	**39,7**	322	236	240	315	314	288	236	244	334	244
total area under the curve; range: 5°2T; 80°2T			blender	3349	2959	-	3323	-	-	-	-	3396	2938
			spatula	3383	-	3500	-	3389	3756	3290	3268	-	-

Tab.A4- 8: characteristic peak areas of hydrated cement pastes from powder XRD_hydration stage T6 & T8

pastes at T6	reference values unhyd.			area under the peak									
mineral phase	peak	ref.	s.d.	CP00.00	CP11.00	CP13.00	CP23.00	CP33.00	CP53.00	CP 00.11	CP00.13	CP 13.11	CP13.13
[-]	[°2T]	[Cts*2T]	[Cts*2T]	[Cts*2T]	[Cts*2T]	[Cts*2T]	[Cts*2T]	[Cts*2T]	[Cts*2T]	[Cts*2T]	[Cts*2T]	[Cts*2T]	[Cts*2T]
Ettringite	9,0	-	-	42	46	56	48	53	46	42	42	54	44
Monocarbonate	11,9	-	-	0	0	47	0	2	16	35	43	46	46
Ferrit	12,2	**37**	**9**	18	14	30	19	33	23	30	3	23	20
Ettringite	15,9	-	-	25	23	34	34	25	27	25	26	24	16
Portlandite	18,1	-	-	551	620	361	603	656	1319	827	542	224	338
Gypsum	20,7	-	-	34	28	22	29	26	37	10	4	17	26
C_3S	29,5	**330**	**31,1**	137	131	120	145	128	158	149	157	145	120
C_3S	30,1	**68**	**6,2**	25	32	33	32	21	36	31	28	34	33
C_3S; C_2S	32,2	**477**	**45,2**	182	175	164	168	185	146	98	177	146	183
C_3S; C_2S	32,6	**401**	**37,9**	149	156	175	173	130	123	155	123	163	142
Aluminate	33,3	**73**	**8**	24	39	32	45	45	35	27	27	36	34
Ferrite / Portlandite	33,9	**99**	**21**	335	151	119	166	201	171	131	151	162	122
C_3S	34,4	**281**	**39,7**	143	114	172	121	134	112	178	111	187	131
total area under the curve; range: 5°2T; 80°2T			blender	2481	2356	2214	-	-	-	-	2296	-	1969
			spatula	-	-	-	2471	2441	3053	-	-	-	-

pastes at T8	reference values unhyd.			area under the peak									
mineral phase	peak	ref.	s.d.	CP00.00	CP11.00	CP13.00	CP23.00	CP33.00	CP53.00	CP 00.11	CP00.13	CP 13.11	CP13.13
[-]	[°2T]	[Cts*2T]	[Cts*2T]	[Cts*2T]	[Cts*2T]	[Cts*2T]	[Cts*2T]	[Cts*2T]	[Cts*2T]	[Cts*2T]	[Cts*2T]	[Cts*2T]	[Cts*2T]
Ettringite	9,0	-	-	31	44	40	61	43	41	39	27	40	31
Monocarbonate	11,9	-	-	28	31	19	1	26	27	41	41	30	35
Ferrit	12,2	**37**	**9**	25	21	30	26	24	19	32	3	20	2
Ettringite	15,9	-	-	18	20	27	31	36	27	30	20	23	15
Portlandite	18,1	-	-	793	772	552	688	835	1492	573	756	382	303
Gypsum	20,7	-	-	26	9	6	26	31	40	5	6	3	3
C_3S	29,5	**330**	**31,1**	159	97	108	142	102	104	96	117	109	141
C_3S	30,1	**68**	**6,2**	27	26	29	24	2	24	34	32	31	37
C_3S; C_2S	32,2	**477**	**45,2**	151	101	131	127	107	121	154	113	140	169
C_3S; C_2S	32,6	**401**	**37,9**	110	103	92	107	94	73	121	110	121	168
Aluminate	33,3	**73**	**8**	25	20	2	27	22	17	34	24	32	22
Ferrite / Portlandite	33,9	**99**	**21**	369	145	150	223	215	169	167	251	149	93
C_3S	34,4	**281,00**	**39,7**	110	130	134	124	94	88	125	114	156	164
total area under the curve; range: 5°2T; 80°2T			blender	2970	2268	1994	-	-	-	-	2300	-	1991
			spatula	-	-	-	2503	2342	2985	-	-	-	-

Tab.A4- 9: Total organic carbon content of admixtures

carbon content of admixture		
adm.	[g_C/g]	comment
SRA1	0,62	product
SRA2	0,49	product
SRA3	0,56	product
SRA5	0,37	product
SP-PCE	0,5	solid content

Tab.A4- 10: Total organic carbon content of mixing water and extracted pore solutions

TOC raw data	hydration stages								
	initial	T1	T2	T3	T4	T5	T6	T7	T8
	carbon content of extracted pore solution [mg/l]								
CP00.00	11	145	156	88	112	81	95	102	233
CP11.00	6809	8168	8052	8615	9731	14560	18780	21480	24420
CP13.00	31190	31360	31730	34010	41900	51370	61420	73660	77900
CP23.00	24350	24030	23200	-	-	-	-	-	-
CP33.00	28240	21110	22910	-	-	-	-	-	-
CP53.00	19220	14400	13360	-	-	-	-	-	-
CP00.11	1700	1340	1387	1767	2305	3822	4125	4604	4971
CP00.13	7700	6155	5434	7790	10040	12700	16720	19250	19880
CP13.11	32890	32970	33620	35620	52610	56090	67920	75800	79030
CP13.13	38890	37830	40250	57900	64520	74960	76860	87450	91800

Tab.A4- 11: Calculated admixture concentration in extracted pore solution

hydration stage	initial	T1	T2	T3	T4	T5	T6	T7	T8
	concentration of admixture in extracted pore solution [g/l]								
CP00.00	-	-	-	-	-	-	-	-	-
CP11.00	12,5	12,8	12,6	13,6	15,3	23,1	29,8	34,1	38,6
CP13.00	50,0	49,8	50,4	54,1	66,6	81,8	97,8	117,3	123,9
CP23.00	50,0	49,0	47,3	-	-	-	-	-	-
CP 33.00	50,0	37,1	40,3	-	-	-	-	-	-
CP53.00	50,0	38,1	35,3	-	-	-	-	-	-
CP00.11	3,4	2,4	2,5	3,4	4,4	7,5	8,1	9,0	9,5
CP00.13	13,4	12,0	10,6	15,4	19,9	25,2	33,3	38,3	39,3
CP 13.__	50,0	50,2	51,1	54,0	79,4	81,4	101,7	113,6	119,1
CP__.11	3,4	2,4	2,5	3,2	5,2	9,7	8,0	8,8	7,9
CP 13.__	50,0	50,1	54,5	77,7	83,6	100,1	97,3	108,8	121,9
CP__.13	13,4	12,2	11,6	17,9	23,8	24,1	31,3	38,0	29,9

Tab.A4- 12: Calculated reduction of liquid phase due to hydration progress –relative amounts

hydration stage	initial	T1	T2	T3	T4	T5	T6	T7	T8
	reduction of liquid phase during hydration [m.-%]								
CP00.00	100%	92%	90%	78%	67%	51%	34%	33%	23%
CP11.00	100%	93%	91%	73%	64%	46%	34%	31%	22%
CP13.00	100%	92%	90%	71%	58%	44%	33%	28%	22%
CP23.00	100%	93%	91%	-	-	-	32%	-	22%
CP 33.00	100%	93%	91%	-	-	-	31%	-	19%
CP53.00	100%	94%	91%	-	-	-	33%	-	18%
CP00.11	100%	92%	90%	66%	54%	51%	31%	26%	23%
CP00.13	100%	89%	86%	57%	46%	38%	30%	27%	23%
CP13.11	100%	91%	88%	68%	46%	40%	31%	26%	27%
CP13.13	100%	88%	78%	49%	39%	39%	32%	27%	30%

Tab.A4- 13: Theoretical bulk concentration of admixture for assumed “zero” adsorption at the solid/liquid interface

hydration stage	initial	T1	T2	T3	T4	T5	T6	T7	T8
	theoretical amount of admixture for "zero" adsorption [g/l]								
CP00.00	-	-	-	-	-	-	-	-	-
CP11.00	12,5	13,5	13,7	17,2	19,5	27,4	36,8	39,9	57,7
CP13.00	50,0	54,2	55,3	70,5	85,6	112,9	150,8	175,4	226,8
CP23.00	50,0	53,8	54,9	-	-	-	154	-	224
CP 33.00	50,0	53,7	54,9	-	-	-	161	-	262
CP53.00	50,0	53,5	55,0	-	-	-	150	-	285
CP00.11	3,4	3,7	3,8	5,2	6,3	6,6	11,0	13,2	15,1
CP00.13	13,4	15,1	15,7	23,4	28,9	35,7	44,2	49,4	58,9
CP 13.__	50,0	54,9	56,6	73,2	109,8	126,2	160,8	190,2	184,9
CP__.11	3,4	3,7	3,9	5,0	7,5	8,6	10,9	12,9	12,6
CP 13.__	50,0	57,1	64,0	101,6	129,3	127,3	155,6	183,2	167,5
CP__.13	13,4	15,3	17,2	27,2	34,6	34,1	41,7	49,1	44,9

Tab.A4- 14: Loss of admixture in the course of hydration – absolute & relative amounts

hydration stage	initial	T1	T2	T3	T4	T5	T6	T7	T8
	[g/100g]	loss of admixture [g/100g unhydrated cement]							
CP00.00	0,00	-	-	-	-	-	-	-	-
CP11.00	0,50	0,03	0,04	0,10	0,11	0,08	0,09	0,07	0,17
CP13.00	2,00	0,16	0,18	0,47	0,44	0,55	0,70	0,66	0,91
CP23.00	2,00	0,18	0,28	-	-	-	-	-	-
CP 33.00	2,00	0,62	0,53	-	-	-	-	-	-
CP53.00	2,00	0,58	0,72	-	-	-	-	-	-
CP00.11	0,13	0,05	0,05	0,05	0,04	-0,02	0,04	0,04	0,05
CP00.13	0,54	0,11	0,17	0,18	0,17	0,16	0,13	0,12	0,18
CP 13.__	2,00	0,17	0,20	0,53	0,55	0,71	0,74	0,81	0,71
CP__.11	0,13	0,05	0,05	0,05	0,04	-0,02	0,04	0,04	0,05
CP 13.__	2,00	0,24	0,30	0,47	0,71	0,43	0,75	0,81	0,54
CP__.13	0,54	0,11	0,17	0,18	0,17	0,16	0,13	0,12	0,18

Tab.A4- 15: ICP OES – raw data from extracted pore solution

Ca 422.673	initial	10min	T1	T2	T3	T4	T5	T6	T7	T8
	[mmol/l]									
CP00.00	-	-	19,9	22,5	18,8	11,0	2,7	1,9	1,8	1,7
CP11.00	b.d.l.	-	19,4	21,2	17,4	10,9	2,6	1,8	1,6	1,4
CP13.00	b.d.l.	15,0	15,4	17,3	14,6	6,0	1,9	1,5	1,2	1,0
CP23.00	-	16,2	17,2	20,1	-	-	-	-	-	-
CP33.00	-	19,4	20,0	23,0	-	-	-	-	-	-
CP00.11	b.d.l.	-	21,8	25,1	10,6	4,2	2,2	1,9	1,7	1,5
CP00.13	b.d.l.	-	23,6	28,3	5,1	2,6	2,2	1,9	1,7	1,7
CP13.11	b.d.l.	-	15,8	18,7	13,2	2,0	1,9	1,4	1,2	1,3
CP13.13	b.d.l.	-	18,5	18,1	2,2	1,3	1,6	1,3	1,2	1,2

K 766.491	initial	10min	T1	T2	T3	T4	T5	T6	T7	T8
	[mmol/l]									
CP00.00	-	-	435	409	435	486	537	588	639	665
CP11.00	b.d.l.	-	384	409	409	486	537	563	614	665
CP13.00	b.d.l.	358	358	358	358	486	512	537	537	588
CP23.00	-	384	358	358	-	-	-	-	-	-
CP33.00	-	409	409	384	-	-	-	-	-	-
CP00.11	b.d.l.	-	409	435	486	512	588	614	639	716
CP00.13	b.d.l.	-	435	435	512	588	639	691	716	793
CP13.11	b.d.l.	-	358	358	384	537	537	537	563	588
CP13.13	b.d.l.	-	358	409	537	537	588	563	639	614

S 181.972	initial	10min	T1	T2	T3	T4	T5	T6	T7	T8
	[mmol/l]									
CP00.00	-	-	178	168	165	156	27	8	12	16
CP11.00	b.d.l.	-	171	159	159	165	34	9	10	15
CP13.00	b.d.l.	156	140	128	128	125	20	7	7	11
CP23.00	-	165	156	137	-	-	-	-	-	-
CP33.00	-	165	187	162	-	-	-	-	-	-
CP00.11	b.d.l.	-	187	171	153	72	10	9	11	14
CP00.13	b.d.l.	-	190	171	81	8	8	11	13	20
CP13.11	b.d.l.	-	147	125	128	16	12	6	7	11
CP13.13	b.d.l.	-	153	128	9	5	6	6	7	11

Na 589.592	initial	10min	T1	T2	T3	T4	T5	T6	T7	T8
	[mmol/l]									
CP00.00	-	-	39	43	48	52	65	70	78	83
CP11.00	b.d.l.	-	43	43	48	57	65	70	78	87
CP13.00	b.d.l.	48	48	48	52	57	57	61	65	74
CP23.00	-	48	48	48	-	-	-	-	-	-
CP33.00	-	48	57	61	-	-	-	-	-	-
CP00.11	1,7	-	48	48	61	65	74	78	83	91
CP00.13	8,7	-	65	65	78	83	91	104	113	130
CP13.11	1,7	-	52	52	61	65	65	65	70	78
CP13.13	8,7	-	70	74	83	78	83	83	91	87

OH-	initial	10min	T1	T2	T3	T4	T5	T6	T7	T8
	[mmol/l]									
CP00.00	-	-	146	189	158	212	451	591	568	588
CP11.00	-	-	152	182	140	223	483	592	610	610
CP13.00	-	-	157	182	190	292	569	668	632	684
CP23.00	-	-	-	-	-	-	-	-	-	-
CP33.00	-	-	-	-	-	-	-	-	-	-
CP00.11	-	-	146	182	204	404	569	546	661	607
CP00.13	-	-	146	189	364	555	616	661	739	736
CP13.11	-	-	152	203	182	616	616	634	686	631
CP13.13	-	-	146	243	639	642	754	754	827	765

* b.d.l. - **b**elow **d**etection **l**imit

Tab.A4- 16: Water activity of extracted pore solution (calculated from TOC measurement)

hydration stage	initial	T1	T2	T3	T4	T5	T6	T7	T8
	water activity in liquid phase [%]								
CP00.00	100%	100%	100%	100%	100%	100%	100%	100%	100%
CP11.00	99%	99%	99%	99%	98%	98%	97%	97%	96%
CP13.00	95%	95%	95%	95%	93%	92%	90%	88%	88%
CP23.00	95%	95%	95%	-	-	-	-	-	-
CP 33.00	95%	96%	96%	-	-	-	-	-	-
CP53.00	95%	96%	96%	-	-	-	-	-	-
CP00.11	100%	100%	100%	100%	100%	99%	99%	99%	99%
CP00.13	99%	99%	99%	98%	98%	97%	97%	96%	96%
CP13.11	95%	95%	95%	94%	92%	91%	89%	88%	87%
CP13.13	94%	94%	93%	90%	89%	88%	87%	85%	85%

Tab.A4- 17: Ionic content of pore solution adjusted for admixture content

Ca 422.673	hydration stages							
	T1	T2	T3	T4	T5	T6	T7	T8
	Calcium ion concentration adjusted for admixture [mmol/l]							
CP00.00	19,9	22,5	18,8	11,0	2,7	1,9	1,8	1,7
CP11.00	19,7	21,5	17,6	11,1	2,7	1,9	1,7	1,5
CP13.00	16,3	18,2	15,5	6,4	2,1	1,7	1,4	1,2
CP23.00	18,1	21,1	-	-	-	-	-	-
CP33.00	20,7	24,0	-	-	-	-	-	-
CP00.11	21,9	25,1	10,6	4,3	2,2	2,0	1,7	1,6
CP00.13	23,9	28,6	5,2	2,7	2,3	2,0	1,8	1,8
CP13.11	16,7	19,7	14,0	2,2	2,1	1,6	1,3	1,5
CP13.13	19,7	19,4	2,5	1,5	1,8	1,5	1,4	1,5
K 766.491	T1	T2	T3	T4	T5	T6	T7	T8
	Potassium ion concentration adjusted for admixture [mmol/l]							
CP00.00	435	409	435	486	537	588	639	665
CP11.00	389	414	415	494	550	580	635	692
CP13.00	377	377	379	521	557	595	608	671
CP23.00	377	376	-	-	-	-	-	-
CP33.00	425	400	-	-	-	-	-	-
CP00.11	410	436	488	514	593	619	645	723
CP00.13	440	439	520	600	656	714	745	825
CP13.11	378	378	407	587	591	603	641	674
CP13.13	382	438	594	602	672	646	749	724
S 181.972	T1	T2	T3	T4	T5	T6	T7	T8
	Sulphate ion concentration adjusted for admixture [mmol/l]							
CP00.00	178	168	165	156	27	8	12	16
CP11.00	174	161	161	168	35	10	10	15
CP13.00	148	135	135	134	21	8	8	12
CP23.00	164	144	-	-	-	-	-	-
CP33.00	194	169	-	-	-	-	-	-
CP00.11	188	172	153	72	10	9	11	14
CP00.13	193	173	82	8	8	11	14	20
CP13.11	155	132	136	17	13	7	7	12
CP13.13	163	137	10	6	7	7	9	12
Na 589.592	T1	T2	T3	T4	T5	T6	T7	T8
	Sodium ion concentration adjusted for admixture [mmol/l]							
CP00.00	39	43	48	52	65	70	78	83
CP11.00	44	44	49	57	67	72	81	90
CP13.00	50	50	55	61	62	67	74	84
CP23.00	50	50	-	-	-	-	-	-
CP33.00	59	63	-	-	-	-	-	-
CP00.11	48	48	61	66	75	79	83	92
CP00.13	66	66	80	84	94	108	118	136
CP13.11	55	55	65	71	72	73	79	90
CP13.13	74	79	91	88	94	95	107	103
OH^-	T1	T2	T3	T4	T5	T6	T7	T8
	Hydroxy ion content adjusted for admixture content [mmol/l]							
CP00.00	146	189	158	212	451	591	568	588
CP11.00	154	184	142	227	495	610	631	635
CP13.00	166	191	201	313	620	741	715	780
CP23.00	-	-	-	-	-	-	-	-
CP33.00	-	-	-	-	-	-	-	-
CP00.11	147	182	205	406	574	550	667	613
CP00.13	148	191	369	567	632	684	769	766
CP13.11	160	214	193	673	678	712	782	723
CP13.13	156	260	707	719	861	866	969	901

* b.d.l. - **b**elow **d**etection **l**imit

Tab.A4- 18: Changes in content of the main ion species in the course of hydration

Ca 422.673	hydration stages							
	T1	T2	T3	T4	T5	T6	T7	T8
	Changes in Calcium ion concentration [%]							
CP00.00	0%	0%	0%	0%	0%	0%	0%	0%
CP11.00	-1%	-4%	-6%	1%	1%	0%	-5%	-13%
CP13.00	-18%	-19%	-18%	-42%	-22%	-10%	-21%	-30%
CP23.00	-9%	-6%	-	-	-	-	-	-
CP33.00	4%	7%	-	-	-	-	-	-
CP00.11	10%	12%	-44%	-61%	-17%	5%	-5%	-8%
CP00.13	20%	27%	-72%	-76%	-15%	6%	0%	4%
CP13.11	**-24%**	**-21%**	**32%**	**-48%**	**-6%**	**-17%**	**-22%**	**-5%**
CP13.13	**-17%**	**-32%**	**-53%**	**-46%**	**-20%**	**-22%**	**-23%**	**-17%**

K 766.491	T1	T2	T3	T4	T5	T6	T7	T8
	Changes in Potassium ion concentration [%]							
CP00.00	0%	0%	0%	0%	0%	0%	0%	0%
CP11.00	-11%	1%	-5%	2%	2%	-1%	-1%	4%
CP13.00	-13%	-8%	-13%	7%	4%	1%	-5%	1%
CP23.00	-13%	-8%	-	-	-	-	-	-
CP33.00	-2%	-2%	-	-	-	-	-	-
CP00.11	-6%	7%	12%	6%	10%	5%	1%	9%
CP00.13	1%	7%	19%	24%	22%	21%	16%	24%
CP13.11	**-8%**	**-13%**	**-17%**	**14%**	**0%**	**-3%**	**-1%**	**-7%**
CP13.13	**-13%**	**0%**	**14%**	**0%**	**2%**	**-10%**	**1%**	**-12%**

S 181.972	T1	T2	T3	T4	T5	T6	T7	T8
	Changes in Sulphate ion concentration [%]							
CP00.00	0%	0%	0%	0%	0%	0%	0%	0%
CP11.00	-2%	-4%	-2%	8%	31%	19%	-16%	-4%
CP13.00	-17%	-20%	-18%	-14%	-20%	-2%	-31%	-22%
CP23.00	-8%	-14%	-	-	-	-	-	-
CP33.00	9%	0%	-	-	-	-	-	-
CP00.11	6%	2%	-7%	-54%	-63%	16%	-7%	-9%
CP00.13	8%	3%	-50%	-95%	-70%	39%	15%	29%
CP13.11	**-18%**	**-23%**	**-12%**	**-76%**	**26%**	**-29%**	**-32%**	**-16%**
CP13.13	**-15%**	**-21%**	**-87%**	**-30%**	**-15%**	**-37%**	**-36%**	**-39%**

Na 589.592	T1	T2	T3	T4	T5	T6	T7	T8
	Changes in Sodium ion concentration [%]							
CP00.00	0%	0%	0%	0%	0%	0%	0%	0%
CP11.00	13%	1%	1%	10%	2%	3%	4%	9%
CP13.00	29%	16%	15%	16%	-6%	-3%	-6%	2%
CP23.00	29%	15%	-	-	-	-	-	-
CP33.00	50%	46%	-	-	-	-	-	-
CP00.11	23%	10%	28%	26%	14%	13%	7%	12%
CP00.13	69%	52%	66%	62%	44%	55%	50%	64%
CP13.11	**15%**	**15%**	**6%**	**9%**	**-4%**	**-7%**	**-5%**	**-3%**
CP13.13	**12%**	**20%**	**15%**	**4%**	**1%**	**-12%**	**-9%**	**-24%**

OH^-	T1	T2	T3	T4	T5	T6	T7	T8
	Changes in Hydroxy ion content [%]							
CP00.00	0%	0%	0%	0%	0%	0%	0%	0%
CP11.00	5%	-2%	-10%	7%	10%	3%	11%	8%
CP13.00	13%	2%	27%	48%	37%	25%	26%	33%
CP23.00	-	-	-	-	-	-	-	-
CP33.00	-	-	-	-	-	-	-	-
CP00.11	0%	-3%	30%	92%	27%	-7%	17%	4%
CP00.13	1%	1%	134%	167%	40%	16%	35%	30%
CP13.11	**9%**	**17%**	**-6%**	**66%**	**18%**	**29%**	**17%**	**18%**
CP13.13	**6%**	**43%**	**245%**	**77%**	**50%**	**57%**	**45%**	**47%**

*** grey boxes: values related to the pastes with the referring SP-PCE dosage (SP-PCE only)**

Tab.A4- 19: Evaluation of the C_3S conversion after 14 days of hydration

Evaluation of C3S hydration / degree of hydration			C_3S_C0 plain paste	C_3S_C1 C_{SRA}=3,2g/l =10mg/g	C_3S_C2 C_{SRA}=6,4g/l =19mg/g	C_3S_C3 C_{SRA}=16g/l =48mg/g	C_3S_C4 C_{SRA}=32g/l =96mg/g	C_3S_C5 C_{SRA}=64g/l =192mg/g	C_3S_C6 C_{SRA}=128g/l =384mg/g
phase composition before TGA measurement	unhydrated C_3S	[%]	39,0	23,9	27,1	45,0	44,2	52,7	67,6
	C-S-H	[%]	38,0	48,6	46,1	33,8	33,3	27,0	18,0
	Portlandite*	[%]	**19,7**	**25,2**	**23,9**	**17,5**	**17,3**	**14,0**	**9,3**
	phys. bound water**	[%]	3,4	2,2	2,9	3,8	5,1	6,2	5,1
	sum	[%]	100,0	100,0	100,0	100,0	100,0	100,0	100,0
assumed degree of hydration		[%]	**54%**	**71%**	**67%**	**48%**	**48%**	**38%**	**24%**
phase composition referring to initial amount of 100g C_3S	unhydrated C_3S	[g]	46,0	29,0	32,8	52,5	52,4	61,8	75,7
	C-S-H	[g]	44,8	58,9	55,8	39,4	39,5	31,7	20,2
	Portlandite	[g]	23,2	30,5	28,9	20,4	20,5	16,4	10,4
	phys. bound water**	[g]	4,00	2,70	3,50	4,40	6,10	7,30	5,70
	sum	[g]	118,0	121,2	121,0	116,8	118,5	117,2	112,0
composition of dehydrated phases/ residue at 980°C	unhydrated C_3S	[%]	39,0	23,9	27,1	45,0	44,2	52,7	67,6
	C-S-H	[%]	30,5	39,1	37,0	27,1	26,8	21,7	14,5
	Portlandite	[%]	14,9	19,0	18,1	13,2	13,1	10,6	7,1
	calculated residue	[%]	84,3	82,0	82,2	85,3	84,1	85,0	89,1
	measured residue*	[%]	**84,3**	**82,0**	**82,2**	**85,3**	**84,1**	**85,0**	**89,1**

* obtained from TGA

** calculated to maintain balance between measured and calculated values for a) Portlandite content; b) residue at 980°C

A4.2 Figures

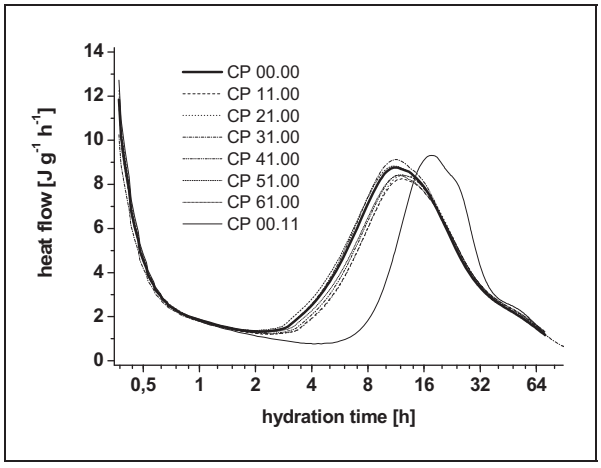

Fig.A4- 1:Heat flow of CEM I paste with low dosage of different SRA and SP-PCE; C_{SRA}=0.5wt.-% of cement

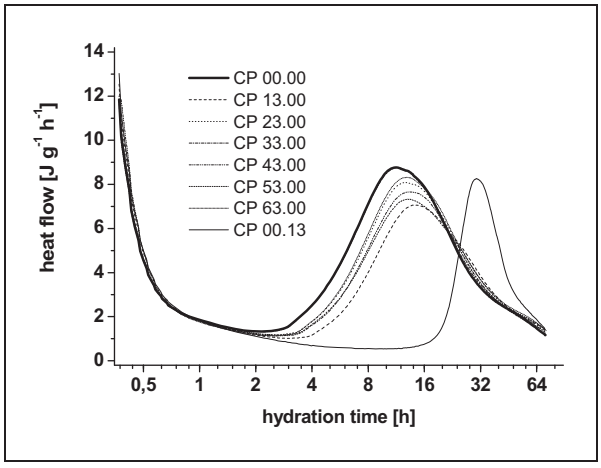

Fig.A4- 2: Heat flow of CEM I paste with high dosage of different SRA and SP-PCE; C_{SRA}=2wt.-% of cement

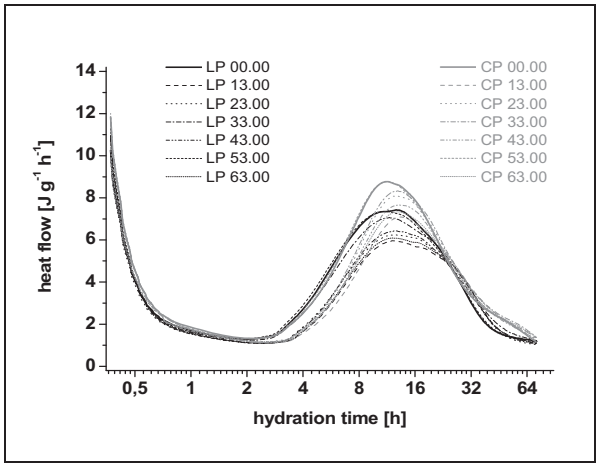

Fig.A4- 3: Heat flow of CEM I & CEM II A-L paste with high dosage of different SRA; C_{SRA}=2wt.-% of binder

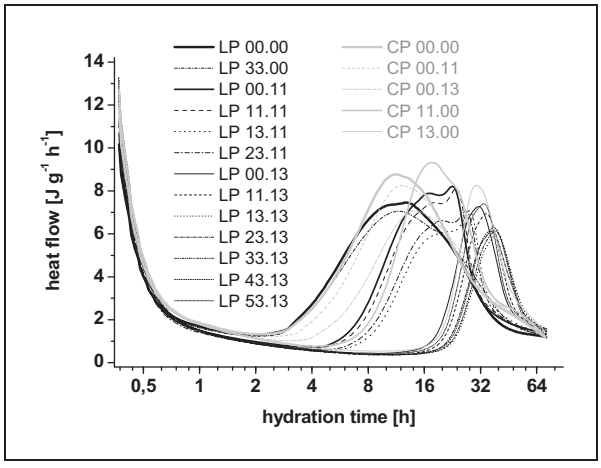

Fig.A4- 4: Heat flow of CEM I & CEM II A-L paste with different admixture combinations

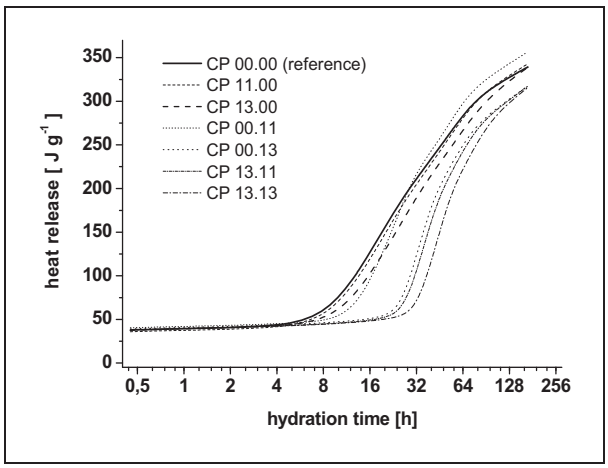

Fig.A4- 5: Heat release of CEM I cement paste with different dosages and combinations of SRA1 and SP-PCE

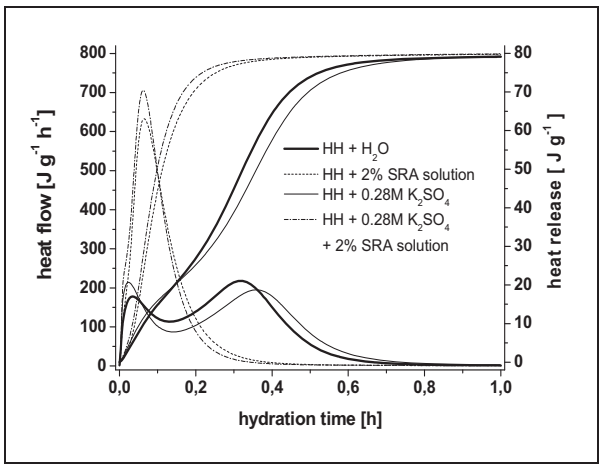

Fig.A4- 6: Heat flow and heat release of hemihydrat hydrating in the presence of water, potassium sulphate solution or/and SRA1

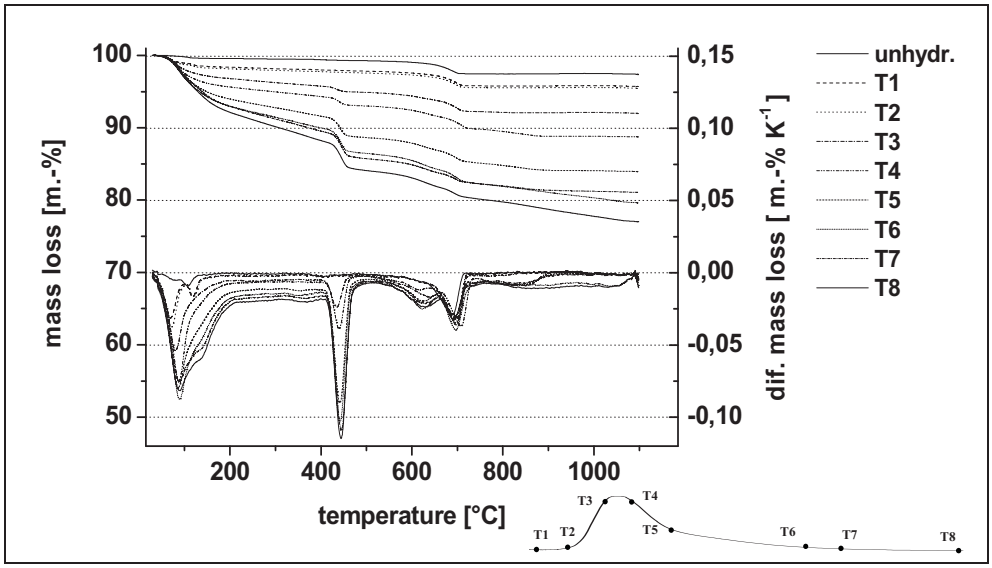

Fig.A4- 7: Thermo analysis of CP 00.00

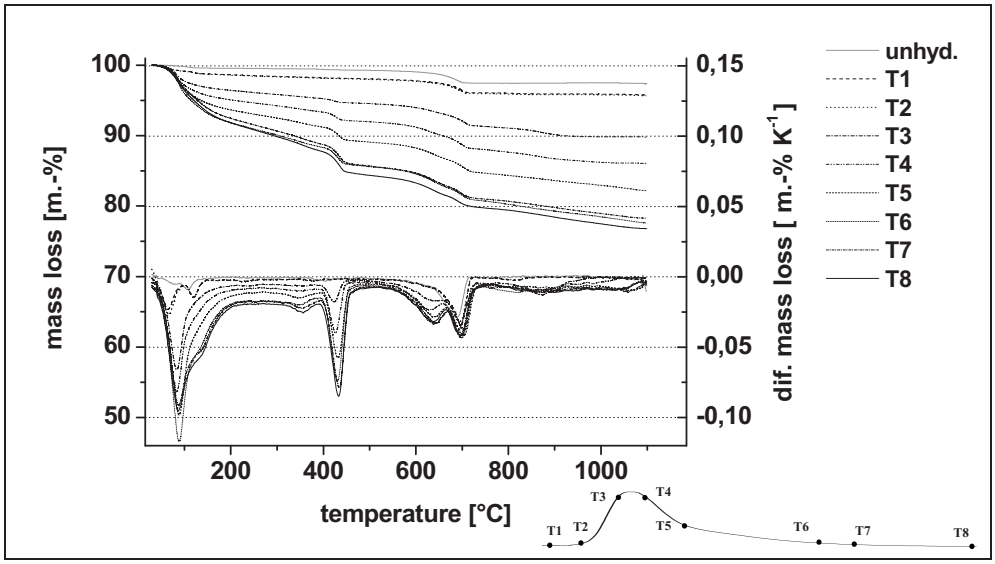

Fig.A4- 8: Thermo analysis of CP 13.00

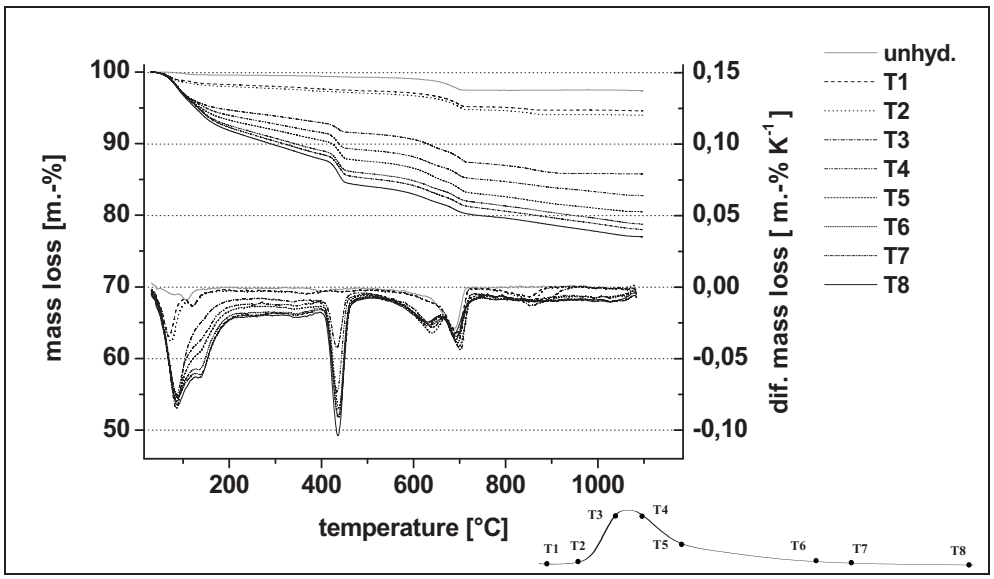

Fig.A4- 9:
Thermo analysis
of CP 00.13

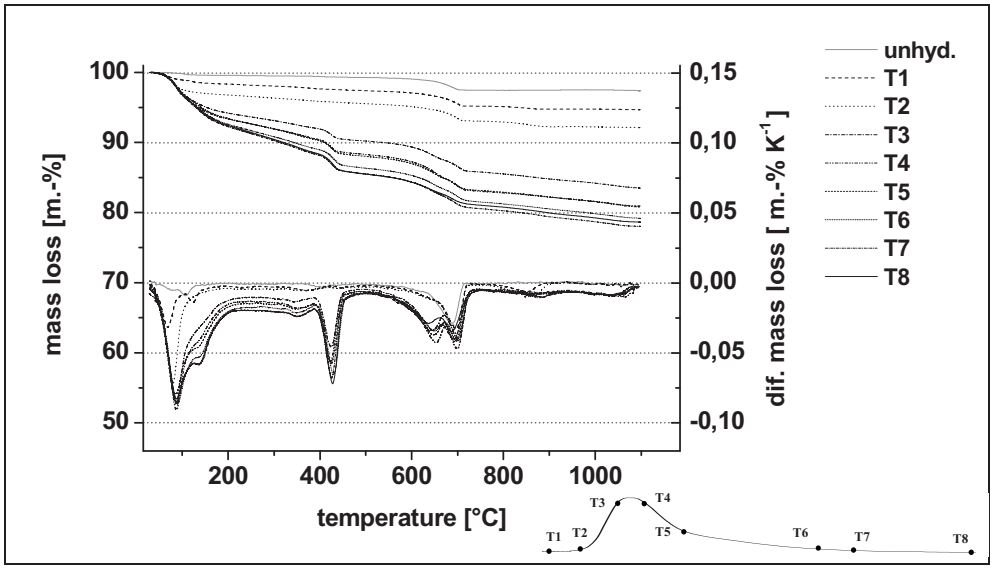

Fig.A4- 10:
Thermo analysis
of CP 13.13

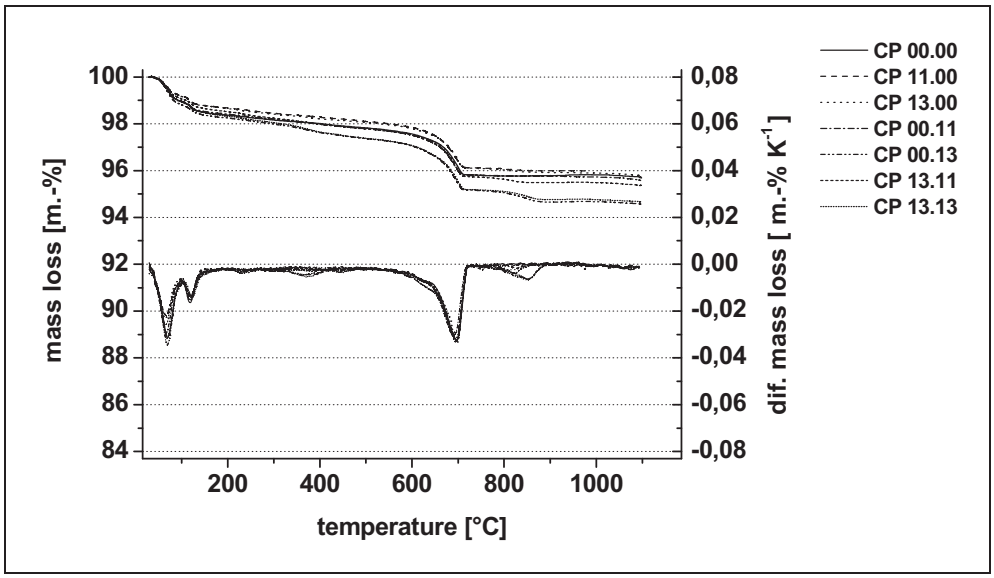

Fig.A4- 11:
Thermo analysis
of pastes for one
hydrated (T1)

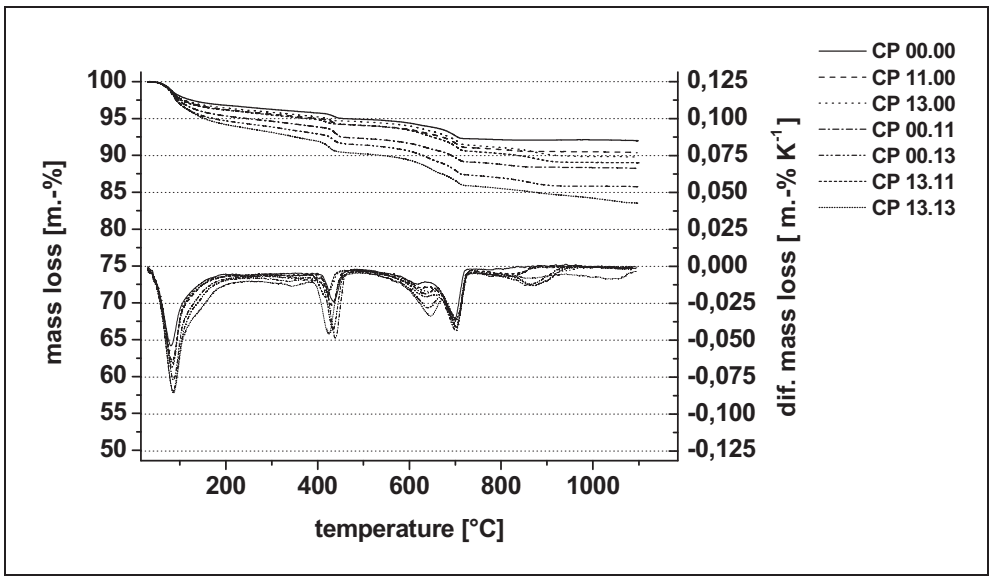

Fig.A4- 12: Thermo analysis of pastes before main heat release (T3)

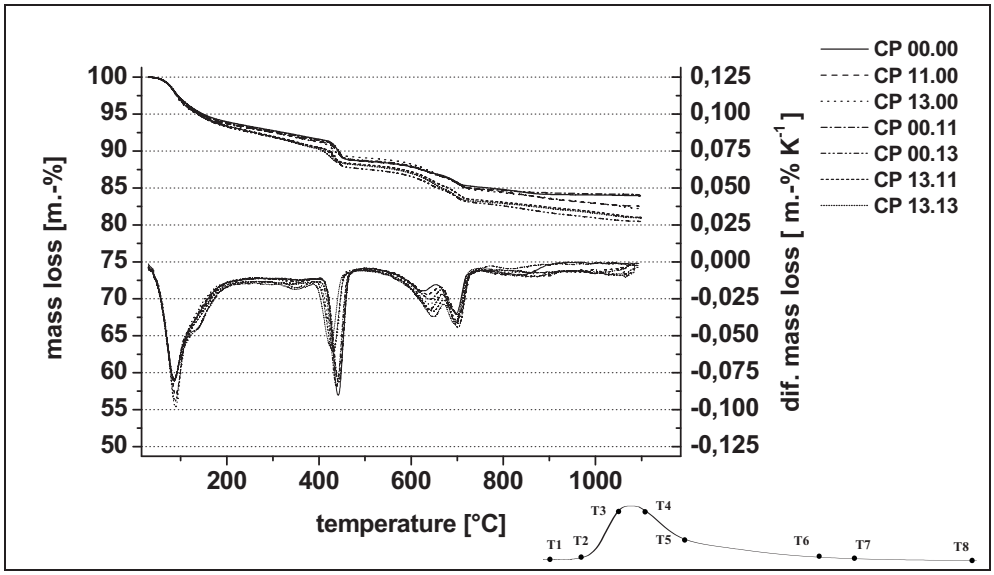

Fig.A4- 13: Thermo analysis of pastes at the end of the deceleration period (T5)

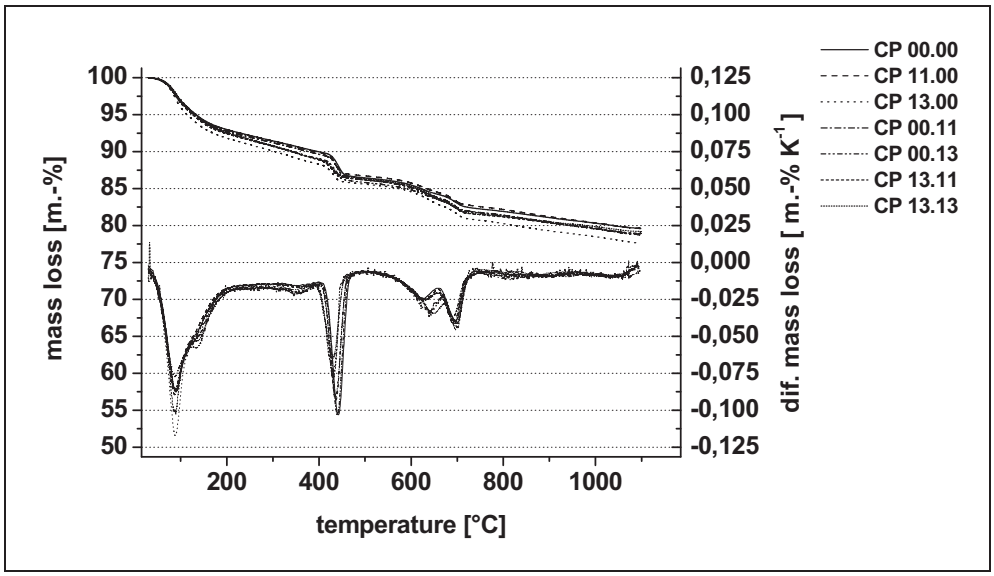

Fig.A4- 14: Thermo analysis of pastes at the beginning of the final period (T6)

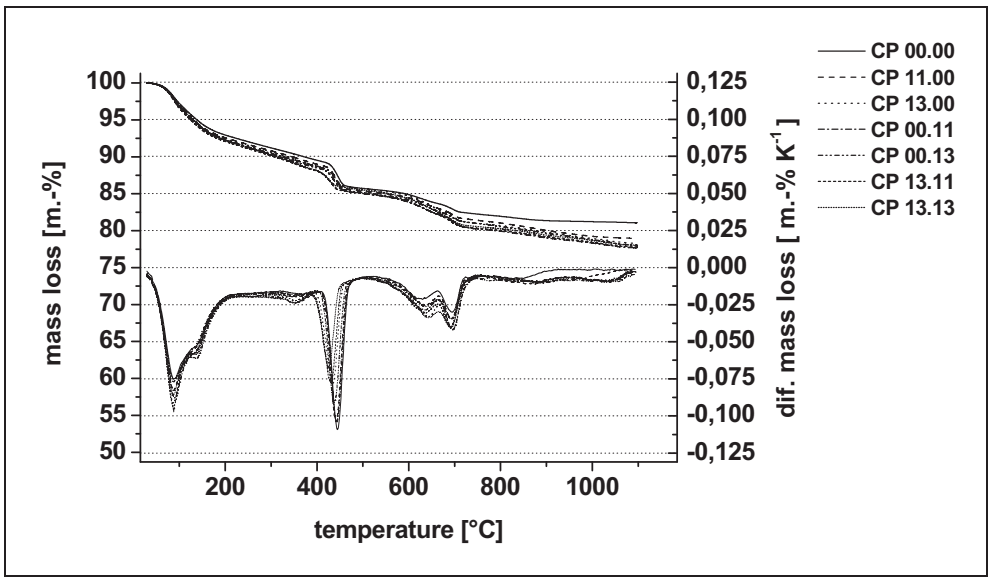

Fig.A4- 15: Thermo analysis of pastes after 7 days of hydration (T7)

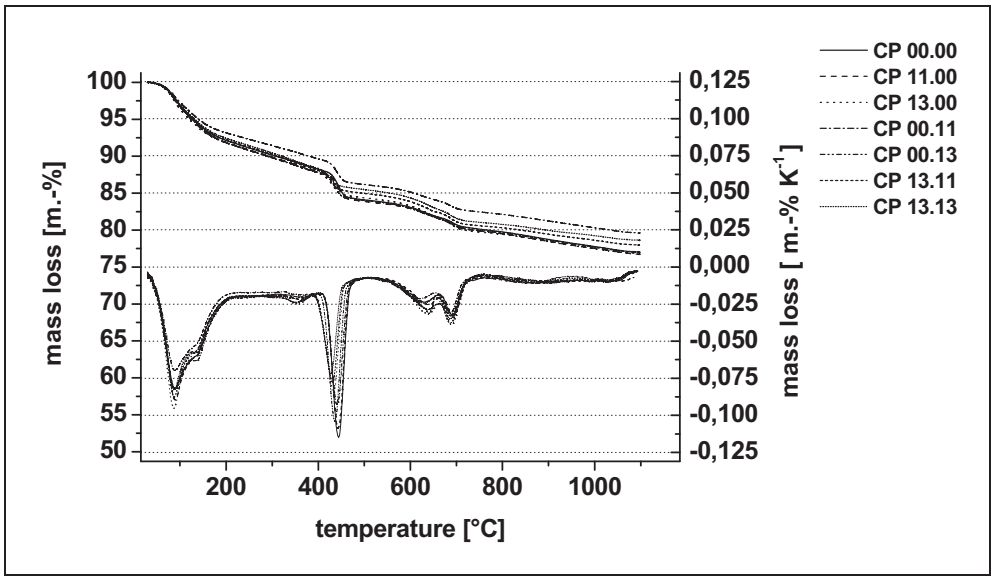

Fig.A4- 16: Thermo analysis of pastes after 28 days of hydration (T8)

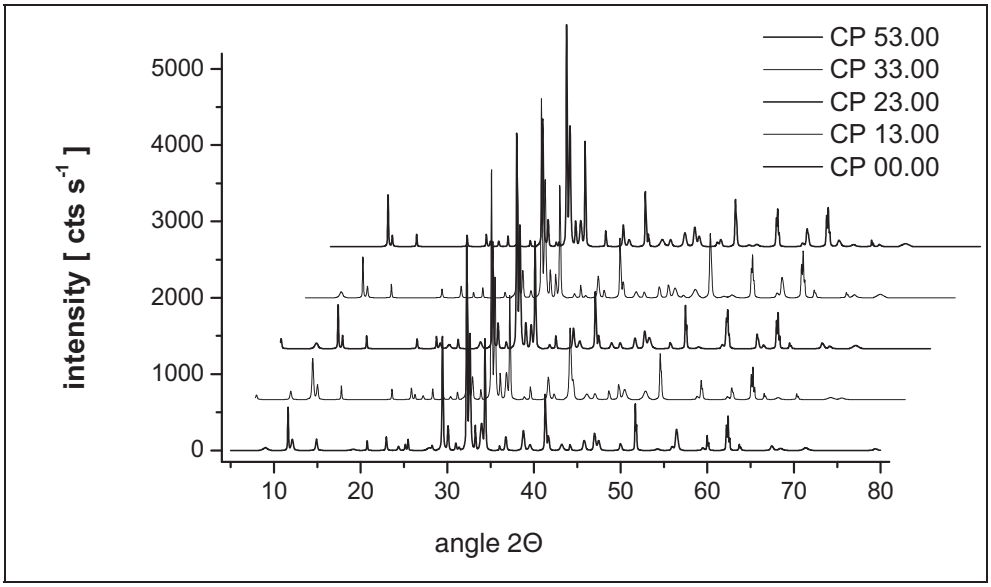

Fig.A4- 17: Diffracto grams of pastes hydrated for 10min

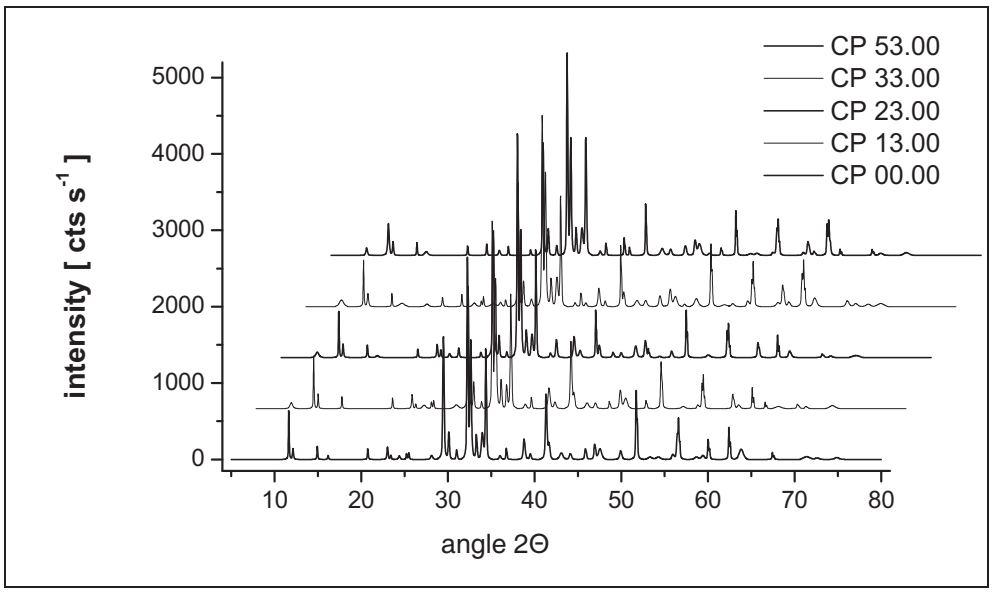

Fig.A4- 18: X-ray diffractograms for pastes at hydration stage T1

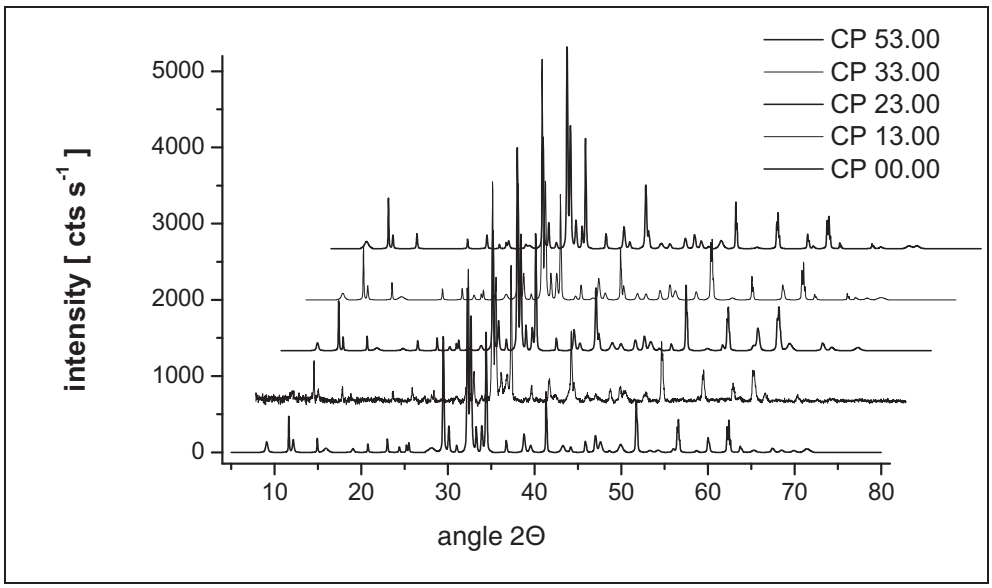

Fig.A4- 19: X-ray diffractograms of paste at hydration stage T2

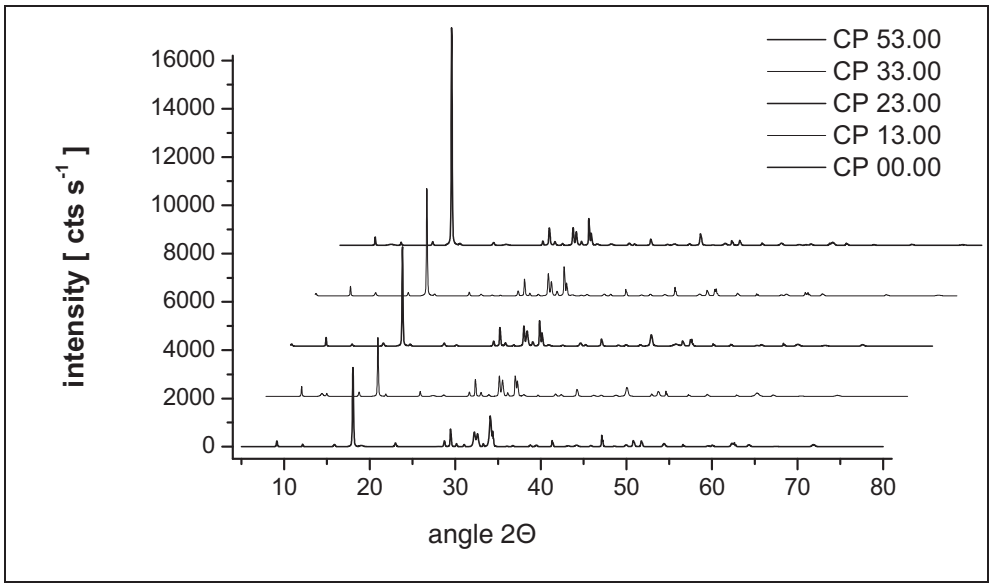

Fig.A4- 20: X-ray diffractograms of paste at hydration stage T6

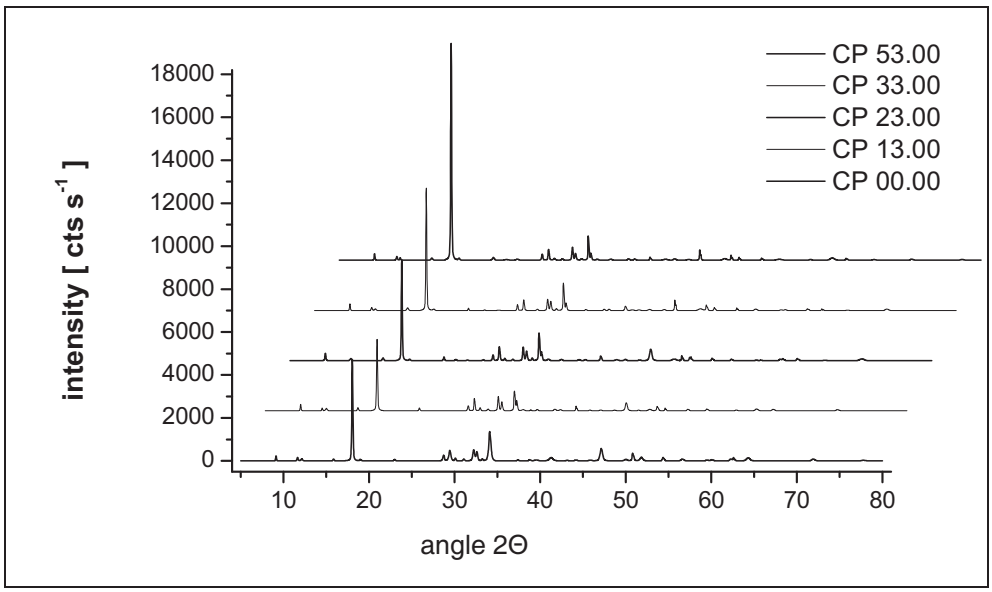

Fig.A4- 21: X-ray diffractograms of paste at hydration stage T8

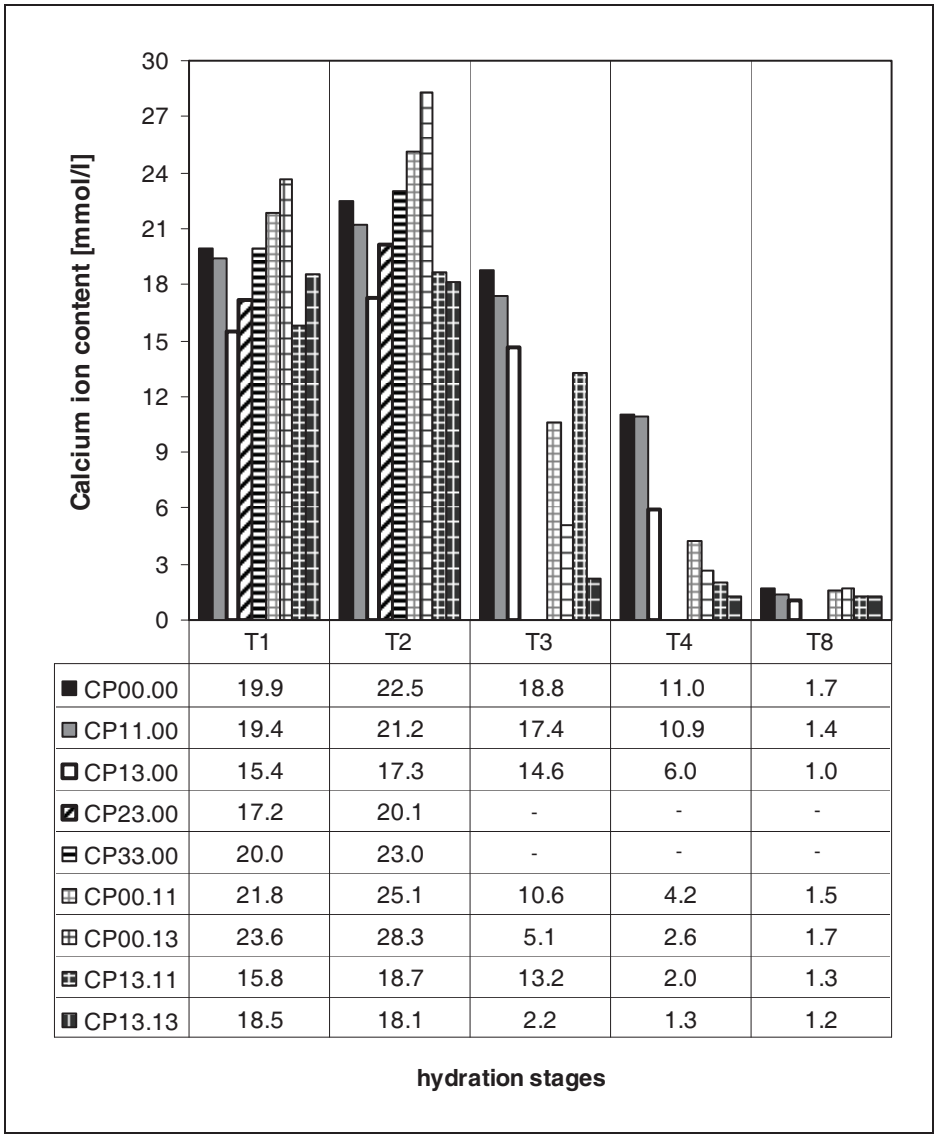

	T1	T2	T3	T4	T8
CP00.00	19.9	22.5	18.8	11.0	1.7
CP11.00	19.4	21.2	17.4	10.9	1.4
CP13.00	15.4	17.3	14.6	6.0	1.0
CP23.00	17.2	20.1	-	-	-
CP33.00	20.0	23.0	-	-	-
CP00.11	21.8	25.1	10.6	4.2	1.5
CP00.13	23.6	28.3	5.1	2.6	1.7
CP13.11	15.8	18.7	13.2	2.0	1.3
CP13.13	18.5	18.1	2.2	1.3	1.2

Fig.A4- 22: Calcium ion concentration of extracted pore solution

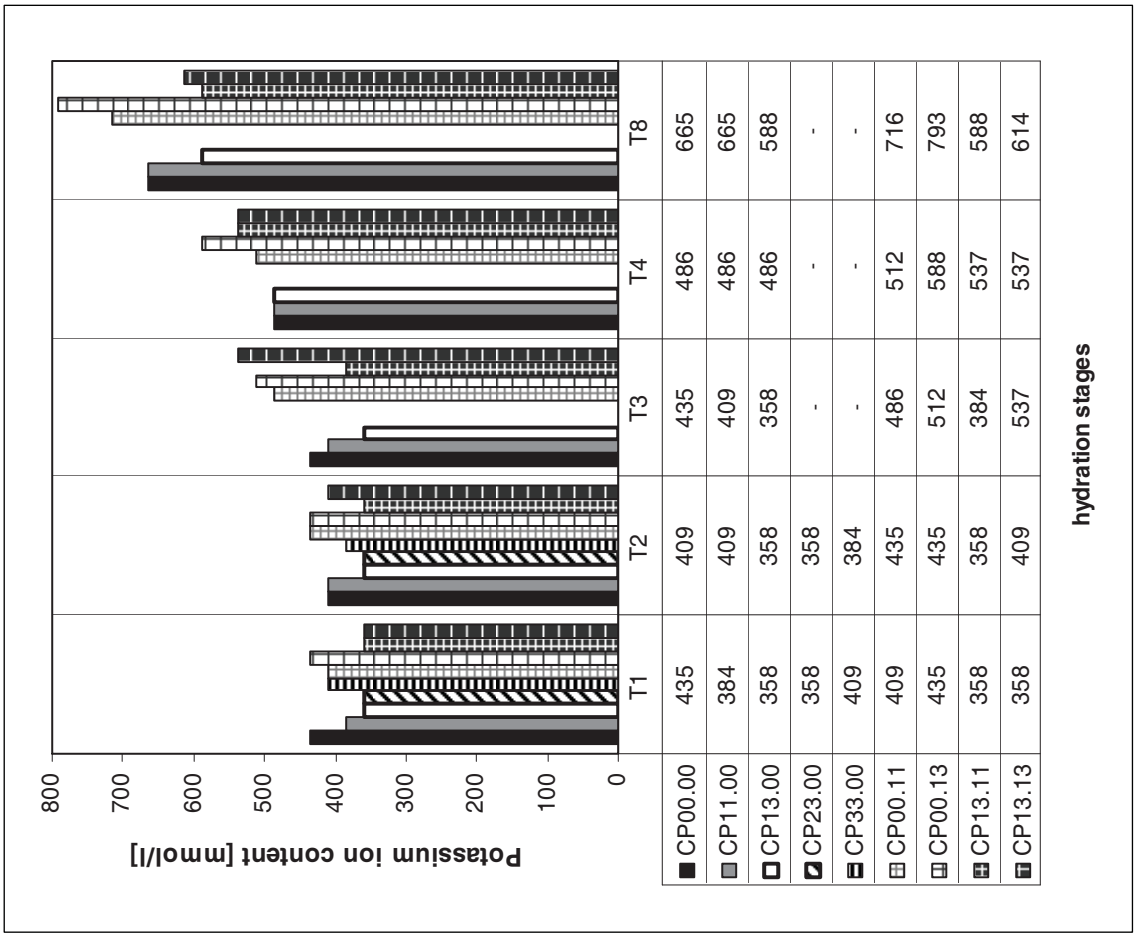

Fig.A4- 23: Potassium ion concentration of extracted pore solution

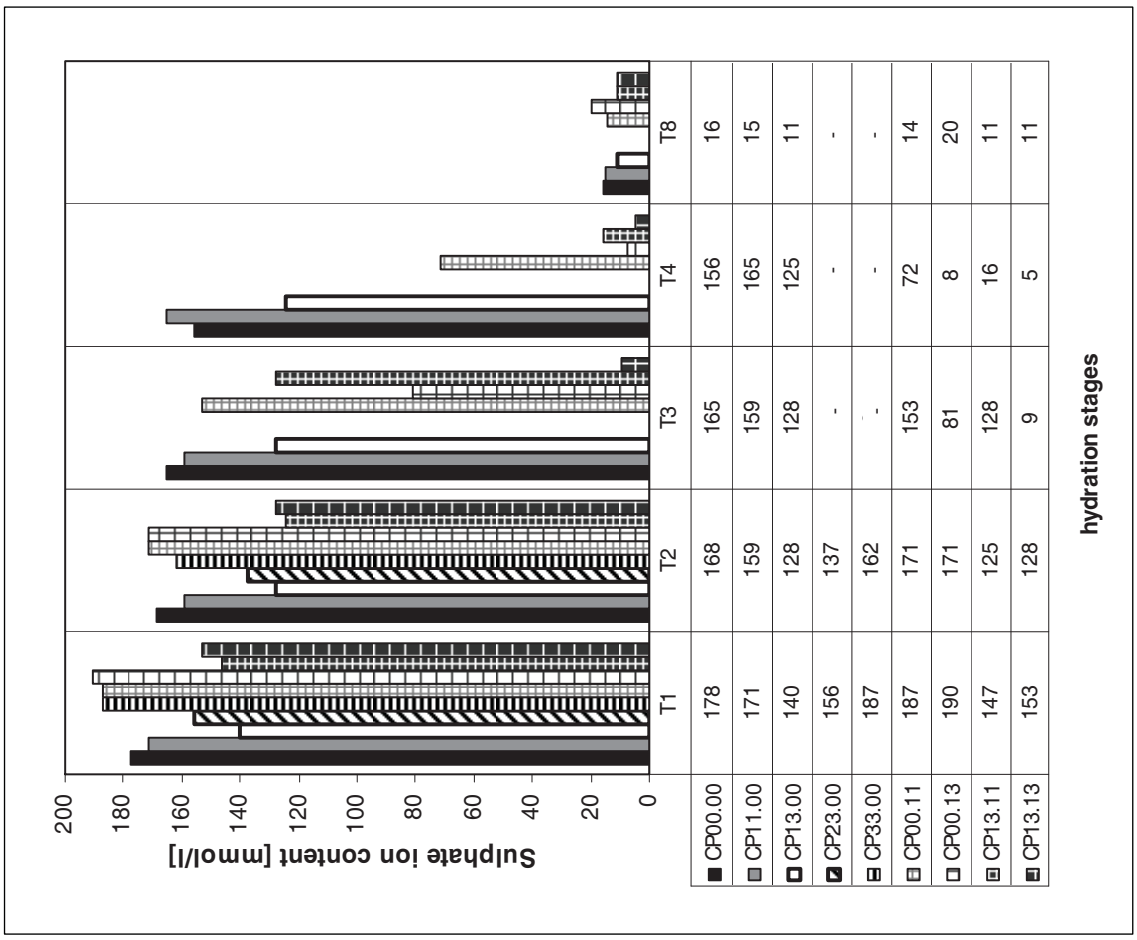

Fig.A4- 24: Sulphate ion concentration of extracted pore solution

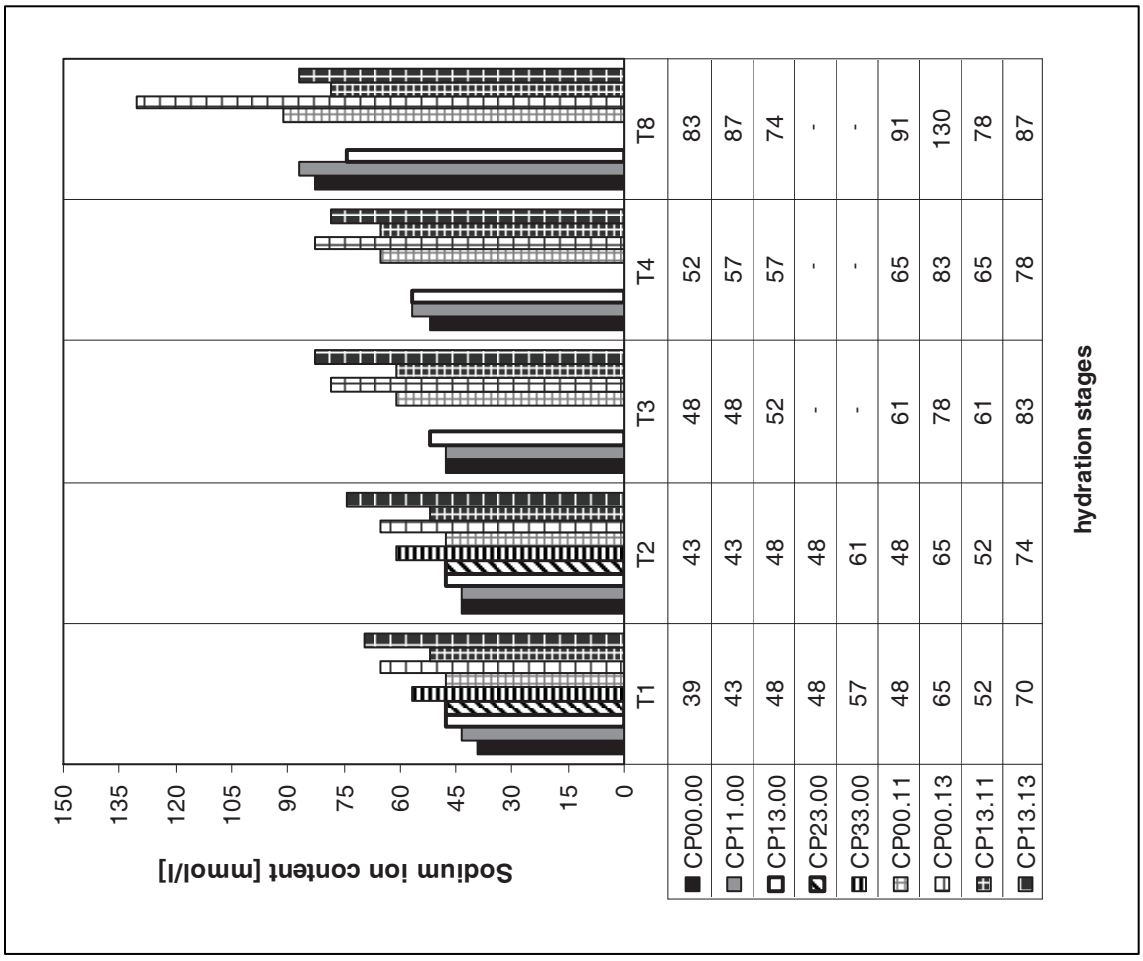

Fig.A4- 25: Sodium ion concentration of extracted pore solution

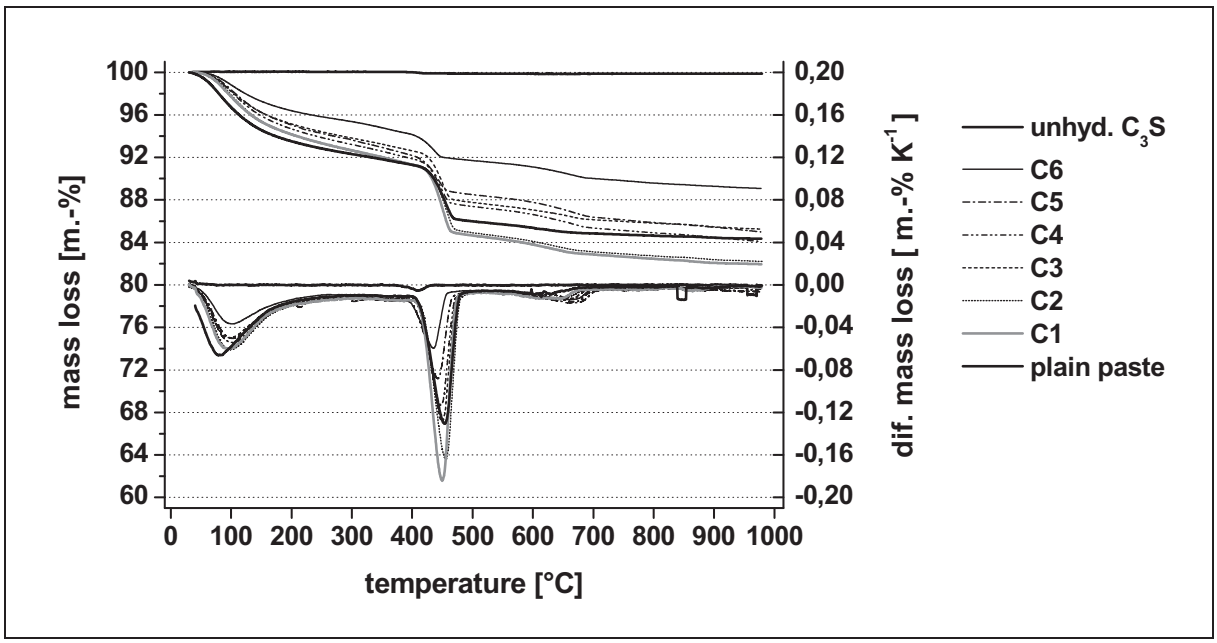

Fig.A4- 26: TGA curves of SRA1 modified C_3S pastes after 14 days of hydration

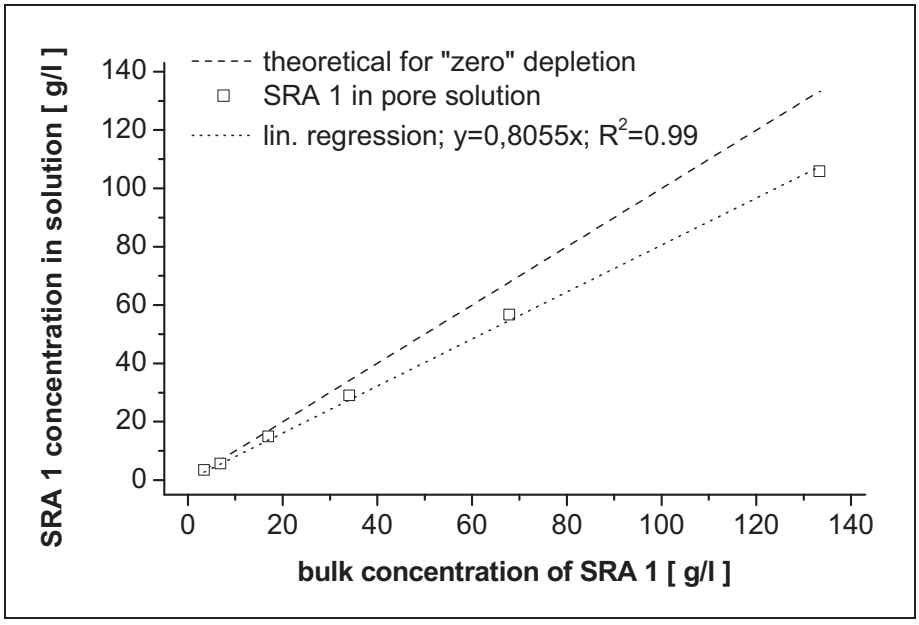

Fig.A4- 27: Depletion of SRA1 from bulk solution of dilute C_3S-suspensions

A5 - Microstructure of cement paste and mortar

A5.1 Tables

Tab.A5- 1: Porosity of paste samples after wet curing for one year

paste		water sorption	gel pores		capillary pores		total pores	
			avg	sd	avg	sd	avg	sd
		[m.-%]	[vol.-%]	[vol.-%]	[vol.-%]	[vol.-%]	[vol.-%]	[vol.-%]
ref.	CP 00.00	1,2%	**23,2%**	0,0%	**15,0%**	0,2%	**38,2%**	0,2%
SRA 1	CP 11.00	1,2%	**24,2%**	0,2%	**13,3%**	0,3%	**37,4%**	0,2%
	CP 12.00	1,3%	**24,7%**	0,2%	**12,5%**	0,3%	**37,2%**	0,5%
	CP 13.00	1,8%	**25,6%**	0,2%	**11,4%**	0,2%	**37,0%**	0,4%
SRA 2	CP 21.00	0,4%	**23,6%**	0,2%	**14,2%**	0,2%	**37,8%**	0,1%
	CP 22.00	1,3%	**24,3%**	0,2%	**14,0%**	0,2%	**38,3%**	0,2%
	CP 23.00	1,7%	**25,5%**	0,2%	**12,4%**	0,3%	**37,9%**	0,1%
SRA 3	CP 31.00	1,0%	**25,9%**	0,3%	**11,5%**	0,0%	**37,4%**	0,3%
	CP 32.00	1,1%	**26,5%**	0,2%	**10,5%**	0,1%	**37,0%**	0,1%
	CP 33.00	1,5%	**26,7%**	0,1%	**9,6%**	0,2%	**36,3%**	0,1%
SRA 5	CP 51.00	1,5%	**26,3%**	0,2%	**11,4%**	0,0%	**37,6%**	0,2%
	CP 52.00	1,8%	**26,1%**	0,1%	**10,6%**	0,2%	**36,7%**	0,2%
	CP 53.00	2,3%	**26,8%**	0,2%	**10,1%**	0,1%	**37,0%**	0,2%

* capillary pores from evaporable water content; ovendrying of saturated samples at 50°C

** gel porosity from non-evaporable water content; mass loss between 50°C and 110°C ovendrying

Tab.A5- 2: Porosity of mortar samples after wet curing for 273 days

mortar		water sorption	gel pores		capillary pores		total pores	
			avg	sd	avg	sd	avg	sd
		[m.-%]	[vol.-%]	[vol.-%]	[vol.-%]	[vol.-%]	[vol.-%]	[vol.-%]
ref.	CM 00	1,8%	**11,4%**	0,1%	**7,0%**	0,3%	**18,5%**	0,2%
SRA1	CM 12	1,9%	**12,2%**	0,1%	**6,7%**	0,1%	**18,8%**	0,1%
	CM 13	2,1%	**12,4%**	0,1%	**6,2%**	0,5%	**18,6%**	0,4%
ref.	LM 00	1,4%	**9,7%**	0,2%	**9,9%**	0,3%	**19,7%**	0,3%
SRA1	LM 12	1,7%	**11,2%**	0,1%	**9,3%**	0,1%	**20,6%**	0,1%
	LM 13	1,6%	**11,8%**	0,1%	**8,4%**	0,3%	**20,2%**	0,3%
ref.	SM 00	0,5%	**9,0%**	0,2%	**8,7%**	0,2%	**17,7%**	0,3%
SRA1	SM 13	1,4%	**11,2%**	0,1%	**8,2%**	0,2%	**19,4%**	0,1%

* capillary pores from evaporable water content; ovendrying of saturated samples at 50°C

** gel porosity from non-evaporable water content; mass loss between 50°C and 110°C ovendrying

A5.2 Figures

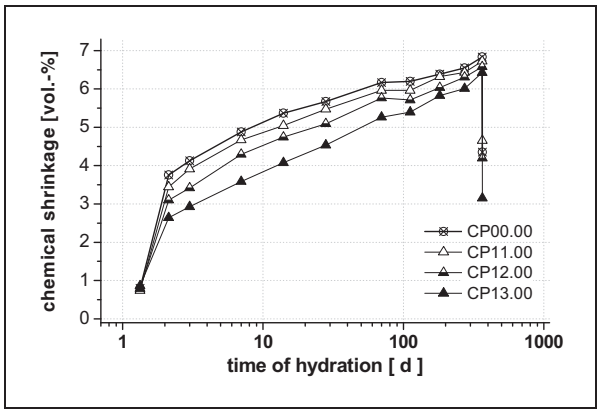

Fig.A5- 1: Chemical shrinkage of paste series containing SRA1

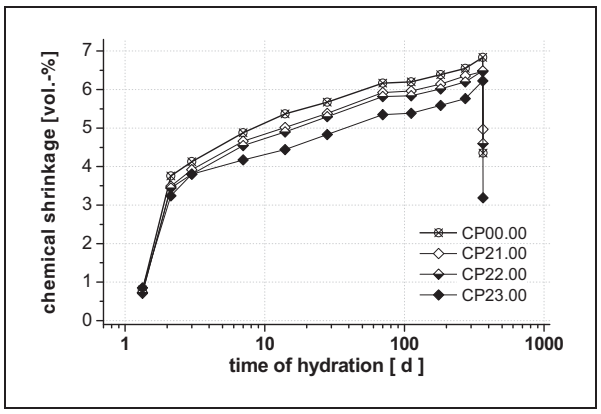

Fig.A5- 2: Chemical shrinkage of paste series containing SRA2

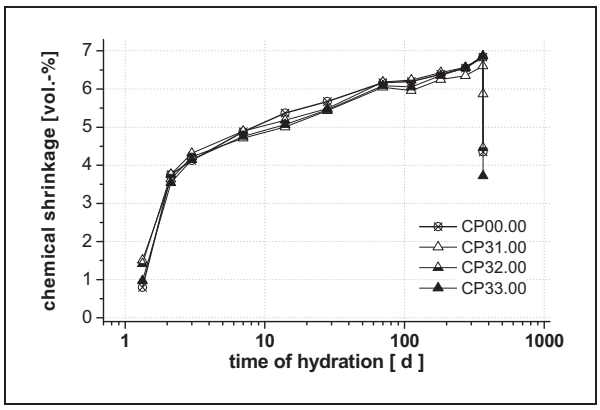

Fig.A5- 3: Chemical shrinkage of paste series containing SRA3

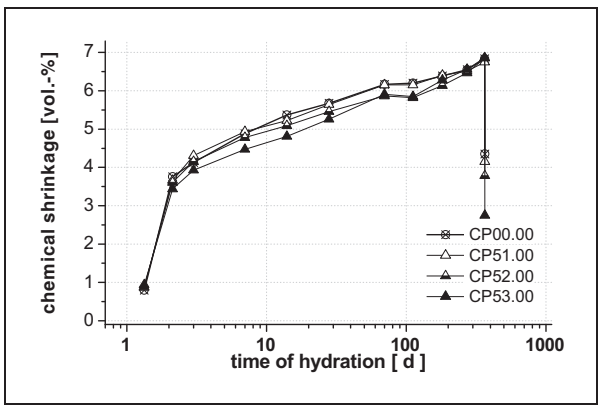

Fig.A5- 4: Chemical shrinkage of paste series containing SRA5

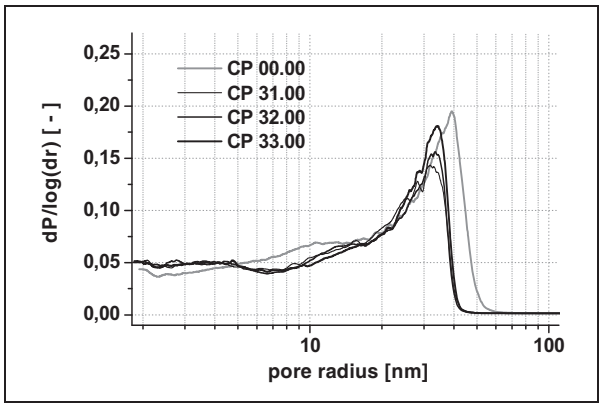

Fig.A5- 5: Mercury intrusion porosimetry of cement paste with increasing amount of SRA3

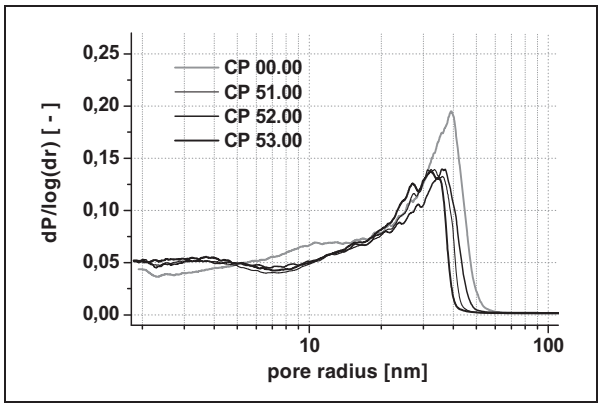

Fig.A5- 6: Mercury intrusion porosimetry of cement paste with increasing amount of SRA5

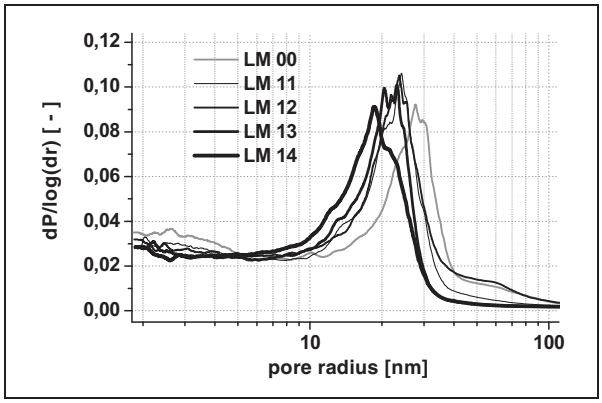

Fig.A5- 7: Mercury intrusion porosimetry of mortar series LM (lime stone composite binder; with increasing amount of SRA1)

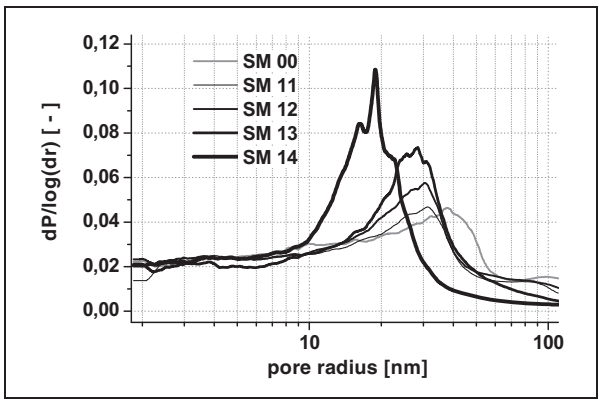

Fig.A5- 8: Mercury intrusion porosimetry of mortar series SM (standard mortar acc. EN 196; with increasing amount of SRA1)

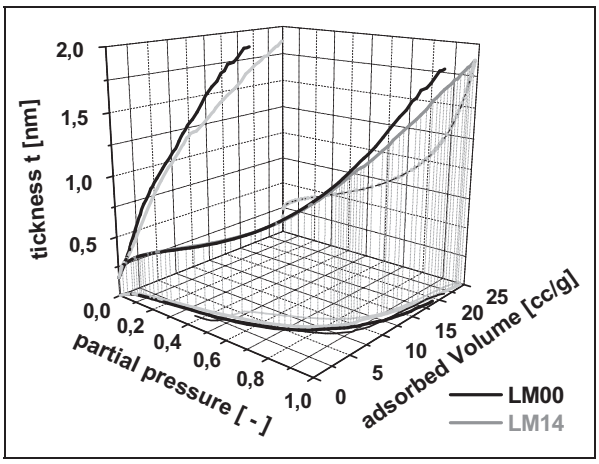

Fig.A5- 9: Influence of SRA1 on nitrogene sorption of mortar series LM

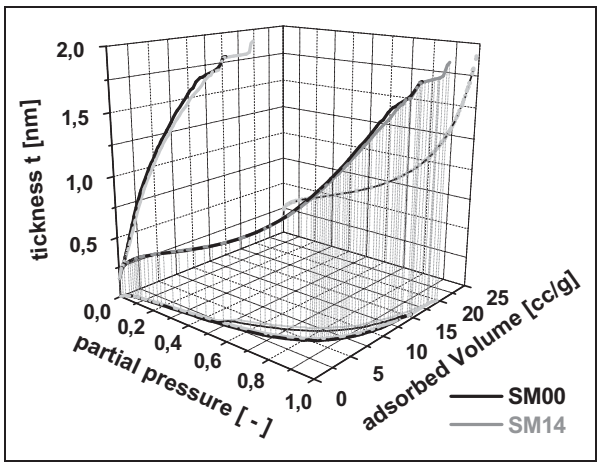

Fig.A5- 10: Influence of SRA1 on nitrogene sorption of mortar series SM

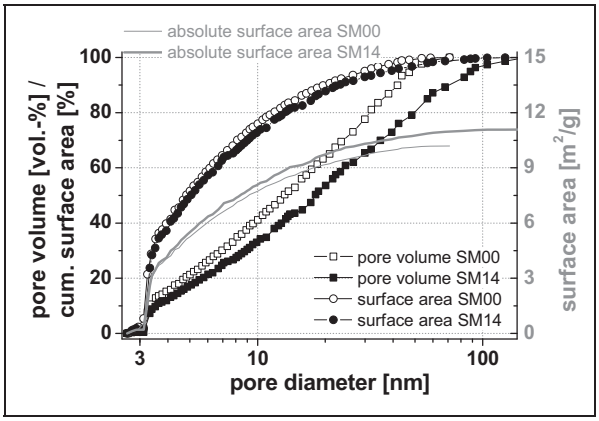

Fig.A5- 11: Influence of SRA1 on specific surface area of mortar series LM according Modelless-method (nitrogene desorption)

A6 - Leaching

A6.1 Tables

Tab.A6- 1: Rawdata leaching tests

mortar type	[-]	SM0	SM1	SM2	SM3	CM0	CM1	CM2	CM3	LM0	LM1	LM2	LM3
mass	[g]	1712	1768	1721	1786	1750	1729	1722	1704	1748	1722	1720	1786
volume	[m³]	7,5E-04	7,8E-04	7,5E-04	7,8E-04	7,5E-04	7,5E-04	7,4E-04	7,3E-04	7,6E-04	7,5E-04	7,5E-04	7,7E-04
area exposed	[m²]	0,1910	0,1910	0,1910	0,1910	0,1910	0,1910	0,1910	0,1910	0,1910	0,1910	0,1910	0,1910
$C_{SRA;t=O}$	[g/m³]	0	2515	5019	9994	0	3630	7257	14485	0	3637	7277	14597
C_{Carbon_SRA}	[g/m³]	0	1585	3162	6296	0	2287	4572	9126	0	2291	4585	9196
$C_{SP\_PCE;t=O}$	[g/m³]	0	0	0	0	12242	12234	12230	12206	4789	4785	4775	4766
$C_{Carbon\_SP\_PCE}$	[g/m³]	0	0	0	0	1653	1652	1651	1648	647	646	645	643
tot C_{Carbon}	[g/m³]	0	1585	3162	6296	1653	3938	6223	10774	647	2937	5229	9839

volume eluent		SM0	SM1	SM2	SM3	CM0	CM1	CM2	CM3	LM0	LM1	LM2	LM3
cycle 1	[l]	7,08	7,07	7,10	7,07	7,07	7,07	7,11	7,08	7,11	7,07	7,07	7,07
cycle 2		7,09	7,23	7,05	7,15	7,07	7,07	7,06	7,08	7,06	7,06	7,07	7,12
cycle 3		7,06	7,18	7,11	7,07	7,07	7,08	7,03	7,11	7,14	7,07	7,10	7,28
cycle 4		7,06	7,07	7,06	7,06	7,06	7,08	7,07	7,07	7,06	7,06	7,06	7,07
cycle 5		7,06	7,06	7,06	7,06	7,06	7,06	7,06	7,07	7,06	7,06	7,07	7,07
cycle 6		7,06	7,06	7,06	7,06	7,10	7,07	7,06	7,06	7,06	7,06	7,07	7,07
cycle 7		7,06	7,06	7,06	7,06	7,06	7,06	7,06	7,06	7,06	7,06	7,06	7,06
cycle 8		7,06	7,06	7,06	7,06	7,06	7,07	7,07	7,06	7,07	7,06	7,06	7,06

TOC eluat		SM0	SM1	SM2	SM3	CM0	CM1	CM2	CM3	LM0	LM1	LM2	LM3
cycle 1	[mg/l]	0	45	87	169	4	45	84	159	1	85	168	338
cycle 2		0	23	42	81	2	27	53	96	1	44	76	168
cycle 3		0	11	24	53	3	20	37	68	1	24	53	98
cycle 4		0	9	15	35	3	16	26	54	1	13	35	63
cycle 5		3	7	14	31	2	14	26	49	1	10	19	42
cycle 6		0	4	8	17	1	7	15	28	0	5	8	20
cycle 7		0	4	7	16	0	9	15	30	0	4	9	16
cycle 8		0	2	6	20	1	16	28	53	1	4	9	18

SP-PCE		SM0	SM1	SM2	SM3	CM0*	CM1**	CM2**	CM3**	LM0*	LM1**	LM2**	LM3**
cycle 1	[g/m³]	-	-	-	-	**278**	1319	2858	4878	**69**	2328	5031	7205
cycle 2		-	-	-	-	**139**	662	1412	2250	**69**	942	1726	3707
cycle 3		-	-	-	-	**208**	743	1102	2256	**69**	703	3723	2793
cycle 4		-	-	-	-	**208**	549	658	1558	**91**	270	0	1493
cycle 5		-	-	-	-	**139**	373	657	977	**91**	170	51	540
cycle 6		-	-	-	-	**70**	196	391	617	**14**	101	0	173
cycle 7		-	-	-	-	**30**	210	193	462	**29**	0	101	154
cycle 8		-	-	-	-	**69**	248	0	140	**69**	0	0	0
sum	[% ini]	-	-	-	-	**9**	35	59	108	**10**	94	223	337

* evaluated acc. TOC

** evaluated acc. gas chromatography & residual carbon content from TOC

SRA1 - TOC		SM0	SM1	SM2	SM3	CM0	CM1*	CM2*	CM3*	LM0	LM1*	LM2*	LM3*
cycle 1	[g/m³]	-	651	1298	2420	-	618	1216	2370	-	1254	2505	4886
cycle 2		-	340	623	1173	-	376	771	1438	-	642	1125	2439
cycle 3		-	154	351	759	-	256	504	999	-	343	783	1450
cycle 4		-	130	223	496	-	196	353	779	-	179	499	895
cycle 5		-	58	168	406	-	173	368	717	-	129	265	590
cycle 6		-	55	110	235	-	93	212	415	-	66	120	290
cycle 7		-	52	93	225	-	133	216	458	-	49	128	228
cycle 8		-	31	95	286	-	218	408	794	-	41	124	246
sum	[% ini]	-	58	59	60	-	57	56	55	-	74	76	76

* assuming SP-PCE is leached similar to the plain reference

SRA1 - Gas Chrom.		SM0	SM1	SM2	SM3	CM0	CM1	CM2	CM3	LM0	LM1	LM2	LM3
cycle 1	[g/m³]	-	-	-	-	-	395	665	1386	-	770	1442	3357
cycle 2		-	-	-	-	-	264	498	986	-	455	770	1660
cycle 3		-	-	-	-	-	143	313	562	-	208	- *	866
cycle 4		-	-	-	-	-	123	257	490	-	141	719*	594
cycle 5		-	-	-	-	-	123	257	539	-	113	274	493
cycle 6		-	-	-	-	-	66	143	298	-	47	132	256
cycle 7		-	-	-	-	-	95	181	365	-	56	113	201
cycle 8		-	-	-	-	-	180	428	779	-	75	179	310
sum	[% ini]	-	-	-	-	-	38	38	37	-	51	50	53

* eluat not tested in cycle 3

cycle length	[d]	[s]
cycle 1; ... ; cycle 7	28	2419200
cycle 8	56	4838400

total running time	[d]	[s]
	252	21772800

Tab.A6- 2: Efficient coefficient of diffusion for different time til equilibrium, mortar series, all series

mortar	Deff.{t}	assumed time to equilibrium [d]					
		1	2	4	7	21	28
SM1	[m²/s]	3,00E-10	1,50E-10	7,50E-11	5,00E-11	2,14E-11	1,07E-11
SM2		2,84E-10	1,42E-10	7,10E-11	4,73E-11	2,03E-11	1,01E-11
SM3		3,06E-10	1,53E-10	7,65E-11	5,10E-11	2,19E-11	1,09E-11
avg		**2,97E-10**	**1,48E-10**	**7,42E-11**	**4,94E-11**	**2,12E-11**	**1,06E-11**
sd		**1,13E-11**	**5,64E-12**	**2,82E-12**	**1,88E-12**	**8,06E-13**	**4,03E-13**
rel.sd	[-]	**4%**	**4%**	**4%**	**4%**	**4%**	**4%**
CM1	[m²/s]	2,78E-10	1,38E-10	6,92E-11	4,61E-11	1,98E-11	9,89E-12
CM2		2,74E-10	1,37E-10	6,87E-11	4,58E-11	1,96E-11	9,81E-12
CM3		2,69E-10	1,35E-10	6,73E-11	4,48E-11	1,92E-11	9,61E-12
avg		**2,74E-10**	**1,37E-10**	**6,84E-11**	**4,56E-11**	**1,95E-11**	**9,77E-12**
sd		**4,54E-12**	**2,00E-12**	**1,00E-12**	**6,66E-13**	**2,86E-13**	**1,43E-13**
rel.sd	[-]	**2%**	**1%**	**1%**	**1%**	**1%**	**1%**
LM1	[m²/s]	2,81E-10	1,41E-10	7,04E-11	4,69E-11	2,01E-11	1,01E-11
LM2		2,79E-10	1,40E-10	6,98E-11	4,65E-11	1,99E-11	9,97E-12
LM3		2,98E-10	1,49E-10	7,46E-11	4,97E-11	2,13E-11	1,07E-11
avg		**2,86E-10**	**1,43E-10**	**7,16E-11**	**4,77E-11**	**2,05E-11**	**1,02E-11**
sd		**1,05E-11**	**5,19E-12**	**2,59E-12**	**1,73E-12**	**7,41E-13**	**3,70E-13**
rel.sd	[-]	**4%**	**4%**	**4%**	**4%**	**4%**	**4%**
all series	**Deff.{t}**	**assumed time to equilibrium [d]**					
		1	**2**	**4**	**7**	**21**	**28**
avg	[m²/s]	**2,86E-10**	**1,43E-10**	**7,14E-11**	**4,76E-11**	**2,04E-11**	**1,02E-11**
sd		**1,29E-11**	**6,39E-12**	**3,19E-12**	**2,13E-12**	**9,12E-13**	**4,56E-13**
rel.sd	[-]	**5%**	**4%**	**4%**	**4%**	**4%**	**4%**

A6.2 Figures

Fig.A6- 1: leaching of superplasticizer SP-PCE

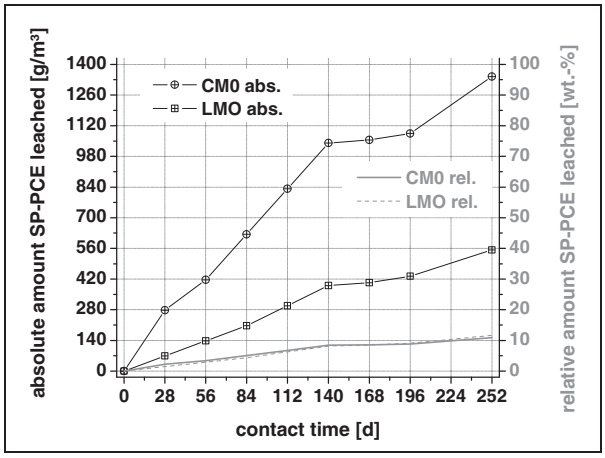

Fig.A6- 2: leaching of SRA1 from mortar type SM

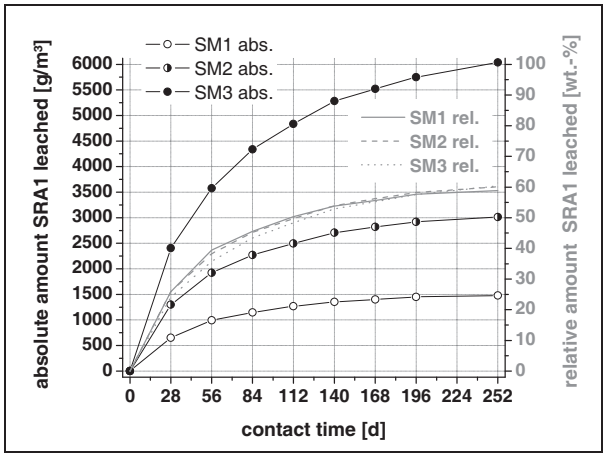

Fig.A6- 3: leaching of SRA1 from mortar type CM

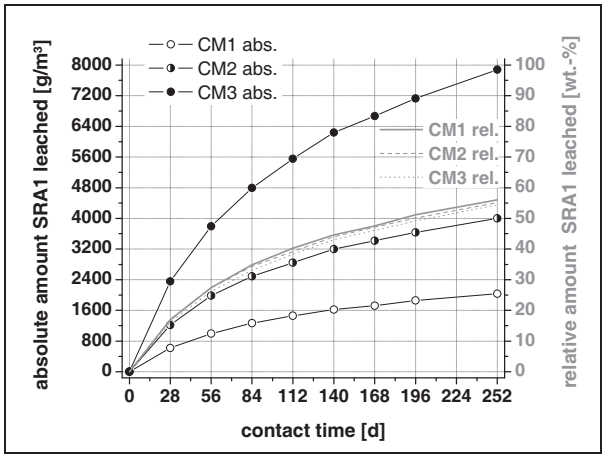

Fig.A6- 4: leaching of SRA1 from mortar type LM

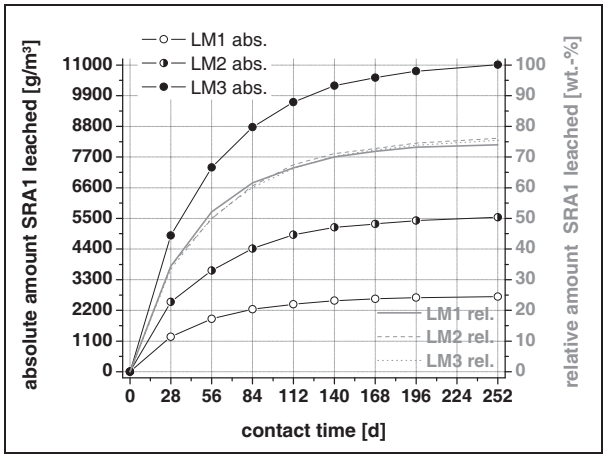

Fig.A6- 5: Estimation of mobile SRA fraction for mortar series CM

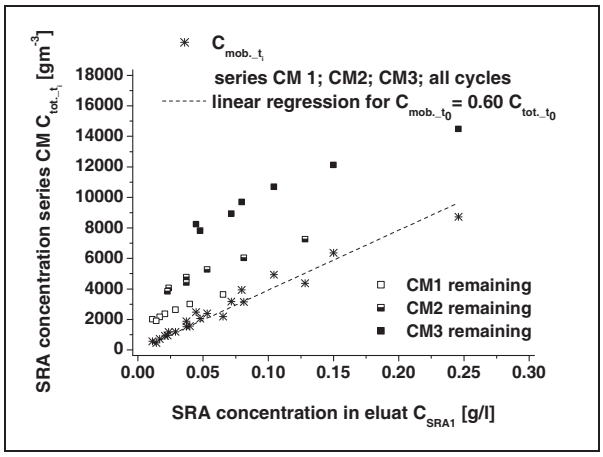

Fig.A6- 6: Estimation of mobile SRA fraction for mortar series SM

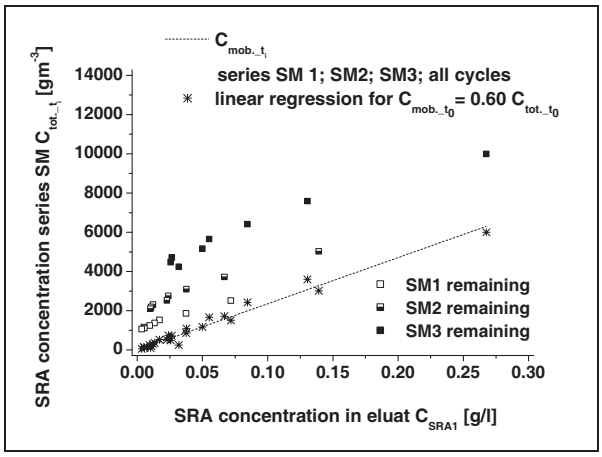

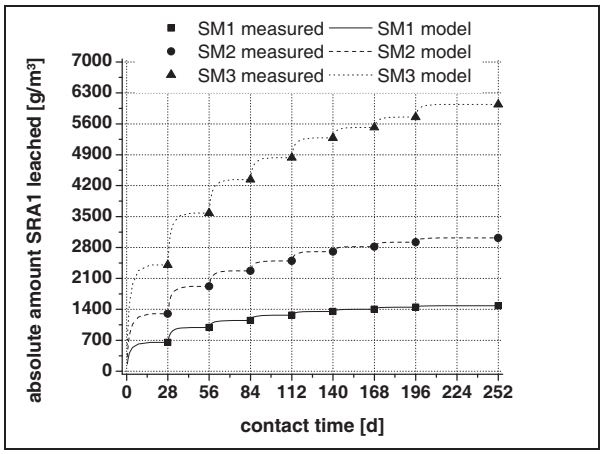

Fig.A6- 7: modeled leaching SM/tank test

Approximated diffusion coefficients for equibrium before 21d:

SM1: $D_{eq.\_28d}$ = 1.34 1E-11 m²/s

SM2: $D_{eq.\_28d}$ = 1.30 1E-11 m²/s

SM3: $D_{eq.\_28d}$ = 1.39 1E-11 m²/s

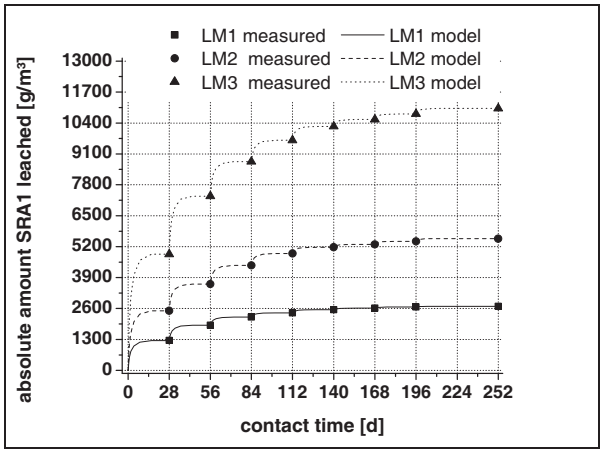

Fig.A6- 8: modeled leaching LM/tank test

Approximated diffusion coefficients:

LM1: $D_{eq.\_28d}$= 1.44 1E-11 m²/s

LM2: $D_{eq.\_28d}$= 1.45 1E-11 m²/s

LM3: $D_{eq.\_28d}$= 1.53 1E-11 m²/s

Fig.A6- 9: shrinkage of mortar series LM during cyclic leaching / drying and cyclic rewetting / drying

a) LM0 – cyclic leaching

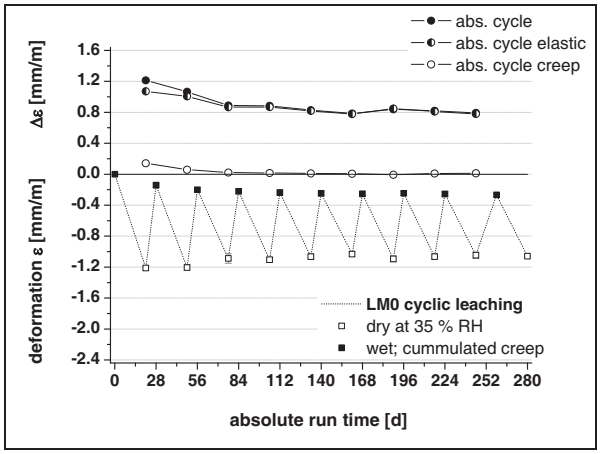

b) LM3 – cyclic leaching

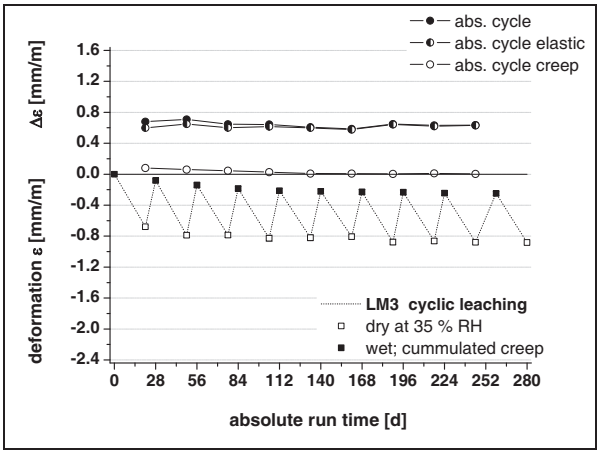

c) LM0 – inert resaturation

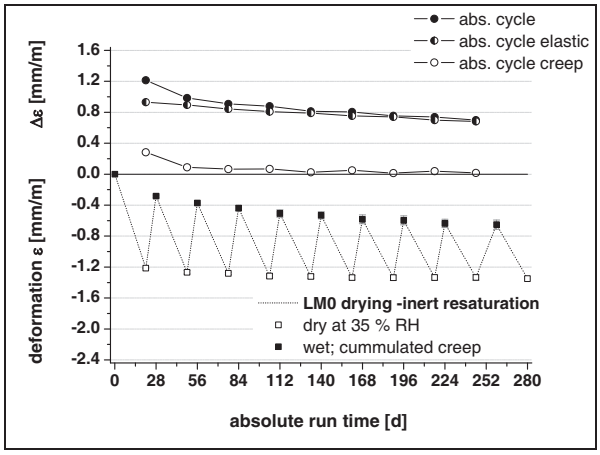

d) LM3 – inert resaturation

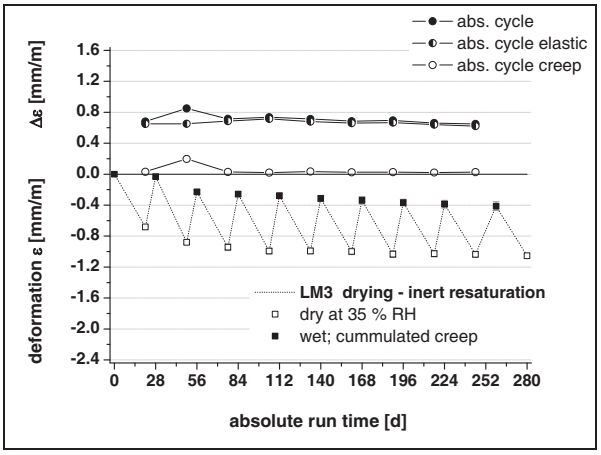

Fig.A6- 10: adsorption/desorption and cumulated creep in the cyclic regimes of mortars LM0 and LM3; cyclic drying and leaching on the left side, cyclic drying and rewetting on the right side

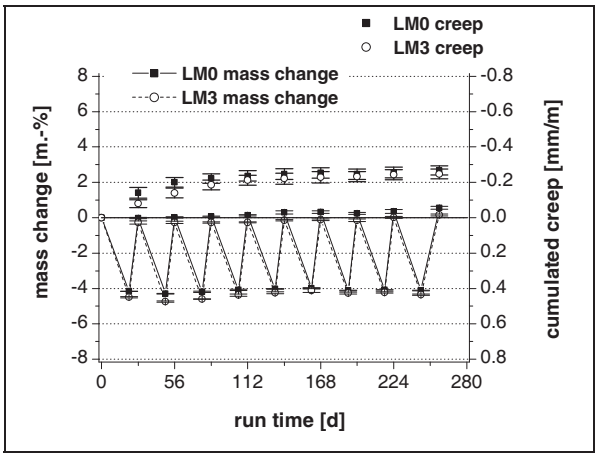

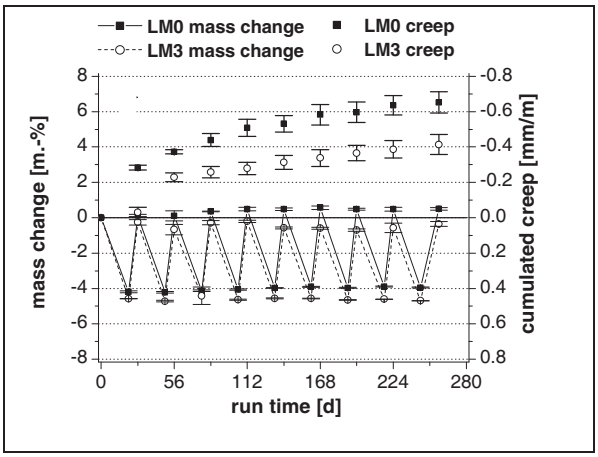

Fig.A6- 11: shrinkage of mortar series SM during cyclic leaching / drying and cyclic rewetting / drying

a) SM0 – cyclic leaching

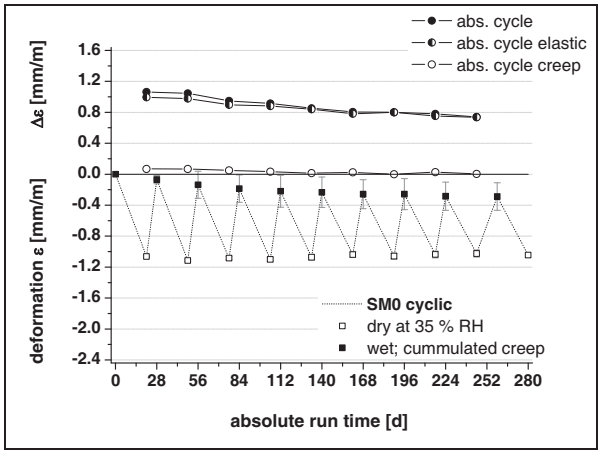

b) SM3 – cyclic leaching

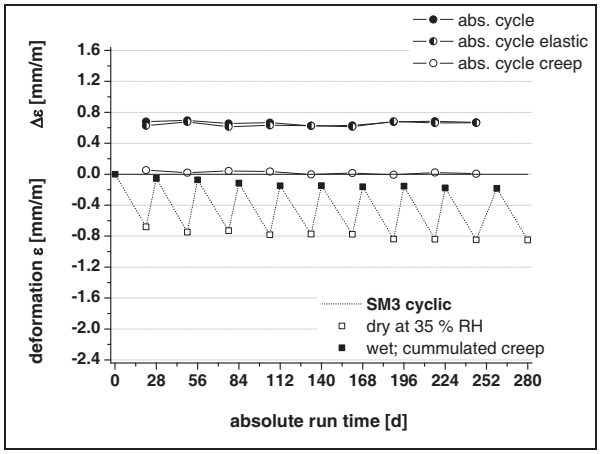

c) SM0 – inert resaturation

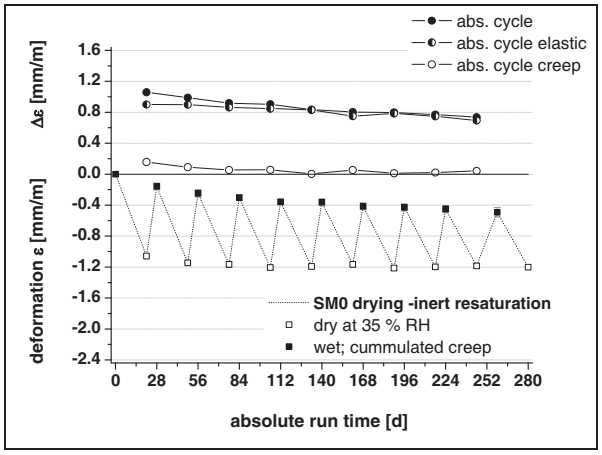

d) SM3 – inert resaturation

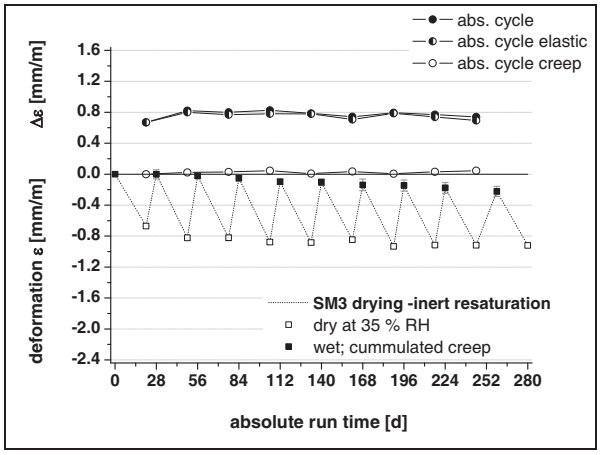

Fig.A6- 12: adsorption/desorption and cumulated creep in the cyclic regimes of mortars SM0 and SM3; cyclic drying and leaching on the left side, cyclic drying and rewetting on the right side

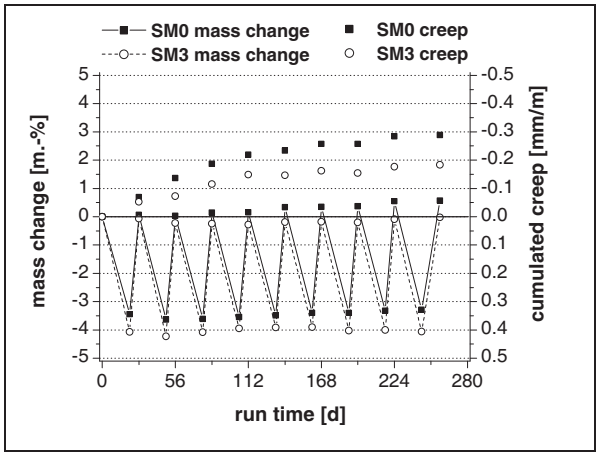

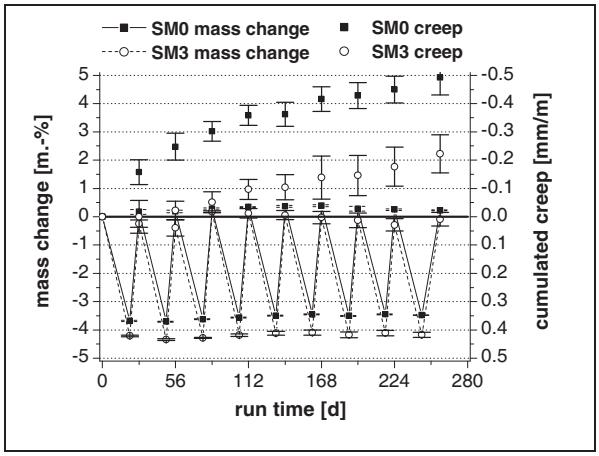

A7 - Drying and shrinkage of cement paste and mortar

A7.1 Tables

Tab.A7- 1: Elastic properties of mortars and pastes

mortar series *v=* 0.2		LM0	LM1	LM2	LM3	CM0	CM1	CM2	CM3	SM0	SM1	SM2	SM3
time [d]	**RH [%]**	modulus of elasticity ***E*** [GPa]				modulus of elasticity ***E*** [GPa]				modulus of elasticity ***E*** [GPa]			
7	90	28	26	26	26	30	28	29	32	26	25	25	26
28	90	32	30	30	31	35	34	35	36	29	29	29	30
91	35	32	32	33	34	37	-	38	39	29	-	-	33
91	70	31	30	30	30	38	35	38	37	32	31	31	33
91	90	32	32	33	-	-	-	37	39	31	-	-	-
time [d]	**RH [%]**	bulk modulus ***K*** *[GPa]*				bulk modulus ***K*** *[GPa]*				bulk modulus ***K*** *[GPa]*			
7	90	16	15	15	15	17	16	16	18	15	14	14	14
28	90	18	17	17	17	19	19	19	20	16	16	16	16
91	35	18	18	18	19	21	-	21	22	16	-	-	18
91	70	17	17	17	17	21	20	21	21	18	17	17	18
91	90	18	18	18	-	-	-	20	21	17	-	-	-

* sd{E_{LM}} = 0.75 GPa * sd{E_{CM}} = 0.91 GPa * sd{E_{SM}} = 0.51 GPa

paste series *v= 0.2*	cement paste CP	limestone composite paste LP
modulus of elasticity ***E*** [GPa]	20	16.8
bulk modulus ***K*** *[GPa]*	11	9.2

Tab.A7- 2: Reversible and irreversible shrinkage of mortar CM stored at different relative humidities (30% RH; 50% RH & 70% RH; climate chamber with nitrogen as protective gas)

30% RH	shrinkage	reduction	irreversible fraction		reversible fraction		mass (resat.)
	[mm/m]	[%]	[mm/m]	[%]	abs [mm/m]	[red.-%]	[% of ini. wt.]
CM0	-1.406	0%	-0.790	**56%**	-0.617	**0%**	99.89%
0.5% SRA1	-0.833	41%	-0.273	33%	-0.560	9%	99.92%
1.0% SRA1	-0.755	46%	-0.174	23%	-0.582	6%	99.70%
2.0% SRA1	-0.680	52%	-0.176	26%	-0.504	18%	99.73%
2.0% SRA2	-0.680	52%	-0.255	37%	-0.425	31%	99.94%
2.0% SRA3	-0.760	46%	-0.350	46%	-0.410	33%	99.91%
2.0% SRA6	-0.667	53%	-0.171	26%	-0.496	19%	99.86%
			average SRA	**32%**			

50% RH	shrinkage	reduction	irreversible fraction		reversible fraction		mass (resat.)
	[mm/m]	[%]	[mm/m]	[%]	abs [mm/m]	[red.-%]	[% of ini. wt.]
CM0	-0.933	0%	-0.399	**43%**	-0.534	**0%**	100.07%
0.5% SRA1	-0.849	9%	-0.394	46%	-0.455	15%	100.14%
1.0% SRA1	-0.706	24%	-0.278	39%	-0.428	20%	100.03%
2.0% SRA1	-0.586	37%	-0.243	42%	-0.342	36%	99.92%
2.0% SRA2	-0.730	22%	-0.361	49%	-0.369	31%	100.15%
2.0% SRA3	-0.505	46%	-0.176	35%	-0.329	38%	100.18%
2.0% SRA6	-0.589	37%	-0.271	46%	-0.318	41%	100.16%
			average SRA	**43%**			

70% RH	shrinkage	reduction	irreversible fraction		reversible fraction		mass (resat.)
	[mm/m]	[%]	[mm/m]	[%]	abs [mm/m]	[red.-%]	[% of ini. wt.]
CM0	-0.746	0%	-0.472	**63%**	-0.274	**0%**	99.84%
0.5% SRA1	-0.685	8%	-0.440	64%	-0.246	10%	99.86%
1.0% SRA1	-0.618	17%	-0.377	61%	-0.241	12%	99.75%
2.0% SRA1	-0.536	28%	-0.360	67%	-0.176	36%	99.77%
2.0% SRA2	-0.585	22%	-0.362	62%	-0.223	19%	99.86%
2.0% SRA3	-0.455	39%	-0.311	68%	-0.144	47%	99.87%
2.0% SRA6	-0.553	26%	-0.311	56%	-0.241	12%	99.85%
			average SRA	**63%**			

Tab.A7- 3: Reversible and irreversible shrinkage of mortar CM stored at different relative humidities and carbonation (climate chamber without protective gas)

65% RH	shrinkage	reduction	irreversible fraction		reversible fraction		mass (resat.)
	[mm/m]	[%]	[mm/m]	[%]	abs [mm/m]	[red.-%]	[% of ini. wt.]
CM0	-1.252	0%	-0.979	**78%**	-0.273	**0%**	99.87%
0.5% SRA1	-0.638	49%	-0.384	60%	-0.254	7%	100.09%
1.0% SRA1	-0.672	46%	-0.453	67%	-0.219	20%	100.22%
2.0% SRA1	-0.541	57%	-0.366	68%	-0.175	36%	100.17%
2.0% SRA2	-0.783	37%	-0.574	73%	-0.209	23%	100.36%
2.0% SRA3	-0.435	65%	-0.229	53%	-0.206	25%	100.26%
2.0% SRA6	-0.574	54%	-0.357	62%	-0.217	21%	100.37%
			average SRA	**64%**			

80% RH	shrinkage	reduction	irreversible fraction		reversible fraction		mass (resat.)
	[mm/m]	[%]	[mm/m]	[%]	abs [mm/m]	[red.-%]	[% of ini. wt.]
CM0	-0.518	0%	-0.353	**68%**	-0.165	**0%**	100.08%
0.5% SRA1	-0.426	18%	-0.251	59%	-0.175	-6%	100.18%
1.0% SRA1	-0.468	10%	-0.249	53%	-0.219	-33%	100.00%
2.0% SRA1	-0.476	8%	-0.307	65%	-0.169	-2%	100.24%
2.0% SRA2	-0.403	22%	-0.264	65%	-0.140	16%	100.41%
2.0% SRA3	-0.416	20%	-0.277	67%	-0.139	16%	100.17%
2.0% SRA6	-0.460	11%	-0.304	66%	-0.156	6%	100.18%
			average SRA	**62%**			

Tab.A7- 4: Reversible and irreversible shrinkage of mortar CM stored with change of relative humidity after 44 days (climate chamber with nitrogen as protective gas)

a) 44 days at 40% RH, then 20% RH up to 64 days

40% RH	shrinkage	reduction
	[mm/m]	[%]
CM0	-1.012	0%
0.5% SRA1	-0.818	19%
1.0% SRA1	-0.768	24%
2.0% SRA1	-0.664	34%
2.0% SRA2	-0.686	32%
2.0% SRA3	-0.547	46%
2.0% SRA6	-0.582	43%

20% RH	shrinkage	reduction	irreversible fraction		reversible fraction	
	[mm/m]	[%]	[mm/m]	[%]	abs [mm/m]	[red.-%]
CM0	-1.689	0%	-0.445	**26%**	-1.244	**0%**
0.5% SRA1	-1.015	40%	-0.227	22%	-0.788	37%
1.0% SRA1	-0.997	41%	-0.243	24%	-0.753	39%
2.0% SRA1	-0.871	48%	-0.218	25%	-0.653	48%
2.0% SRA2	-0.932	45%	-0.239	26%	-0.693	44%
2.0% SRA3	-0.768	55%	-0.129	17%	-0.638	49%
2.0% SRA6	-0.814	52%	-0.140	17%	-0.675	46%
			average SRA	**22%**		

a) 44 days at 87% RH, then 50% RH up to 64 days

87% RH	shrinkage	reduction
	[mm/m]	[%]
CM0	-0.429	0%
0.5% SRA1	-0.283	34%
1.0% SRA1	-0.290	32%
2.0% SRA1	-0.241	44%
2.0% SRA2	-0.328	24%
2.0% SRA3	-0.207	52%
2.0% SRA6	-0.219	49%

50% RH*	shrinkage	reduction	irreversible fraction		reversible fraction	
	[mm/m]	[%]	[mm/m]	[%]	abs [mm/m]	[red.-%]
CM0	-0.986	0%	-0.429	**44%**	-0.557	**0%**
0.5% SRA1	-0.735	25%	-0.260	35%	-0.475	15%
1.0% SRA1	-0.702	29%	-0.297	42%	-0.404	27%
2.0% SRA1	-0.574	42%	-0.253	44%	-0.322	42%
2.0% SRA2	-0.553	44%	-0.259	47%	-0.294	47%
2.0% SRA3	-0.467	53%	-0.146	31%	-0.322	42%
2.0% SRA6	-0.532	46%	-0.219	41%	-0.313	44%
			average SRA	**40%**		

A7.2 Figures

Fig.A7- 1: Desorption isotherms of cement paste with SRA1

a) Cement paste

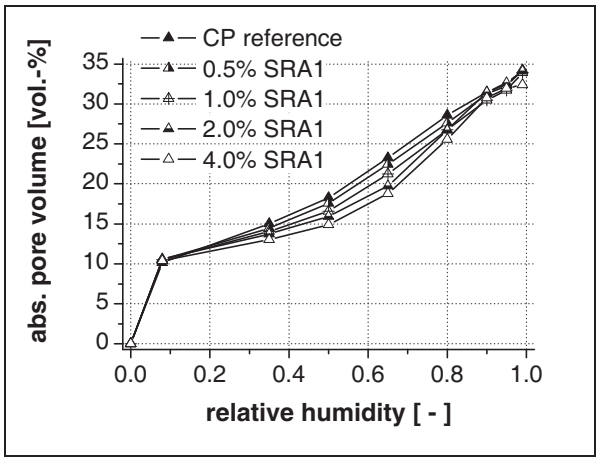

b) Limestone composite binder

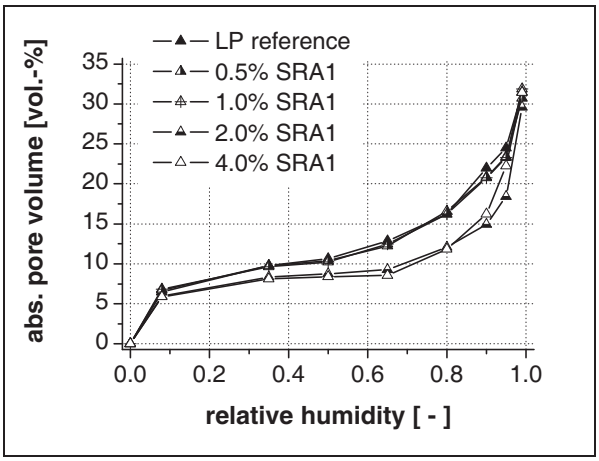

Fig.A7- 2: Desorption isotherms of cement paste with SRA2

a) absolute saturation

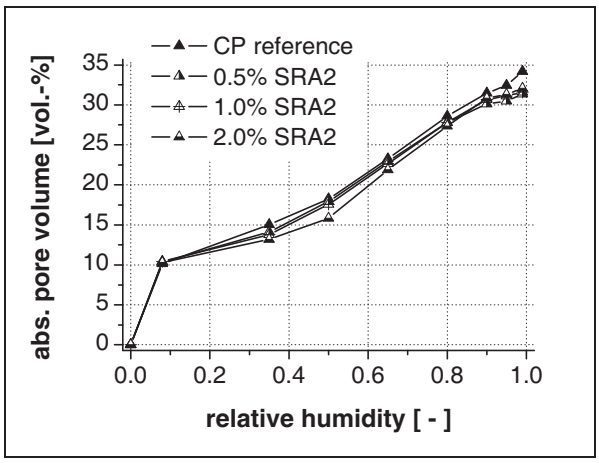

b) degree of saturation

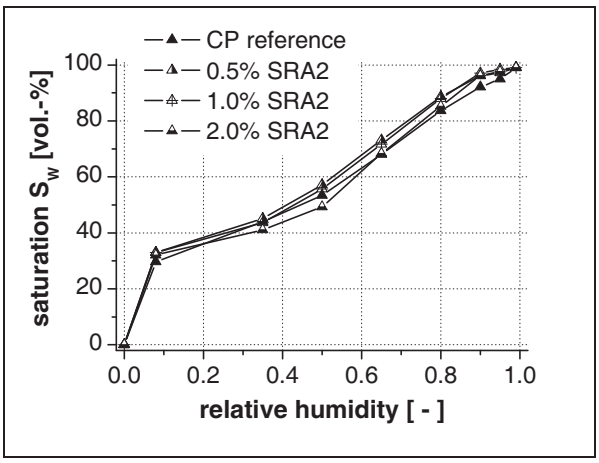

Fig.A7- 3: Desorption isotherms of cement paste with SRA3

a) absolute saturation

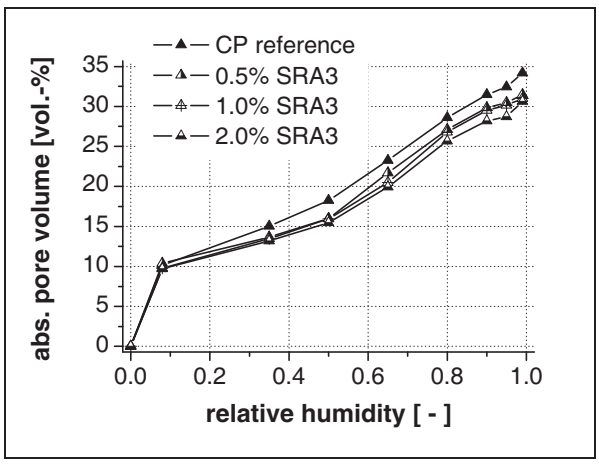

b) degree of saturation

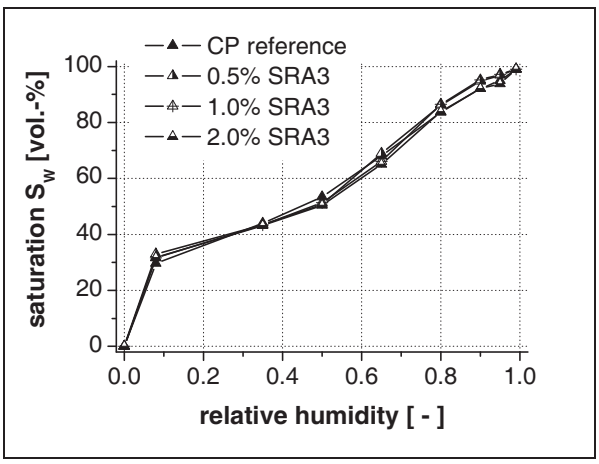

Fig.A7- 4: Desorption isotherms of cement paste with SRA5

a) absolute saturation

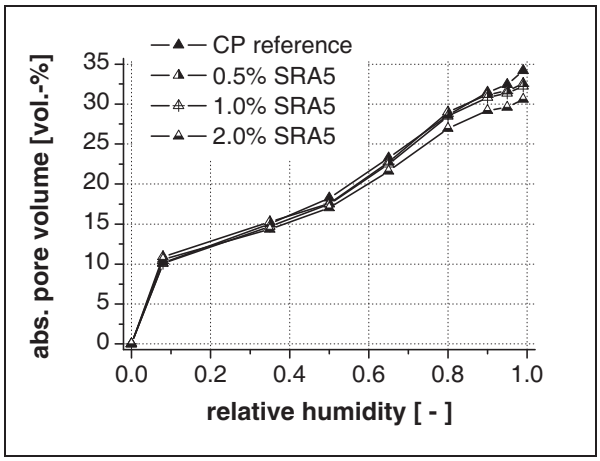

b) degree of saturation

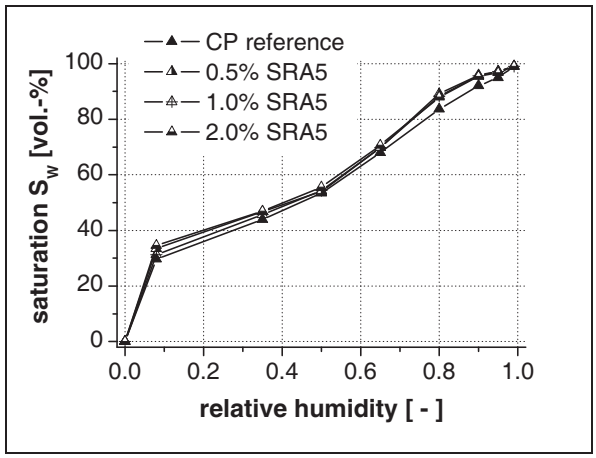

Fig.A7- 5: Desorption isotherms of cement mortar with SRA1

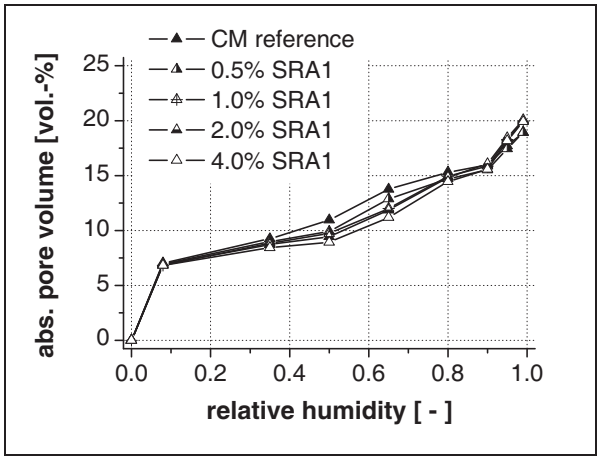

Fig.A7- 6: Desorption isotherms of mortar with limestone composite binder and SRA1

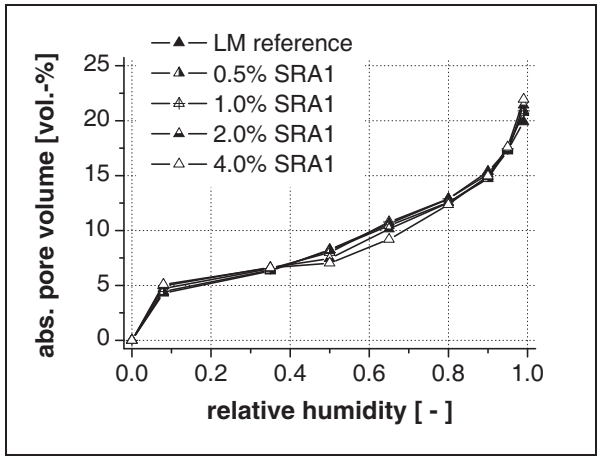

Fig.A7- 7: Desorption isotherms of standard mortar with SRA1

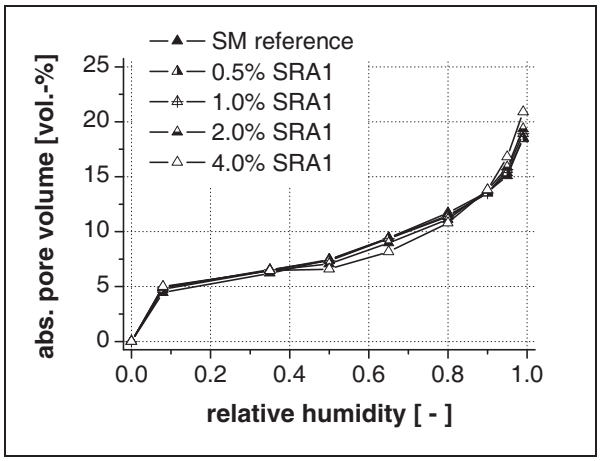

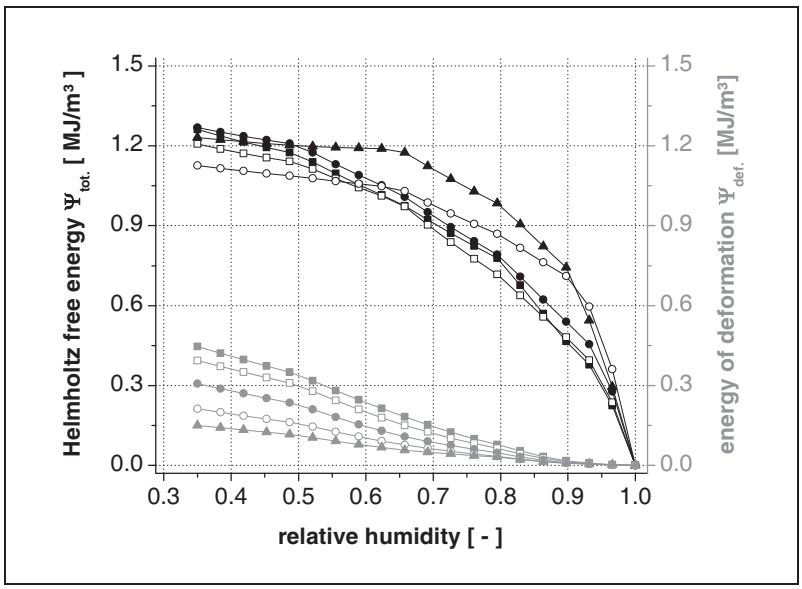

Fig.A7- 8: Energy balance for limestone composite paste containing SRA1

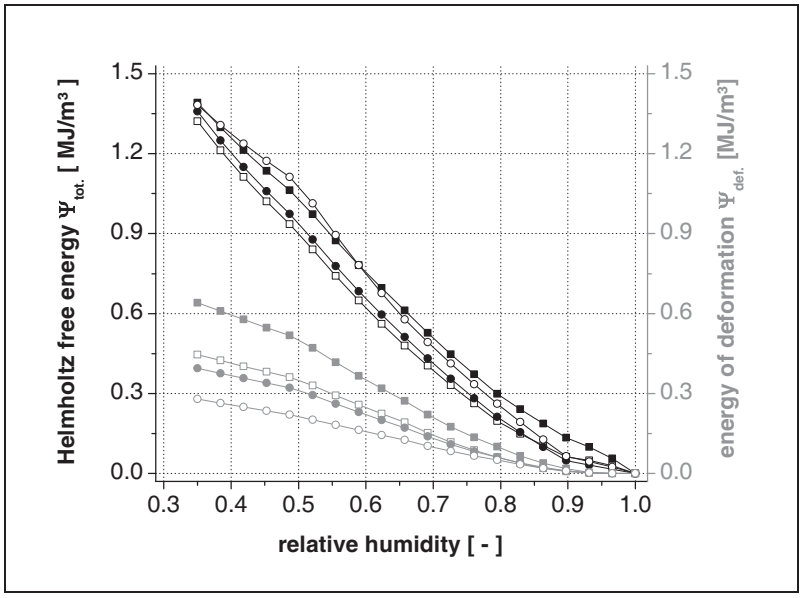

Fig.A7- 9: Energy balance for cement paste containing SRA2

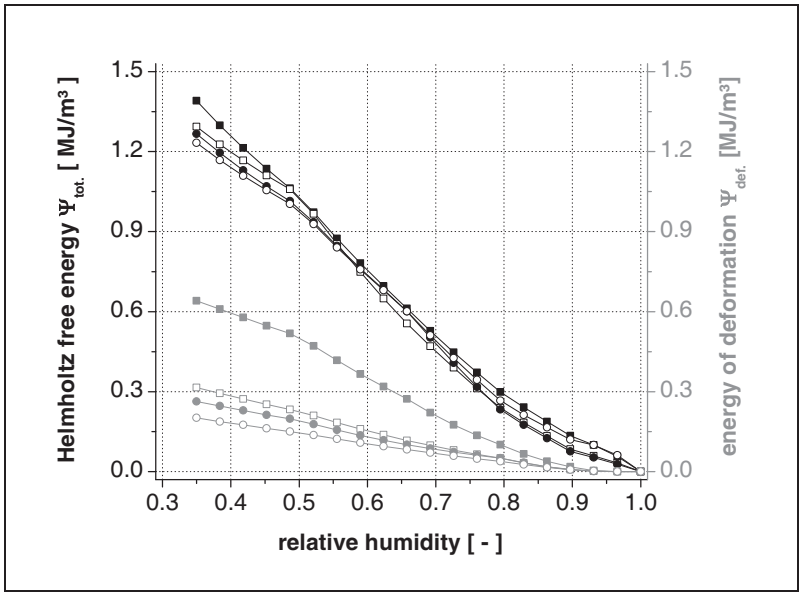

Fig.A7- 10: Energy balance for cement paste containing SRA3

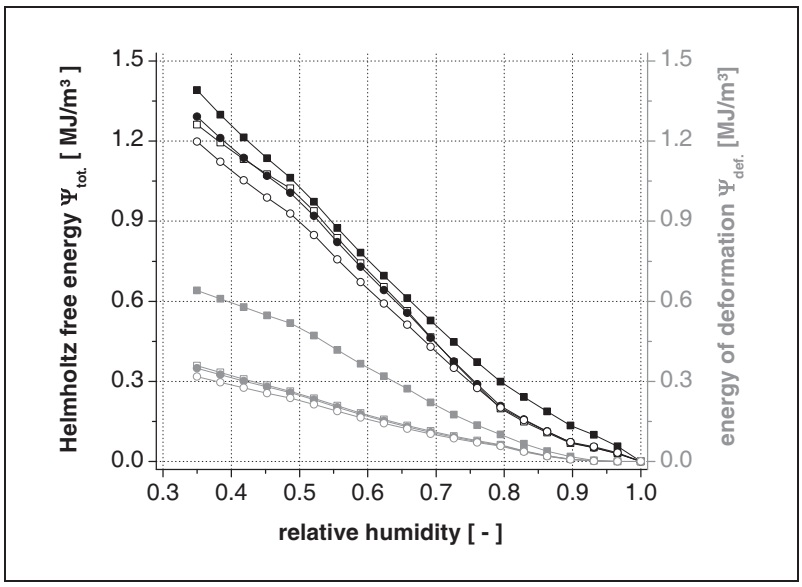

Fig.A7- 11: Energy balance for cement paste containing SRA5

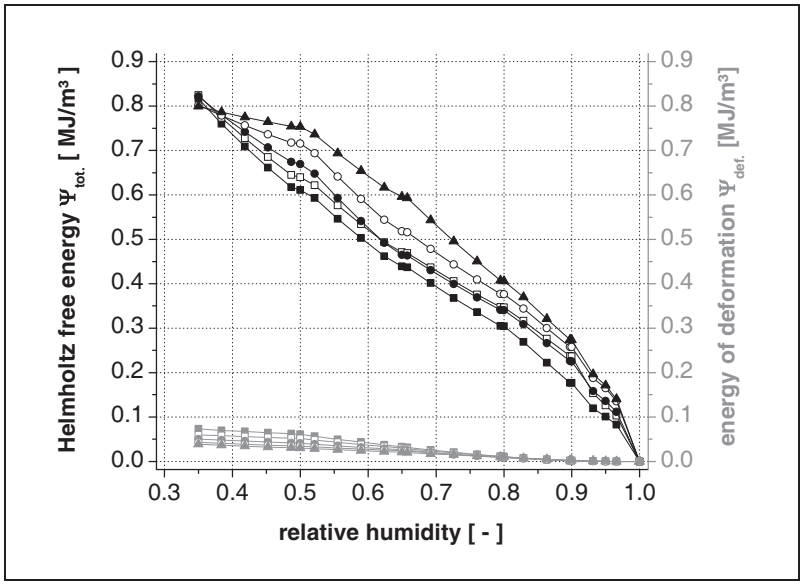

Fig.A7- 12: Energy balance for mortar type LM with SRA1

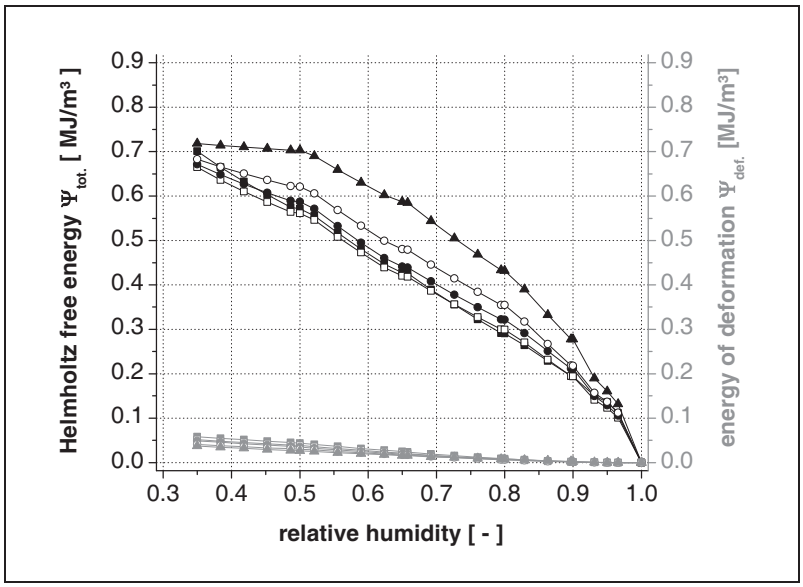

Fig.A7- 13: Energy balance for mortar type SM with SRA1

Fig.A7- 14: Interfacial area exposed to the liquid/vapour interface and evolution of surface tension in pore fluid of paste LP

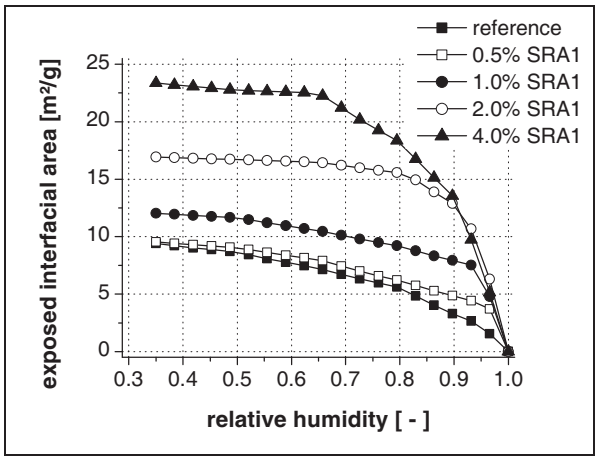

a) interfacial area exposed in the course of drying

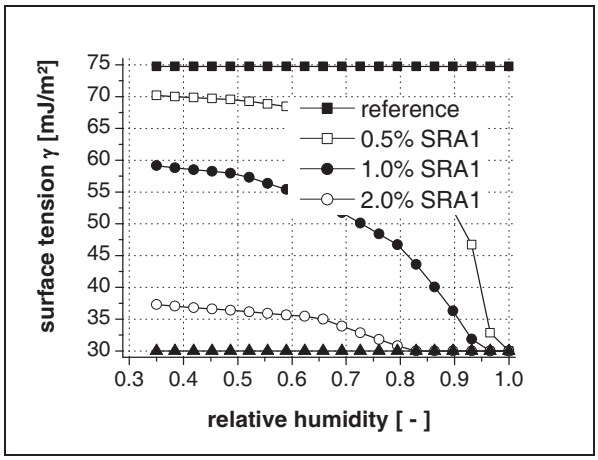

b) evolution of surface tension

Fig.A7- 15: Interfacial area exposed to the liquid/vapour interface and evolution of surface tension in pore fluid of paste CP

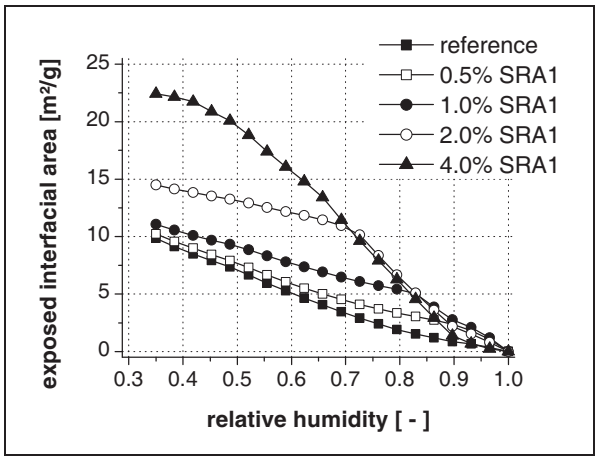

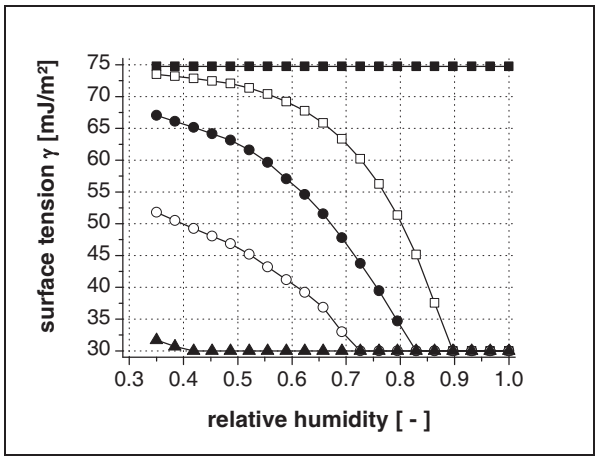

ISBN 978-3-8440-0027-6